Western University
Scholarship@Western

Digitized Theses | Digitized Special Collections

1996

Simulation And Modelling Of Thin Film Phi(rho-z) Curves For Electron Probe Microanalysis

Ka Shing Chan

Follow this and additional works at: https://ir.lib.uwo.ca/digitizedtheses

Recommended Citation

Chan, Ka Shing, "Simulation And Modelling Of Thin Film Phi(rho-z) Curves For Electron Probe Microanalysis" (1996). *Digitized Theses*. 2609.
https://ir.lib.uwo.ca/digitizedtheses/2609

This Dissertation is brought to you for free and open access by the Digitized Special Collections at Scholarship@Western. It has been accepted for inclusion in Digitized Theses by an authorized administrator of Scholarship@Western. For more information, please contact tadam@uwo.ca, wlswadmin@uwo.ca.

National Library of Canada

Bibliothèque nationale du Canada

Acquisitions and Bibliographic Services Branch

Direction des acquisitions et des services bibliographiques

395 Wellington Street
Ottawa, Ontario
K1A 0N4

395, rue Wellington
Ottawa (Ontario)
K1A 0N4

Your file Votre référence

Our file Notre référence

NOTICE

The quality of this microform is heavily dependent upon the quality of the original thesis submitted for microfilming. Every effort has been made to ensure the highest quality of reproduction possible.

If pages are missing, contact the university which granted the degree.

Some pages may have indistinct print especially if the original pages were typed with a poor typewriter ribbon or if the university sent us an inferior photocopy.

Reproduction in full or in part of this microform is governed by the Canadian Copyright Act, R.S.C. 1970, c. C-30, and subsequent amendments.

AVIS

La qualité de cette microforme dépend grandement de la qualité de la thèse soumise au microfilmage. Nous avons tout fait pour assurer une qualité supérieure de reproduction.

S'il manque des pages, veuillez communiquer avec l'université qui a conféré le grade.

La qualité d'impression de certaines pages peut laisser à désirer, surtout si les pages originales ont été dactylographiées à l'aide d'un ruban usé ou si l'université nous a fait parvenir une photocopie de qualité inférieure.

La reproduction, même partielle, de cette microforme est soumise à la Loi canadienne sur le droit d'auteur, SRC 1970, c. C-30, et ses amendements subséquents.

Canada

SIMULATION AND MODELLING OF THIN FILM $\phi(\rho z)$ CURVES FOR ELECTRON PROBE MICROANALYSIS

by

Albert K.S. Chan

Faculty of Engineering Science

Department of Materials Engineering

Submitted in partial fulfilment
of the requirements for the degree of
Doctor of Philosophy

Faculty of Graduate Studies
The University of Western Ontario
London, Ontario, Canada
February, 1996

© Albert K.S. Chan 1996

National Library of Canada

Bibliothèque nationale du Canada

Acquisitions and Bibliographic Services Branch

Direction des acquisitions et des services bibliographiques

395 Wellington Street
Ottawa, Ontario
K1A 0N4

395, rue Wellington
Ottawa (Ontario)
K1A 0N4

Your file Votre référence

Our file Notre référence

The author has granted an irrevocable non-exclusive licence allowing the National Library of Canada to reproduce, loan, distribute or sell copies of his/her thesis by any means and in any form or format, making this thesis available to interested persons.

L'auteur a accordé une licence irrévocable et non exclusive permettant à la Bibliothèque nationale du Canada de reproduire, prêter, distribuer ou vendre des copies de sa thèse de quelque manière et sous quelque forme que ce soit pour mettre des exemplaires de cette thèse à la disposition des personnes intéressées.

The author retains ownership of the copyright in his/her thesis. Neither the thesis nor substantial extracts from it may be printed or otherwise reproduced without his/her permission.

L'auteur conserve la propriété du droit d'auteur qui protège sa thèse. Ni la thèse ni des extraits substantiels de celle-ci ne doivent être imprimés ou autrement reproduits sans son autorisation.

ISBN 0-612-09854-0

Canada

Name CHAN KA SHING ALBERT

Dissertation Abstracts International is arranged by broad, general subject categories. Please select the one subject which most nearly describes the content of your dissertation. Enter the corresponding four-digit code in the spaces provided.

MATERIALS SCIENCE — SUBJECT TERM

0794 — SUBJECT CODE

U·M·I

Subject Categories

THE HUMANITIES AND SOCIAL SCIENCES

COMMUNICATIONS AND THE ARTS

Architecture 0729
Art History 0377
Cinema 0900
Dance 0378
Fine Arts 0357
Information Science 0723
Journalism 0391
Library Science 0399
Mass Communications 0708
Music 0413
Speech Communication 0459
Theater 0465

EDUCATION

General 0515
Administration 0514
Adult and Continuing 0516
Agricultural 0517
Art 0273
Bilingual and Multicultural 0282
Business 0688
Community College 0275
Curriculum and Instruction 0727
Early Childhood 0518
Elementary 0524
Finance 0277
Guidance and Counseling 0519
Health 0680
Higher 0745
History of 0520
Home Economics 0278
Industrial 0521
Language and Literature 0279
Mathematics 0280
Music 0522
Philosophy of 0998
Physical 0523
Psychology 0525
Reading 0535
Religious 0527
Sciences 0714
Secondary 0533
Social Sciences 0534
Sociology of 0340
Special 0529
Teacher Training 0530
Technology 0710
Tests and Measurements 0288
Vocational 0747

LANGUAGE, LITERATURE AND LINGUISTICS

Language
- General 0679
- Ancient 0289
- Linguistics 0290
- Modern 0291

Literature
- General 0401
- Classical 0294
- Comparative 0295
- Medieval 0297
- Modern 0298
- African 0316
- American 0591
- Asian 0305
- Canadian (English) 0352
- Canadian (French) 0355
- English 0593
- Germanic 0311
- Latin American 0312
- Middle Eastern 0315
- Romance 0313
- Slavic and East European 0314

PHILOSOPHY, RELIGION AND THEOLOGY

Philosophy 0422
Religion
- General 0318
- Biblical Studies 0321
- Clergy 0319
- History of 0320
- Philosophy of 0322

Theology 0469

SOCIAL SCIENCES

American Studies 0323
Anthropology
- Archaeology 0324
- Cultural 0326
- Physical 0327

Business Administration
- General 0310
- Accounting 0272
- Banking 0770
- Management 0454
- Marketing 0338

Canadian Studies 0385
Economics
- General 0501
- Agricultural 0503
- Commerce-Business 0505
- Finance 0508
- History 0509
- Labor 0510
- Theory 0511

Folklore 0358
Geography 0366
Gerontology 0351
History
- General 0578
- Ancient 0579
- Medieval 0581
- Modern 0582
- Black 0328
- African 0331
- Asia, Australia and Oceania 0332
- Canadian 0334
- European 0335
- Latin American 0336
- Middle Eastern 0333
- United States 0337

History of Science 0585
Law 0398
Political Science
- General 0615
- International Law and Relations 0616
- Public Administration 0617

Recreation 0814
Social Work 0452
Sociology
- General 0626
- Criminology and Penology 0627
- Demography 0938
- Ethnic and Racial Studies 0631
- Individual and Family Studies 0628
- Industrial and Labor Relations 0629
- Public and Social Welfare 0630
- Social Structure and Development 0700
- Theory and Methods 0344

Transportation 0709
Urban and Regional Planning 0999
Women's Studies 0453

THE SCIENCES AND ENGINEERING

BIOLOGICAL SCIENCES

Agriculture
- General 0473
- Agronomy 0285
- Animal Culture and Nutrition 0475
- Animal Pathology 0476
- Food Science and Technology 0359
- Forestry and Wildlife 0478
- Plant Culture 0479
- Plant Pathology 0480
- Plant Physiology 0817
- Range Management 0777
- Wood Technology 0746

Biology
- General 0306
- Anatomy 0287
- Biostatistics 0308
- Botany 0309
- Cell 0379
- Ecology 0329
- Entomology 0353
- Genetics 0369
- Limnology 0793
- Microbiology 0410
- Molecular 0307
- Neuroscience 0317
- Oceanography 0416
- Physiology 0433
- Radiation 0821
- Veterinary Science 0778
- Zoology 0472

Biophysics
- General 0786
- Medical 0760

EARTH SCIENCES

Biogeochemistry 0425
Geochemistry 0996
Geodesy 0370
Geology 0372
Geophysics 0373
Hydrology 0388
Mineralogy 0411
Paleobotany 0345
Paleoecology 0426
Paleontology 0418
Paleozoology 0985
Palynology 0427
Physical Geography 0368
Physical Oceanography 0415

HEALTH AND ENVIRONMENTAL SCIENCES

Environmental Sciences 0768
Health Sciences
- General 0566
- Audiology 0300
- Chemotherapy 0992
- Dentistry 0567
- Education 0350
- Hospital Management 0769
- Human Development 0758
- Immunology 0982
- Medicine and Surgery 0564
- Mental Health 0347
- Nursing 0569
- Nutrition 0570
- Obstetrics and Gynecology 0380
- Occupational Health and Therapy 0354
- Ophthalmology 0381
- Pathology 0571
- Pharmacology 0419
- Pharmacy 0572
- Physical Therapy 0382
- Public Health 0573
- Radiology 0574
- Recreation 0575
- Speech Pathology 0460
- Toxicology 0383

Home Economics 0386

PHYSICAL SCIENCES

Pure Sciences

Chemistry
- General 0485
- Agricultural 0749
- Analytical 0486
- Biochemistry 0487
- Inorganic 0488
- Nuclear 0738
- Organic 0490
- Pharmaceutical 0491
- Physical 0494
- Polymer 0495
- Radiation 0754

Mathematics 0405
Physics
- General 0605
- Acoustics 0986
- Astronomy and Astrophysics 0606
- Atmospheric Science 0608
- Atomic 0748
- Electronics and Electricity 0607
- Elementary Particles and High Energy 0798
- Fluid and Plasma 0759
- Molecular 0609
- Nuclear 0610
- Optics 0752
- Radiation 0756
- Solid State 0611

Statistics 0463

Applied Sciences

Applied Mechanics 0346
Computer Science 0984

Engineering
- General 0537
- Aerospace 0538
- Agricultural 0539
- Automotive 0540
- Biomedical 0541
- Chemical 0542
- Civil 0543
- Electronics and Electrical 0544
- Heat and Thermodynamics 0348
- Hydraulic 0545
- Industrial 0546
- Marine 0547
- Materials Science 0794
- Mechanical 0548
- Metallurgy 0743
- Mining 0551
- Nuclear 0552
- Packaging 0549
- Petroleum 0765
- Sanitary and Municipal 0554
- System Science 0790

Geotechnology 0428
Operations Research 0796
Plastics Technology 0795
Textile Technology 0994

PSYCHOLOGY

General 0621
Behavioral 0384
Clinical 0622
Developmental 0620
Experimental 0623
Industrial 0624
Personality 0625
Physiological 0989
Psychobiology 0349
Psychometrics 0632
Social 0451

ABSTRACT

Quantitative analysis of homogeneous bulk unknowns using an electron probe microanalyzer requires the accurate knowledge of the depth distributions of x-ray production($\phi(\rho z)$ curves). Straight line behaviour is observed in the plot of $\ln\phi(\rho z)$ versus $(\rho z)^2$ for most experimentally measured data. Monte Carlo calculations can be used to simulate $\phi(\rho z)$ curves. However, $\ln \phi(\rho z)$ versus $(\rho z)^2$ plots of these $\phi(\rho z)$ curves, in general, are nonlinear and concave downward. By introducing the concept of electron straggling into a multiple scattering Monte Carlo model, agreement with the behaviour of experimental curves is achieved.

Electron probe microanalysis can also be used for the characterization of thin films on substrates. The multiple scattering Monte Carlo program was used to simulate more than 300 thin film $\phi(\rho z)$ curves with different film/substrate combinations. The simulations were made at normal electron incidence in the energy range from 10-30 keV. Using these data and based on the concept of the ratio of $\phi(\rho z)$ values from the thin film to the corresponding bulk $\phi(\rho z)$ value at the same thickness, general equations were developed which allow prediction of thin film $\phi(\rho z)$ curves for any film/substrate combination at any electron energy. The equations can be used with any bulk $\phi(\rho z)$ model. Comparisons were made with literature values of measured k-ratios in order to confirm the validity of the present model.

ACKNOWLEDGEMENTS

The author wishes to express his deepest thanks to Professor J.D. Brown for his suggestions, time and patience. The laboratory help provided by B. Verhagen is also appreciated.

The author would also like to thank his wife Carmen and his other family members for the support they have offered through the years, which has allowed him to pursue his interest in science, often at the expense of family obligations.

TABLE OF CONTENTS

Page

CERTIFICATE OF EXAMINATION ii

ABSTRACT iii

ACKNOWLEDGEMENTS iv

TABLE OF CONTENTS v

LIST OF APPENDICES vii

LIST OF TABLES viii

LIST OF FIGURES ix

NOMENCLATURE xxiv

CHAPTER 1 - INTRODUCTION 1
- 1.1 Background 1
- 1.2 Objectives and Methods of Attack 2

CHAPTER 2 - X-RAY PHYSICS AND INSTRUMENTATION 4
- 2.1 Theory 4
- 2.2 Production of X-rays by Electrons 5
- 2.3 The Electron Probe Microanalyzer 6
- 2.4 Detection of X-rays 9
- 2.4.1 Wavelength Dispersive Spectrometer 9
- 2.4.2 Energy Dispersive Spectrometer 13
- 2.4.3 Advantages of WDS over EDS for Thin Film Measurements 14

CHAPTER 3 - MATRIX CORRECTION FOR EPMA 16
- 3.1 Quantitative Electron Probe Microanalysis 16
- 3.1.1 Introduction 16
- 3.1.2 $\phi(\rho z)$ and the Tracer Technique 17
- 3.1.3 Quantitative Analysis of Bulk Specimens 23

Page

3.2 ZAF Method 28
3.2.1 The Absorption Correction 28
3.2.2 Atomic Number Correction 28
3.2.3 Fluorescence Correction 29
3.3 $\phi(\rho z)$ Method 30
3.4 Review of Models for $\phi(\rho z)$ Curves 31
3.5 An Example of the $\phi(\rho z)$ Method 41

CHAPTER 4 - MONTE CARLO SIMULATION OF BULK $\phi(\rho z)$ CURVES 45
4.1 Electron Interaction with Solids 45
4.2 The Monte Carlo Method 47
4.3 Single Scattering Model 49
4.4 Multiple Scattering Model 56
4.5 Modifications to the Multiple Scattering Model 60
4.5.1 Electron Straggling 61
4.5.2 Multiple Scattering Angles 66
4.5.3 Other Changes 74
4.6 Results on Bulk Specimens 75

CHAPTER 5 - MOTT THEORY OF ELECTRON SCATTERING 80
5.1 Introduction 80
5.2 Mott Scattering Angles for the Multiple Scattering Model 82
5.3 Results 85
5.3.1 General Comments 103
5.3.2 Specific Systems 108
5.3.3 Summary 113

CHAPTER 6 - THIN FILM ANALYSIS 119
6.1 Introduction 119
6.2 Monte Carlo Method for Thin Films 125
6.3 Simulation Results 131
6.4 Mathematical Model for Thin Film $\phi(\rho z)$ Curves 137
6.5 K-ratio Calculations and Comparisons 196
6.6 Sources of Error 208

CHAPTER 7 - CONCLUSIONS ..... 21[illegible]
7.1 Future Work 211

Page

APPENDIX 1	Fortran Program to Calculate Bulk $\phi(\rho z)$ Curves (Rutherford Scattering)	212
APPENDIX 2	Fortran Program to Calculate Bulk $\phi(\rho z)$ Curves (Mott Scattering)	225
APPENDIX 3	Fortran Program to Calculate Thin Film $\phi(\rho z)$ Curves by the Monte Carlo Method	239
APPENDIX 4	Summary of the Set of Equations to Calculate Thin Film $\phi(\rho z)$ Curves	255
APPENDIX 5	Fortran Program to Calculate Thin Film $\phi(\rho z)$ Curves by Equations	257
APPENDIX 6	Fortran Program to Calculate Film K-Ratios as a Function of Electron Energy	263
APPENDIX 7	Fortran Program to Calculate Film K-Ratios as a Function of Film Thickness	269
APPENDIX 8	Fortran Program to Calculate Unknown Film Thickness from the K-Ratio	275
REFERENCES		281
VITA		293

LIST OF TABLES

Table	Description	Page
1	Absorption and Atomic Number Correction for an Alloy (Cu-5 wt% Al)	44
2	The 15 Different Systems for the Comparison of $\phi(\rho z)$ Curves Between Experimental and M.C. Calculations	87
3	Comparison of α Value Between Experimentally Measured and Monte Carlo Calculated $\phi(\rho z)$ Curves	106
4	Comparison of Mass Depth at Maximum $\phi(\rho z)$ Between Experimentally Measured and Monte Carlo Calculated $\phi(\rho z)$ Curves	109
5	10 keV Electron Energy Tables for Si Kα	129
6	Summary Table for the Energy and Location of a 10 keV Electron in a Si Film on Au Substrate	132
7	Monte Carlo Thin Film Calculations	133
8a	Comparison of c2 Values as Calculated by Equations 81 and 92 for Light Element Film on Heavy Element Substrate	185
8b	Comparison of c2 Values as Calculated by Equations 88 and 93 for Heavy Element Film on Light Element Substrate	185
9a	Comparison of Calculated Film Thicknesses from Various Methods Using the Measured K-ratio Data from Reuter [133], Take-off Angle (ψ=52.5°)	207
9b	Comparison of Calculated Film Thicknesses with the Measured K-ratio Data from Willich [155], Take-off Angle (ψ=40°)	207

LIST OF FIGURES

Figure	Description	Page
1	Schematic illustration of characteristic and continuum x-ray production by electron excitation	7
2	Schematic diagram of an electron microprobe	8
3	X-rays are diffracted from a crystal if Bragg's law is satisfied	10
4	Schematic diagram of Johann semi-focusing spectrometer	12
5	Schematic diagram of Johansson fully focusing spectrometer	12
6	Measurement of $\phi(\rho z)$ curve by the tracer technique	19
7	Generated and emitted $\phi(\rho z)$ curves from a tracer of element B in a matrix A	20
8a-d	Different shapes of $\phi(\rho z)$ curves from Philibert, Bishop, Wittry and Packwood and Brown	33
8e-h	Different shapes of $\phi(\rho z)$ curves from Pouchou and Pichoir, Love et al., Gaber and Merlet	38
9a	Schematic of the emitted and generated $\phi(\rho z)$ curves for Al Kα from a Cu-5 wt% Al alloy	42
9b	Schematic of the emitted and generated $\phi(\rho z)$ curves for Al Kα from a pure Al standard	42
10	Schematic diagram of laboratory frame of reference	53
11	Schematic diagram of scattering frame of reference	53
12a	Monte Carlo simulated $\phi(\rho z)$ curve of Cu Kα from Cu at 30 keV from Henoc and Maurice [4]	62
12b	Plot of $\ln\phi(\rho z)$ versus $(\rho z)^2$ from Figure 12a	62

Figure	Description	Page

13a	Monte Carlo simulated $\phi(\rho z)$ curve of Al Kα from Al at 30 keV from Henoc and Maurice [4]	63
13b	Plot of ln$\phi(\rho z)$ versus $(\rho z)^2$ from Figure 13a	63
14a-c	Unmodified, modified with linear random number generator, modified with Gaussian random number generator	65
15	Range straggling assumed in an Al matrix	67
16a	Scattering angles for Cu Kα in Cu matrix at 10 keV from Henoc and Maurice [4]	69
16b	Scattering angles for Cu Kα in Cu matrix at 10 keV from Werner and Heydenreich [102]	69
17a	Scattering angles for Au Mα in Au matrix at 30 keV from Henoc and Maurice [4]	71
17b	Scattering angles for Au Mα in Au matrix at 30 keV from Werner and Heydenreich [102]	71
18a	Scattering angles for Cu Kα in Cu matrix at 30 keV from Henoc and Maurice [4]	72
18b	Scattering angles for Cu Kα in Cu matrix at 30 keV from Werner and Heydenreich [102]	72
19a	Scattering angles for Al Kα in Al matrix at 30 keV from Henoc and Maurice [4]	73
19b	Scattering angles for Al Kα in Al matrix at 30 keV from Werner and Heydenreich [102]	73
20a	Experimentally measured and Monte Carlo simulated $\phi(\rho z)$ curves for Cd Lα in Al at 30 keV	76
20b	Plots of ln$\phi(\rho z)$ versus $(\rho z)^2$ from Figure 20a	76

Figure	Description	Page
21a	Experimentally measured and Monte Carlo simulated $\phi(\rho z)$ curves for Cd Lα in Ag at 20 keV	77
21b	Plots of ln$\phi(\rho z)$ versus $(\rho z)^2$ from Figure 21a	77
22a	Experimentally measured and Monte Carlo simulated $\phi(\rho z)$ curves for Bi Lα in Al at 30 keV	78
22b	Plots of ln$\phi(\rho z)$ versus $(\rho z)^2$ from Figure 22a	78
23a	Scattering angle distributions as calculated from equation (72) for Au at 30 keV	83
23b	Scattering angle distributions as calculated from equation (73) for Au at 30 keV	84
24a	Experimentally measured and Monte Carlo simulated $\phi(\rho z)$ curves for Cd Lα in Ag at 15 keV	86
24b	Plots of ln$\phi(\rho z)$ versus $(\rho z)^2$ from Figure 24a	86
25a	Experimentally measured and Monte Carlo simulated $\phi(\rho z)$ curves for Cd Lα in Au at 25 keV	88
25b	Plots of ln$\phi(\rho z)$ versus $(\rho z)^2$ from Figure 25a	88
26a	Experimentally measured and Monte Carlo simulated $\phi(\rho z)$ curves for Si Kα in Au at 10 keV	89
26b	Plots of ln$\phi(\rho z)$ versus $(\rho z)^2$ from Figure 26a	89
27a	Experimentally measured and Monte Carlo simulated $\phi(\rho z)$ curves for Si Kα in Au at 30 keV	90
27b	Plots of ln$\phi(\rho z)$ versus $(\rho z)^2$ from Figure 27a	90
28a	Experimentally measured and Monte Carlo simulated $\phi(\rho z)$ curves for Si Kα in Ag at 20 keV	91
28b	Plots of ln$\phi(\rho z)$ versus $(\rho z)^2$ from Figure 28a	91

Figure	Description	Page
29a	Experimentally measured and Monte Carlo simulated $\phi(\rho z)$ curves for Bi Lα in Ag at 30 keV	92
29b	Plots of ln$\phi(\rho z)$ versus $(\rho z)^2$ from Figure 29a	92
30a	Experimentally measured and Monte Carlo simulated $\phi(\rho z)$ curves for Cd Lα in Ag at 15 keV	93
30b	Plots of ln$\phi(\rho z)$ versus $(\rho z)^2$ from Figure 30a	93
31a	Experimentally measured and Monte Carlo simulated $\phi(\rho z)$ curves for Cd Lα in Ag at 20 keV	94
31b	Plots of ln$\phi(\rho z)$ versus $(\rho z)^2$ from Figure 31a	94
32a	Experimentally measured and Monte Carlo simulated $\phi(\rho z)$ curves for Cd Lα in Ag at 30 keV	95
32b	Plots of ln$\phi(\rho z)$ versus $(\rho z)^2$ from Figure 32a	95
33a	Experimentally measured and Monte Carlo simulated $\phi(\rho z)$ curves for Zn Kα in Cu at 20 keV	96
33b	Plots of ln$\phi(\rho z)$ versus $(\rho z)^2$ from Figure 33a	96
34a	Experimentally measured and Monte Carlo simulated $\phi(\rho z)$ curves for Zn Kα in Cu at 30 keV	97
34b	Plots of ln$\phi(\rho z)$ versus $(\rho z)^2$ from Figure 34a	97
35a	Experimentally measured and Monte Carlo simulated $\phi(\rho z)$ curves for Si Kα in Cu at 15 keV	98
35b	Plots of ln$\phi(\rho z)$ versus $(\rho z)^2$ from Figure 35a	98
36a	Experimentally measured and Monte Carlo simulated $\phi(\rho z)$ curves for Cu Kα in Al at 15 keV	99
36b	Plots of ln$\phi(\rho z)$ versus $(\rho z)^2$ from Figure 36a	99

Figure	Description	Page

Figure	Description	Page
37a	Experimentally measured and Monte Carlo simulated $\phi(\rho z)$ curves for Si Kα in Al at 10 keV	100
37b	Plots of ln$\phi(\rho z)$ versus $(\rho z)^2$ from Figure 37a	100
38a	Experimentally measured and Monte Carlo simulated $\phi(\rho z)$ curves for Cr Lα in Al at 10 keV	101
38b	Plots of ln$\phi(\rho z)$ versus $(\rho z)^2$ from Figure 38a	101
39a	Experimentally measured and Monte Carlo simulated $\phi(\rho z)$ curves for Cu Lα in Ag at 10 keV	102
39b	Plots of ln$\phi(\rho z)$ versus $(\rho z)^2$ from Figure 39a	102
40a-d	Plots of ln$\phi(\rho z)$ versus $(\rho z)^2$ from Figures 20, 34, 31 and 27 respectively	105
41a,b	Absolute and relative comparison of optimized α values between experimentally measured and Monte Carlo calculated $\phi(\rho z)$ curves from Table 3	107
42	Comparison of absolute difference between Monte Carlo simulated and measured $\phi(\rho z)$ curves for the depth of maximum x-ray production with the corresponding simulated layer interval (Table 4)	110
43a	Experimentally measured and Monte Carlo simulated $\phi(\rho z)$ curves for Si Kα in Au at 10 keV	114
43b	Plots of ln$\phi(\rho z)$ versus $(\rho z)^2$ from Figure 43a	114
44a	Experimentally measured and Monte Carlo simulated $\phi(\rho z)$ curves for Zn Kα in Cu at 20 keV	115
44b	Plots of ln$\phi(\rho z)$ versus $(\rho z)^2$ from Figure 44a	115
45a	Experimentally measured and Monte Carlo simulated $\phi(\rho z)$ curves for Si Kα in Cu at 15 keV	116
45b	Plots of ln$\phi(\rho z)$ versus $(\rho z)^2$ from Figure 45a	116

Figure	Description	Page

46a Experimentally measured and Monte Carlo simulated $\phi(\rho z)$ curves for Cu Lα in Ag at 10 keV 117

46b Plots of $\ln\phi(\rho z)$ versus $(\rho z)^2$ from Figure 46a 117

47a Measurement of x-ray intensity (I_A^L) from thin film on substrate 123

47b Area under the curve represents I_A^L from Figure 47a 123

48a Measurement of x-ray intensity (I_A^A) from bulk standard 123

48b Area under the curve represents I_A^A from Figure 48a 123

49 Schematic diagram of six possible electron trajectories in a thin film on substrate specimen 127

50a Monte Carlo simulated thin film $\phi(\rho z)$ curves of 10 different silicon film thicknesses on gold substrate at 30 keV 135

50b Ratio plots of film $\phi(\rho z)$ curves from Figure 50a 135

51a Monte Carlo simulated thin film $\phi(\rho z)$ curves of 10 different gold film thicknesses on silicon substrate at 30 keV 138

51b Ratio plots of film $\phi(\rho z)$ curves from Figure 51a 138

52a $\phi(\rho z)$ curves for bulk Si and five Si films on Au substrate at 30 keV 140

52b Ratio versus ρz for five Si films on Au substrate 140

52c $(\text{Ratio-1})^{1/8}$ versus ρz for five Si films on Au substrate 140

53a Plots of c1 versus Si film thickness ρt on Au substrate at 10, 15, 20, 25 and 30 keV 142

Figure	Description	Page

53b Plots of $\ln(0.93\text{-c1})$ versus $\ln(\rho t/(\mu g/cm^2))$ from Figure 53a 142

53c Plot of c2 versus $\ln(E_o/keV)$ from Figure 53b 142

54a Plot of $1/(m1.\rho t+c1)$ versus ρt_{norm} for different Si film thicknesses on Au substrate at 10, 15, 20, 25 and 30 keV electron energies 145

54b Corresponding ln-ln plot of Figure 54a 145

55a Monte Carlo simulated thin film $\phi(\rho z)$ curves of 10 different silicon film thicknesses on gold substrate at 30 keV 146

55b Calculated thin film $\phi(\rho z)$ curves at 10 different silicon film thicknesses on gold substrate at 30 keV 146

56a Comparison of ratios calculated from Figures 55a and 55b 147

56b Error plots calculated from Figure 56a 147

57a Monte Carlo simulated thin film $\phi(\rho z)$ curves of 10 different silicon film thicknesses on gold substrate at 25 keV 148

57b Calculated thin film $\phi(\rho z)$ curves at 10 different silicon film thicknesses on gold substrate at 25 keV 148

58a Comparison of ratios calculated from Figures 57a and 57b 149

58b Error plots calculated from Figure 58a 149

59a Monte Carlo simulated thin film $\phi(\rho z)$ curves of 10 different silicon film thicknesses on gold substrate at 20 keV 150

59b Calculated thin film $\phi(\rho z)$ curves at 10 different silicon film thicknesses on gold substrate at 20 keV 150

60a Comparison of ratios calculated from Figures 59a and 59b 151

Figure	Description	Page
60b	Error plots calculated from Figure 60a	151
61a	Monte Carlo simulated thin film $\phi(\rho z)$ curves of 10 different silicon film thicknesses on gold substrate at 15 keV	152
61b	Calculated thin film $\phi(\rho z)$ curves at 10 different silicon film thicknesses on gold substrate at 15 keV	152
62a	Comparison of ratios calculated from Figures 61a and 61b	153
62b	Error plots calculated from Figure 62a	
63a	Monte Carlo simulated thin film $\phi(\rho z)$ curves of 10 different silicon film thicknesses on gold substrate at 10 keV	154
63b	Calculated thin film $\phi(\rho z)$ curves at 10 different silicon film thicknesses on gold substrate at 10 keV	154
64a	Comparison of ratios calculated from Figures 63a and 63b	155
64b	Error plots calculated from Figure 64a	
65a	$\phi(\rho z)$ curves for bulk Au and five Au films on Si substrate at 30 keV	157
65b	Ratio versus ρz for five Au films on Si substrate	157
65c	$(1\text{-Ratio})^{1/3}$ versus ρz for five Au films on Si substrate	157
66a	Plots of c1 versus Au film thickness ρt on Si substrate at 10, 15, 20, 25 and 30 keV	159
66b	Plots of $\ln(0.85\text{-c1})$ versus $\ln(\rho t/(\mu g/cm^2))$ from Figure 66a	159
66c	Plot of c2 versus $\ln(E_o/keV)$ from Figure 66b	159
67a	Plot of $1/(m1 \cdot \rho t + c1)$ versus ρt_{norm} for different Au film thicknesses on Si substrate at 10, 15, 20, 25 and 30 keV electron energies	161

Figure	Description	Page

Figure	Description	Page
67b	Corresponding ln-ln plot of Figure 67a	161
68a	Monte Carlo simulated thin film $\phi(\rho z)$ curves of 10 different gold film thicknesses on silicon substrate at 30 keV	162
68b	Calculated thin film $\phi(\rho z)$ curves at 10 different gold film thicknesses on silicon substrate at 30 keV	162
69a	Comparison of ratios calculated from Figures 68a and 68b	163
69b	Error plots calculated from Figure 69a	163
70a	Monte Carlo simulated thin film $\phi(\rho z)$ curves of 10 different gold film thicknesses on silicon substrate at 25 keV	164
70b	Calculated thin film $\phi(\rho z)$ curves at 10 different gold film thicknesses on silicon substrate at 25 keV	164
71a	Comparison of ratios calculated from Figures 70a and 70b	165
71b	Error plots calculated from Figure 71a	165
72a	Monte Carlo simulated thin film $\phi(\rho z)$ curves of 10 different gold film thicknesses on silicon substrate at 20 keV	166
72b	Calculated thin film $\phi(\rho z)$ curves at 10 different gold film thicknesses on silicon substrate at 20 keV	166
73a	Comparison of ratios calculated from Figures 72a and 72b	167
73b	Error plots calculated from Figure 73a	167
74a	Monte Carlo simulated thin film $\phi(\rho z)$ curves of 10 different gold film thicknesses on silicon substrate at 15 keV	168
74b	Calculated thin film $\phi(\rho z)$ curves at 10 different gold film thicknesses on silicon substrate at 15 keV	168

Figure	Description	Page
75a	Comparison of ratios calculated from Figures 74a and 74b	169
75b	Error plots calculated from Figure 75a	169
76a	Monte Carlo simulated thin film $\phi(\rho z)$ curves of 10 different gold film thicknesses on silicon substrate at 10 keV	170
76b	Calculated thin film $\phi(\rho z)$ curves at 10 different gold film thicknesses on silicon substrate at 10 keV	170
77a	Comparison of ratios calculated from Figures 76a and 76b	171
77b	Error plots calculated from Figure 77a	171
78a	Monte Carlo simulated thin film $\phi(\rho z)$ curves of 5 different copper film thicknesses on silver substr . e a 30 keV	173
78b	Calculated thin film $\phi(\rho z)$ curves of 5 different copper film thicknesses on silver substrate at 30 keV	173
78c	Error plots calculated from Figures 78a and 78b	173
79a	Monte Carlo simulated thin film $\phi(\rho z)$ curves of 5 different copper film thicknesses on gold substrate at 30 keV	174
79b	Calculated thin film $\phi(\rho z)$ curves of 5 different copper film thicknesses on gold substrate at 30 keV	174
79c	Error plots calculated from Figures 79a and 79b	174
80a	Monte Carlo simulated thin film $\phi(\rho z)$ curves of 5 different silver film thicknesses on gold substrate at 30 keV	175
80b	Calculated thin film $\phi(\rho z)$ curves of 5 different silver film thicknesses on gold substrate at 30 keV	175
80c	Error plots calculated from Figures 80a and 80b	175

Figure	Description	Page
81a	Monte Carlo simulated thin film $\phi(\rho z)$ curves of 5 different silicon film thicknesses on silver substrate at 30 keV	176
81b	Calculated thin film $\phi(\rho z)$ curves of 5 different silicon film thicknesses on silver substrate at 30 keV	176
81c	Error plots calculated from Figures 81a and 81b	176
82a	Monte Carlo simulated thin film $\phi(\rho z)$ curves of 5 different silicon film thicknesses on copper substrate at 30 keV	177
82b	Calculated thin film $\phi(\rho z)$ curves of 5 different silicon film thicknesses on copper substrate at 30 keV	177
82c	Error plots calculated from Figures 82a and 82b	177
83a	Monte Carlo simulated thin film $\phi(\rho z)$ curves of 5 different silver film thicknesses on copper substrate at 30 keV	178
83b	Calculated thin film $\phi(\rho z)$ curves of 5 different silver film thicknesses on copper substrate at 30 keV	178
83c	Error plots calculated from Figures 83a and 83b	178
84a	Monte Carlo simulated thin film $\phi(\rho z)$ curves of 5 different gold film thicknesses on copper substrate at 30 keV	179
84b	Calculated thin film $\phi(\rho z)$ curves of 5 different gold film thicknesses on copper substrate at 30 keV	179
84c	Error plots calculated from Figures 84a and 84b	179
85a	Monte Carlo simulated thin film $\phi(\rho z)$ curves of 5 different gold film thicknesses on silver substrate at 30 keV	180

Figure	Description	Page
85b	Calculated thin film $\phi(\rho z)$ curves of 5 different gold film thicknesses on silver substrate at 30 keV	180
85c	Error plots calculated from Figures 85a and 85b	180
86a	Monte Carlo simulated thin film $\phi(\rho z)$ curves of 5 different silver film thicknesses on silicon substrate at 30 keV	181
86b	Calculated thin film $\phi(\rho z)$ curves of 5 different silver film thicknesses on silicon substrate at 30 keV	181
86c	Error plots calculated from Figures 86a and 86b	181
87a	Monte Carlo simulated thin film $\phi(\rho z)$ curves of 5 different copper film thicknesses on silicon substrate at 30 keV	182
87b	Calculated thin film $\phi(\rho z)$ curves of 5 different copper film thicknesses on silicon substrate at 30 keV	182
87c	Error plots calculated from Figures 87a and 87b	182
88a	Plot of c2 versus $\ln((E_o-(E_c/3))/keV)$ for three x-ray lines at six different electron energies	184
88b	Plots of $\ln(0.75-c1)$ versus $\ln(\rho t/(\mu g/cm^2))$ for different thicknesses of copper films on silver substrates at 15, 20 and 30 keV energies respectively	184
89a	Monte Carlo simulated thin film $\phi(\rho z)$ curves of 5 different silver film thicknesses on gold substrate at 30 keV	186
89b	Calculated thin film $\phi(\rho z)$ curves of 5 different silver film thicknesses on gold substrate at 30 keV	186
89c	Error plots calculated from Figures 89a and 89b	186

Figure	Description	Page
90a	Plot of c3 versus $\lvert\Delta\eta\rvert\cdot(1-\eta_{Film})$ for light element film on heavy element substrate	188
90b	Plot of ln(c3) versus $\ln\lvert\Delta\eta\rvert\cdot(1-\eta_{Film})$ for light element film on heavy element substrate	188
90c	Plot of c4 versus $\lvert\Delta\eta\rvert\cdot(1-\eta_{Film})$ for light element film on heavy element substrate	188
90d	Plot of ln(c4) versus $\ln(1+\lvert\Delta\eta\rvert\cdot(1-\eta_{Film}))$ for light element film on heavy element substrate	188
91a	Plot of c3 versus $\lvert\Delta\eta\rvert\cdot(1+\eta_{substrate})$ for heavy element film on light element substrate	190
91b	Plot of ln(c3) versus $\ln\lvert\Delta\eta\rvert\cdot(1+\eta_{substrate})$ for heavy element film on light element substrate	190
91c	Plot of c4 versus $\lvert\Delta\eta\rvert\cdot(1+\eta_{substrate})$ for heavy element film on light element substrate	190
91d	Plot of ln(c4) versus $\ln(1+\lvert\Delta\eta\rvert\cdot(1+\eta_{substrate}))$ for heavy element film on light element substrate	190
92	Error plot of constants c3 as calculated from Figures 90a and 91a and c4 from Figures 90c and 91c	192
93a	$\phi(\rho z)$ curves for 300 nm of Al on W, Ag, Cu, B and Al bulk at 10 keV	194
93b	$\phi(\rho z)$ curves for various thicknesses of Al films on W at 10 keV	194
93c	Reprint from Pouchou and Pichoir [122, Figure 8]	194
93d	Reprint from Pouchou and Pichoir [122, Figure 9]	194
94a	Comparison of calculated k-ratios with those measured by Bolon and Lifshin [137] for 5 different Au films on Si substrate	198

Figure	Description	Page
94b	Comparison of calculated k-ratios with those measured by Hutchins [138] for various Au films on Si substrate at 10, 20 and 30 keV electron energies	198
95a	Comparison of calculated k-ratios with those measured by Gillies et al. [163] for 3 different Ag films on Si substrate	200
95b	Reprint from Gillies et al. [163, Figure 2]	200
96a	Comparison of calculated k-ratios with those measured and fitted by Laurie et al. [175] for various Cu films on C substrate at 15 and 25 keV electron energies	201
96b	Comparison of calculated k-ratios with those measured by Bastin et al. [169] for two Ti films on Si substrate at different electron energies	201
97a	Comparison of calculated k-ratios with those measured by Packwood et al. [181] for Cu films on Si substrate at 15 keV electron energy. The corner plot [181,Figure 5] is copyrighted and reprinted with the permission of San Francisco Press, Inc.	203
97b	Comparison of calculated k-ratios with those measured by Packwood et al. [181] for Cu films on Si substrate at 10 keV electron energy. The corner plot [181,Figure 6] is copyrighted and reprinted with the permission of San Francisco Press, Inc.	203
98a	Comparison of calculated k-ratios with those measured by Pouchou and Pichoir [75] for a Cu film on W substrate at different electron energies	204
98b	Comparison of calculated k-ratios with those measured by Pouchou and Pichoir [75] for two Cu films on Mo substrate at different electron energies	204

Figure	Description	Page
99a	Comparison of calculated k-ratios with those measured by Packwood et al. [181] for Cu films on Pb substrate at 15 and 20 keV electron energies. The corner plot [181,Figure 5] is copyrighted and reprinted with the permission of San Francisco Press, Inc.	206
99b	Comparison of calculated k-ratios with those measured by Packwood et al. [181] for Cu films on Sn substrate at 15 and 20 keV electron energies. The corner plot [181,Figure 5] is copyrighted and reprinted with the permission of San Francisco Press, Inc.	206

NOMENCLATURE

A	=	Atomic weight, absorption correction in ZAF
B	=	Background count rate
C_A	=	Weight fraction of element A in a specimen
d	=	Spacing between diffracting planes
E_o	=	Energy of incident electrons
E_c	=	Critical excitation potential
EI(x)	=	Exponential integral
e	=	Charge of electron, basis of natural logarithms
erfc(x)	=	Complementary error function
FWHM	=	Full width at half maximum
$f(\chi)$	=	Philibert's absorption factor
H	=	Constant $\phi(\rho z)$ value from Bishop's rectangular model
h	=	$1.2A/Z^2$
I	=	X-ray intensities
I_A^{AB}	=	Emitted x-ray intensities of element A from the specimen alloy AB. (The subscripts and superscripts refer to the analyzed element and matrix material respectively.)
J	=	Mean ionization potential
k^A	=	K-ratio, ratio of measured x-ray intensities from unknown and standard, sometimes written as k_A
K	=	K-level x-ray emission line
L	=	L-level x-ray emission line
M	=	M-level x-ray emission line
N_A	=	Avogadro number

N_t	=	Total number of steps in one electron trajectory
n	=	Order of diffraction, number of trajectories
P	=	Peak count rate
P(s)	=	Probability of an electron travelling a distance s
Q	=	Ionization cross-section
R	=	Backscattering factor, a random number between zero and one
r	=	Electron or x-ray range
S	=	Stopping power
s	=	Step length of an electron
T	=	Total counting time
U	=	Overvoltage ratio (E_o/E_c)
Z	=	Atomic number, atomic number correction in ZAF, axis normal to the specimen surface
ZAF	=	A correction scheme with three multiplication factors
α	=	Screening parameter
η	=	Backscatter coefficient
θ	=	Bragg angle, electron scattering angle
λ	=	Wavelength, mean free path
μ	=	X-ray mass absorption coefficient
$\mu g/cm^2$	=	Mass thickness unit
ρ	=	Density
ρt	=	Thin film mass thickness
ρz	=	Mass depth

$(\rho z)_{max}$ = ρz value at $\phi(\rho z)$ maximum, also written as ρz_o from Wittry (Eqn. 19)

$\overline{\rho z}$ = Mean depth of x-ray production

$\Delta\rho z$ = Infinitely thin layer

σ = Lenard coefficient of electron beam attenuation, electron scattering cross-section, standard deviation

$\sigma(E)$ = Total elastic scattering cross-section

ϕ = Azimuthal angle

$\phi(o)$ = Surface ionization, also written as ϕ_o

$\phi(\rho z)$ = Depth distribution of the x-ray production

χ = $\mu \csc\psi$ (x-ray absorption parameter)

ψ = X-ray take off angle

Ω = Solid angle

Parameters from equations:

w = Parameter from Tanuma and Nagashima (Eqn. 21)

a,n = Parameters from Buchner (Eqn. 23)

$D,k,n,\rho z_o$ = Parameters from Parobek (Eqn. 24)

α,β,γ = Parameters from Packwood and Brown (Eqn. 25)

R_c,R_m,R_x = Parameters from Pouchou and Pichoir (Eqn. 27)

$\rho z_m,\rho z_r,\phi_m$ = Parameters from Sewell et al. (Eqn. 29)

$\alpha,\beta,\rho z_m,\phi_m$ = Parameters from Merlet (Eqn. 30)

f = Parameter from Werner and Heydenreich for inelastic scattering (Eqn. 62)

R^*,α,β,β^* = Parameters from Drouin et al. (Eqn. 68)

$c1,c2,c3,c4,c5,m1,\rho t_{norm}$ = Parameters from this work

The author of this thesis has granted The University of Western Ontario a non-exclusive license to reproduce and distribute copies of this thesis to users of Western Libraries. Copyright remains with the author.

Electronic theses and dissertations available in The University of Western Ontario's institutional repository (Scholarship@Western) are solely for the purpose of private study and research. They may not be copied or reproduced, except as permitted by copyright laws, without written authority of the copyright owner. Any commercial use or publication is strictly prohibited.

The original copyright license attesting to these terms and signed by the author of this thesis may be found in the original print version of the thesis, held by Western Libraries.

The thesis approval page signed by the examining committee may also be found in the original print version of the thesis held in Western Libraries.

Please contact Western Libraries for further information:
E-mail: libadmin@uwo.ca
Telephone: (519) 661-2111 Ext. 84796
Web site: http://www.lib.uwo.ca/

CHAPTER 1

INTRODUCTION

1.1 BACKGROUND

Electron probe microanalysis (EPMA) is a well established analytical technique which has been widely used in materials characterization of unknown composition since the early 1960s. The principle is based on detecting the emitted characteristic x-rays from an unknown sample that is bombarded by a beam of electrons with energies between 5 and 35 keV. Quantitative analysis can be performed by comparing the emission from one line of each element from the unknown sample to that from the same line of a pure element standard or a standard with known composition. This simple ratio, to a first approximation, gives the weight fraction of the element concerned. However, appropriate matrix corrections are required for more accurate results. The $\phi(\rho z)$ approach to calculate matrix corrections relies on the accurate modelling on the distribution with depth of the x-rays which are generated in the sample. Packwood and Brown [1] pointed out that at sufficient mass depth in many experimentally measured $\phi(\rho z)$ curves, $\ln\phi(\rho z)$ varies with $(\rho z)^2$ in a linear fashion. They proposed that the $\phi(\rho z)$ curves should consist of a gaussian, centered at the specimen surface, but modified by a transient term to take into account the initial collimation of the incident electron beam.

Monte Carlo calculations can be used to simulate $\phi(\rho z)$ curves. Each electron trajectory is composed of a series of straight line segments. Random numbers are

used to predict the scattering angle and energy loss for each scattering event. When $\ln\phi(\rho z)$ was plotted against $(\rho z)^2$ for many Monte Carlo simulated $\phi(\rho z)$ curves, these curves are not linear but concave downward in clear disagreement with all experimentally measured data.

Knowledge of how to calculate $\phi(\rho z)$ in bulk samples does not necessarily lead to accurate distributions in the case of thin films on substrates. This is because the film $\phi(\rho z)$ distribution is influenced by the scattering of the electrons as they penetrate from the film into the substrate. Thus the $\phi(\rho z)$ distribution will be different for the film and the pure element standard even if the film is a pure element. Many researchers have suggested that thin film distributions can be described by bulk distributions in which the parameters are modified on the basis of the thin film and substrate compositions and film thickness. Even though these methods had some success in the calculation of thin film mass thickness, the resulting thin film $\phi(\rho z)$ curves do not agree with the Monte Carlo calculations from Karduck et al. [2] and Ding and Wu [3] who state that any weighting scheme which attempts to preserve the basic shape of bulk $\phi(\rho z)$ for a fictitious homogeneous specimen will lead to unrealistic film $\phi(\rho z)$ curves if the film and substrate atomic number deviate substantially.

1.2 OBJECTIVES AND METHODS OF ATTACK

A Monte Carlo program from Henoc and Maurice [4] served as the basis to explore modifications which would result in better agreement between simulated and measured $\phi(\rho z)$ curves for bulk specimens. In particular, the straight line behaviour

for the plot of $\ln\phi(\rho z)$ versus $(\rho z)^2$ was used as criterion to judge the success of the modifications. The concept of electron straggling was introduced so that each electron trajectory undergoes a variable range of travel instead of the original fixed range. Both Rutherford and Mott multiple scattering angles were investigated. Although many studies of quantitative thin film analysis have been reported, systematic investigation of $\phi(\rho z)$ curves for thin films on a substrate are still limited. If there is a difference in atomic number between film and substrate, then the film $\phi(\rho z)$ distribution for $Z_{film} < Z_{substrate}$ will be enhanced near the interface and for $Z_{film} > Z_{substrate}$ the $\phi(\rho z)$ distribution will be suppressed. Therefore, the objective of this work is to investigate these effects more closely and to derive an analytical expression based on Monte Carlo simulated thin film $\phi(\rho z)$ curves which is suitable for all film/substrate combinations and for all electron energies. The equations to describe the thin film $\phi(\rho z)$ curves are based on a model in which the bulk $\phi(\rho z)$ curve for the thin film composition is modified from the interface back toward the surface.

CHAPTER 2

X-RAY PHYSICS AND INSTRUMENTATION

2.1 THEORY

Properties of materials are often controlled by their microstructure. Most natural or artificial solid substances are chemically heterogeneous on the microscopic scale. Quantitative x-ray microanalysis which involves the excitation of x-rays within a microscopic volume of the specimen provides the tool to characterize the elemental composition of material on a micro scale.

Electron probe x-ray microanalysis is a well established microanalytical technique. Many excellent discussions on EPMA can be found in the literature, in particular by Heinrich [5], Scott and Love [6], Heinrich and Newbury [7], Reed [8] and Scott et al. [9]. This chapter is meant to review briefly the generation, diffraction and detection of x-rays as occurs in a typical electron probe microanalyzer.

When a solid is bombarded by energetic electrons, a variety of interaction processes occur. Electron probe microanalysis is concerned in particular with the x-ray emission spectrum which can be measured and recorded by either a crystal spectrometer (WDS method) or a solid state detector (EDS method). The principle of the method is to irradiate a selected point on a specimen surface with a finely focused beam of electrons that can be of less than 1 μm in diameter. Typical accelerating voltage applied to the electrons is in the range of 5-35 kV. X-rays are generated from excited atoms at depths of a few tenths of μm at low energies and of

a few μm at 30 keV. The wavelengths present identify the emitting element and the line intensities are related to the concentration of the corresponding elements. X-rays are detected by either a wavelength dispersive spectrometer in which a single crystal is used to diffract a chosen wavelength of x-rays into a gas proportional detector, or a solid state energy dispersive spectrometer in which x-rays are converted to a small quantity of charge which is then electronically sorted to obtain the x-ray spectrum. Instrumental design has improved to the point that stability considerations are no longer an issue for a modern microprobe and the observed x-ray spectrum can be assumed to be reliable. Since the focused electron beam is nondestructive to the specimen, other techniques can be used to confirm the analysis results.

2.2 PRODUCTION OF X-RAYS BY ELECTRONS

X-rays are electromagnetic radiation having wavelengths from about 0.1 to 100Å and photon energies from less than 1 keV to approximately 100 keV. X-ray continuum results when the incident beam electrons interact inelastically with the Coulomb field of the nucleus of atoms of the specimen. The energy the electrons lose is radiated in a continuous spectrum. The continuum extends up to a limiting energy sometimes called the Duane-Hunt limit which is equal to the incident electron energy.

Characteristic x-rays are produced by the inelastic interaction of incident electrons with the inner shell electrons of atoms in the specimen. If the incident electron has enough energy, it may dislodge a K, L or M inner shell electron, losing

energy equivalent to the binding energies of that shell and leave the atom in an ionized state. The minimum energy for ionization of a particular shell is called the critical excitation potential or absorption edge energy. An outer electron can lower its energy by filling the inner shell vacancy. In this process the energy can be emitted as an x-ray photon or can be transferred to a second electron which is emitted from the atom (Auger process). The efficiency of ionization by electron bombardment is rather low, typically only one electron per thousand produces a K shell vacancy. Therefore, a great number of electrons is required to produce reasonable x-ray count rates.

An element can emit more than one type of x-ray because of a cascading effect of interactions. For example, a vacancy in the K shell might be filled by an electron from the L shell, producing a $K\alpha$ x-ray, then the vacancy in the L shell might be filled by an electron from the M shell producing an $L\alpha$ x-ray and so on. Figure 1 illustrates how continuum and characteristic x-rays are generated by incident electrons.

The energy of the x-ray photon is equal to the difference in energy between the two orbitals involved in the transition, which is thus characteristic of the element. Therefore, the wavelengths of the characteristic radiation are unique for atoms of a given atomic number.

2.3 THE ELECTRON PROBE MICROANALYZER

Figure 2 is a schematic diagram of a typical electron microprobe. At the top of the electron optical column is an electron gun which provides the stable source of

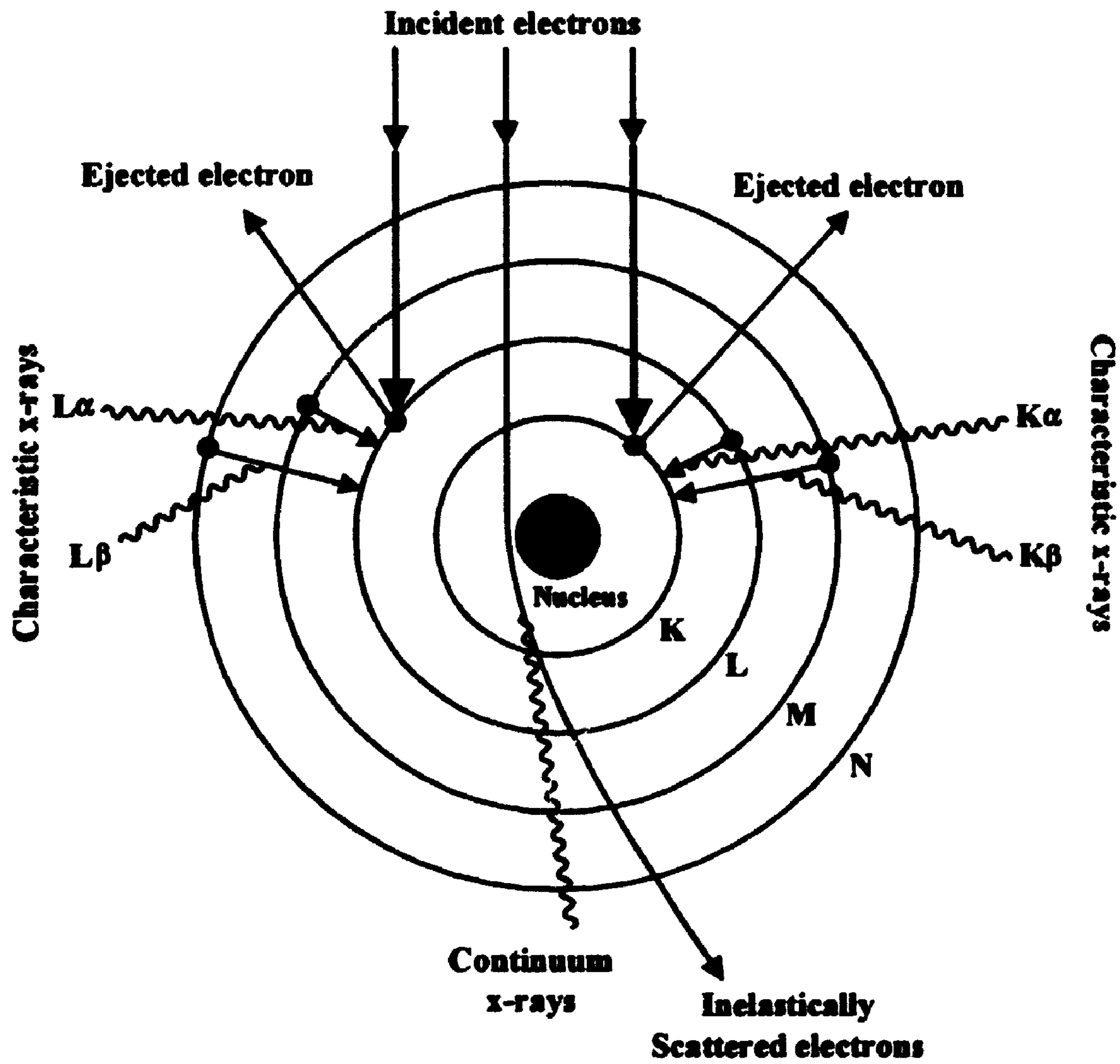

Figure 1. Schematic illustration of characteristic and continuum x-ray production by electron excitation

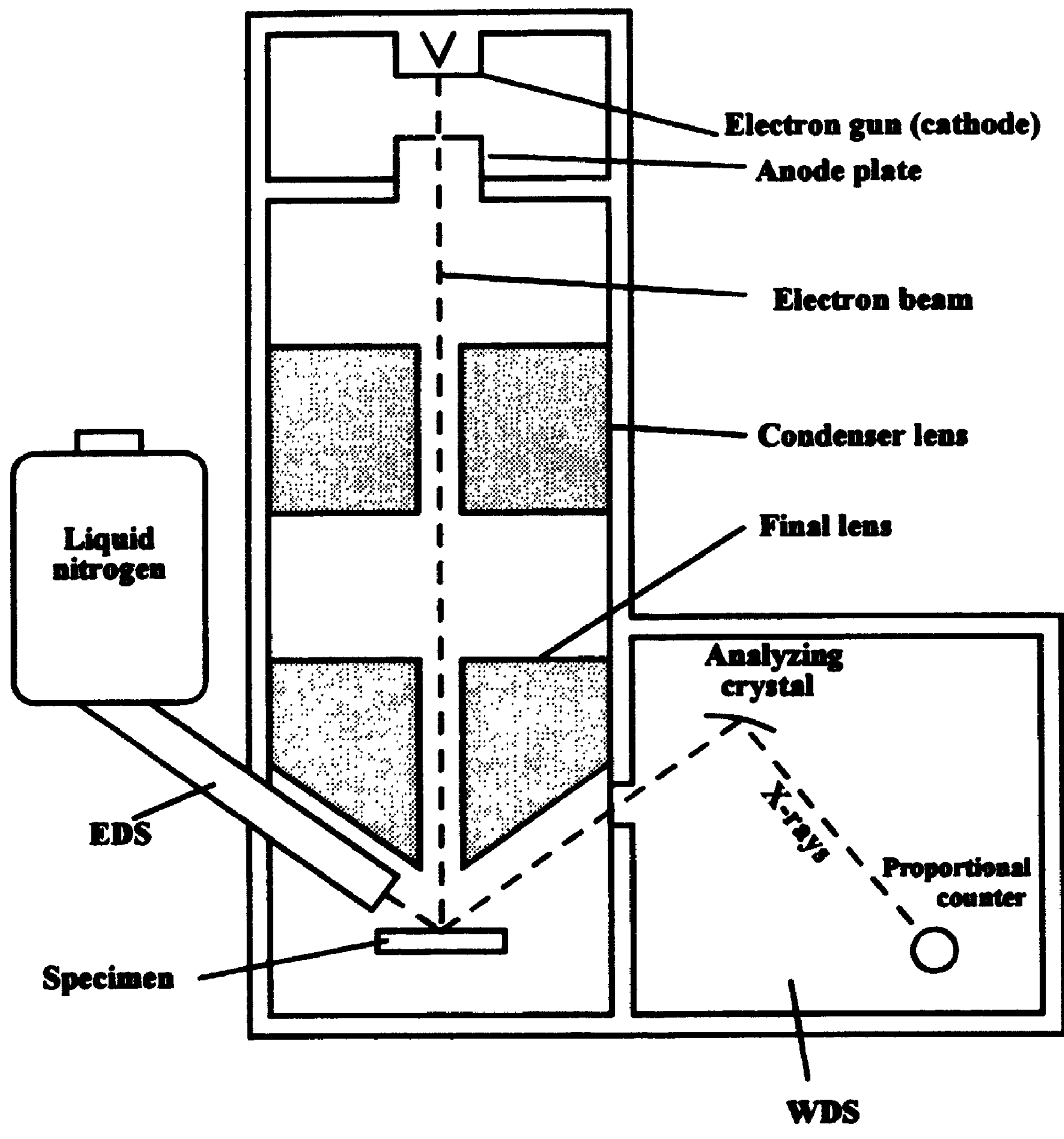

Figure 2. Schematic diagram of an electron microprobe

electrons used to form the electron beam. The gun consists of a filament which is a tungsten wire bent in the shape of a hairpin enclosed within a cylindrical cathode called the Wehnelt cylinder. During operation, the filament is heated and electrons are emitted by a process called thermionic emission to form a space charge near the tip. This space charge is confined by an electrical potential of a few hundred volts negative on the cathode relative to the filament. Electrons are accelerated through a small hole in the cathode toward the grounded anode plate and into the electron optical column attaining an electron energy (keV) equal to the accelerating potential (kV) applied to the gun. A series of electron lenses are used to focus the electron beam to less than 1 μm at the surface of the specimen. A Faraday cup for probe current monitoring can be inserted into the path of the electron beam between counting periods to obtain accurate current readings. On entering the specimen, electrons will generate x-rays within a small volume near the surface. A good vacuum of about 10^{-6} torr is required.

2.4 DETECTION OF X-RAYS

2.4.1 Wavelength Dispersive Spectrometer

The x-rays emitted from the specimen are detected by either a crystal (wavelength dispersive spectrometer) or a solid state detector (energy dispersive spectrometer). In the wavelength dispersive spectrometer, separation of wavelengths depends on diffraction from a single crystal which is a very selective process depending on Bragg's law (Figure 3) which is given by :

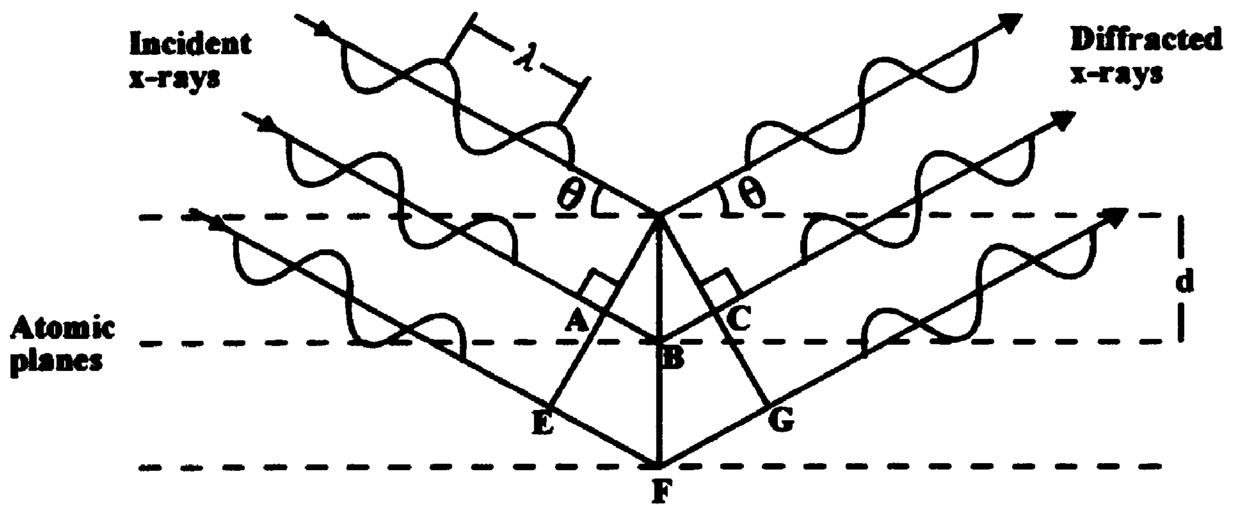

AB+BC=2dsin θ

AB+BC= λ

EF+FG=2λ

Reinforcement occurs when

diffracted x-rays are in phase

Figure 3. X-rays are diffracted from a crystal if Bragg's law is satisfied

$$n\lambda = 2d\sin\theta \quad \text{(Eqn. 1)}$$

where λ = wavelength of the diffracted x-rays

d = interplanar spacing of the crystal

θ = angle between the crystal surface and the incident and diffracted x-rays

n = integer

When Bragg's law is satisfied, the diffracted x-rays from the crystal planes combine in phase to produce an intensity maximum due to constructive interference. As a consequence, diffracted peaks are strong and the peak to background ratio is large.

In order to focus x-rays on the detector, the distance between the x-ray source (specimen) and diffracting crystal has to be the same as the distance between the diffracting crystal and x-ray detector. To accomplish this, the Johann spectrometer was developed where the specimen, diffracting crystal and x-ray detector are all on the circumference of a circle called the Rowland focusing circle with a specified radius. Bragg's law can be satisfied by sliding the crystal and the detector along the focal circle so that the detector travels at twice the angular speed of the crystal. The crystal is bent to a radius twice that of the focal circle but only a portion of the diffracting surface lies exactly on the circumference of the Rowland circle. A crystal of this shape focuses only a portion of the x-rays onto the detector, resulting in low angular resolution in the recorded spectra (Figure 4). A better solution was given by Johansson who not only bent but also ground away the inner surface of the crystal to a radius equal to that of the spectrometer circle. This ensured that Bragg's law

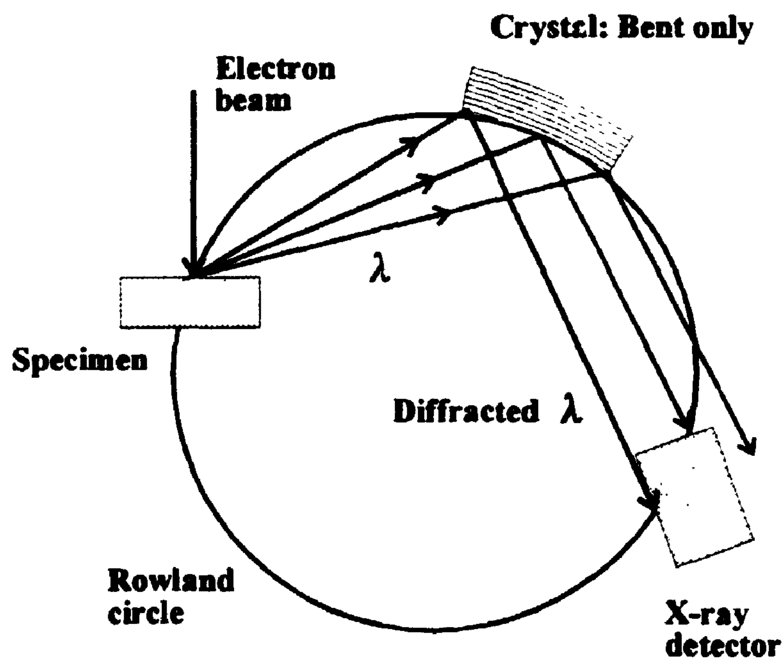

Figure 4. Schematic diagram of Johann semi-focusing spectrometer

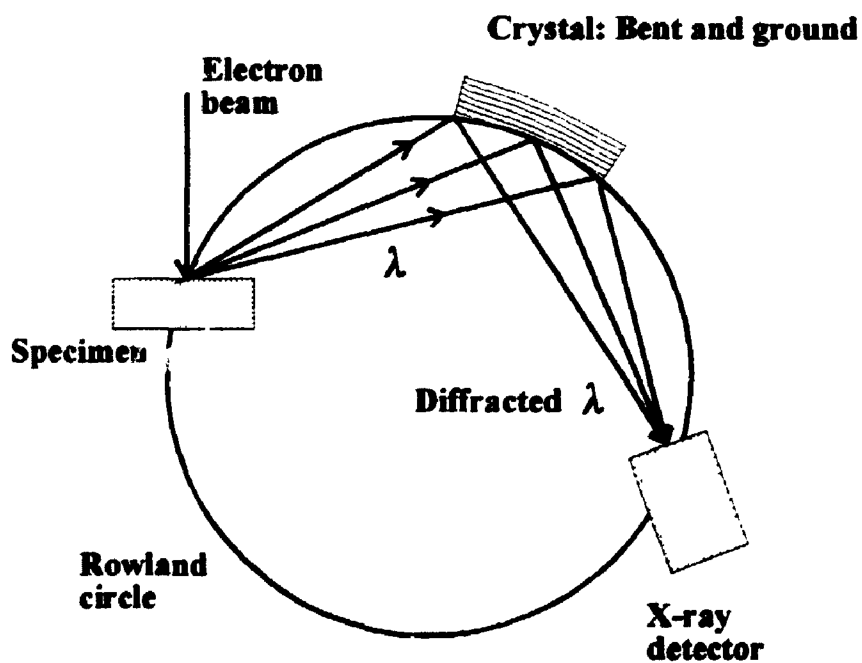

Figure 5. Schematic diagram of Johansson fully focusing spectrometer

remained satisfied over the length of the crystal in the plane of the Rowland circle (Figure 5). Wittry and Sun [10,11] reported that doubly curved crystals would improve the overall efficiency over the existing Johansson geometry. This crystal would be very difficult to produce in practice. A method was described by Wittry and Sun [12] to approximate the ideal shape by fabricating 'stepped' crystals.

The type of detector usually used in a WDS is a gas proportional counter, consisting of a tube filled with P10 gas (90% argon, 10% methane). When x-rays enter through a thin window, they are absorbed by the argon atoms resulting in the production of energetic photoelectrons (photoelectric effect). The total number of electron ion pairs (e^-, Ar^+) generated is proportional to the energy of the incident x-ray photon and hence it is called a proportional counter. Further ionisation occurs as a consequence of electron collisions with other argon atoms as these electrons are accelerated towards the thin tungsten wire held at a positive potential of 1-3 kV at the centre of the tube. The charge pulses from the centre wire of the counter are amplified, selected according to amplitude in a single channel analyzer and then counted in a scalar/timer.

2.4.2 Energy Dispersive Spectrometer

The energy dispersive spectrometer consists of a lithium-drifted silicon semiconductor (Si(Li)) detector, an amplifier system, a multichannel analyzer and a computer system with an output display. The Si(Li) detector itself is a reverse biased p-i-n diode structure with a thin x-ray transparent surface gold contact on the p-region

and a thicker gold contact on the n-region. When an x-ray photon enters the active region of the Si(Li) crystal, its energy is released as a series of interactions which produce electron-hole pairs. The formation of an electron-hole pair requires an average energy of about 3.8 eV, therefore the number of pairs generated is directly proportional to the energy of incoming x-ray photons. The electrons and holes are attracted to opposite gold contacts. A small pulse of electrons is collected as a charge pulse on the back gold contact which is closely coupled to the gate of a field-effect transistor (FET). The FET converts the charge pulse to a voltage change which is then amplified further. The magnitude of these voltage signals is digitized and sorted into memory locations (channels) in the multichannel analyzer (MCA). Thus x-ray photons are sorted according to energy and stored in memory making quasi-simultaneous multi-element analysis possible. The complete spectrum can be printed out or displayed on a video screen at the same time as the spectrum is being accumulated.

2.4.3 Advantages of WDS over EDS for Thin Film Measurements

Although a particular characteristic x-ray line is monochromatic, the statistical nature of electron-hole generation results in a finite energy width in the peaks in the EDS spectrum. Conventionally the spectral resolution is defined as the full width at half-maximum height (FWHM) of the Mn Kα peak at 5.9 keV. At present, a top quality EDS detector has a spectral resolution of about 130 eV. On the other hand, in a WDS spectrometer, diffraction by the single crystal which is used to separate

photons of different energy has a resolution in the 5 to 10 eV range. Because the x-ray line photons in WDS appear over a very much smaller range of energy of the continuum, better peak to background ratios, fewer peak overlaps and lower minimum detectable limits of elements are achieved. The other advantage concerns total count rates. An EDS has an optimal count rate of 3000 to 5000 counts per second which is spread over the entire spectrum entering the detector whereas a WDS can have count rates of 100,000 counts per second for a single photon energy without loss in energy resolution. Therefore, electron beam currents are severely limited for EDS. Thus, EDS is more appropriate for quick qualitative analysis but WDS is more reliable and sensitive for quantitative analysis of thin films.

CHAPTER 3

MATRIX CORRECTION FOR EPMA

3.1 QUANTITATIVE ELECTRON PROBE MICROANALYSIS

3.1.1 Introduction

The purpose of quantitative microanalysis is to identify and determine the concentration of elements present in the specimen. The results are usually expressed as the weight fraction of each element in the unknown. Quantitative microanalysis consists of four basic steps:

(1) Obtain an x-ray spectrum from the unknown to determine qualitatively the presence of elements in the specimen. Additional information may be required about the source of the specimen and the purpose of the analysis, particularly for low concentration elements which may not appear in a relatively quick and insensitive scan of the spectrum.

(2) Measure x-ray count rates for the same characteristic lines from the unknown and from appropriate standards under identical conditions of electron energy and beam current. Measure the background count rates. The specimens must be infinitely thick (from the standpoint of x-ray generation), have a flat surface and be homogeneous in the volume analyzed by the electron beam. Generally the electron energy should be at least twice the excitation potential for the highest energy characteristic line. All standards must be homogeneous and if not pure elements be of accurately known composition. For example, for

phosphorus for which the pure element cannot be used, GaP or InP are good standards that are easily obtained and of high purity.

(3) Correct the measured count rates from both specimen and standards for instrumental effects such as dead time and background to determine peak count rates. Calculate the k-ratios (see section 3.1.3 and Eqn. 9) which are the input data from which composition is to be determined. It was pointed out by Bastin and Heijligers [13] that while studying different types of carbides, the position and shape of the C Kα peak can vary as a result of chemical bonding. They developed the area/peak factor (APF) for intensity measurement which is useful for light element analysis.

(4) Apply corrections for x-ray absorption, atomic number effects and any fluorescence effects to obtain the composition by an iterative procedure from the k-ratios. The accuracy of these corrections rests on the accuracy of the modelling of the x-ray depth distribution curves ($\phi(\rho z)$ curves) for the particular correction procedure.

3.1.2 $\phi(\rho z)$ and the Tracer Technique

In practice, it is very difficult to measure or calculate an absolute value for the generated x-ray intensity as a function of depth. For that reason, $\phi(\rho z)$ is defined as the x-ray intensity generated in a layer interval, $d(\rho z)$, in the depth, ρz, divided by the intensity that is excited in an isolated layer of the same material with the same thickness and under the same measuring conditions. $\phi(\rho z)$ is a ratio and is therefore

dimensionless. Measurements of the depth distribution of characteristic x-rays were first performed experimentally using the tracer technique by Castaing and Deschamps [14]. The tracer technique requires depositing a thin film (tracer) of element B onto a solid substrate target of element A. The thin tracer is then covered successively by thicker and thicker layers of element A. X-ray intensity is then measured from the tracer as a function of its depth below the surface. This is normalized by comparing it to that measured from an isolated layer of element B of identical thickness and under the same analysis conditions. The reference layer was used to remove x-ray collection efficiency of the spectrometers from the calculations. A schematic diagram of the tracer technique is shown in Figure 6.

Since the tracer x-rays are created at some depth below the surface of the specimen, they must pass through the matrix layers on top on their way out to the detector. The generated $\phi(\rho z)$ curve (Figure 7) can be calculated from the measured or emitted $\phi(\rho z)$ curve after the absorption correction given by the following equation is made for each individual data point:

$$I_{Generated} = I_{measured}/\exp(-\mu\rho z \csc\psi) \quad \text{(Eqn. 2)}$$

where μ is the x-ray mass absorption coefficient of the tracer x-ray line by the overlayer material, $\rho z \csc\psi$ is the absorption path length and ψ is the takeoff angle between the x-ray detector and the specimen surface.

The following requirements have to be met for the tracer layer:

(1) As proposed by Castaing and Deschamps [14] in determining the absorption correction, the tracer element should be chosen to have similar electron

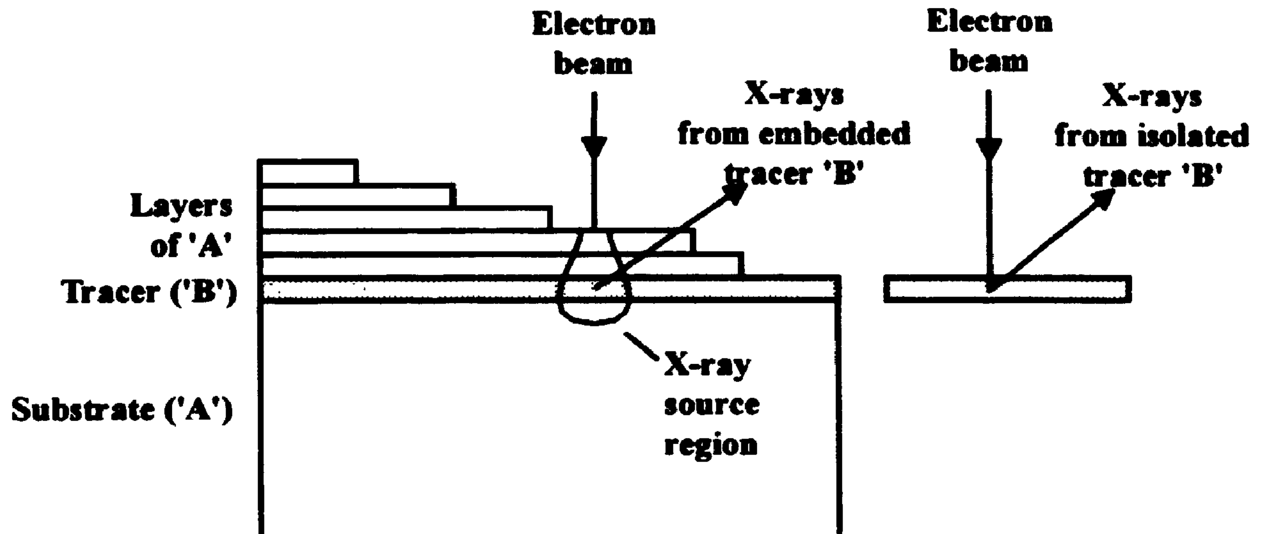

Figure 6. Measurement of $\Phi(\rho z)$ curve by the tracer technique.

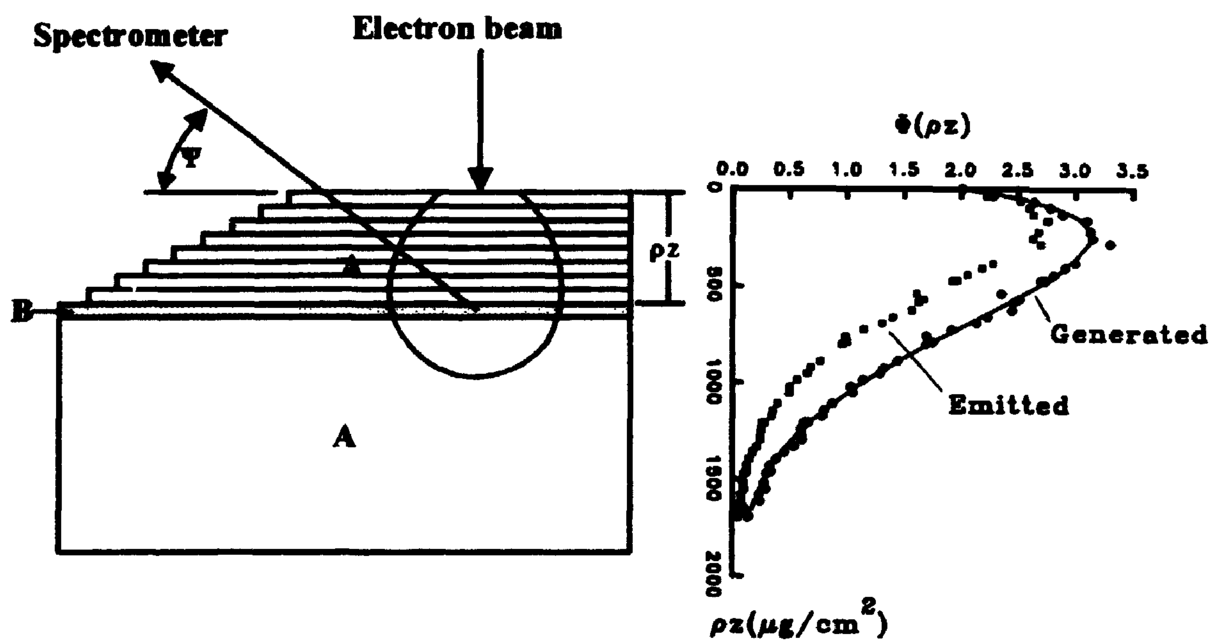

Figure 7. Generated and emitted $\Phi(\rho z)$ curves from a tracer of element B in a matrix A.

scattering properties as the matrix element so that the x-ray depth distribution would be unperturbed by the tracer layer. A typical example is Zn tracer in Cu matrix. Later, Brown and Parobek [15] suggested that the atomic number effect can be studied if layers of identical thickness of a single tracer element are deposited within the sandwich samples with atomic numbers quite different from that of the matrix element. Here, the assumption is that the tracer layer is thin enough that the electron scattering properties of the matrix are not significantly perturbed.

(2) The tracer should be chosen so that its characteristic x-ray line is not strongly fluoresced by an intense line of the matrix.

(3) By definition, the tracer has to be so thin that the electrons suffer no significant scattering nor backscattering in it. Karduck et al. [2] and Karduck and Rehbach [16] demonstrated that for a thick tracer the $\phi(\rho z)$ maximum value can be reduced by 10%. When the electrons are partly scattered in the tracer, the tracer intensity will increase by a factor of approximately $1/\langle\cos\omega\rangle$ where $\langle\cos\omega\rangle$ is the mean angular deflection of the incident electrons in the tracer. This gives a compressed $\phi(\rho z)$ curve since the isolated tracer intensity is too high. Therefore, tracer thickness must be thin enough not to significantly perturb the scattering of the electrons in order to yield the true shape of the $\phi(\rho z)$ curve. At the same time, the layers must be thick enough to obtain measurable x-ray intensities.

(4) There is no one standard tracer thickness. For optimal results, different tracer

thicknesses should be used. For example, very thin films are required at low incident electron energy (E_o) in order to improve the accuracy on the maximum $\phi(\rho z)$ value. On the other hand, thicker films are required at high E_o in order to increase the peak to background ratio. Typically film thicknesses of the order of 2-20 $\mu g/cm^2$ have been used. (In microprobe analysis, mass thickness is used because mass absorption coefficients are used for x-ray absorption, the absorption path is in mass units and film thicknesses are more easily measured in mass thickness. Mass thickness is simply the linear thickness multiplied by the density of the material.)

With a few exceptions, most of the experimentally measured $\phi(\rho z)$ curves have been done by a handful of research groups, namely those of Castaing and co-workers [14,17], Shimizu and co-workers [18], Sewell and co-workers [19], Brown [20, 15, 21 and 22] and Parobek [23]. Karduck [24] and Rehbach [25 and 26] extended the measured curves to low electron energy and low energy x-ray lines. A table listing the measured $\phi(\rho z)$ curves was updated by Heinrich [27], Brown [28], Scott [29], Karduck [30] and Scott [31].

All measured $\phi(\rho z)$ curves have the following common characteristics:

(1) In general shape of the $\phi(\rho z)$ curve rises from the surface, passes through a maximum then decays away to zero at sufficiently large depths.

(2) The surface ionisation, $\phi(o)$, is always greater than unity. Due to backscattering of the electrons, x-ray intensities of all tracers at the surface are increased by their underlying substrates above the isolated layer intensity.

(3) The initial rise in the $\phi(\rho z)$ curve is due to the increase in the average electron path length through each elemental layer, $d(\rho z)$, as the initially collimated electrons suffer greater and greater scattering. In addition, the average ionization cross-section may be increasing as the mean electron energy decreases with depth.

(4) The maximum in $\phi(\rho z)$ corresponds to the depth at which any increase in ionizations due to average path length increase is balanced by decreases in the number of electrons reaching that depth and perhaps decreases in average ionization cross-section as the energy of the electrons reduces.

(5) The $\phi(\rho z)$ value decreases at great depths because there are fewer electrons reaching these depths and even if they do, these electrons will either be less effective or, if their energies have fallen below E_c, be incapable of producing further x-rays.

3.1.3 Quantitative Analysis of Bulk Specimens

The first step in the analysis of an unknown is the identification of the elements present, i.e., qualitative analysis. Major and minor elements can quickly be identified using an energy dispersive system, however the presence of trace elements may require careful searching with a wavelength dispersive spectrometer. Because of the simplicity of x-ray spectra, misidentification of elements is seldom a problem.

The purpose of electron probe microanalysis is to transform the measured x-ray intensities into weight fraction estimates of the elements present. There are a few

requirements for accurate bulk analysis:

(1) The volume of the specimen excited by the electrons and through which the x-rays pass to reach the spectrometer must be uniform or homogeneous in composition.

(2) The analyzed specimen has to be thicker than the depth of penetration of the incident electron beam.

(3) Both specimen and standard must have flat surfaces.

(4) Both specimen and standard must be conductive. For non-conducting specimens, a thin conducting layer of identical thickness deposited on the surface of both specimen and standards can partially solve this problem.

(5) Preferably, the electron beam strikes the specimen at normal incidence although modifications to allow for the effect of non-normal incidence as in the case of tilted specimens in a scanning electron microscope have been developed by Sewell et al. [32], Packwood et al. [33] and Pouchou et al. [34].

Quantitative EPMA was first proposed by Castaing [35] who indicated that quantitative data may be obtained by comparing the x-ray intensity measured with the same instrumental conditions from the element of interest in a specimen with that from a pure element standard. A knowledge of the absolute intensity of emission is not important because of the cancellation of factors which occurs when comparing intensities of the same characteristic line from specimen and standard. Since x-rays of the same energy are measured, it is not necessary to know the efficiency of the spectrometer and the fluorescence yield of the x-ray line. To a first approximation,

the calibration curve of intensity versus weight fraction is linear and is given by the following equation:

$$\frac{I_{specimen}}{I_{standard}} = C \qquad \text{(Eqn. 3)}$$

where C is the weight fraction of the element of interest inside the specimen. However, only rarely does this relationship hold and usually corrections are required which take into account the difference in electron and x-ray scattering and absorption between specimen and standard. According to Castaing, the total intensity generated inside the specimen is given by:

$$I_{generated} = \phi(\Delta\rho z)\int_{0}^{\infty}\phi(\rho z)\,d(\rho z) \qquad \text{(Eqn. 4)}$$

where $\phi(\Delta\rho z)$ corresponds to the x-rays emitted from an isolated thin film of the target material with mass thickness $\Delta\rho z$. The emitted intensity is given by:

$$I_{emitted} = \phi(\Delta\rho z)\int_{0}^{\infty}\phi(\rho z)\exp(-\chi\rho z)\,d(\rho z) \qquad \text{(Eqn. 5)}$$

where

$$\chi = \mu csc\psi \qquad \text{(Eqn. 6)}$$

The emitted intensity can be rewritten as:

$$I_{emitted} = \phi(\Delta\rho z)\cdot f(\chi)\cdot\int_{0}^{\infty}\phi(\rho z)\,d(\rho z) \qquad \text{(Eqn. 7)}$$

where

$$f(\chi) = \frac{\int_{0}^{\infty} \phi(\rho z) \exp(-\chi \rho z)\, d(\rho z)}{\int_{0}^{\infty} \phi(\rho z)\, d(\rho z)} \qquad \text{(Eqn. 8)}$$

represents the fraction of generated x-rays which escape from the specimen. This fraction is less than one due to x-ray absorption.

Consider a simple binary alloy specimen containing elements A and B. The weight fraction of A is to be measured by reference to a pure element standard A. The ratio of the emitted intensity of element A from alloy to standard is known as the k-ratio and can be represented by:

$$\frac{I_A^{AB}}{I_A^{A}} = k^A = \frac{\phi(\Delta\rho z)_A^{AB}}{\phi(\Delta\rho z)_A^{A}} \cdot \frac{[\int_{0}^{\infty} \phi(\rho z)\, d(\rho z)]_A^{AB}}{[\int_{0}^{\infty} \phi(\rho z)\, d(\rho z)]_A^{A}} \cdot \frac{f(\chi)_A^{AB}}{f(\chi)_A^{A}} \qquad \text{(Eqn. 9)}$$

The ratio of intensity from the isolated thin films can be shown to be equal to the ratio of the weight fractions, thus:

$$\frac{\phi(\Delta\rho z)_A^{AB}}{\phi(\Delta\rho z)_A^{A}} = C_A \qquad \text{(Eqn. 10)}$$

where C_A is the weight fraction of element A in alloy AB.

The second term of Eqn. (9)

$$[\int_0^\infty \phi(\rho z)\, d(\rho z)]_A^{AB} / [\int_0^\infty \phi(\rho z)\, d(\rho z)]_A^A$$

represents the ratio of the number of x-rays generated per unit concentration in the alloy relative to the standard. This ratio is dependent on the average atomic number of the alloy relative to the standard and has become known as the atomic number effect, Z. The ratio

$$f(\chi)_A^{AB} / f(\chi)_A^A$$

corrects for differences in absorption within the alloy and standard. This correction is known as the absorption correction, A.

In some systems, characteristic fluorescence may be important in which case an additional term, fluorescence correction F, is required and Eqn. (9) becomes:

$$\frac{I_A^{AB}}{I_A^A} = k^A = C_A Z \cdot A \cdot F \qquad \text{(Eqn. 11)}$$

Each correction factor is usually treated separately in a ZAF approach. To use Eqn. (11) to correct the measured k-ratio to obtain concentrations, an iterative process is necessary since some parameters used in the calculation depend upon the composition of the specimen and this is unknown to begin with. The usual practice is to use the x-ray k-ratios as the first estimate of the weight fraction and then use

iterative loops to carry out successive approximations until the results converge.

3.2 ZAF METHOD

3.2.1 The Absorption Correction

The earliest commonly used analytical expression to approximate Eqn. (8) is that proposed by Philibert [36]. The complete derivation and description on Philibert's full absorption model have been reviewed by Heinrich [37] and Scott et al. [38]. Philibert's simple $f(\chi)$ formula is based on assumptions which include zero generated x-ray intensity at the specimen surface and therefore this formula should not be used when strong absorption effects are present. In general, absorption of x-rays is strong for low energy x-ray lines, high energy electron beams and in specimens containing high atomic number elements. Modifications have been made by Duncumb and Shields [39], Duncumb et al. [40], Love et al. [41] and Scott and Love [42], for example, who have derived alternate formulae to approximate $f(\chi)$. Nevertheless the simple Philibert's $f(\chi)$ formula was still the most widely used expression for calculating absorption correction in microanalysis.

3.2.2 Atomic Number Correction

The atomic number correction is a consequence of energy lost to the ionization process and carried away by electrons backscattered from the specimen, and of the differences in rate of energy loss between low and high atomic number elements. Z is usually calculated as follows:

$$Z = \frac{[R/S]_{specimen}}{[R/S]_{standard}} \qquad \text{(Eqn. 12)}$$

where R is the backscattering factor which is related to the backscattering coefficient η (see Ref. [8], p. 205 and p. 211) and S is the stopping power or penetration factor. Thomas [43] was the first to identify R and S as the factors important in the atomic number correction. Calculation of R has been reported by Bishop [44], Duncumb and Reed [45], Springer [46] and Love et al. [47]. Calculation of S has been reported by Duncumb and Reed [45], Philibert and Tixier [48], Love et al. [49] and Pouchou and Pichoir [50]. The dependence on atomic number is such that the rate of energy loss per unit mass thickness is greater in low Z than in high Z elements since the stopping power of heavy atoms is less. Conversely, the mass penetration or range in mass thickness units varies roughly as A/Z where A is the atomic weight and so increases with atomic number. However, backscattering increases with the atomic number of the specimen and that tends to compensate for the increase in mass penetration with atomic number. In short, due to backscattering a lot of electrons are lost from a heavy element but those that remain in the specimen are more effective at producing x-rays.

3.2.3 Fluorescence Correction

The fluorescence correction factor should include fluorescence contributions due to both characteristic x-rays and continuum x-rays. Fluorescence is a consequence of the strong absorption of the characteristic radiation of one (exciting) element by another (excited) element in the specimen which subsequently emits its

own characteristic x-rays. This phenomenon occurs only when the energy of the exciting radiation is greater than the critical excitation potential (E_c) for the particular electron shell of the excited. The effect is seen as an increase in the intensity of the excited element. The magnitude of the fluorescence effect is greatest when the exciting x-ray energy just exceeds E_c for the excited element.

Castaing [51] derived a characteristic fluorescence correction equation which was modified by Reed [52, 53]. A general expression for the characteristic fluorescence correction has been developed by Armstrong and Buseck [54] who claimed the geometry-independent expression can apply to bulk specimens, thin films and even spherical particles.

A correction for fluorescence due to continuum radiation was published by Springer [55] and Henoc [56]. Although the magnitude of the continuum correction is generally small, it can amount to 7% of the directly excited radiation as reported by Springer and Rosner [57].

3.3 $\phi(\rho z)$ METHOD

Although historically the ZAF approach was developed as the first method of choice for quantitative analysis, Eqn. (5) suggests that if the $\phi(\rho z)$ curves are accurately known, quantitative analysis can be carried out based on that knowledge. In principle, the equation as written is exact and the more accurate the description of $\phi(\rho z)$ the more accurate the analysis. In terms of $\phi(\rho z)$, the k-ratio (from Eqn. (9)) can be written as:

$$\frac{I_A^{AB}}{I_A^A} = k^A = C_A \cdot \frac{[\int_0^\infty \phi(\rho z)\, d(\rho z)]_A^{AB}}{[\int_0^\infty \phi(\rho z)\, d(\rho z)]_A^A} \cdot \frac{\dfrac{[\int_0^\infty \phi(\rho z) \exp(-\chi \rho z)\, d(\rho z)]_A^{AB}}{[\int_0^\infty \phi(\rho z)\, d(\rho z)]_A^{AB}}}{\dfrac{[\int_0^\infty \phi(\rho z) \exp(-\chi \rho z)\, d(\rho z)]_A^A}{[\int_0^\infty \phi(\rho z)\, d(\rho z)]_A^A}}$$

(Eqn. 13)

Equation (13) can be reduced to:

$$\frac{I_A^{AB}}{I_A^A} = k^A = C_A \frac{[\int_0^\infty \phi(\rho z) \exp(-\chi \rho z)\, d(\rho z)]_A^{AB}}{[\int_0^\infty \phi(\rho z) \exp(-\chi \rho z)\, d(\rho z)]_A^A} = C_A [ZA] \qquad \text{(Eq. 14)}$$

where the atomic number correction (Z) and absorption correction (A) can be obtained by comparing Eqn. (14) with Eqn. (13).

In the $\phi(\rho z)$ method, the rather artificial separation into atomic number and absorption effects inherent in the ZAF approach can be avoided. Instead, the combined correction is contained in a single term provided both the shape and the total area under the $\phi(\rho z)$ curves are accurately known.

3.4 REVIEW OF MODELS FOR $\phi(\rho z)$ CURVES

Several approaches have been used for developing an equation for $\phi(\rho z)$. Philibert [36] adopted a theoretical method which employed principles of electron and

x-ray physics. The implied $\phi(\rho z)$ curve associated with Philibert's simple $f(\chi)$ expression is one in which $\phi(\rho z)$ increases exponentially from the surface and then decreases again exponentially from the maximum value in the curve (Figure 8a). Its analytical form is as follows:

$$\phi(\rho z) = A \cdot \exp(-\sigma\rho z)\,[1-\exp(-\sigma\rho z/h)] \qquad \text{(Eqn. 15)}$$

where A is a constant, σ is the Lenard coefficient [58] and

$$h = 1.2A/Z^2 \qquad \text{(Eqn. 16)}$$

where Z and A are the atomic number and atomic weight of the sample respectively. Although the general shape of the calculated $\phi(\rho z)$ curve resembled much experimental $\phi(\rho z)$ data, the assumption that $\phi(o) = 0$ is clearly inappropriate as $\phi(o)$ must be greater than unity.

Castaing [51] in deriving his fluorescence correction assumed that the $\phi(\rho z)$ curve decayed exponentially from the surface of the specimen according to Lenard's law:

$$\phi(\rho z) = \phi_o \exp(-\sigma\rho z) \qquad \text{(Eqn. 17)}$$

Criss and Birks [58a] used a five term polynomial exponential expression to fit the $\phi(\rho z)$ curves measured by Castaing and Deschamps [14].

Bishop [59] assumed that $\phi(\rho z)$ can be represented as a rectangle (Figure 8b) with constant intensity (H) of x-ray generation with depth up to a depth of twice the mean depth of x-ray production, $\overline{\rho z}$, whereupon the intensity falls abruptly to zero. The mean ionization depth or mean depth of x-ray production is defined as:

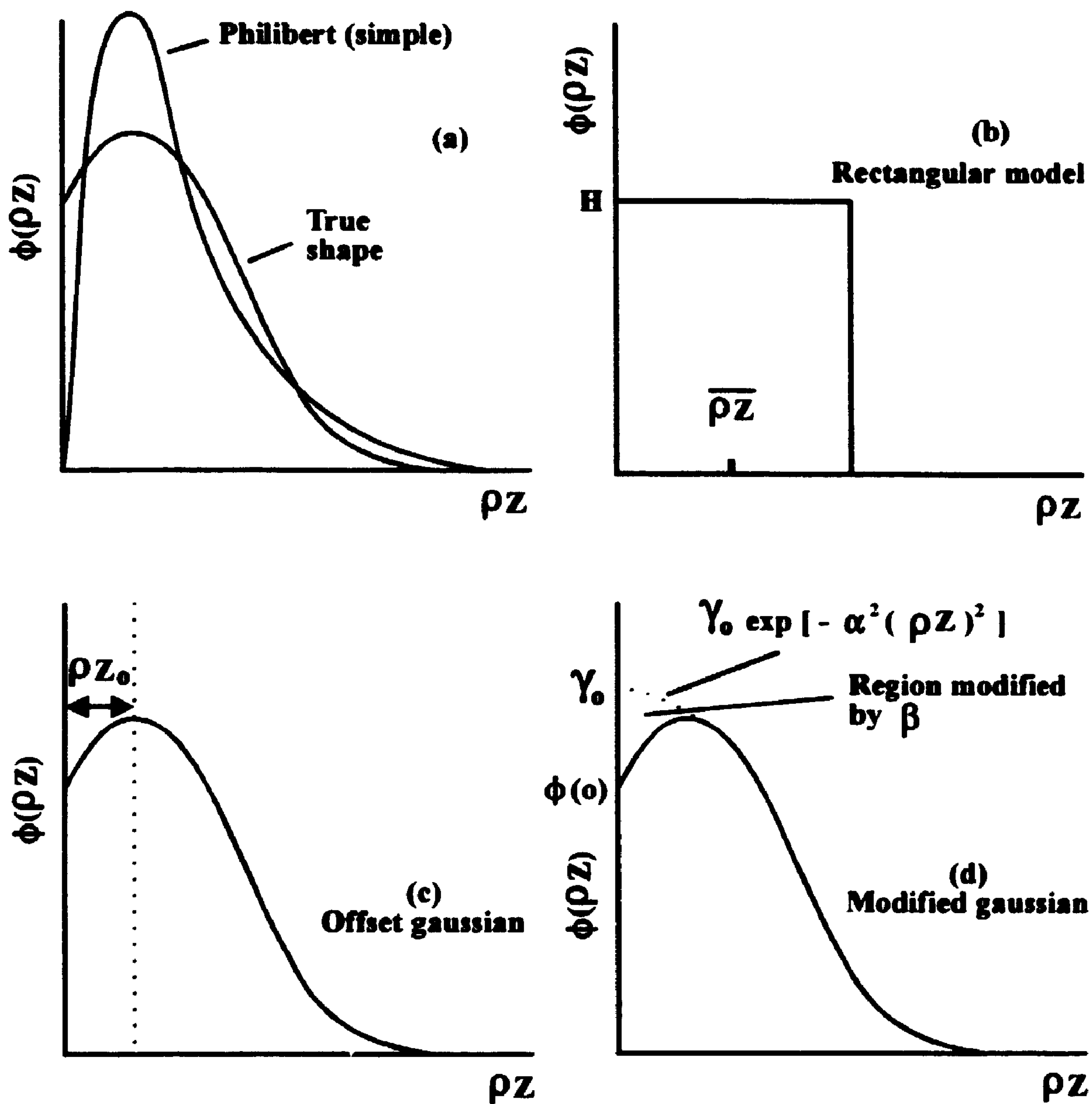

Figure 8 (a,b,c and d). Different shapes of $\phi(\rho z)$ curves from Philibert, Bishop, Wittry and Packwood and Brown.

$$\overline{\rho z} = \frac{\int_0^\infty \phi(\rho z) \cdot \rho z \cdot d(\rho z)}{\int_0^\infty \phi(\rho z)\, d(\rho z)} \qquad \text{(Eqn. 18)}$$

An alternative empirical curve fitting approach is possible in determining the generated x-ray depth distribution curves by using the experimental $\phi(\rho z)$ data by tracer measurements and simulated $\phi(\rho z)$ data by Monte Carlo calculations. Wittry [60] proposed that $\phi(\rho z)$ could be represented by a gaussian profile with the peak at some depth along the mass depth axis (Figure 8c).

$$\phi(\rho z) = A \cdot \exp\left[-\left(\frac{\rho z - \rho z_o}{\Delta \rho z}\right)^2\right] \qquad \text{(Eqn. 19)}$$

where A is a constant, ρz_o is the mass depth of the peak and $\Delta\rho z$ is proportional to the half-width of the gaussian. A modification of this function was suggested by Kyser [61] to take account of the asymmetry of the distribution about the peak value. He simply subtracted an exponential term giving

$$\phi(\rho z) = A_1 \exp\left[-\left(\frac{\rho z - \rho z_o}{\Delta \rho z}\right)^2\right] - A_2 \exp\left(-\frac{b \rho z}{\rho z_o}\right) \qquad \text{(Eqn. 20)}$$

where A_1, A_2 and b are constants. Tanuma and Nagashima [62] adopted the original idea of Wittry and represented $\phi(\rho z)$ as a gaussian profile which is displaced by some distance from the origin. In the updated version [63], a second gaussian centred at the surface is subtracted from the displaced gaussian curve in order to obtain a

reasonable $\phi(o)$ value. They normalize the $\phi(\rho z)$ curve using the mean value of x-ray production. The equation which resulted is

$$\begin{aligned}\phi(w) &= 0.664\exp[-0.665^2-(w-0.3)^2] \\ &\quad -0.2\exp[-10.4329w^2]\end{aligned} \qquad \text{(Eqn. 21)}$$

where

$$w = \frac{\rho z}{\overline{\rho z}} \qquad \text{(Eqn. 22)}$$

and $\overline{\rho z}$ can be expressed as a function of incident electron energy, critical excitation potential, the atomic number and the atomic weight of the material.

Buchner et al. [64, 65, 66] developed the wedge method to measure $\phi(\rho z)$ curves and derived an empirical expression for $\phi(\rho z)$, given by:

$$\phi(\rho z) = a \cdot n \cdot (a\rho z)^{n-1}\exp[-(a\rho z)^n] \qquad \text{(Eqn. 23)}$$

where a is a function of E_o and E_c and n is a function of Z. This equation has the same problem as the simple Philibert model in that $\phi(o)$ equals to zero. Buchner [67] extended the application to light elements by shifting the $\phi(\rho z)$ curve to obtain a realistic $\phi(o)$ value and a better agreement for small ρz.

Extensive tracer experiments were carried out by Parobek and Brown [23] which were the basis for deducing an analytical expression for $\phi(\rho z)$. The Parobek-Brown approach is essentially empirical and is given by:

$$\phi(\rho z) = D \cdot k \cdot n[k(\rho z+\rho z_o)]^{n-1}\exp[-(k(\rho z+\rho z_o))^n] \qquad \text{(Eqn. 24)}$$

The parameters D, k, n and ρz_o were obtained by fitting the equation to numerous measured $\phi(\rho z)$ curves using a simplex optimization process. The

dependence of the four parameters on E_o, E_c, Z and A were from appropriate plots of the optimized parameters. Brown and Robinson [68] extended these $\phi(\rho z)$ curves by publishing parameters suitable for higher electron beam energies.

On the basis of an analysis of experimentally measured $\phi(\rho z)$ curves, in particular from Parobek and Brown [23], Packwood and Brown [1] adopted a gaussian profile for the $\phi(\rho z)$ curve with the centre of the gaussian at the surface and introduced a 'transient function' near the surface to account for the directed nature of the original electron beam. The basis for the Packwood and Brown gaussian model is that a plot of $\ln\phi(\rho z)$ versus the square of the mass depth is a straight line which has been confirmed by a large number of published experimental $\phi(\rho z)$ curves. This implies that x-ray production does not decrease in an exponential fashion with increasing depth but rather in a gaussian or normal distribution fashion. The modified gaussian (Figure 8d) has the following form:

$$\phi(\rho z) = \gamma_o \exp(-\alpha^2(\rho z)^2)\left[1 - \left(\frac{\gamma_o - \phi(o)}{\gamma_o}\right)\exp(-\beta\rho z)\right] \quad \text{(Eqn. 25)}$$

The constants α, β and γ_o given originally by Packwood and Brown were derived from physical considerations on the interaction between electrons and target atoms modified by fitting to experimental data. The value of α establishes the rate at which the $\phi(\rho z)$ decays from the maximum of the gaussian. It is derived on the assumption of a random walk by individual electrons. The value γ_o is the amplitude of the gaussian function. It represents what the $\phi(o)$ value would be if the incident electrons were incident from random directions instead of in a collimated beam. As the

electron beam at and just below the surface of the specimen is still collimated, the rate at which electrons are generating x-rays in the surface and near surface layers is not at a maximum. This region is described by a transient function and β is related to how quickly the electrons that originally travel in a specific direction become randomized by scattering by the atoms of the solid. A particular advantage of the form of Eqn. (25) is that the integral of the gaussian can be solved in closed form. It can be shown mathematically [70] that the combined [ZA] correction has the form:

$$[ZA] = \frac{\{\gamma_o erfc(\frac{\chi}{2\alpha}) - [\gamma_o - \phi(o)]\, erfc(\frac{\beta+\chi}{2\alpha})\}_{specimen} \cdot \alpha_{standard}}{\{\gamma_o erfc(\frac{\chi}{2\alpha}) - [\gamma_o - \phi(o)]\, erfc(\frac{\beta+\chi}{2\alpha})\}_{standard} \cdot \alpha_{specimen}} \quad \text{(Eqn. 26)}$$

where erfc(x) represents the value of the complementary error function for the argument in parentheses.

The parameters in the modified gaussian approach have been optimized by Brown and Packwood [69], Bastin et al. [70] and Bastin and Heijligers [71] who extended the application to ultralight elements. Efforts were also made by Tirira and Riveros [72], Tirira et al. [73] and Giorgio [74] to further improve the performance of the original model.

Pouchou and Pichoir [75, 76] proposed that the x-ray depth distribution is described by a smoothly joined pair of parabolae. The $\phi(\rho z)$ curve is defined by four parameters: the surface ionization function ($\phi(o)$), the depth at which the maximum in the $\phi(\rho z)$ curve occurs (R_m), the x-ray range (R_x) and the area under the $\phi(\rho z)$ curve (Figure 8e). The resulting curve is given by:

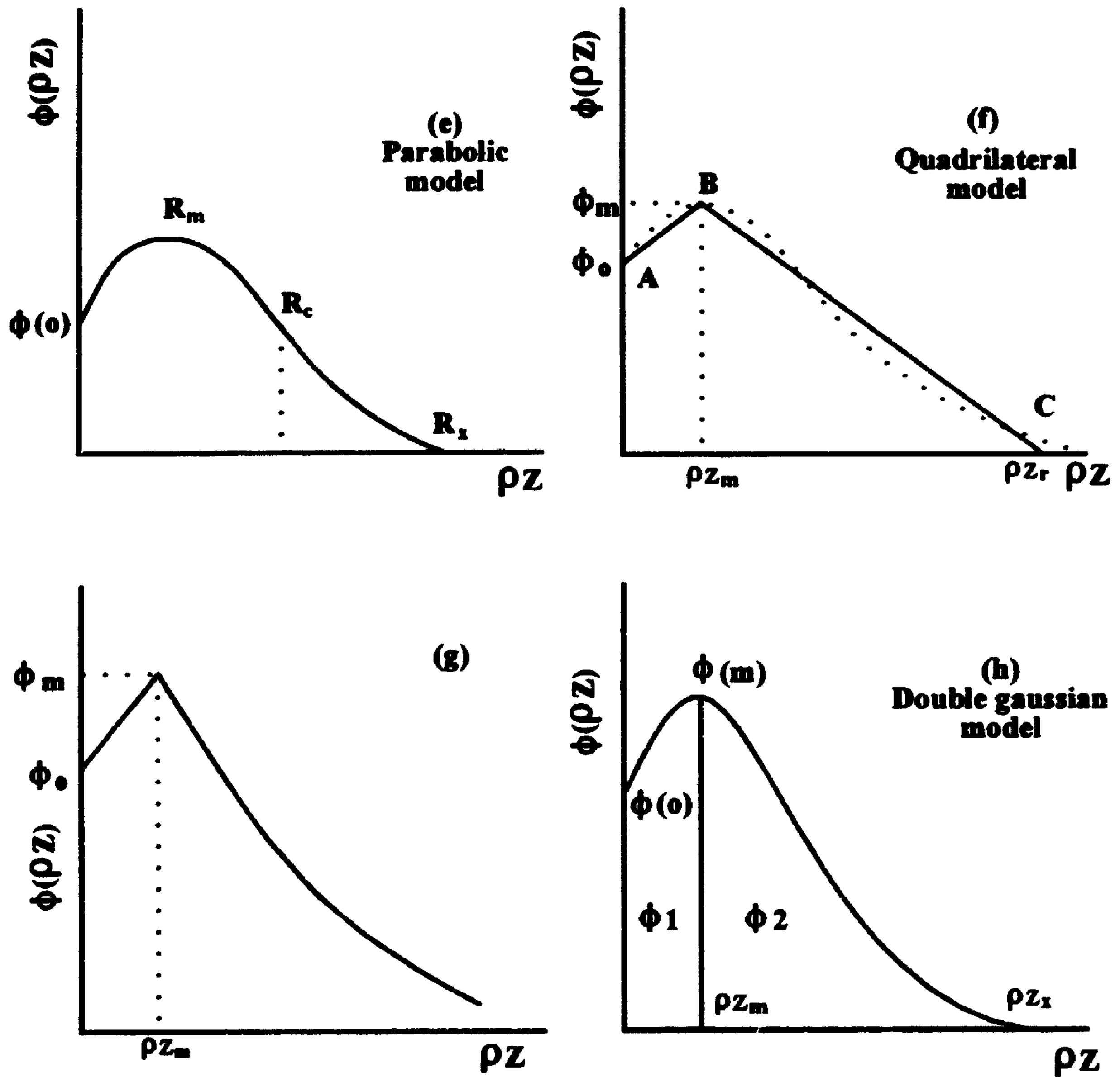

Figure 8 (e,f,g and h). Different shapes of $\phi(\rho Z)$ curves from Pouchou and Pichoir, Love et al., Gaber and Merlet

$$\phi(\rho z) = \begin{cases} A_1(\rho z - R_m)^2 + B_1 & for \quad 0 \le \rho z \le R_c \\ A_2(\rho z - R_x)^2 & for \quad R_c < \rho z \le R_x \end{cases} \qquad \text{(Eqn. 27)}$$

where A_1, A_2 and B_1 are expressed in terms of R_m, R_x, $\phi(o)$ and R_c which is the crossover point of the parabolae. Pouchou and Pichoir [77] modified their original model and later developed a simplified model [78] which gives $\phi(\rho z)$ in the following form:

$$\phi(\rho z) = A\exp(-a\rho z) + (B\rho z + \phi_o - A)\exp(-b\rho z) \qquad \text{(Eqn. 28)}$$

where the parameters a, b, A and B are derived from ϕ_o, the total generated intensity, the slope of $\phi(\rho z)$ at the surface and the mean depth of x-ray production.

In the quadrilateral model of Love et al. [79] and Sewell et al. [19], $\phi(\rho z)$ was approximated by two straight line segments joining the points A, B and C on the curve (Figure 8f). Point A represents the magnitude of x-ray generation at the sample surface, point B refers to the height and position of the maximum and point C is close to the x-ray range. The resulting function is:

$$\phi(\rho z) = \begin{cases} \phi(o) + [\phi_m - \phi(o)] \cdot \dfrac{\rho z}{\rho z_m} & for \quad 0 \le \rho z \le \rho z_m \\ \phi_m \left(\dfrac{\rho z_r - \rho z}{\rho z_r - \rho z_m}\right) & for \quad \rho z_m \le \rho z \le \rho z_r \end{cases} \qquad \text{(Eqn. 29)}$$

Formulation of the parameters ρz_m, ρz_r, ϕ_m and $\phi(o)$ are described in Sewell et al. [80].

Gaber [81] modified the quadrilateral model by assuming that $\phi(\rho z)$ increases linearly with the depth ρz up to the depth ρz_m at which the function $\phi(\rho z)$ reaches its maximum value ϕ_m and then subsequently decreases exponentially with increasing ρz.

Therefore, the shape of $\phi(\rho z)$ is still described by two segments, the first being linear but the second decreasing exponentially (Figure 8g).

Merlet [82] proposed that $\phi(\rho z)$ could be approximated by a double partial gaussian profile (Figure 8h) in which the profile was described by three values which are at the surface $(0, \phi(o))$, at the maximum of the $\phi(\rho z)$ curve $(\rho z_m, \phi_m)$ and at the x-ray range $(\rho z_x, \phi_{m/100})$. $\phi(\rho z)$ is expressed as:

$$\phi(\rho z)\begin{cases}\phi_1=\phi_m\exp\{-(\frac{\rho z-\rho z_m}{\beta})^2\} & for \quad 0\le\rho z\le\rho z_m\\ \phi_2=\phi_m\exp\{-(\frac{\rho z-\rho z_m}{\alpha})^2\} & for \quad \rho z_m\le\rho z\le\rho z_x\end{cases} \qquad \text{(Eqn. 30)}$$

where β is a function of $\phi(o)$, ϕ_m and ρz_m and α is a function of ϕ_m, ρz_m and ρz_x

August and Wernisch [83] derived a theoretical model for calculating $\phi(\rho z)$ based on a single electron scattering model making use of physical quantities which include electron transmission, backscattering coefficients, angular distributions and ionization cross-section. August and Wernisch [84] claimed that their predicted $\phi(\rho z)$ curves agree well with measured ones.

The assessment employed in order to evaluate the performance of different $\phi(\rho z)$ models for microanalysis usually refers to a histogram with its horizontal axis labelled as k'/k, where k is the measured x-ray intensity ratio for the element of interest and k' is the predicted intensity ratio with a given specimen composition. The wider the range of composition and experimental conditions used in the analysis, the more comprehensive the evaluations would be. When k'/k =1, the correction is working properly, while k'/k <1 indicates overcorrection and vice versa. The mean

value of k'/k, the skewness of the distribution and the root mean square error are all taken as evaluation criteria. Ultralight element (Z<11) data are usually separately assessed due to uncertainty in the accuracy of mass absorption coefficient and difficulties in x-ray measurements. Recent assessments were made and reviewed by Scott and Love [85], Riveros and Castellano [86] and Scott et al. [87]. In general the better the agreement between the predicted and the true shape of the $\phi(\rho z)$ curve, the more accurate the model would be for all systems. At present, a successful correction procedure should give a rms error of less than 3% for heavier element analysis whereas for ultralight element analysis a 5% rms error is considered satisfactory.

3.5 AN EXAMPLE OF THE $\phi(\rho z)$ METHOD

The following example is meant to demonstrate how one can make use of the $\phi(\rho z)$ equations and the combined ZA correction to calculate the true content of an unknown; in this case, an alloy of 95 wt% Cu and 5 wt% Al. These data are for an electron energy of 15 keV and a 40° x-ray take-off angle. Figure 9(a-b) shows the calculated $\phi(\rho z)$ curves for AlKα for the alloy and pure element. The dotted curves show the portion of the x-rays which can escape from the specimen. Note that for the generated curves, the alloy curve lies above the pure aluminum curve indicating that more x-rays are generated per unit concentration in the alloy which has a higher average atomic number. Quantitatively, the atomic number correction in terms of Figure 9 is:

$$Z = \frac{Area(1) + Area(2)}{Area(3) + Area(4)} \qquad \text{(Eqn. 31)}$$

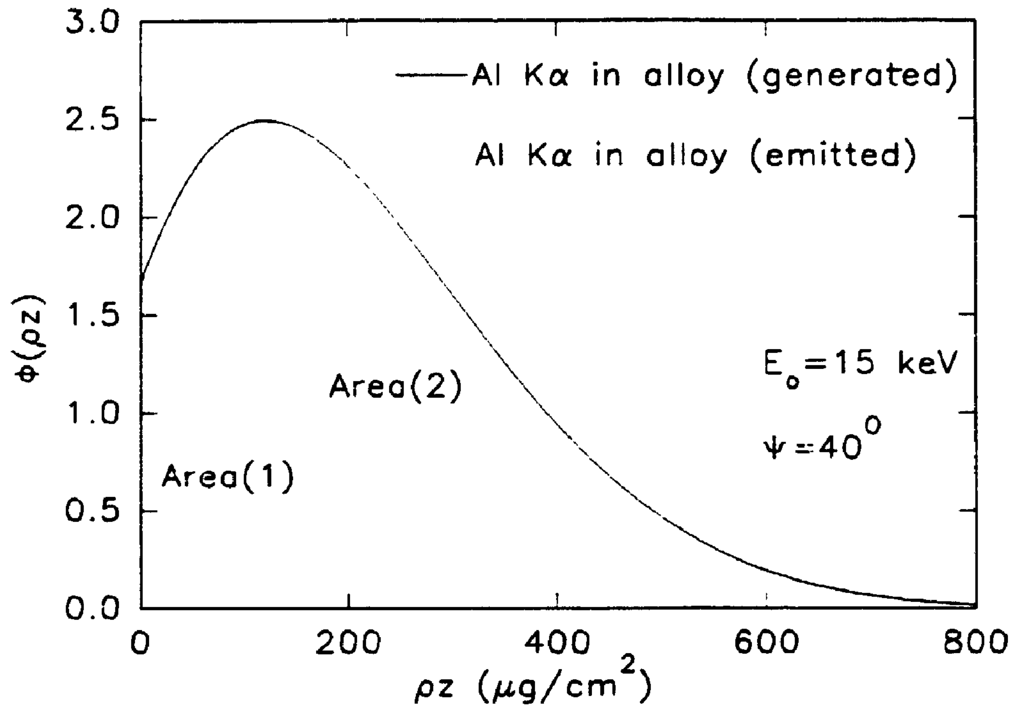

Figure 9a. Schematic of the emitted and generated $\Phi(\rho z)$ curves for Al Kα from a Cu−5wt% Al alloy.

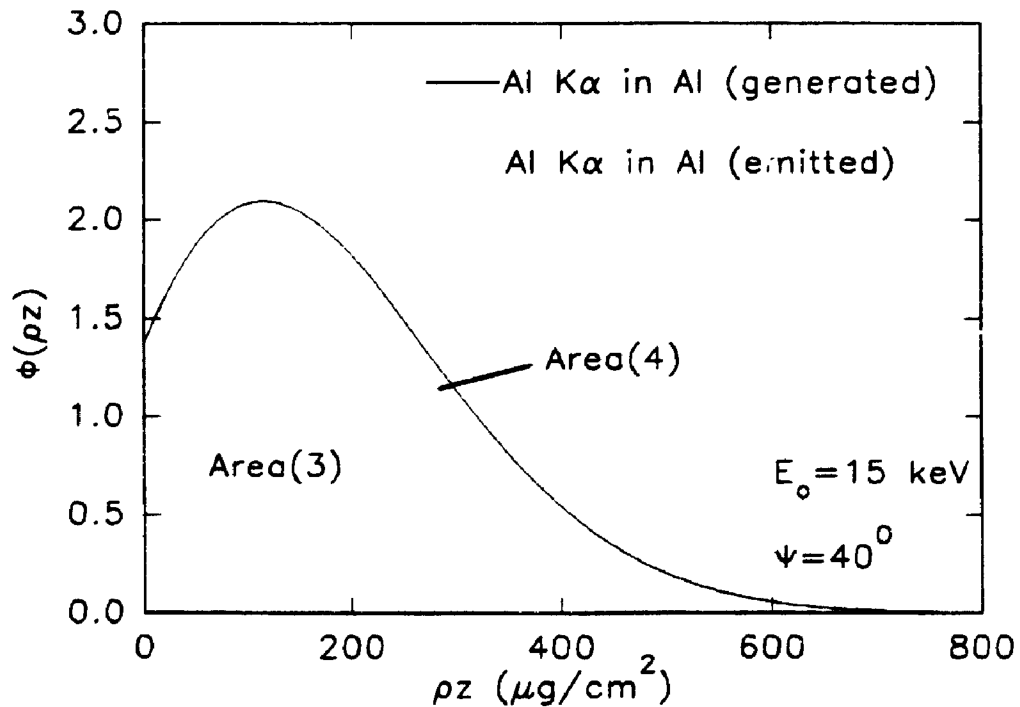

Figure 9b. Schematic of the emitted and generated $\Phi(\rho z)$ curves for Al Kα from a pure Al standard.

The fraction of x-rays which escape from the alloy is:

$$f(\chi)_{AlCu} = \frac{Area(1)}{Area(1) + Area(2)} \quad \text{(Eqn. 32)}$$

and from the pure element is:

$$f(\chi)_{Al} = \frac{Area(3)}{Area(3) + Area(4)} \quad \text{(Eqn. 33)}$$

The absorption correction is then:

$$A = \frac{\dfrac{Area(1)}{Area(1) + Area(2)}}{\dfrac{Area(3)}{Area(3) + Area(4)}} \quad \text{(Eqn. 34)}$$

Clearly, the fraction of x-rays absorbed in the alloy is much greater than in pure element. The combined correction gives:

$$ZA = \frac{Area(1)}{Area(3)} \quad \text{(Eqn. 35)}$$

Since characteristic fluorescence does not occur in this system, the measured k-ratio

$$k_{Al} = 0.05 * \frac{Area(1)}{Area(3)} \quad \text{(Eqn. 36)}$$

will be less than the weight fraction since x-ray absorption is the dominant effect in this system. These results are tabulated in Table 1.

In an actual analysis, the k-ratio is measured and the concentration calculated which requires an iterative procedure since the actual $\phi(\rho z)$ curve is unknown until the composition is known.

TABLE 1: ABSORPTION AND ATOMIC NUMBER CORRECTION FOR AN ALLOY (Cu-5 wt% Al)

Sample	X-ray Line	$\phi(\rho z)_{generated}$	$\phi(\rho z)_{emitted}$	A	Z	ZA
Pure Al Standard	Al Kα	Area (3) + Area (4)	Area (3)	1.00	1.00	1.00
Alloy (Cu-5 wt% Al)	Al Kα	Area (1) + Area (2)	Area (1)	$\dfrac{\frac{Area(1)}{Area(1)+Area(2)}}{\frac{Area(3)}{Area(3)+Area(4)}}$	$\dfrac{Area(1)+Area(2)}{Area(3)+Area(4)}$	$\dfrac{Area(1)}{Area(3)}$

CHAPTER 4

MONTE CARLO SIMULATION OF BULK $\phi(\rho z)$ CURVES

4.1 ELECTRON INTERACTION WITH SOLIDS

Electrons on entering a solid specimen undergo scattering processes which control their subsequent behaviour. Understanding these processes is important in optimizing and extending the use of electron beams. This chapter will specifically address x-ray generation by electrons, the understanding of which is crucial in electron probe microanalysis.

Electron scattering is the interaction between a moving electron and the target atoms that results in a change in the electron trajectory, direction of travel and/or energy. Electron-specimen interactions can be divided into elastic scattering and inelastic scattering. In elastic scattering, the direction of the moving electron changes but the kinetic energy remains unchanged. Each electron is scattered by Coulombic interaction with the charge of the atomic nucleus of the target atom (Rutherford scattering), as partially screened by the orbital electrons. In general, less than 1 eV of energy is transferred from the beam electron to the nucleus; this loss is negligible compared to the incident energy which ranges from up to 30 keV on entering the specimen and down to E_c at which energy they are no longer capable of exciting x-rays in x-ray microanalysis applications. Elastic scattering angles lie in the range of 0-π radians (0°-180°) with the most probable value per interaction being less than 5°. Thus, for most elastic scattering events, the electron continues to travel in the same

general direction and very rarely in a single event is its direction of motion reversed. Elastic scattering is responsible for most of the angular scattering phenomena such as electron backscattering.

In inelastic scattering, energy is transferred from the beam electrons to those in the atoms. Depending on the particular process, a single inelastic event can transfer any amount of energy ranging from a fraction of an electron volt to the entire energy carried by a given electron. As a consequence, this can lead to the generation of characteristic and continuum x-rays, Auger electrons, secondary electrons, lattice vibrations (phonons) and electron plasma oscillations in metals (plasmons). This type of electron-electron scattering process causes the incident electron to lose energy but with relatively little angular deflection, typically less than 0.1°.

In discussing scattering, two key concepts emerge that are closely related, cross-section and mean free path. Cross-section is a measure of the probability that an event will occur. It is usually denoted by the symbol Q or σ with dimensions of cm^2. Mean free path is the average distance an electron travels in the specimen between events of a certain type. Mean free path is usually denoted by the symbol λ or Λ with dimensions of cm. Mean free path is related to cross-section by the following relation:

$$\lambda = \frac{A}{N_A \rho \sigma} \quad cm \qquad \text{(Eqn. 37)}$$

where A is the atomic weight (g/mol)

N_A is the Avogadro's number (6.02×10^{23} atoms/mol)

ρ is the density (g/cm^3).

The mean free path for a certain type of event is obtained by substituting the appropriate cross-section σ into Eqn. (37). Thus λ can be calculated for elastic scattering and that is a crucial calculation used in models to describe electron interactions.

4.2 THE MONTE CARLO METHOD

One method to develop microanalytical correction procedures is to formulate a model of the interaction of the electron beam with the specimen. Monte Carlo electron trajectory simulation is one method which provides a powerful tool for theoretical studies of electron interactions in solid targets. The great power of the Monte Carlo technique arises from the stepwise treatment used to construct each electron trajectory in the target. This approach provides a continuous record of electron position and kinetic energy. The technique was first applied to microprobe analysis in the early 1960s by Green [88] and Bishop [89] and has since been revolutionized by modern high speed and low-cost computing. Progress was reviewed in 1975 at a special workshop organized by the NBS [90], subsequent advances have been reported primarily at the Microbeam Analysis Society and ICXOM meetings. Recently, a book was written by Joy [91] who reviewed his most up to date work on Monte Carlo method.

The Monte Carlo procedure is based on the simulation of a large number of trajectories of primary electrons within the target and averaging the results. The

effects of elastic and inelastic scattering are based on probabilities calculated from appropriate models to determine scattering angles, distances between scattering sites and energy loss rates. From these parameters and equations of analytical geometry, the electron trajectory can be simulated in a stepwise fashion from the location at which it enters the specimen to a final point at which either the energy has decreased to an arbitrary cut-off energy such as the critical excitation potential for a particular shell due to inelastic scattering or the electron passes through the surface of the target and escapes. From the product of the ionization cross-section and the path length for each small section of the electron trajectory, calculated for thousands of trajectories, the probability of x-ray ionization in a given layer in the specimen may be summed to build up the distribution of x-ray production, $\phi(\rho z)$, with depth ρz below the surface. In general, direct comparison with experimental values needs to be made to evaluate the accuracy of the Monte Carlo simulation and the limits of applicability. These calculated $\phi(\rho z)$ curves are important since the total number of measured $\phi(\rho z)$ curves are limited and are available only for a certain range of incident electron energies and target materials. In addition, quantities such as the position and energy distributions of electrons in the specimen that are not obtainable directly by experiment can also be calculated by the Monte Carlo technique.

Several assumptions are necessary to make the calculations practical. First, the crystalline structure and lattice orientation of the solid is ignored. That is, atoms are assumed to be distributed randomly as if in an amorphous solid. The effects of inelastic large angle scattering are also neglected. Individual trajectories differ sharply

from each other because of the random nature of individual scattering events, therefore a large number of trajectories, typically 10,000, must be followed to achieve statistical significance. The precision of a Monte Carlo calculation depends on the number of events calculated, with the standard deviation, σ, given by:

$$\sigma = n^{1/2} \qquad \text{(Eqn. 38)}$$

where n refers to the number of trajectories which contribute to the event of interest. Sometimes relative standard deviation is used and is given by:

$$RSD = \frac{\sigma}{n} = \frac{1}{n^{1/2}} \qquad \text{(Eqn. 39)}$$

4.3 SINGLE SCATTERING MODEL

The basic structure of a single scattering Monte Carlo code for bulk specimens is as follows: the length of the basic repetitive step is usually set equal to the elastic mean free path for the electrons. From the rate of energy loss due to inelastic scattering, the decreasing energy can be calculated along the path of the electron. After the electron travels a distance equal to a mean free path, the next scattering site is reached and a new scattering angle is chosen for the next step based upon the new value of the energy. The scattering angle is calculated only from expressions based upon elastic scattering since inelastic scattering causes negligible angular deviation (see Bishop in ref. [90], p.6). In short, it is assumed that all scattering events which produce directional changes are elastic and that between such collisions the electron travels in a straight line, losing energy continuously.

Cross-sections for the individual inelastic scattering processes are difficult to obtain for the target. Instead, an average rate of energy loss for all inelastic processes grouped together is denoted by dE/ds where s represents the distance travelled in the target. The continuous energy loss expression of Bethe [92] provides a useful approximation for dE/ds for energies greater than 5 keV. It is represented by the following equation:

$$\frac{dE}{ds}\left(\frac{keV}{cm}\right) = -7.85x10^{4}\frac{Z\rho}{AE_m}\ln\left(\frac{1.166E_m}{J}\right) \qquad \text{(Eqn. 40)}$$

where Z is the atomic number

A is the atomic weight

ρ is the density

E_m is the average energy along the path segment s

J is the mean ionization potential.

The constant 1.166 is the square root of half the base of natural logarithm (see Heinrich in ref. [5], p.226). The mean ionization potential is the average energy loss per inelastic interaction considering all the energy loss processes and one approximation is given by Berger and Seltzer [93] as:

$$J(keV) = (9.76Z+58.5Z^{-0.19})*10^{-3} \qquad \text{(Eqn. 41)}$$

Many other expressions have been reported for J (see Heinrich in ref. [5], p. 231) but, fortunately, any uncertainty in J enters via a logarithmic term in the Bethe equation and hence the sensitivity to this uncertainty is reduced accordingly. For the calculation of the elastic scattering cross-section and ionization cross-section, the mean

energy of the electron at a particular step must be known. This is calculated by applying a Runge-Kutta type numerical method to the Bethe equation. The energy loss ΔE along a segment of path of length s is given by

$$\Delta E = s\left(\frac{dE}{ds}\right) \quad \text{(Eqn. 42)}$$

The continuous slowing down assumption is very attractive because of its simplicity and low computer cost as no detailed consideration of inelastic interaction processes are used in this scheme. For a $\phi(\rho z)$ calculation, mass depth (g/cm^2) is used instead of linear depth (cm). Hence, the stopping power is simply the continuous energy loss expression expressed in terms of mass depth units (g/cm^2) rather than linear distance units (cm).

Before calculating the scattering angle, a coordinate system needs to be established. Since the direction of the electron changes relative to its current direction at each scattering event, there are clearly two important frames of reference to consider. First, there is the laboratory frame. Second, there is the frame which co-moves with the electron. This frame undergoes many sudden relative changes in its reference directions. For calculation of x-ray production, the laboratory frame is the most convenient to use as the fundamental frame of reference. On the other hand, the physics and kinematics of the scattering events are most simple to describe in the co-moving frame. Therefore, the geometrical relation between the two frames must be found. The chosen convention is as follows: The positive Z axis is normal to the specimen surface and directed into the specimen, the X axis is parallel to the tilt axis, the X-Y plane is the surface plane of an untilted flat specimen and the Y axis

completes a right hand set of axes. Figure 10 shows the laboratory frame of reference and Figure 11 shows the scattering frame of reference.

In the laboratory frame, the angles after the scattering event θ_{n+1}, ϕ_{n+1} can now be determined in terms of the angles prior to the event θ_n, ϕ_n and the scattering angle θ and the azimuthal angle ϕ. Electron interaction with a solid is a 3-D phenomenon but as far as the $\phi(\rho z)$ depth distribution is concerned, the Z coordinate is sufficient to locate the electron in the forward direction. The new Z coordinate can be calculated from the following two equations:

$$\cos\theta_{n+1} = \cos\theta_n\cos\theta + \sin\theta_n\sin\theta\cos\phi \qquad \text{(Eqn. 43)}$$

$$Z_{n+1} = Z_n + s_n\cos\theta_{n+1} \qquad \text{(Eqn. 44)}$$

where s_n is the step length of the electron.

Elastic scattering results from the deflection of the beam electron by the positive charge of the nucleus of the atom, as screened by the orbital electrons. Because a convenient analytic formula exists for the screened Rutherford cross-section, it is mathematically simple to implement in a Monte Carlo simulation. The elastic cross-section can be calculated for any electron energy and scattering atom of interest. The discussion of the concept of Rutherford scattering and the complete derivation of its related formulae were reviewed throughoutly by Reimer [94].

Electrons from a parallel beam which pass thro[illegible] area $d\sigma$ are scattered into a cone of solid angle $d\Omega$. The ratio $d\sigma/d\Omega$ is called the differential cross-section which represents the probability of an incident electron being scattered per unit solid angle Ω by a given atom. A total cross-section can then be found by integrating over

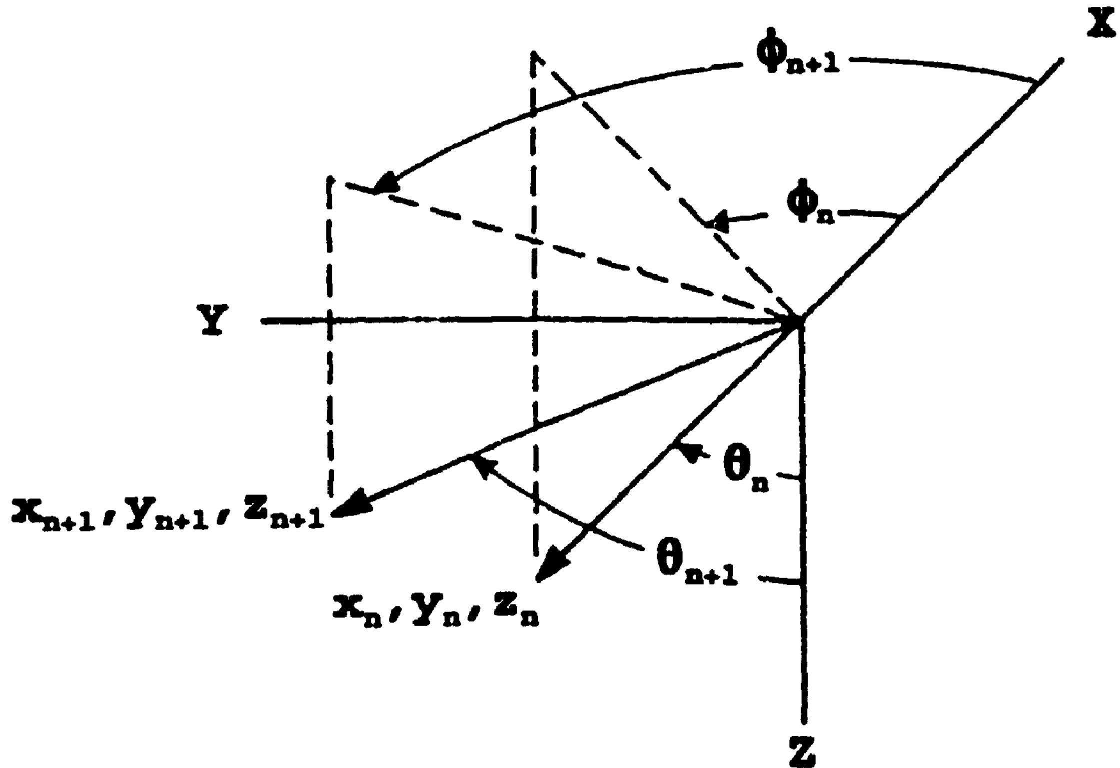

Figure 10. Schematic diagram of laboratory frame of reference.

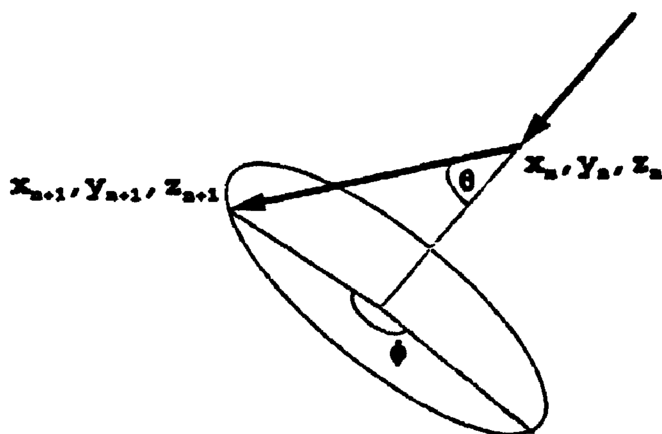

Figure 11. Schematic diagram of scattering frame of reference.

the complete range of angles. After solving the related equations (see ref. [95]), two important final equations are found. The total elastic scattering cross-section $\sigma(E)$ is given by:

$$\sigma(E) = const.\ \frac{Z^2}{E^2}\frac{\pi}{\alpha(1+\alpha)} \quad \text{(Eqn. 45)}$$

The probability for elastic scattering into an angular range from zero to a given angle θ or the distribution function is given by:

$$P(\theta) = (1+\alpha)\{1-\frac{2\alpha}{1-\cos\theta+2\alpha}\} \quad \text{(Eqn. 46)}$$

α in Eqns. (45) and (46) is the screening parameter and has been given by Henoc and Maurice [90] as:

$$\alpha = \frac{3.4x10^{-3}Z^{2/3}}{E(keV)} \quad \text{(Eqn. 47)}$$

According to Eqn. (45), elastic scattering is more probable for high atomic number materials and for low electron energy. The effect of elastic scattering is to randomize the trajectories, hence for low atomic number material, randomization may only occur at a depth relatively far from the surface of the material. The mean free path, λ, was calculated by substituting Eqn. (45) into Eqn. (37). Recall that λ represents the average distance that an electron will travel between encountering elastic scattering events. The actual distance that an electron travels between successive scatterings will of course vary in a random fashion. The probability P(s) of an electron travelling a distance s without any scattering, when the mean free path is λ, is given by:

$$P(s) = \exp(-s/\lambda) \qquad \text{(Eqn. 48)}$$

An estimate for the distance actually travelled can then be found by sampling this distribution with a random number R_s which involves solving:

$$R_s = \frac{\int_0^s \exp(-s/\lambda)\,ds}{\int_0^\infty \exp(-s/\lambda)\,ds} \qquad \text{(Eqn. 49)}$$

Solving and rearranging will give:

$$s = -\lambda \ln R_s \quad for \quad 0 < R_s < 1 \qquad \text{(Eqn. 50)}$$

where s is the step length.

The right nand side of Eqn. (46) represents the probability of the electron being scattered through an angle less than θ. For any given scattering event, a random number is pulled from the computer, equated to the probability in order to choose an angle for which this value of probability would be appropriate. So Eqn. (46) becomes:

$$R_\theta = \frac{(1+\alpha)(1-\cos\theta)}{1+2\alpha-\cos\theta} \qquad \text{(Eqn. 51)}$$

Rearranging and isolating cosθ on the left hand side,

$$\cos\theta = 1 - \frac{2\alpha R_\theta}{1+\alpha-R_\theta} \qquad \text{(Eqn. 52)}$$

where θ is the scattering angle.

The azimuthal angle ϕ is assumed to be uniformly distributed around the axis

of the electron travelling direction. Hence, in principle, it can be any angle between 0 and 2π and ϕ is given by:

$$\phi = 2\pi R_{\phi} \quad for \quad 0 < R_{\phi} < 1. \qquad \text{(Eqn. 53)}$$

Therefore, three random numbers need to be generated in each iteration. They are required for Eqns. (50), (52) and (53) respectively.

The value of electron energy for a given step in the simulation is used for the calculation of the ionization cross-section. Therefore, the trajectory of the electron is followed incrementally through the target, at all time knowing the electron's position, energy and direction of motion. The accuracy of the calculation is limited by the accuracy of the cross-sections used for calculation of the scattering angles and mean free path and also the model used for the ionization cross-section.

The single scattering treatment results in simpler equations but lengthy calculations owing to the greater number of steps. This is because the mean free path is proportional to energy and therefore the step length gets progressively smaller along the electron trajectory and the total number of steps per trajectory can be very large.

4.4 THE MULTIPLE SCATTERING MODEL

Calculations for the single scattering model are very time consuming and expensive. The multiple scattering model allows elastic scattering events to be grouped together giving a fixed number of steps in a condensed path rather than treating each elastic scattering event individually. Therefore, the elementary path length in the calculations may be an order of magnitude greater than the mean free

path. Consequently, the number of steps in the calculation as well as the computing time is reduced. In other words, the electron trajectory is arbitrarily divided into segments and the scattering acts within each segment are replaced by a single hypothetical scattering event. The parameters of this hypothetical event are adjusted so that, on average, it would alter the path of the electron in the same way as the collisions that would occur in a real target along the same length of electron trajectory.

In the multiple scattering approach, the step length has been chosen in two ways. One way is to choose a constant length for each step throughout the trajectory for all trajectories. Bishop [89] and Henoc [90] adopted the fixed step length method as this was more convenient to use in conjunction with the scattering matrix method of recording the results. The relation is given by:

$$\Delta s_i = \frac{r}{N_t} \qquad \text{(Eqn. 54)}$$

where r is a range

N_t is the total number of steps which form the whole electron trajectory under consideration

For $\phi(\rho z)$ calculations, the range refers to the x-ray range. Therefore, the step length represents a constant fraction of the x-ray range.

The second way is to keep the mean number of scattering events in each step constant; this allows for increased scattering as the electron loses energy. The relation is given by:

$$\Delta s_i = \frac{E_i}{E_o} * \Delta s_o \qquad \text{(Eqn. 55)}$$

where E_i is the residual electron energy after the ith collision and Δs_o is the first step length, therefore

$$E_i = E_{i-1} - \left|\frac{dE}{ds}\right|_{E=E_{i-1}} * \Delta s_{i-1} \qquad \text{(Eqn. 56)}$$

Since this work is meant to improve on Henoc's program, the former multiple scattering approach will be discussed. In order to find the constant step length from Eqn. (54), r must be calculated. The total distance or full range travelled by an average electron is given by:

$$r = \int_{E_o}^{E=0} \frac{1}{dE/ds}\, dE \qquad \text{(Eqn. 57)}$$

The Bethe expression (Eqn. 40) for dE/ds can be used so that the integral gives the so-called Bethe range. The expression must be integrated numerically. An approximation to the integrated form of the equation is given by Henoc and Maurice [90] as:

$$r\,(cm) = \frac{J^2}{7.85x10^4} * \frac{A}{Z} * \frac{1}{\rho} * [EI(2\ln\frac{1.166E_o}{J}) - EI(2\ln\frac{1.166E_i}{J})]$$

(Eqn. 58)

where E_i = 1.03 J

J is the mean ionization potential

EI(x) is the exponential integral.

The value 1.03 is chosen to give convergence of the integral. For the purpose of x-ray range calculation, a particular inner-shell ionization energy E_c is used to substitute for E_i. The exponential integral EI can be represented by a series which converges in approximately 20 terms.

After finding the constant step length, computation of energies for every half-step and full-step is next. Values of half-step and full-step energies are calculated by integrating Bethe's equation using a fourth order Runge-Kutta solution. The values are stored in a table. The half-step energy is used in calculating scattering angles of equal probability and the full-step energy is used in calculating the value of ionization cross-section in each step.

The scattering at each step was calculated from the multiple scattering theory of Goudsmit and Saunderson [96] with the Rutherford single scattering cross-section modified to take account of screening of the nucleus by bound electrons, and a small additional modification to allow for angular deflections occurring in inelastic collisions. This convolution method is based on an electron being scattered a certain number of times, n, after which it has a certain direction, θ. The mathematics is rather complicated. Preparation of the set of angles of equal scattering probability is equally time consuming. A total of more than 100 lines of Fortran programming was used to accommodate this portion of the code. An important consequence of this change is the modification of the angular distribution of the scattered electrons from that given by Eqn. (52) to a more complex form. Therefore, the scattering angle θ or for that matter $\cos\theta$ was calculated differently inasmuch as step length is now

calculated by Eqn. (54) instead of Eqn. (50). The azimuthal angle calculation remains the same.

Usually the scattering point, where the electron changes its energy and direction of motion abruptly, may be taken at the beginning of each step. However, these simulations result in discrepancies from experimental results. Hence, Henoc introduced the concept of substeps in each step Δs_i, lengths of which were given by a random number R between zero and one. Therefore, the electron keeps its direction of motion of the previous step until a point determined by R as $R\Delta s_i$ is found. The electron will change its direction neither at the end point of Δs_{i-1} nor the end point of Δs_i but at the endpoint of a substep $R\Delta s_i$.

As far as the cross-section for inner shell ionization is concerned, numerous models can be found in the literature. These have been reviewed by Powell [[illegible] 97] and Rez [98]. The basic form of the cross-section is:

$$Q = const.\ \frac{\ln U}{E_c^2 U^a} \quad for \quad 0.7 \le a \le 1 \qquad \text{(Eqn. 59)}$$

where E_c is the critical excitation energy of the shell

U is the overvoltage ratio denoted by $U=E/E_c$

where E is the instantaneous energy.

4.5 MODIFICATIONS TO THE MULTIPLE SCATTERING MODEL

As seen in Chapter 3, Packwood and Brown [1] found for measured $\phi(\rho z)$ curves the plot of $\ln\phi(\rho z)$ versus $(\rho z)^2$ is a straight line. However, such plots tend to

be concave downward when the results of the Monte Carlo simulations of Henoc and Maurice [4] are used. Two such examples are shown in Figures 12 and 13. It can be seen that as the atomic number of the matrix element decreases, the non-linearity of the curve is more pronounced.

4.5.1 Electron Straggling

Electrons lose energy in penetration through matter. If one assumes that the energy loss is continuous along the electron path, the distance travelled until the electron comes to rest (or loses energy to some pre-determined value) must be a well defined value, the same for all electrons with the same initial energy in the same type of material. This is an assumption used in the Monte Carlo program of Henoc and Maurice. However, the passage of electrons through matter is much more complicated than is the case with heavier particles like protons. The differences are caused by the much smaller mass of the electron and its greater speed for the same energy. An electron will lose a large fraction of its energy in a single collision with an atomic electron with the result that straggling is much more marked in the case of electrons. Electrons are also scattered much more easily by nuclei and their paths are usually not straight. Therefore, the range, whether electron range or x-ray range, is a less precisely defined quantity for electrons. This concept has been supported experimentally by Tung et al. [99]. The energy loss is in fact not continuous but statistical in nature. Two identical electrons with the same initial energy will not in general suffer the same number of collisions and hence the same energy loss in

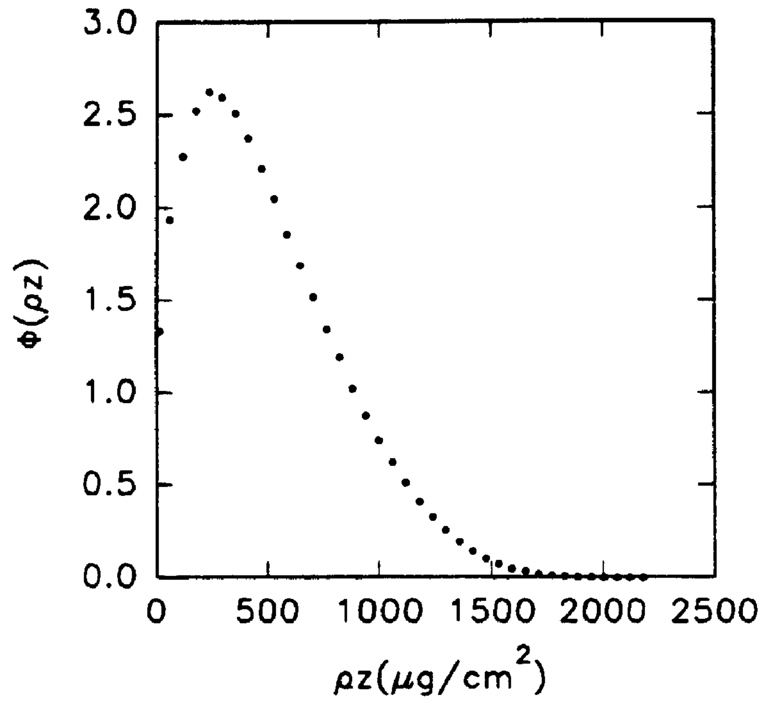

Figure 12a. Monte Carlo simulated $\Phi(\rho z)$ curve of Cu Kα from Cu at 30 keV from Henoc and Maurice [4].

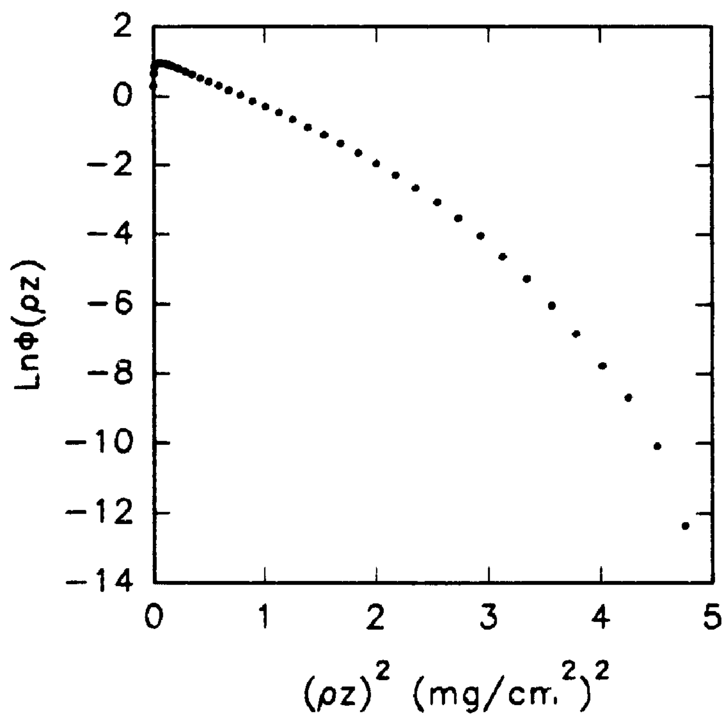

Figure 12b. Plot of $\ln\Phi(\rho z)$ versus $(\rho z)^2$ from figure 12a.

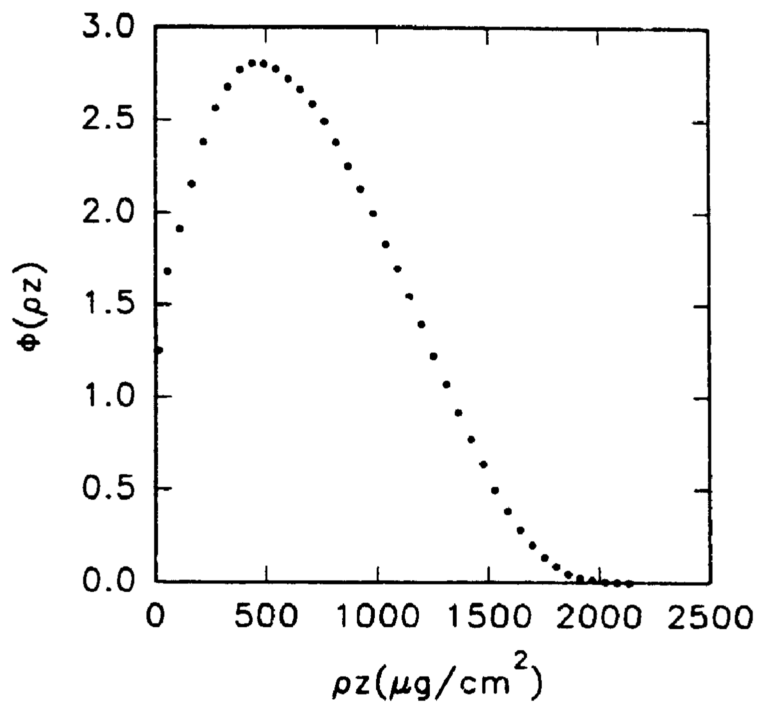

Figure 13a. Monte Carlo simulated $\Phi(\rho z)$ curve of Al Kα from Al at 30 keV from Henoc and Maurice [4].

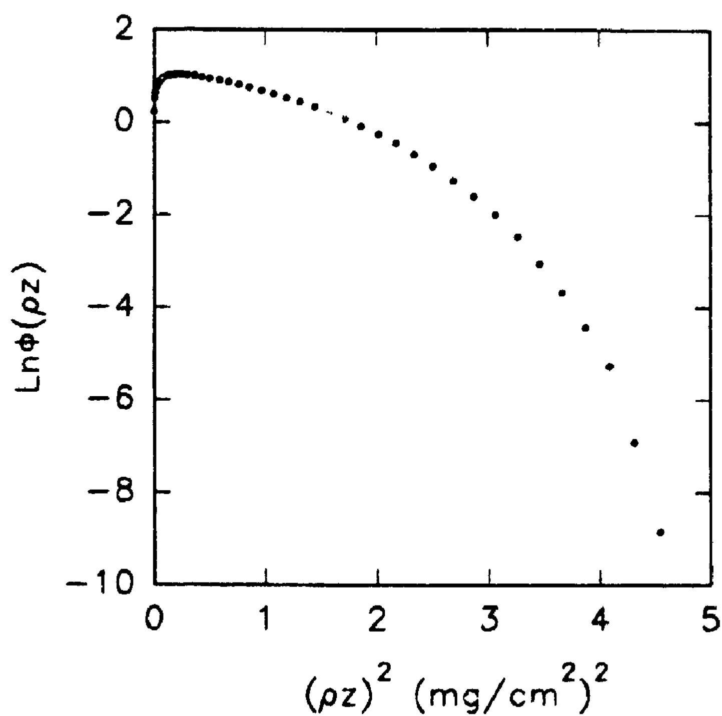

Figure 13b. Plot of $\ln\Phi(\rho z)$ versus $(\rho z)^2$ from figure 13a.

travelling the same distance through a material. Rather, a statistical distribution of ranges centred about some mean value is observed. This phenomenon is known as straggling. To a first approximation, the distribution of ranges is gaussian in form.

As far as the $\phi(\rho z)$ calculation is concerned, there is an effect of straggling on x-ray production. The total characteristic x-ray production is roughly proportional to the distance an electron travels before its energy is reduced to the excitation potential of the ionization of interest. Because of straggling, some electrons travel farther and others less far than average. Straggling becomes more important in the later stage of electron travel and as a consequence ionization can occur at increased depths as a result of the increased range of some electrons.

Equation (50) indicates in a single scattering model that instead of setting step length equal to the mean free path, it was actually modified by a random number. However, in Henoc's multiple scattering model, the range equation (Eqn. 58) takes no account of straggling effects which can blur the deceleration process. Recall that in the original program the step length is a constant for each step throughout the whole trajectory for all electron trajectories via Eqn. (54). One possible correction for the effects of straggling on x-ray production could be introduced by associating with each path length a distribution of energies about a mean and hence a distribution of ionization cross-sections about a mean. This calculation is quite complicated as pointed out by Landau [100] because the energy will become an extra variable that must be selected at random. Therefore, an approximate range straggling distribution was proposed instead. To incorporate the idea of range straggling, the modified

program will still use constant step length for each step within the same trajectory but a different step length from one electron to the next. The step length for each complete trajectory is now given by:

$$\Delta s_i = \frac{r}{N_t(1+a*(RND-0.5))} \qquad \text{(Eqn. 60)}$$

where Δs_i, r and N_t were defined in Eqn. (54),

RND is a random number, and

a is a constant where $0 < a < 1$.

The value of RND is supplied by the random number generator which can be linear or gaussian in nature. The following figure (Figure 14) illustrates the effect of this modification.

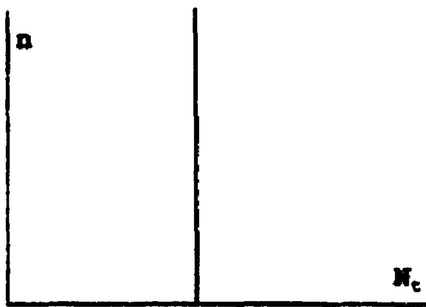

Figure 14a Unmodified

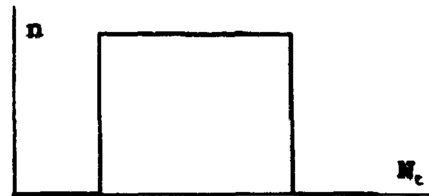

Figure 14b Modified with linear random number generator

Figure 14c Modified with gaussian random number generator

Electrons passing through targets of different atomic number will have a different degree of range straggling. Figure 15 shows the distribution of the x-ray range for 10,000 electron trajectories in an aluminum matrix using the gaussian random number generator.

In the multiple scattering Monte Carlo program, an energy table is pre-calculated to avoid the time consuming energy calculation for each electron trajectory. To implement the variable range, the size of the array of the original energy table had to be expanded. This was done by setting up an energy index table of 200 rows (previously the table had the same number of rows as the fixed number of steps) as if the value of N_t is 200 in Eqn. (54). This is required since a finer grid of electron energy from E_o down to E_c is needed to accommodate the variable step size. For each trajectory, instead of using all energy values from the table, energies for each specific electron trajectory were picked at regular intervals throughout the table. For example, if the number of steps calculated from the expression $N_t(1+a_s(RND-0.5))$ is 50, then each interval is simply 200 divided by 50 which equals four. It follows that 50 energies were chosen from the corresponding index of 4, 8, 12,...,196, 200.

4.5.2 Multiple Scattering Angles

The central idea of a multiple scattering model is that a large number of collisions can be condensed in one event which accounts for the combined effect of many single collisions. To derive the angular distribution of a multiple scattering event, Henoc and Maurice used a convolution method of Goudsmit and Saunderson

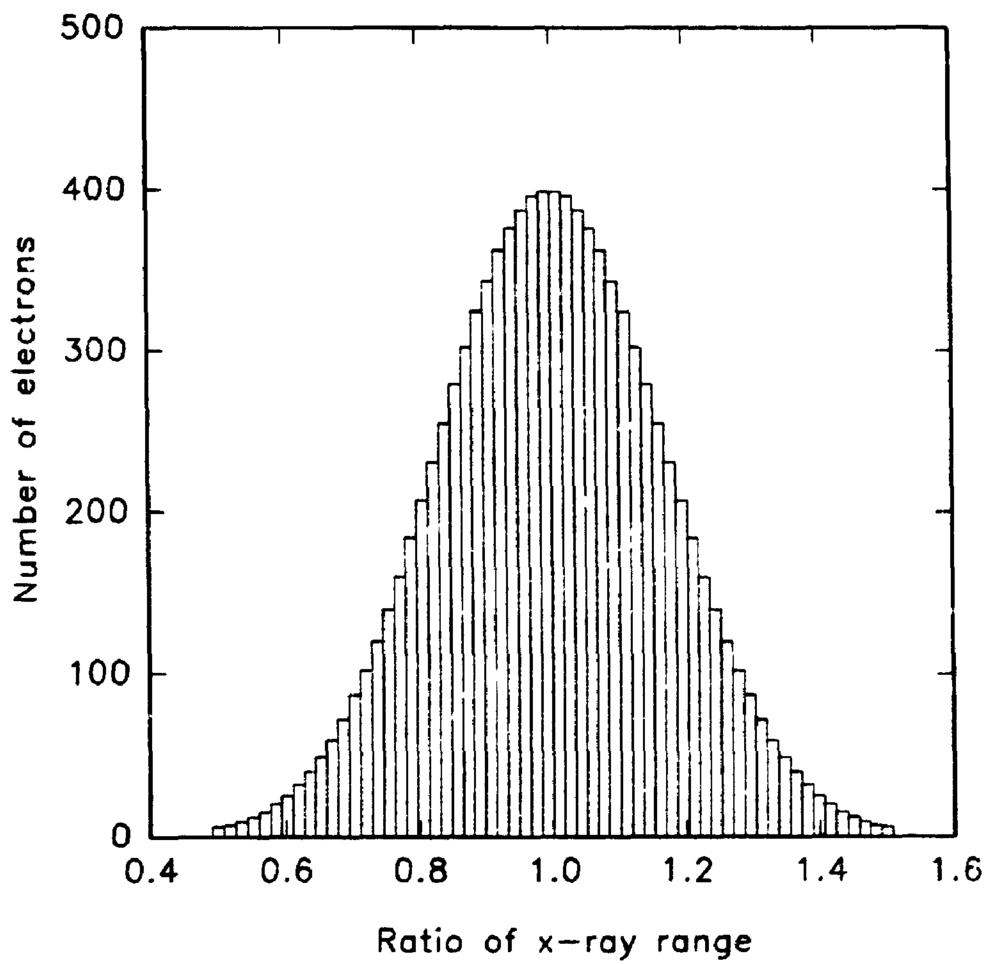

Figure 15. Range straggling assumed in an Al matrix.

2

PM-1 3½"x4' PHOTOGRAPHIC MICROCOPY TARGET
NBS 1010a ANSI/ISO #2 EQUIVALENT

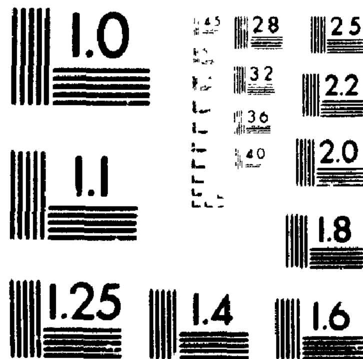

[96] which requires extensive arrays of calculated scattering angles and series expansions. Legendre coefficients were obtained from a simple recursive relationship. It is essential that precautions be taken to avoid rounding off errors. After some careful investigation of the code using specific input values to test the program, it was found that some of the series in fact did not converge in a reasonable number of terms. Depending on the choice of rounding error and the local maximum and local minimum of various functions, the outcome was not as straightforward as one might expect. In order to get the best result, some of the rounding parameters had to be changed for different systems of interest instead of using one universal value. Merlet [101] also reported that there are restrictions below 10 keV for Monte Carlo calculations based on the Goudsmit and Saunderson theory. The problem can be illustrated by a specific example. If the input E_o value is 10 keV, E_c is 8.98 keV for Cu Kα with an atomic number of 29 and atomic weight of 63.54, then the scattering angle distribution has a discontinuity and this is illustrated in Figure 16a. Also, for random numbers below 0.1, negative angles are calculated which are not allowed according to the definition used for scattering angles. As a result, the accuracy of the final $\phi(\rho z)$ distribution will be in jeopardy. Thus, the Henoc and Maurice program works quite well in some systems but gives incorrect results in others.

Werner and Heydenreich [102] developed another multiple collision scheme which is applicable in the energy range between 5 and 100 keV. A simple screened Rutherford cross-section was used to monitor the angular distribution of a multiple scattering event. Such a formula is exact for two limiting cases; a single scattering

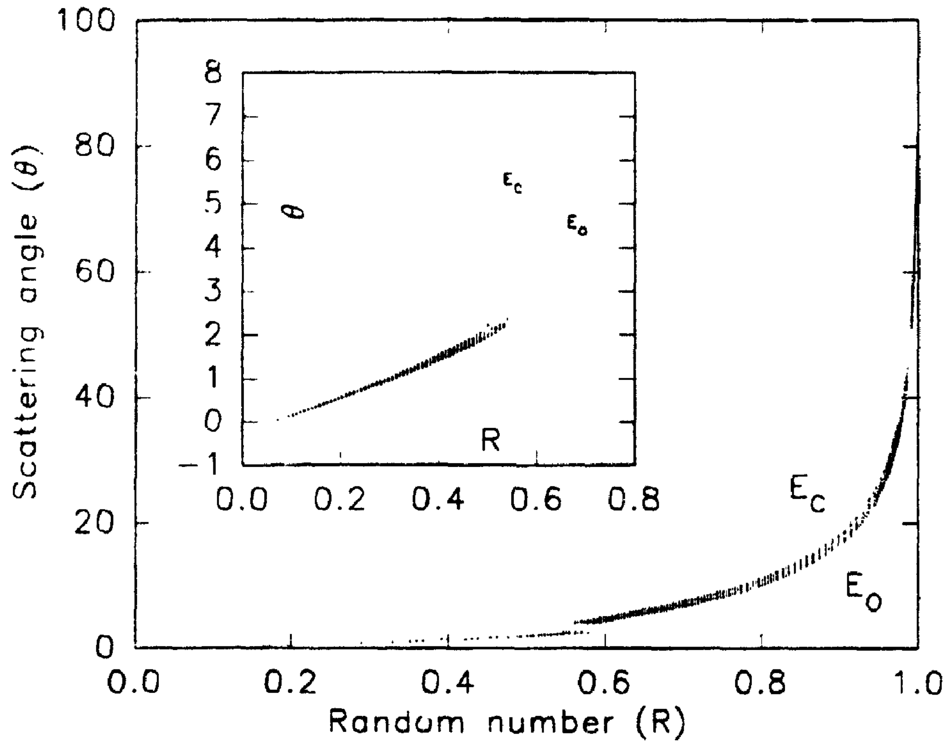

Figure 16a. Scattering angles for Cu Kα in Cu matrix at 10 keV from Henoc and Maurice [4].

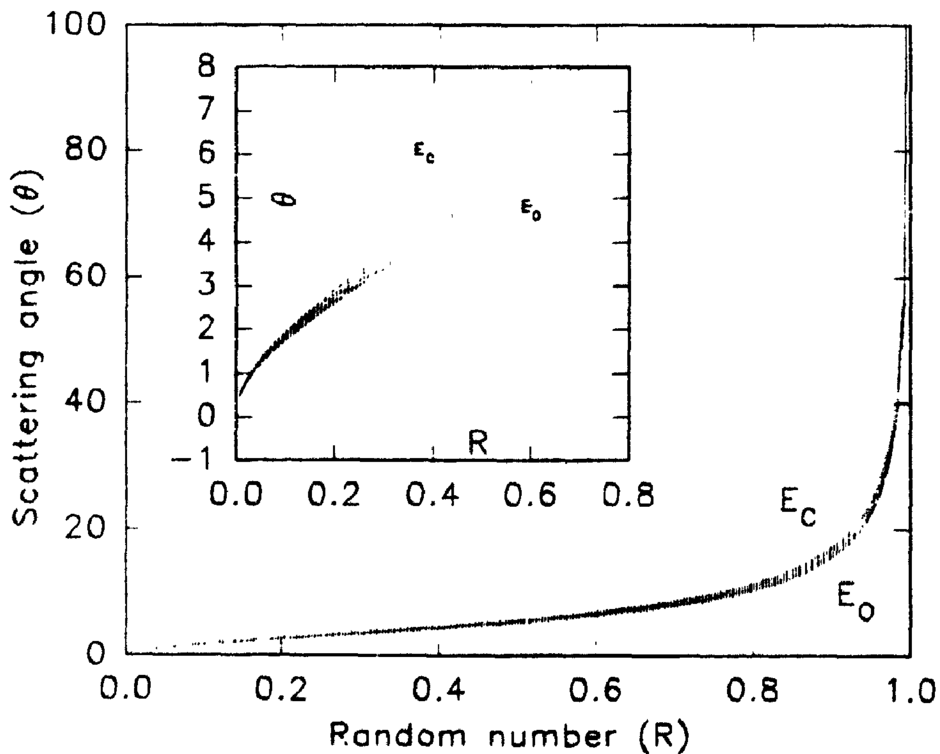

Figure 16b. Scattering angles for Cu Kα in Cu matrix at 10 keV from Werner and Heydenreich [102].

collision and an infinite number of collisions giving an isotropic distribution while a multiple scattering event presumably corresponds to an intermediate situation. The final result was the development of an equation for the screening parameter:

$$\alpha_i = \frac{C_1 Z^{2.4} f^{1.3} (\rho \Delta s)^{1.3}}{(C_2 A)^{1.3} E_i^{2.3}} \qquad \text{(Eqn. 61)}$$

where C_1 = 4.34 eV

C_2 = 4.43 nm gcm^{-3}/keV

$$f = 1 + \frac{0.8}{Z} \qquad \text{(Eqn. 62)}$$

The f factor is meant to include the inelastic angular scattering caused by the electron-electron interaction. This correction factor will have a bigger effect for low atomic number material. Calculation of the scattering angle θ is straightforward in that the α of Eqn. (61) is substituted into Eqn. (52). Figure 16b shows a plot of scattering angles using the new expression for α. The discontinuity is removed and there are no negative scattering angles. Comparisons between the old and new expressions for scattering angle show similar distributions for all systems. Examples are illustrated in Figures 17, 18 and 19 for Au, Cu and Al at 30 keV. Note that as the energy of the electron decreases from E_o towards E_c, the scattering angles increase due to an increase in the elastic scattering cross-section. This method of finding scattering angles has reduced the size of the computer program substantially yet has not sacrificed any accuracy in the determination of the scattering angles.

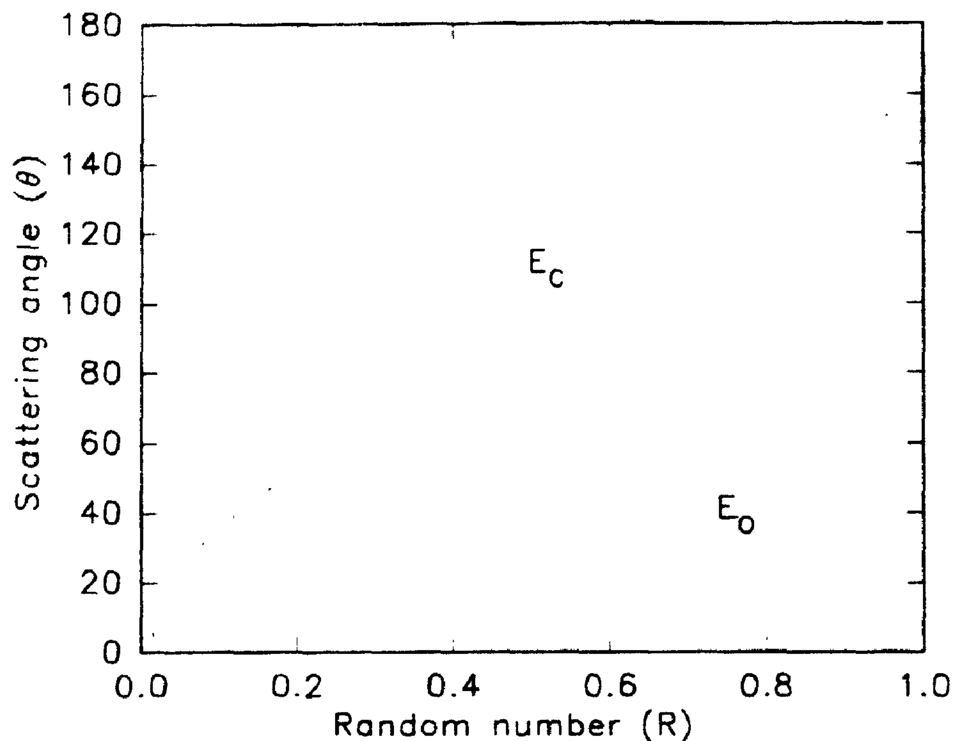

Figure 17a. Scattering angles for Au Mα in Au matrix at 30 keV from Henoc and Maurice [4].

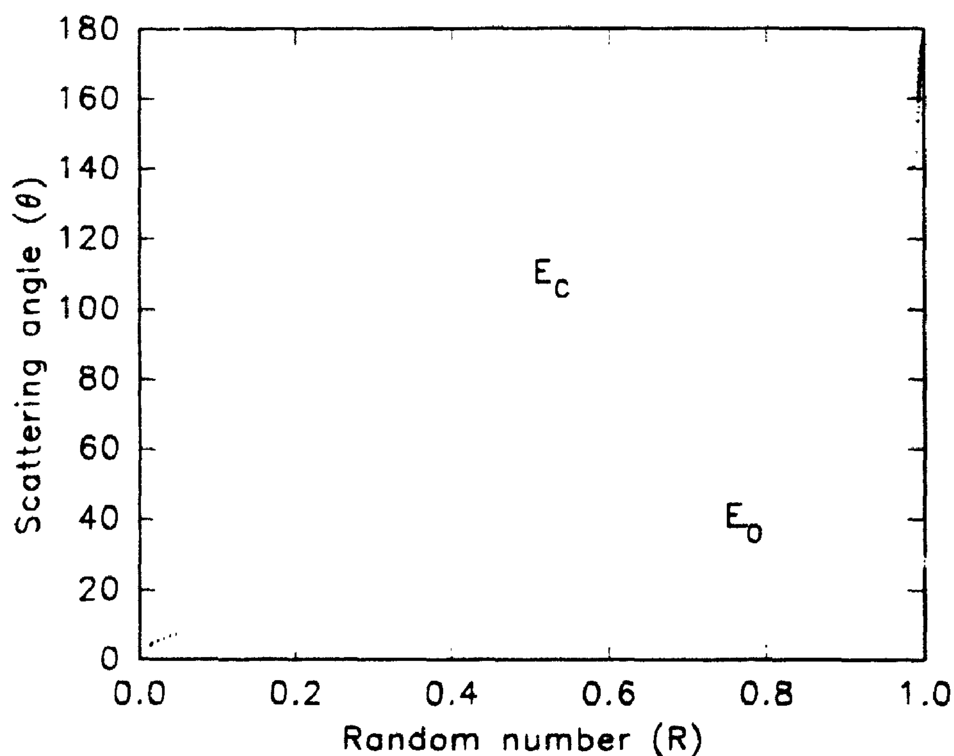

Figure 17b. Scattering angles for Au Mα in Au matrix at 30 keV from Werner and Heydenreich [102].

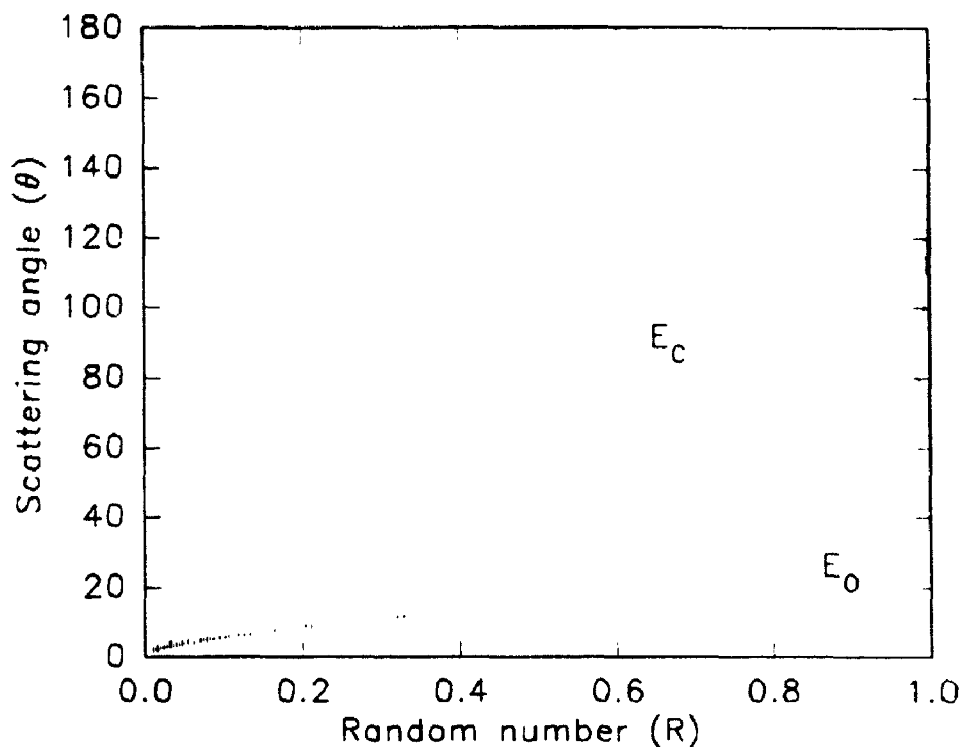

Figure 18a. Scattering angles for Cu Kα in Cu matrix at 30 keV from Henoc and Maurice [4].

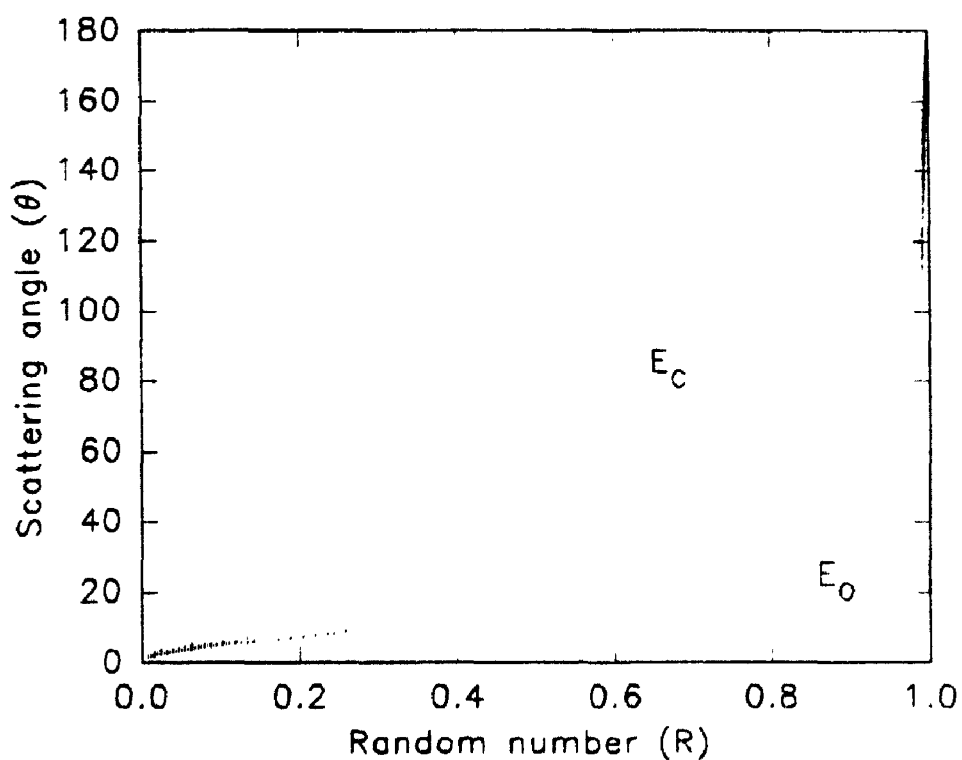

Figure 18b. Scattering angles for Cu Kα in Cu matrix at 30 keV from Werner and Heydenreich [102].

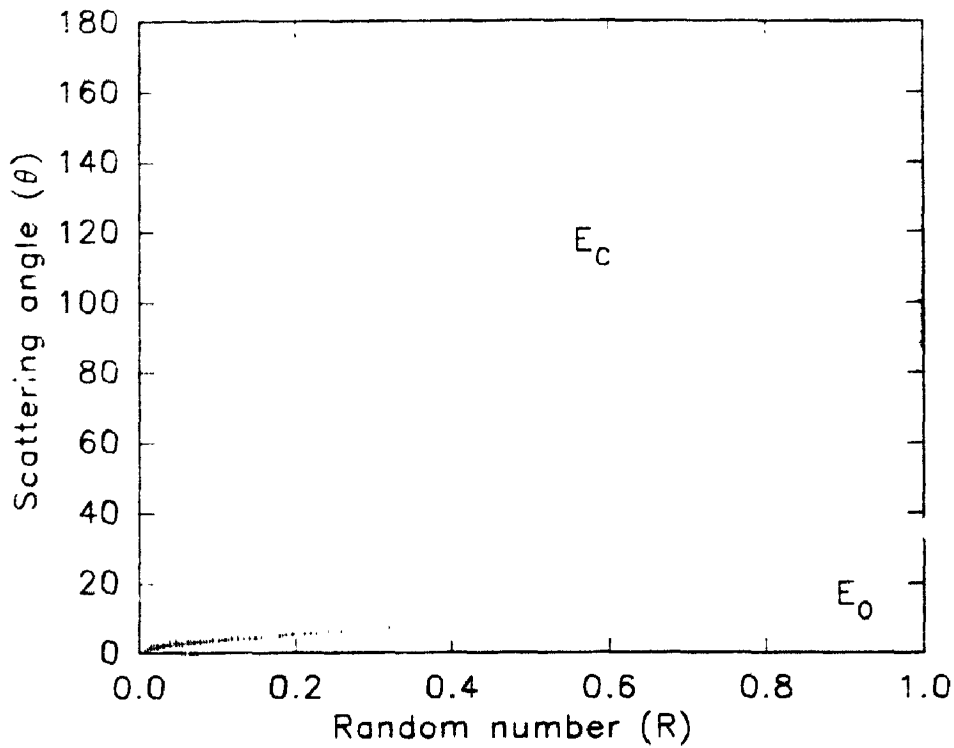

Figure 19a. Scattering angles for Al Kα in Al matrix at 30 keV from Henoc and Maurice [4].

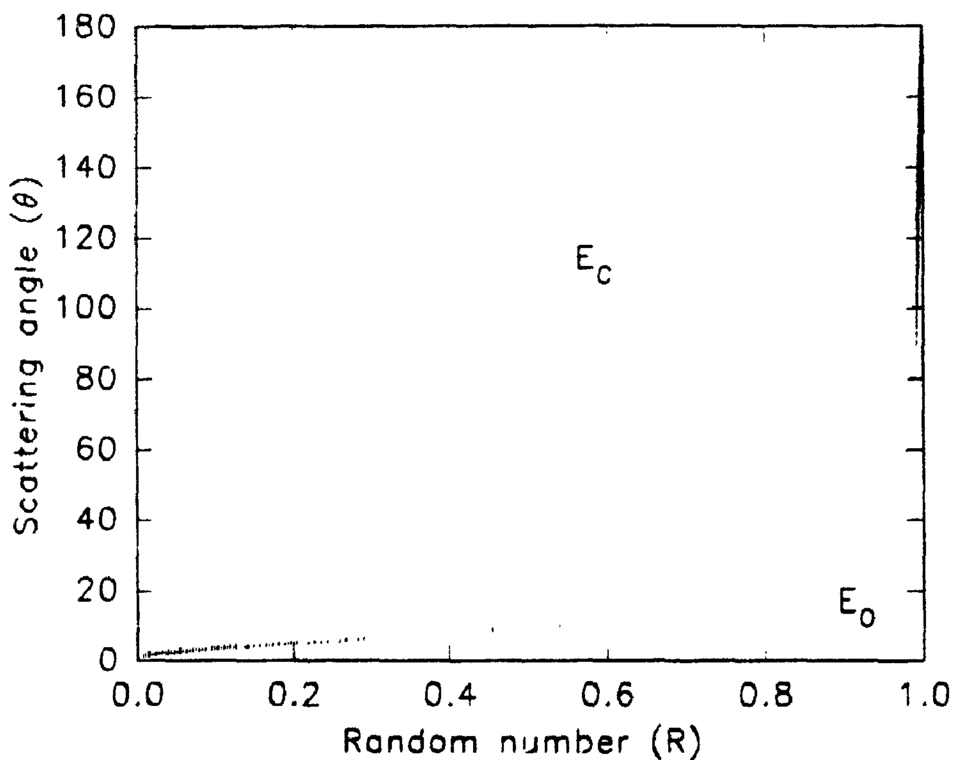

Figure 19b. Scattering angles for Al Kα in Al matrix at 30 keV from Werner and Heydenreich [102].

4.5.3 Other Changes

The surface ionization values, $\phi(o)$, calculated in the original program were found to be too small when compared with experimental data. In the original program, the electron position after each step is stored in an electron position table. The idea is to sum up all the electrons with the same energy and in the same layer so that the $\phi(\rho z)$ distribution can be calculated. The relation between electron position from the surface, z, and the layer number J is:

$$J = \frac{z}{\Delta z} + 1.5 \qquad \text{(Eqn. 63)}$$

where Δz is the layer thickness which was chosen to be equal to the step length. Equation (63) has the following implication given by:

$$IF \begin{Bmatrix} 0 < z/\Delta z < 0.5 \\ 0.5 < z/\Delta z < 1.5 \\ 1.5 < z/\Delta z < 2.5 \end{Bmatrix} \quad THEN \quad \begin{Bmatrix} J=1 \\ J=2 \\ J=3 \end{Bmatrix}$$

Thus the total number of electrons in the first layer is smaller than it should have been since some of the incident electrons never appear in the first layer. To overcome this problem, the initial position of the step was reduced to a half step and the electrons moved into the specimen without scattering. The exact position at the end of this first step, because of the introduction of straggling is approximately in the centre of the first layer. Likewise, the starting energy is now smaller than E_o as the electron is approximately half-way through the first layer at the start of the trajectory calculations. Equation (63), to calculate the layer index, was changed to:

$$J = z/\Delta z + 1.0 \qquad \text{(Eqn. 64)}$$

The situation becomes:

$$IF \begin{Bmatrix} 0 < z/\Delta z < 1.0 \\ 1.0 < z/\Delta z < 2.0 \\ 2.0 < z/\Delta z < 3.0 \end{Bmatrix} \quad THEN \quad \begin{Bmatrix} J=1 \\ J=2 \\ J=3 \end{Bmatrix}$$

Calculated $\phi(o)$ values now agree more closely with the experimental values.

To calculate the $\phi(\rho z)$ distribution, the number of electrons at each energy in a particular layer is multiplied by the ionization cross-section. Many expressions for ionization cross-section have been published but the following relation was used:

$$Q = const. \ \frac{\ln U}{E_c^2 U^{0.8}} \qquad \text{(Eqn. 65)}$$

This was chosen simply because it gives better agreement between Monte Carlo generated $\phi(\rho z)$ curves and experimental curves than the original model from Henoc and Maurice [4].

Conceptually, it should be better to use the half-step energy to calculate the ionization cross-section and full-step energy to calculate the scattering angle although in the original program the opposite was used. This has been changed, however no significant difference in $\phi(\rho z)$ curves was found as a result of this change.

4.6 RESULTS ON BULK SPECIMENS

Good agreement was found when comparing calculated $\phi(\rho z)$ curves based on the modified Monte Carlo method (Appendix 1) with experimentally measured $\phi(\rho z)$ curves. Three examples are given in Figures 20a, 21a and 22a for Cd Lα in Al at 30 keV, Cd Lα in Ag at 20 keV and Bi Lα in Al at 30 keV respectively. Experimental

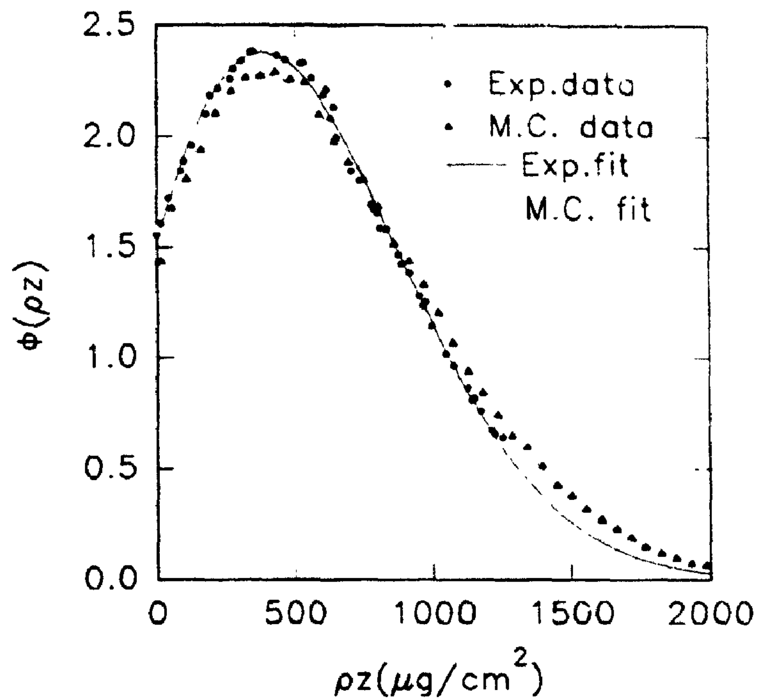

Figure 20a. Experimentally measured and Monte Carlo simulated $\Phi(\rho z)$ curves for Cd $L\alpha$ in Al at 30 keV.

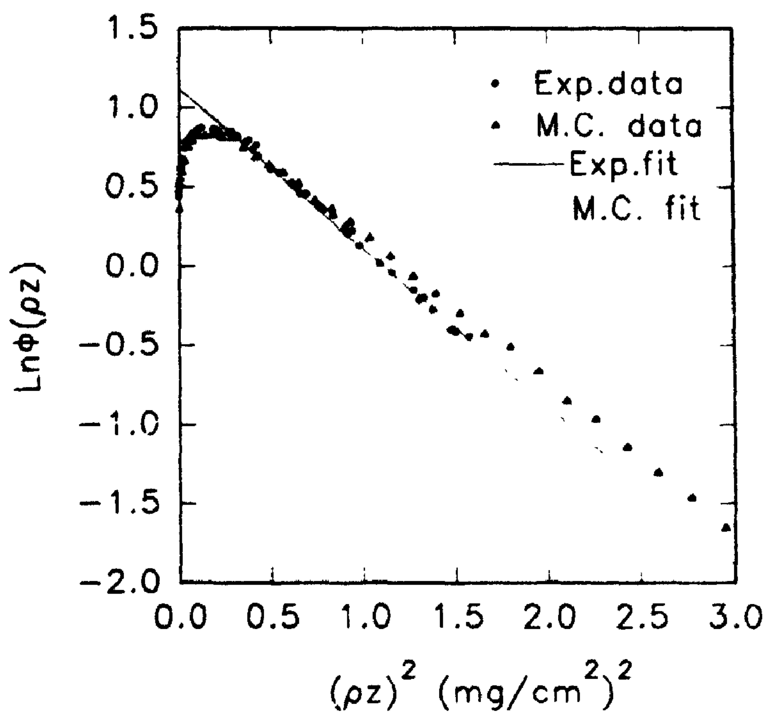

Figure 20b. Plots of $\ln\Phi(\rho z)$ versus $(\rho z)^2$ from figure 20a.

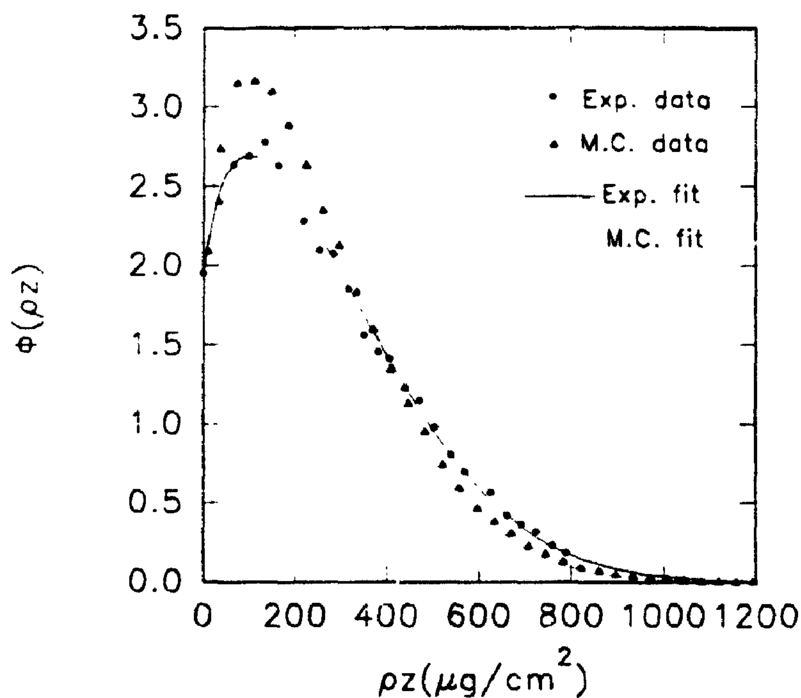

Figure 21a. Experimentally measured and Monte Carlo simulated $\Phi(\rho z)$ curves for Cd $L\alpha$ in Ag at 20 keV.

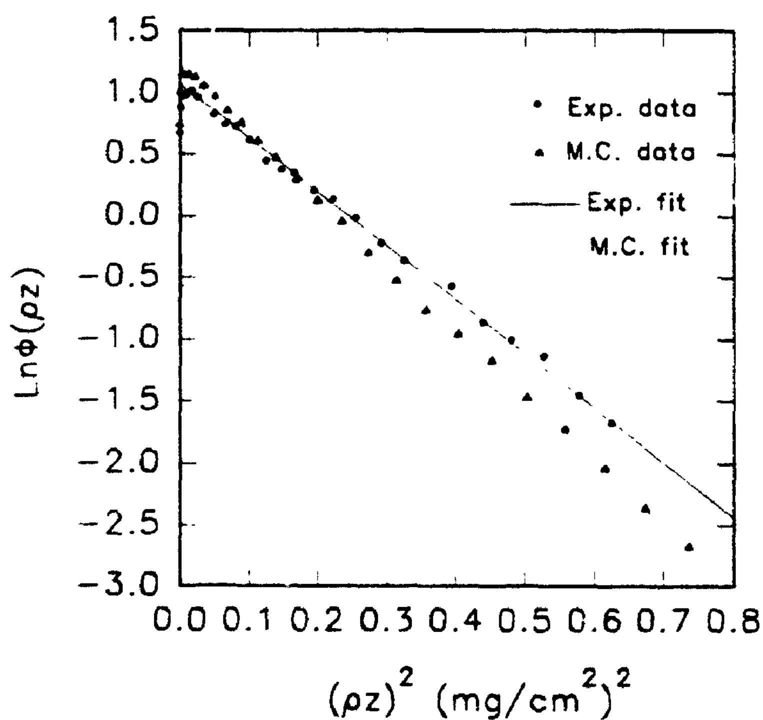

Figure 21b. Plots of $\ln\Phi(\rho z)$ versus $(\rho z)^2$ from figure 21a.

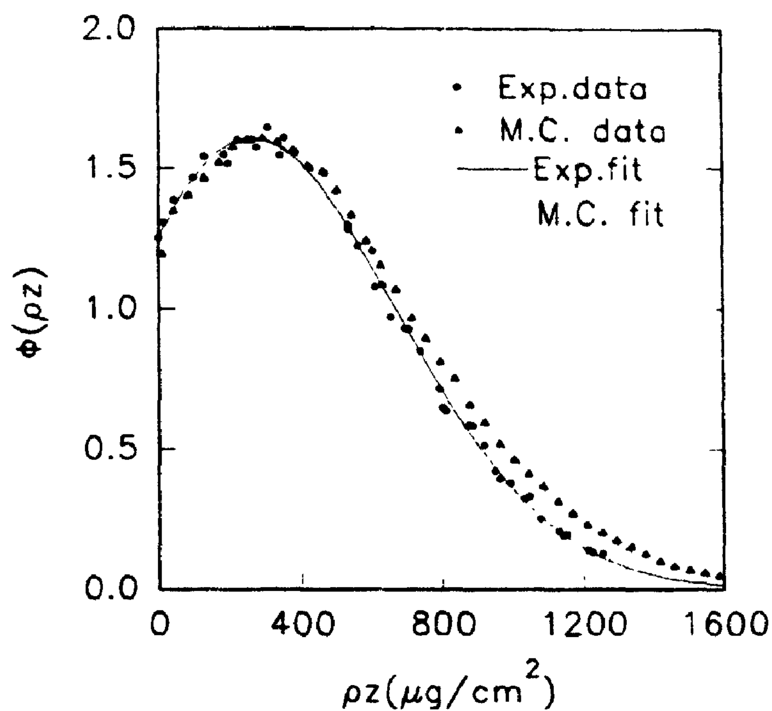

Figure 22a. Experimentally measured and Monte Carlo simulated $\Phi(\rho z)$ curves for Bi Lα in Al at 30 keV.

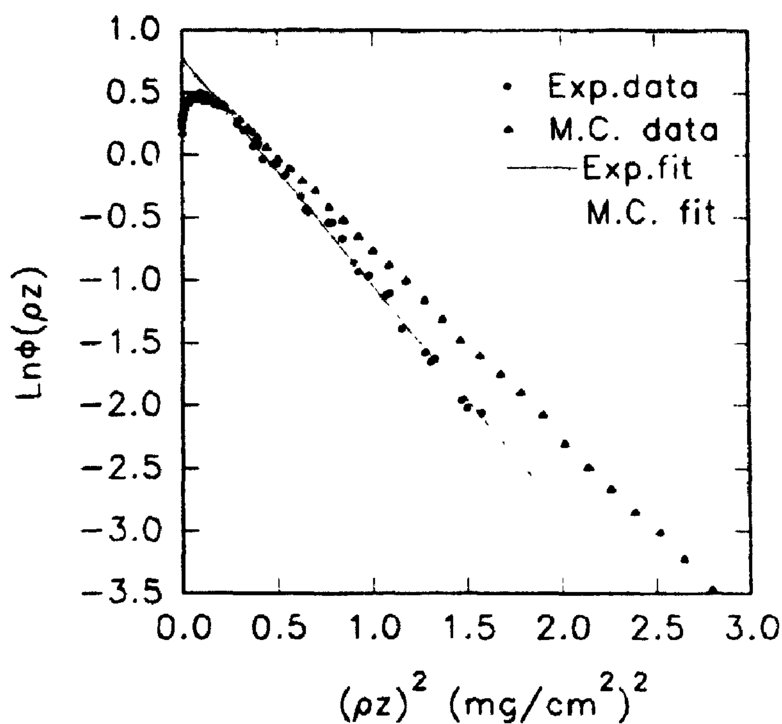

Figure 22b. Plots of $\ln\Phi(\rho z)$ versus $(\rho z)^2$ from figure 22a.

data, if not specified otherwise, were taken from Parobek and Brown [23], Brown and Parobek [15, 21, 22] and unpublished data from Parobek throughout this work. The calculated curves follow the experimentally observed straight line behaviour (Figures 20b, 21b and 22b) but the slopes in the tail portion of the curves vary from the experimental measurements. Mott scattering is examined in the next chapter to determine if the scattering model is the source of these differences.

CHAPTER 5

MOTT THEORY OF ELECTRON SCATTERING

5.1 INTRODUCTION

Monte Carlo simulations of electron scattering in a target normally are based on one of two elastic cross-sections, either the screened Rutherford cross-section or the Mott cross-section. The use of the Mott [103] scattering cross-section was first proposed by Reimer and Krefting [90]. In general, the screened Rutherford cross-section gives acceptable results for high energies and light element targets but Mott cross-sections are better for low to medium incident electron energies and heavy element targets.

Only limited energy and element ranges were investigated in previous studies by Kotera et al. [104, 105], Reimer and Lodding [106], Reimer and Stelter [107] and Czyzewski et al. [108]. Moreover, individual cross-section values were obtained by numerical interpolation since results were reported in a tabular form and no explicit equation was available to determine individual values. To describe the elastic scattering of electrons in solids, the probability distribution of the angles of elastic collisions must be known. It can be shown that the scattering angle θ_i can be found by solving the following equation:

$$R = \frac{\int_0^{\theta_i} \left(\frac{d\sigma}{d\Omega}\right) \sin\theta d\theta}{\int_0^{\pi} \left(\frac{d\sigma}{d\Omega}\right) \sin\theta d\theta} \qquad \text{(Eqn. 66)}$$

where R is a random number uniformly distributed between zero and one and $d\sigma/d\Omega$ is the partial elastic cross-section. Because a convenient analytical formula exists for the screened Rutherford cross-section, it is mathematically simple to represent $d\sigma/d\Omega$. For any electron energy and scattering atom of interest, Eqn. (66) has an analytical solution of the following form:

$$\cos\theta_i = 1 - \frac{2\alpha R}{1+\alpha-R} \qquad \text{(Eqn. 67)}$$

where α is the screening parameter. However, when $d\sigma/d\Omega$ is taken from the exact Mott theory although the needed accuracy was obtained, no simple analytical solution could be found and complex mathematical computation must be used to obtain the value θ_i. Recently, Drouin et al. [109] developed the following formula to compute this scattering angle θ from partial elastic Mott cross-sections which is valid for the energy range from 0.1 to 30 keV:

$$\cos(\theta_i^{\beta}) = 1 - \frac{2\alpha R^*}{1+\alpha-R^*} \qquad \text{(Eqn. 68)}$$

where θ_i is in degrees

$$\log_{10}(\alpha) = a + b\log_{10}(E) + c\log_{10}^2(E) + \frac{d}{\exp(\log_{10}(E))} \qquad \text{(Eqn. 69)}$$

$$\beta^* = e + f\sqrt{E}\log_e(E) + \frac{g\log_e(E)}{E} + \frac{h}{E} \qquad \text{(Eqn. 70)}$$

and $\beta = 1$ if $\beta^* > 1$

$\beta = \beta^*$ if $\beta^* \le 1$

where a-h are constants. Values for these constants were given by Drouin et al. [109]

for the first 94 elements in the periodic table. Finally,

$$R^* = R \times \frac{\cos(180^\beta) + \alpha\cos(180^\beta) - 1 - \alpha}{\cos(180^\beta) - 1 - 2\alpha} \quad \text{(Eqn. 71)}$$

5.2 MOTT SCATTERING ANGLES FOR THE MULTIPLE SCATTERING MODEL

Formulae are available to calculate scattering angle probabilities for Rutherford single and multiple electron scattering and for Mott single scattering (Eqns. 52, 61 and 68). To date, no published results are available to describe quantitatively the scattering angle distribution for a multiple scattering model based on the Mott scattering cross-section. Since, in general, the $\theta_{Mott,single}$ distribution falls below the $\theta_{R,single}$ distribution, it is reasonable to assume that qualitatively $\theta_{Mott,multiple}$ falls below $\theta_{R,multiple}$. Two approaches were developed in this work to find values for $\theta_{Mott,multiple}$ by knowing the other three distributions. The two equations are:

$$\theta_{Mott,multiple} = \theta_{R,multiple} \star \left(\frac{\theta_{Mott,single}}{\theta_{R,single}} \right) \quad \text{(Eqn. 72)}$$

and

$$\theta_{Mott,multiple} = \theta_{R,multiple} + (\theta_{Mott,single} - \theta_{R,single}) \quad \text{(Eqn. 73)}$$

Figures 23a and 23b show the distribution of scattering angles for Au at 30 keV based on these two equations. Clearly, the ratio assumption gives a larger difference in scattering angles than the difference assumption.

The effect of the two different methods for calculating $\theta_{Mott,multiple}$ is illustrated

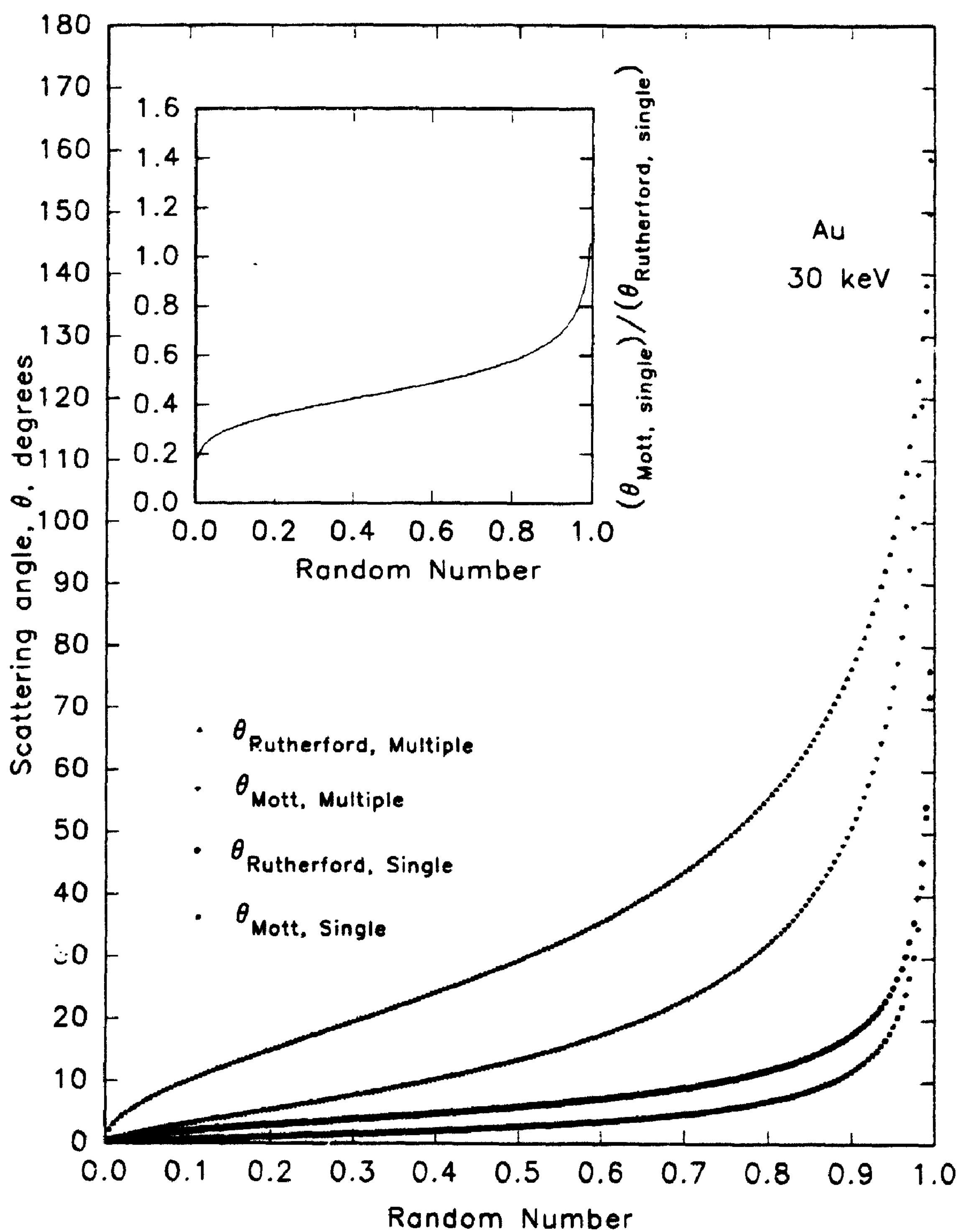

Figure 23a. Scattering angle distributions as calculated from equation (72) for Au at 30 keV.

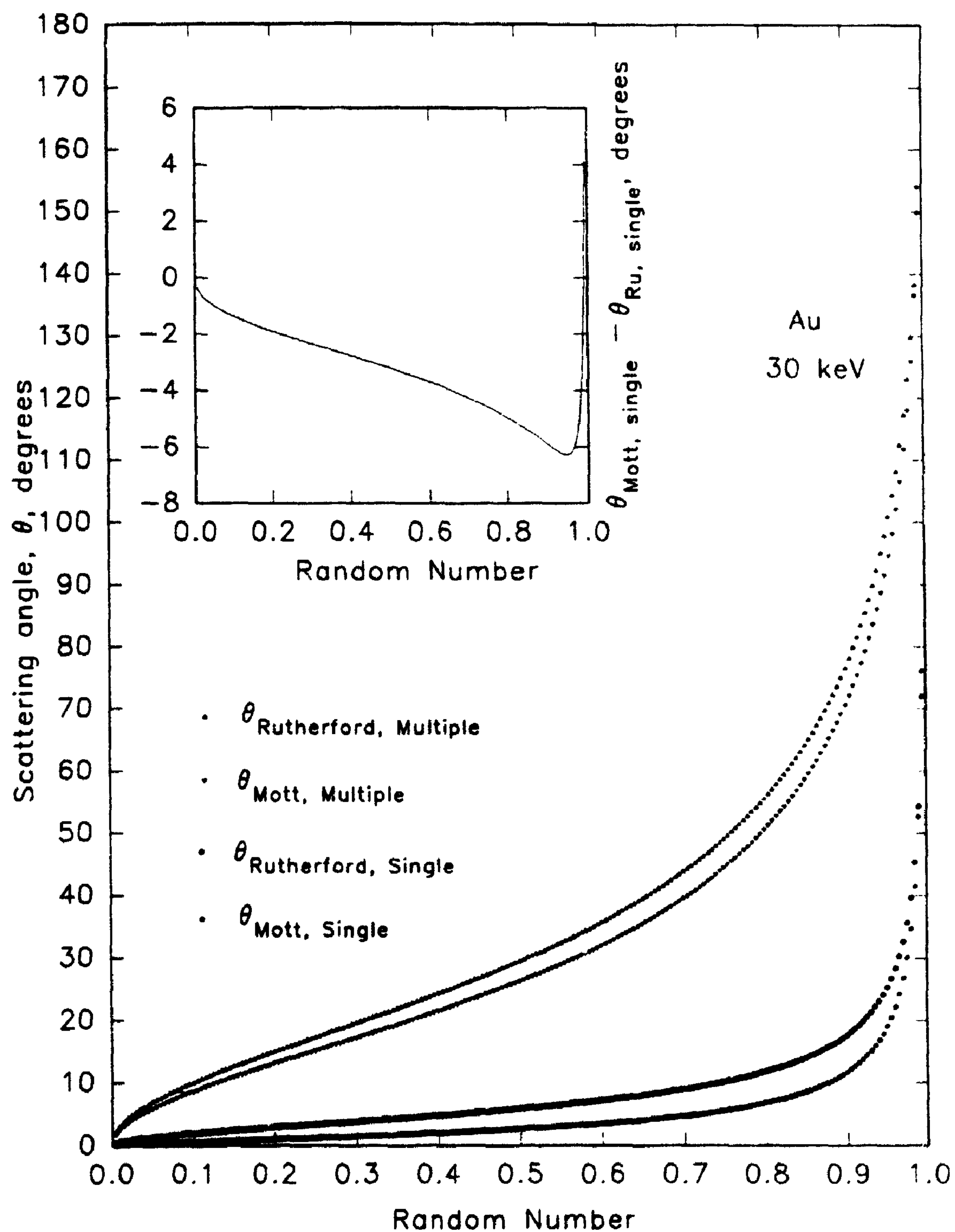

Figure 23b. Scattering angle distributions as calculated from equation (73) for Au at 30 keV.

in Figures 24a and 24b. The position of the maximum of the $\phi(\rho z)$ curve is essentially unaffected by the choice of Mott multiple scattering angle distribution. However, the slope of the line in Figure 24b for Mott using Eqn. (72) was found to be less than the experimental data whereas for Mott using Eqn. (73) (Appendix 2) a steeper slope is observed. In short, when using Eqn. (72) instead of Eqn. (73) in determining $\theta_{Mott,multiple}$, since the angles are generally smaller, there is a transfer of ionizations in that the peak region is suppressed and the tail region will be enhanced.

5.3 RESULTS

The $\phi(\rho z)$ expression is a critical quantity in determining accuracy in the $\phi(\rho z)$ methods for quantitative electron probe microanalysis. For the absorption correction, the shape of the curve, particularly with respect to the position of the maximum and the tail of the distribution is most important. For the atomic number correction, the total area under the curve is critical. One should always keep in mind however that in any calculations, ratios involving two different $\phi(\rho z)$ curves at the same electron energy are used. The measured $\phi(\rho z)$ curves are being used as the standard against which the Monte Carlo curves are being judged. It must be recognized that the measured curves can suffer from errors because of tracer layer thickness, overlayer thickness measurements, x-ray intensity measurements and inaccuracies in mass absorption coefficients.

A total of 15 systems were chosen to compare the Monte Carlo $\phi(\rho z)$ curves calculated using both the Rutherford (Eqn. 67) and Mott (Eqn. 73) multiple scattering

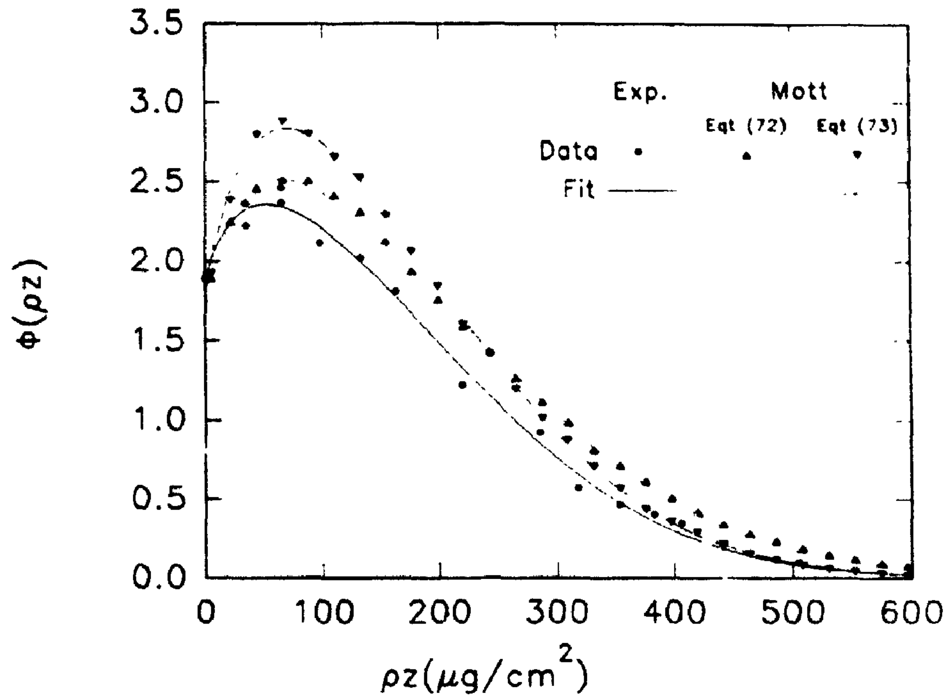

Figure 24a. Experimentally measured and Monte Carlo simulated $\Phi(\rho z)$ curves for Cd $L\alpha$ in Ag at 15 keV.

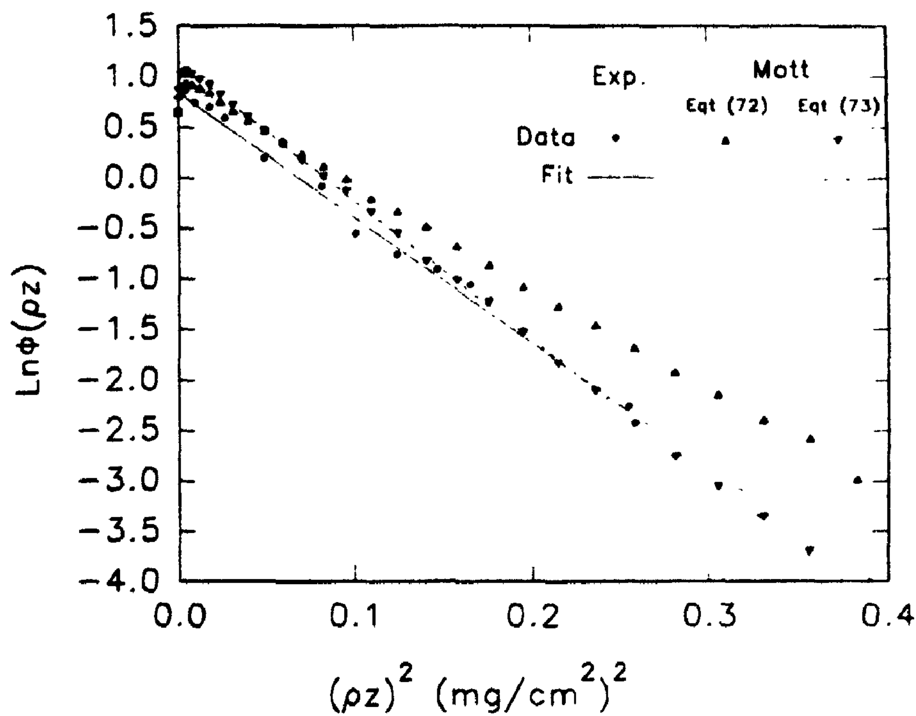

Figure 24b. Plots of $\ln\Phi(\rho z)$ versus $(\rho z)^2$ from figure 24a.

Table 2

The 15 different systems for the comparison of $\phi(\rho z)$ curves experimental and Monte Carlo calculations.

Figure number	E_o (keV)	Tracer X-ray line	E_c (keV)	Matrix
25	25	Cd Lα	3.538	Au
26	10	Si Kα	1.838	Au
27	30	Si Kα	1.838	Au
28	20	Si Kα	1.838	Ag
29	30	Bi Lα	13.42	Ag
30	15	Cd Lα	3.538	Ag
31	20	Cd Lα	3.538	Ag
32	30	Cd Lα	3.538	Ag
33	20	Zn Kα	9.660	Cu
34	30	Zn Kα	9.660	Cu
35	15	Si Kα	1.838	Cu
36	15	Cu Kα	8.980	Al
37	10	Si Kα	1.838	Al
38	10	Cr Lα	0.574	Al
39	10	Cu Lα	0.933	Ag

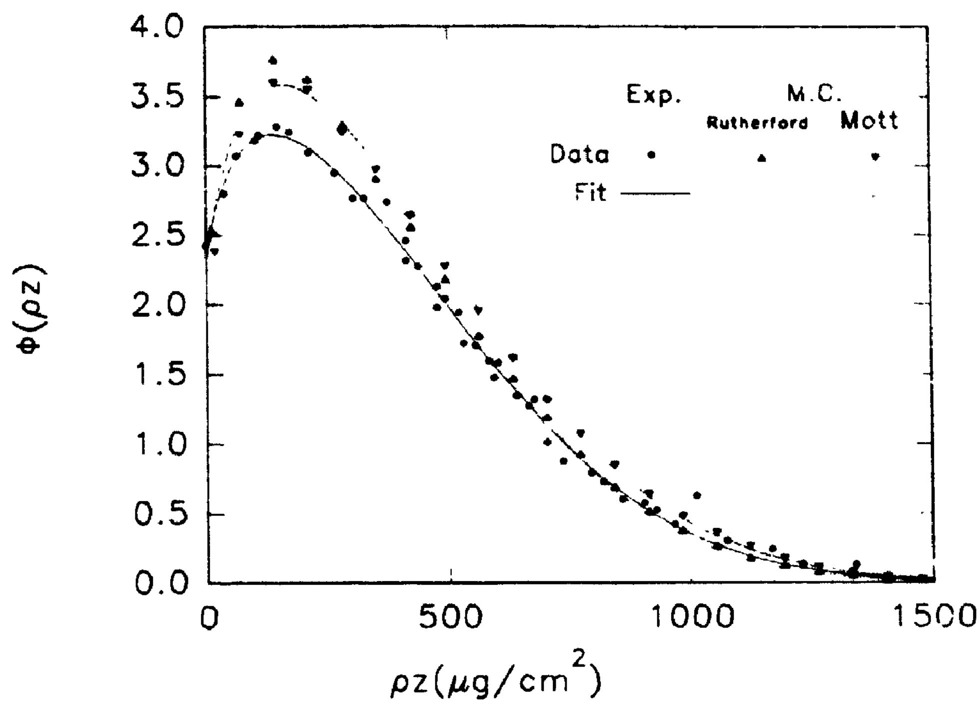

Figure 25a. Experimentally measured and Monte Carlo simulated $\Phi(\rho z)$ curves for Cd Lα in Au at 25 keV.

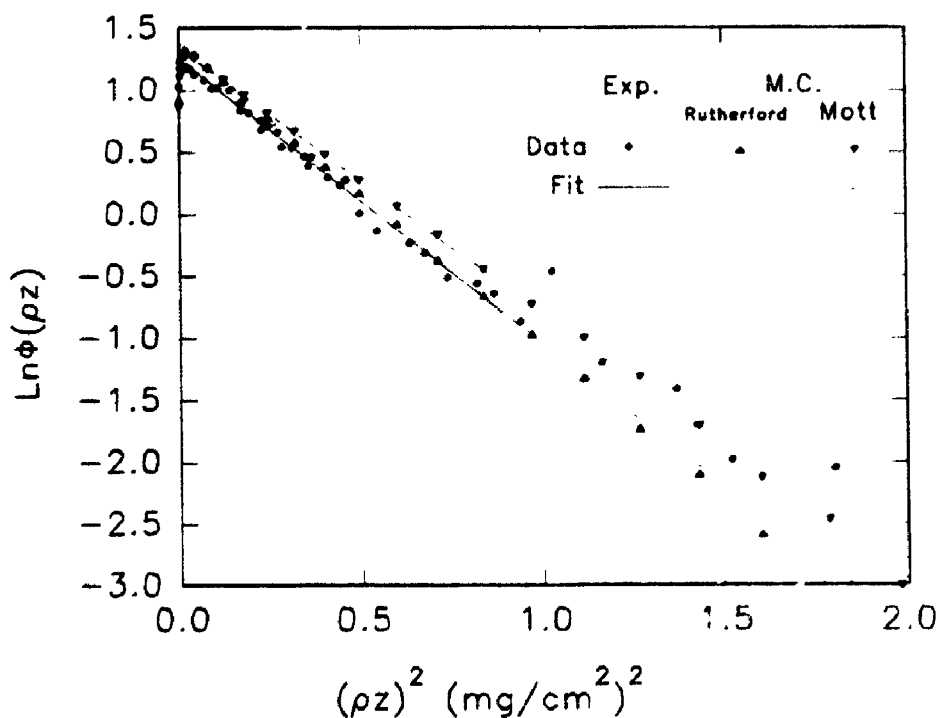

Figure 25b. Plots of $\ln\Phi(\rho z)$ versus $(\rho z)^2$ from figure 25a.

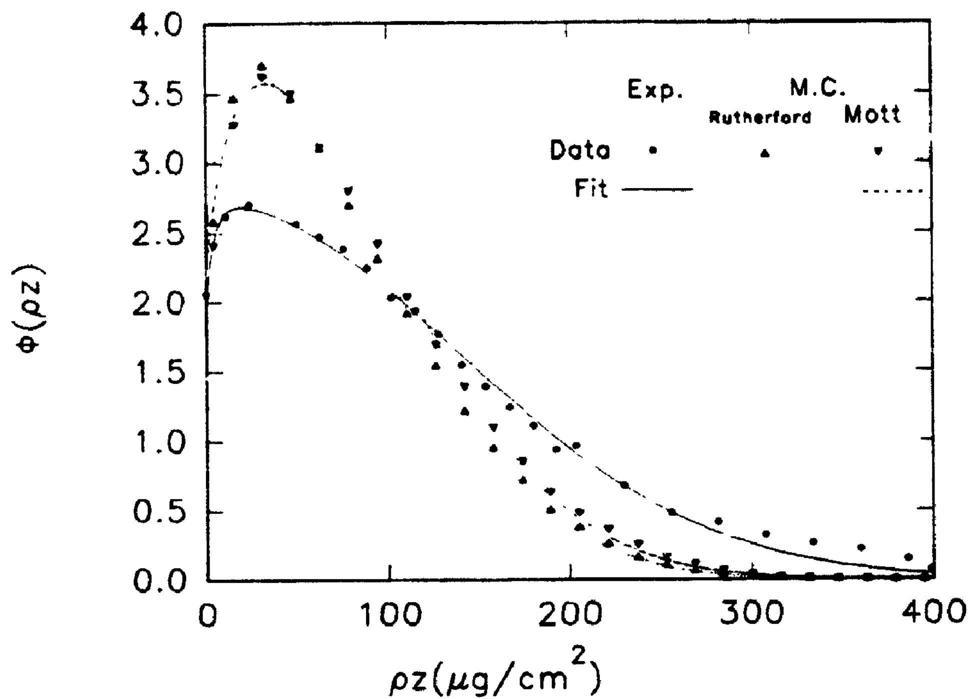

Figure 26a. Experimentally measured and Monte Carlo simulated $\Phi(\rho z)$ curves for Si $K\alpha$ in Au at 10 keV.

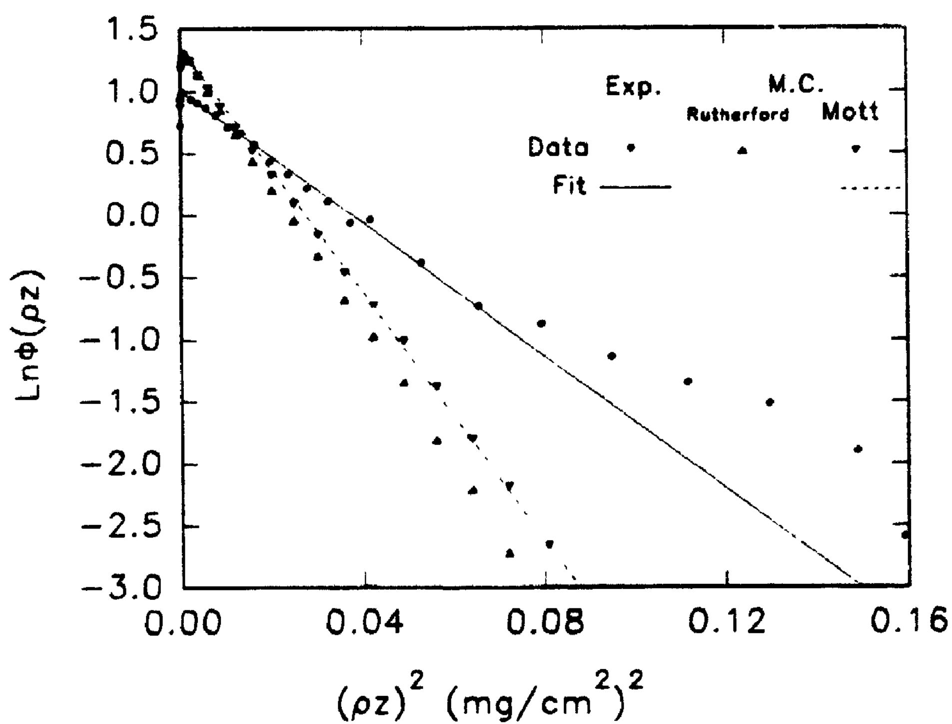

Figure 26b. Plots of $\ln\Phi(\rho z)$ versus $(\rho z)^2$ from figure 26a.

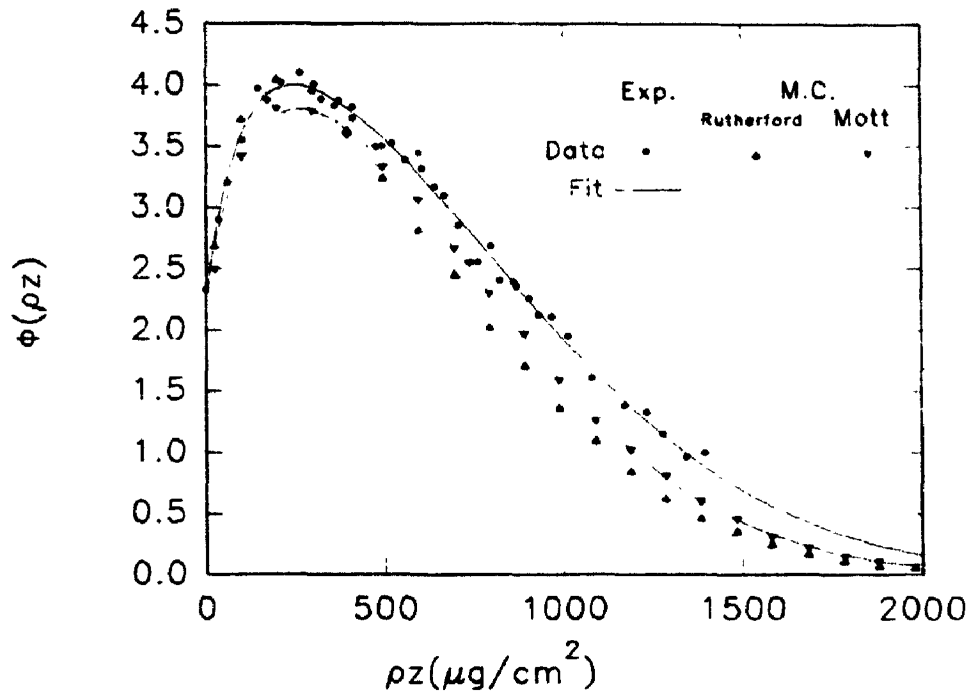

Figure 27a. Experimentally measured and Monte Carlo simulated $\Phi(\rho z)$ curves for Si Kα in Au at 30 keV.

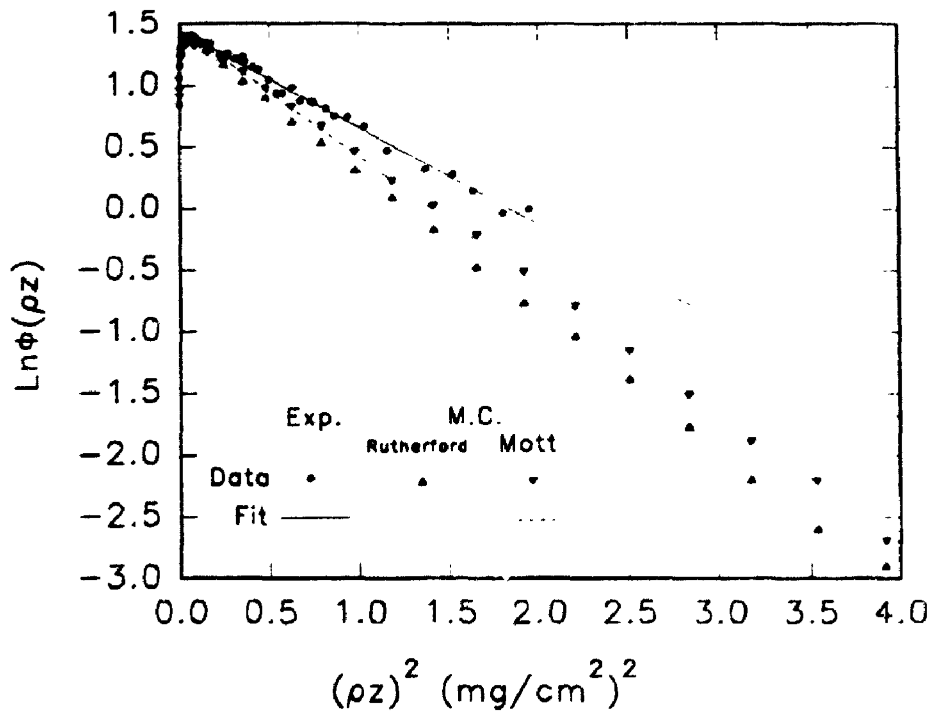

Figure 27b. Plots of $\ln\Phi(\rho z)$ versus $(\rho z)^2$ from figure 27a.

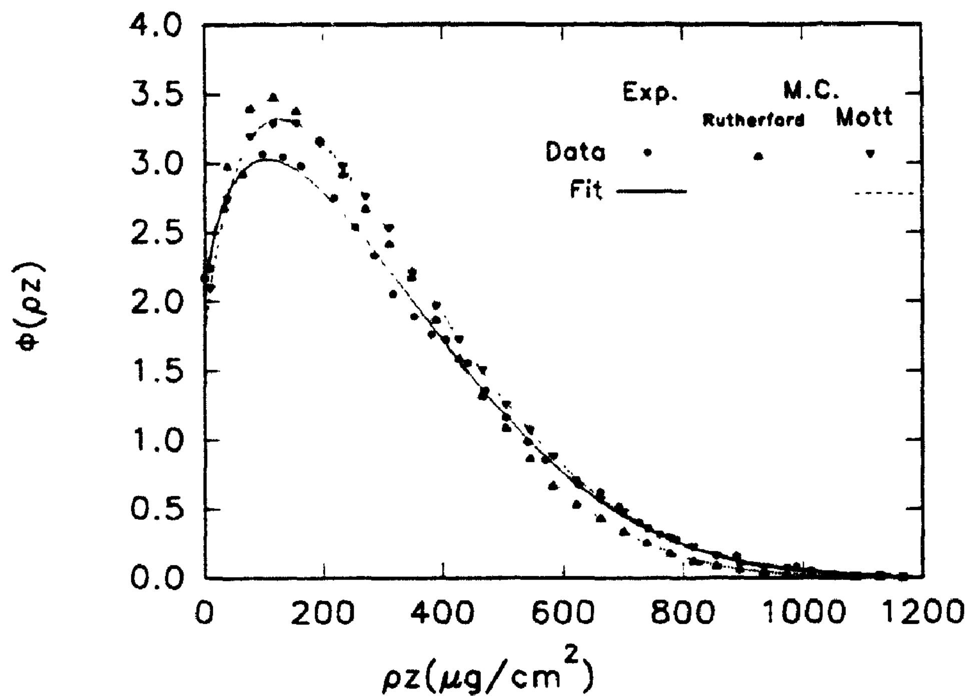

Figure 28a. Experimentally measured and Monte Carlo simulated $\Phi(\rho z)$ curves for Si Kα in Ag at 20 keV.

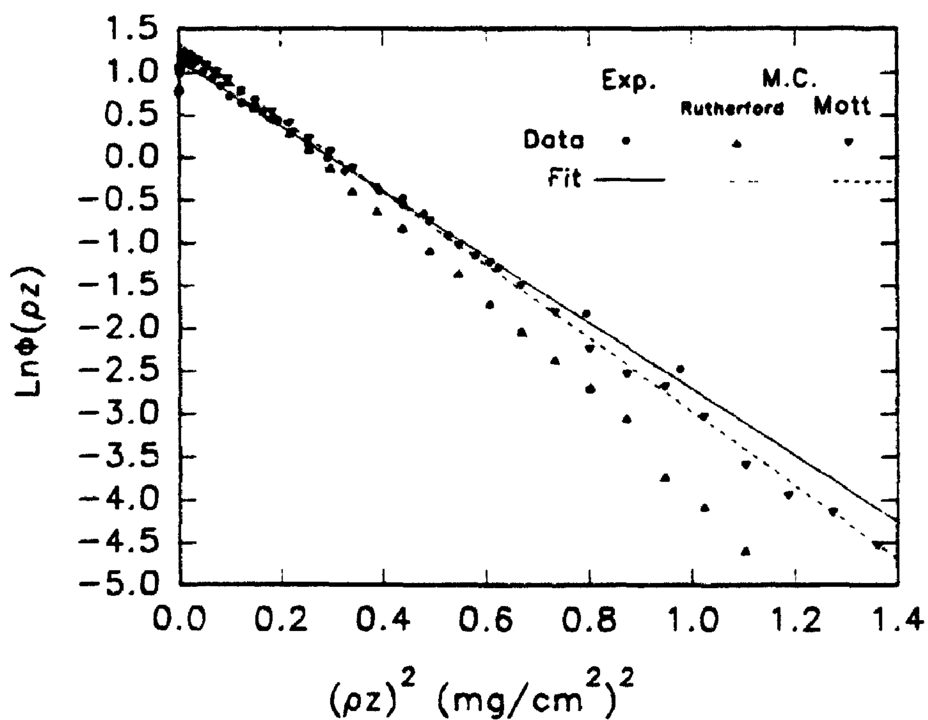

Figure 28b. Plots of $\ln\Phi(\rho z)$ versus $(\rho z)^2$ from figure 28a.

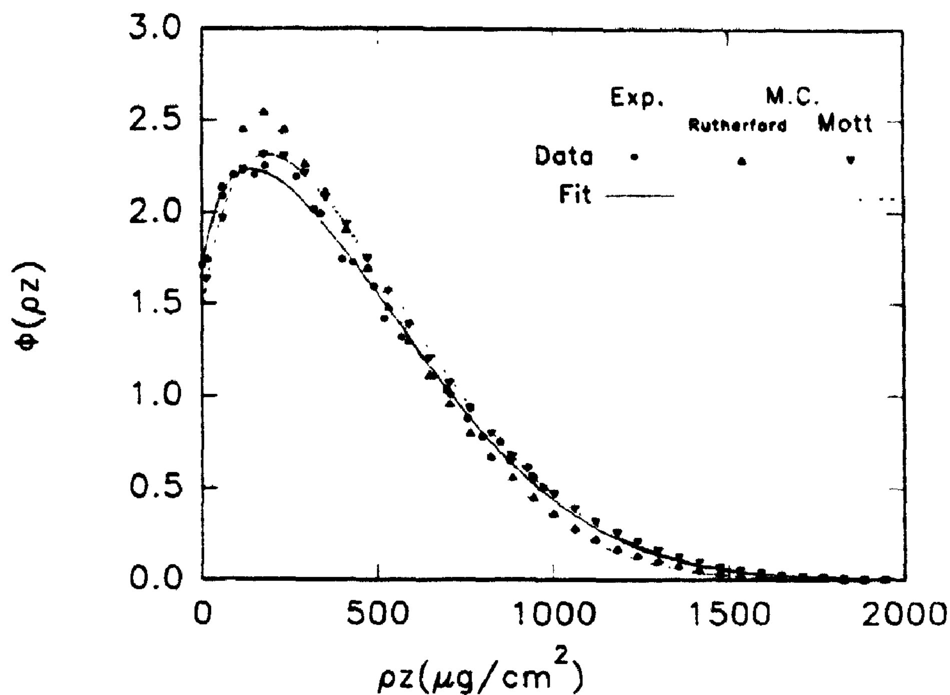

Figure 29a. Experimentally measured and Monte Carlo simulated $\Phi(\rho z)$ curves for Bi $L\alpha$ in Ag at 30 keV.

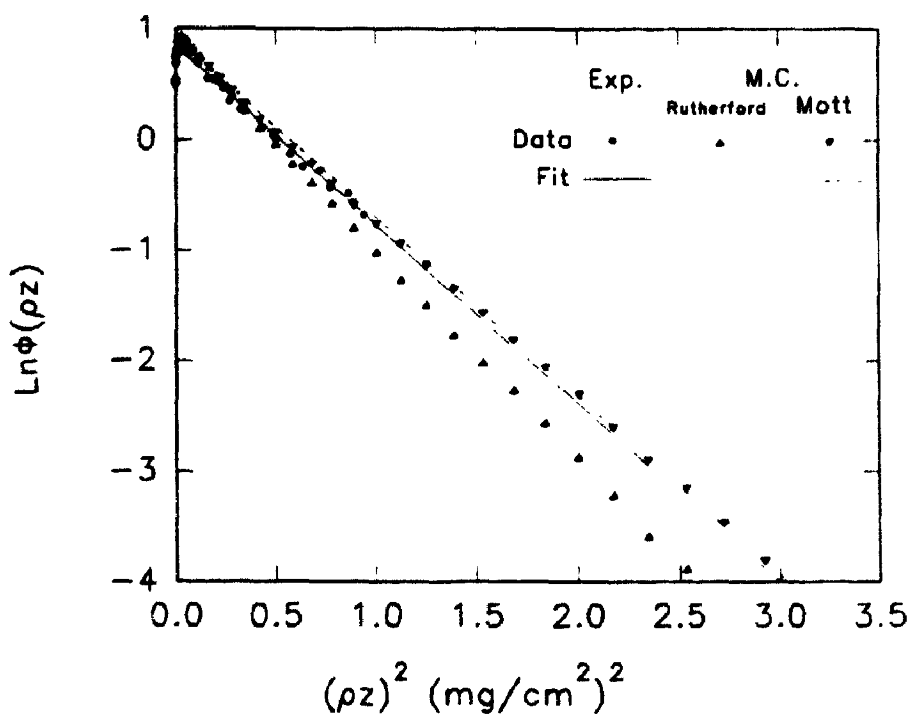

Figure 29b. Plots of $\ln\Phi(\rho z)$ versus $(\rho z)^2$ from figure 29a.

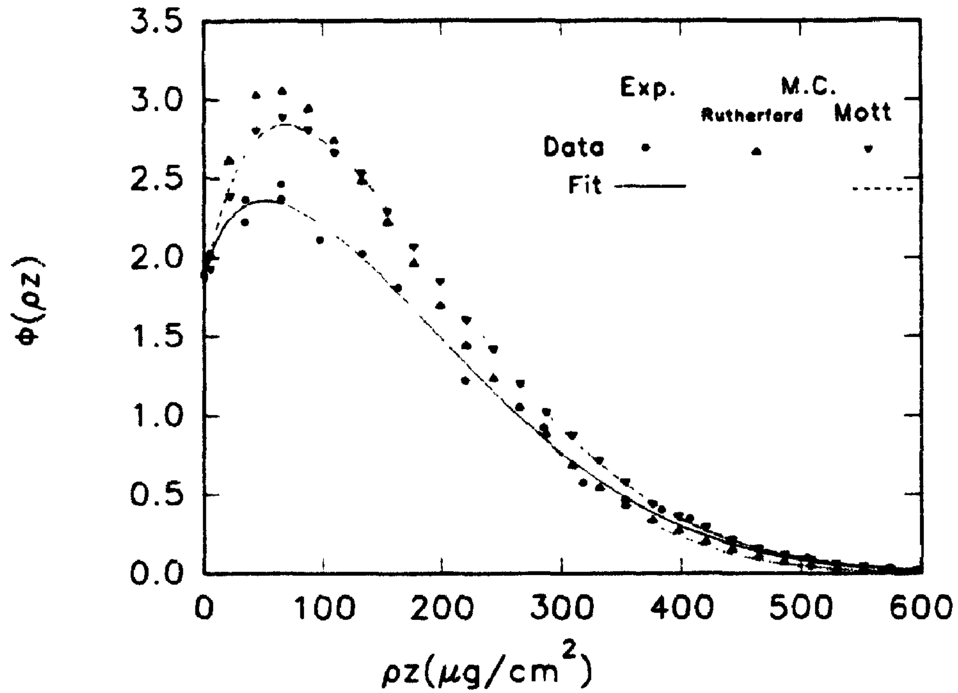

Figure 30a. Experimentally measured and Monte Carlo simulated $\Phi(\rho z)$ curves for Cd Lα in Ag at 15 keV.

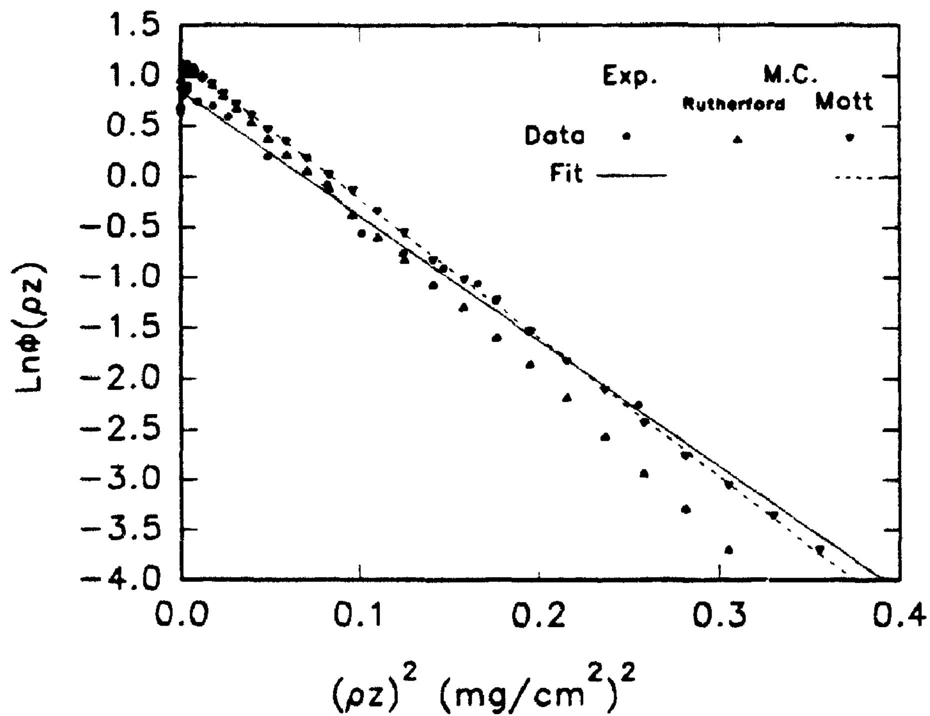

Figure 30b. Plots of $\ln\Phi(\rho z)$ versus $(\rho z)^2$ from figure 30a.

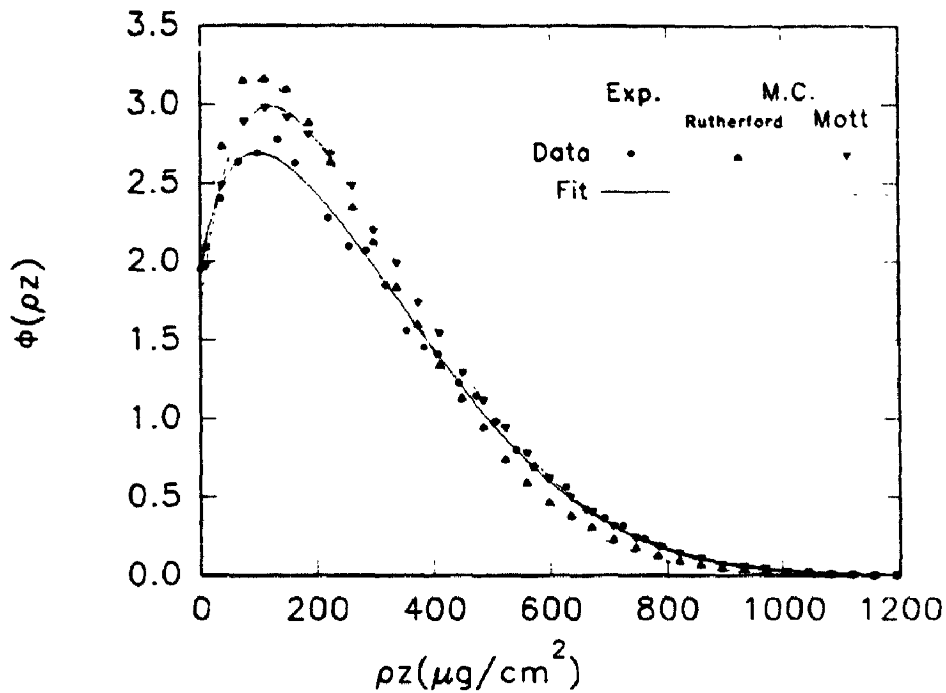

Figure 31a. Experimentally measured and Monte Carlo simulated Φ(ρz) curves for Cd Lα in Ag at 20 keV.

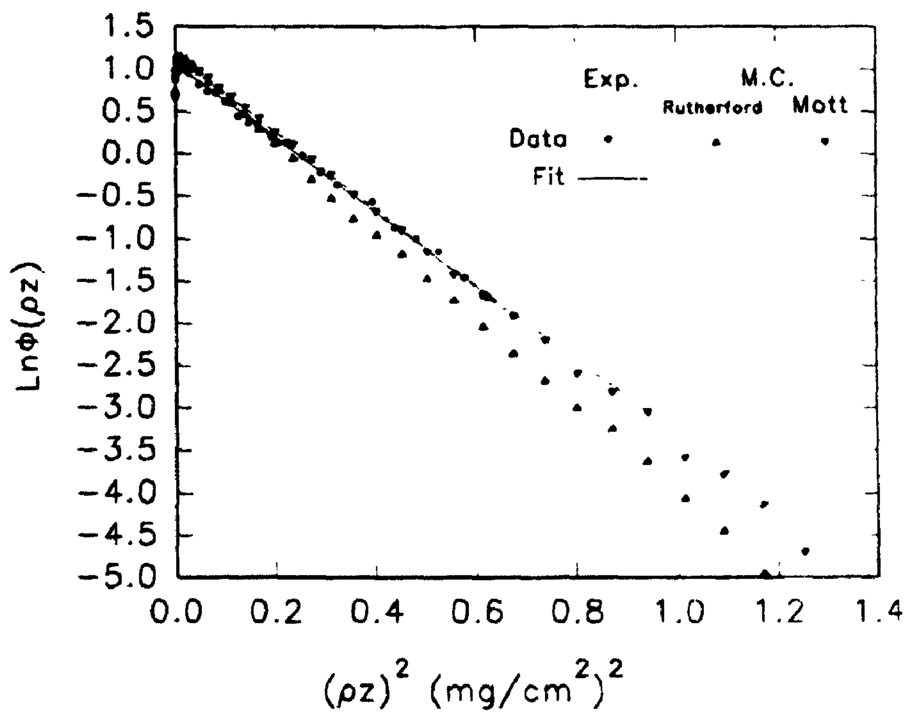

Figure 31b. Plots of lnΦ(ρz) versus $(\rho z)^2$ from figure 31a.

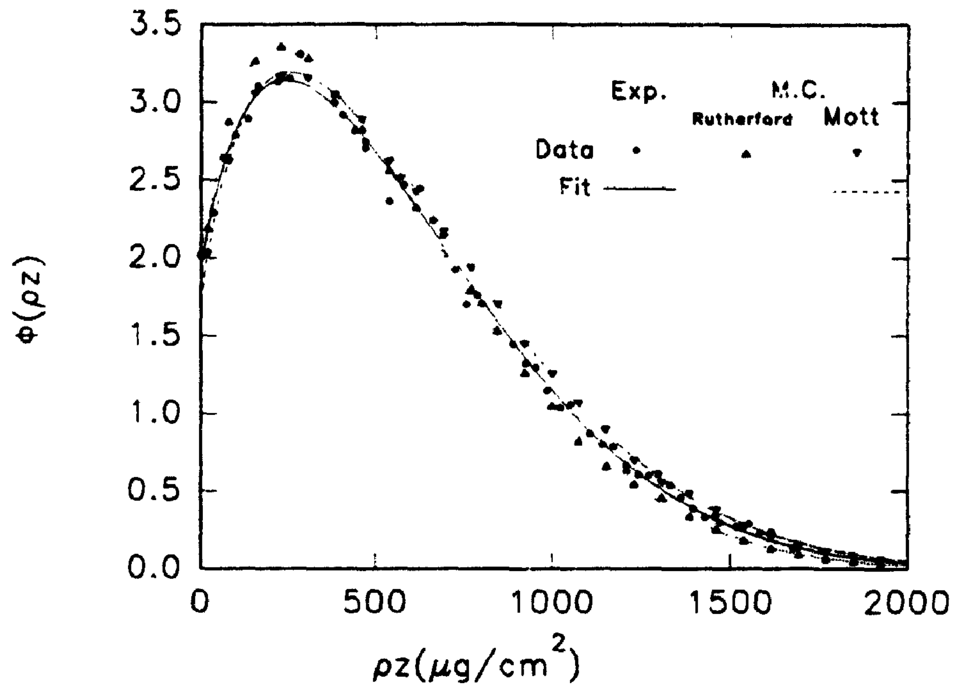

Figure 32a. Experimentally measured and Monte Carlo simulated $\Phi(\rho z)$ curves for Cd Lα in Ag at 30 keV.

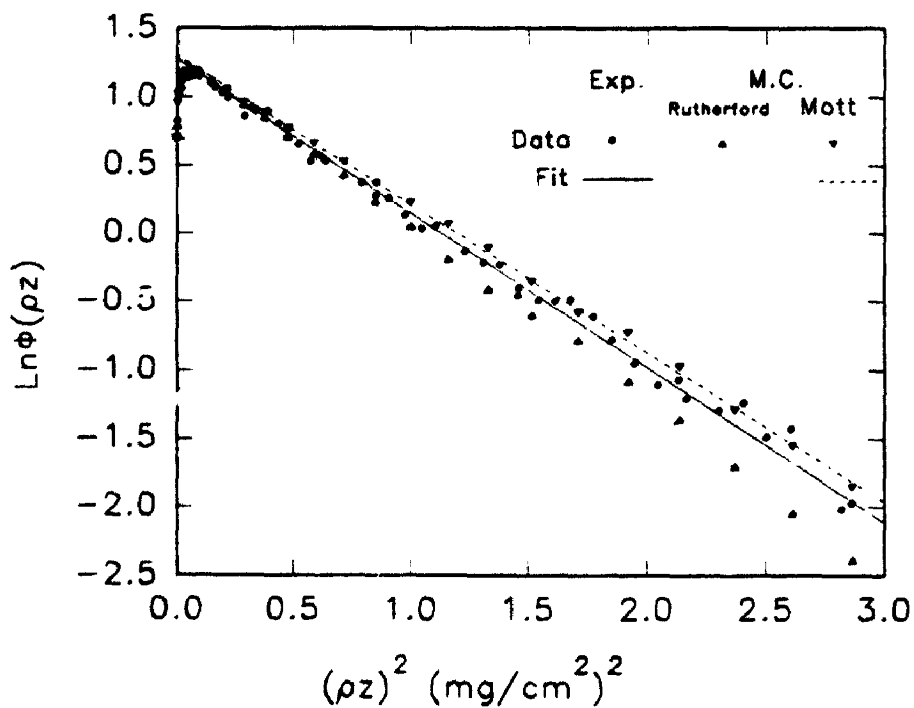

Figure 32b. Plots of $\ln\Phi(\rho z)$ versus $(\rho z)^2$ from figure 32a.

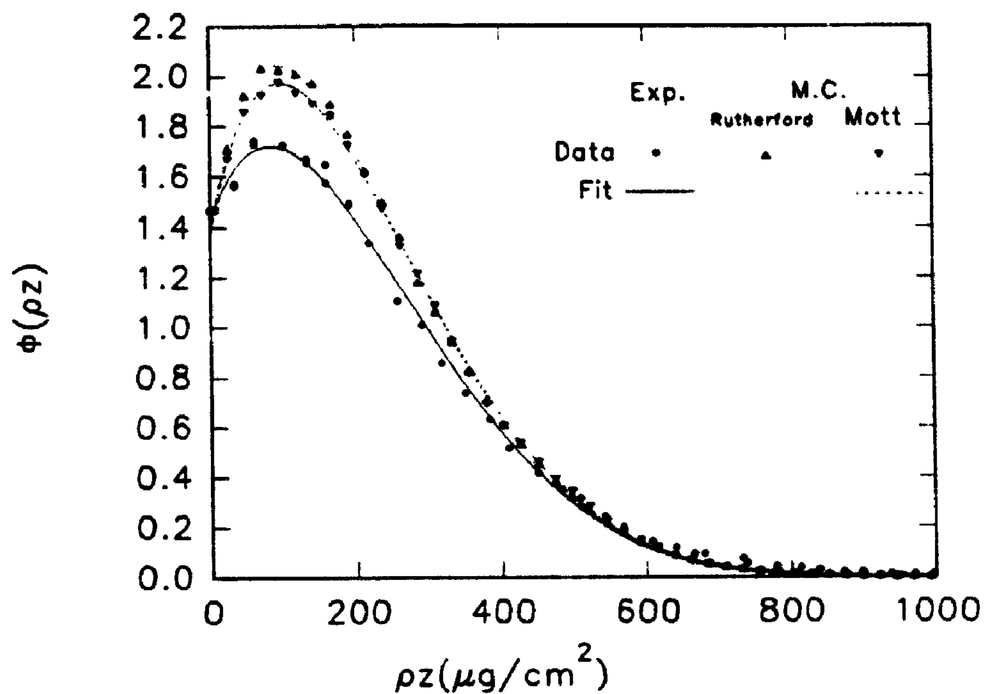

Figure 33a. Experimentally measured and Monte Carlo simulated Φ(ρz) curves for Zn Kα in Cu at 20 keV.

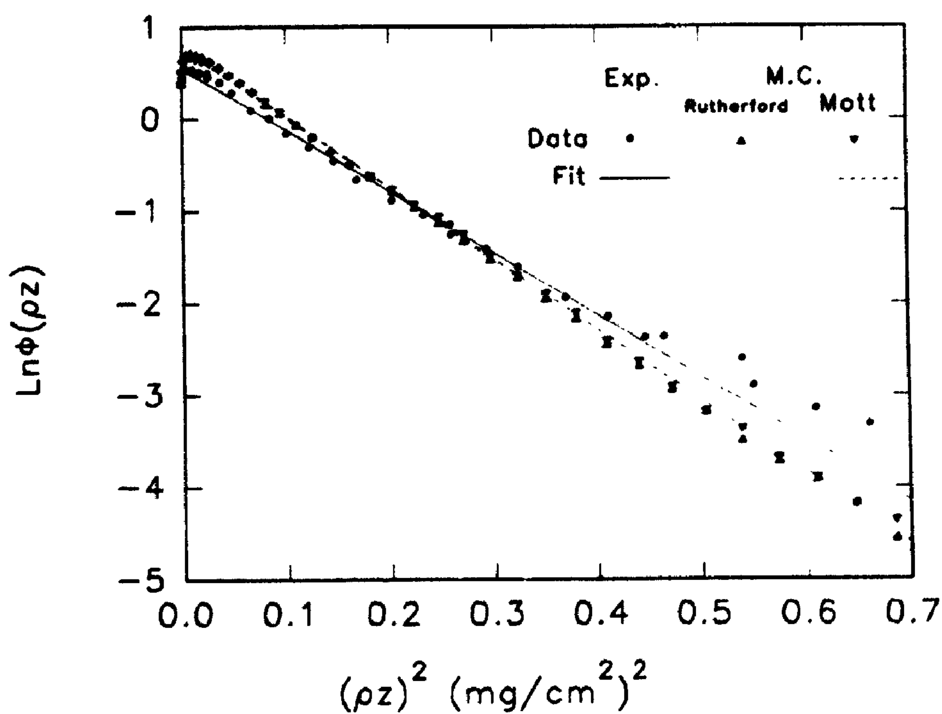

Figure 33b. Plots of lnΦ(ρz) versus $(\rho z)^2$ from figure 33a.

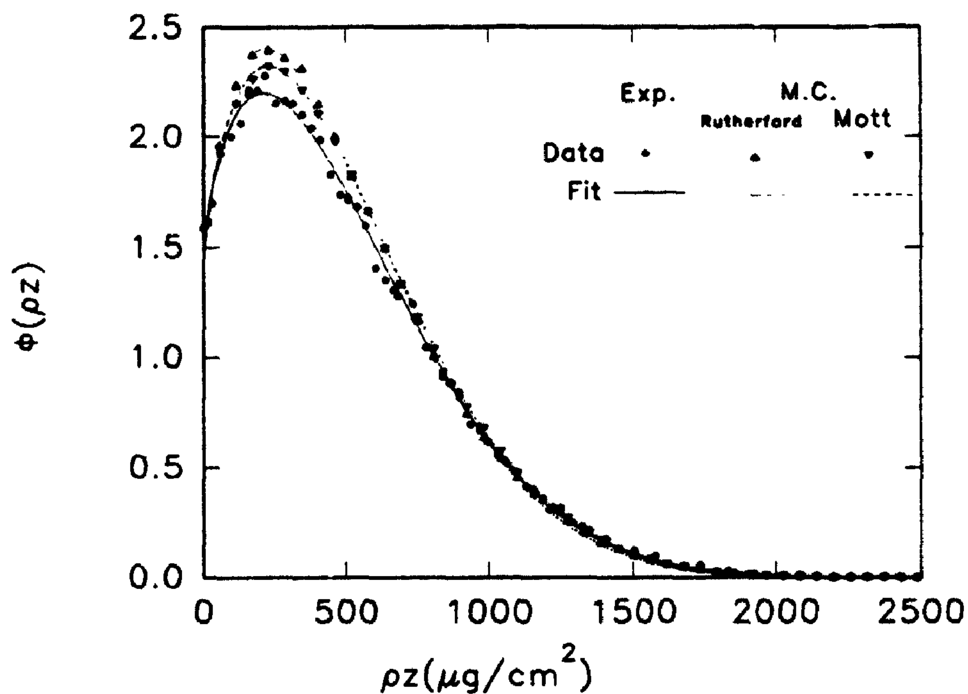

Figure 34a. Experimentally measured and Monte Carlo simulated $\Phi(\rho z)$ curves for Zn $K\alpha$ in Cu at 30 keV.

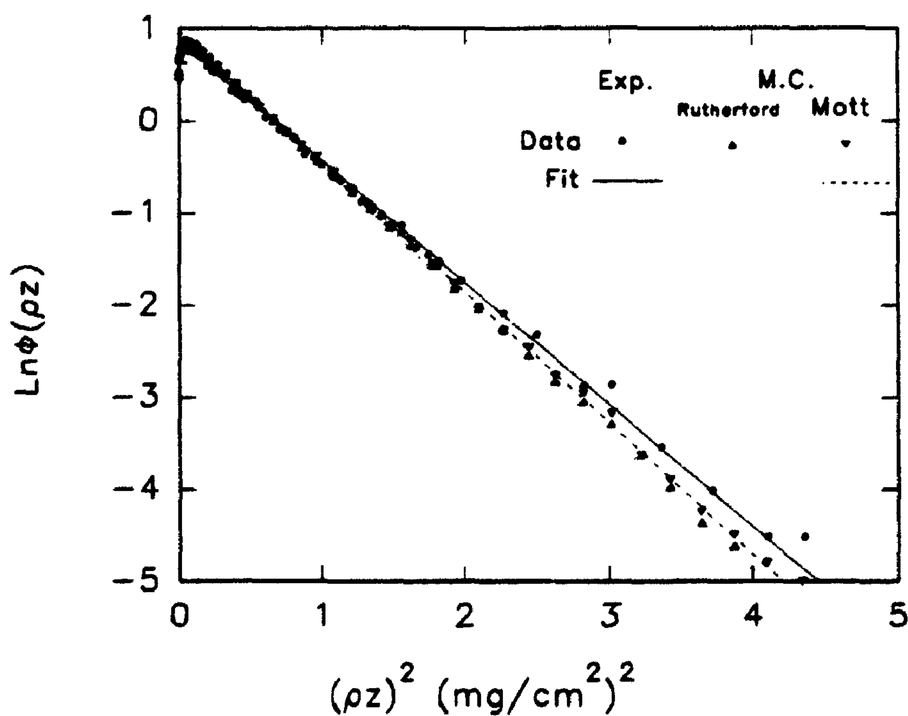

Figure 34b. Plots of $\ln\Phi(\rho z)$ versus $(\rho z)^2$ from figure 34a.

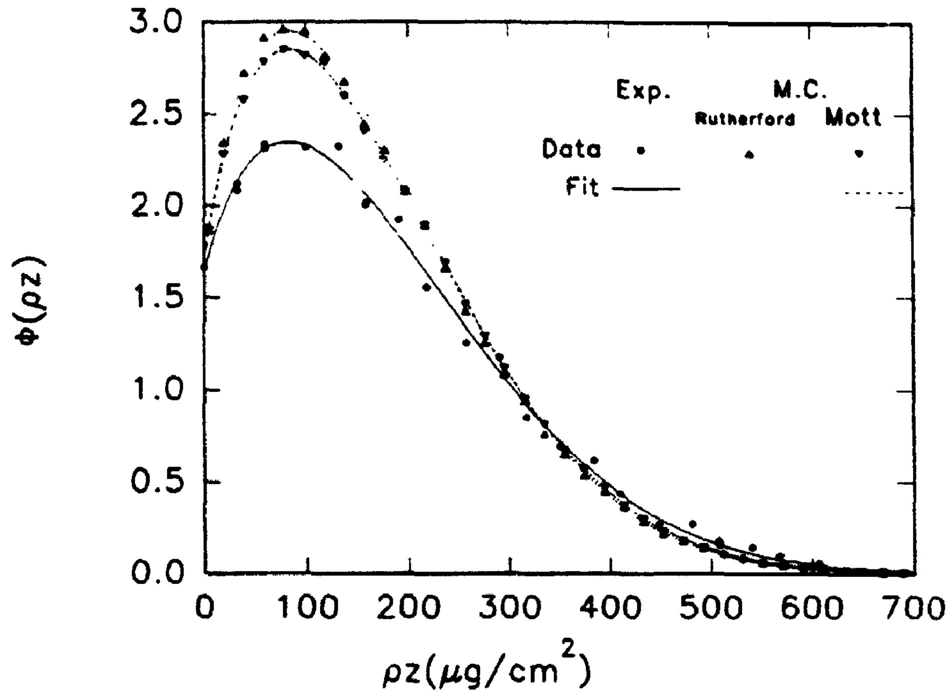

Figure 35a. Experimentally measured and Monte Carlo simulated $\Phi(\rho z)$ curves for Si $K\alpha$ in Cu at 15 keV.

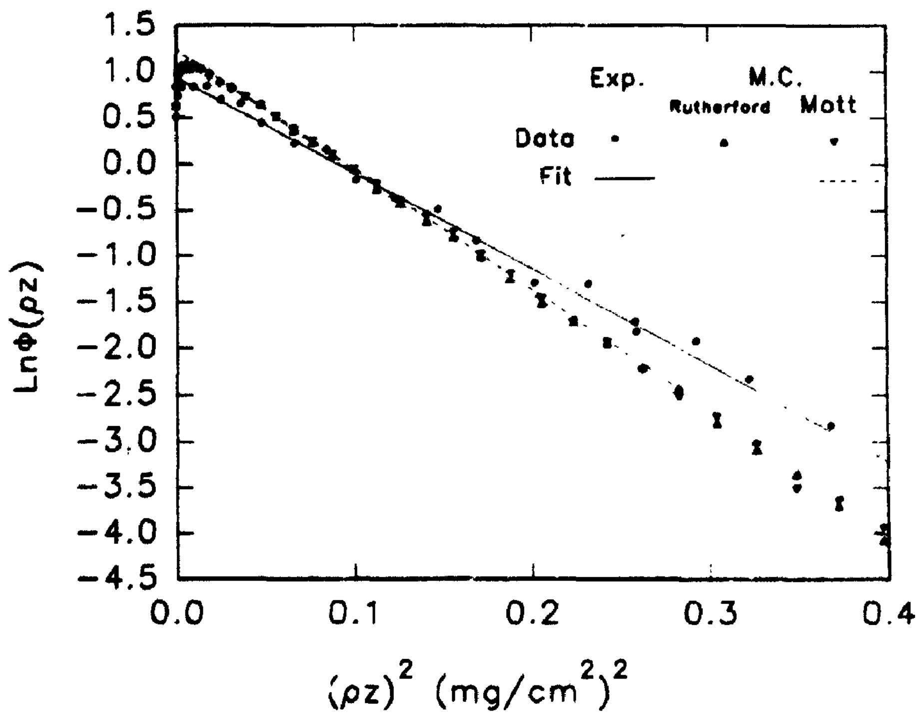

Figure 35b. Plots of $\ln\Phi(\rho z)$ versus $(\rho z)^2$ from figure 35a.

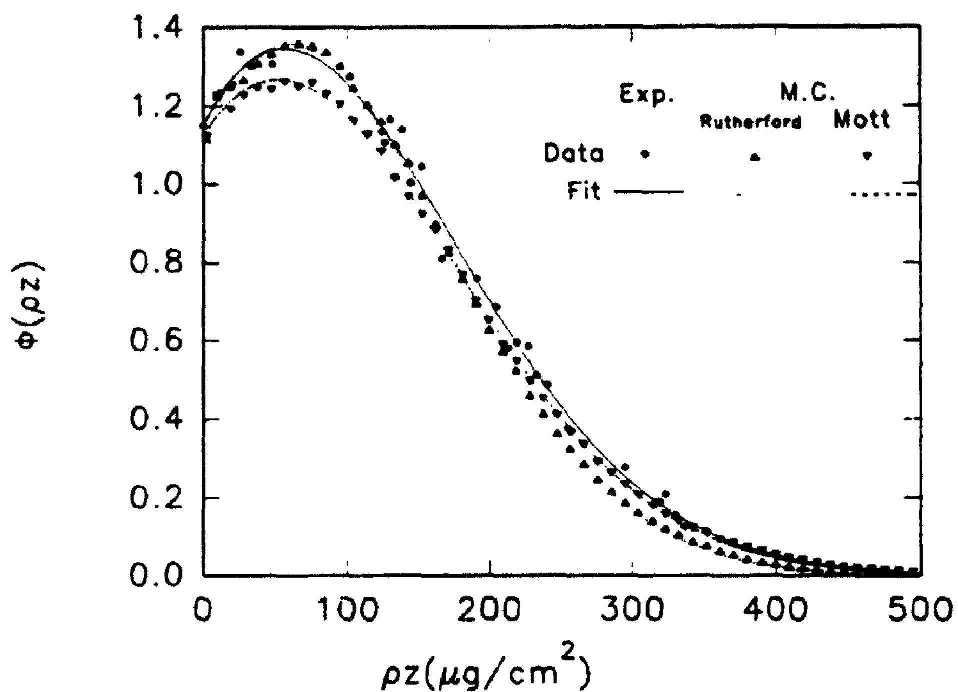

Figure 36a. Experimentally measured and Monte Carlo simulated $\Phi(\rho z)$ curves for Cu Kα in Al at 15 keV.

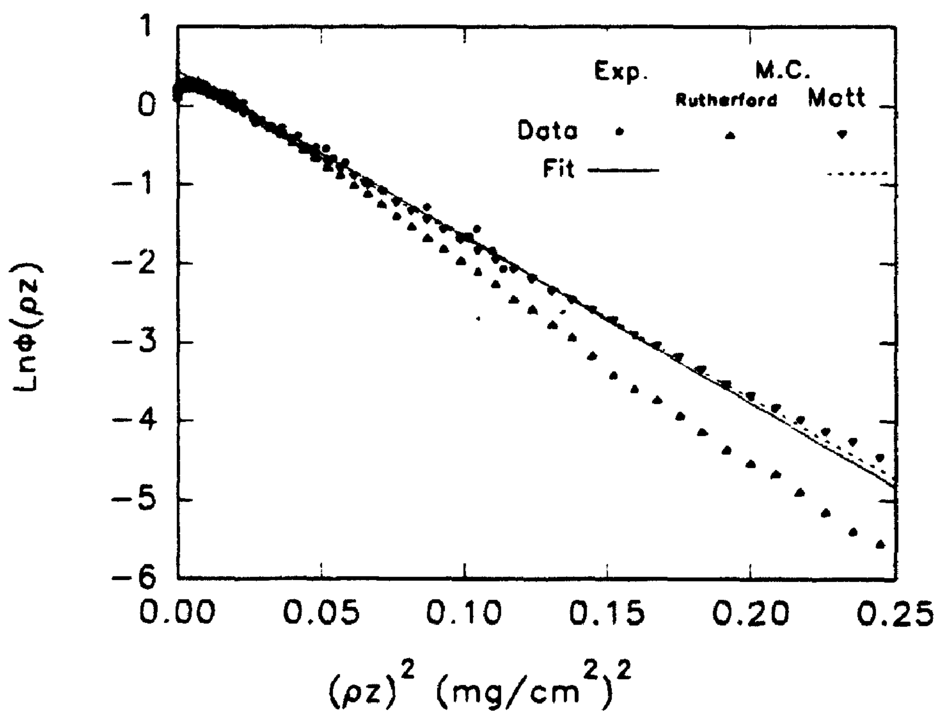

Figure 36b. Plots of $\ln\Phi(\rho z)$ versus $(\rho z)^2$ from figure 36a.

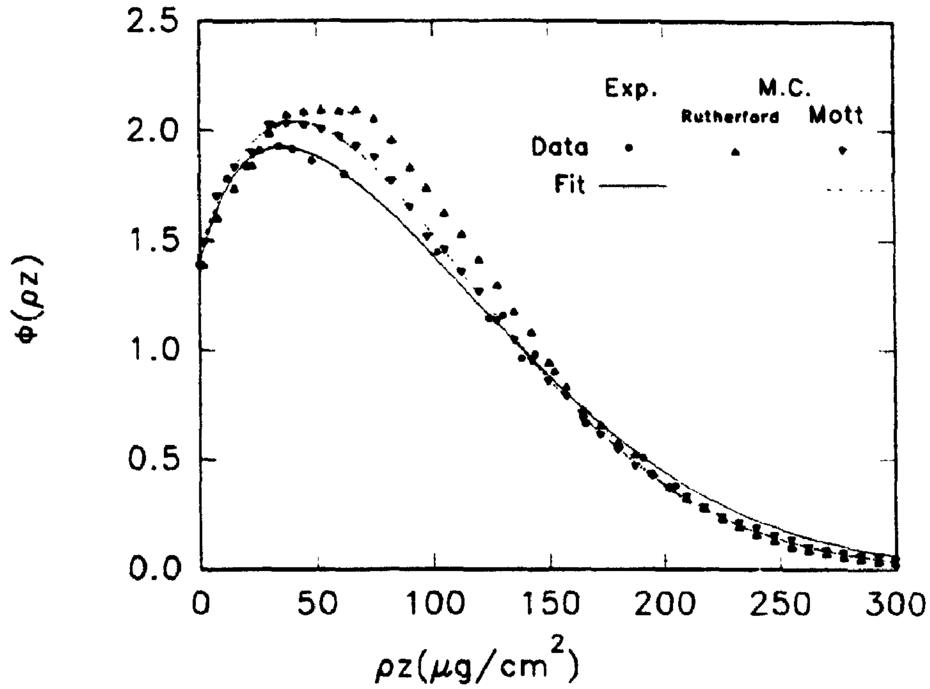

Figure 37a. Experimentally measured and Monte Carlo simulated $\Phi(\rho z)$ curves for Si Kα in Al at 10 keV.

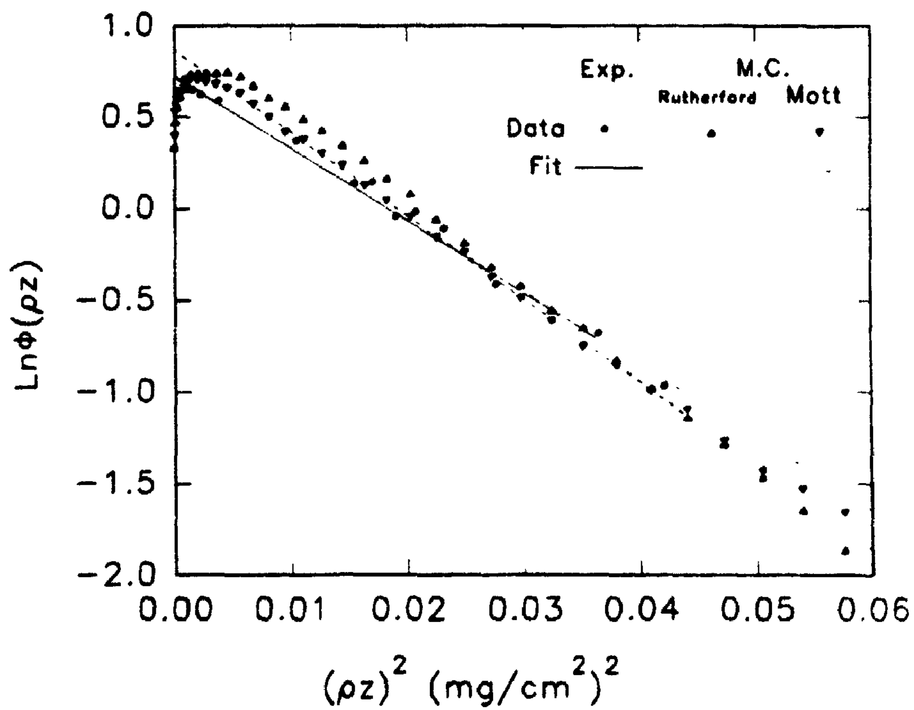

Figure 37b. Plots of $\ln\Phi(\rho z)$ versus $(\rho z)^2$ from figure 37a.

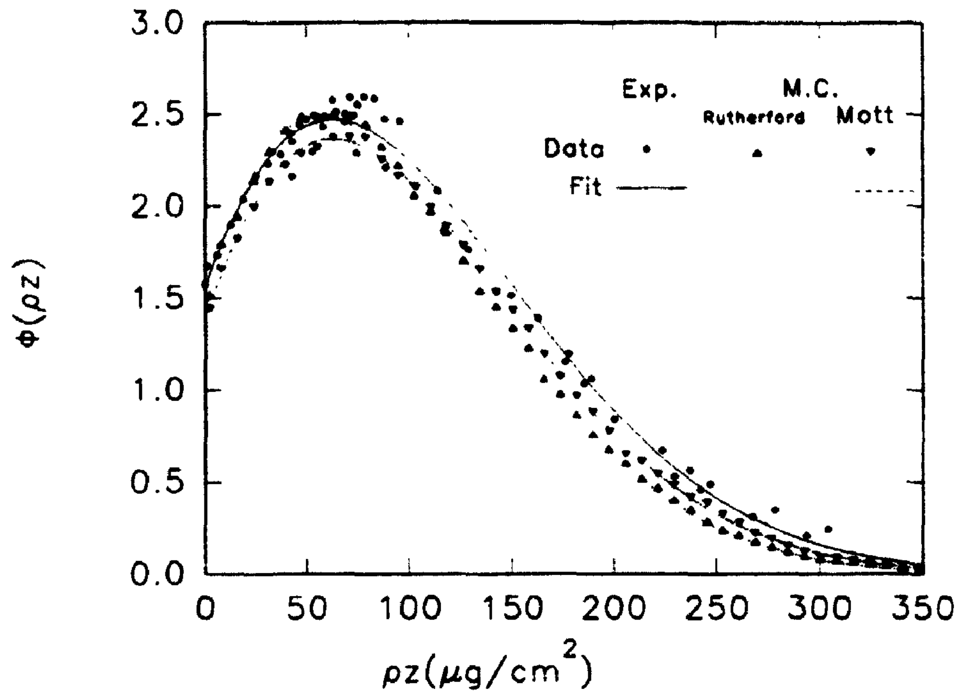

Figure 38a. Experimentally measured and Monte Carlo simulated $\Phi(\rho z)$ curves for Cr Lα in Al at 10 keV.

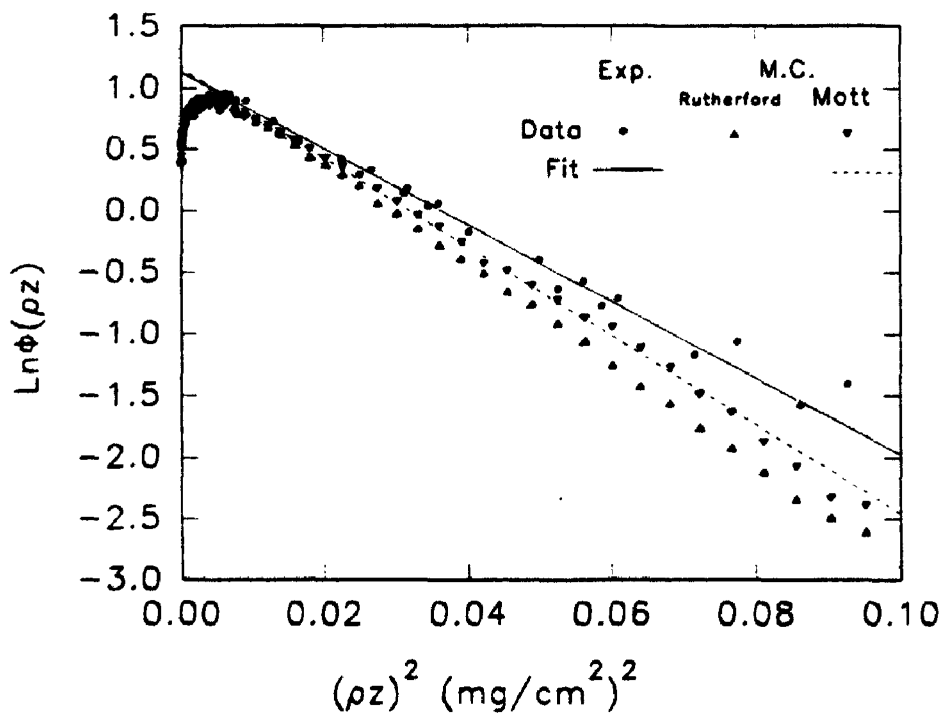

Figure 38b. Plots of $\ln\Phi(\rho z)$ versus $(\rho z)^2$ from figure 38a.

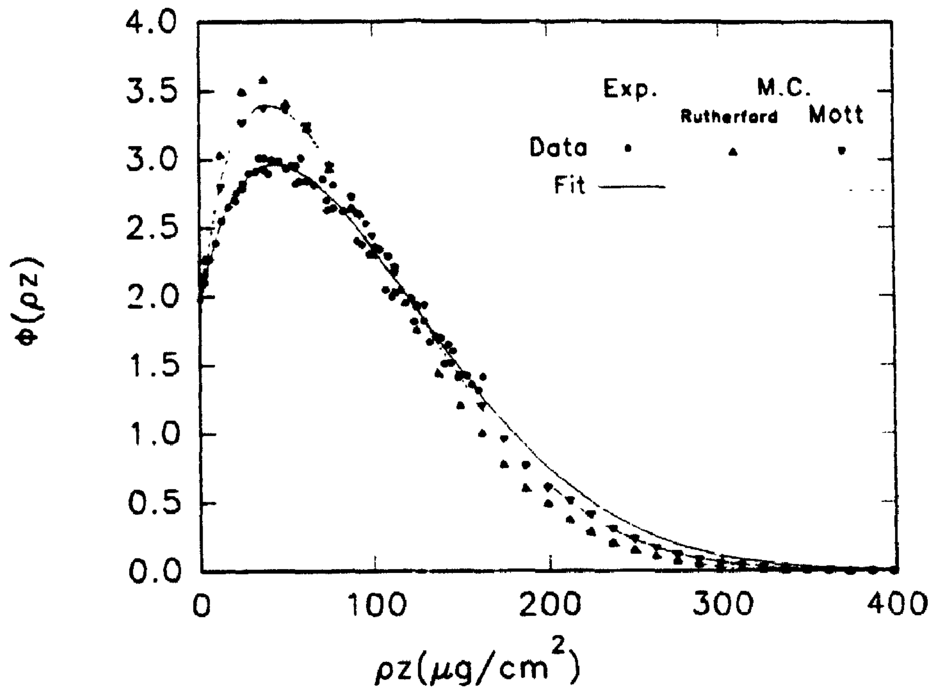

Figure 39a. Experimentally measured and Monte Carlo simulated $\Phi(\rho z)$ curves for Cu Lα in Ag at 10 keV.

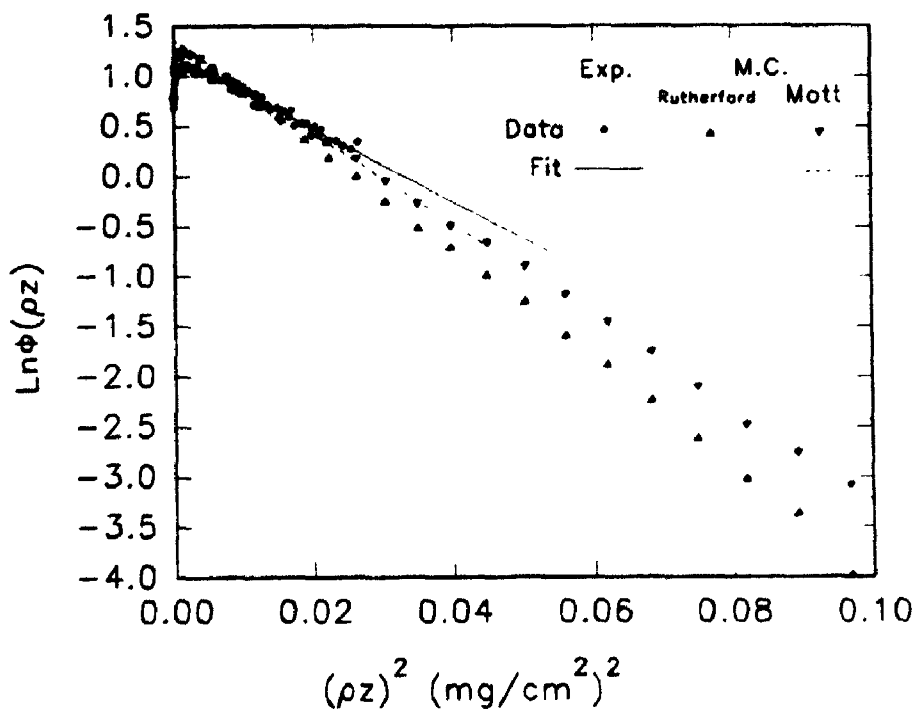

Figure 39b. Plots of $\ln\Phi(\rho z)$ versus $(\rho z)^2$ from figure 39a.

expressions with experimentally measured curves (Figures 25-39). These curves are chosen to cover a variety of incident electron energies, critical excitation potentials and atomic number of the matrix elements. The details are summarized in Table 2. The lines drawn in the figures are fits made to the Packwood and Brown $\phi(\rho z)$ equation by optimizing the four parameters, namely α, β, γ_o and $\phi(o)$.

5.3.1 General Comments

Overall, several comments can be made about the agreement between the Monte Carlo curves and the measured curves. By and large, the general shape, the position of the maximum and the shape of the curves beyond the maximum are in reasonable agreement and the agreement tends to be better as the electron energy increases. The areas under the curves however, are generally overestimated, again more severely at low electron energies. The poorest agreement is for high atomic number matrices at low electron energies. Part of the reason for this may be the experimental difficulty of measuring x-ray intensities from the isolated layer. In theory, the layer must be thin enough so that the electrons pass through without being scattered. (The layer should be infinitely thin.) Any scattering increases intensities of this reference layer to a value greater than it should be. The problem is worse as the electron energy decreases (assuming the same tracer layer thickness). The result is that the x-ray intensity from each layer in the experimental data is divided by a value which is too large, hence lowering the curve by a constant fraction. In many of the graphs at low energies, multiplication of the experimental curves by a constant

fraction (this amounts to a constant shift in the $\ln\phi(\rho z)$ value) would lead to very good agreement indeed.

The experimental data for $\phi(\rho z)$ when plotted as $\ln\phi(\rho z)$ versus the square of the depth shows a linear behaviour (slope = α^2) beyond the maximum in the curve. Data from many calculated $\phi(\rho z)$ curves fail to show this linear behaviour, e.g. Figures 12 and 13. The modifications made to the model, specifically the introduction of electron straggling does lead to this linear behaviour. Four curves are taken and replotted in Figure 40 to demonstrate the predicted behaviour over many orders of magnitude of intensity. This does confirm that the tails for the calculated x-ray generation curves are indeed gaussian.

The curves calculated using the Rutherford scattering expression are generally in poorer agreement with the experimental curves compared to the Mott scattering expression. This is particularly evident at low electron energies and with high atomic number matrices (see Figures 26, 30 and 39). This poorer agreement can also be seen in comparing the α values from the fits for the entire 15 systems. The Rutherford data leads to α values which are too high in most cases by at least 10% while the Mott values are in much better agreement (Table 3). These α values are also plotted in Figures 41a and 41b.

Another characteristic of a $\phi(\rho z)$ curve is the mass depth at maximum $\phi(\rho z)$. This depth can be found by fitting the Packwood and Brown $\phi(\rho z)$ equation (Eqn. 25) to the data then differentiating with respect to ρz and setting the differential equal to zero. The following equation is the reduced form of the differential:

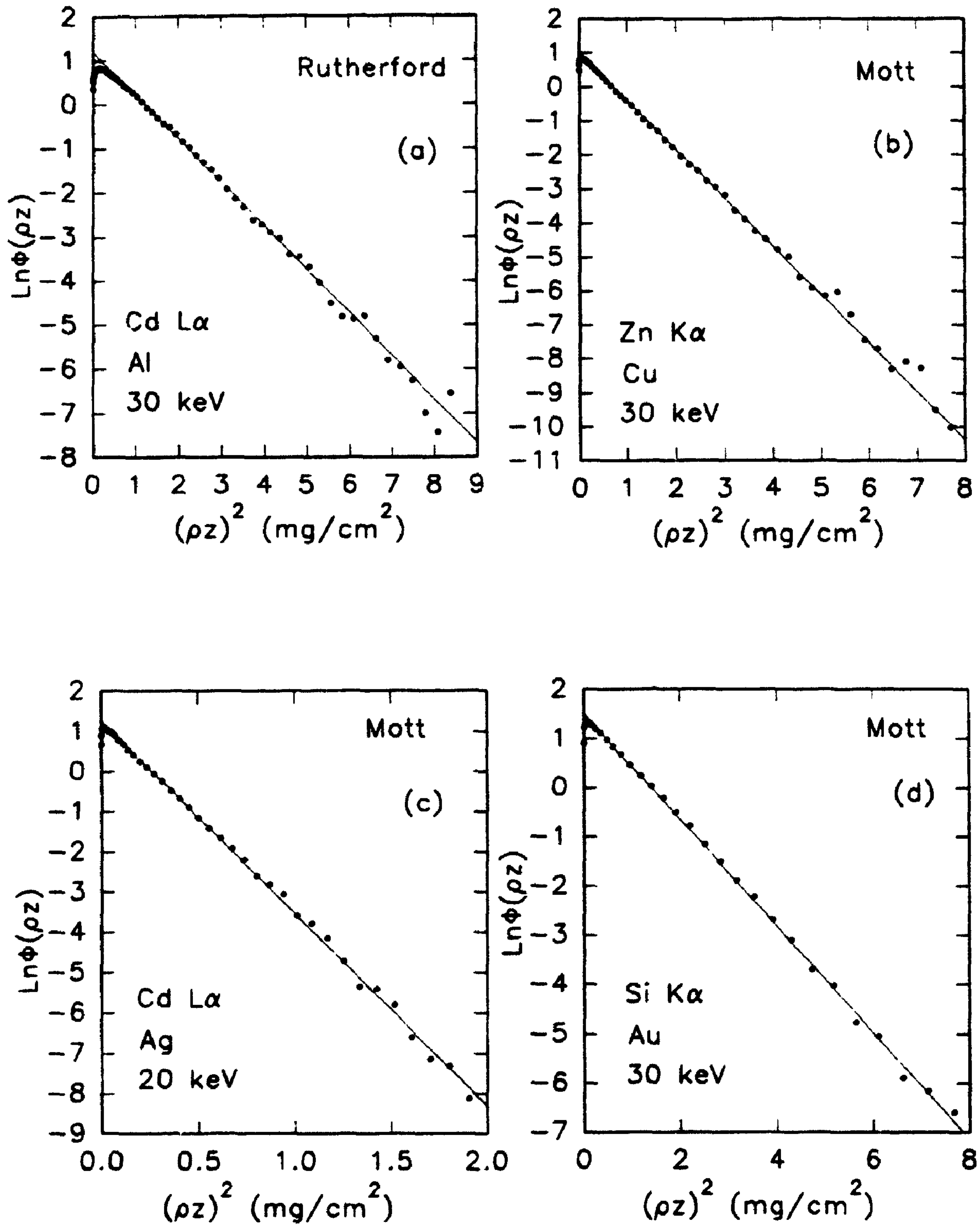

Figure 40(a,b,c and d). Plots of $\ln\Phi(\rho z)$ versus $(\rho z)^2$ from figures 20,34,31 and 27 respectively.

Table 3

Comparison of α value between experimentally measured and Monte Carlo calculated $\phi(\rho z)$ curves.

Figure number	α value Exp. ($cm^2/\mu g$)	α value M.C. Rutherford ($cm^2/\mu g$)	Rel. Diff. from Exp. (%)	α value M.C. Mott ($cm^2/\mu g$)	Rel. Diff. from Exp. (%)
25	1513	1595	5.4	1487	-1.7
26	5129	7598	48.1	7172	39.8
27	905	1096	21.1	1018	12.5
28	2013	2240	11.3	2067	2.7
29	1301	1445	11.1	1309	0.6
30	3650	4100	12.3	3741	2.5
31	2099	2386	13.7	2173	3.5
32	1066	1127	5.7	1035	-2.9
33	2755	2888	4.8	2840	3.1
34	1180	1232	4.4	1205	2.1
35	3320	3668	10.5	3596	8.3
36	4692	5286	12.7	4729	0.8
37	6252	7307	16.9	6790	8.6
38	5893	6493	10.1	6216	5.5
39	6185	7314	18.3	6753	9.2

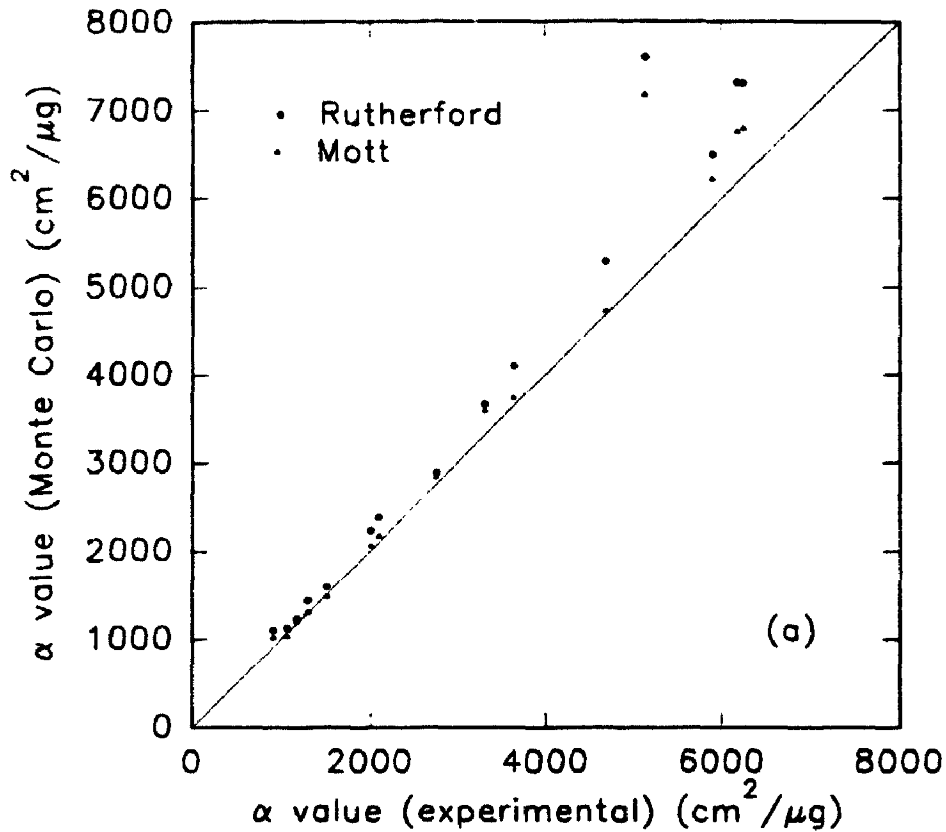

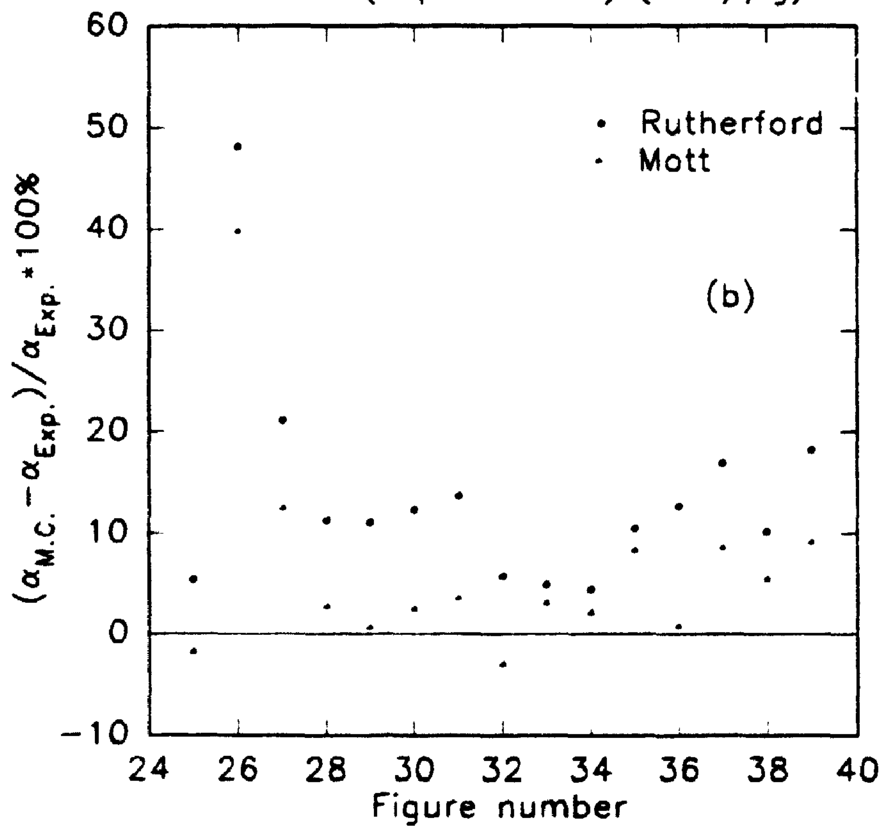

Figure 41(a,b). Absolute and relative comparison of optimized α values between experimentally measured and Monte Carlo calculated $\Phi(\rho z)$ curves from Table 3.

$$(\gamma_o-\phi(o))\,(2\alpha^2(\rho z)_{max}+\beta)\,e^{-\beta(\rho z)_{max}} - 2\alpha^2\gamma_o(\rho z)_{max} = 0 \qquad \text{(Eqn. 74)}$$

$(\rho z)_{max}$ can be solved numerically using Newton's Law. A Fortran computer program was written to calculate the values of ρz_{max}. A comparison of maximum $\phi(\rho z)$ positions between Monte Carlo simulated and measured $\phi(\rho z)$ curves is summarized in Table 4. While there is an obvious advantage of choosing Mott over Rutherford for the α parameter, this is not necessarily the case when comparing ρz_{max} position. For some systems, the Rutherford model is better than the Mott model and for others it is not. The agreement with the maximum is not particularly good. This may be due in part to the layer interval (last column of Table 4) chosen in the Monte Carlo program which results in only a few points from the surface to the maximum. Figure 42 plots the absolute difference between the Monte Carlo and measured maximum $\phi(\rho z)$ values versus the layer interval. The line drawn represents a single layer interval - all points lying below the line have a discrepancy corresponding to less than one layer. Generally, agreement is within one layer thickness which is perhaps as good as one could expect.

5.3.2 Specific Systems

An interesting comparison occurs between Figures 28 and 31. In these figures, data are plotted for the same matrix element and electron energy but for two different x-ray lines, Cd Lα and Si Kα whose critical excitation potentials are 3.538 and 1.838 keV respectively. Since the same matrix and energy are involved, the same electron scattering occurs and hence the same table for number of electrons and energy against

Table 4

Comparison of mass depth at maximum $\phi(\rho z)$ between experimentally measured and Monte Carlo calculated $\phi(\rho z)$ curves.

Figure number	ρz_{max} Exp. ($\mu g/cm^2$)	ρz_{max} M.C. Rutherford ($\mu g/cm^2$)	Diff. from Exp. ($\mu g/cm^2$)	ρz_{max} M.C. Mott ($\mu g/cm^2$)	Diff. from Exp. ($\mu g/cm^2$)	Layer Interval ($\mu g/cm^2$)
25	138.3	141.3	3.0	156.8	18.5	70.4
26	19.0	26.7	7.7	33.7	14.7	15.8
27	246.3	215.7	-30.6	264.0	17.7	99.0
28	105.2	114.3	9.1	127.7	22.5	38.9
29	142.3	161.2	18.9	185.7	43.4	59.0
30	51.6	60.4	8.8	69.0	17.4	22.1
31	97.2	103.7	6.5	119.6	22.4	37.3
32	243.0	218.8	-24.2	256.3	13.3	77.0
33	82.2	92.9	10.8	96.1	13.9	23.7
34	209.5	220.2	10.7	228.2	18.7	57.9
35	82.3	83.3	1.0	83.2	0.9	19.7
36	56.7	60.9	4.2	52.9	-3.8	9.5
37	35.3	52.7	17.4	41.3	6.0	7.5
38	62.6	56.8	-5.9	63.1	0.5	7.9
39	43.9	34.0	-9.9	39.6	-4.3	12.5

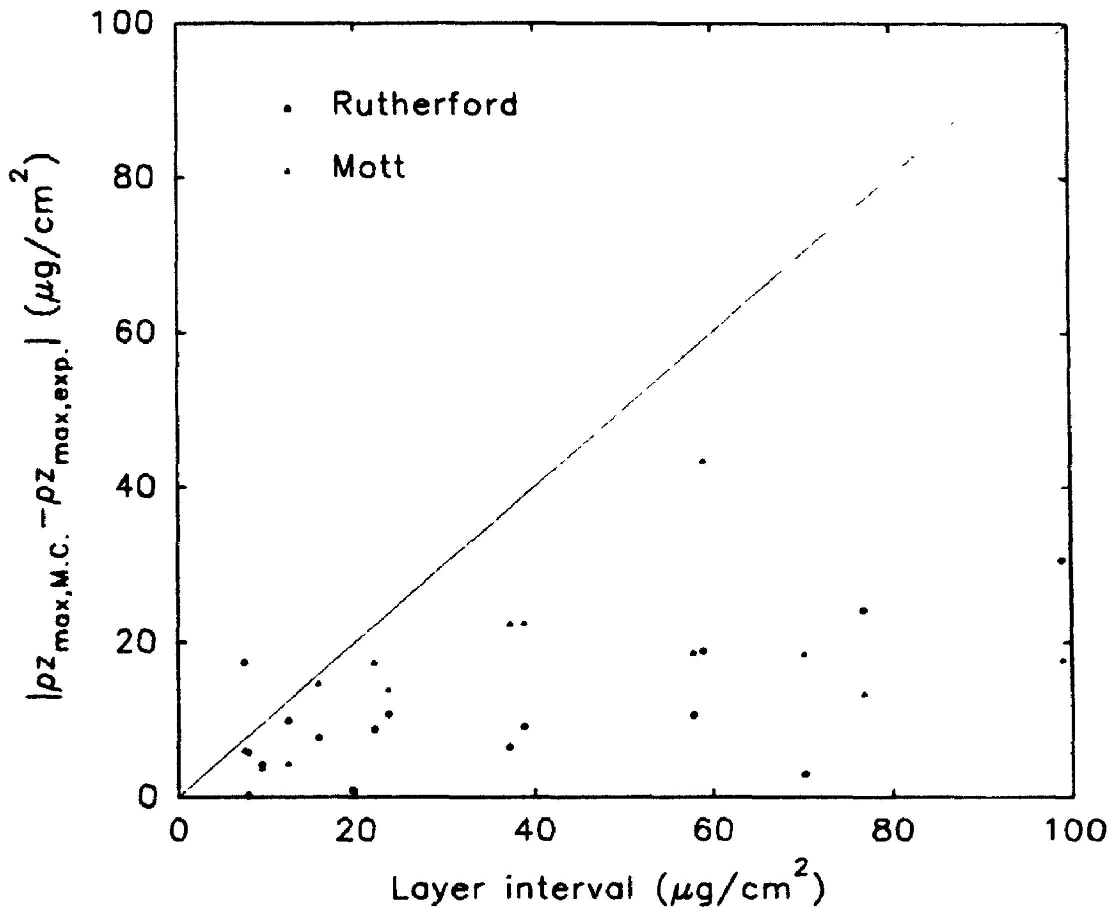

Figure 42. Comparison of absolute difference between Monte Carlo simulated and measured $\Phi(\rho z)$ curves for the depth at maximum $\Phi(\rho z)$ with the corresponding simulated layer interval (Table 4).

layer number can be generated. The only difference in the calculation of the curves is the difference in x-ray cross-section and for the Si Kα, the electrons whose energy lies between 3.538 and 1.838 keV which cannot excite the Cd Lα line. The curves look quite similar, as they should for the same electron distribution in the solid but careful inspection reveals some interesting differences. Relative to the Cd Lα curve, the Si Kα curve is broader (which can be seen most easily in the $\ln\phi(\rho z)$ curve) and is much higher in value (seen best in the $\phi(\rho z)$ curve). The former is a consequence of the low energy electrons which predominate at larger depths in the specimen while the latter effect is due to the higher overvoltage at which the x-ray cross-section will be smaller for electrons passing through the thin film reference layer.

Monte Carlo calculations have been made by other authors on specific systems which are included in this study. In Figure 25a for Cd Lα in Au at 25 keV, the Monte Carlo curves lie above the measured one. Murata et al. [110] had similar results in that their calculated curve also lay above the measured one in particular in the peak region of the curve. However, the position of the maximum occurred at a deeper mass depth from their model which is not the case in Figure 25a.

For Si Kα in Au at 10 keV, perhaps the poorest agreement is attained in this study between the Monte Carlo and measured curves in which both the Rutherford and Mott expression give distributions which are too narrow and high. Similar difficulties were encountered by Murata et al. [111], August and Wernisch [84] and Karduck and Rehbach [16] in that all found that the peak position was too deep and the peak maximum too great in the simulated curves.

In the system Si Kα n Au at 30 keV, Figure 27, the Monte Carlo curves lie below the experimental data. Karduck and Rehbach [24] had similar results from their Monte Carlo simulation in which the simulated curves fell below the measured curves, particularly in the tail region. In contrast, the calculated curves for Si Kα in Ag at 20 keV of Figure 28 lie above the measured curves. For the same system, Ding and Wu [112] compared various experimental curves with Monte Carlo curves based on different energy loss and scattering angle models. A similar difference was found in that even their "best" curve lay completely above the experimental curves. The same comments apply to Figure 31 for Cd Lα in Ag which was also studied by Ding and Wu.

Figures 33 and 34 show plots for Zn Kα in Cu at 20 and 30 keV respectively with better agreement apparent at 30 keV. Karduck and Rehbach [16] had similar results with their Monte Carlo simulation.

For the low atomic number matrix aluminum, August and Wernisch [84] found that their Monte Carlo curve for Cu Kα at 15 keV, which is a fairly low overvoltage ratio, agreed well with the experimental curve for the initial rise of the curve to depths of 50 $\mu g/cm^2$ but fell away for depths from 50 to 300 $\mu g/cm^2$ and finally lay above the experimental curve for greater depths. Figure 36 shows the curves from this system. Note that although the Mott scattering expression yields a poorer fit through the peak, the tail of the curve is in good agreement (Figure 36b). The August and Wernisch curve gives a very low slope in the plot of $\ln\phi(\rho z)$ versus the square of depth. Murata et al. [113] for Si Kα in the same matrix at 10 keV, found that their

Monte Carlo curve fell below the experimental curve in contrast to the curves of Figure 37.

Figures 43, 44, 45 and 46 were meant to illustrate that the disagreement in some α values between experimentally measured $\phi(\rho z)$ curves and those calculated by the Mott multiple scattering angle (Figures 26, 33, 35 and 39) can be reduced if Eqn. (73) was replaced by Eqn. (72).

5.3.3 Summary

The assumed scattering angle model has a significant effect on the simulated $\phi(\rho z)$ curves. In general, for low atomic number matrices and high electron energy, the Rutherford scattering model is accurate enough to describe $\phi(\rho z)$ curves. However, as the atomic number of the matrix increases and the electron energy decreases, the Mott scattering model performs better in particular for the tail part of the $\phi(\rho z)$ curve where the predicteu behaviour comes closer to the experimental data. While there is no formal equation to calculate $\theta_{Mott,multiple}$ quantitatively, qualitatively, in general, a small correction from $\theta_{Rutherford,multiple}$ is sufficient to obtain a better simulated $\phi(\rho z)$ curve. Although Eqns. (72) and (73) appear to be quite simple, they do give good results and made significant improvement over the original Rutherford model. What is further required is to further modify the two existing formulae.

It is important to point out that discussions of ways to improve Monte Carlo simulations have usually concentrated on topics such as the effect of the choice of

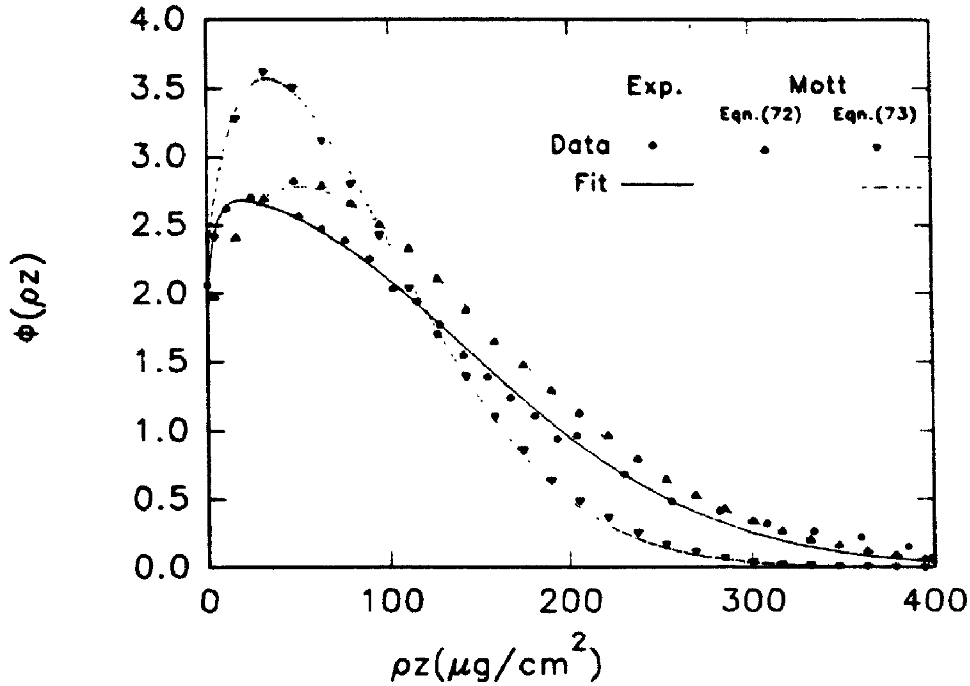

Figure 43a. Experimentally measured and Monte Carlo simulated $\Phi(\rho z)$ curves for Si $K\alpha$ in Au at 10 keV.

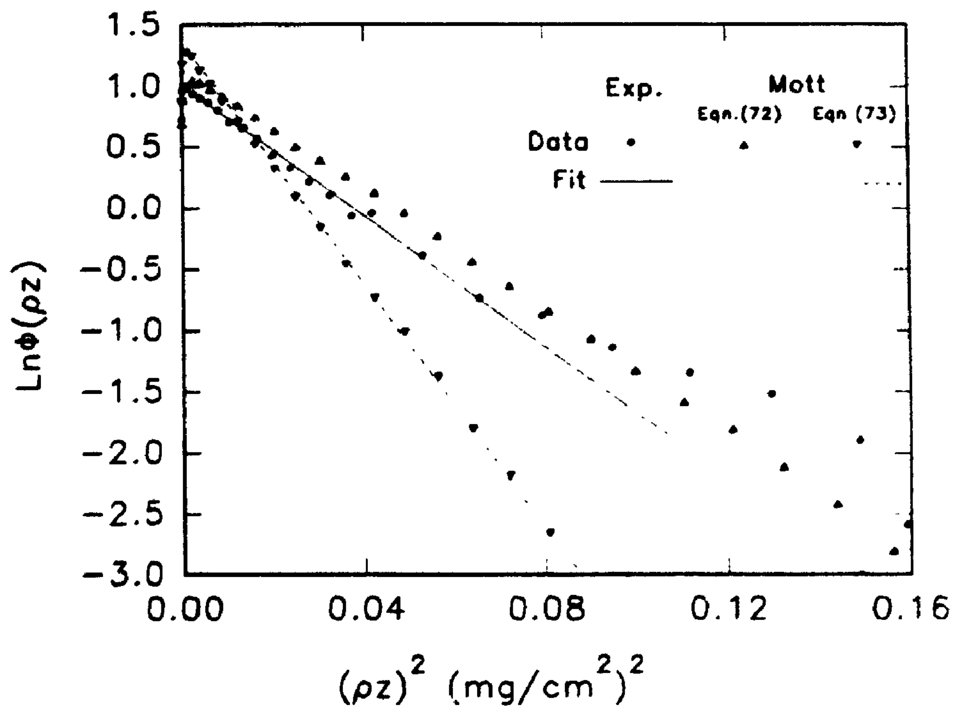

Figure 43b. Plots of $\ln\Phi(\rho z)$ versus $(\rho z)^2$ from figure 43a.

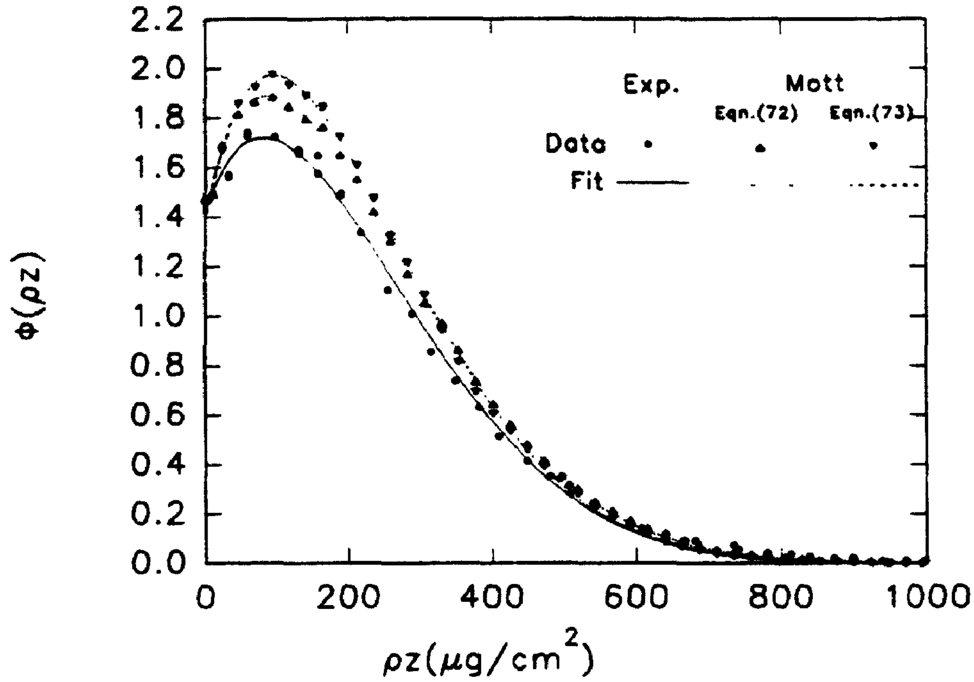

Figure 44a. Experimentally measured and Monte Carlo simulated $\Phi(\rho z)$ curves for Zn Kα in Cu at 20 keV.

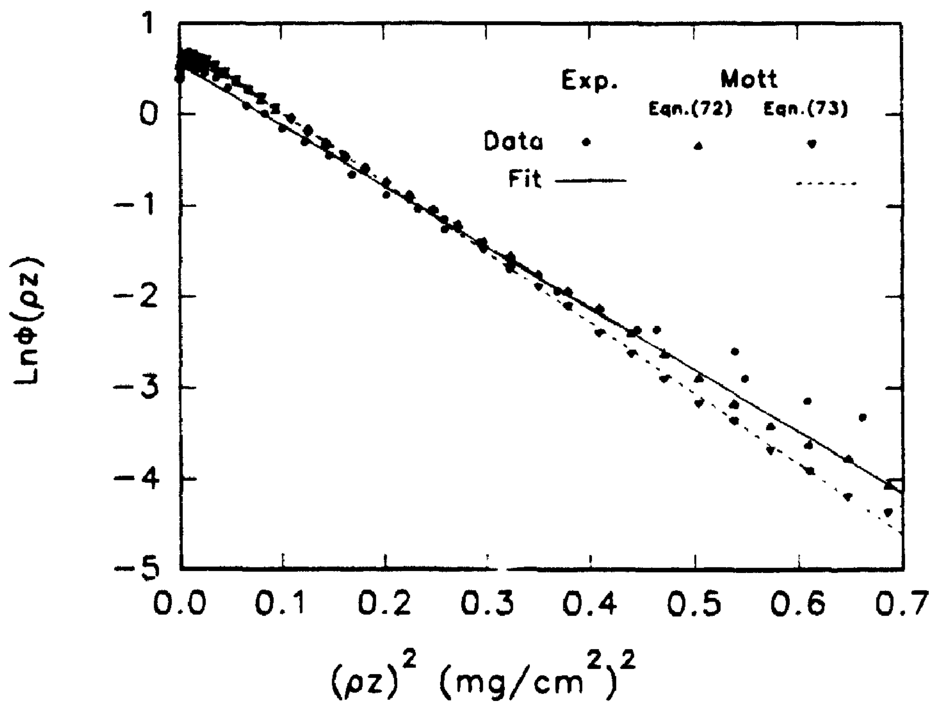

Figure 44b. Plots of $\ln\Phi(\rho z)$ versus $(\rho z)^2$ from figure 44a.

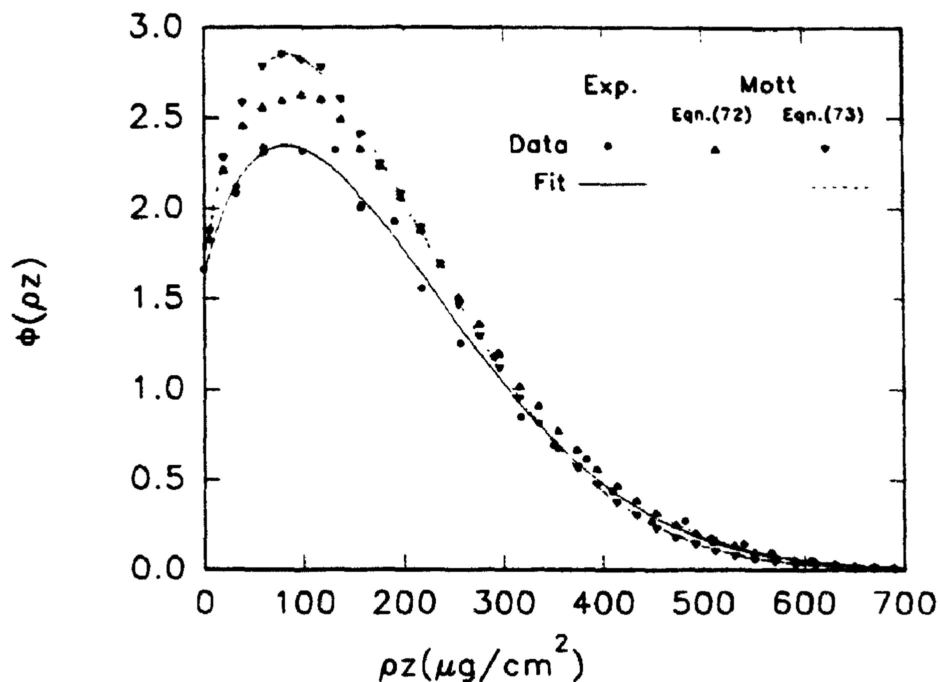

Figure 45a. Experimentally measured and Monte Carlo simulated $\Phi(\rho z)$ curves for Si Kα in Cu at 15 keV.

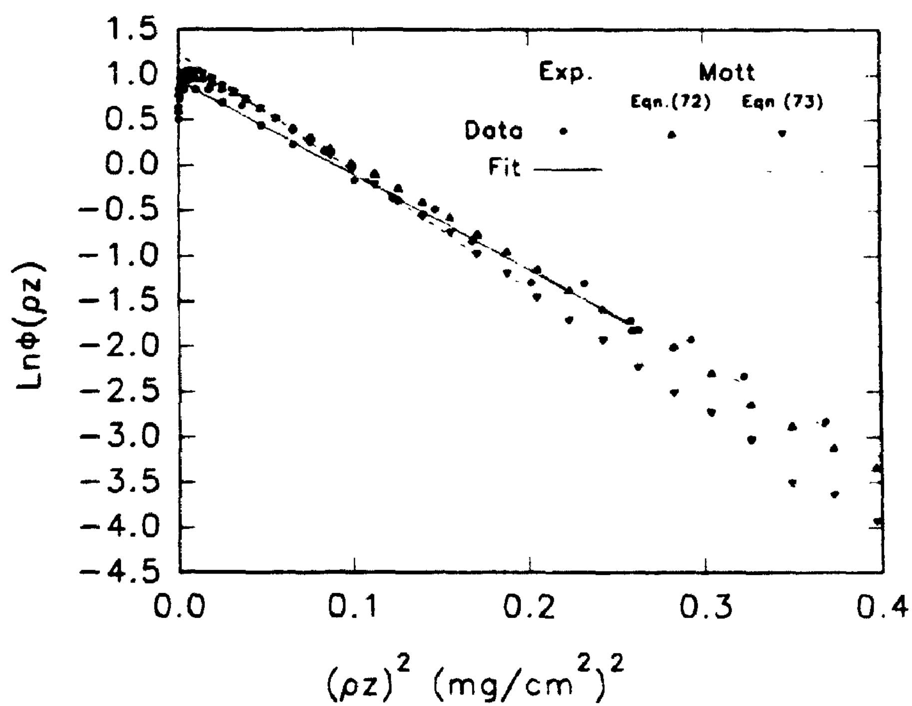

Figure 45b. Plots of $\ln\Phi(\rho z)$ versus $(\rho z)^2$ from figure 45a.

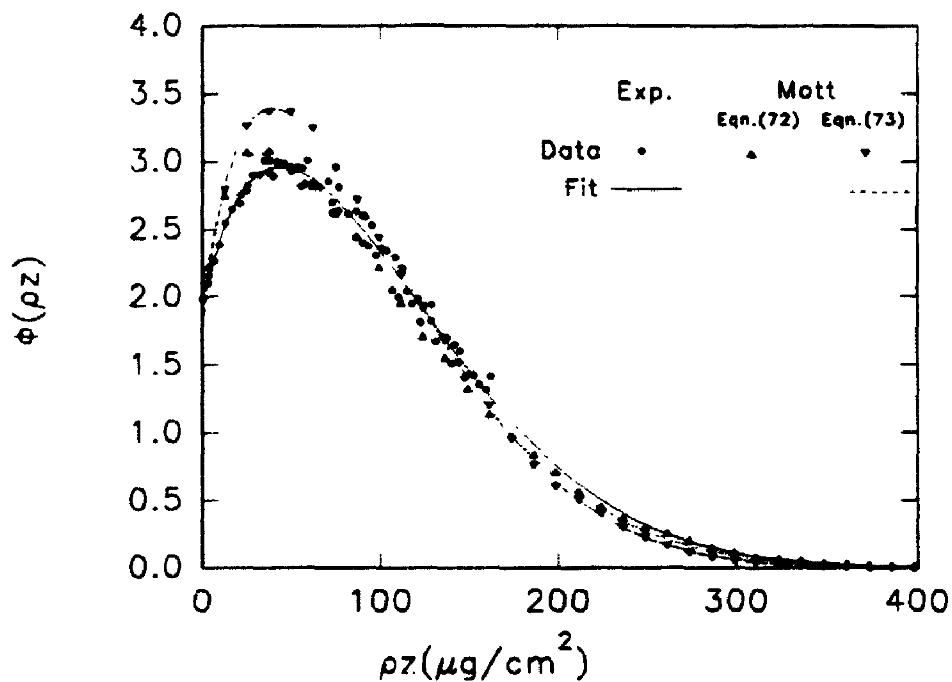

Figure 46a. Experimentally measured and Monte Carlo simulated $\Phi(\rho z)$ curves for Cu Lα in Ag at 10 keV.

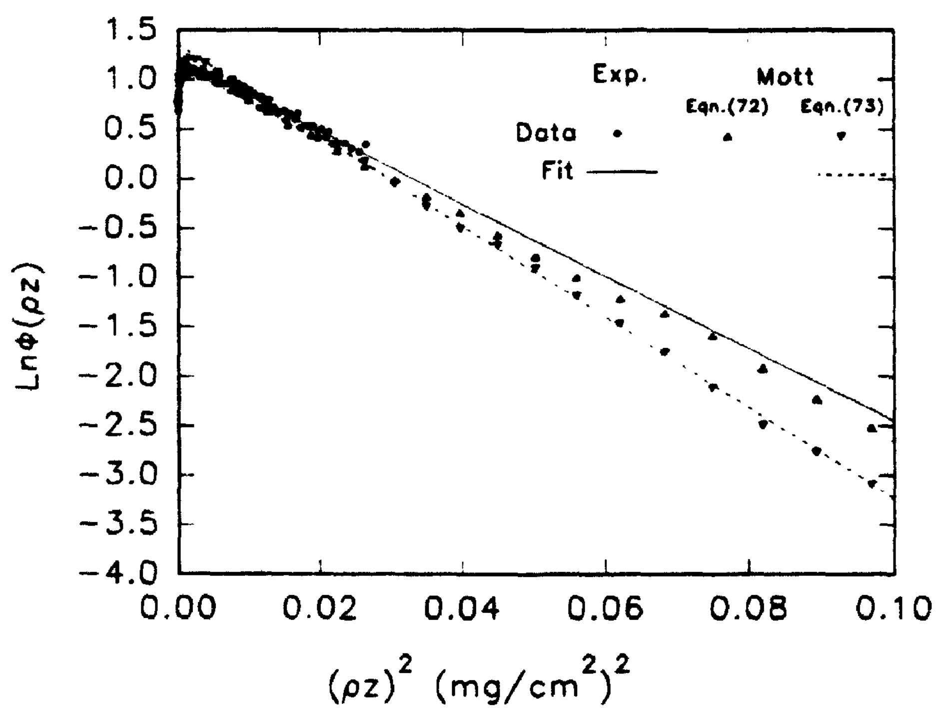

Figure 46b. Plots of $\ln\Phi(\rho z)$ versus $(\rho z)^2$ from figure 46a.

scattering cross-section, ionization cross-section, or the appropriate electron energy loss equations. Much less attention has been focused on the reliability of the experimental data before a comparison of simulated and measured $\phi(\rho z)$ curves were made. Similarly, little attention has been placed on the experimental observation that $\phi(\rho z)$ curves follow a modified gaussian behaviour. The many comparisons made in this work confirm that the modifications made have led to satisfactory agreement with the experimental measurements.

CHAPTER 6

THIN FILM ANALYSIS

6.1 INTRODUCTION

Thin films on thick substrates are used in many fields, in particular, in semiconductor technology where many devices are fabricated by depositing metallic films onto semiconductor substrates and in metallurgy, in which metallic substrates are coated in various ways to protect them from oxidation, corrosion or wear. In these applications, the coatings must be characterized in terms of composition and thickness, preferably in a non-destructive way. The use of electron probe microanalysis for the characterization of thin films on substrates is a proven technique for quality control in a variety of industrial applications. For example, it was reported by Nassiopoulou and Valamontes [114] that EPMA can be used in microelectronics applications to measure film thicknesses and determine the distribution and homogeneity of aluminum structures (integrated circuits) buried under copper layers of different thicknesses.

When it comes to surface analysis, there is a general belief that Auger electron spectroscopy (AES), electron spectroscopy for chemical analysis (ESCA) and secondary ion mass spectroscopy (SIMS) are the most appropriate techniques. However, as early as 1970, Butz and Wagner [115] reported that molybdenum layers could be detected in an electron microprobe down to the monolayer range when deposited on a tungsten substrate. The minimum detection limit (MDL) or the lowest concentration of a given element that can be detected is a measure of the sensitivity

of the analysis system. In EPMA this depends on the element analyzed, the matrix elements, the instrument and the time allowed for the analysis. For thin films, the problem is to decide how small an x-ray peak can be detected above the background from the substrate. One criterion which is used is based on 95% confidence that a measurement has successfully detected the presence of the film. On that basis the minimum detection limit can be estimated from the following equation assuming that a linear relation exists between film thickness ρL and count rate:

$$\rho L_{MDL} = \frac{3}{P}\sqrt{\frac{B}{T}} \qquad \text{(Eqn. 75)}$$

where B = background count rate

P = count rate per unit film thickness

T = counting time for both peak and background

A monolayer detection limit for electron probe microanalysis was further confirmed by subsequent studies from Butz and Wagner [116], Wendt et al. [117], Brown [118, 119] and Murata and Sugiyama [120]. With improving instrumental electronics, an even lower detection limit was reported by Hasegawa et al. [121], Pouchou and Pichoir [122] and Scott et al. [123]. It was reported by Bastin and Heijligers [124] that an oxygen peak was detected on a pure gold specimen. As the solubility of oxygen in gold is negligible, the oxygen must be physically adsorbed on the specimen surface and that shows how surface sensitive a microprobe can be.

Determination of the mass thickness of thin films whose mass thickness is smaller than the range of x-ray production is an opportunity in electron probe

microanalysis and is being addressed with increasing accuracy. Sweeny et al. [125] were the first to try to determine the thickness of various metallic films evaporated on glass. Other studies include Cockett and Davis [126], Marshall and Hall [127, 128], Philibert and Penot [129], Philibert and Tixier [130], Colby [131], Djuric and Cerovic [132], Reuter [133, 134], Bishop and Poole [135, 136], Bolon and Lifshin [137], Hutchins [138], Kyser and Murata [139], Yakowitz and Newbury [140], Duzevic and Bonefacic [141], Cvikevich and Pihl [142], Hunger and Kuchler [143], Murata et al. [110, 111, 120, 144], Sewell et al. [145], Pouchou and Pichoir [75, 122], Pouchou et al. [34], Packwood and co-workers [146-149], Willich and co-workers [150-155], Churms and Kritzinger [156], Brown [118, 157], August [158-160], Hunger [161], Waldo [162], Gillies et al. [163], Cazaux et al. [164], Fitzgerald and co-workers [165-167], Bastin et al. [168-170], Karduck and Ammann [2, 171], Ammann and Karduck [172, 173], Wernisch [174], Laurie et al. [175], Scott and Love [176] and Ding and Wu [3]. However, some of these methods are completely empirical, some are graphical, some are based on calibration curves, some include ZAF formalism and some may only apply to a particular system rather than more generally. Comparisons between some of these methods were made and commented by Wernisch [174], Mackenzie [177] and Scott et al. [178].

In conventional bulk microanalysis the specimen is homogeneous within the depth probed by the electron beam. However, in thin film analysis the above criterion is no longer valid. Electron penetration into the substrate and subsequent electron backscattering gives rise to complex interactions which the conventional ZAF

approach cannot accommodate. On the other hand, the $\phi(\rho z)$ method has the advantage of naturally representing layered specimens even though properties of the $\phi(\rho z)$ function change abruptly at any interface. Whereas for bulk analysis the $\phi(\rho z)$ curve must be integrated between zero and infinity, for thin films, the integration is between distinct limits (see Packwood and Milliken [146]).

The term EPMA of thin films is used to describe the situation in which the film thickness is less than the ultimate depth of x-ray production. The geometry of analysis of thin films is shown in Figures 47 and 48. The x-ray excitation volume extends through the film of mass thickness ρt into the substrate in Figure 47a. Measurement of film thickness starts from the depth distribution function of characteristic x-rays. The ratio, k_A, between the characteristic x-ray count rate of element A measured from the thin film to the count rate measured from a pure element standard under identical instrumental conditions is given by:

$$\frac{I_A^L}{I_A^A} = k_A = W_A \frac{\int_0^{\rho t} \phi_A^L(\rho z) \exp(-\mu_A^L \rho z \csc\psi)\, d(\rho z)}{\int_0^{\infty} \phi_A^A(\rho z) \exp(-\mu_A^A \rho z \csc\psi)\, d(\rho z)} \qquad \text{(Eqn. 76)}$$

where W_A is the weight fraction of element A in the film layer L, the denominator represents the count rate from the bulk pure element standard A and the numerator represents the count rate from the thin film of mass thickness ρt. μ_A^L and μ_A^A are the mass absorption coefficients for the characteristic radiation of element A in the film

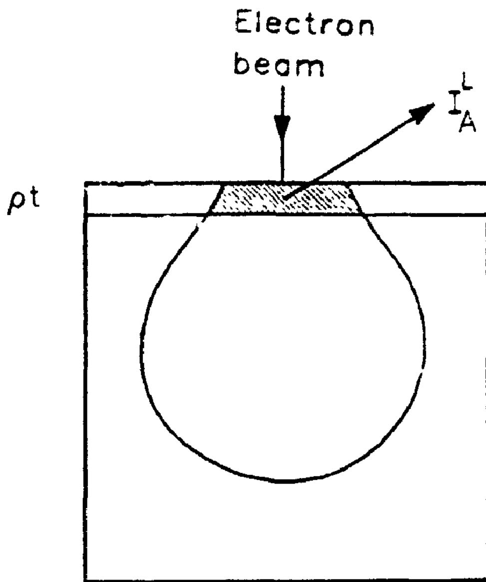

Fig 47a. Measurement of x-ray intensity (I_A^L) from thin film on substrate.

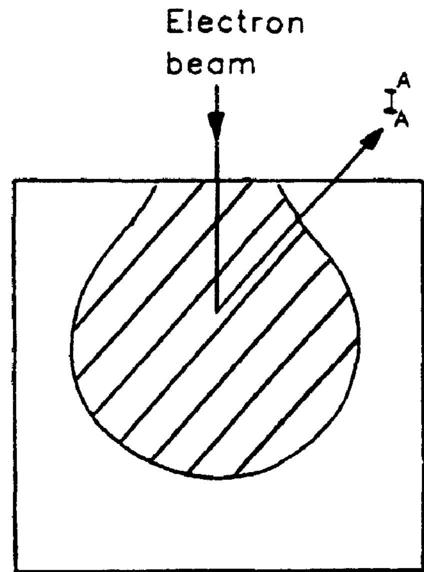

Fig 48a. Measurement of x-ray intensity (I_A^A) from bulk standard.

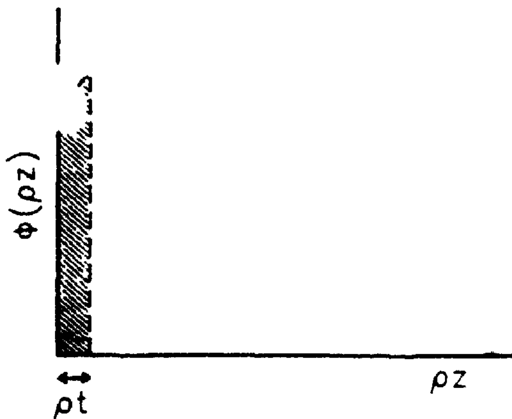

Fig 47b. Area under the curve represents I_A^L from Fig. 47a.

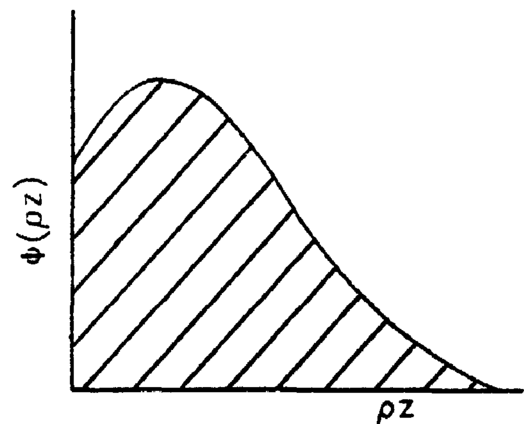

Fig 48b. Area under the curve represents I_A^A from Fig. 48a.

L and pure element standard A respectively. If the film consists of a single element or in other words pure element film, then W_A equals to unity and the only unknown in Eqn. (76) is the film mass thickness ρt. Since I_A^L and I_A^A can be accurately measured by a modern microprobe and therefore accuracy in determining ρt is limited only by the prediction of the $\phi(\rho z)$ curves both for the pure element standard and the layer. Because of the complex nature of Eqn. (76), the measured intensity ratio can not be explicitly expressed as a function of the film mass thickness. Fortunately, an iterative procedure is possible, provided that algorithms to compute $\phi(\rho z)$ functions are available. By successive modifications of ρt the final value of the film thickness for which the calculated k_A is identical to the measured k-ratio can be computed. The accuracy of this method also depends on the accuracy of the mass absorption coefficients chosen. Other assumptions are that there are no fluorescence effects by elements present in the substrate or layer and that the analyzed element in the film is not present in the substrate.

The main problem in the determination of film thickness, using $\phi(\rho z)$ equations, is the influence of the substrate on the $\phi(\rho z)$ distribution within the film. $\phi(\rho z)$ will be different for the pure element standard and layer even if the layer is a pure element due to the differences in energy loss and backscattering that occur at the film/substrate interface. If the film and substrate are of similar atomic number, then no special difficulties arise. If there is a marked difference in atomic number between film and substrate, then the $\phi(\rho z)$ distribution for $Z_{film} < Z_{substrate}$ will be enhanced near the interface and for $Z_{film} > Z_{substrate}$ the $\phi(\rho z)$ distribution will be suppressed.

Therefore, the objective of this work is to investigate these effects more closely and to derive an analytical expression for thin film $\phi(\rho z)$ distribution which is suitable for all film/substrate combinations, at all energies for microprobe analysis. Up to now, thin film $\phi(\rho z)$ expressions have been rather unknown and inaccurate. Systematic investigations of $\phi(\rho z)$ curves for thin film on substrate are still limited. Existing approaches use empirical approximations based upon the well established expressions for $\phi(\rho z)$ in homogeneous materials. Therefore, a detailed study of thin film $\phi(\rho z)$ curves is necessary to put EPMA of thin films on a firm basis.

6.2 MONTE CARLO METHOD FOR THIN FILMS

Due to scattering phenomena, electrons can move from regions of greater mass depth to regions of smaller mass depth. Therefore, the substrate material in a thin film specimen will influence the shape of the depth distribution function of the film. This will produce $\phi(\rho z)$ curves which are different from the bulk curves. The Monte Carlo method can be adapted to accommodate interfaces and calculate appropriate thin film $\phi(\rho z)$ curves.

The present Monte Carlo method for bulk analysis has been extensively modified to take care of this idea. It is assumed that a sample is divided into two regions by a horizontal plane which is parallel to the surface of the sample at a certain mass depth given by the mass thickness of the film. In the case of bulk homogeneous samples, the two regions consist of the same material. For a thin film specimen, the top region refers to the film and the bottom region refers to the substrate. Some

possible electron paths are shown in Figure 49. The influence of the substrate comes about when electrons pass through the film, penetrate into the substrate but then scatter back into the film as in trajectories 1-4. All electrons initially enter the film. The computer program was modified such that when the electron stays in the film, the electron follows the energy loss and scattering angle changes for the film medium but when the electron crosses into and stays in the substrate, the electron follows the energy loss and scattering angle changes appropriate for the substrate medium.

When an electron passes from the film into the substrate, a portion of the step length will be in the film and a portion in the substrate and in an exact calculation the step should be broken up into two parts in which each portion will suffer a different energy loss. The same is true when an electron moves from the substrate into the film. However, to simplify calculations, in the case where the electron passes from the film into the substrate, the whole step is assumed to take place as if it were in the film medium. In a similar manner, when the electron passes from the substrate into the film, the whole step is assumed to occur as if it were in the substrate medium. As a consequence, the interface is treated essentially as a rough interface. However, since each electron trajectory may cross the interface a few times and since a large number of trajectories (10,000) are followed, any errors introduced by electrons passing from film to substrate will be offset by electrons passing from substrate to film.

In the bulk analysis Monte Carlo program, only one electron energy loss table is required. However, two such tables are needed in a film/substrate specimen

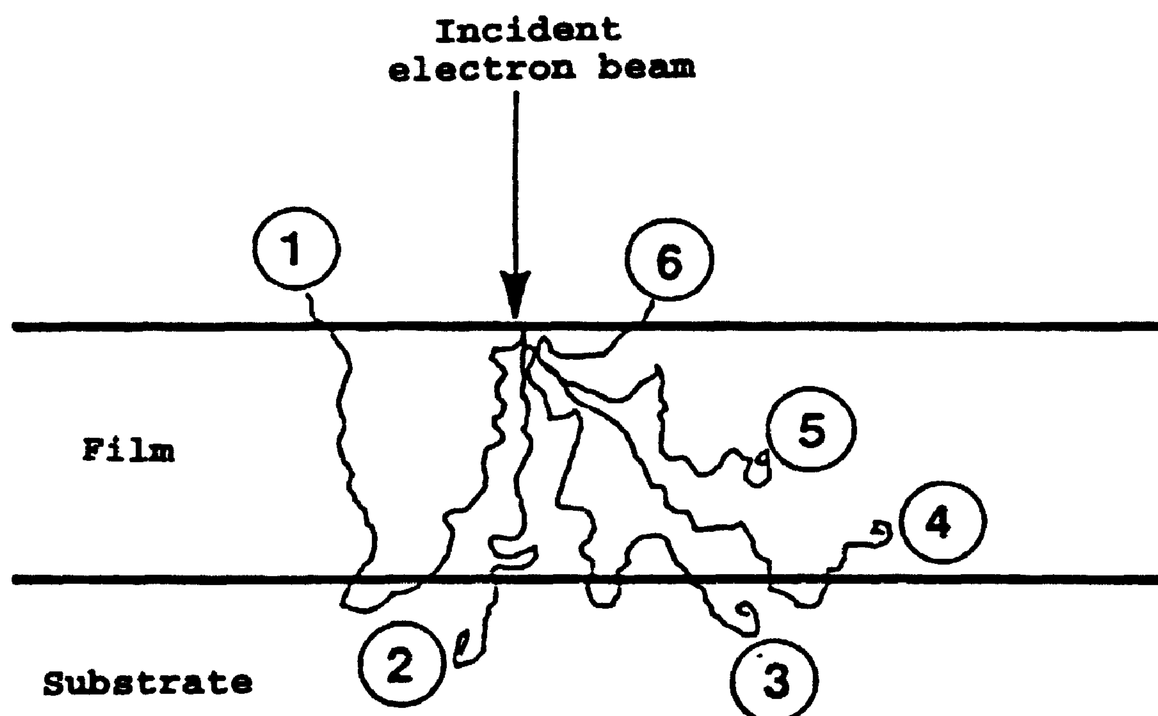

Trajectory number	Start	Route	End
1	film	substrate, film	backscattered
2	film	substrate	substrate
3	film	substrate, film	substrate
4	film	substrate	film
5	film	film	film
6	film	film	backscattered

Figure 49. Schematic diagram of six possible electron trajectories in a thin film on substrate specimen.

calculation, one for electron energy loss in the film medium and the other for the substrate medium. The computer program was designed such that the energy value is taken from the film energy table initially and for as long as the electron moves around in the film. However, if the electron passes through the interface into the substrate, the energy table from the substrate medium is used immediately and vice versa. Similarly, the electron scattering angle distributions are switched when the electron passes through the interface.

There are a few complications in connection with the energy tables. In bulk specimens in order to allow for electron straggling the number of values needed is larger than the actual number of steps taken for each trajectory, the exact index for each electron in a particular step is predetermined by a random number so that the energy for the electron at a particular step is established. However, in the case of a thin film on a substrate, the energy of an electron at a particular step cannot be predetermined except during the first few scattering events while the electron remains in the film. When the electron passes through the interface the energy of the electron remains essentially the same but the corresponding energy index may be different. For example, Table 5 shows the electron energy tables for silicon and gold with 10 keV electron incidence energy for the Si Kα line. Suppose the electron has been scattered from the film through the interface into the substrate and that the energy index at the end of the step would have been 50 in the film (Si). The energy therefore is 8.555 keV. In the substrate (Au), the closest corresponding energy is 8.551 keV at index 46. As a consequence, the energy index would be changed to 46

Table 5
10 keV electron energy tables for Si Kα

	Matrix			Matrix	
Index	Si	Au	Index	Si	Au
1	9.973	9.970	51	*8.524	8.385
2	*9.945	9.940	52	8.493	8.351
3	9.918	9.910	53	8.462	8.318
4	9.890	9.879	54	8.431	8.284
5	9.863	9.849	55	*8.400	8.250
6	9.835	9.819	56	8.369	8.216
7	*9.808	9.788	57	8.338	8.182
8	9.780	9.758	58	8.306	8.148
9	9.752	9.727	59	*8.275	8.114
10	9.724	9.697	60	8.243	8.080
11	*9.696	9.666	61	8.212	8.046
12	9.668	9.635	62	8.180	8.011
13	9.640	9.604	63	8.148	7.977
14	9.612	9.574	64	*8.116	7.942
15	*9.584	9.543	65	8.084	7.908
16	9.556	9.512	66	8.052	7.873
17	9.527	9.481	67	8.020	7.838
18	9.499	9.450	68	*7.988	7.803
19	9.471	9.418	69	7.955	7.768
20	*9.442	9.387	70	7.923	7.733
21	9.414	9.356	71	7.890	7.698
22	9.385	9.324	72	7.857	7.663
23	9.356	9.293	73	*7.825	7.627
24	*9.328	9.262	74	7.792	7.592
25	9.299	9.230	75	7.759	7.556
26	9.270	9.198	76	7.725	7.521
27	9.241	9.167	77	*7.692	7.485
28	9.212	9.135	78	7.659	7.449
29	*9.183	9.103	79	7.625	7.413
30	9.154	9.071	80	7.592	7.377
31	9.124	9.039	81	*7.558	7.341
32	9.095	9.007	82	7.525	7.305
33	*9.066	8.975	83	7.491	7.268
34	9.036	8.943	84	7.457	7.232
35	9.007	8.911	85	7.422	7.195
36	8.977	8.878	86	*7.388	7.158
37	*8.948	8.846	87	7.354	7.122
38	8.918	8.814	88	7.319	7.085
39	8.888	8.781	89	7.285	7.048
40	8.858	8.748	90	*7.250	7.011
41	8.828	8.716	91	7.215	6.973
42	*8.798	8.683	92	7.180	6.936
43	8.768	8.650	93	7.145	6.898
44	8.738	8.617	94	*7.110	6.861
45	8.707	8.584	95	7.075	6.823
46	*8.677	8.551	96	7.039	6.785
47	8.647	8.518	97	7.004	6.747
48	8.616	8.485	98	6.968	6.709
49	8.586	8.452	99	*6.932	6.671
50	8.555	8.418	100	6.896	6.633

Table 5 (continued)
10 keV electron energy tables for Si Kα

Index	Matrix Si	Matrix Au	Index	Matrix Si	Matrix Au
101	6.860	6.594	151	4.819	*4.478
102	6.823	6.556	152	4.772	4.431
103	*6.787	6.517	153	4.725	4.383
104	6.750	6.478	154	4.677	4.336
105	6.714	6.439	155	4.629	4.288
106	6.677	6.400	156	4.581	*4.240
107	6.640	6.361	157	4.532	4.192
108	*6.603	6.322	158	4.483	4.143
109	6.565	6.282	159	4.434	4.094
110	6.528	6.243	160	4.384	4.045
111	6.490	6.203	161	4.334	*3.996
112	*6.452	6.163	162	4.283	3.946
113	6.414	6.123	163	4.232	3.896
114	6.376	6.083	164	4.180	3.846
115	6.338	6.042	165	4.128	3.795
116	*6.299	6.002	166	4.076	*3.745
117	6.261	5.961	167	4.023	3.694
118	6.222	5.921	168	3.969	3.642
119	6.183	5.880	169	3.915	3.591
120	6.143	5.839	170	3.861	3.539
121	*6.104	5.797	171	3.806	3.487
122	6.064	*5.756	172	3.750	3.434
123	6.025	5.714	173	3.694	3.381
124	5.985	5.673	174	3.637	3.328
125	*5.945	5.631	175	3.580	3.275
126	5.904	5.589	176	3.522	3.221
127	5.864	*5.547	177	*3.463	3.167
128	5.823	5.504	178	3.404	3.113
129	5.782	5.462	179	3.344	3.058
130	5.741	5.419	180	3.283	3.003
131	5.699	5.376	181	*3.222	2.947
132	5.658	*5.333	182	3.159	2.892
133	5.616	5.290	183	3.096	2.836
134	5.574	5.246	184	3.032	2.779
135	5.532	5.203	185	*2.967	*2.723
136	5.489	5.159	186	2.901	2.666
137	5.446	*5.115	187	2.834	2.608
138	5.403	5.071	188	2.766	2.551
139	5.360	5.026	189	2.697	2.493
140	5.316	4.982	190	2.626	*2.434
141	5.273	4.937	191	2.555	2.376
142	5.229	*4.892	192	2.482	2.317
143	5.184	4.847	193	2.407	2.258
144	5.140	4.802	194	2.332	2.198
145	5.095	4.756	195	2.254	*2.139
146	5.050	*4.710	196	2.175	2.079
147	5.004	4.664	197	2.094	2.019
148	4.958	4.618	198	2.011	1.959
149	4.912	4.572	199	1.926	1.898
150	4.866	4.525	200	1.838	*1.838

and the index increment adjusted to ensure that the energy would be equal to 1.838 (E_c for Si K) at the end of the last step. An example of a trajectory calculation is given to clarify the process of energy value selection from the two tables. Trajectory number 3 from Figure 49 with 46 steps was chosen as an illustration where the electron starts in the film, crosses the interface into the substrate but scatters back into the film and finally ends up in the substrate. The asterisk (*) marks the actual energy that the electron had in each step along its path. Due to the nature of the trajectory, the electron crosses the interface a few times and that is reflected in the choice of the energy which moves back and forth between the two matrices. The energies of the electron and its positions are summarized in Table 6.

6.3 SIMULATION RESULTS

Table 7 lists the combinations used to determine how thin film $\phi(\rho z)$ curves depend on the atomic number of the film and substrate materials, the thickness of the film and experimental conditions such as the primary beam energy and the choice of x-ray line. Over 300 thin film $\phi(\rho z)$ curves were simulated (Appendix 3). The systems outlined in Table 7 are meant to cover a wide range of elements from the periodic table and practical electron energies for EPMA. Twenty bulk $\phi(\rho z)$ curves were also simulated as control curves for the four elements at 10, 15, 20, 25 and 30 keV electron energies. To date, very little detailed experimental information is available about $\phi(\rho z)$ distributions for thin films on substrates primarily because these data are not directly accessible by experiment. Fortunately, two independent studies

Table 6
Summary table for the energy and location of an 10 keV electron in a Si film on Au substrate.

Step number	Energy index(Si)	Energy index(Au)	Electron energy(keV)	Previous location	Present location
1	2	NA	9.945	film	film
2	7	NA	9.808	film	film
3	11	NA	9.696	film	film
4	15	NA	9.584	film	film
5	20	NA	9.442	film	film
6	24	NA	9.328	film	film
7	29	NA	9.183	film	film
8	33	NA	9.066	film	film
9	37	NA	8.948	film	film
10	42	NA	8.798	film	film
11	46	NA	8.677	film	film
12	51	NA	8.524	film	film
13	55	NA	8.400	film	film
14	59	NA	8.275	film	film
15	64	NA	8.116	film	film
16	68	NA	7.988	film	film
17	73	NA	7.825	film	film
18	77	NA	7.692	film	film
19	81	NA	7.558	film	film
20	86	NA	7.388	film	film
21	90	NA	7.250	film	film
22	94	NA	7.110	film	film
23	99	NA	6.932	film	film
24	103	NA	6.787	film	film
25	108	NA	6.603	film	film
26	112	NA	6.452	film	film
27	116	NA	6.299	film	film
28	121	NA	6.104	film	film
29	125	NA	5.945	film	film
30	NA	122	5.756	film	substrate
31	NA	127	5.547	substrate	substrate
32	NA	132	5.333	substrate	substrate
33	NA	137	5.115	substrate	substrate
34	NA	142	4.892	substrate	substrate
35	NA	146	4.710	substrate	substrate
36	NA	151	4.478	substrate	substrate
37	NA	156	4.240	substrate	substrate
38	NA	161	3.996	substrate	substrate
39	NA	166	3.745	substrate	substrate
40	177	NA	3.463	substrate	film
41	181	NA	3.222	film	film
42	185	NA	2.967	film	film
43	NA	185	2.723	film	substrate
44	NA	190	2.434	substrate	substrate
45	NA	195	2.139	substrate	substrate
46	NA	200	1.838	substrate	substrate

Table 7
Monte Carlo thin film calculations

X-ray line	Film	Substrate	E_o (keV)	Thickness range ($\mu g/cm^2$)	# of films	Figure #
Kα	Si	Au	30	80-2100	13	55
Kα	Si	Au	25	100-1000	13	57
Kα	Si	Au	20	50- 700	10	59
Kα	Si	Au	15	40- 400	10	61
Kα	Si	Au	10	10- 290	12	63
Mα	Au	Si	30	200-1300	10	68
Mα	Au	Si	25	100-1000	13	70
Mα	Au	Si	20	60- 700	13	72
Mα	Au	Si	15	50- 400	13	74
Mα	Au	Si	10	20- 200	13	76
Kα	Cu	Ag	30	200- 600	5	78
Kα	Cu	Ag	20	50- 250	5	--
Kα	Cu	Ag	15	50- 150	5	--
Kα	Cu	Au	30	200- 600	5	79
Kα	Cu	Au	20	50- 250	5	--
Kα	Cu	Au	15	50- 150	5	--
Lα	Ag	Au	30	300- 700	5	80
Lα	Ag	Au	20	100- 300	5	--
Lα	Ag	Au	10	40- 100	5	--
Lα	Ag	Au	5	4- 16	5	89
Kα	Si	Ag	30	200- 800	5	81
Kα	Si	Ag	20	100- 500	5	--
Kα	Si	Ag	10	40- 100	5	--
Kα	Si	Cu	30	200- 800	5	82
Kα	Si	Cu	20	100- 500	5	--
Kα	Si	Cu	10	40- 100	5	--
Lα	Ag	Cu	30	300- 700	5	83
Lα	Ag	Cu	20	100- 300	5	--
Lα	Ag	Cu	10	40- 100	5	--
Mα	Au	Cu	30	300- 700	5	84
Mα	Au	Cu	20	100- 300	5	--
Mα	Au	Cu	10	40- 100	5	--
Mα	Au	Ag	30	300- 700	5	85
Mα	Au	Ag	20	100- 300	5	--
Mα	Au	Ag	10	40- 100	5	--
Lα	Ag	Si	30	300- 700	5	86
Lα	Ag	Si	20	100- 300	5	--
Lα	Ag	Si	10	40- 100	5	--
Lα	Ag	Si	5	4- 16	5	--
Kα	Cu	Si	30	200- 600	5	87
Kα	Cu	Si	20	50- 250	5	--
Kα	Cu	Si	15	50- 150	5	--

were made on Si/Au and Au/Si systems by August and Wernisch [159, 174] and Ding and Wu [3]. Theoretical calculations were used by the former and a single scattering model by the latter to arrive at the thin film $\phi(\rho z)$ curves. Although quantitatively the results from this work can not easily be compared to theirs, qualitatively similar shapes were observed for the thin film $\phi(\rho z)$ curves at 10 and 30 keV in that:

(1) In the case of a low atomic number film (Si) on a high atomic number substrate (Au), the film $\phi(\rho z)$ curves all lie above the bulk $\phi(\rho z)$ curve. The largest changes in the thin film $\phi(\rho z)$ curve were found near the film/substrate interface where the magnitude of $\phi(\rho z)$ approaching the interface was considerably higher than it would be in the same depth of the bulk material (Figure 50a). One reason is that a heavy element substrate generates an increase in electrons backscattered into the film which results in additional ionizations in the film.

(2) Although the $\phi(\rho z)$ value for film and bulk will differ the most at the interface where the substrate influence is the biggest, the difference decreases in moving through the film towards the surface. This can be clearly seen in the plots of the ratio of $\phi(\rho z)$ values for the film to bulk at the same depth as plotted in Figure 50b. In fact, the effect of the interface may vanish near the surface if the film is thick enough. For example, there is no effect of the Au (substrate) on the 1400 $\mu g/cm^2$ Si film at depths less than about 1000 $\mu g/cm^2$ at 30 keV electron energy (Figure 50a).

(3) The maximum of the low atomic number thin film $\phi(\rho z)$ curves on high atomic

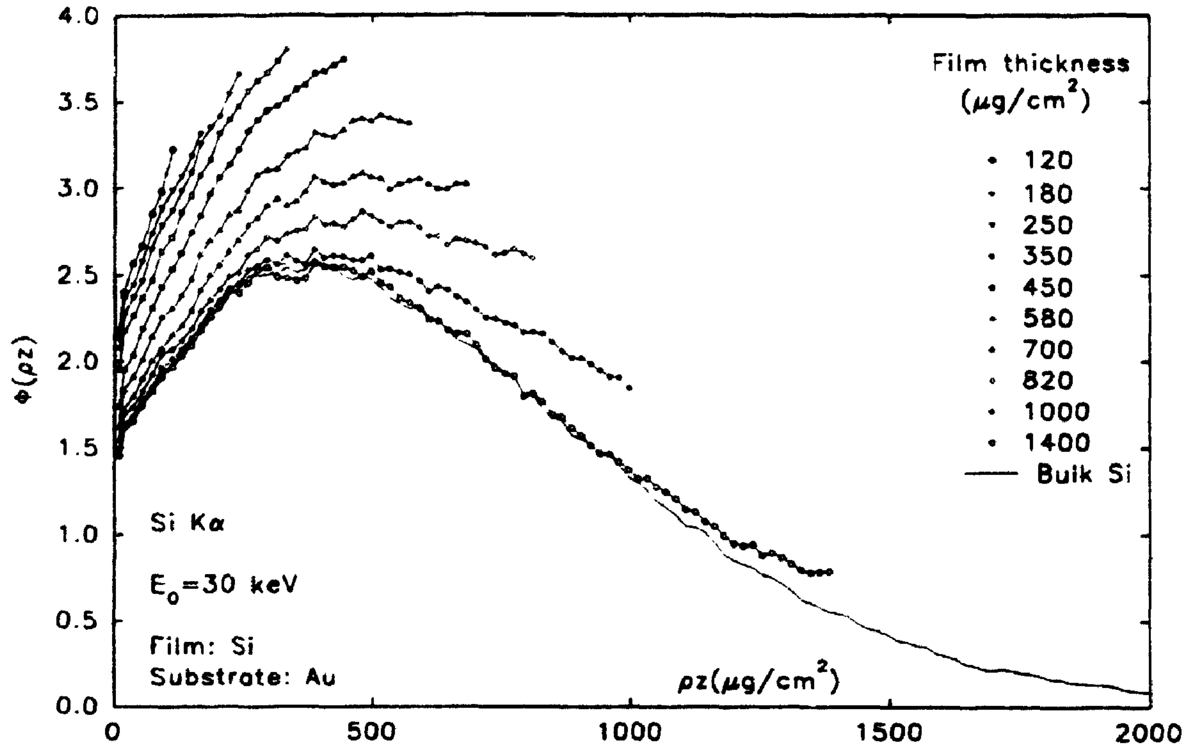

Figure 50a. Monte Carlo simulated thin film $\Phi(\rho z)$ curves of 10 different silicon film thicknesses on gold substrate at 30 keV.

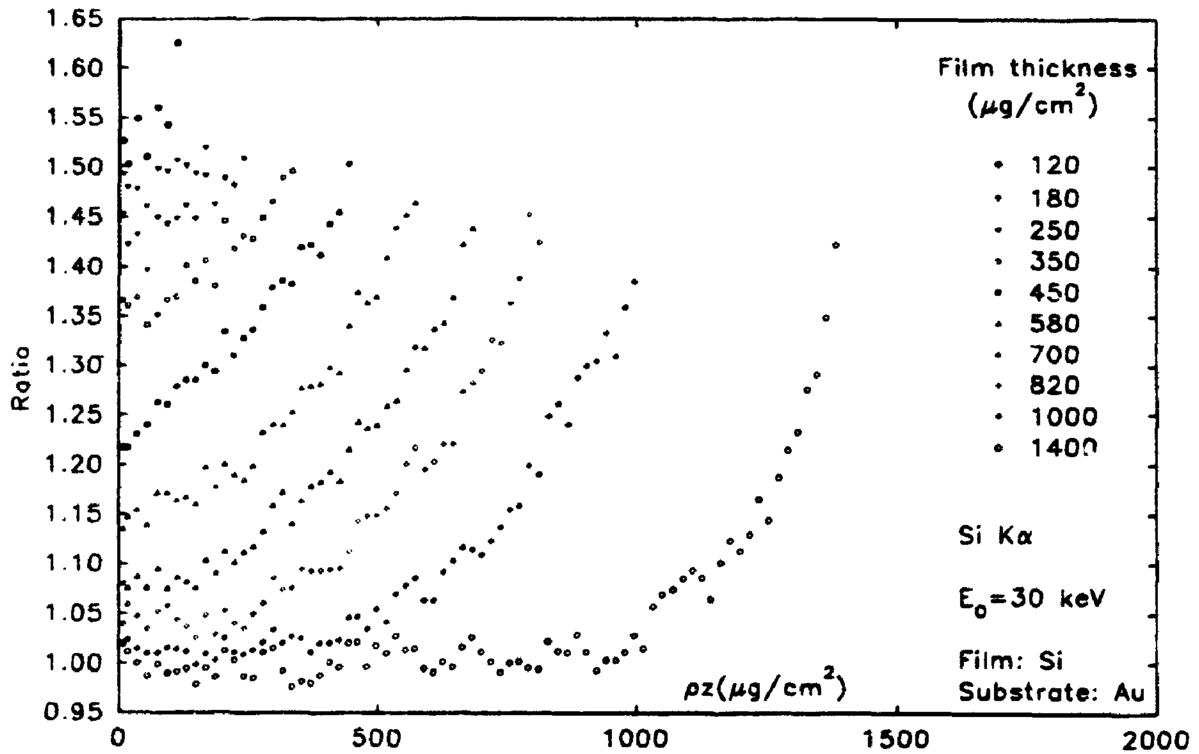

Figure 50b. Ratio plots of film $\Phi(\rho z)$ curves from Fig. 50a.

number substrates was observed to shift towards deeper mass depths. For example, the 700 $\mu g/cm^2$ Si film on Au substrate (Figure 50a) has a maximum which occurs at a greater depth than the corresponding Si bulk $\phi(\rho z)$ curve. For very thick films, the thin film $\phi(\rho z)$ curve lies on top of the corresponding bulk curve and the maximum occurs at the same depth. Thus, it can be argued that the maximum of thin film $\phi(\rho z)$ shifts to greater depths with decreasing film thickness. However, Ammann and Karduck [173] suggested that the maximum of thin film $\phi(\rho z)$ should initially shift to greater depths with increasing film thickness, pass through a maximum value, then beyond that thickness the maximum position shifts rapidly back to the bulk material position. There is no evidence in the data for Si films on Au, at any electron energy of a shift in the position of the $\phi(\rho z)$ maximum to other than greater depths with decreasing film thickness even in those cases where the film is too thin to observe a maximum value but yet thick enough that the maximum position can be estimated.

(4) The value of $\phi(o)$ for a thin film depends on the substrate scattering and the film thickness. For very thick films, the $\phi(o)$ value is the same as the bulk Si $\phi(o)$ value. As the film thickness decreases, the $\phi(o)$ value increases (Figure 50a) and at the limit for a very thin film, the film $\phi(o)$ value will equal to the $\phi(o)$ value for the substrate material.

(5) In the case of a high atomic number film (Au) on a low atomic number substrate (Si), the film $\phi(\rho z)$ curves all lie below the bulk $\phi(\rho z)$ curve (Figure

51a). A reduction in the $\phi(\rho z)$ value at the interface is observed due to a decrease in electrons backscattered from the substrate into the film. This effect will decay away from the interface towards the surface (Figure 51b). For example, there is a reduction of ionization for 1300 $\mu g/cm^2$ of Au film on Si substrate (Figure 51a) at the interface but decays away and there is no difference for the bulk curve for depths less than 750 $\mu g/cm^2$. The maximum of the thin film $\phi(\rho z)$ curves was observed to shift from the bulk maximum position towards shallower mass depths with decreasing film thicknesses (Figure 51a). Again, Ammann and Karduck [173] suggested the 'reversal concept' which is not supported by this system at any energy. For all thicknesses, the Au on Si thin film $\phi(\rho z)$ curves were observed to possess a maximum position and there is no 'plateau' problem around the peak as in the case of light on heavy. The $\phi(o)$ value will be lower in the case of Au film on Si substrate than the bulk Au $\phi(o)$ value. It is apparent that the thinner the film, the lower the $\phi(o)$ value and at the limit for a very th· film, the film $\phi(o)$ value will resemble the $\phi(o)$ value of the substrate material.

6.4 MATHEMATICAL MODEL FOR THIN FILM $\phi(\rho z)$ CURVES

Although the Monte Carlo technique gives remarkable simulation results for thin film $\phi(\rho z)$ curves, it is too time consuming for routine analysis since a complete simulation would be required for each iteration in any quantitative calculation (as well as a bulk $\phi(\rho z)$ simulation for each film element). Therefore, the objective of this

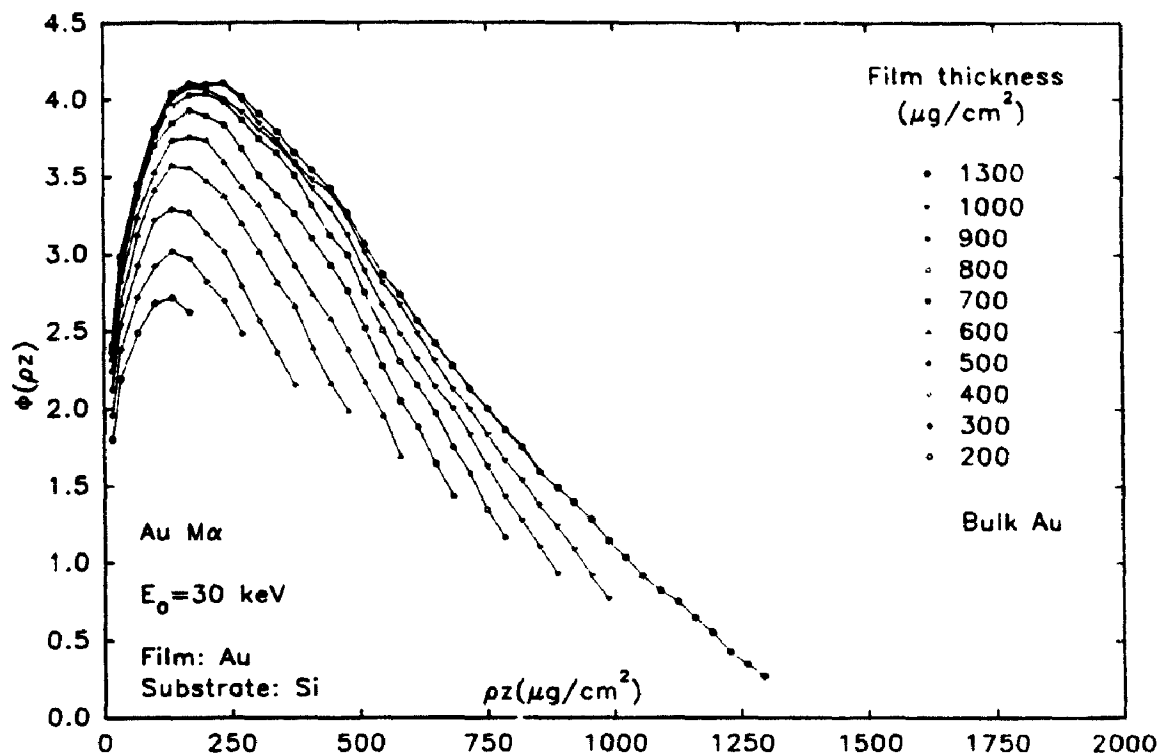

Figure 51a. Monte Carlo simulated thin film $\Phi(\rho z)$ curves of 10 different gold film thicknesses on silicon substrate at 30 keV.

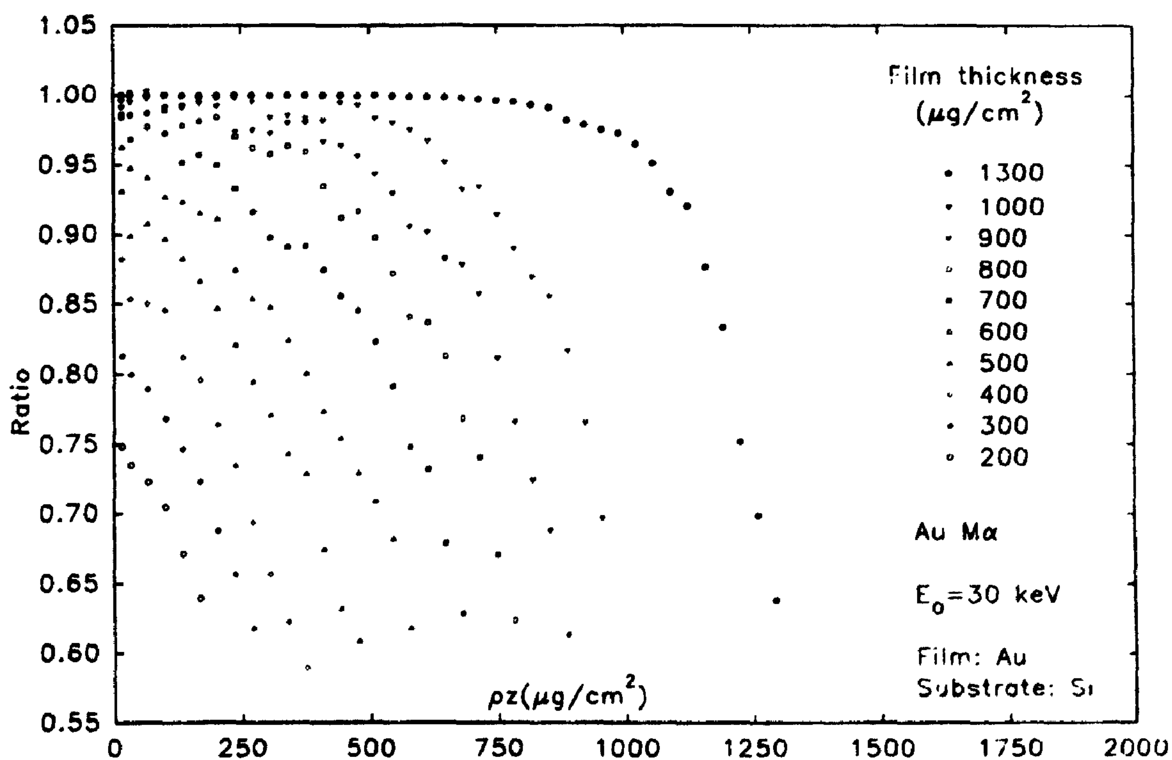

Figure 51b. Ratio plots of film $\Phi(\rho z)$ curves from Fig. 51a.

work is to develop a simple and easy to use analytical model for thin film analysis based on Monte Carlo simulated $\phi(\rho z)$ curves. A model was sought in which the same equations could be used for all circumstances. Preliminary analysis of the thin film simulation results showed that thin film $\phi(\rho z)$ curves in general cannot be described by functions such as a gaussian or parabola which have been used in bulk $\phi(\rho z)$ curves. In addition, exponential function which decay away from the interface towards the surface had been investigated but the agreement was not satisfactory. Therefore, an alternative method was developed in this work.

When a thin film $\phi(\rho z)$ curve is compared to the corresponding bulk curve, the biggest effect is at the interface and the effect decays away from the interface towards the surface. For very thick films there is practically no difference near the surface. This suggests that the film $\phi(\rho z)$ curve can be derived from the bulk $\phi(\rho z)$ curve with an appropriate correction. In investigating the absolute differences between the curves, the values varied drastically depending on the film thickness. A more successful approach was to look at the ratio of the curves at each depth so that the film value could be written as:

$$\phi(\rho z)_{Film} = \phi(\rho z)_{Bulk} * Ratio \qquad \text{(Eqn. 77)}$$

The variable termed 'Ratio' is simply a range of values given by dividing each individual Monte Carlo simulated point on the thin film $\phi(\rho z)$ curve by the equivalent point on the bulk $\phi(\rho z)$ curve. Therefore, 'Ratio' is dimensionless. To illustrate how 'Ratio' varies with film thickness and depth in the film, the five thin film $\phi(\rho z)$ curves for Si films on Au substrate at 30 keV illustrated in Figure 52a together with

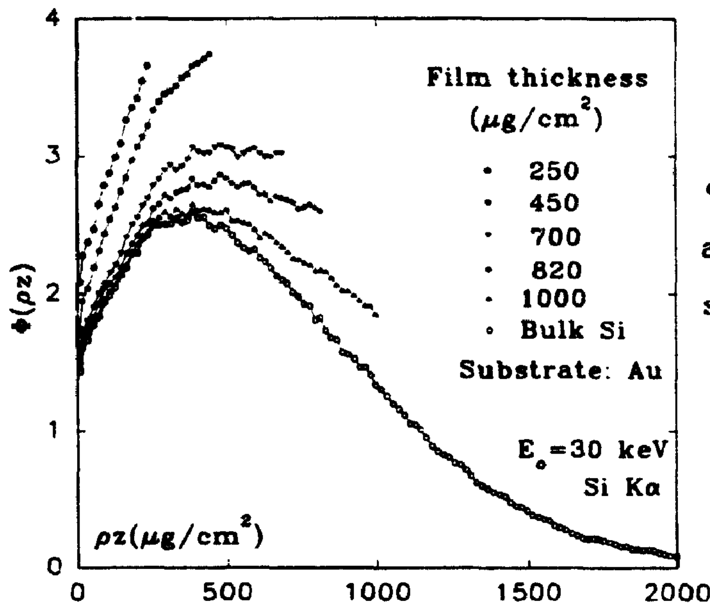

Figure 52a.

$\Phi(\rho z)$ curves for bulk Si and five Si films on Au substrate at 30 keV.

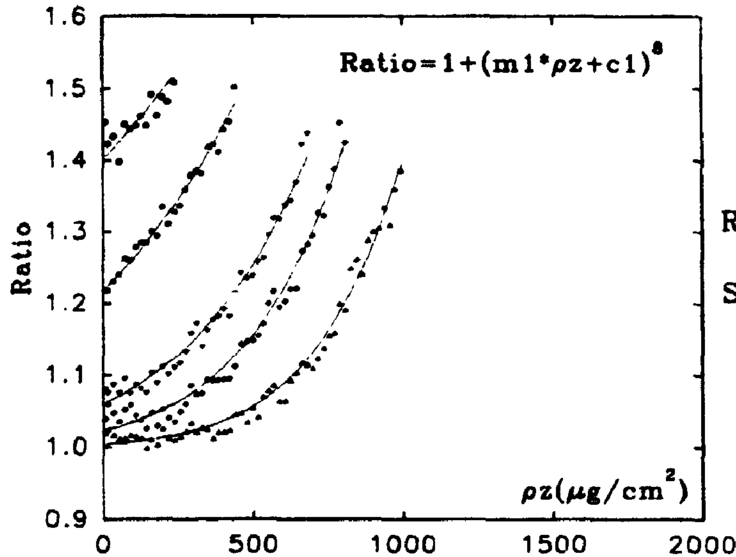

Figure 52b.

Ratio versus ρz for five Si films on Au substrate.

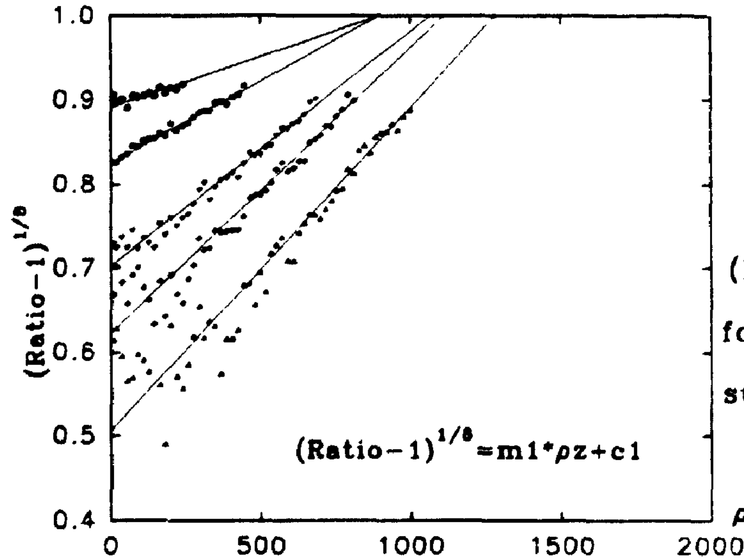

Figure 52c.

$(Ratio-1)^{1/8}$ versus ρz for five Si films on Au substrate.

the Si bulk $\phi(\rho z)$ curve are replotted as 'Ratio' in Figure 52b. To establish the relation between 'ratio' and mass depth, plots of $(Ratio-1)^{1/8}$ versus mass depth give straight lines (Figure 52c) which indicates that the equation of each straight line should be of the form:

$$(Ratio-1)^{1/8} = m1*\rho z+c1 \qquad \text{(Eqn. 78)}$$

where m1 and c1 are the slope and intercept of each individual straight line. The slope has a dimension of $cm^2/\mu g$ and the intercept dimensionless. Rearranging Eqn. (78) gives

$$Ratio = 1+(m1*\rho z+c1)^8 \quad 0 \le \rho z \le \rho t \qquad \text{(Eqn. 79)}$$

The five solid curves in Figure 52b are best fits to Eqn. (79) for each data set. All five curves fit the data very well despite the fact that the data set are quite scattered. The lines in Figure 52b represent these best fits. Further examination of all the thin film $\phi(\rho z)$ curves for low atomic number films on high atomic number substrates indicates that this dependence exists for all film/substrate combinations at all electron energies examined in this work.

The next step is to find how values for c1 and m1 in Eqn. (79) vary with film thickness and electron energy for each film/substrate combination. The first attempts were to view m1 and c1 independently but these were not successful. However, it was later discovered that m1 and c1 are related to each other and that values of c1 versus film thickness fall on relatively smooth curves for each electron energy (Figure 53a). Recall from Eqn. (79) that the two extremes of the curve occur when $\rho z=0$ (at the surface) and $\rho z=\rho t$ (at the interface). Therefore, a plot of c1 versus ρt and

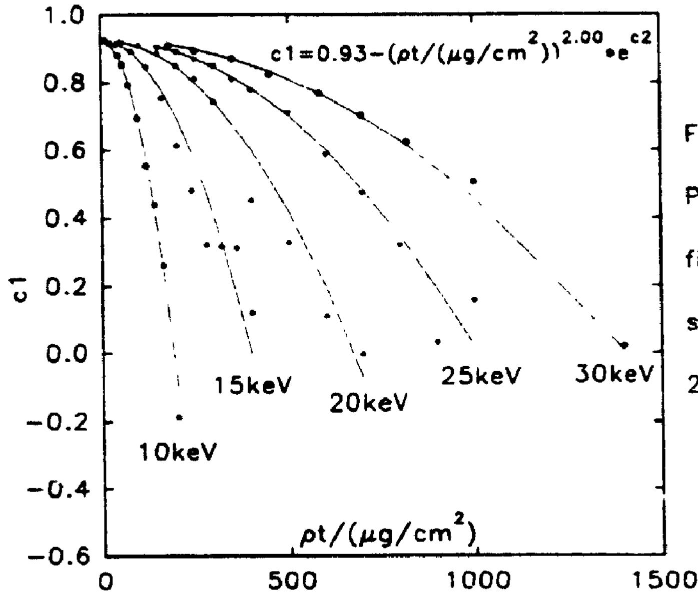

Figure 53a.
Plots of c1 versus Si film thickness ρt on Au substrate at 10, 15, 20, 25 and 30 keV

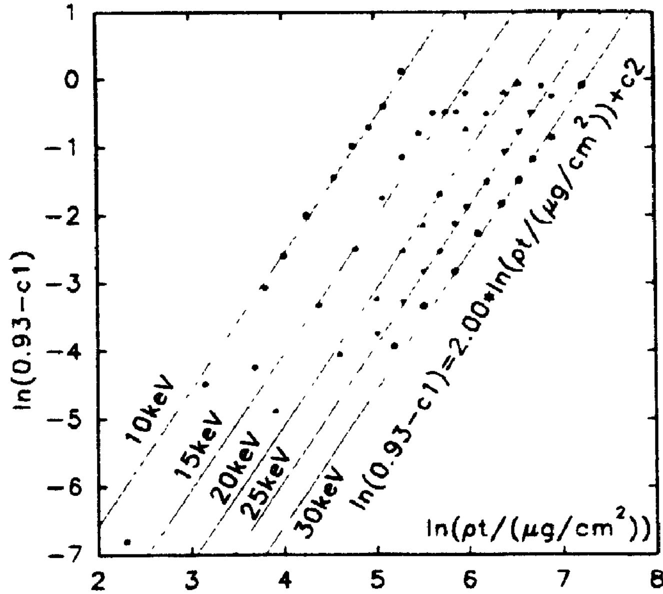

Figure 53b.
Plots of $\ln(0.93-c1)$ versus $\ln(\rho t/(\mu g/cm^2))$ from fig 53a.

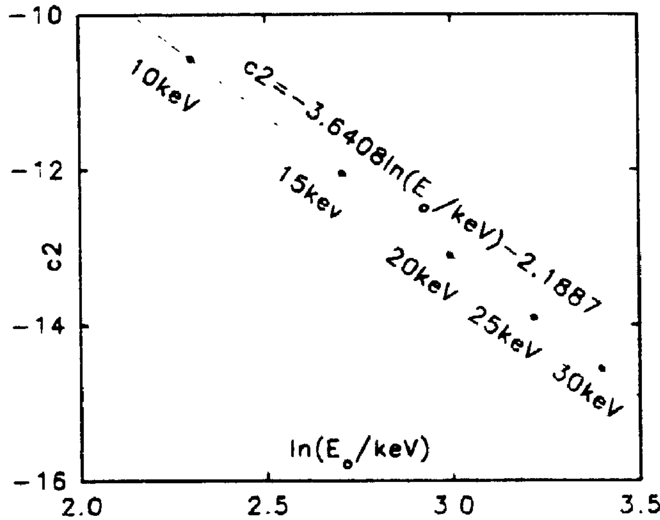

Figure 53c.
Plot of c2 versus $\ln(E_0/keV)$ from fig 53b

(m1.ρt+c1) versus ρt were used to establish the value of c1 and m1 in Eqn. (79). The two end points of the ratio curve were calculated and quantitatively if there is an error at either one or both end points of the curve, the concavity of the curve will be affected and the fit will be off although qualitatively it will at least get the correct trend of the function.

Plots of c1 versus ρt for different Si film thicknesses on Au substrate at five different energies are given in Figure 53a; the values represent optimized c1 values. Five parallel lines were found in the ln-ln plot as indicated in Figure 53b. The slopes of the straight lines are close to 2 and thus the equation to describe these straight lines with slope set to 2 is given by

$$\ln(0.93 - c1) = 2.00 * \ln(\rho t/(\mu g/cm^2)) + c2 \qquad \text{(Eqn. 80)}$$

The constant 0.93 was found to be unique for the Si/Au system, different systems will have different constants. The constant c2 which is the intercept in the ln-ln plot was found to be dependent on electron energy as illustrated in Figure 53c. The corresponding equation has the form:

$$c2 = -3.6408 \ln(E_o/keV) - 2.1887 \qquad \text{(Eqn. 81)}$$

The solid lines in Figure 53a are those obtained from Eqn. (80) which, after rewriting, is

$$c1 = 0.93 - (\rho t/(\mu g/cm^2))^{2.00} * \exp(c2) \qquad \text{(Eqn. 82)}$$

where c2 is given in Eqn. (81).

Instead of plotting (m1.ρt+c1) versus ρt, as mentioned earlier to obtain m1 having got c1 from Eqn. (82), 1/(m1.ρt+c1) versus ρt_{norm} was plotted where ρt_{norm} is

simply the absolute film thickness divided by the corresponding x-ray range. The consequence of using the ratio is that the data set for the five different electron energies now falls into the same range (Figure 54a). The data becomes linear if a ln-ln plot is used (Figure 54b). Although there appears to be considerable scatter of the points, most values fall within 1% of the best fit straight line (shown in Figure 54a). Thus the data can be described by the equation:

$$\ln\left(\frac{1}{m1*\rho t+c1}\right) = 0.02275 * \ln(\rho z_{norm}) + 0.1269 \qquad \text{(Eqn. 83)}$$

or taking antilogs of both sides,

$$\frac{1}{m1*\rho t+c1} = (\rho t_{norm})^{0.02275} * \exp(0.1269) \qquad \text{(Eqn. 84)}$$

m1 can now be found by substituting Eqn. (82) into Eqn. (84). Since both m1 and c1 appear in the equations at a power of one, for every given mass thickness ρt, there will be only one real unique solution for c1 and m1. The advantage of this method in calculating 'ratio' is that the thin film $\phi(\rho z)$ curve can be calculated using Eqn. (77) from the bulk $\phi(\rho z)$ curve using relatively simple equations. The Monte Carlo simulated(a) and empirically calculated(b) thin film $\phi(\rho z)$ curves are shown in Figures 55, 57, 59, 61 and 63 for ten different thicknesses of Si films on Au substrates for electron energies from 10 to 30 keV. To determine how much accuracy is lost in using equations instead of Monte Carlo simulation, ratio curves from the generalized equations were plotted as lines through the ratio data as illustrated in Figures 56a, 58a, 60a, 62a and 64a. Also, error plots of film $\phi(\rho z)_{equation}$/film $\phi(\rho z)_{mc}$ versus ρz were illustrated in Figure 56b, 58b, 60b, 62b and 64b. A 1.00 value indicates no error and

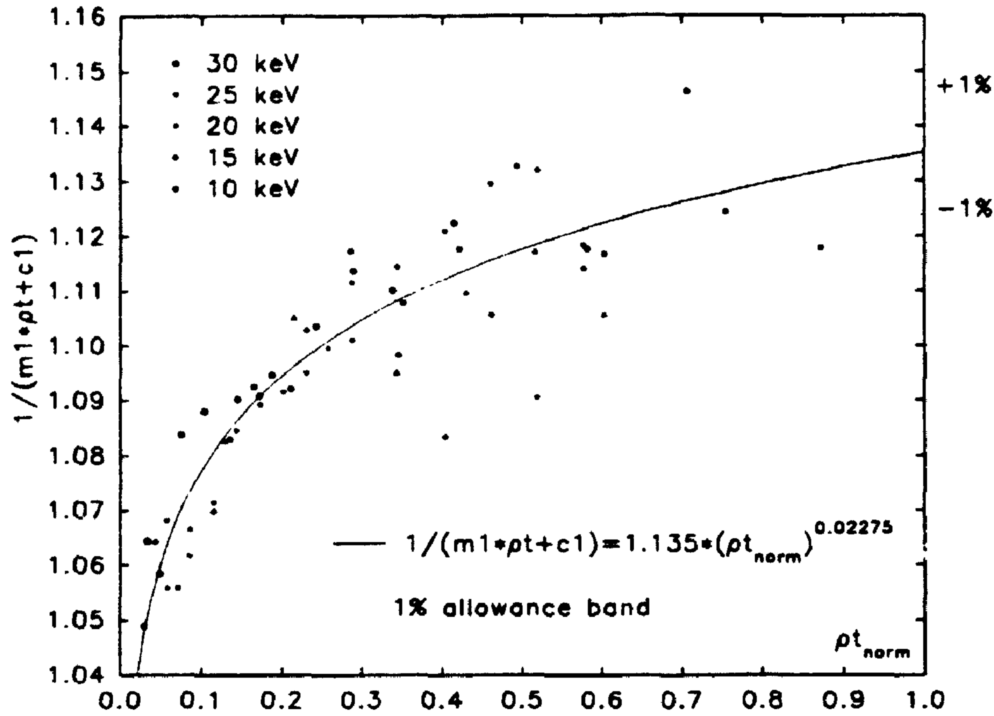

Figure 54a. Plot of $1/(m1*\rho t+c1)$ versus ρt_{norm} for different Si film thicknesses on Au substrate at 10, 15, 20, 25 and 30 keV electron energies.

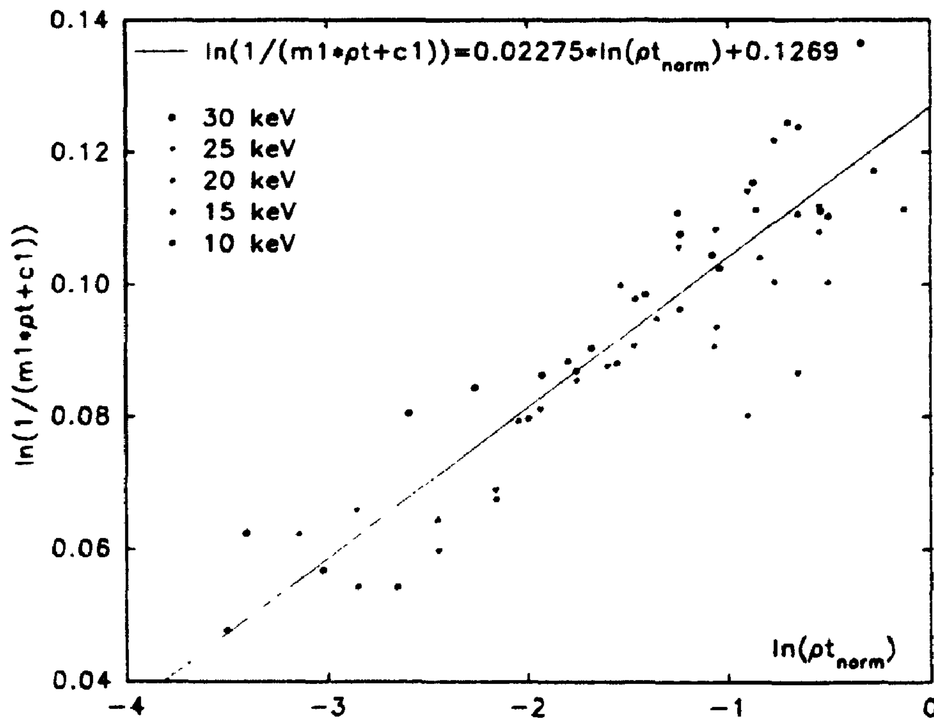

Figure 54b. Corresponding ln−ln plot of figure 54a.

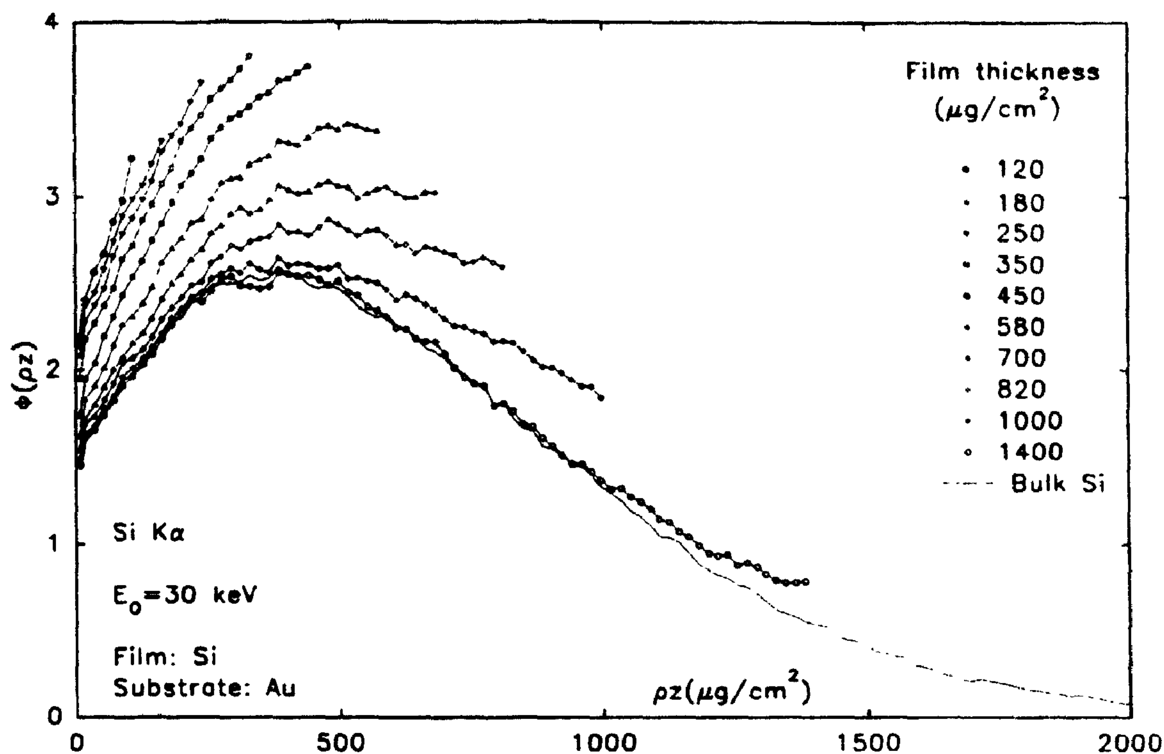

Figure 55a. Monte Carlo simulated thin film $\Phi(\rho z)$ curves of 10 different silicon film thicknesses on gold substrate at 30 keV.

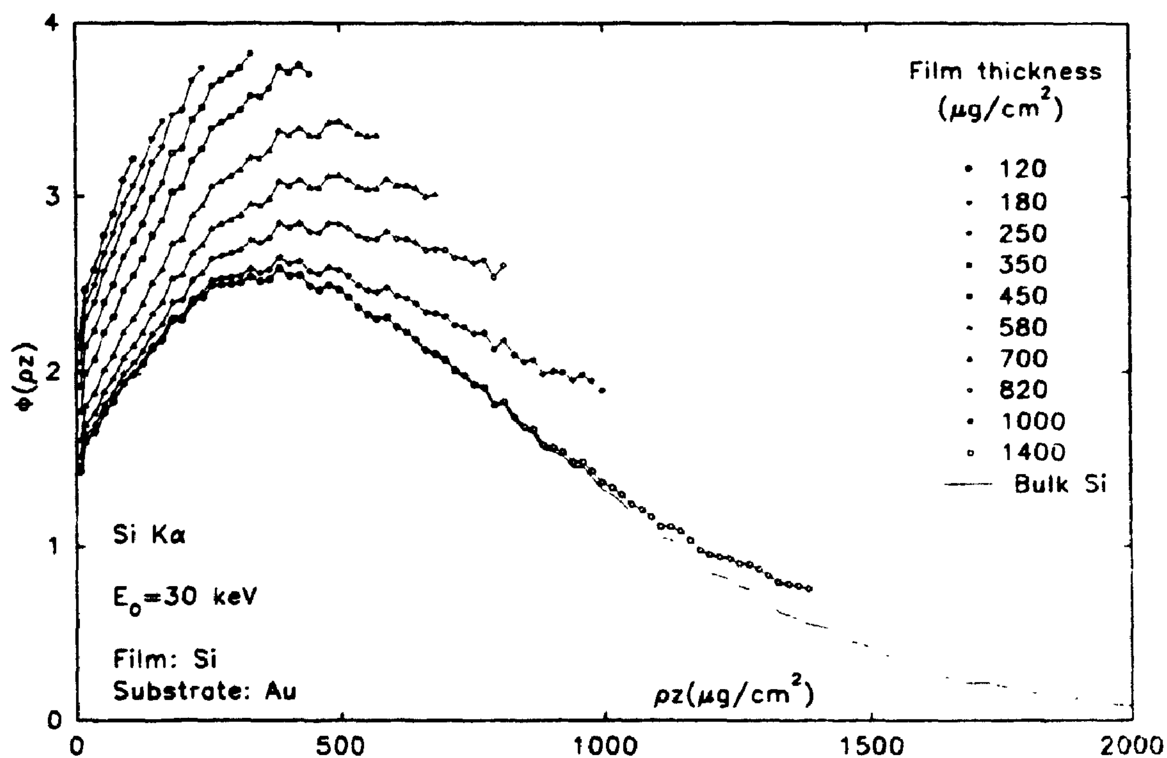

Figure 55b. Calculated thin film $\Phi(\rho z)$ curves of 10 different silicon film thicknesses on gold substrate at 30 keV.

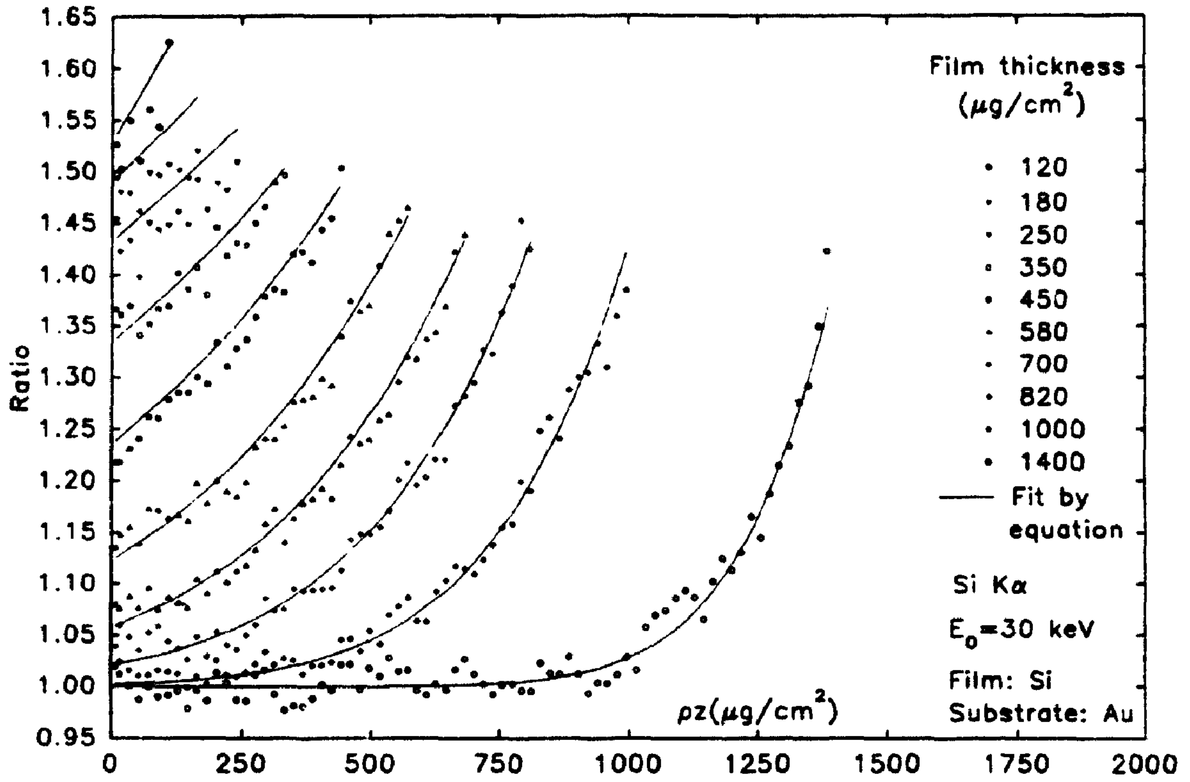

Figure 56a. Comparison of ratios calculated from figure 55a and for 55b.

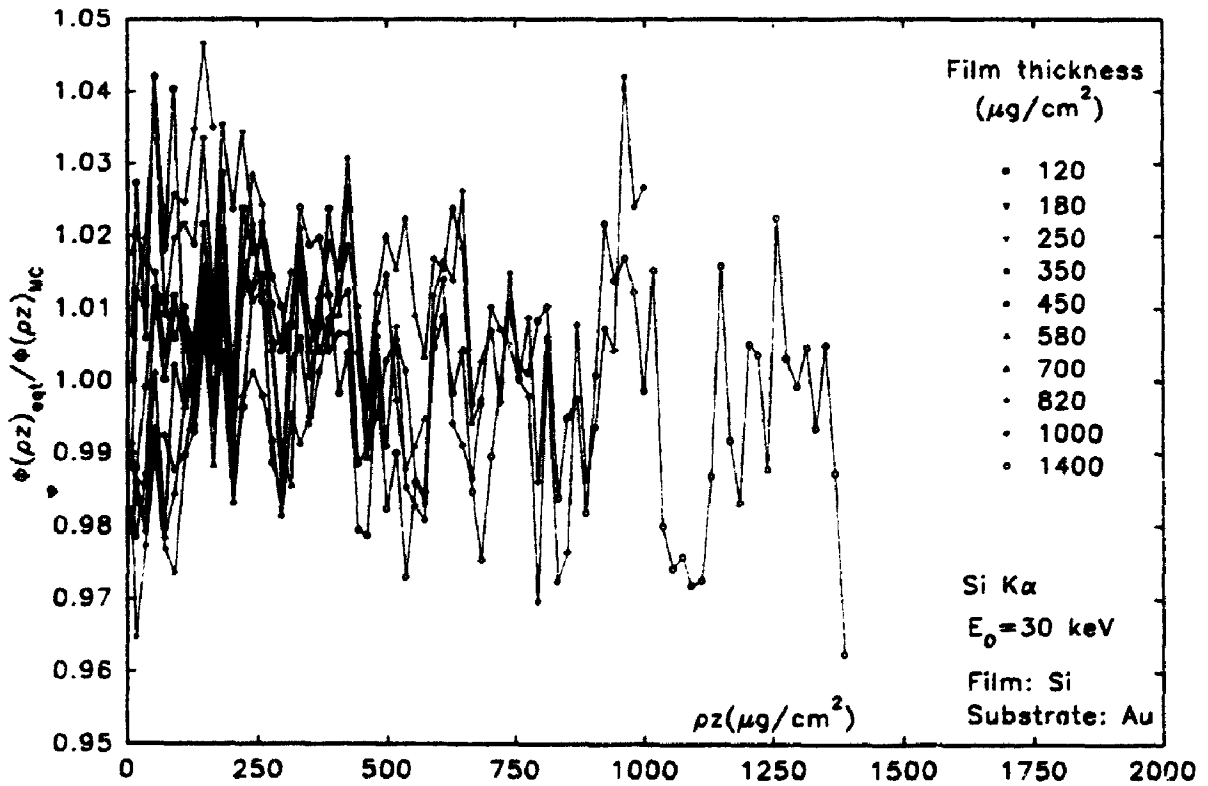

Figure 56b. Error plots calculated from figure 56a.

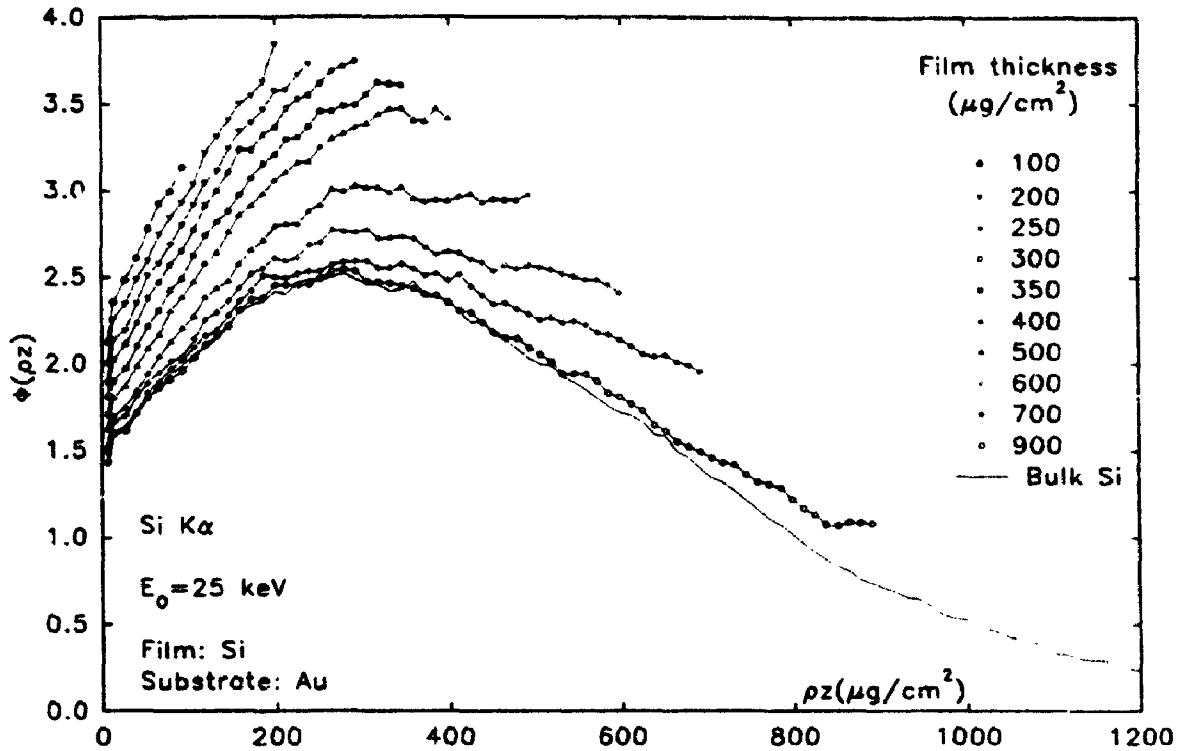

Figure 57a. Monte Carlo simulated thin film $\Phi(\rho z)$ curves of 10 different silicon film thicknesses on gold substrate at 25 keV.

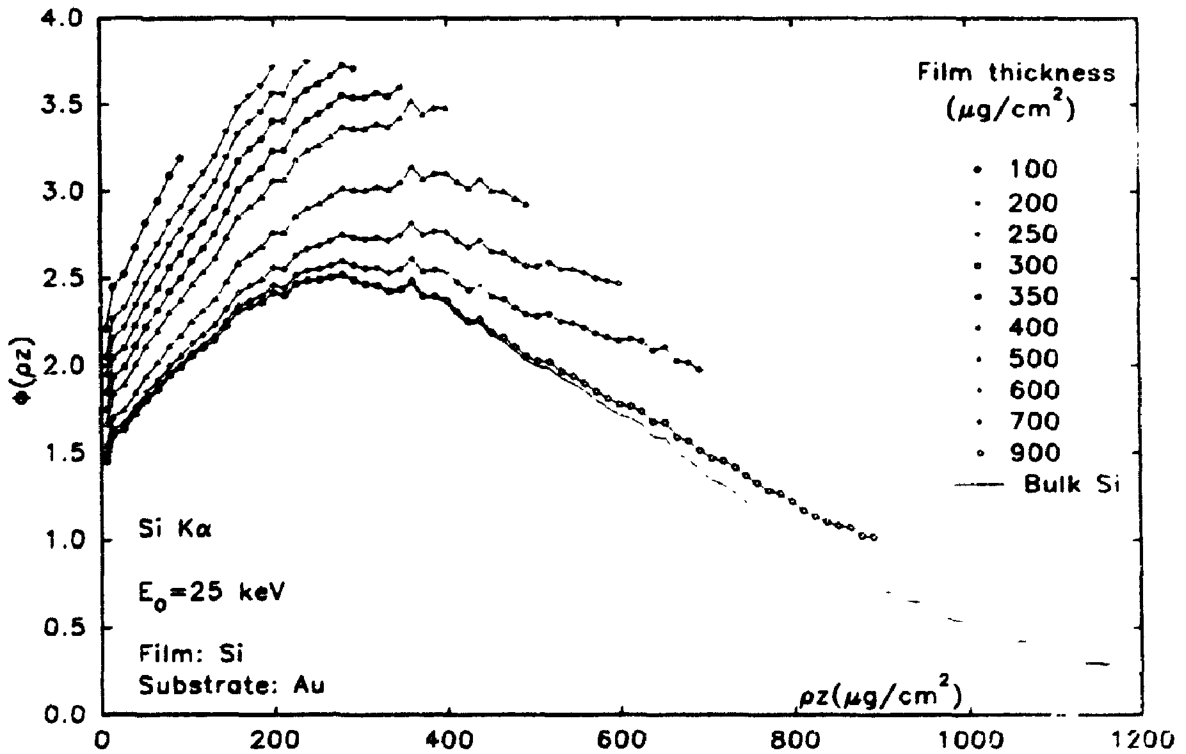

Figure 57b. Calculated thin film $\Phi(\rho z)$ curves of 10 different silicon film thicknesses on gold substrate at 25 keV.

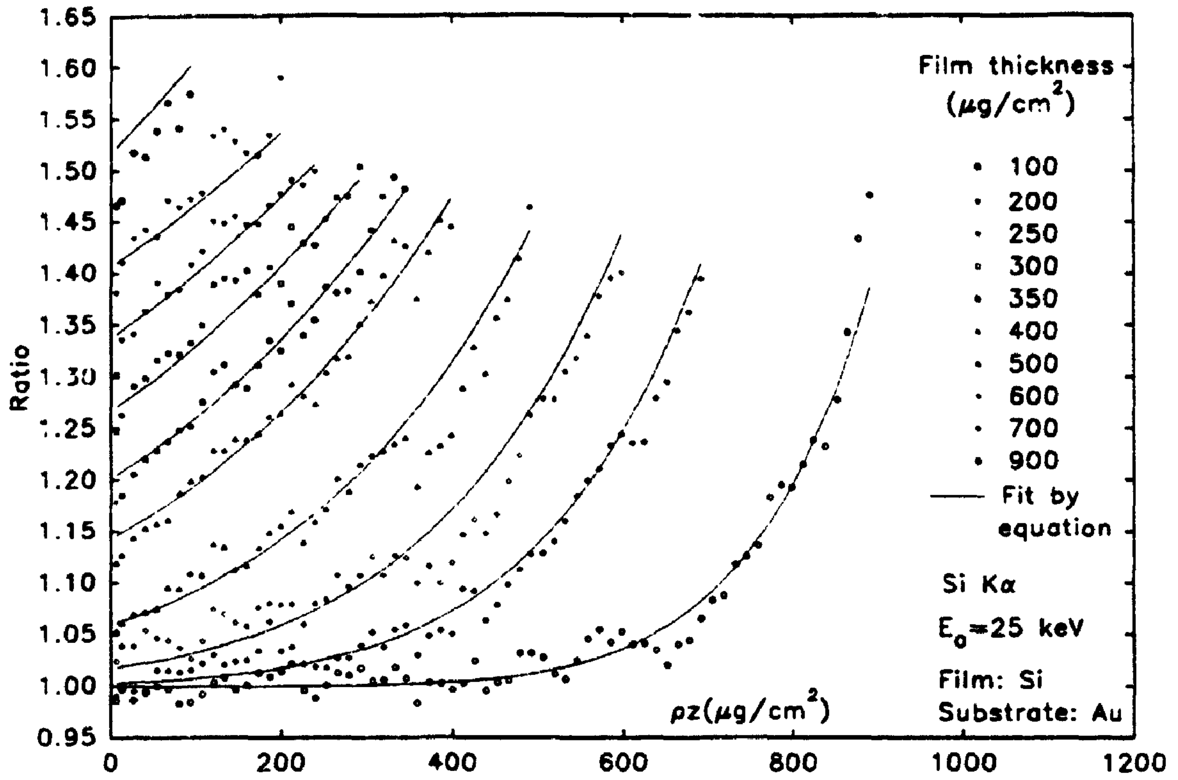

Figure 58a. Comparison of ratios calculated from figure 57a and for 57b.

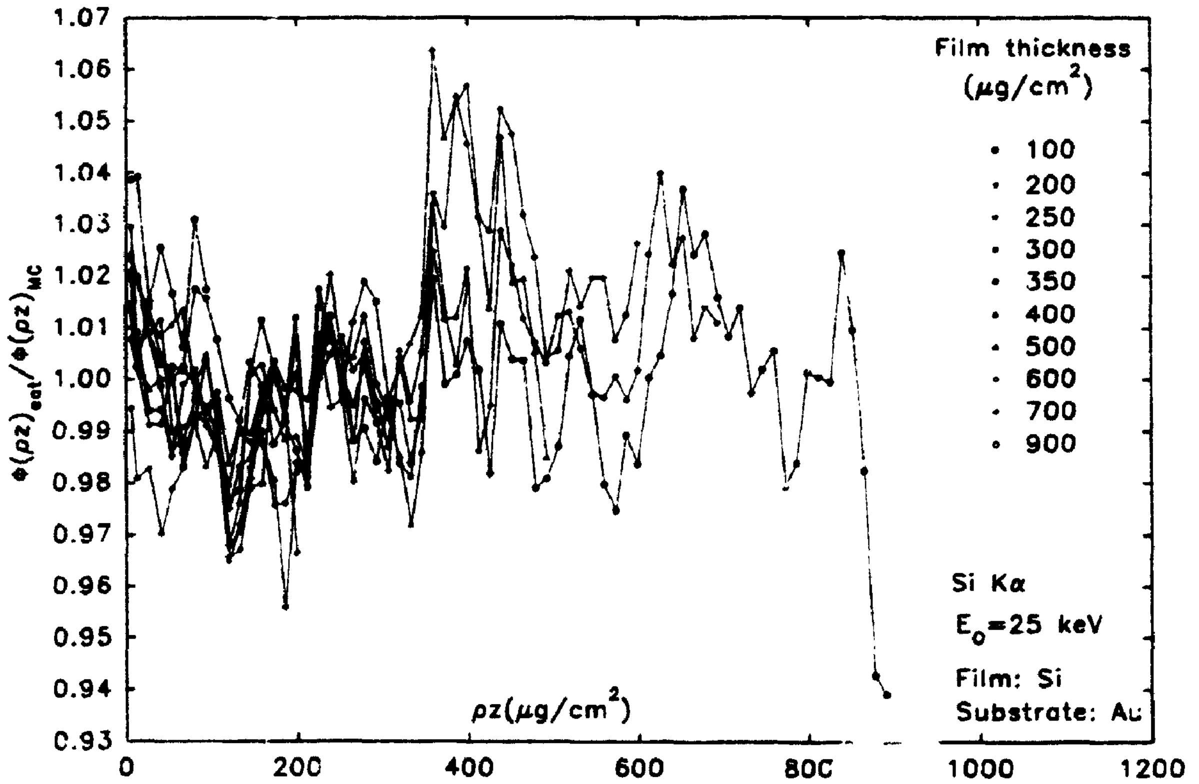

Figure 58b. Error plots calculated from figure 58a.

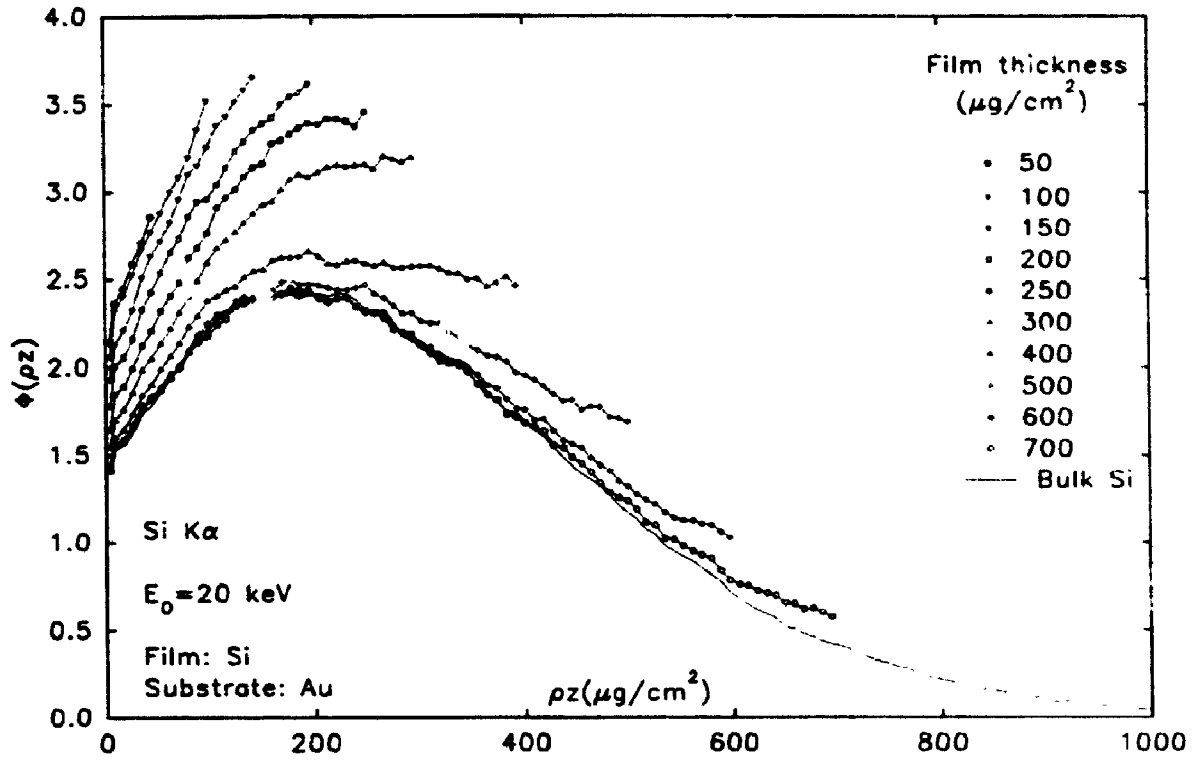

Figure 59a. Monte Carlo simulated thin film Φ(ρz) curves of 10 different silicon film thicknesses on gold substrate at 20 keV.

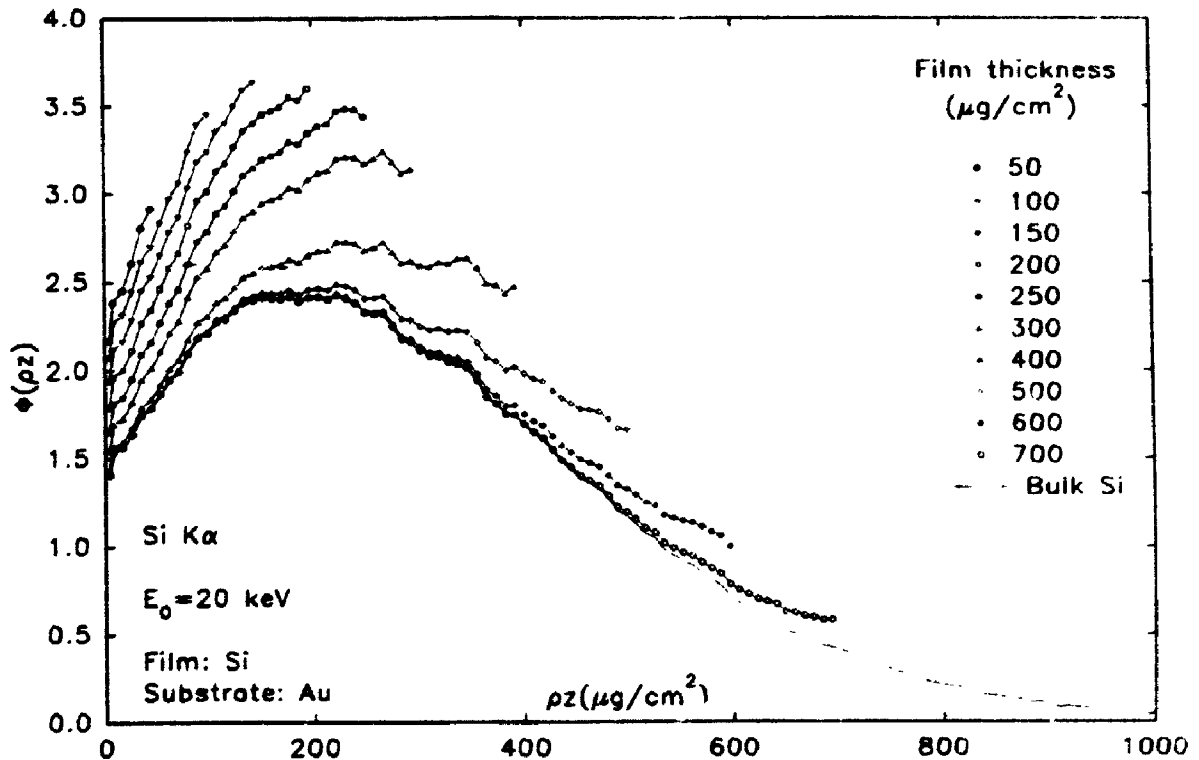

Figure 59b. Calculated thin film Φ(ρz) curves of 10 different silicon film thicknesses on gold substrate at 20 keV.

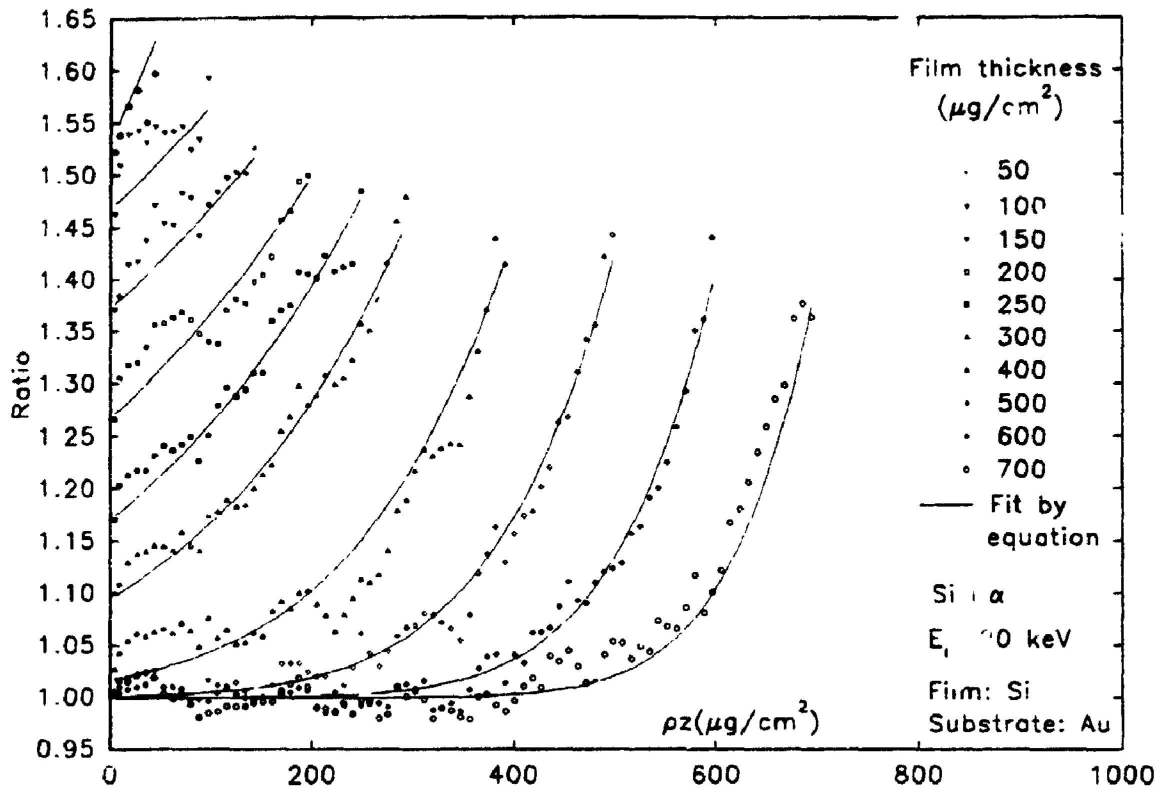

Figure 60a. Comparison of ratios calculated from figure 59a and for 59b.

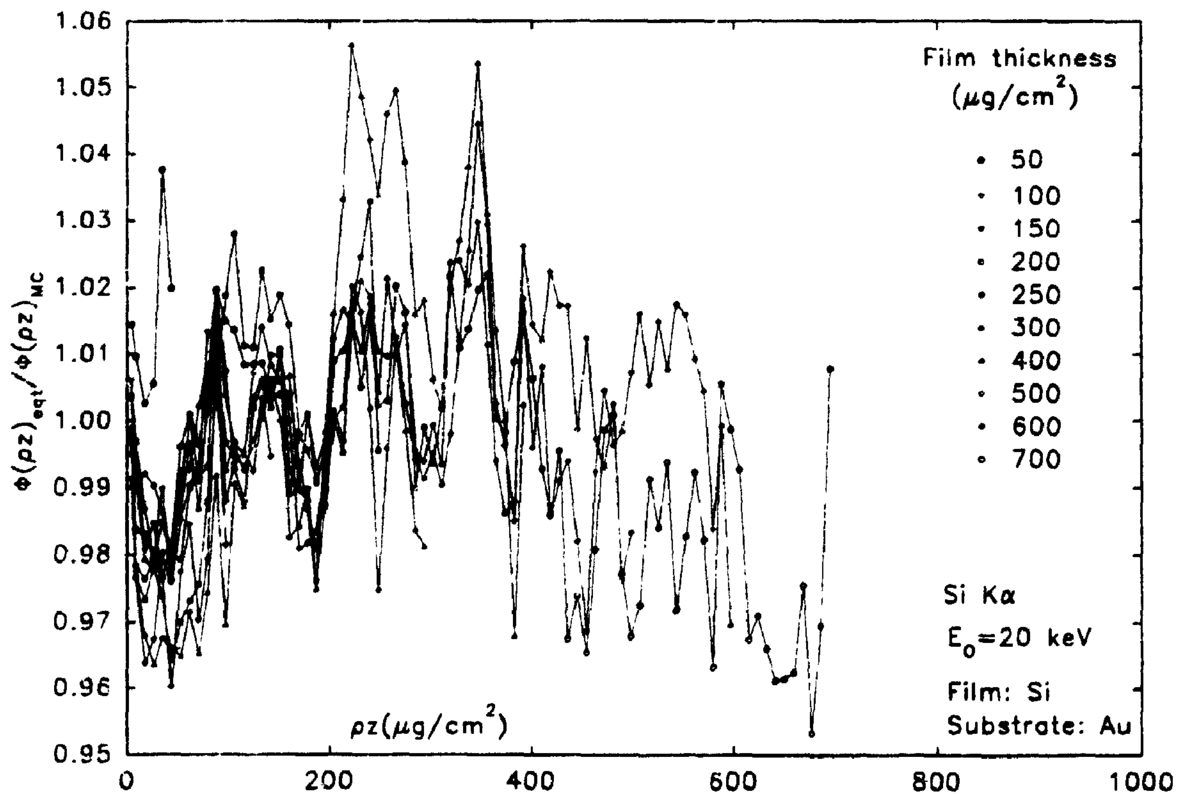

Figure 60b. Error plots calculated from figure 60a.

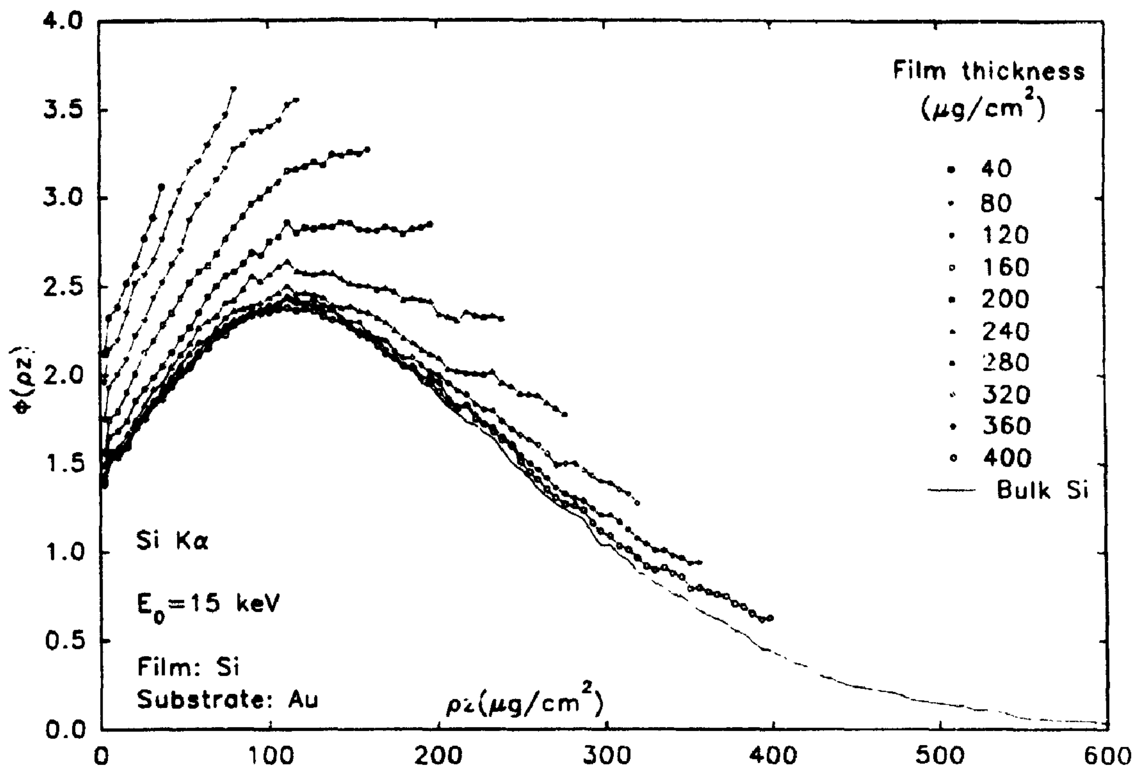

Figure 61a. Monte Carlo simulated thin film $\Phi(\rho z)$ curves of 10 different silicon film thicknesses on gold substrate at 15 keV.

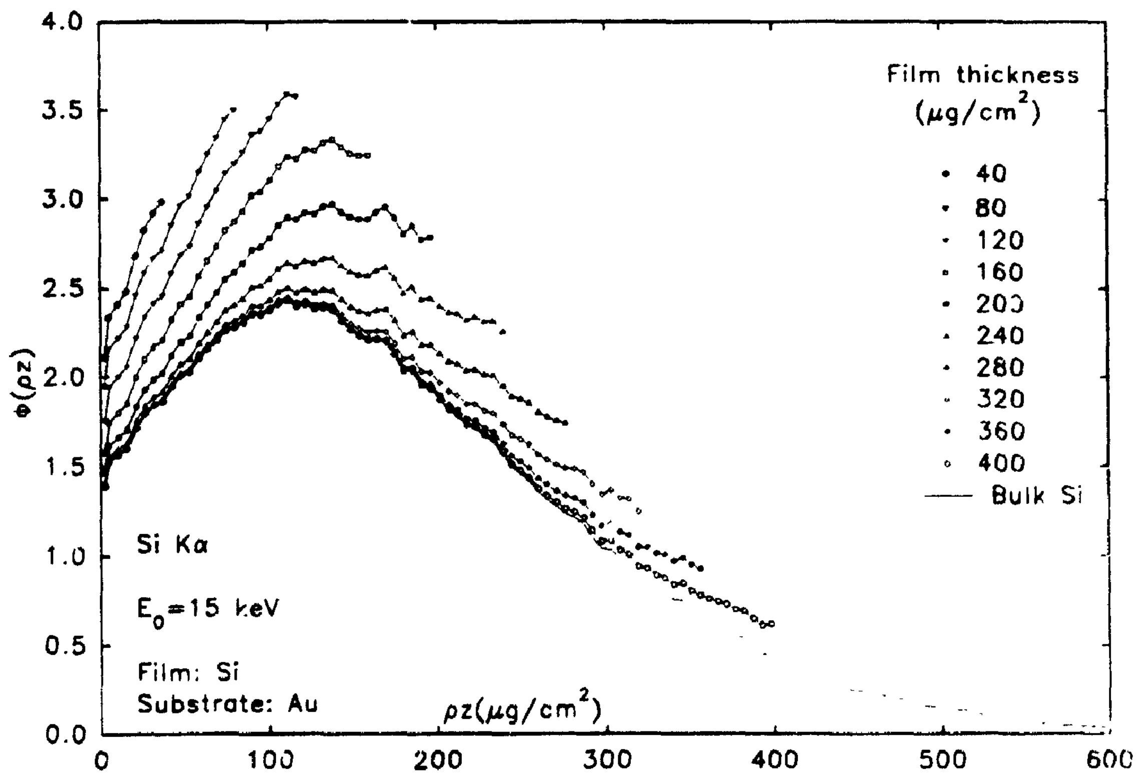

Figure 61b. Calculated thin film $\Phi(\rho z)$ curves of 10 different silicon film thicknesses on gold substrate at 15 keV.

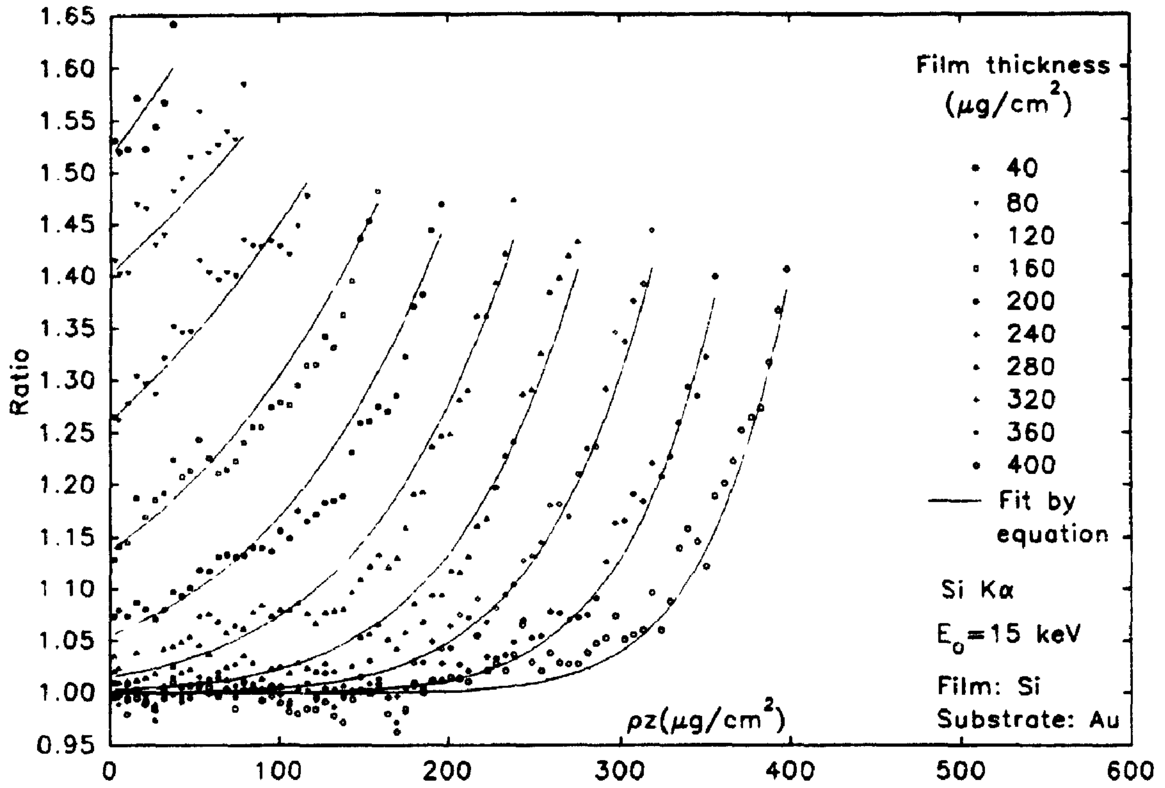

Figure 62a. Comparison of ratios calculated from figure 61a and for 61b.

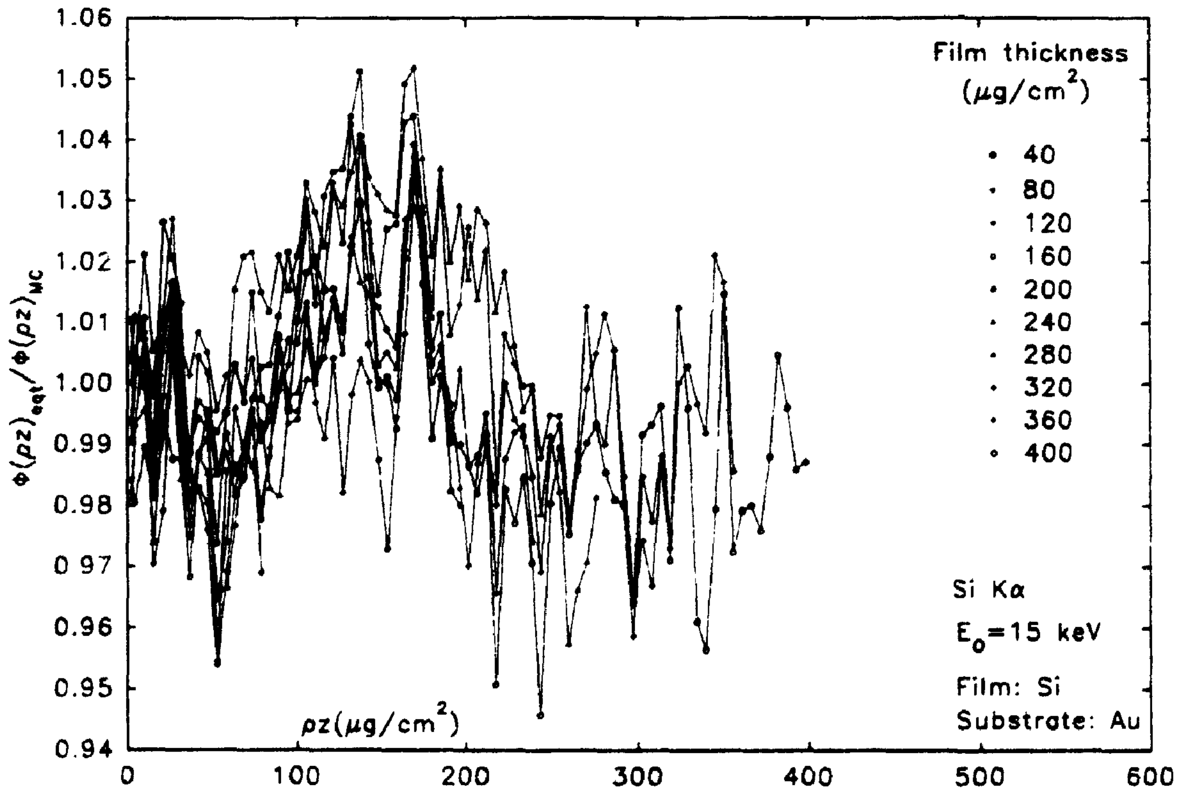

Figure 62b. Error plots calculated from figure 62a.

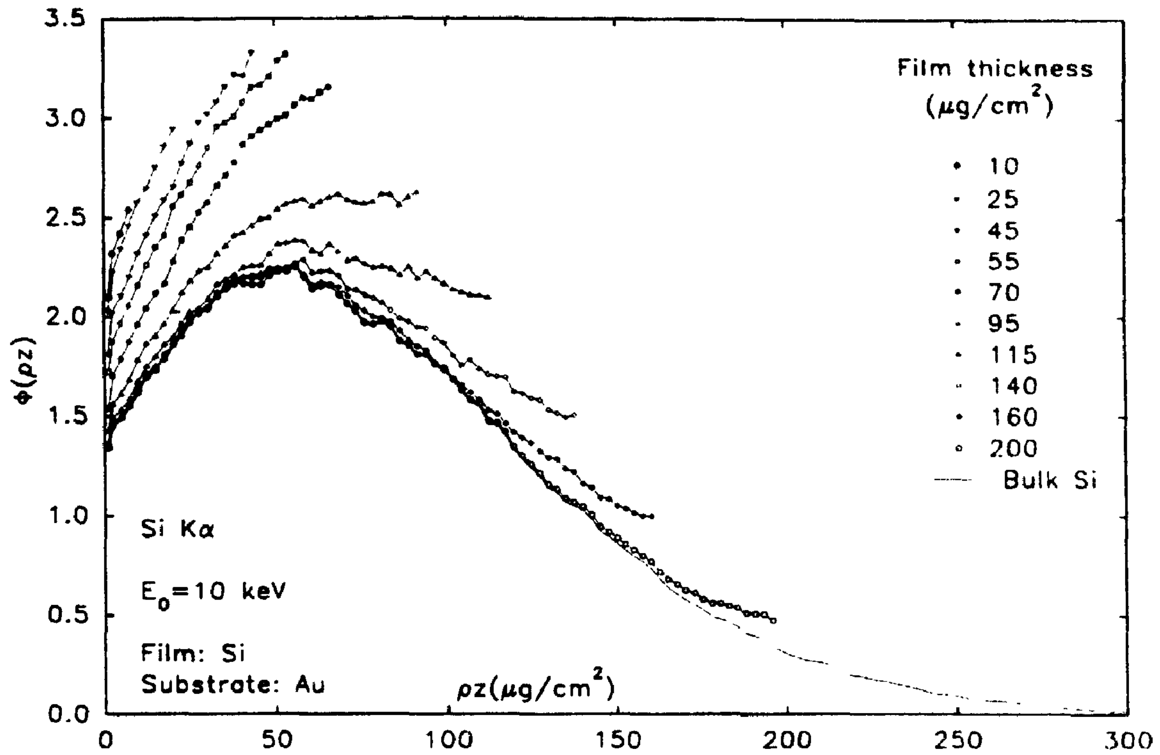

Figure 63a. Monte Carlo simulated thin film $\Phi(\rho z)$ curves of 10 different silicon film thicknesses on gold substrate at 10 keV.

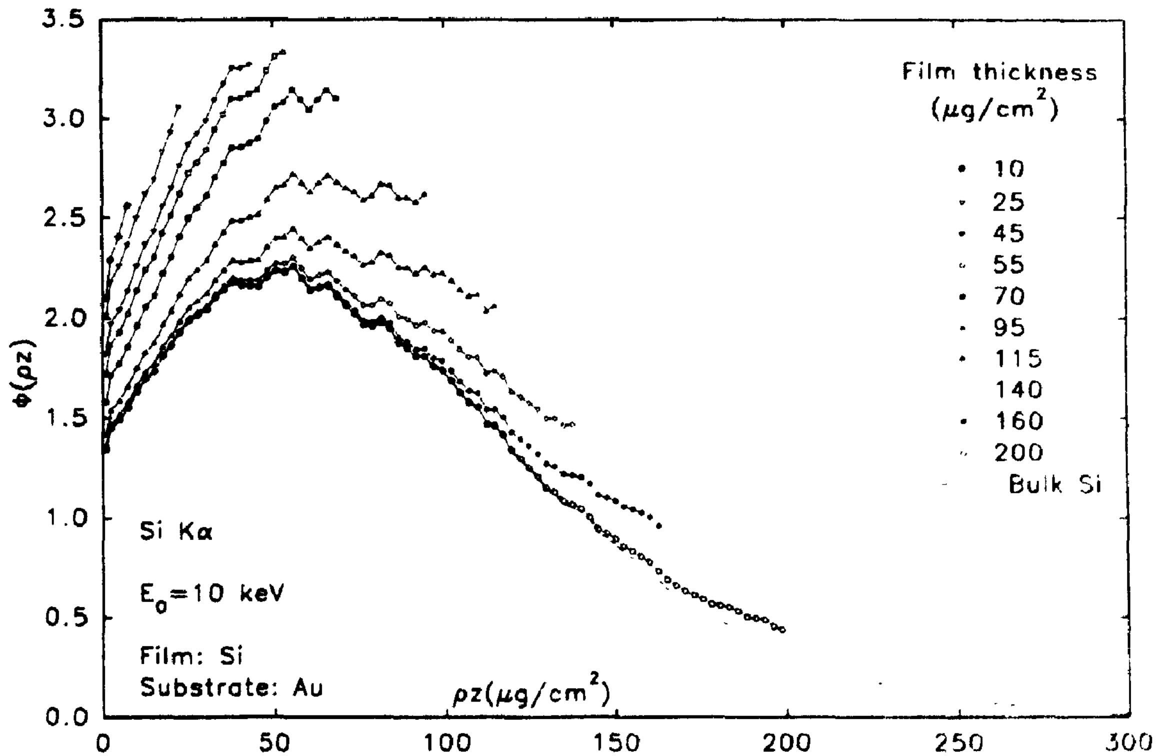

Figure 63b. Calculated thin film $\Phi(\rho z)$ curves of 10 different silicon film thicknesses on gold substrate at 10 keV.

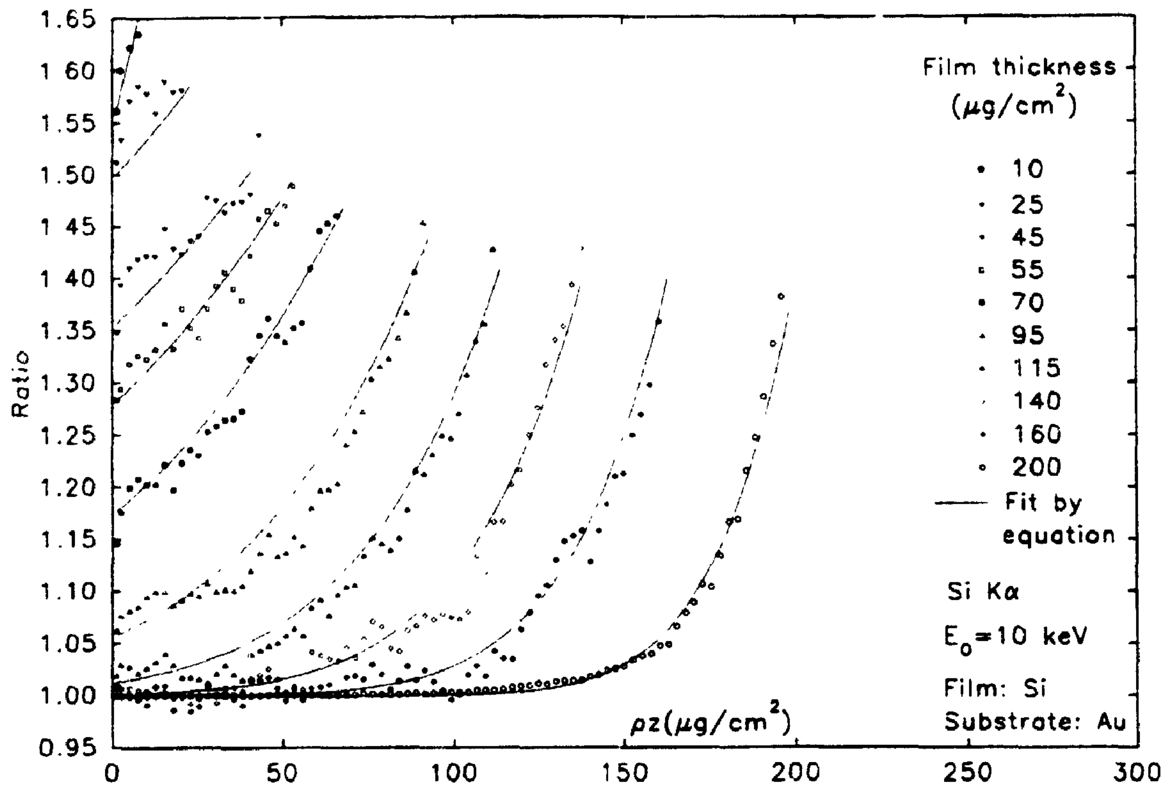

Figure 64a. Comparison of ratios calculated from figure 63a and for 63b.

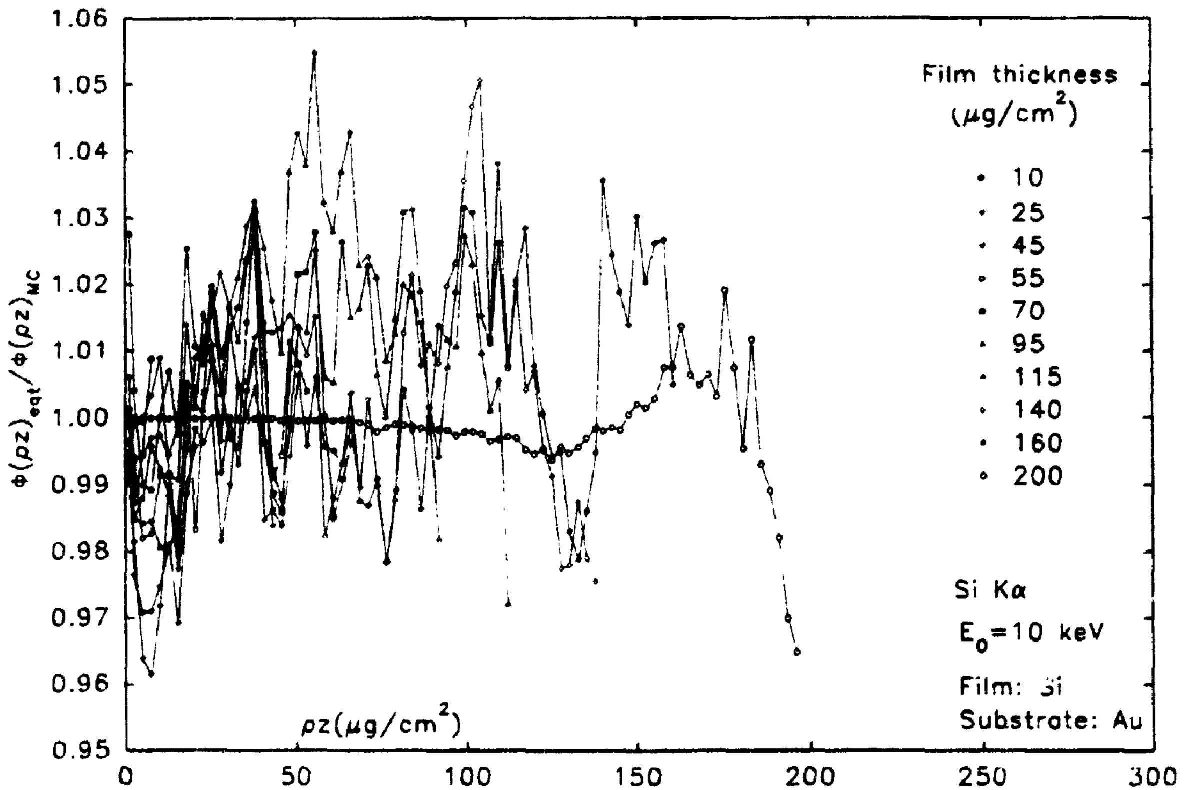

Figure 64b. Error plots calculated from figure 64a.

perfect fit. Since the bulk Monte Carlo values have been used as the basis for the thin film curves, any uncertainties in the bulk curves will carry over into the thin film curves. Because of statistical uncertainty, the Monte Carlo curves have local variations from a smooth curve of a few percent. These variations are different for the bulk curves and thin film curves at the same depth. Thus the Monte Carlo curves themselves have uncertainties of a few percent which will enter in the error plots. It can be seen from the error plots that a ±3% band takes in most of the data points which indicates that the generalized equations fit the data quite well. Also, the mean value of the data points is found to lie very close to 1.00 which indicates that there is neither a positive nor negative bias.

In the case of a high atomic number film on a low atomic number substrate, Eqn. (77) is still valid so that the thin film $\phi(\rho z)$ curves can be expressed in terms of the bulk curves through a ratio. Five thin film $\phi(\rho z)$ curves for Au films on Si substrate at 30 keV are shown in Figure 65a together with the Au bulk curve. The 'Ratio' values versus mass depth were calculated using Eqn. (77) and are plotted in Figure 65b as individual dots. The thin film curves now lie below the bulk curve and a very clear maximum can be seen in each curve. This maximum shifts to smaller mass depth values as the film thickness decreases. The ratio values are now less than one. Thinner films will give a smaller ratio at the surface which indicates a lower $\phi(o)$ value. In analogy with the low atomic number films on high atomic number substrates, in a plot of $(1\text{-Ratio})^{1/8}$ versus mass depth, five straight lines were obtained (Figure 65c). This indicates that the equation for each straight line is of the form:

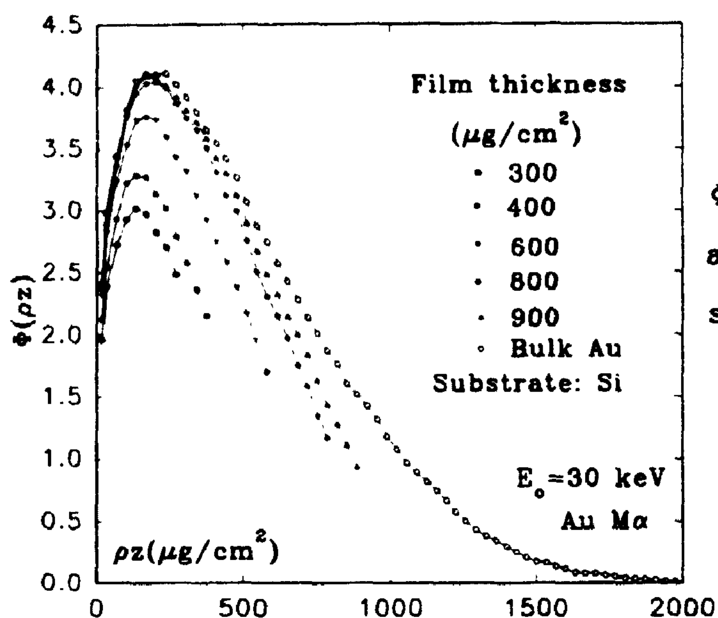

Figure 65a.

$\Phi(\rho z)$ curves for bulk Au and five Au films on Si substrate at 30 keV.

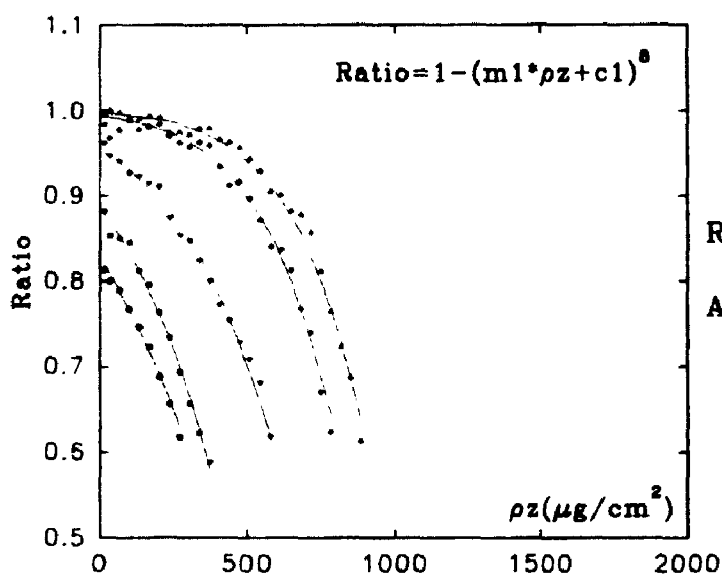

Figure 65b.

Ratio versus ρz for five Au films on Si substrate.

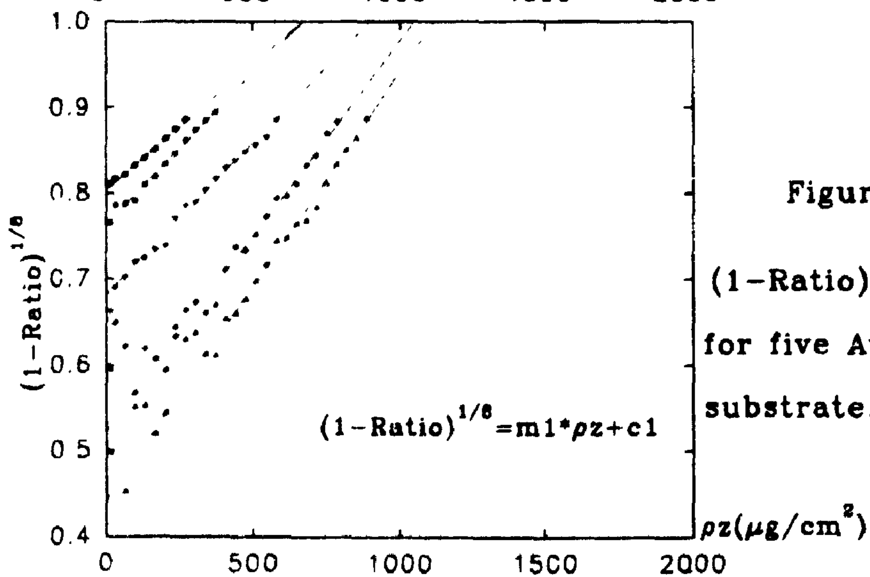

Figure 65c.

$(1-\text{Ratio})^{1/8}$ versus ρz for five Au films on Si substrate.

$$(1-Ratio)^{1/8} = m1 \star \rho z + c1 \quad \text{(Eqn. 85)}$$

The constants m1 and c1 have different values from those in Eqn. (78). By rearranging Eqn. (85),

$$Ratio = 1-(m1 \star \rho z + c1)^{8} \quad 0 \le \rho z \le \rho t \quad \text{(Eqn. 86)}$$

The five solid curves in Figure 65b were drawn according to Eqn. (85) with best fit or optimized c1 and m1 values. All five curves fit the data very well. Further examination of all the thin film $\phi(\rho z)$ curves indicates that this is true for all heavy film/light substrate combinations and at all electron energies examined in this work.

The procedure to find the values for m1 and c1 in the case of a high atomic number film on a low atomic number substrate follows very much the same technique adopted before. Plots of the optimized c1 versus ρt for different Au film thicknesses on Si substrate at five different energies are shown in Figure 66a. Five parallel lines are found in the ln-ln plot of Figure 66b. The corresponding equation is given by:

$$\ln(0.85-c1) = 2.00 \star \ln(\rho t/(\mu g/cm^{2})) + c2 \quad \text{(Eqn. 87)}$$

The constant 0.85 was found to be unique for the Au/Si system, different systems will have different constants. The intercepts of Figure 66b represent the constants c2 which are plotted in Figure 66c. The resulting straight line is given by:

$$c2 = -3.5338 \ln(E_0/keV) - 2.4125 \quad \text{(Eqn. 88)}$$

The solid lines in Figure 66a are obtained from Eqn. (87) by taking antilogs, hence

$$c1 = 0.85-(\rho t/(\mu g/cm^{2}))^{2.00} \star \exp(c2) \quad \text{(Eqn. 89)}$$

where c2 is given by Eqn. (88).

To determine m1, as before, to emphasize the values near the film substrate

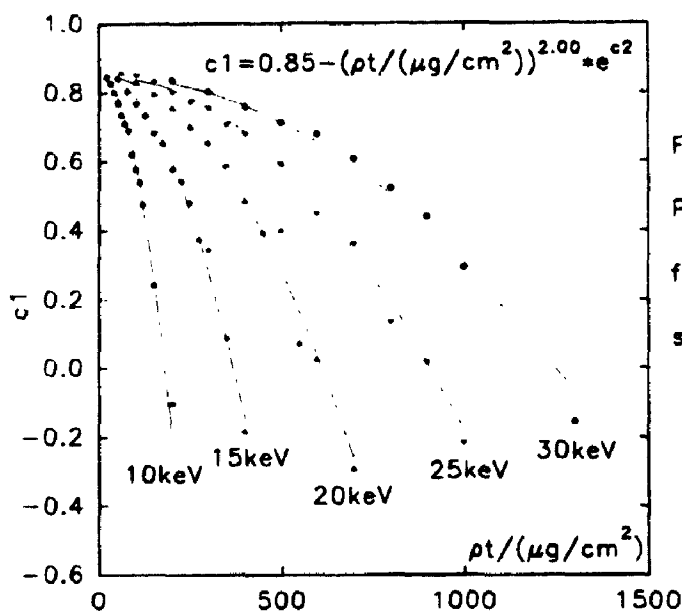

Figure 66a.

Plots of c1 versus Au film thickness ρt on Si substrate at 10, 15, 20, 25 and 30 keV.

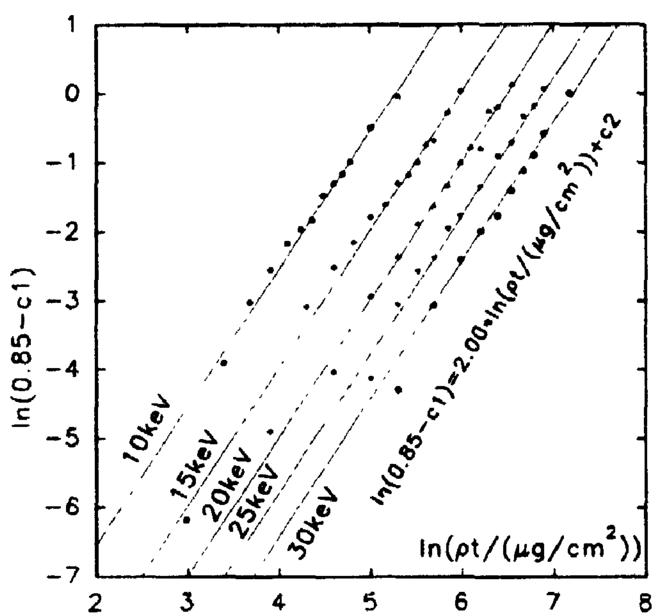

Figure 66b.

Plots of $\ln(0.85-c1)$ versus $\ln(\rho t/(\mu g/cm^2))$ from fig 66a.

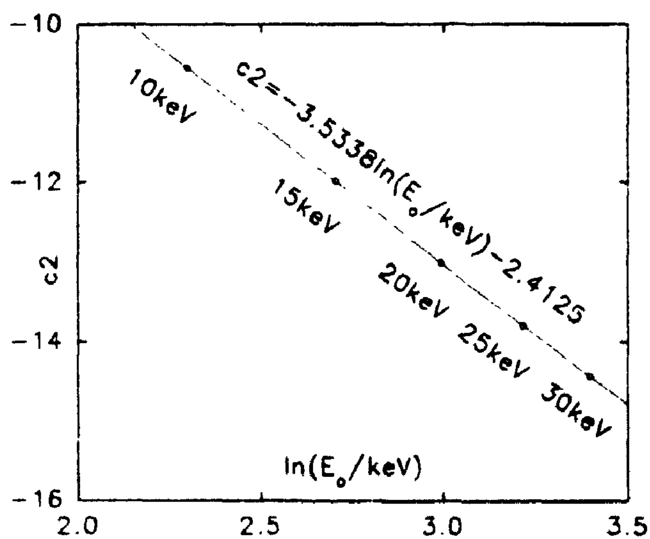

Figure 66c.

Plot of c2 versus $\ln(E_0/keV)$ from fig 66b.

interface, $1/(m1 \cdot \rho t + c1)$ is plotted versus ρt_{norm} in Figure 67a for the Au films on silicon. The data shows that the data are large for small values of ρt_{norm}, passes through a minimum near $\rho t_{norm} = 0.1$, then increases again. Again, in analogy with the previous analysis for low atomic number films on high atomic number substrates, the data are plotted on a ln-ln plot in Figure 67b. These data can be described by a straight line with a mirror at $\ln \rho t_{norm} = -2.303 (\rho t_{norm} = 0.1)$. The equation is:

$$\ln(1/(m1*\rho t+c1)) = 0.02049 * |\ln \rho t_{norm} + 2.303| + 0.0982 \quad \text{(Eqn. 90)}$$

Note that the use of the absolute value ensures that the function increases on both sides of $\ln(\rho t_{norm}) = -2.303$. Taking antilogarithms:

$$\frac{1}{m1*\rho t+c1} = 1.103 * \exp(0.02049 |\ln(10 \rho t_{norm})|) \quad \text{(Eqn. 91)}$$

Except for a few points, all fitted values lie within ±1% of the values predicted by this equation (Figure 67a). m1 can now be found by substituting Eqn. (89) into Eqn. (91). The thin film $\phi(\rho z)$ curves calculated using these values are shown in Figures 68b, 70b, 72b, 74b and 76b for Au films on Si substrates. The corresponding Monte Carlo simulated curves are shown in the 'a' plots. Ratio curves are illustrated in Figures 69a, 71a, 73a, 75a and 77a in which the data points are the Monte Carlo values while the solid curves are from the optimized parameters. The differences between these values are plotted as error plots in Figures 69b, 71b, 73b, 75b and 77b. In the error plots, a ±3% band encloses most of the data points which is excellent agreement in view of the uncertainty in the Monte Carlo values mentioned previously.

Five other systems have been investigated in the case of a low atomic number film on a high atomic number substrate. The systems are Cu/Ag, Cu/Au, Ag/Au,

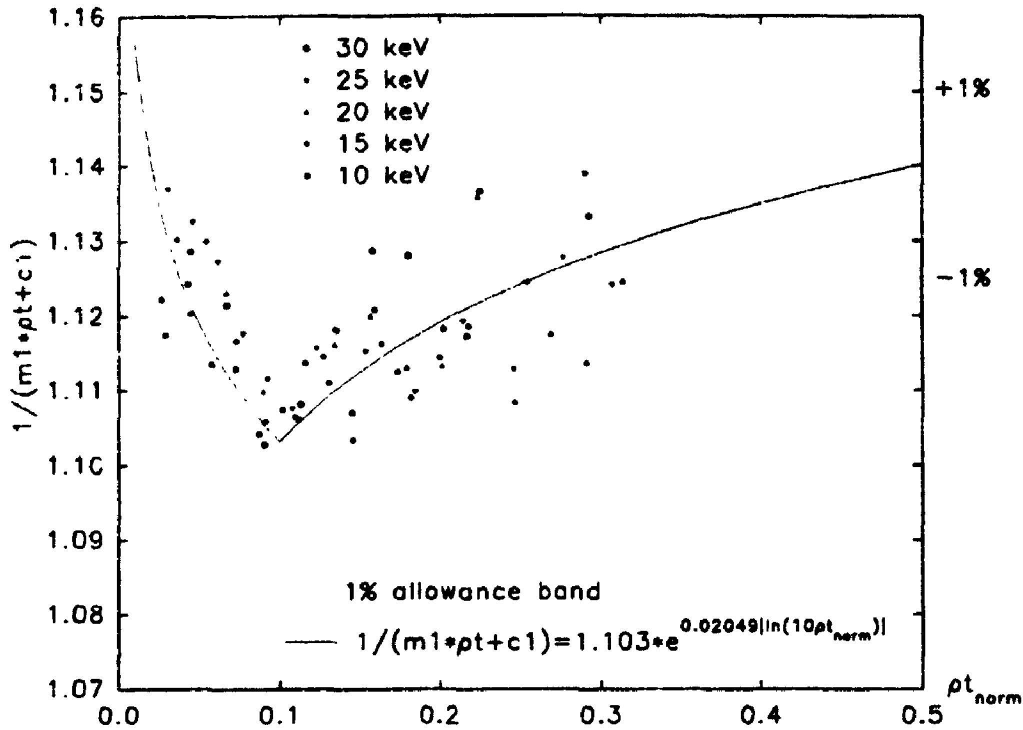

Figure 67a. Plot of $1/(m1*\rho t+c1)$ versus ρt_{norm} for different Au film thicknesses on Si substrate at 10, 15, 20, 25 and 30 keV electron energies.

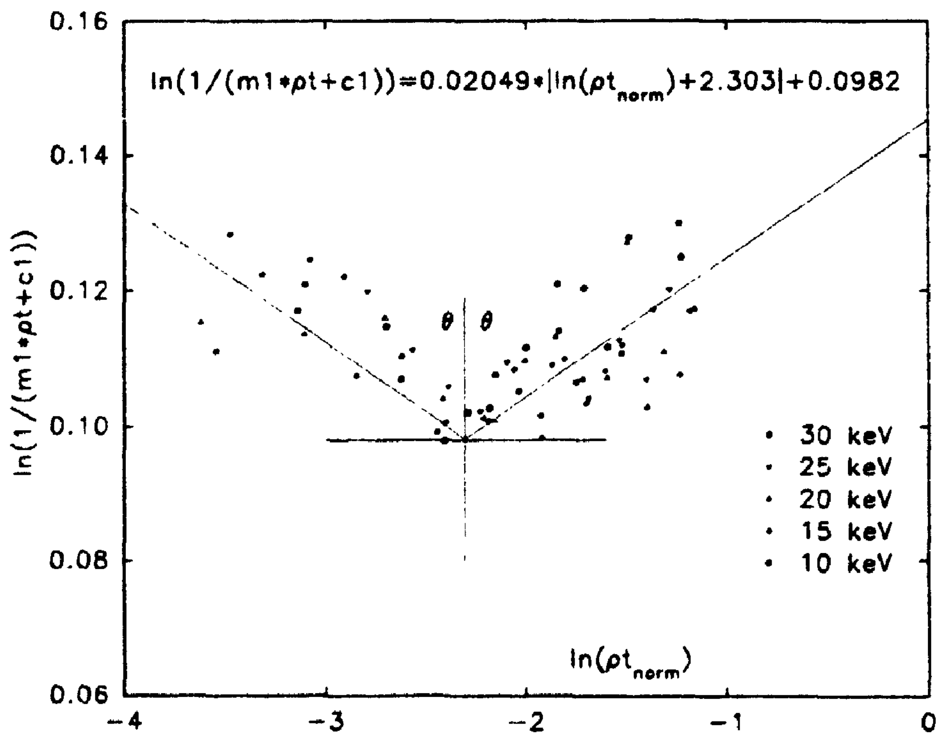

Figure 67b. Corresponding ln–ln plot of figure 67a.

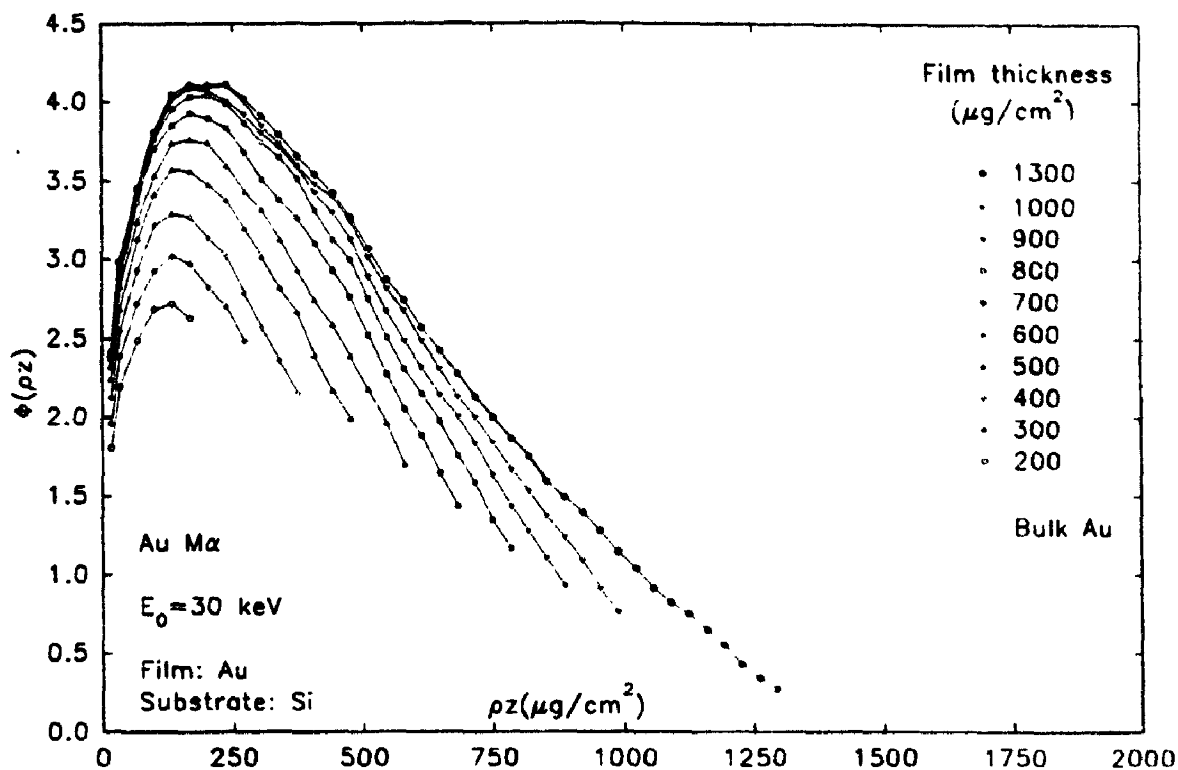

Figure 68a. Monte Carlo simulated thin film $\Phi(\rho z)$ curves of 10 different gold film thicknesses on silicon substrate at 30 keV.

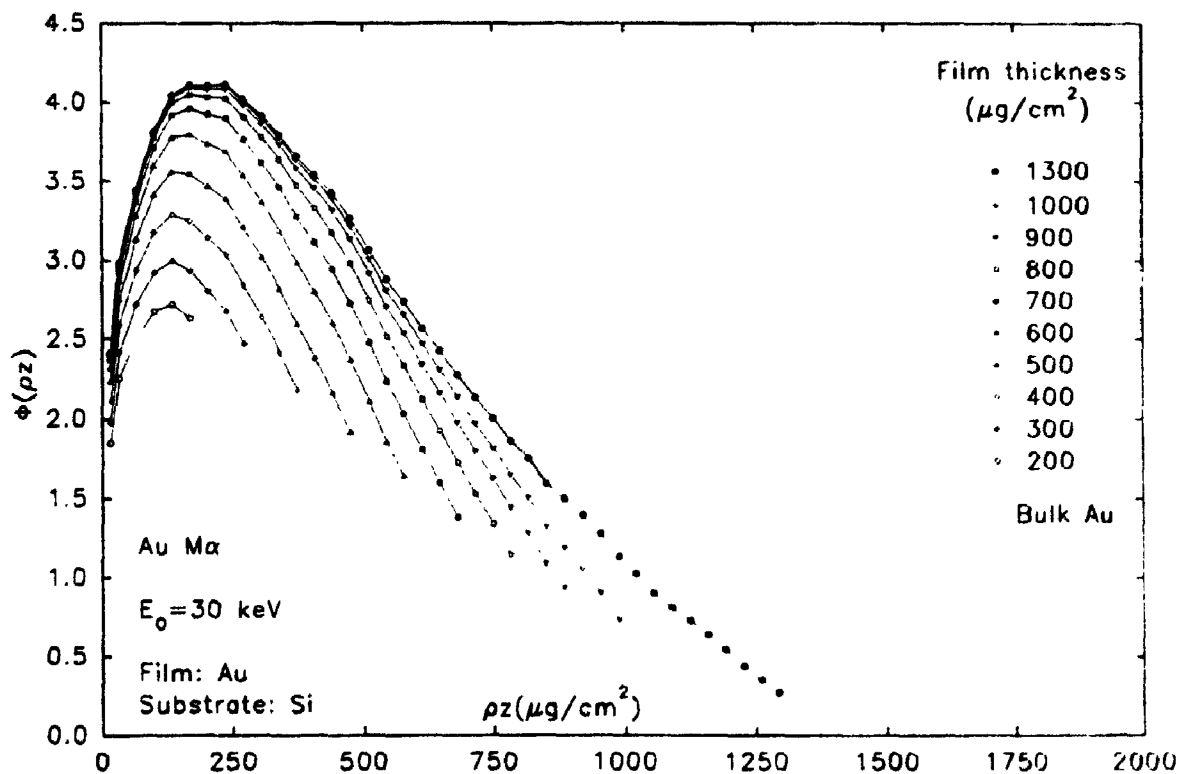

Figure 68b. Calculated thin film $\Phi(\rho z)$ curves of 10 different gold film thicknesses on silicon substrate at 30 keV.

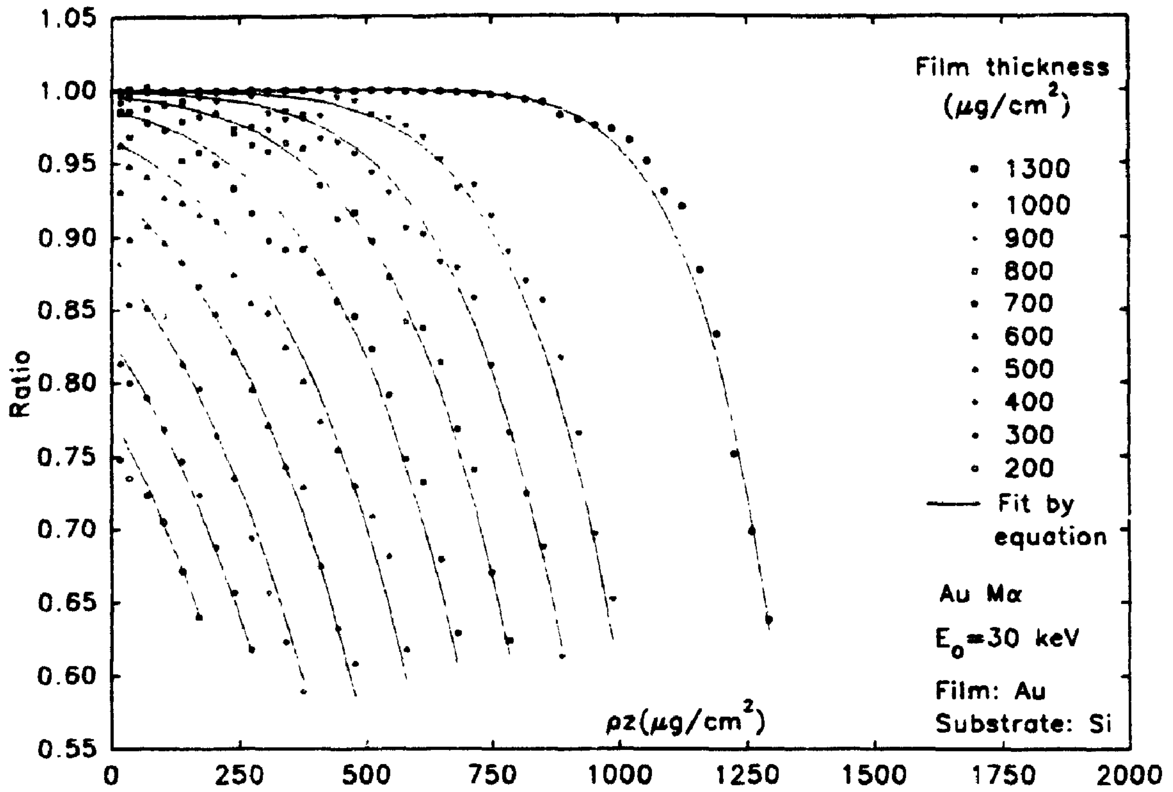

Figure 69a. Comparison of ratios calculated from figure 68a and for 68b.

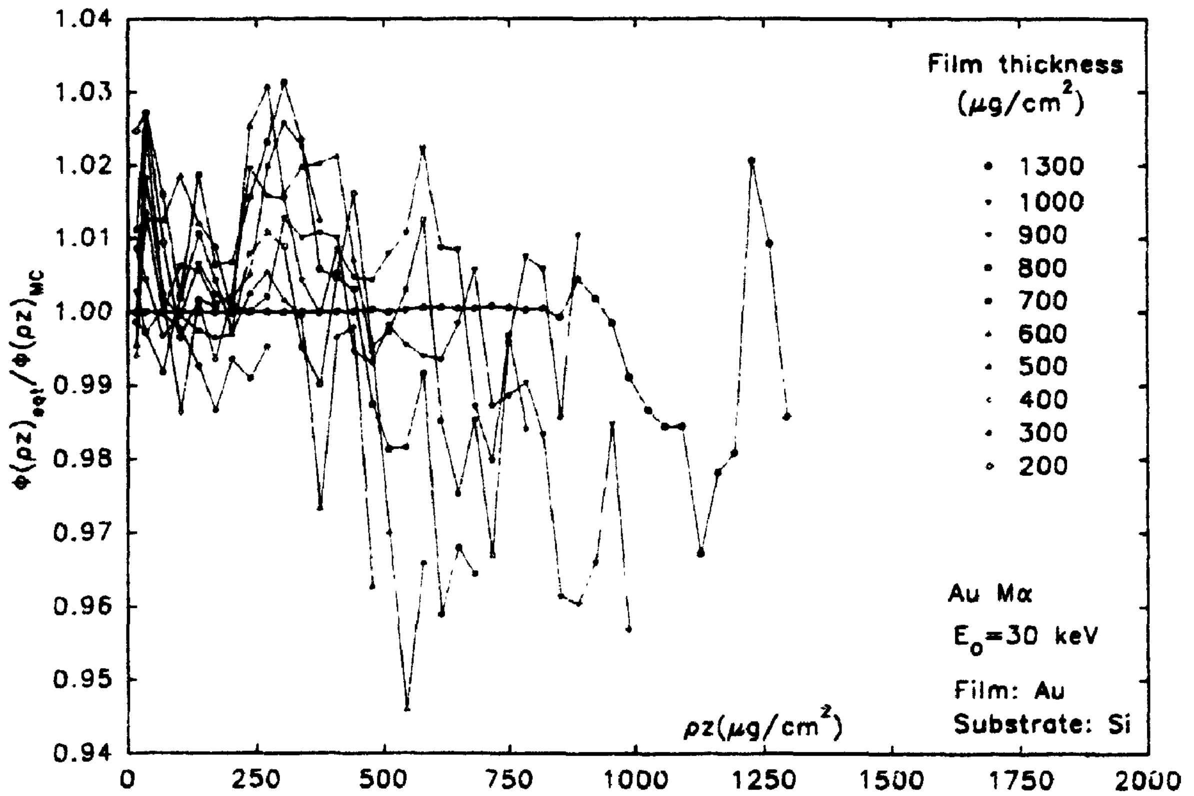

Figure 69b. Error plots calculated from figure 69a.

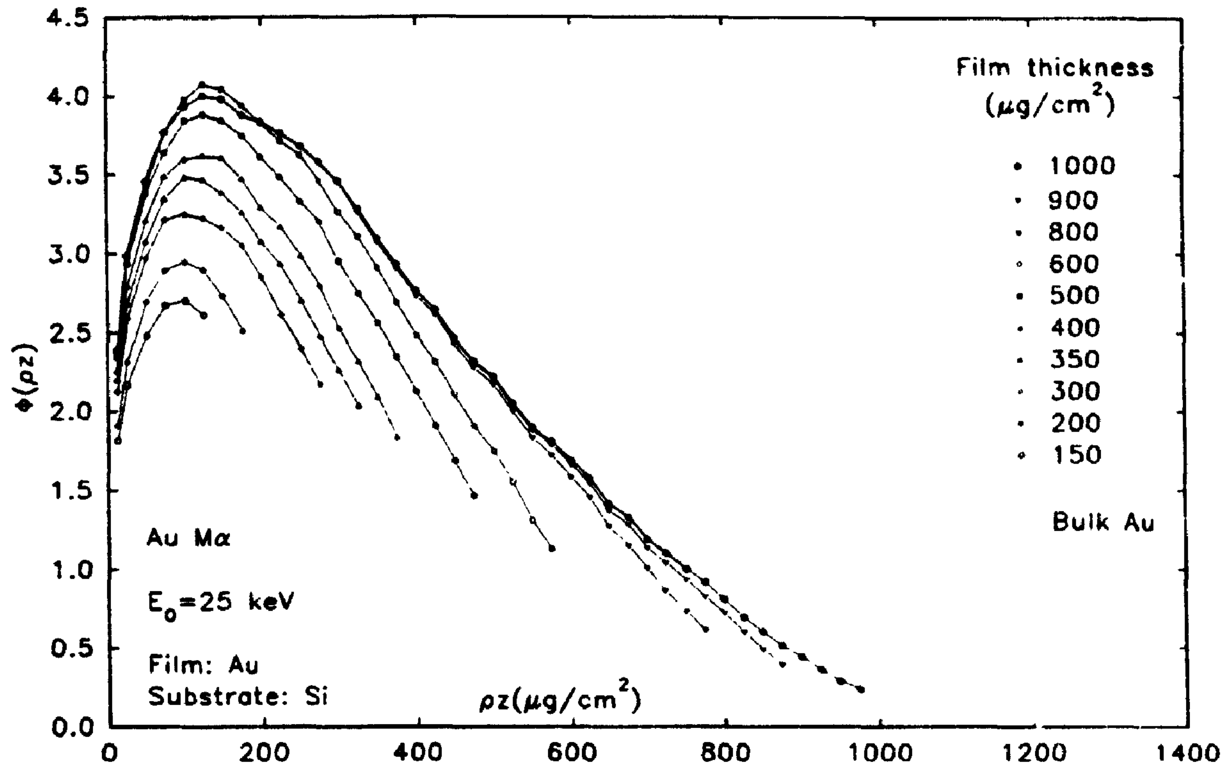

Figure 70a. Monte Carlo simulated thin film $\Phi(\rho z)$ curves of 10 different gold film thicknesses on silicon substrate at 25 keV.

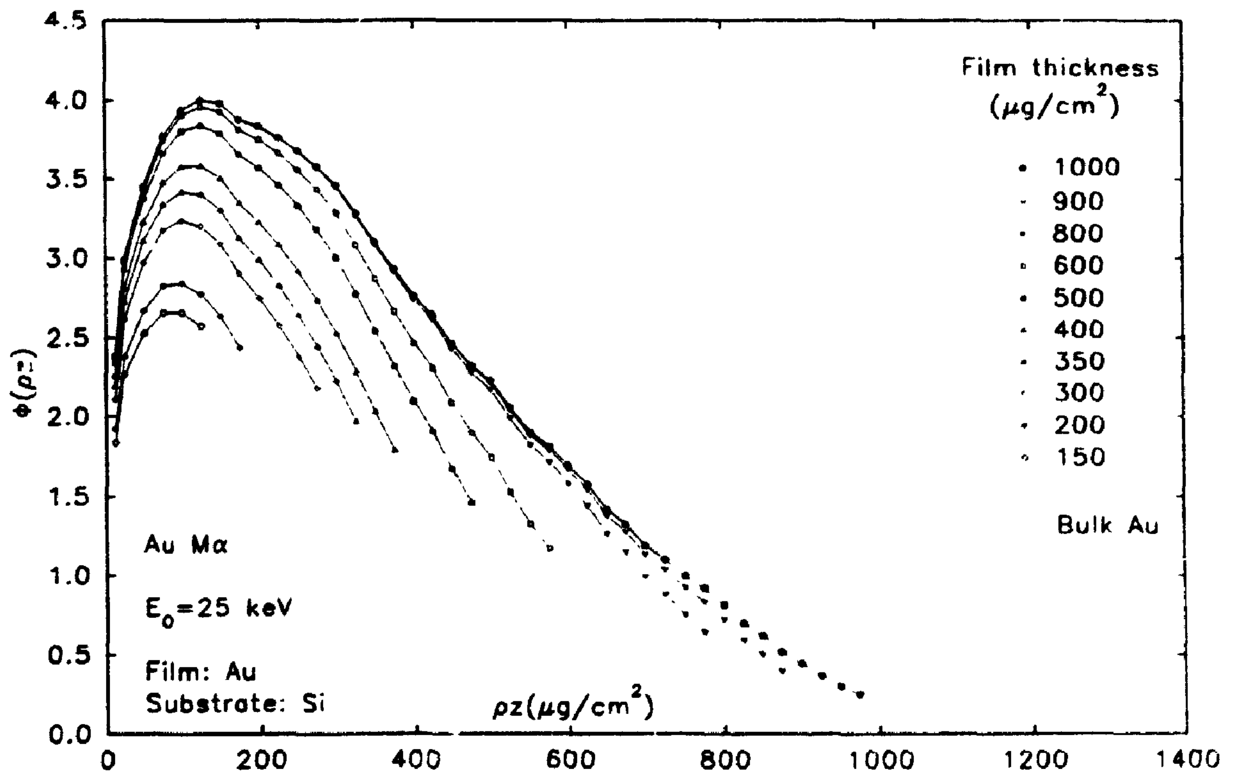

Figure 70b. Calculated thin film $\Phi(\rho z)$ curves of 10 different gold film thicknesses on silicon substrate at 25 keV.

3

PM-1 3½"x4" PHOTOGRAPHIC MICROCOPY TARGET
NBS 1010a ANSI/ISO #2 EQUIVALENT

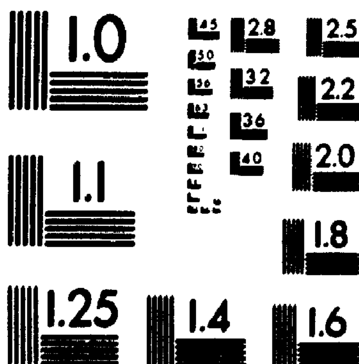

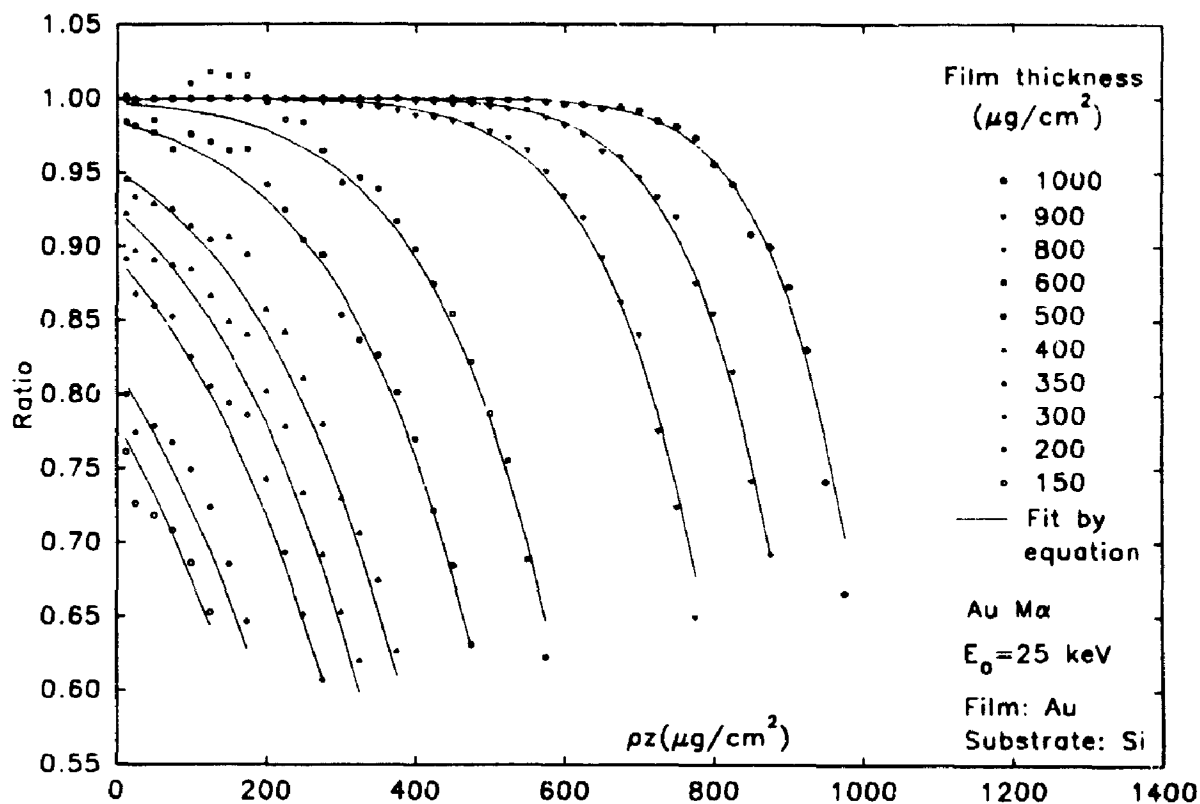

Figure 71a. Comparison of ratios calculated from figure 70a and for 70b.

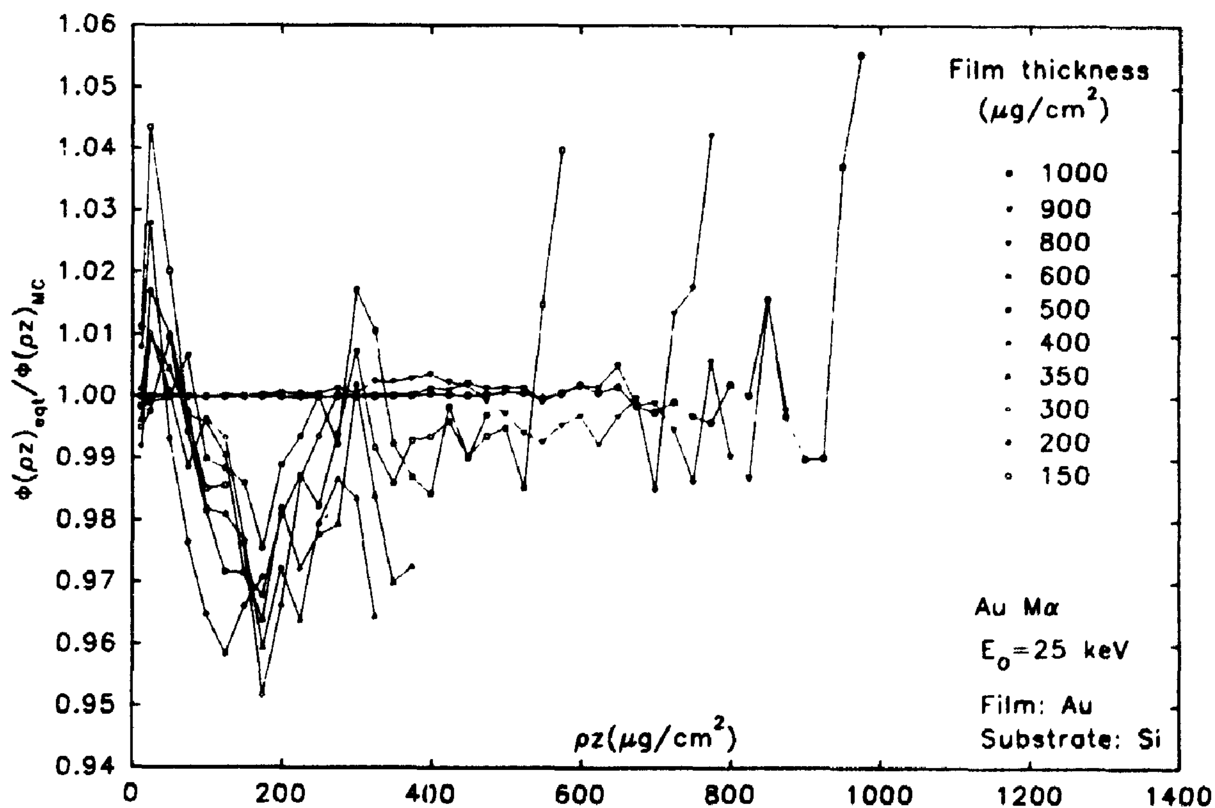

Figure 71b. Error plots calculated from figure 71a.

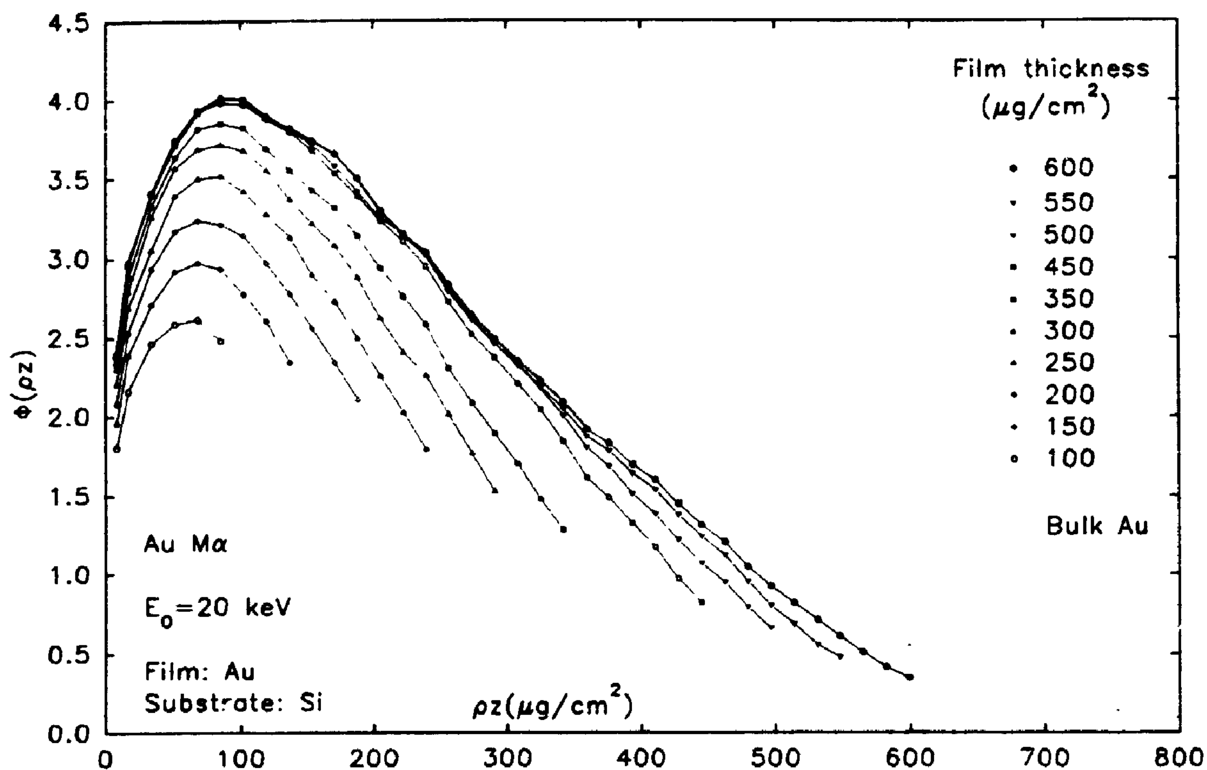

Figure 72a. Monte Carlo simulated thin film $\Phi(\rho z)$ curves of 10 different gold film thicknesses on silicon substrate at 20 keV.

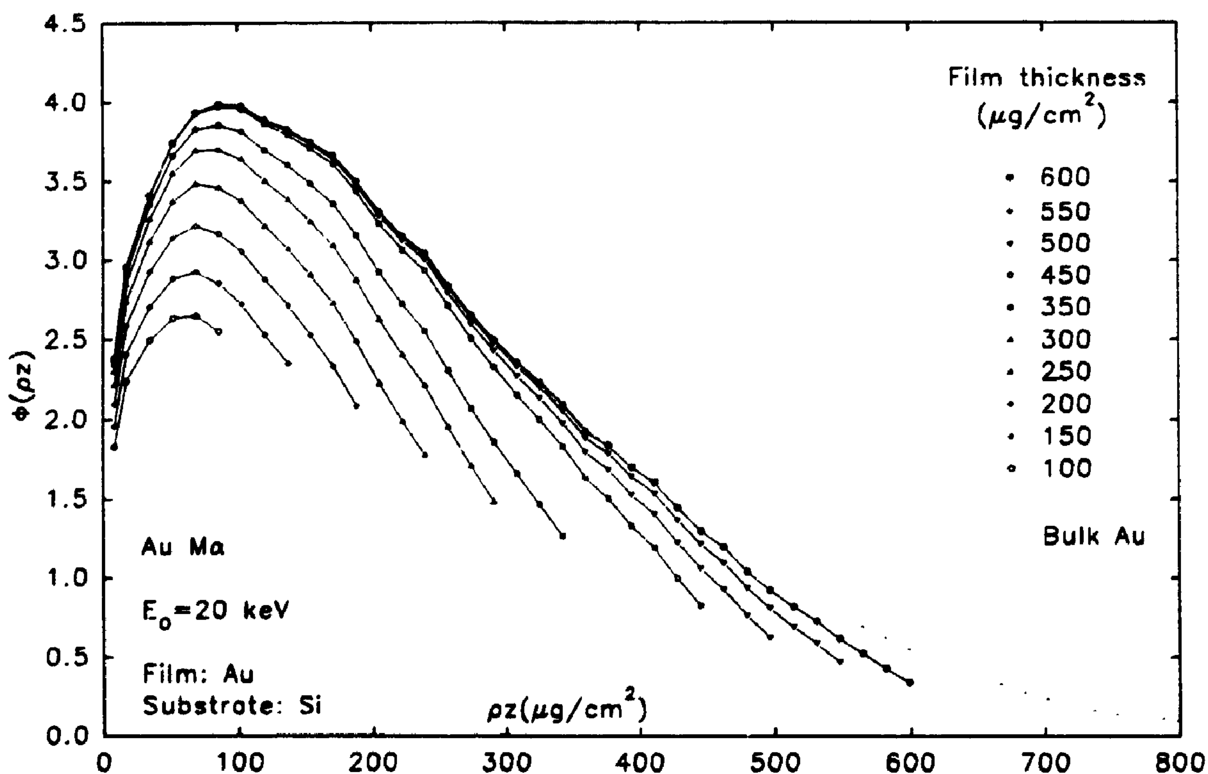

Figure 72b. Calculated thin film $\Phi(\rho z)$ curves of 10 different gold film thicknesses on silicon substrate at 20 keV.

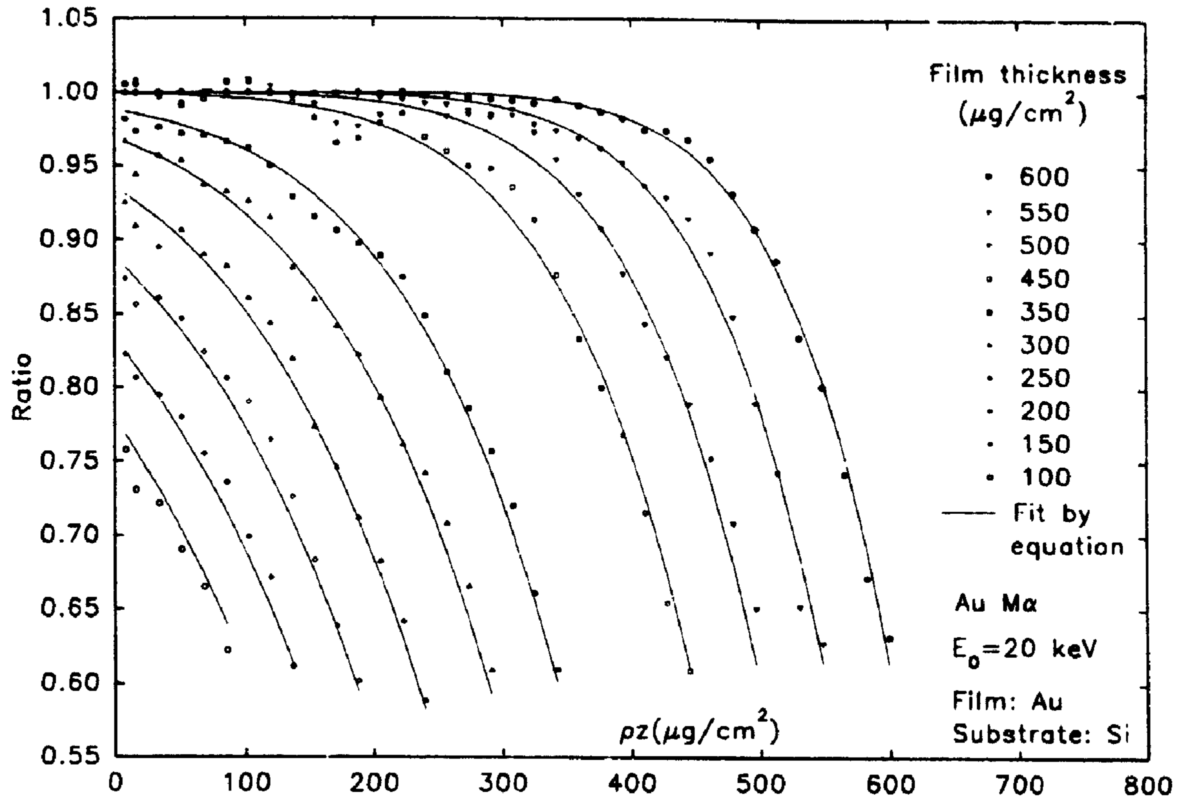

Figure 73a. Comparison of ratios calculated from figure 72a and for 72b.

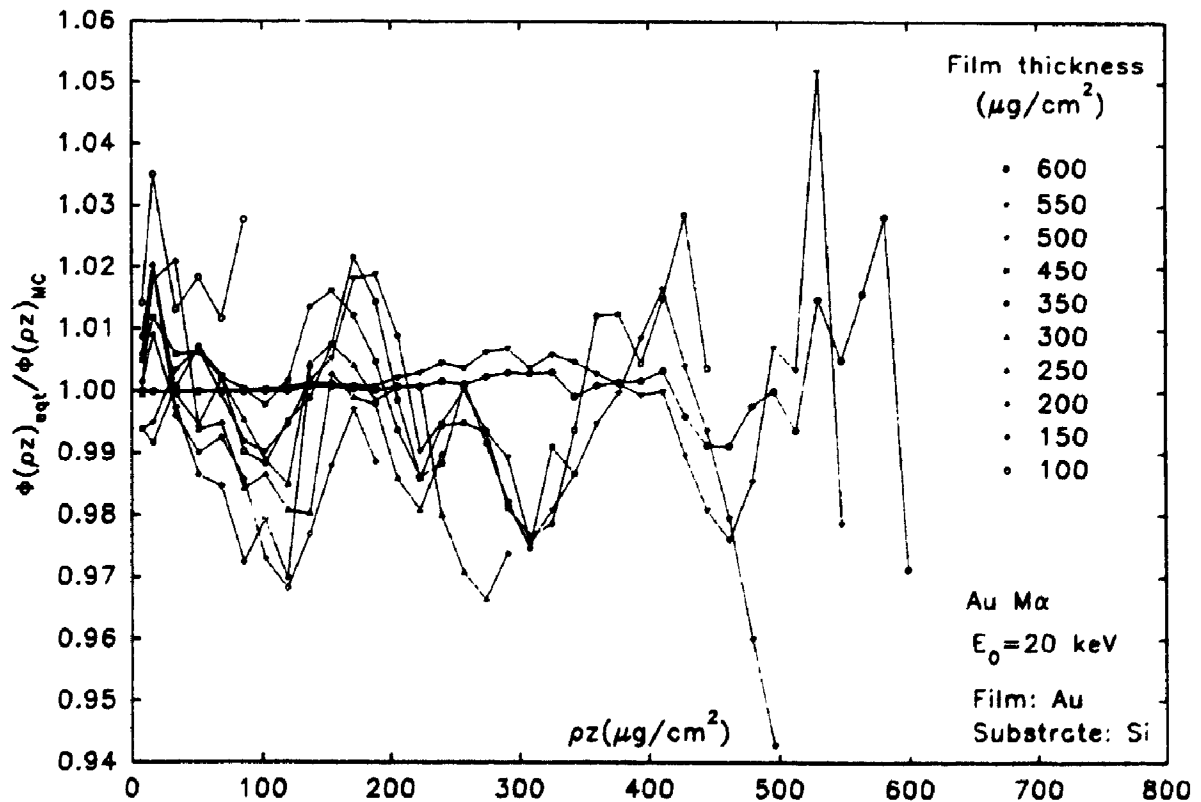

Figure 73b. Error plots calculated from figure 73a.

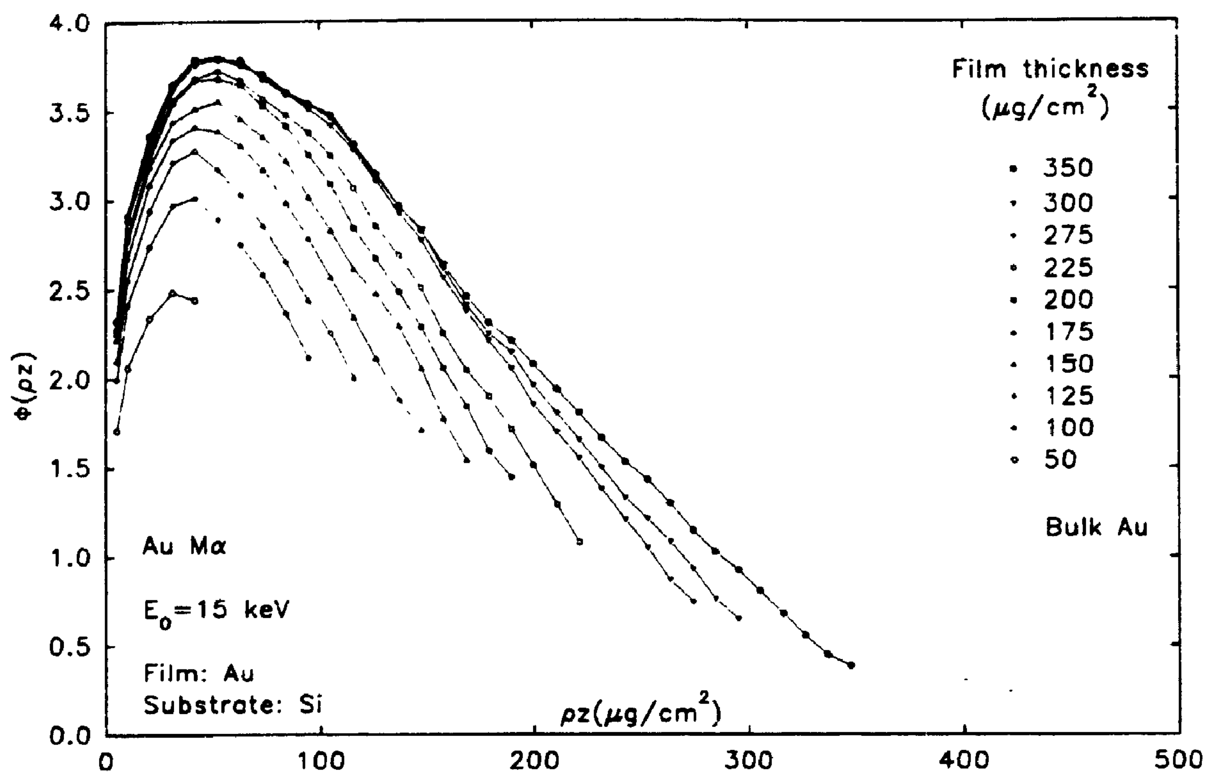

Figure 74a. Monte Carlo simulated thin film Φ(ρz) curves of 10 different gold film thicknesses on silicon substrate at 15 keV.

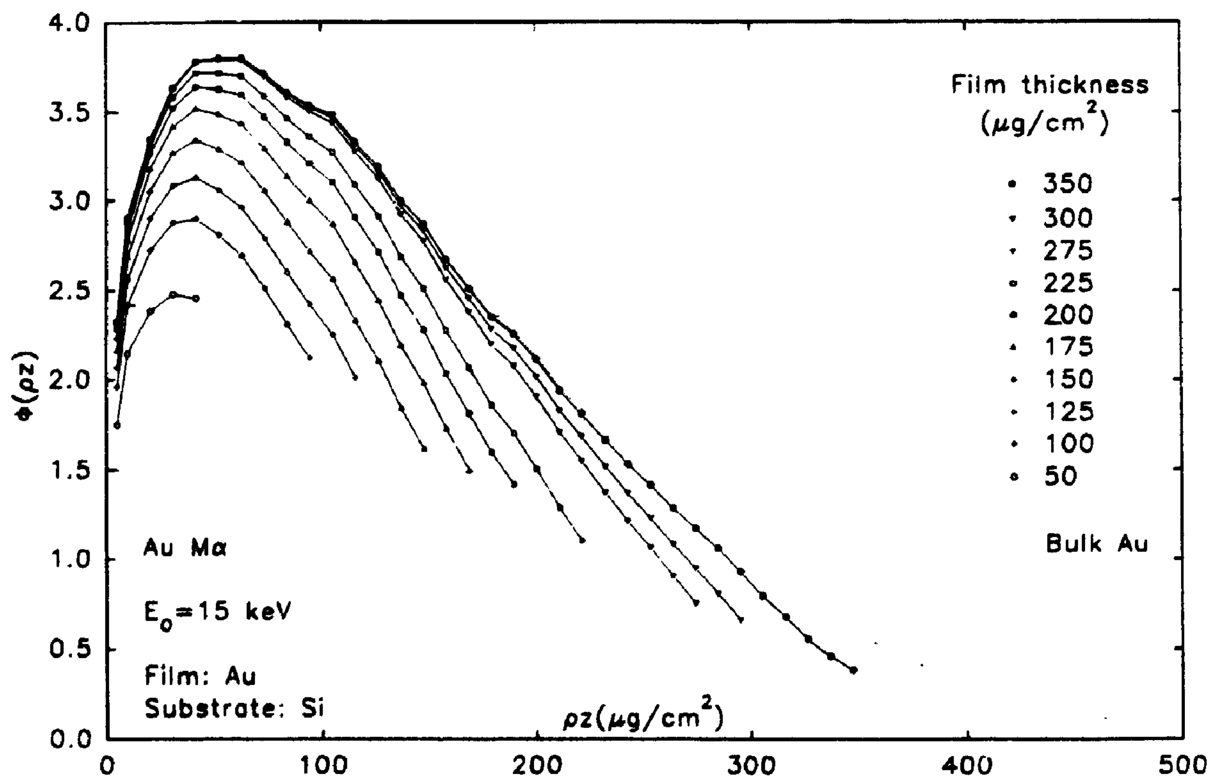

Figure 74b. Calculated thin film Φ(ρz) curves of 10 different gold film thicknesses on silicon substrate at 15 keV.

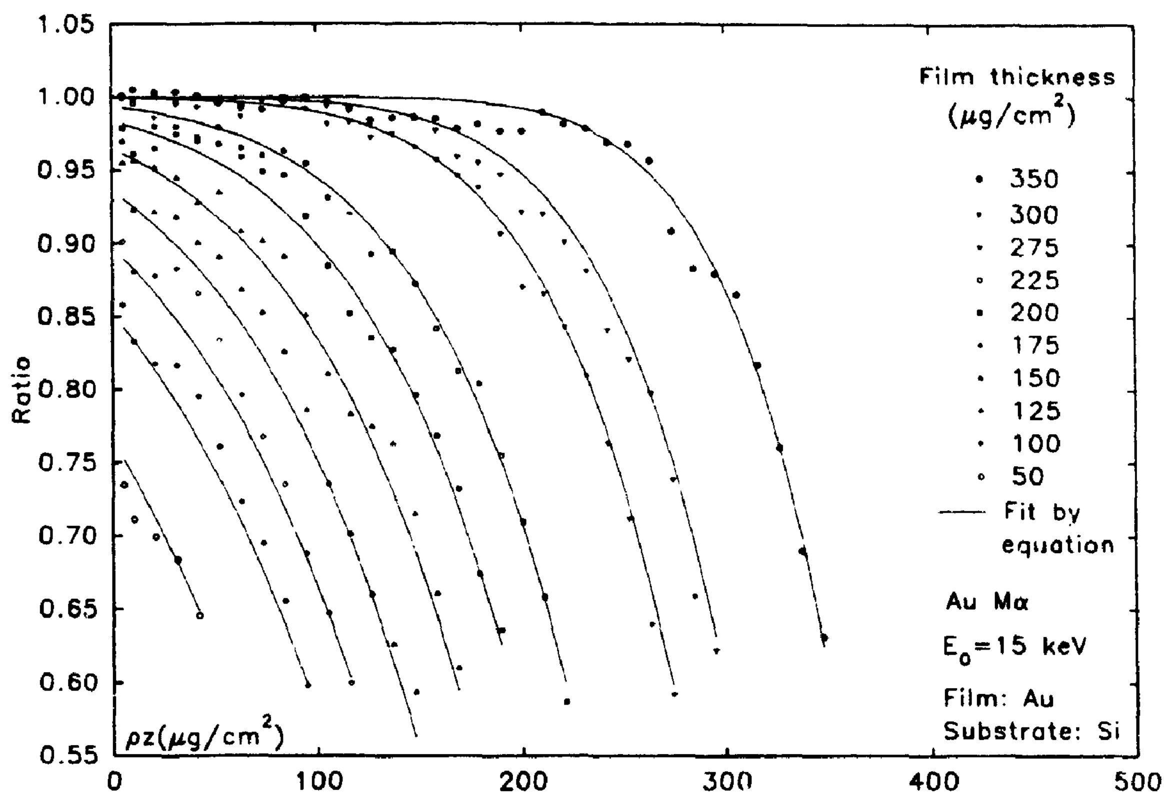

Figure 75a. Comparison of ratios calculated from figure 74a and for 74b.

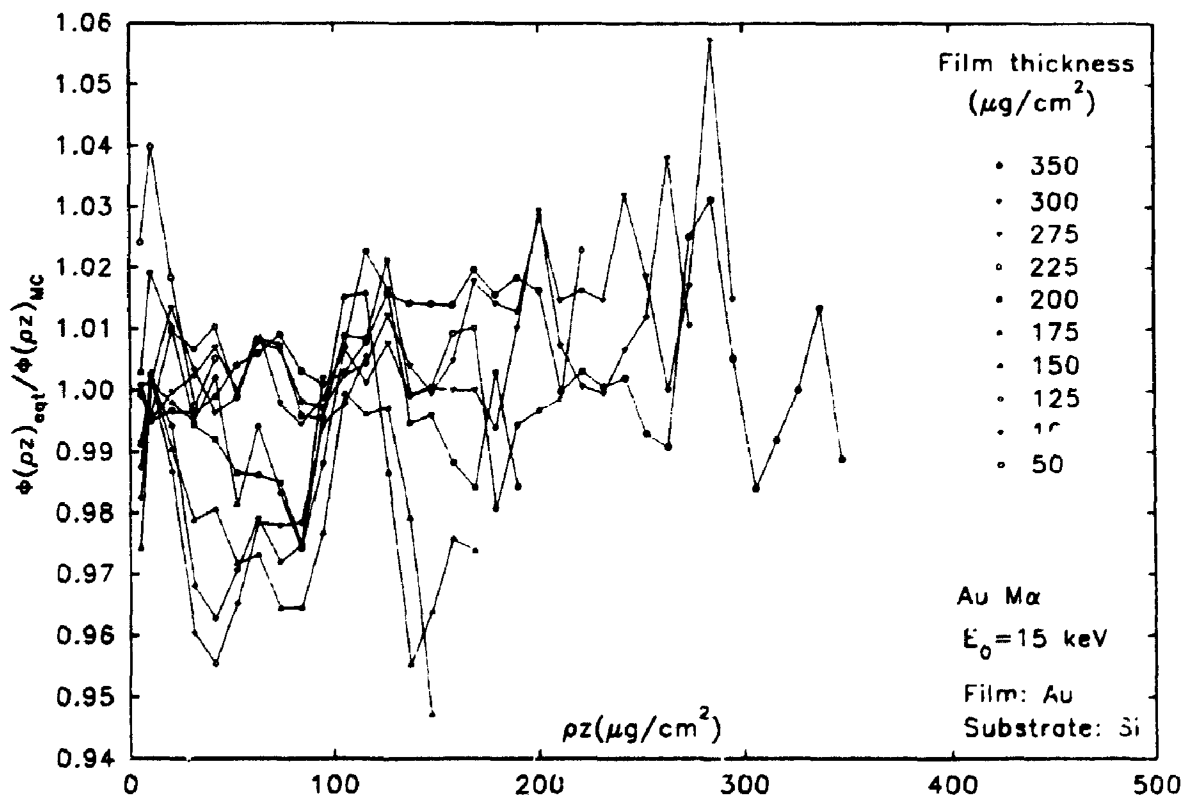

Figure 75b. Error plots calculated from figure 75a.

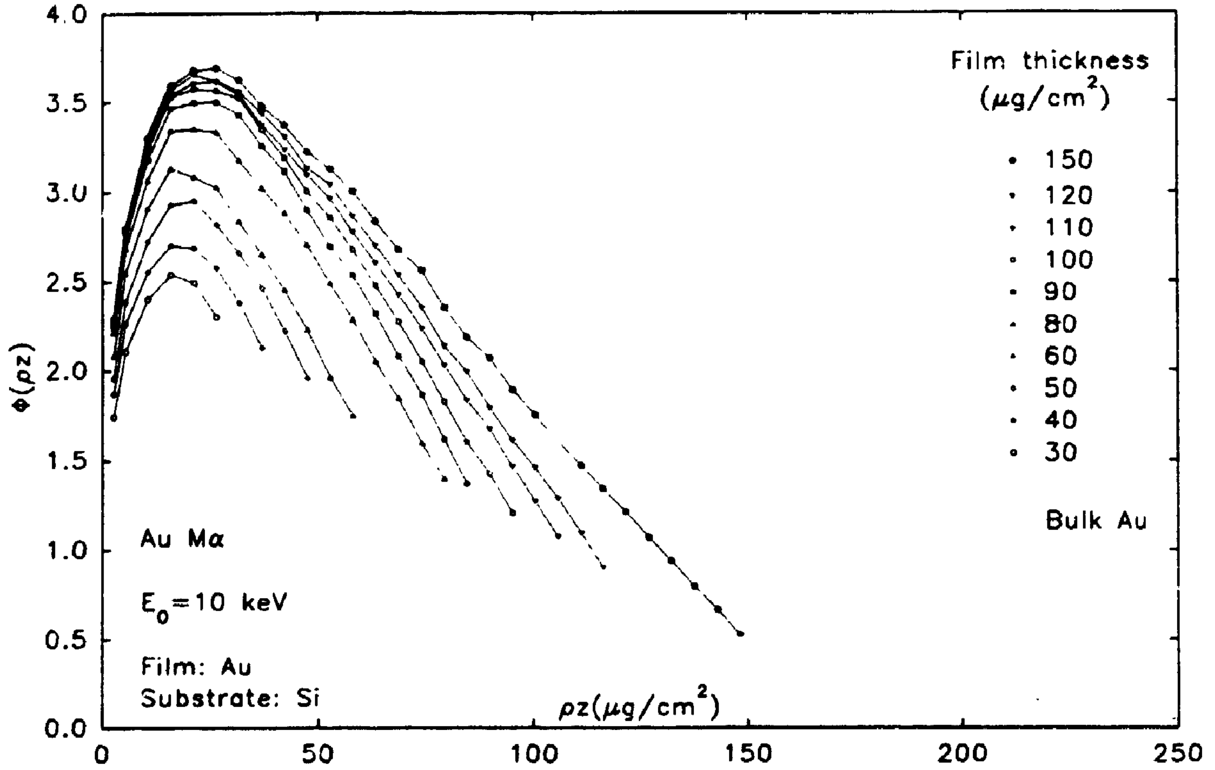

Figure 76a. Monte Carlo simulated thin film $\Phi(\rho z)$ curves of 10 different gold film thicknesses on silicon substrate at 10 keV.

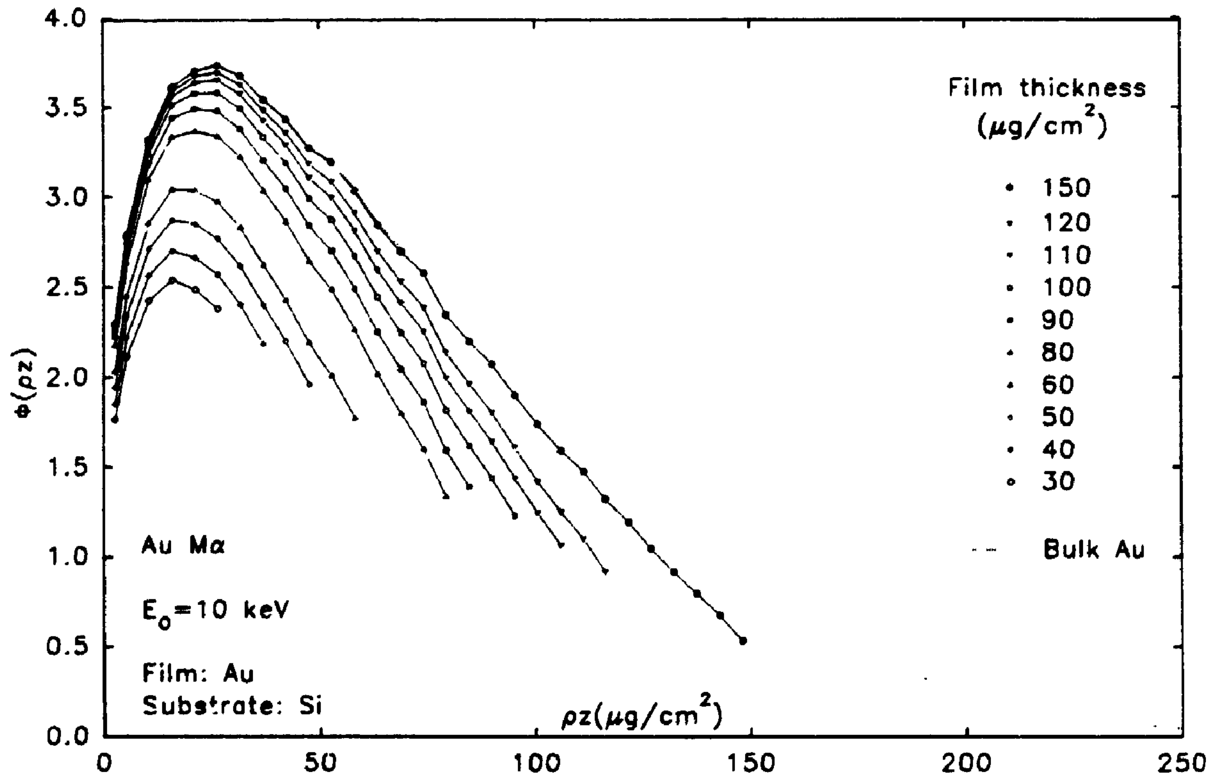

Figure 76b. Calculated thin film $\Phi(\rho z)$ curves of 10 different gold film thicknesses on silicon substrate at 10 keV.

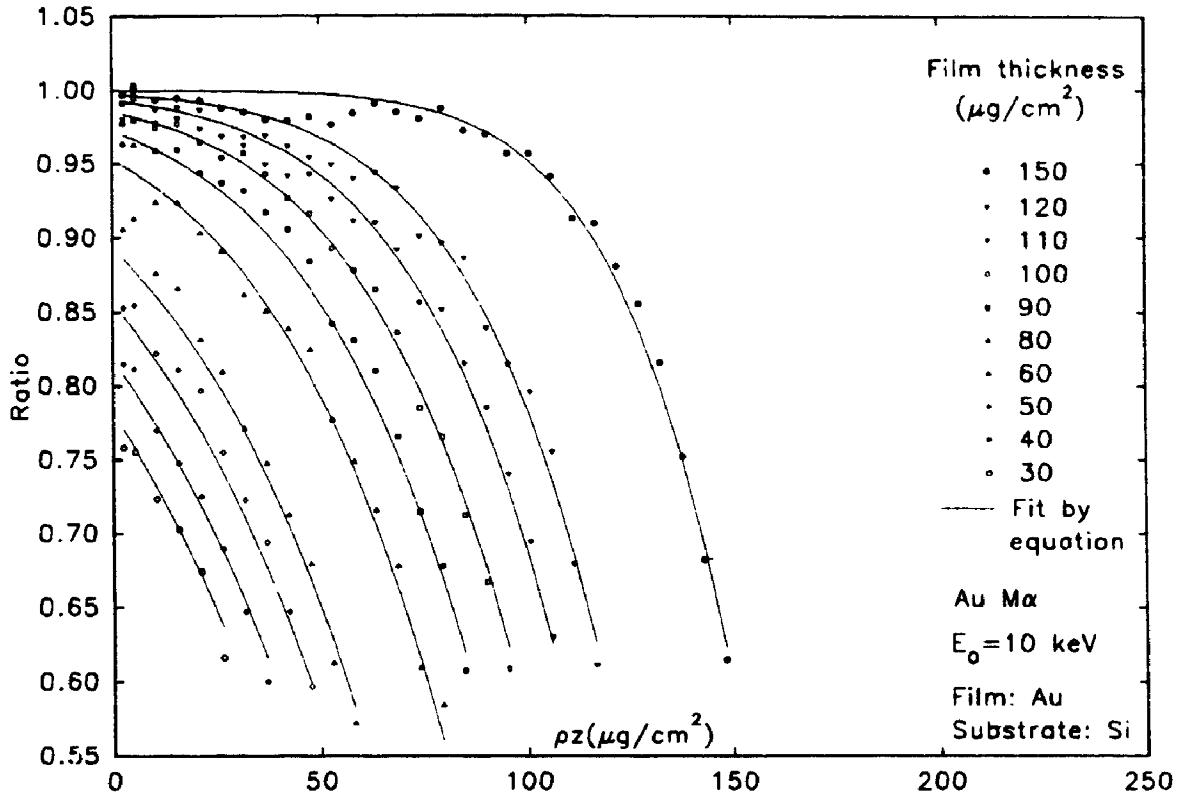

Figure 77a. Comparison of ratios calculated from figure 76a and for 76b.

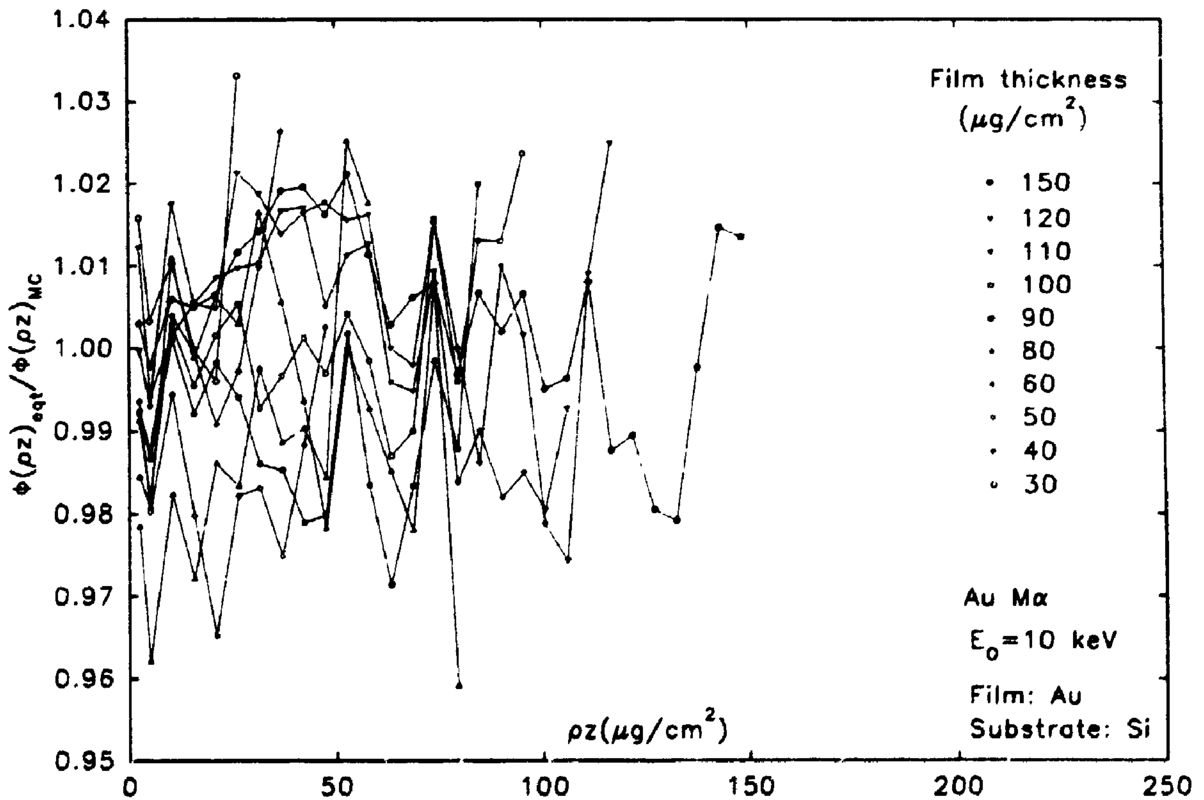

Figure 77b. Error plots calculated from figure 77a.

Si/Ag and Si/Cu (Figures 78 to 82). Each figure includes the Monte Carlo simulated thin film $\phi(\rho z)$ curve (a), the calculated thin film curve (b) and the error plot (c). Although other electron energies were also investigated, only the 30 keV data are reproduced in this work. Ratios were calculated according to Eqns. (82) and (84) except of course that the optimized values used in the equations will be different for each system. The relationship between these parameters will be discussed in detail later. Again in the five error plots (Figures 78c to 82c), a ±3% variation encloses most of the data points which are well centred about the value of 1.00 indicating no significant positive or negative bias. Therefore, good agreement was found between Monte Carlo simulated thin film $\phi(\rho z)$ curves and emperically fitted curves for other systems as well.

Recall that the first step in this approach is to determine the value of ratio which is given by $\phi(\rho z)_{film}/\phi(\rho z)_{bulk}$ from the simulated curves. Therefore, if the atomic numbers of the film and the substrate are very similar, the ratio will be close to unity at all thicknesses. Because of this, no systems were investigated with an atomic number difference less than that of the Si/Cu system.

Five other systems besides Au/Si were studied in the case of a high atomic number film on a low atomic number substrate, Ag/Cu, Au/Cu, Au/Ag, Ag/Si and Cu/Si (Figures 83 to 87). Again, only 30 keV data are reproduced in this work. Ratios were calculated according to Eqns. (89) and (91) and again the optimized values for these equations will be different for each of the systems. Again, most data points in the five error plots (Figures 83c to 87c) lie within ±3%.

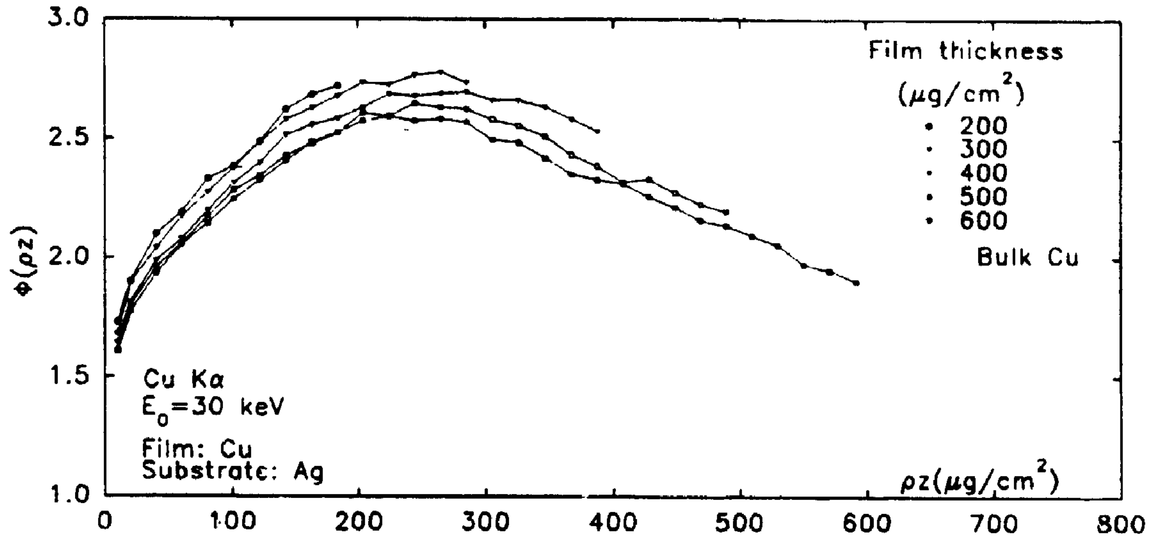

Figure 78a. Monte Carlo simulated thin film $\Phi(\rho z)$ curves of 5 different copper film thicknesses on silver substrate at 30 keV.

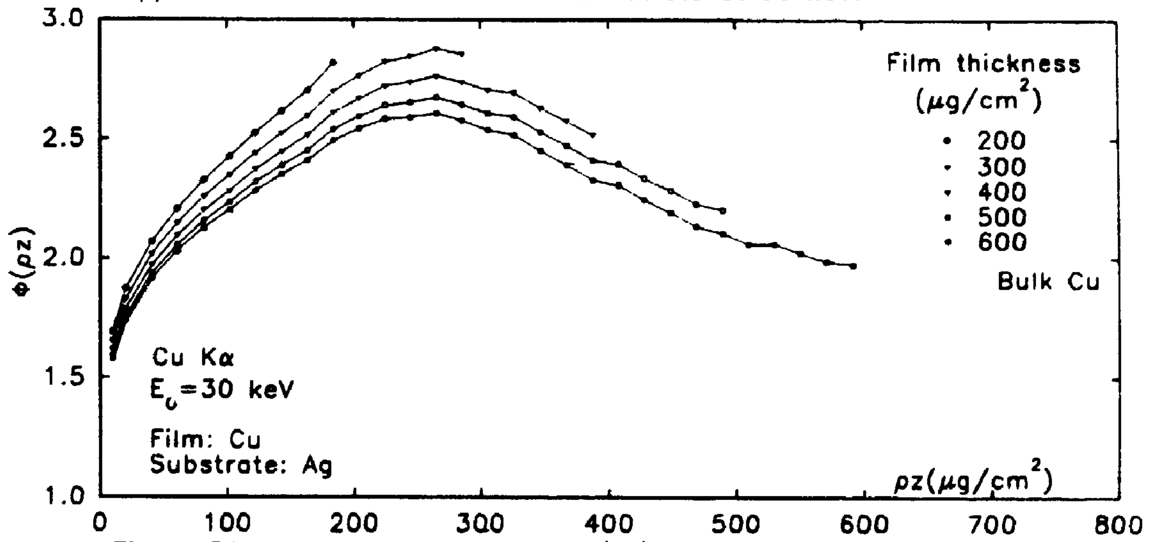

Figure 78b. Calculated thin film $\Phi(\rho z)$ curves of 5 different copper film thicknesses on silver substrate at 30 keV.

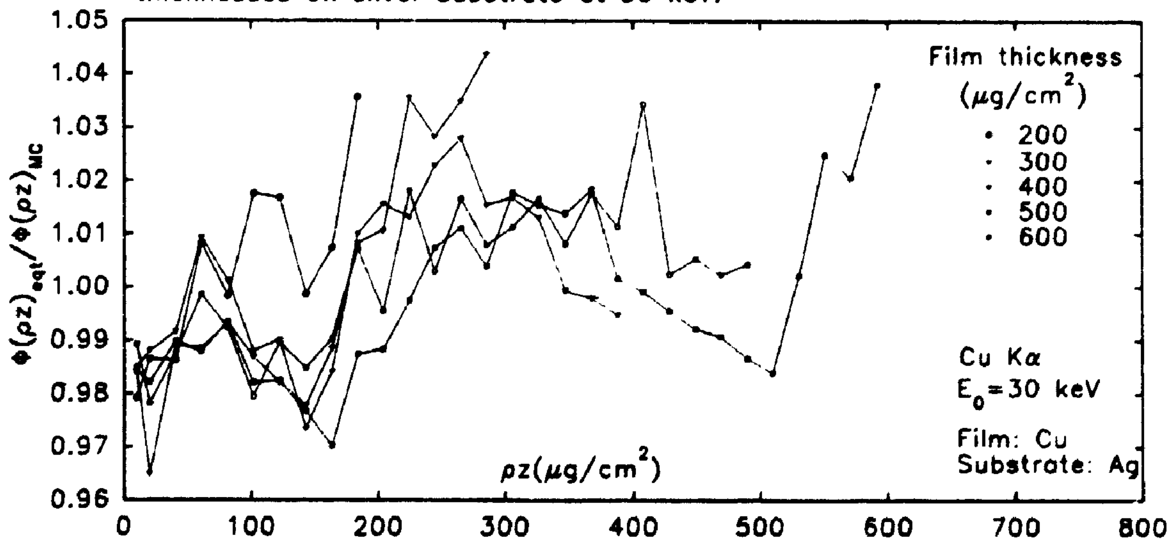

Figure 78c. Error plots calculated from figure 78a and 78b.

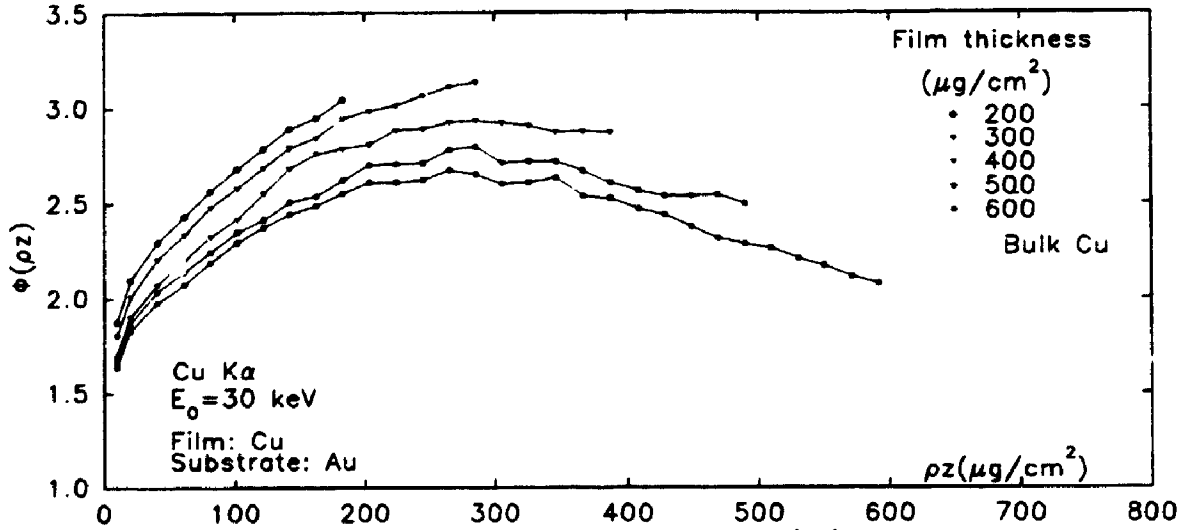

Figure 79a. Monte Carlo simulated thin film $\Phi(\rho z)$ curves of 5 different copper film thicknesses on gold substrate at 30 keV.

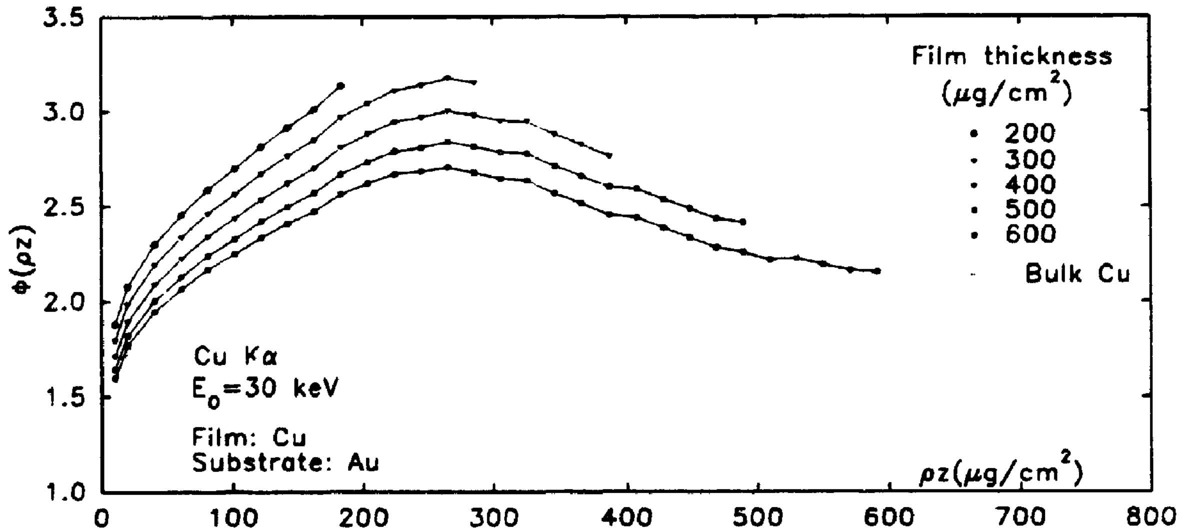

Figure 79b. Calculated thin film $\Phi(\rho z)$ curves of 5 different copper film thicknesses on gold substrate at 30 keV.

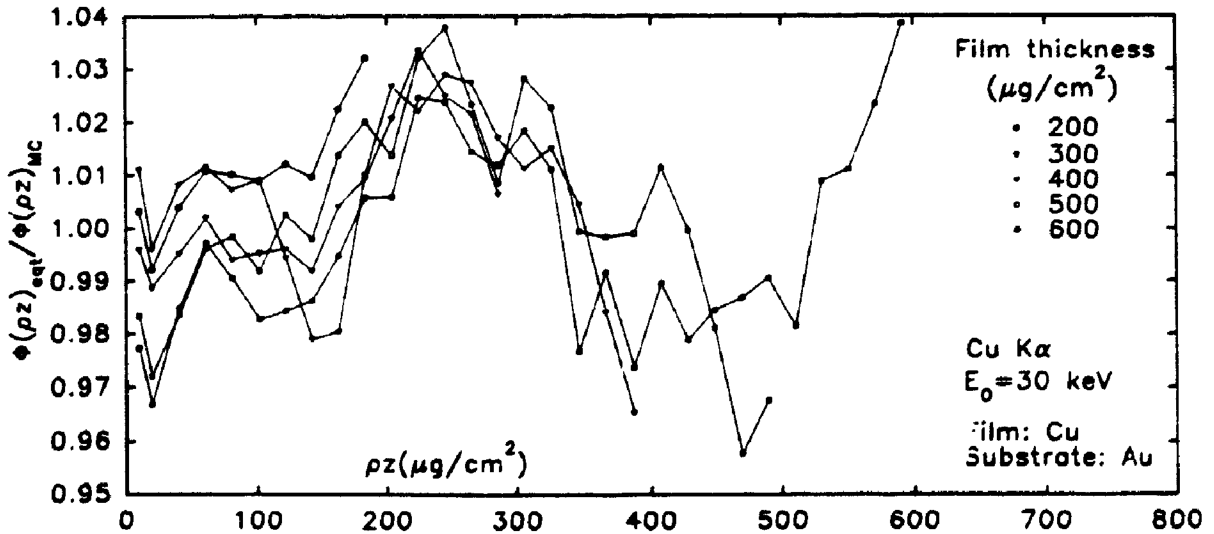

Figure 79c. Error plots calculated from figure 79a and 79b.

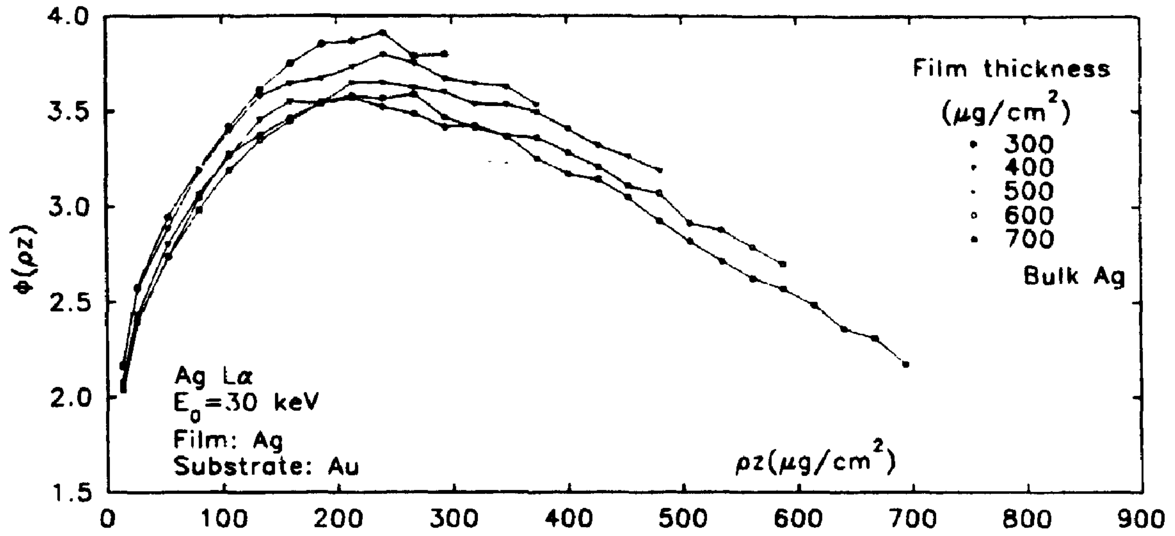

Figure 80a. Monte Carlo simulated thin film $\Phi(\rho z)$ curves of 5 different silver film thicknesses on gold substrate at 30 keV.

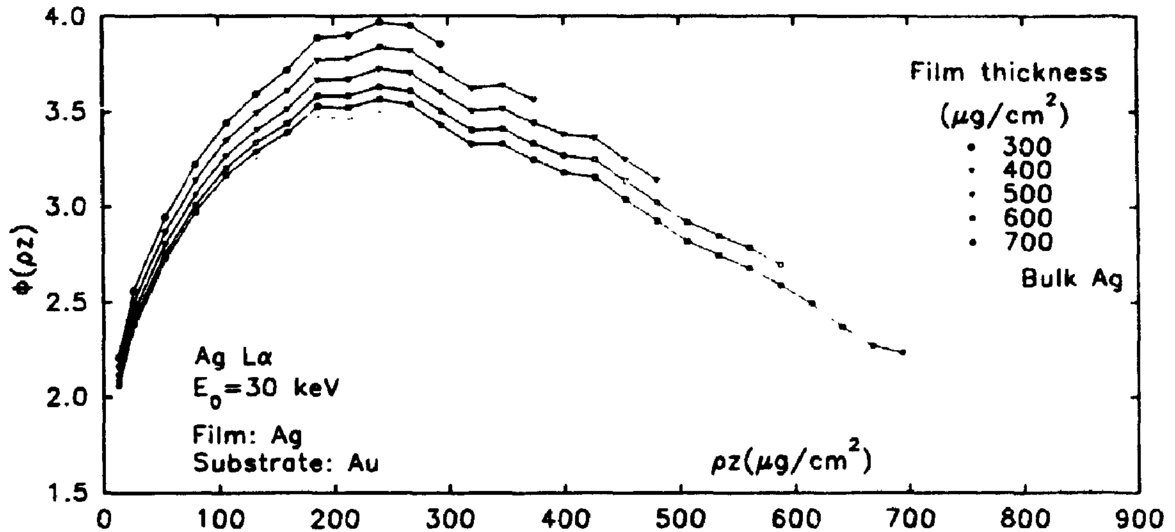

Figure 80b. Calculated thin film $\Phi(\rho z)$ curves of 5 different silver film thicknesses on gold substrate at 30 keV.

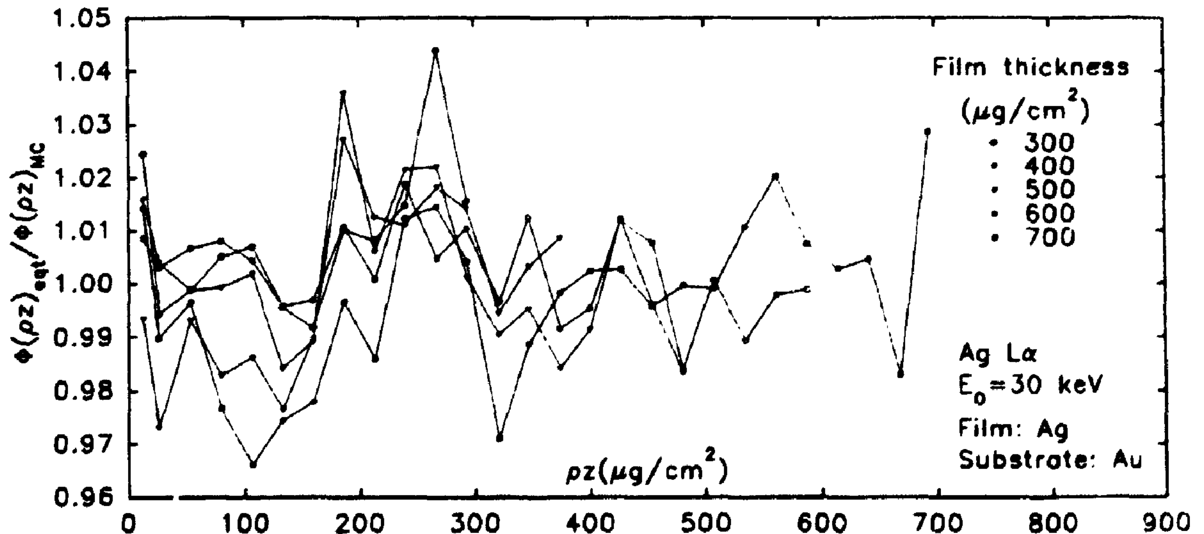

Figure 80c. Error plots calculated from figure 80a and 80b.

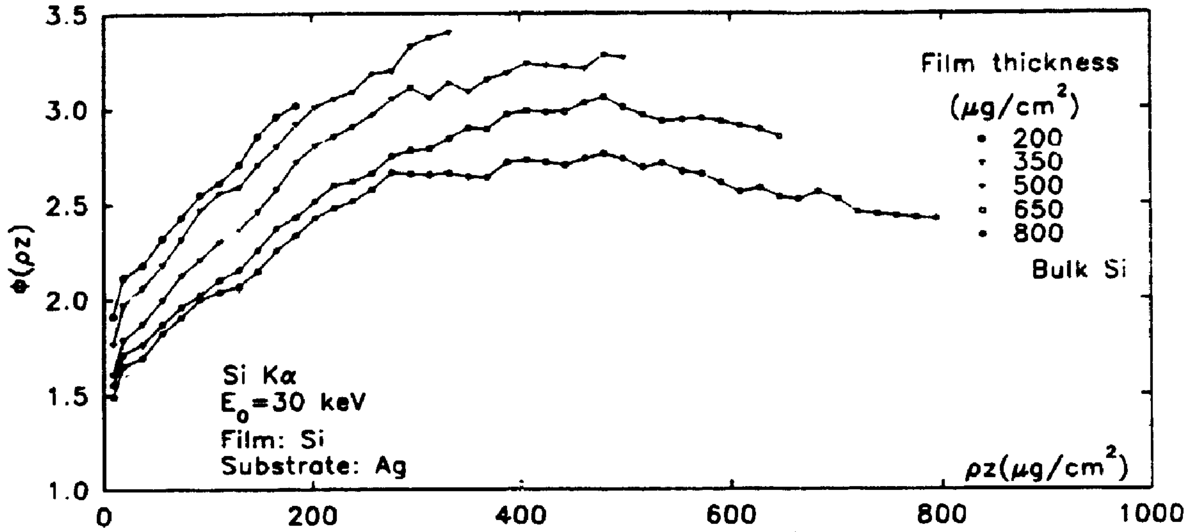

Figure 81a. Monte Carlo simulated thin film $\Phi(\rho z)$ curves of 5 different silicon film thicknesses on silver substrate at 30 keV.

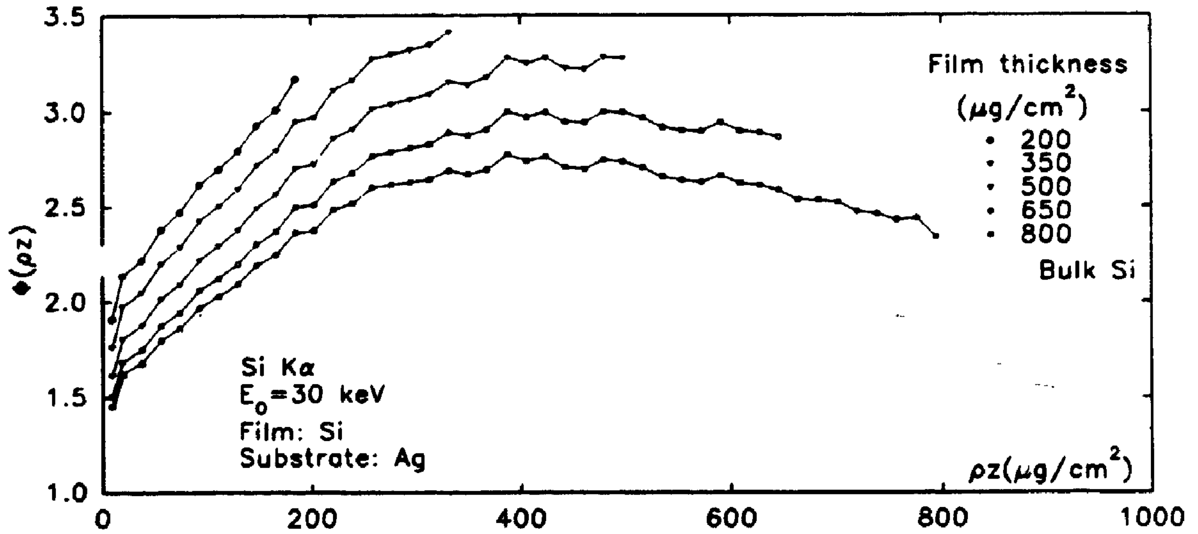

Figure 81b. Calculated thin film $\Phi(\rho z)$ curves of 5 different silicon film thicknesses on silver substrate at 30 keV.

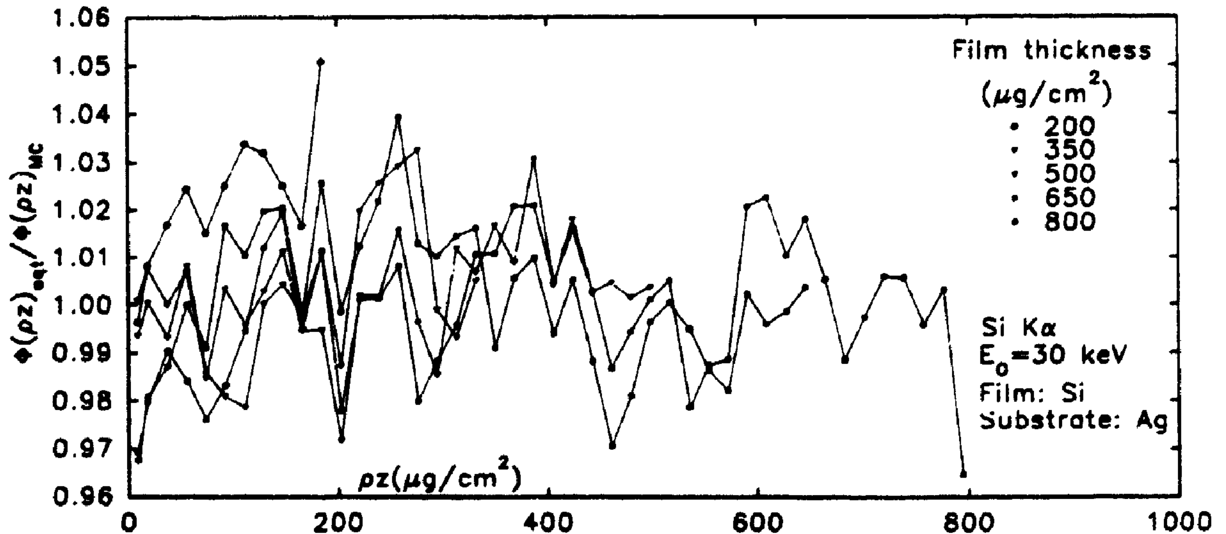

Figure 81c. Error plots calculated from figure 81a and 81b.

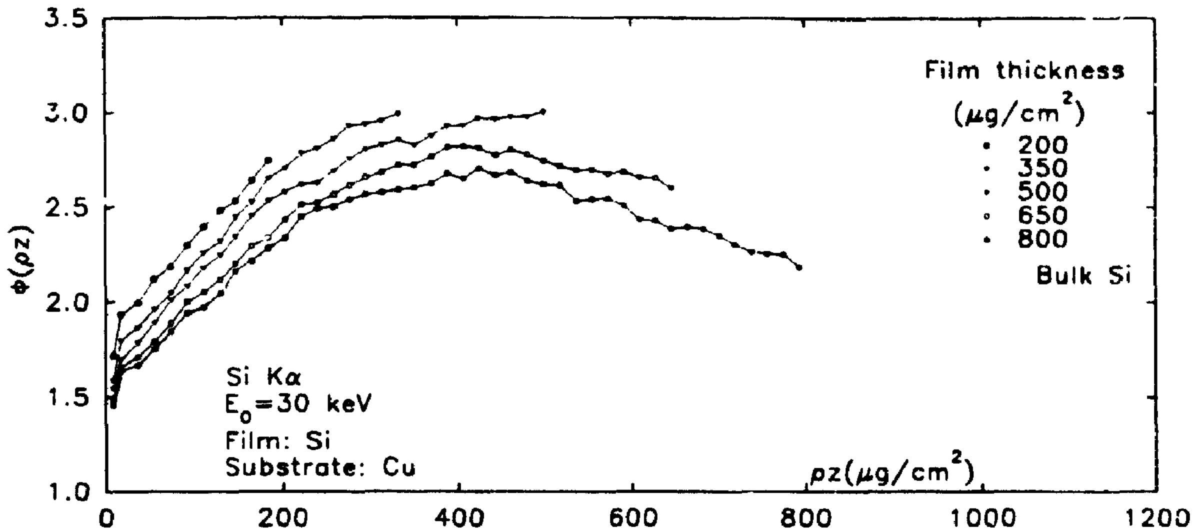

Figure 82a. Monte Carlo simulated thin film $\Phi(\rho z)$ curves of 5 different silicon film thicknesses on copper substrate at 30 keV.

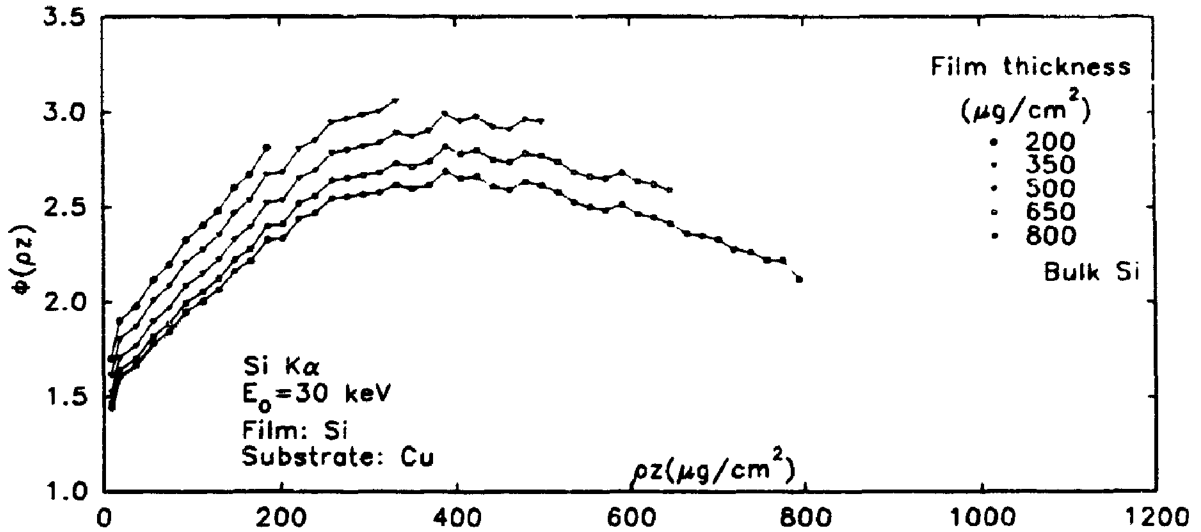

Figure 82b. Calculated thin film $\Phi(\rho z)$ curves of 5 different silicon film thicknesses on copper substrate at 30 keV.

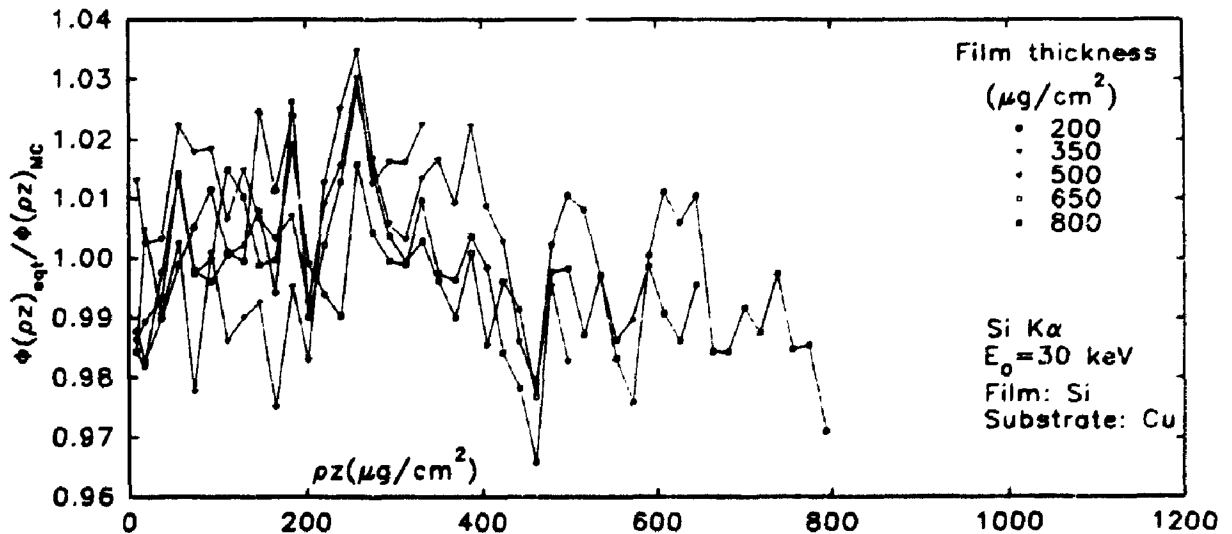

Figure 82c. Error plots calculated from figure 82a and 82b.

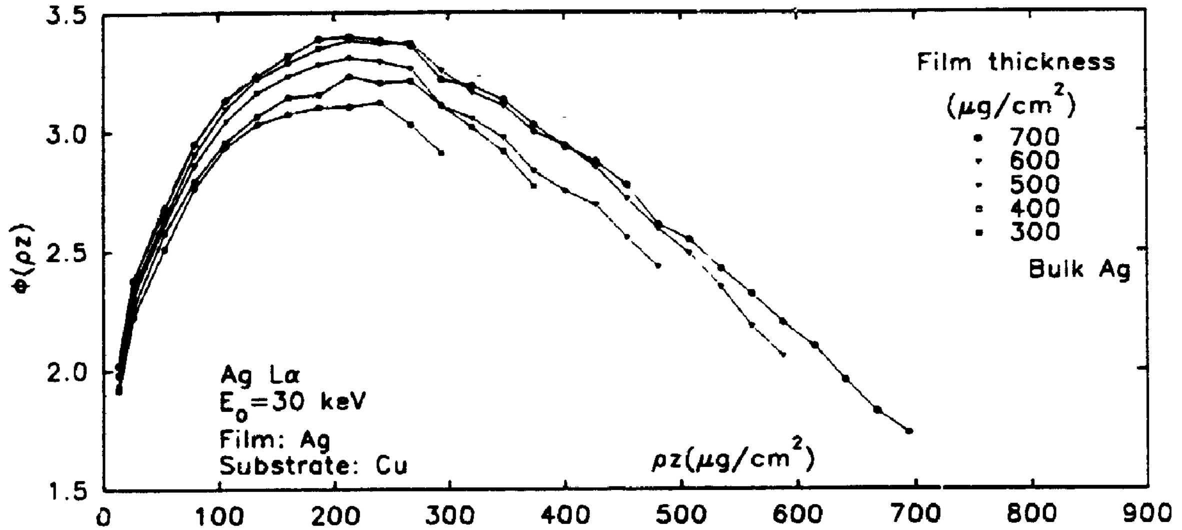

Figure 83a. Monte Carlo simulated thin film $\Phi(\rho z)$ curves of 5 different silver film thicknesses on copper substrate at 30 keV.

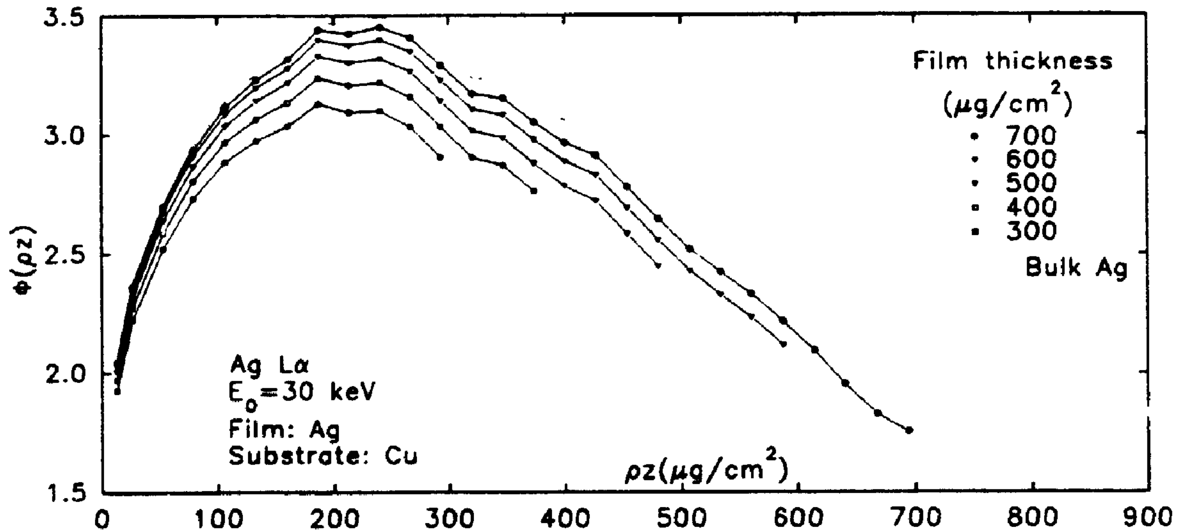

Figure 83b. Calculated thin film $\Phi(\rho z)$ curves of 5 different silver film thicknesses on copper substrate at 30 keV.

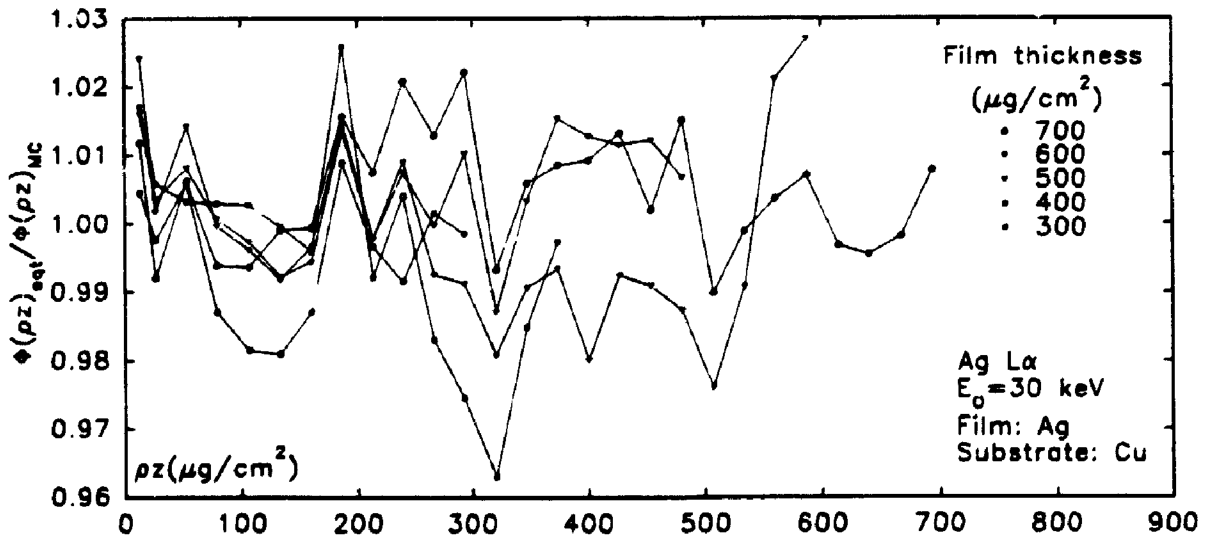

Figure 83c. Error plots calculated from figure 83a and 83b.

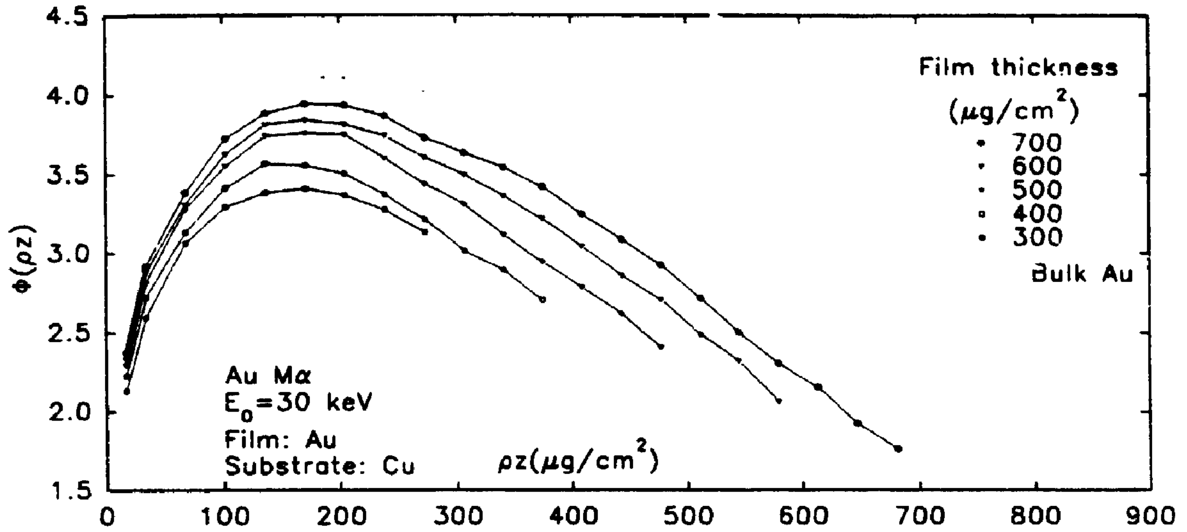

Figure 84a. Monte Carlo simulated thin film $\Phi(\rho z)$ curves of 5 different gold film thicknesses on copper substrate at 30 keV.

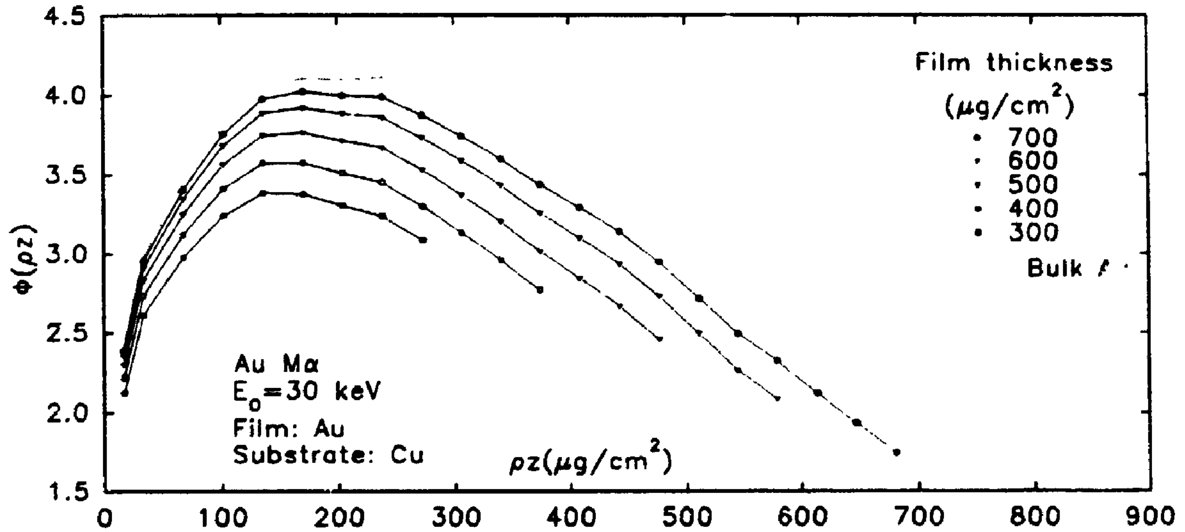

Figure 84b. Calculated thin film $\Phi(\rho z)$ curves of 5 different gold film thicknesses on copper substrate at 30 keV.

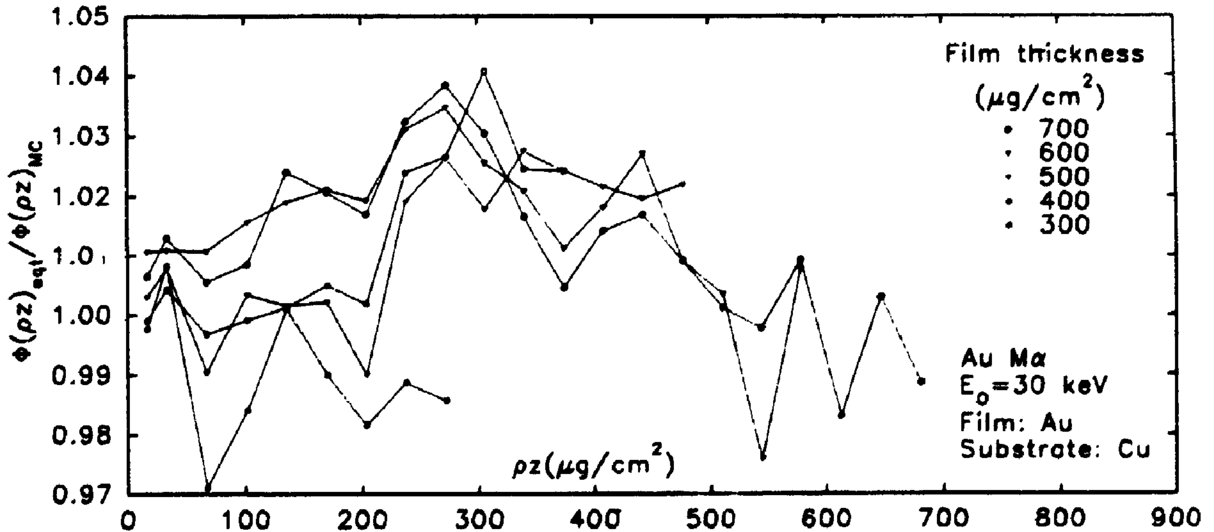

Figure 84c. Error plots calculated from figure 84a and 84b.

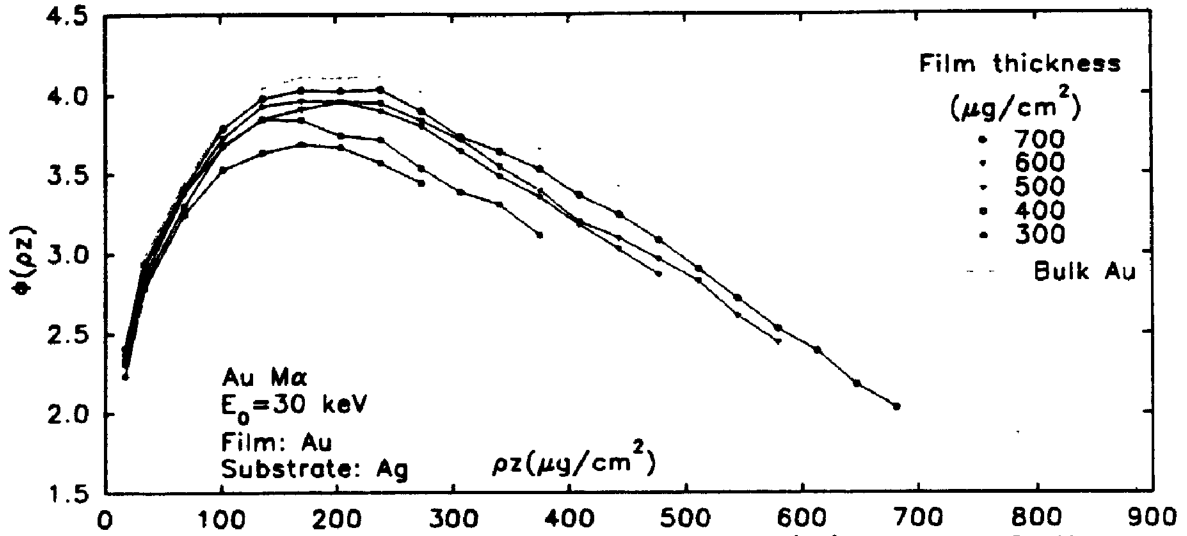

Figure 85a. Monte Carlo simulated thin film $\Phi(\rho z)$ curves of 5 different gold film thicknesses on silver substrate at 30 keV.

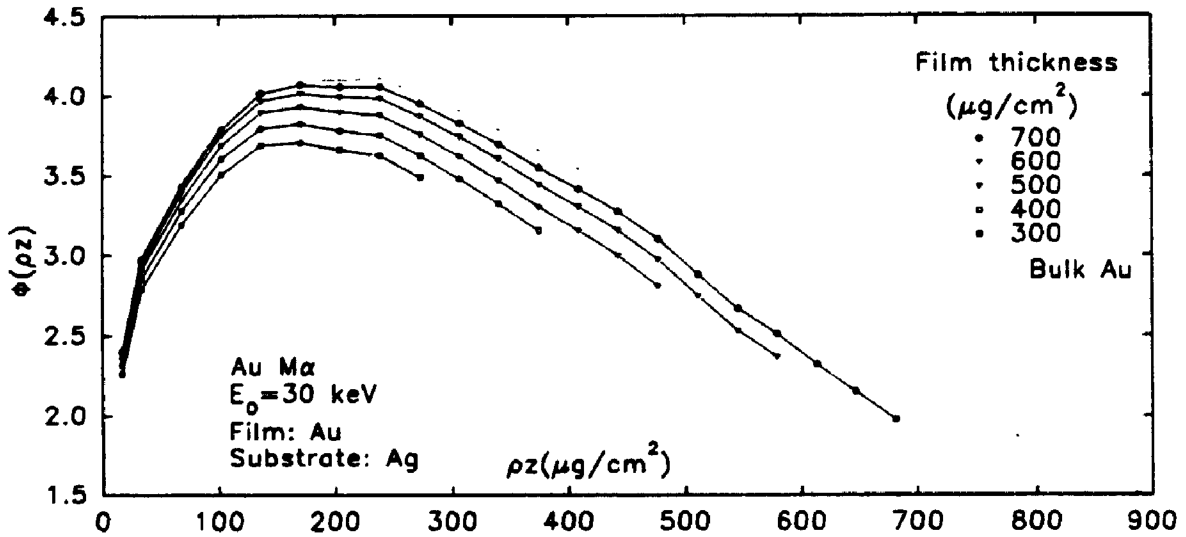

Figure 85b. Calculated thin film $\Phi(\rho z)$ curves of 5 different gold film thicknesses on silver substrate at 30 keV.

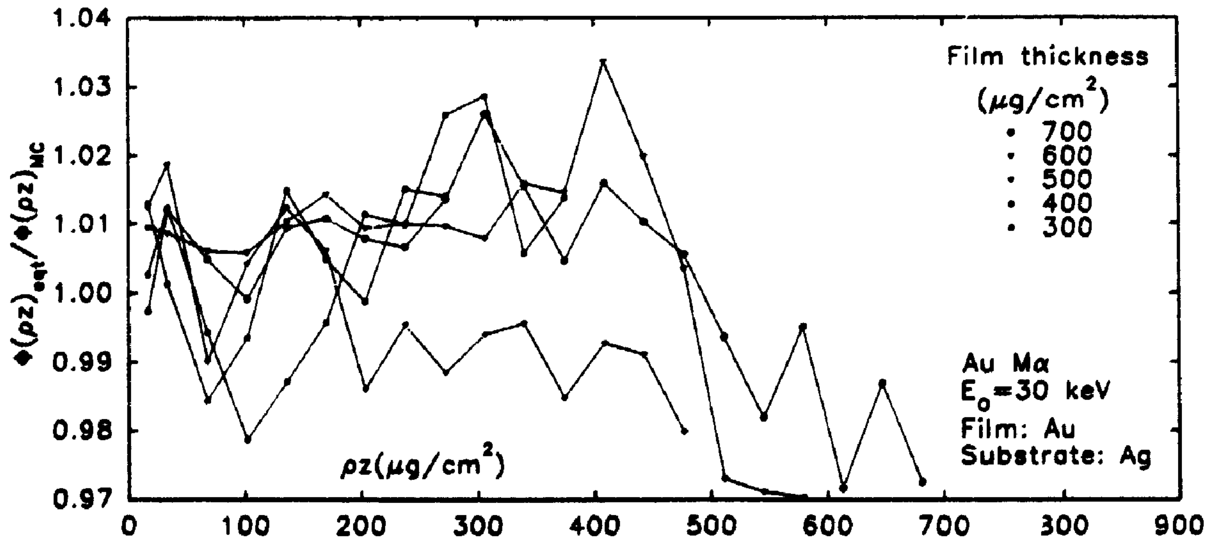

Figure 85c. Error plots calculated from figure 85a and 85b.

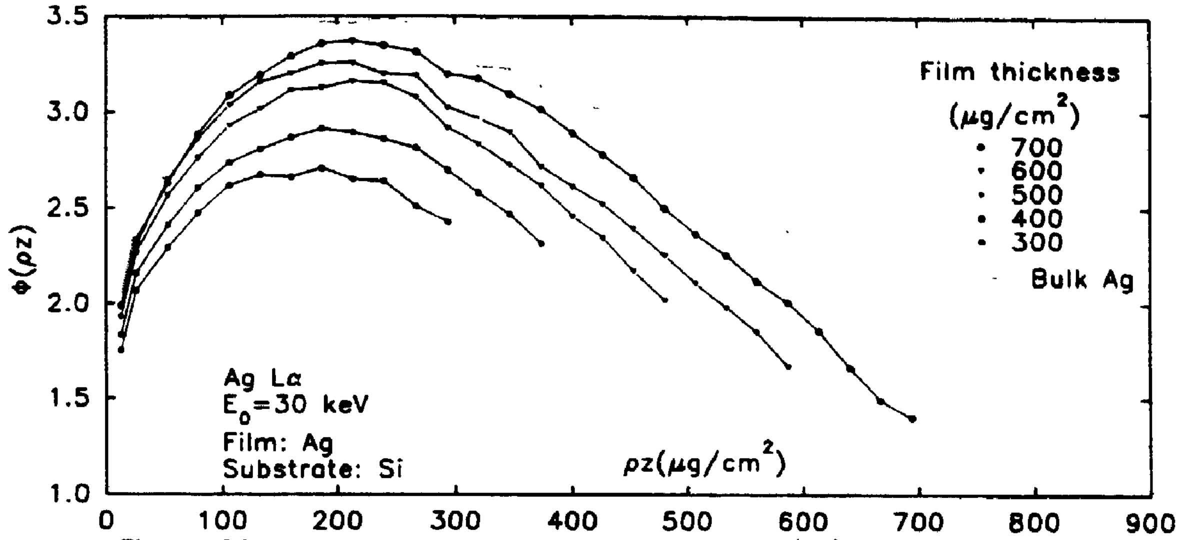

Figure 86a. Monte Carlo simulated thin film $\Phi(\rho z)$ curves of 5 different silver film thicknesses on silicon substrate at 30 keV.

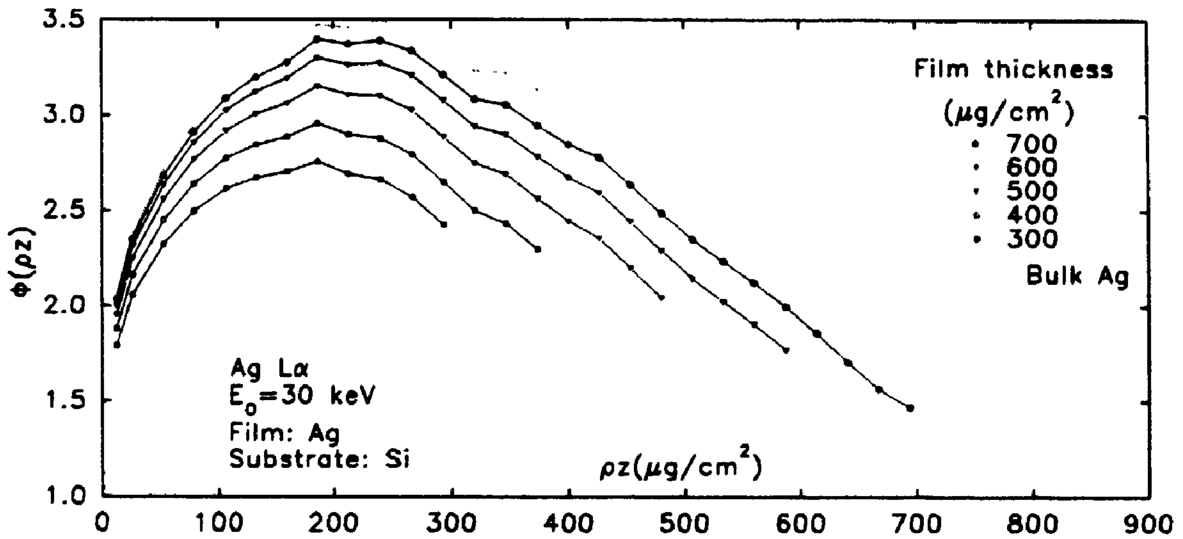

Figure 86b. Calculated thin film $\Phi(\rho z)$ curves of 5 different silver film thicknesses on silicon substrate at 30 keV.

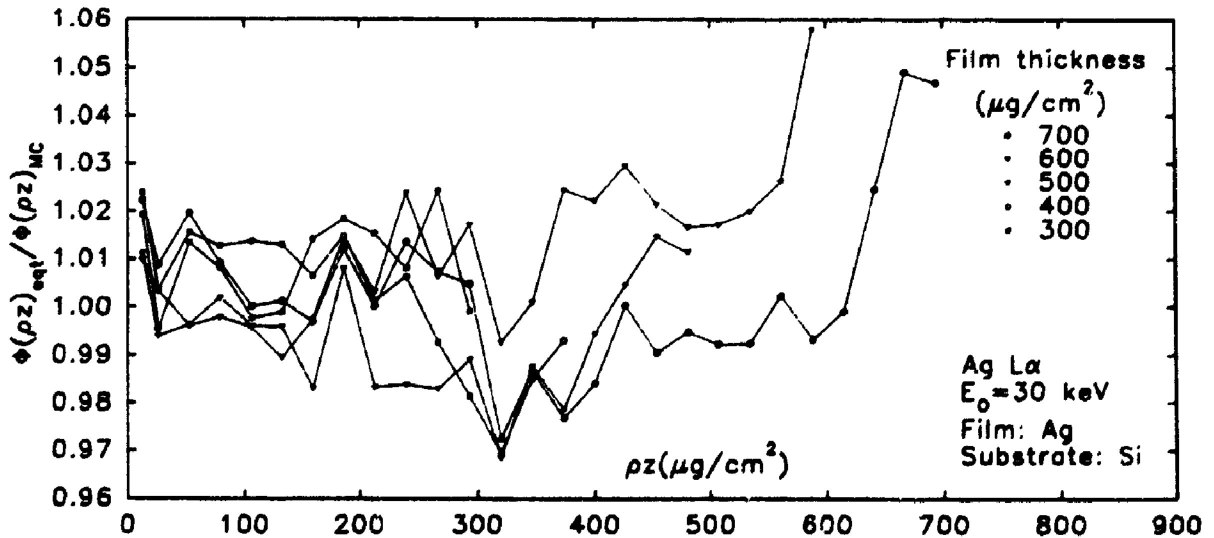

Figure 86c. Error plots calculated from figure 86a and 86b.

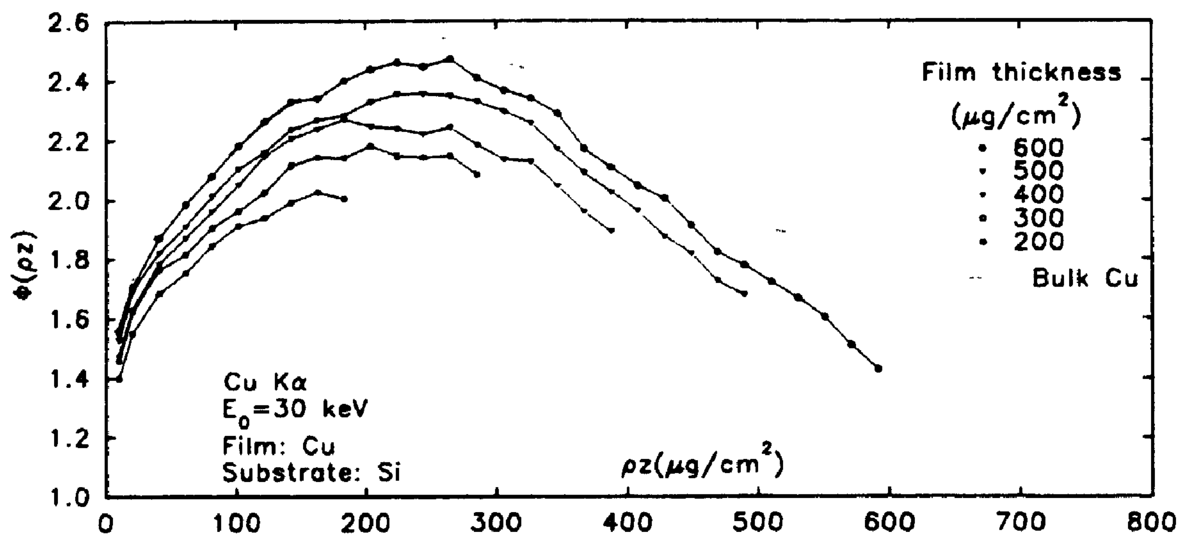

Figure 87a. Monte Carlo simulated thin film $\Phi(\rho z)$ curves of 5 different copper film thicknesses on silicon substrate at 30 keV.

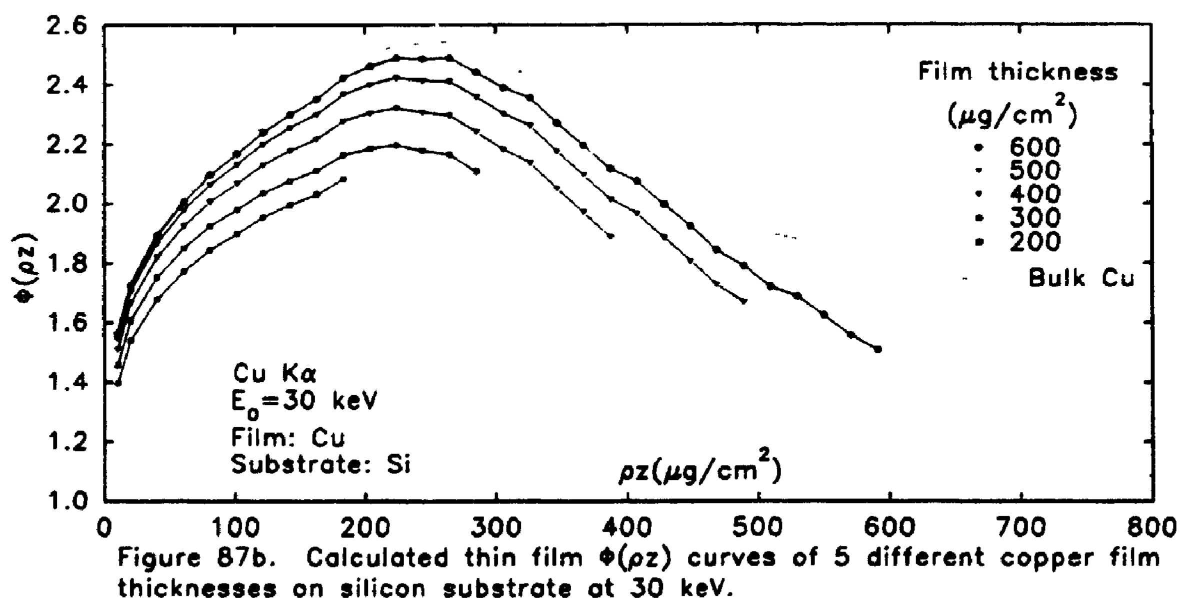

Figure 87b. Calculated thin film $\Phi(\rho z)$ curves of 5 different copper film thicknesses on silicon substrate at 30 keV.

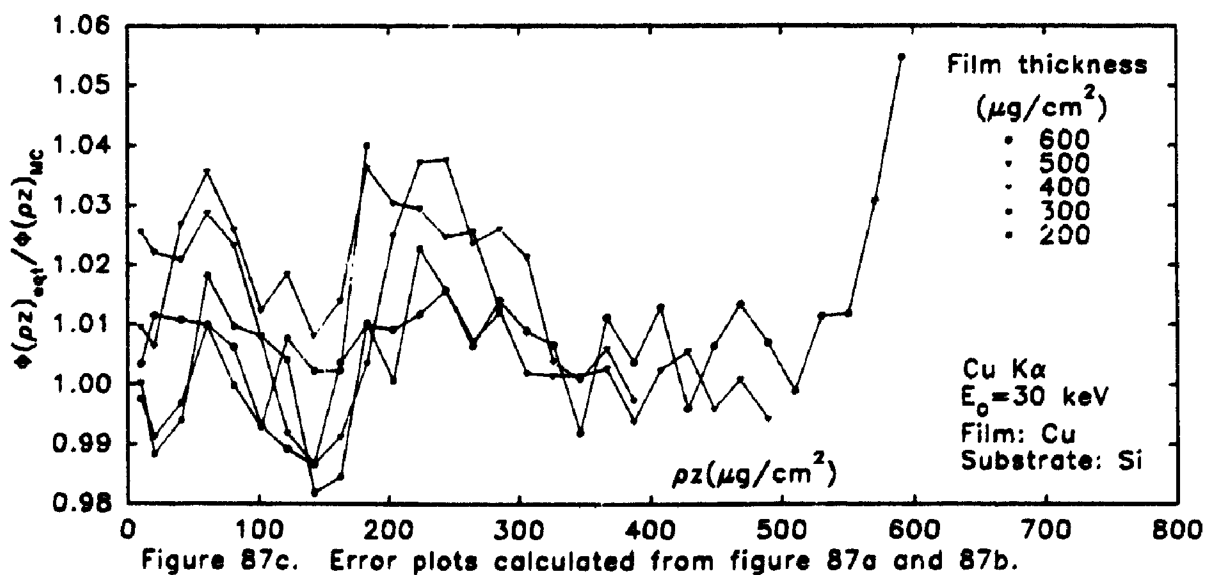

Figure 87c. Error plots calculated from figure 87a and 87b.

In the case of low atomic number films on high atomic number substrates, the constant c2 is calculated by Eqn. (81) which was derived from Figure 53c. As more and more systems were investigated, in particular those having copper as the film where the higher energy Cu Kα x-ray line (E_c = 8.98 keV) was investigated, there is an increasing need to include a dependence on E_c into the equation for c2 which becomes

$$c2 = -3.5050 * \ln\left(\frac{E_o - (E_c/3)}{keV}\right) - 2.7132 \qquad \text{(Eqn. 92)}$$

The data on which this equation is based are shown in Figure 88a. Equation (81) is now replaced by Eqn. (92). The largest effect will be on those systems with a low overvoltage ratio. For example, for copper films on a silver substrate, the effect on the values for c1 which depends on c2 is shown in Figure 88b. The dotted lines represent c2 calculated by the old model (Eqn. (81)) whereas the solid lines represent values calculated by the new model (Eqn. (92)). The fit is obviously improved for this system. The next question is to determine if the new equation significantly changes the c2 value in the Si/Au system or the other systems in a significant way. Fortunately, it does not, as illustrated in Table 8a. The biggest change was found to occur at 5 keV for Ag Lα and hence Ag on the Au system was investigated with five different film thicknesses. This is a severe test to the model since not only is there a low overvoltage ratio but also a low incident electron energy as well. The results are plotted in Figures 89a, b and c. The error plots do not appear any worse than any other previous systems despite the adverse situation of low E_o and low overvoltage

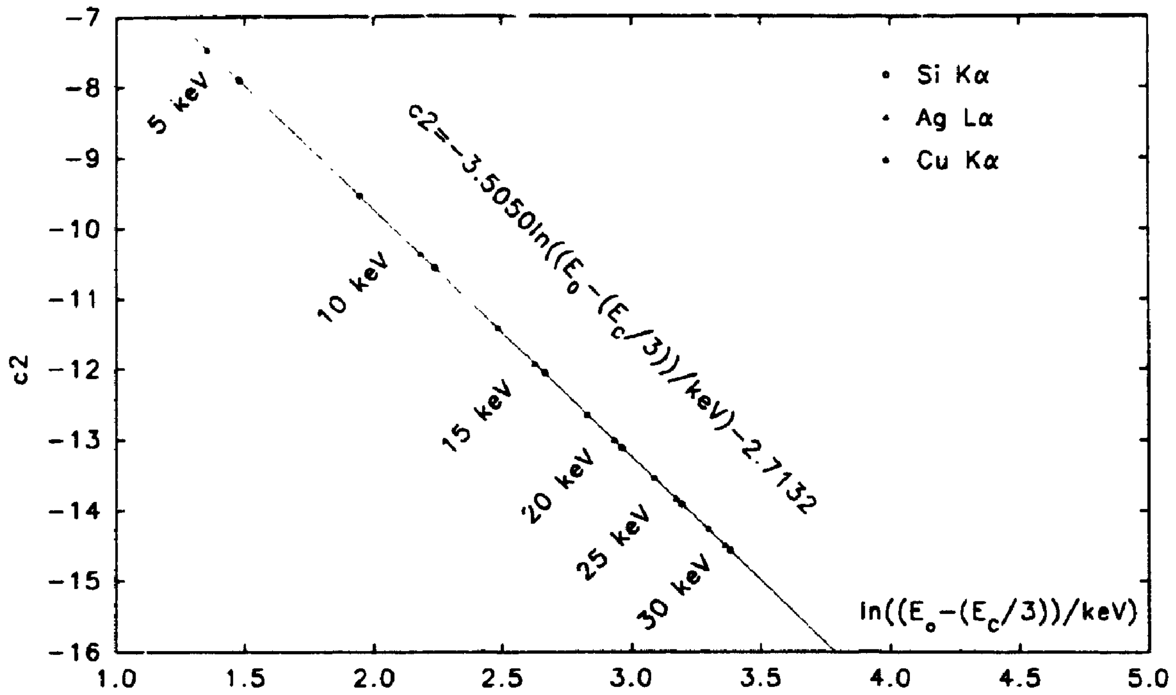

Figure 88a. Plot of c2 versus $\ln((E_0-(E_c/3))/\mathrm{keV})$ for three x-ray lines at six different electron energies.

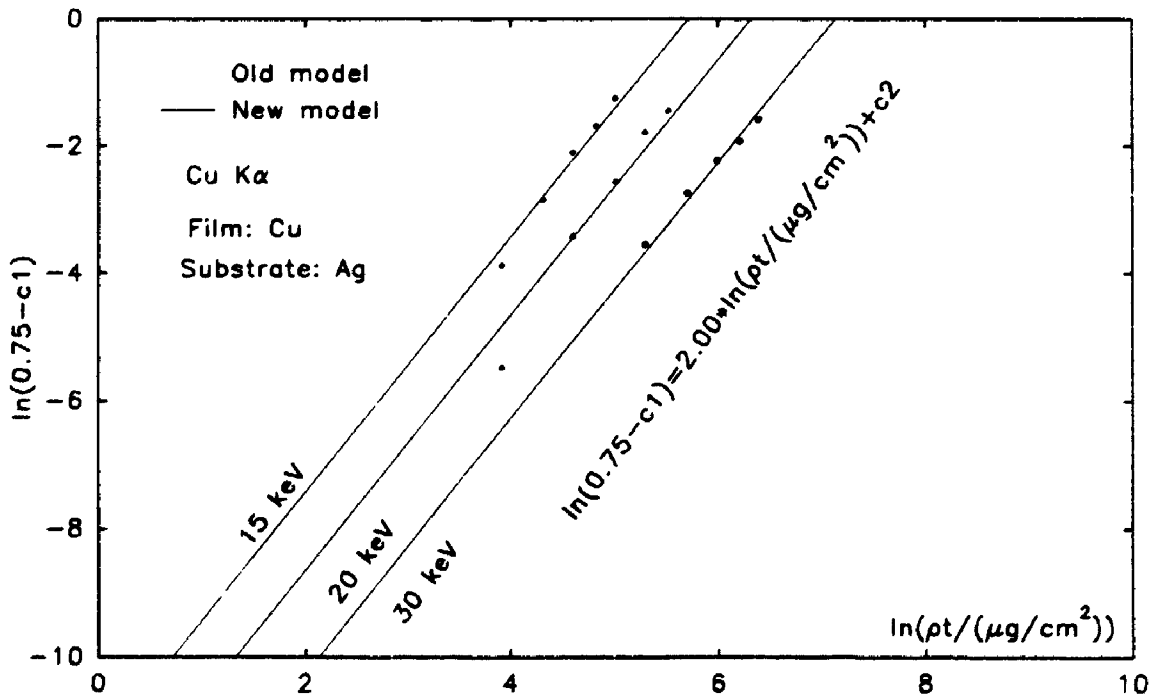

Figure 88b. Plots of $\ln(0.75-c1)$ versus $\ln(\rho t/(\mu g/cm^2))$ for different thicknesses of copper films on silver substrates at 15, 20 and 30 keV electron energies respectively.

Table 8a. Comparison of c2 values as calculated by equations 81 and 92 for light element film on heavy element substrate.

Film x-ray line	E_c(keV)	E_0(keV)	c2 (old)	c2 (new)
Si Kα	1.838	30	-14.572	-14.562
		20	-13.096	-13.104
		10	-10.572	-10.562
Ag Lα	3.351	30	-14.572	-14.502
		20	-13.096	-13.012
		10	-10.572	-10.369
		5	-8.0485	-7.468
Cu Kα	8.980	30	-14.572	-14.266
		20	-13.096	-12.645
		15	-12.048	-11.425

Table 8b. Comparison of c2 values as calculated by equations 88 and 93 for heavy element film on light element substrate.

Film x-ray line	E_c(keV)	E_0(keV)	c2 (old)	c2 (new)
Au Mα	2.220	30	-14.432	-14.414
		20	-12.999	-13.015
		10	-10.549	-10.531
Ag Lα	3.351	30	-14.432	-14.349
		20	-12.999	-12.914
		10	-10.549	-10.315
		5	-8.100	-7.291
Cu Kα	8.980	30	-14.432	-14.004
		20	-12.999	-12.365
		15	-11.982	-11.083

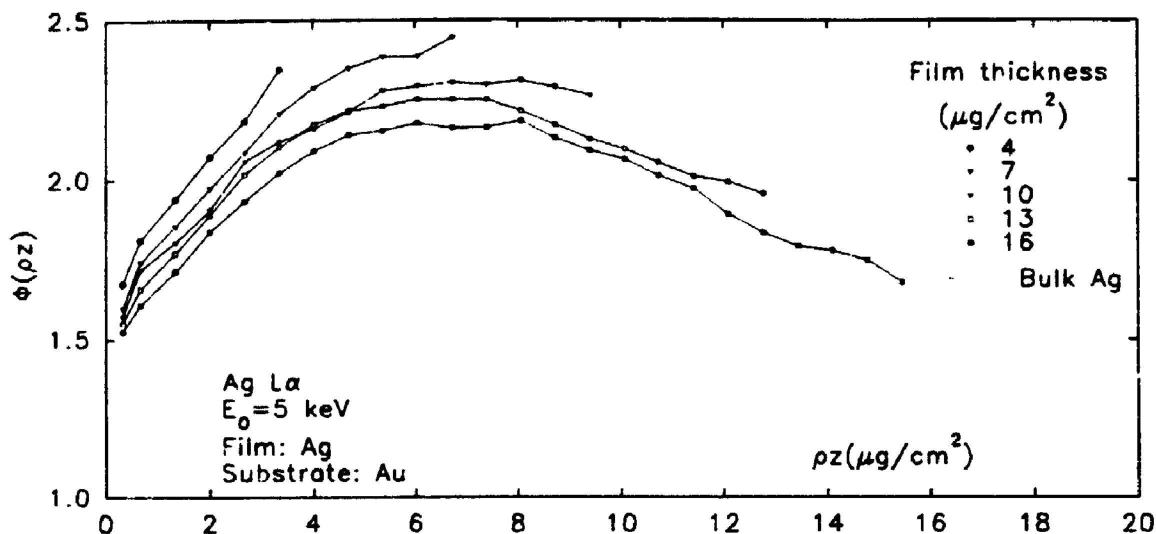

Figure 89a. Monte Carlo simulated thin film $\Phi(\rho z)$ curves of 5 different silver film thicknesses on gold substrate at 30 keV.

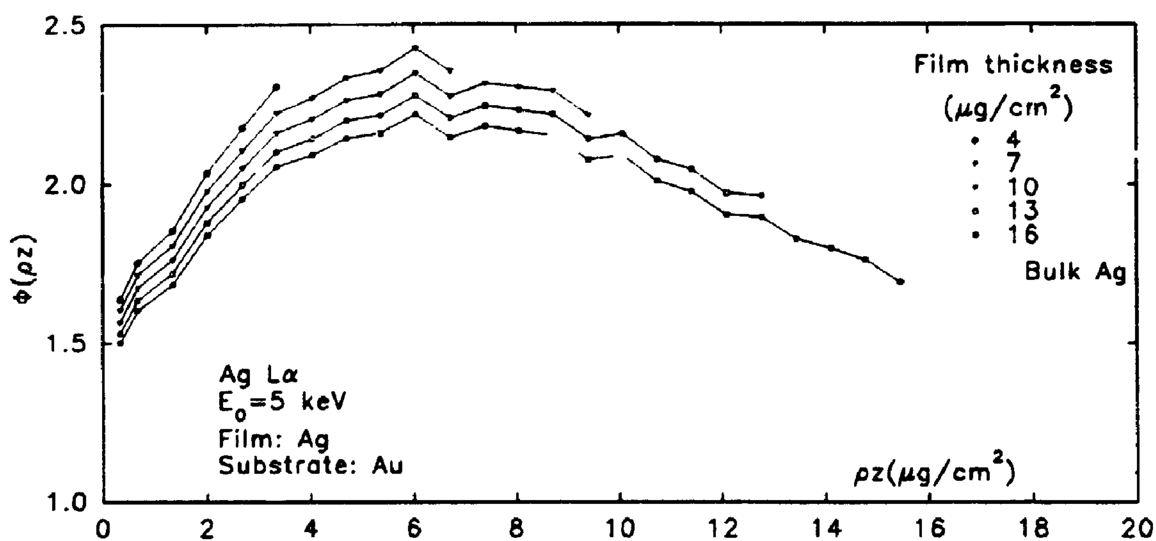

Figure 89b. Calculated thin film $\Phi(\rho z)$ curves of 5 different silver film thicknesses on gold substrate at 30 keV.

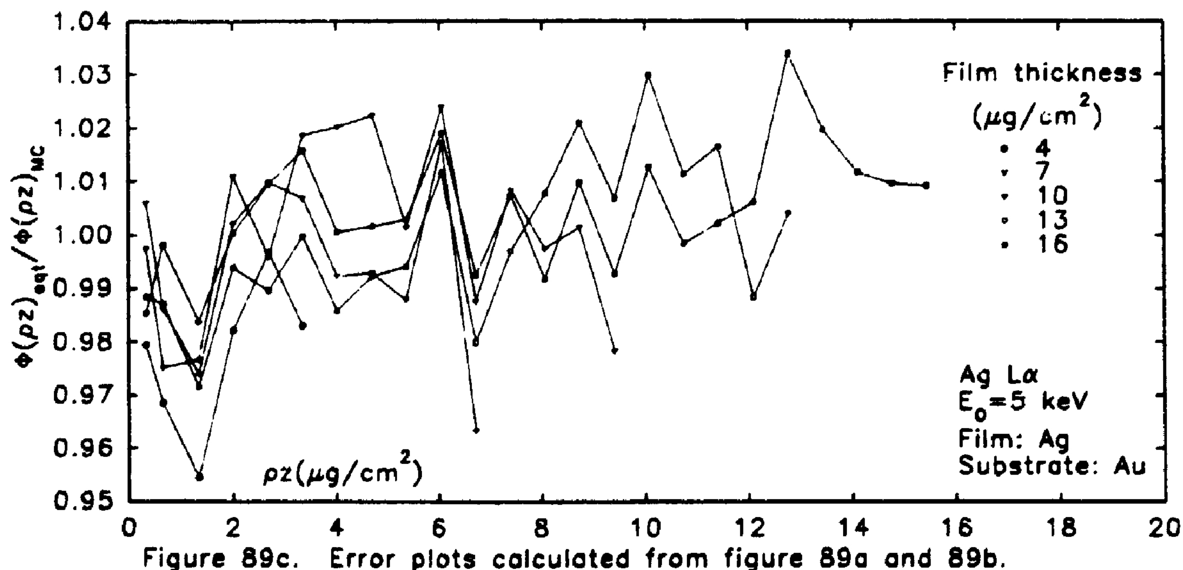

Figure 89c. Error plots calculated from figure 89a and 89b.

ratio.

In the case of high atomic number films on low atomic number substrates, as more and more systems were investigated there is again a need to introduce a dependence on E_c into the equation for c2 which becomes:

$$c2 = -3.2946 * \ln\left(\frac{E_o - (E_c/2)}{keV}\right) - 3.3330 \quad \text{(Eqn. 93)}$$

Thus Eqn. (88) is replaced by Eqn. (93) which now applies to all high on low systems. Table 8b illustrates that there is no significant change to the c2 value at high energy and also low E_c (Au Mα). Satisfactory error plots were found using the new equation.

Electron backscattering from the substrate causes a modification of the thin film $\phi(\rho z)$ curve when compared with the bulk and that the larger the difference in atomic number between the film and the substrate, the larger is the modification. This is the basis for using the backscattering coefficient of the film and substrate to calculate the values of c3 and c4. Recall that c3 = 0.93 is the optimized value in Figure 53b in the case of Si films on Au substrates. Theoretically, c3 should vary with energy whereas the value 0.93 seems to fit all energies. This may be explained by the fact that backscatter coefficient η is not a strong function of E_o (see ref. [179]). Therefore, η values at 30 keV were chosen for the elements used in this work. The values were taken from Heinrich (see ref. [180]). To show the relationship between c3 and η of film and substrate, Figure 90b shows the linear relation between ln(c3) versus $\ln(|\Delta\eta| * (1-\eta_{Film}))$. $|\Delta\eta|$ is simply the absolute difference in

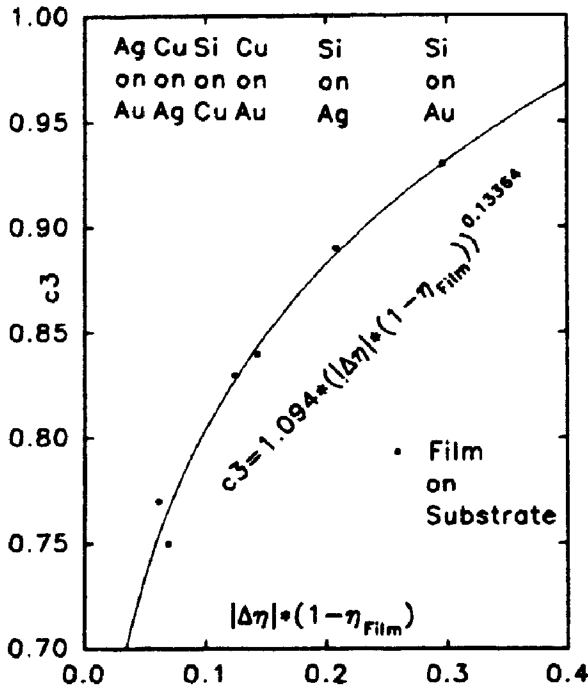

Figure 90a. Plot of c3 versus $|\Delta\eta|*(1-\eta_{Film})$ for light element film on heavy element substrate.

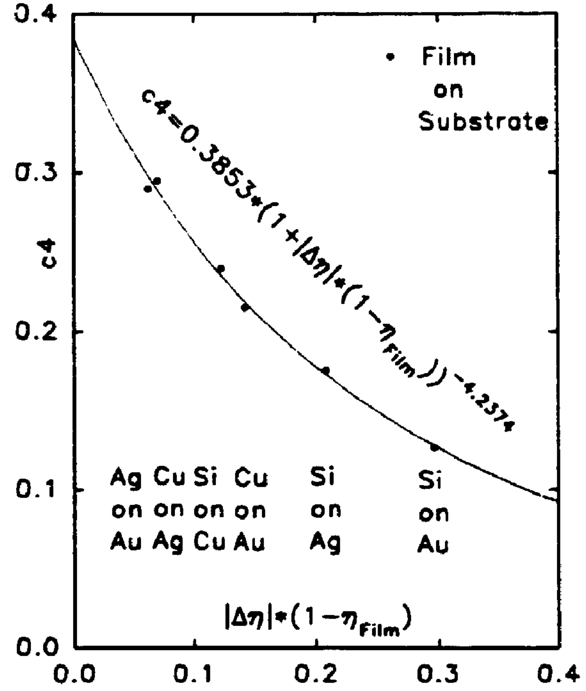

Figure 90c. Plot of c4 versus $|\Delta\eta|*(1-\eta_{Film})$ for light element film on heavy element substrate.

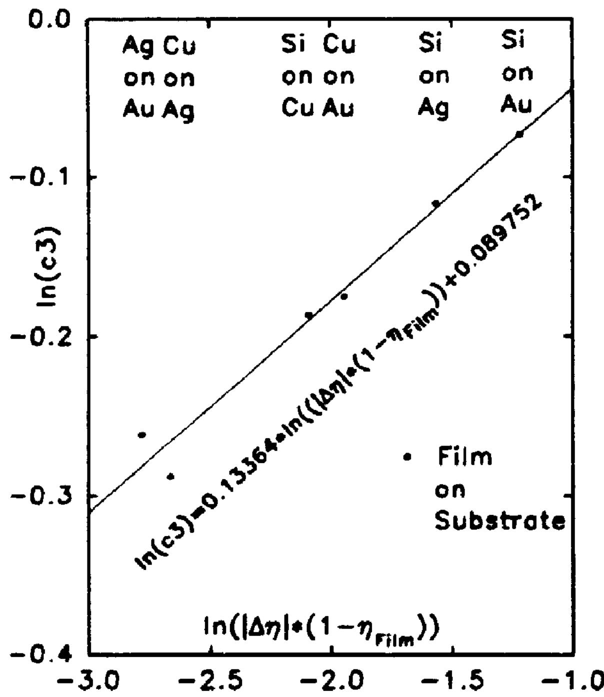

Figure 90b. Plot of ln(c3) versus $\ln(|\Delta\eta|*(1-\eta_{Film}))$ for light element film on heavy element substrate.

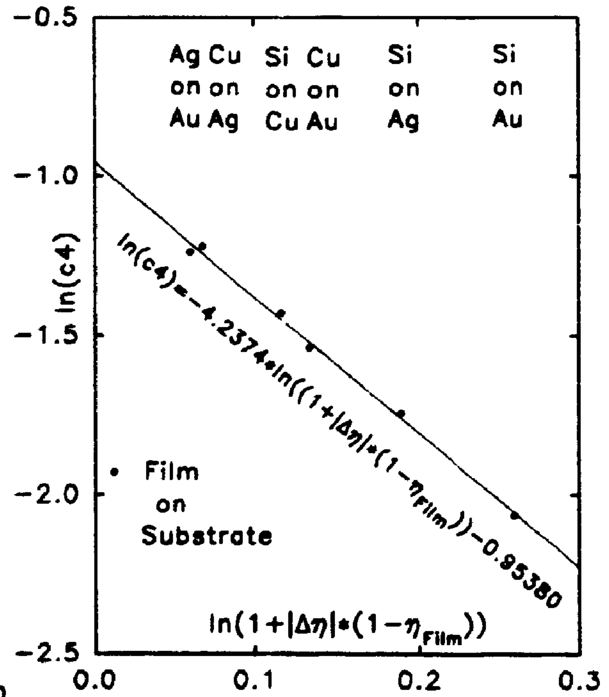

Figure 90d. Plot of ln(c4) versus $\ln(1+|\Delta\eta|*(1-\eta_{Film}))$ for light element film on heavy element substrate.

backscatter coefficient between the film and the substrate. There are six data points in the plot because six systems were investigated in this work. The best fit straight line is given by:

$$\ln(c3) = 0.13364 * \ln(|\Delta\eta| * (1-\eta_{Film})) + 0.089752 \quad \text{(Eqn. 94)}$$

Taking antilogarithms of both sides yields:

$$c3 = 1.094 * (|\Delta\eta| * (1-\eta_{Film}))^{0.13364} \quad \text{(Eqn. 95)}$$

Good agreement was found between the fitted curve and the data points as seen in Figure 90a.

For the values of c4 which represent the intercept of the ln-ln plot in Figure 54b, a plot of ln(c4) versus $\ln(1+|\Delta\eta| * (1-\eta_{Film}))$ will yield a straight line as illustrated in Figure 90d. The equation for the best fit straight line is

$$\ln(c4) = -4.2374 * \ln(1+|\Delta\eta| * (1-\eta_{Film})) - 0.95380 \quad \text{(Eqn. 96)}$$

Taking antilogarithms of both sides gives:

$$c4 = 0.3853 * (1+|\Delta\eta| * (1-\eta_{Film}))^{-4.2374} \quad \text{(Eqn. 97)}$$

Good agreement is found between the fitted curve and the data points as illustrated in Figure 90c.

In the case of high atomic number films on low atomic number substrates, more or less the same approach was applied to determine the value of c3 and c4 except the multiplier in the expression $(1-\eta_{Film})$ was replaced by $(1+\eta_{substrate})$. The best fit straight line in Figure 91b is given by:

$$\ln(c3) = 0.11012 * \ln(|\Delta\eta| * (1+\eta_{substrate})) - 0.062321 \quad \text{(Eqn. 98)}$$

Taking antilogarithms of both sides gives the following:

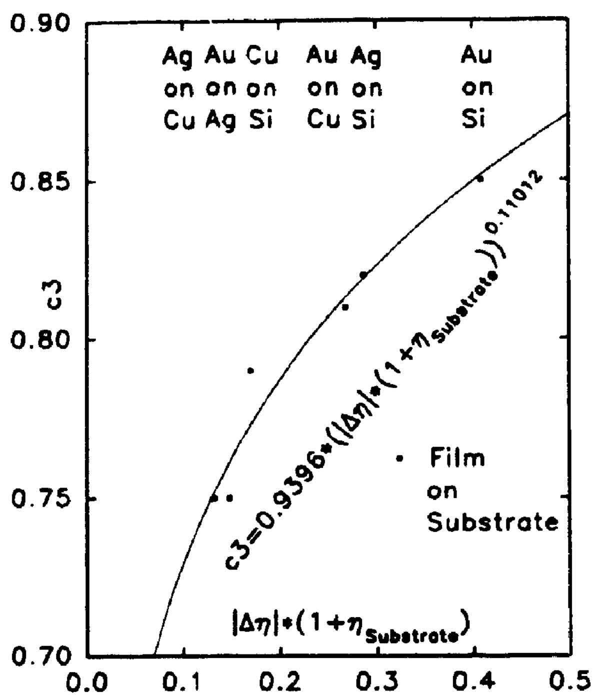

Figure 91a. Plot of c3 versus $|\Delta\eta|*(1+\eta_{Substrate})$ for heavy element film on light element substrate.

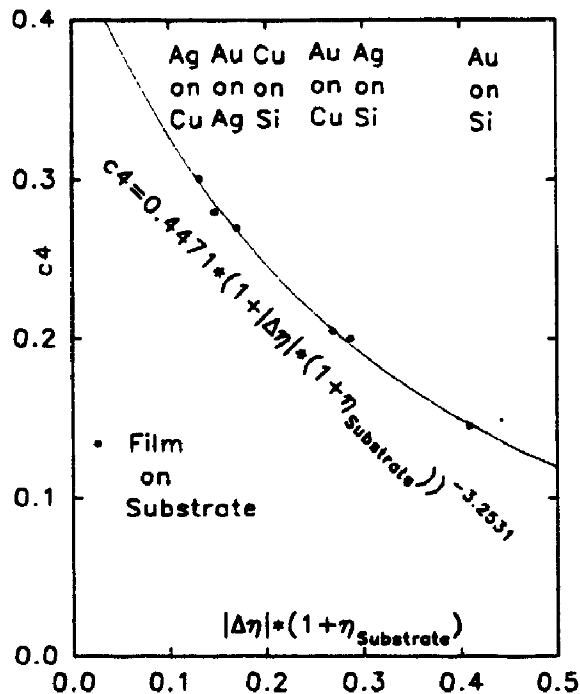

Figure 91c. Plot of c4 versus $|\Delta\eta|*(1+\eta_{Substrate})$ for heavy element film on light element substrate.

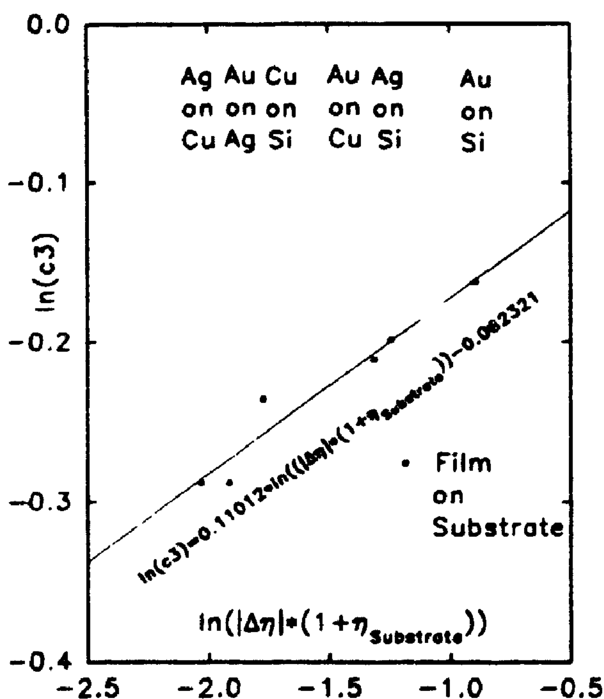

Figure 91b. Plot of $\ln(c3)$ versus $\ln(|\Delta\eta|*(1+\eta_{Substrate}))$ for heavy element film on light element substrate.

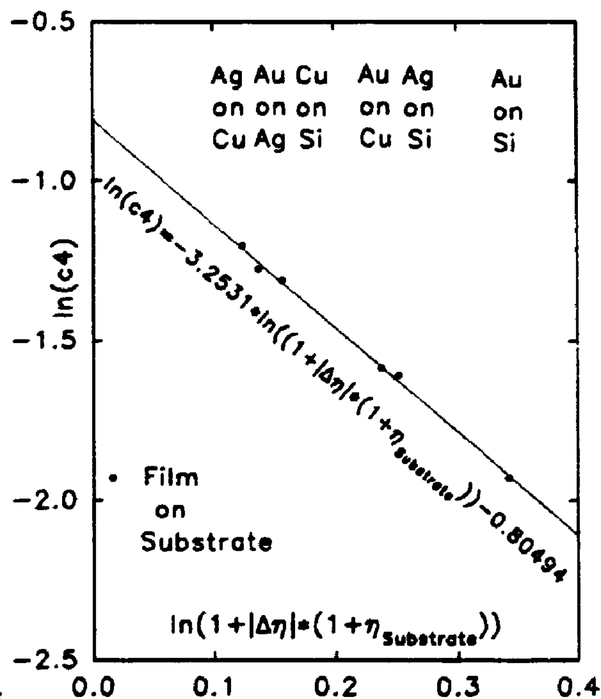

Figure 91d. Plot of $\ln(c4)$ versus $\ln(1+|\Delta\eta|*(1+\eta_{Substrate}))$ for heavy element film on light element substrate.

$$c3 = 0.9396 * (|\Delta\eta| * (1+\eta_{substrate}))^{0.11012} \qquad \text{(Eqn. 99)}$$

Recall the value 0.0982 in Eqn. (90) is the inflection point value for the Au/Si system. The value c4 (0.1454) can be calculated (see Figure 67b) from this inflection point value (c5) by the following equation:

$$c4 = c5 + 0.02049 * 2.303 \qquad \text{(Eqn. 100)}$$

which can be simplified to:

$$c4 = c5 + 0.04719 \qquad \text{(Eqn. 101)}$$

Equation (101) can now be applied to all high atomic number films on low atomic number substrates to calculate c4. The best fit straight line to calculate c4 in Figure 91d is given by:

$$\ln(c4) = -3.2531 * \ln(1 + |\Delta\eta| * (1+\eta_{substrate})) - 0.80494 \qquad \text{(Eqn. 102)}$$

Taking antilogarithms of both sides gives:

$$c4 = 0.4471 * (1 + |\Delta\eta| * (1+\eta_{substrate}))^{-3.2531} \qquad \text{(Eqn. 103)}$$

Good agreement was found between the fitted curve and the data as illustrated in Figure 91c. From the error plot of Figure 92, the fitted c3 and c4 values using Eqns. (95) and (97) for light on heavy and Eqns. (99) and (103) for heavy on light deviate less than 3% from the optimized values which then suggests the agreement is quite good.

Any thin film $\phi(\rho z)$ curve can now be calculated based on the bulk $\phi(\rho z)$ curve (Appendix 4). The only parameters required are the incident electron energy (E_o), the critical excitation potential of the particular x-ray line (E_c), the thickness of the film (ρt), and the atomic number of the film and substrate. Quite a few expressions

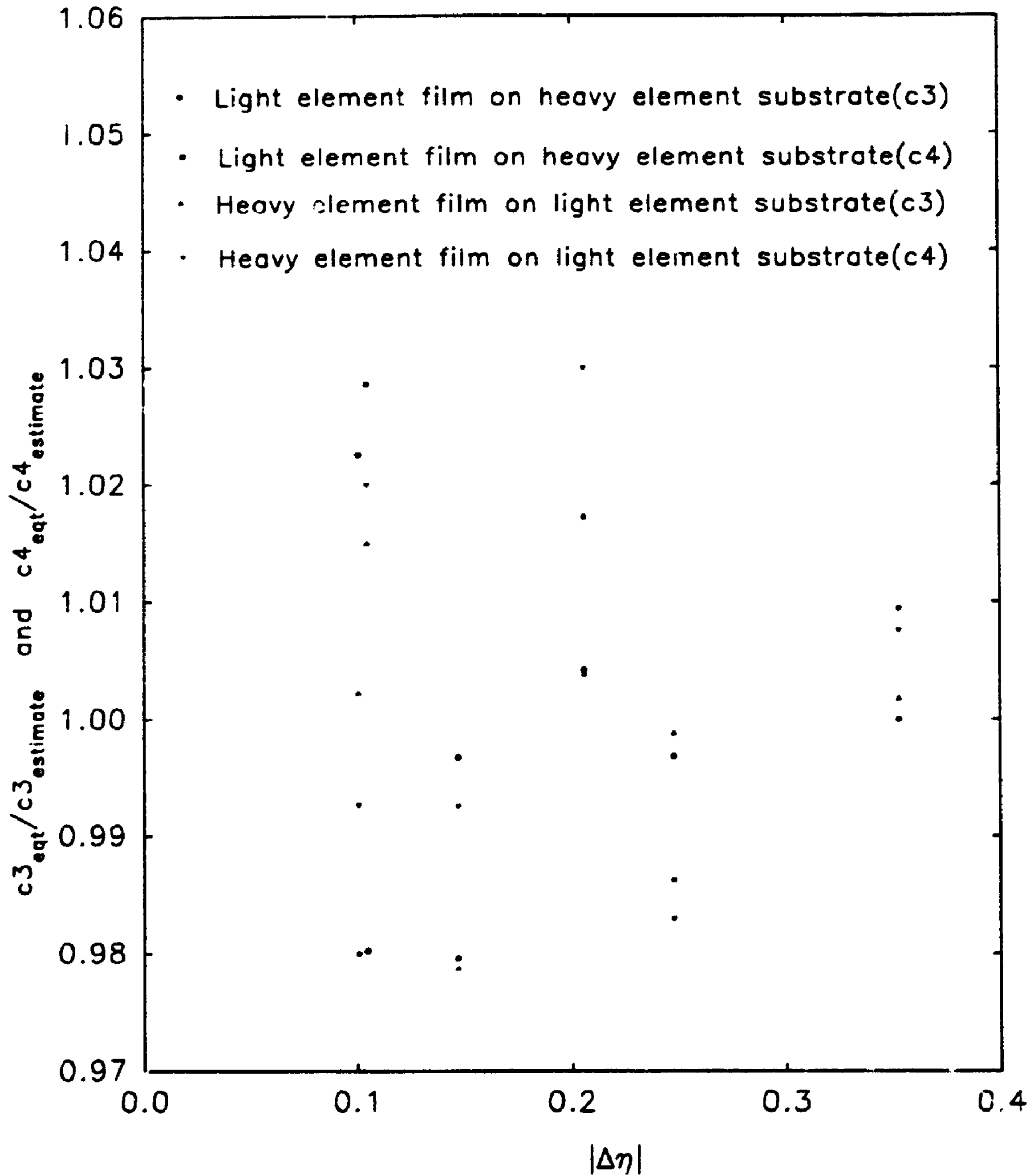

Figure 92. Error plot of constants c3 as calculated from figure 90a and 91a and c4 from figure 90c and 91c.

accurately describe the shape of bulk $\phi(\rho z)$ curve. A computer program was written to calculate the bulk $\phi(\rho z)$ curve based on the Packwood and Brown [1] modified gaussian equation. The four optimized parameters α, β, γ_o and $\phi(o)$ were taken from Brown and Packwood [69]. Four calculated $\phi(\rho z)$ curves (Appendix 5) for a 300 nm (81 $\mu g/cm^2$) Al film at 10 keV on various substrates are plotted in Figure 93a while calculated $\phi(\rho z)$ curves for aluminum films on a tungsten substrate at 10 keV are plotted in Figure 93b. Similar plots made by Pouchou and Pichoir [122] are reprinted for comparison. According to Pouchou and Pichoir as illustrated in Figure 93c, the maximum of the film $\phi(\rho z)$ curve was shifted towards the sample surface as the atomic number of the substrate increases. This result is due to the weighting procedure employed as a compromise between that of the film material and the substrate material with the outcome corresponding to a fictitious homogeneous sample. The resulting curve gave the sample a larger mean atomic number than that of the film material. Since the cross-section for elastic electron scattering increases with increasing atomic number, the maximum of the $\phi(\rho z)$ curve will shift towards the sample surface as the atomic number increases. On the other hand, if the atomic number of the film is larger than that of the substrate material, as in the case of an Al film on a B substrate, then the Pouchou and Pichoir model predicts a shift of the maximum towards deeper regions. However, the very opposite was found in this work as illustrated by Figure 93a in that the maximum of the curve was found to shift to greater depths as the atomic number of the substrate increases and vice versa. The maximum deviation between the thin film $\phi(\rho z)$ curve and the bulk curve was found

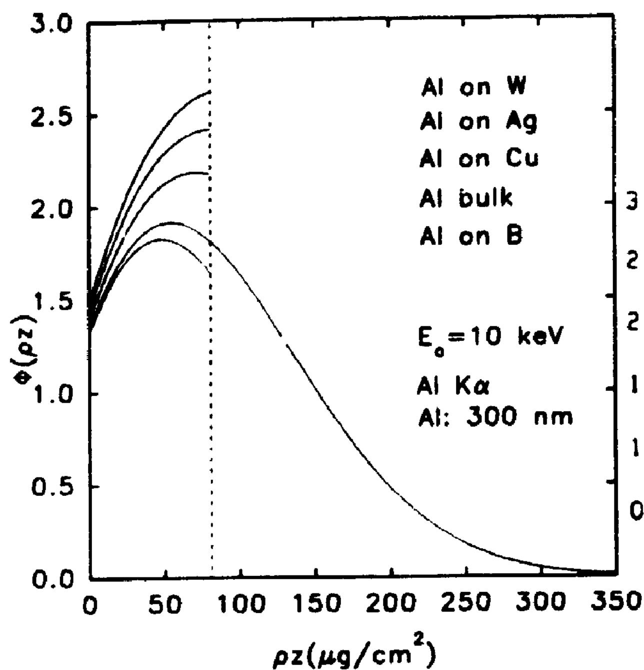

Fig 93a. Φ(ρz) curves for 300 nm of Al on W, Ag, Cu, B and Al bulk at 10 keV.

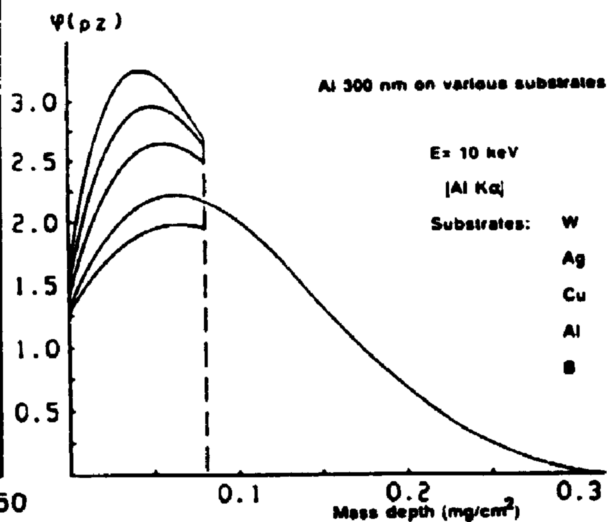

Fig 93c. Reprint from Pouchou and Pichoir [122, Fig 8].

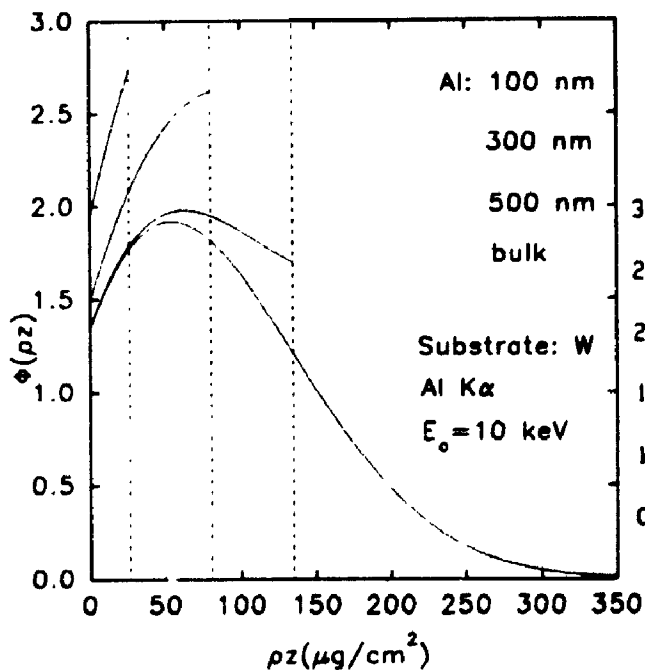

Fig 93b. Φ(ρz) curves for various thicknesses of Al films on W at 10 keV.

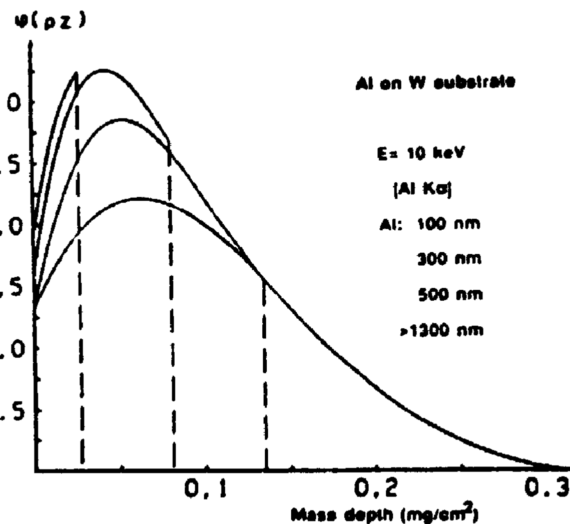

Fig 93d. Reprint from Pouchou and Pichoir [122, Fig 9].

Figures 93c and 93d are copyrighted and reprinted with the permission of SCANNING, and/or the Foundation for Advances of Medicine and Science (FAMS), Box 832, Mahwah, New Jersey 07430, USA.

at the interface from this work. This was not true in the Pouchou and Pichoir model. Also, it is suggested by Figure 93c that the silver substrate has the same effect as the tungsten substrate for the aluminum film at the film/substrate interface. This is not supported by Figure 93a. It was found both from the Pouchou and Pichoir model and this work that the $\phi(o)$ value of the film $\phi(\rho z)$ curve increases as the atomic number of the substrate increases and vice versa. As the film thickness decreases, in the case of a low atomic number film on a high atomic number substrate, the maximum of the curve shifts towards the surface in the Pouchou and Pichoir model (Figure 93d) whereas the very opposite was found from this work (Figure 93b). Also for a 500 nm aluminum film on tungsten, the Pouchou and Pichoir model shows no effect at the film/substrate interface whereas the biggest effect was found at the interface in this work. However, the $\phi(o)$ value was found to increase in both cases as the film thicknesses decrease.

There are basically two lines of thought in connection with how thin film $\phi(\rho z)$ curves should behave compared to the bulk curve. The method suggested in this work agrees better with the Monte Carlo simulation from Karduck et al. [2], Laurie et al. [175] and Ding and Wu [3] and also theoretical calculation from August [159]. On the other hand, the Pouchou and Pichoir model agreed better with the method suggested by Packwood et al. [148, 149], Bastin et al. [170] and Willich et al. [152]. These later methods adopted a weighting process which requires the knowledge of the effective backscattering coefficient or the effective atomic number. They fail to predict thin film $\phi(\rho z)$ curves which agree with the shape predicted by Monte Carlo methods.

6.5 K-ratio CALCULATIONS AND COMPARISONS

The most common method for assessing the validity of a thin film model is to compare the measured k-ratios from well characterized thin films with those calculated from the model. Since no experimental measurements were made in this work, k-ratio data were taken from published data of other research groups. To avoid any bias in the comparison of results, data sets were chosen from different years (1972 to 1992), different microprobes (ψ=13° to 52.5°), different film/substrate combinations, different incident electron energies (4 keV to 30 keV) and different x-ray lines (Ni Lα (E_c=0.87 keV) to Au Lα (E_c=11.9 keV)).

There are basically three kinds of k-ratio measurements. The first is to measure k-ratio versus incident electron energy for a particular thin film of known thickness. This is the simplest from a specimen preparation point of view since one film thickness can generate k-ratios for a series of electron energies, E_o. The second is to measure k-ratio as a function of film thickness at a particular electron energy. More preparation effort is required in that many films of known thickness or a single specimen having many different film thicknesses using a deposit method similar to the sandwich sample technique must be made. These first two methods require accurate knowledge of the film thickness. The third are measurements of films where the film thickness is the unknown. The objective is to convert the measured k-ratio data to film thickness using appropriate equations and an iterative process (see Eqn. (76)). These data can be useful to check consistency of thickness predictions for a range of electron energies or to compare thicknesses calculated by competing methods.

Fortran computer programs were written to either calculate the k-ratio if the film thickness was known (Appendices 6 and 7) or calculate the film thickness from the measured k-ratio by an iterative process (Appendix 8). The first estimate of the film thickness is computed internally in the program and does not require a user input value. Some basic input physical parameters are required such as E_c, Z_{film}, $Z_{substrate}$, A_{film}, ψ and μ. To determine k-ratios, the total areas under the film and bulk $\phi(\rho z)$ curves corrected for absorption were calculated by numerical integration using 200 intervals which were chosen on the basis of primary energy.

A comparison of the calculated k-ratios with experimental data in the case of Au Mα x-ray k-ratios from Au films on a Si substrate is given in Figure 94a. The experimental data are from Bolon and Lifshin [137]. Good agreement was found at $E_o \geq 20$ keV for all thicknesses. At lower electron energies, the predicted values tend to be too high, particularly for the thinner films. The dotted lines show the predicted values for films which are 5% thicker and thinner than the normal values. For the same data set, Kyser and Murata [139] predicted values were too high at 10 keV for all thicknesses and in particular the 1000 Å thick film where their predicted value was very close to unity whereas the experimental data are slightly above 0.8. Similar fitting difficulty was found by Gillies et al. [163] whose predicted values were too high at 10 and 15 keV but too low at 20, 25 and 30 keV.

A different set of k-ratio data for Au films on Si substrate measured by Hutchins [138] at various film thicknesses for 10, 20 and 30 keV are given in Figure 94b. The take off angle in her instrument is unusually low at 13°. Except for the two

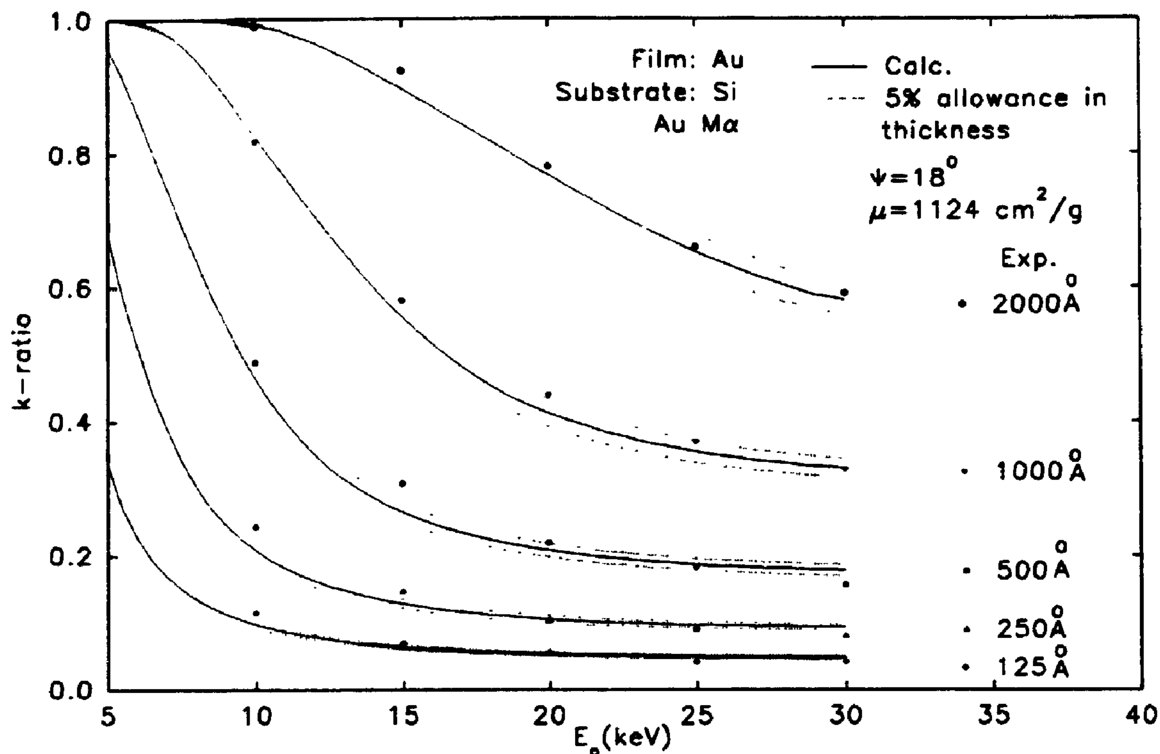

Figure 94a. Comparison of calculated k-ratios with those measured by Bolon and Lifshin [137] for 5 different Au films on Si substrate.

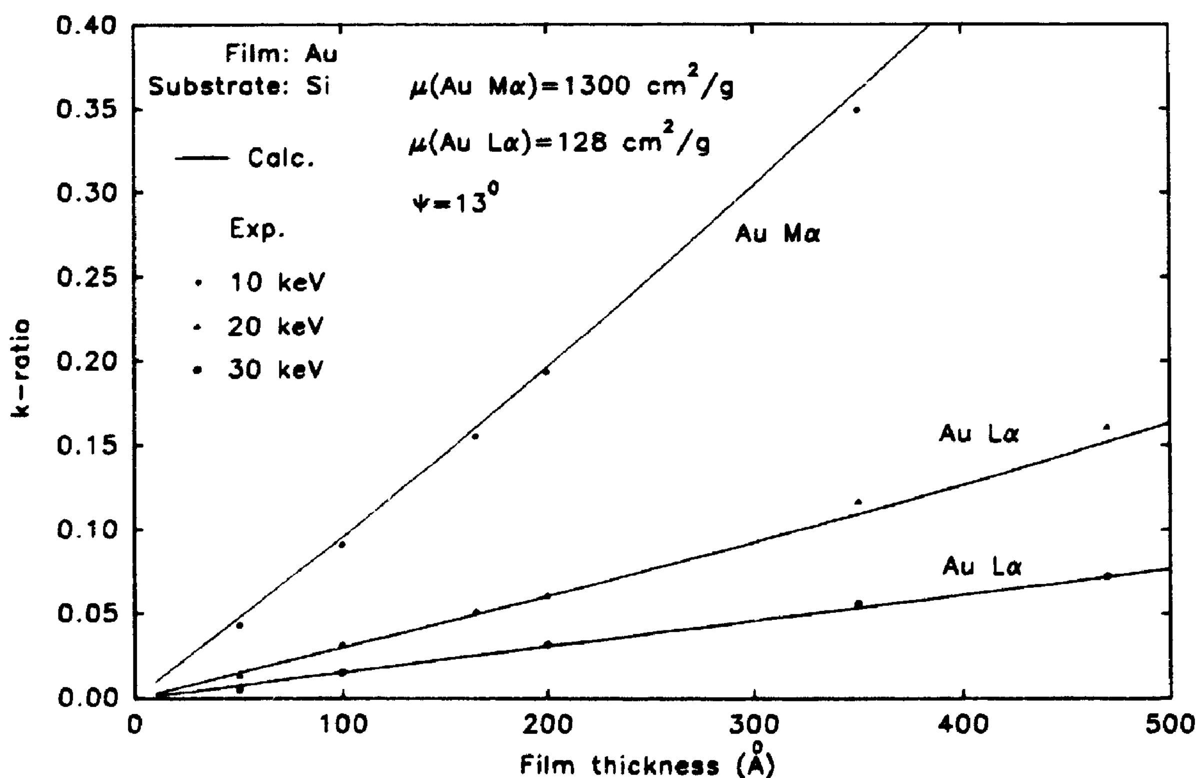

Figure 94b. Comparison of calculated k-ratios with those measured by Hutchins [138] for various Au films on Si substrate at 10,20 and 30 keV electron energies.

thickest films at 20 keV, very good agreement between the measured points and calculated curves occurs for all the Au Lα data. This occurs despite the fact that Au Lα has an excitation potential of 11.9 keV which represents a significant extrapolation from the highest E_c considered in the modelling which was Cu Kα, at 8.98 keV. The Au Mα data at 10 keV of Figure 94b are interesting in that the predicted values lie above the measured values for the Hutchins data whereas they were below the measured values in Figure 94a.

An example of very poor agreement is the comparison in Figure 95a for Ag films on Si substrate from Gillies et al. [163]. The fits at 5 keV are far from satisfactory although a similar difficulty was observed by Gillies et al. who also tried to fit their own data set (Figure 95b). Given that the critical excitation potential for Ag Lα is 3.35 keV, the data at 5 keV is for an overvoltage ratio of less than two. The fit to the experimental values improves as the electron energy increases but, by and large, the calculated data tends to be too low. The predicted values of Gillies et al for the same Ag films tended to be too high, particularly at low electron energies where the fit is very bad. However, at 20 and 25 keV, Gillies et al. have better fits than the present model.

Predicted and measured k-ratios for copper films on carbon from Laurie et al. [175] are given in Figure 96a with the predictions of this model. Good agreement was found between the calculated k-ratios and the experimental data for all thicknesses at 25 keV. The present model fits better than that suggested by Laurie et al. At 15 keV, the model initially underestimates the measured k-ratios but for thicker

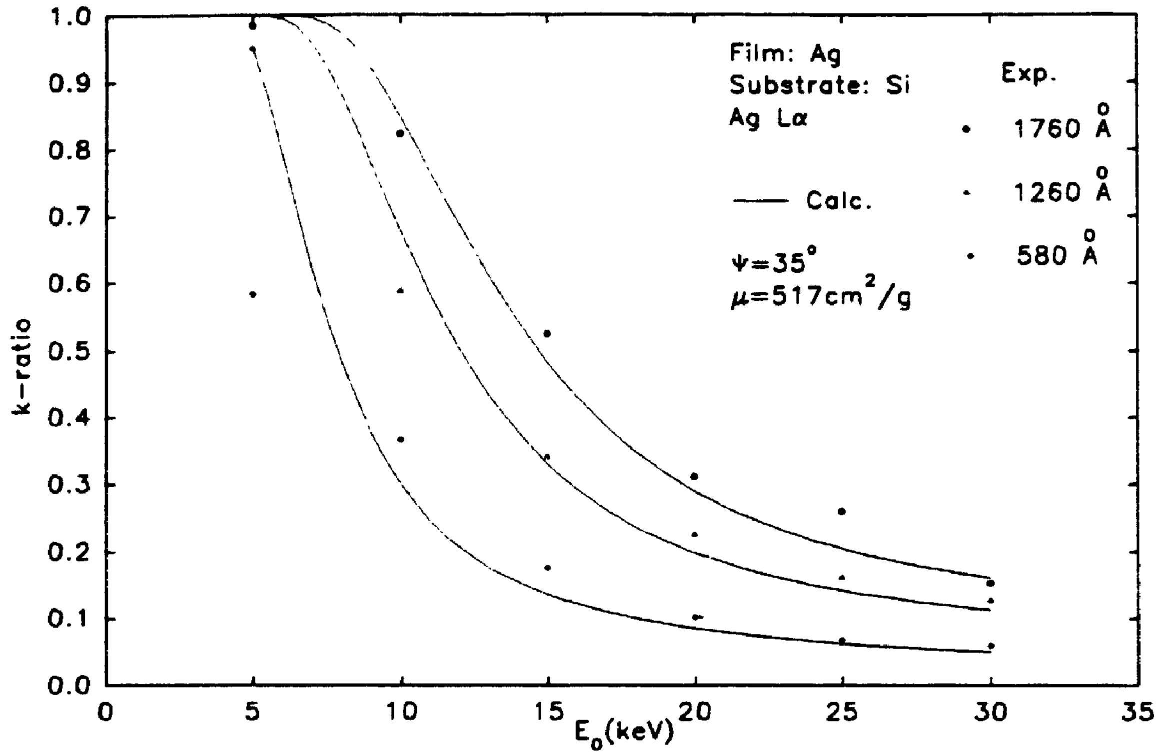

Figure 95a. Comparison of calculated k-ratios with those measured by Gillies et al. [163] for 3 different Ag films on Si substrste.

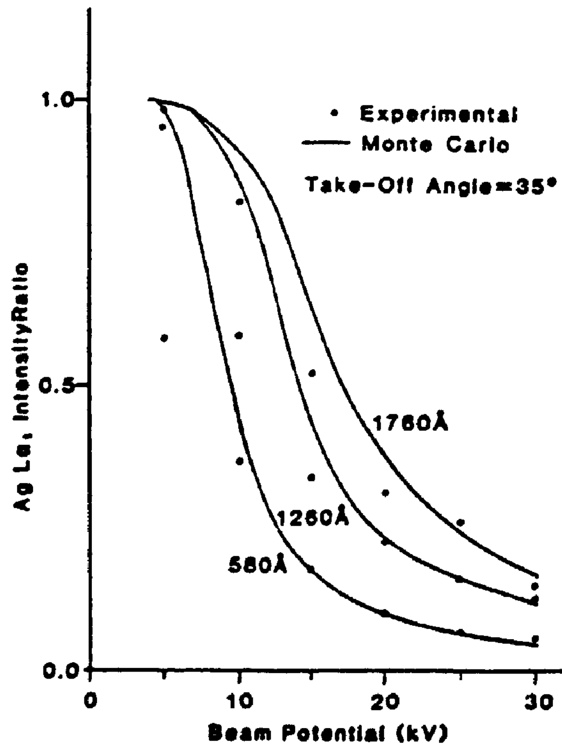

Figure 95b. Reprint from Gillies et al. [163, Fig 2.] .

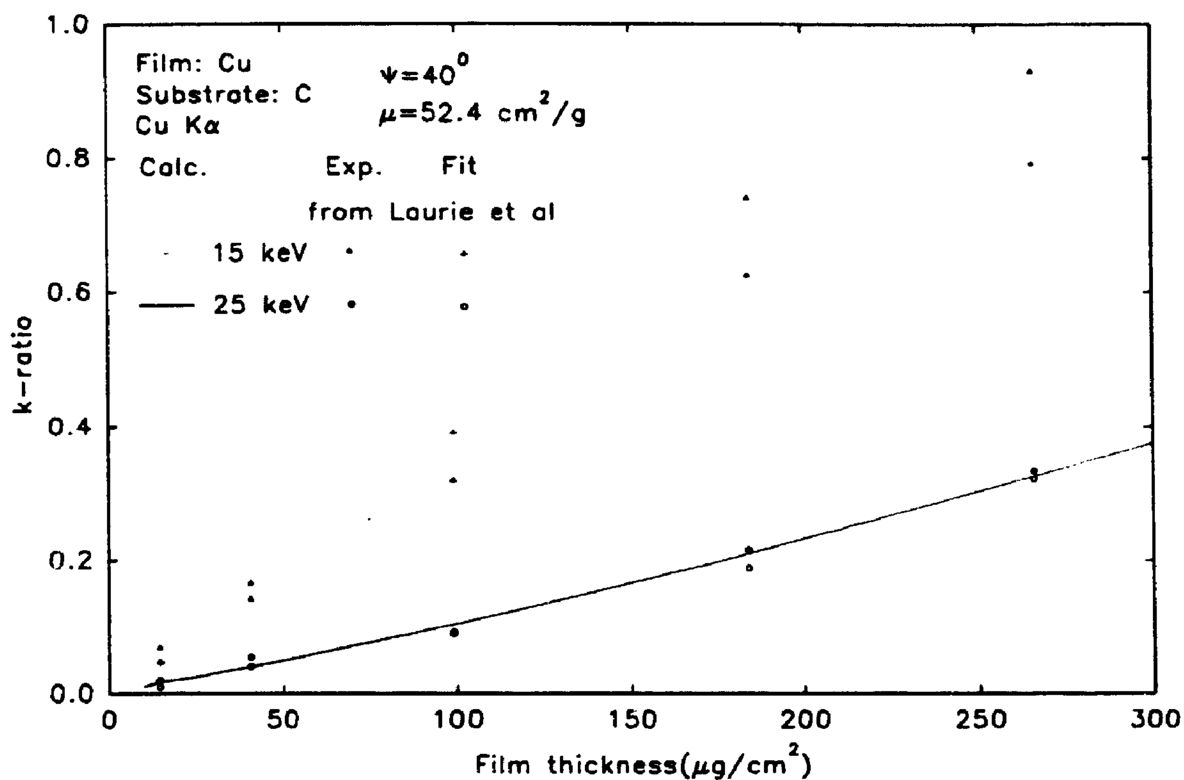

Figure 96a. Comparison of calculated k-ratios with those measured and fitted by Laurie et al. [175] for various Cu films on C substrate at 15 and 25 keV electron energies.

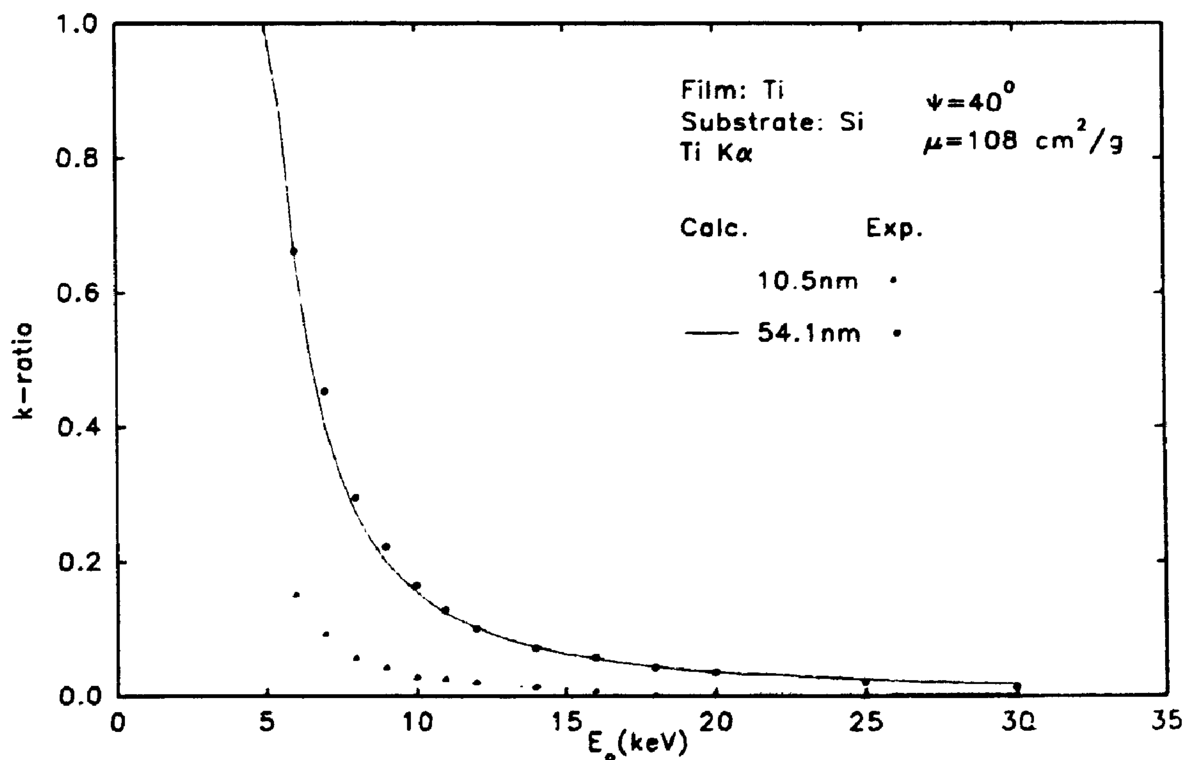

Figure 96b. Comparison of calculated k-ratios with those measured by Bastin et al. [169] for two Ti films on Si substrate at different electron energies.

films overestimation occurs. The model of Laurie et al. tends to overestimate the k-ratios for most films.

More recent (1990) experimental measurements of two Ti films on Si substrate from Bastin et al. [169] are given in Figure 96b. The agreement between the predictions from the present model and the measurements was found to be very good for both thicknesses of film even for relatively low overvoltage ratios below 10 keV electron energy. Another set of more recent data for Cu films on Si by Packwood et al. [181] is shown in Figures 97a and b. For the same films, the Cu Kα line was measured at 15 keV and the Cu Lα line at 10 keV. Here, even at the lower electron energy, the agreement with the Cu Lα data is much better, the model tending to predict values slightly too high for the Cu Kα line. Again, agreement tends to degrade with low overvoltage ratios. These latter sets of data have been measured more recently and the agreement is better than with the earlier data. The more recent measurements may be more reliable (from the standpoint of better equipment and electronics) than those that were measured some time ago.

The previous data have been for heavy element films on light element substrates. Illustrations of light element films on heavy element substrates are given in Figures 98 and 99. Figures 98a and 98b show data for Cu films on higher atomic number substrates measured by Pouchou and Pichoir [75]. For the W substrate except at energies over 25 keV, the predicted values tend to be low. For the Cu films on Mo substrate (Figure 98b), the agreement is excellent except at energies below 15 keV in which the overvoltage ratio has fallen below two (for Cu Kα, E_c = 8.98 keV). Figures

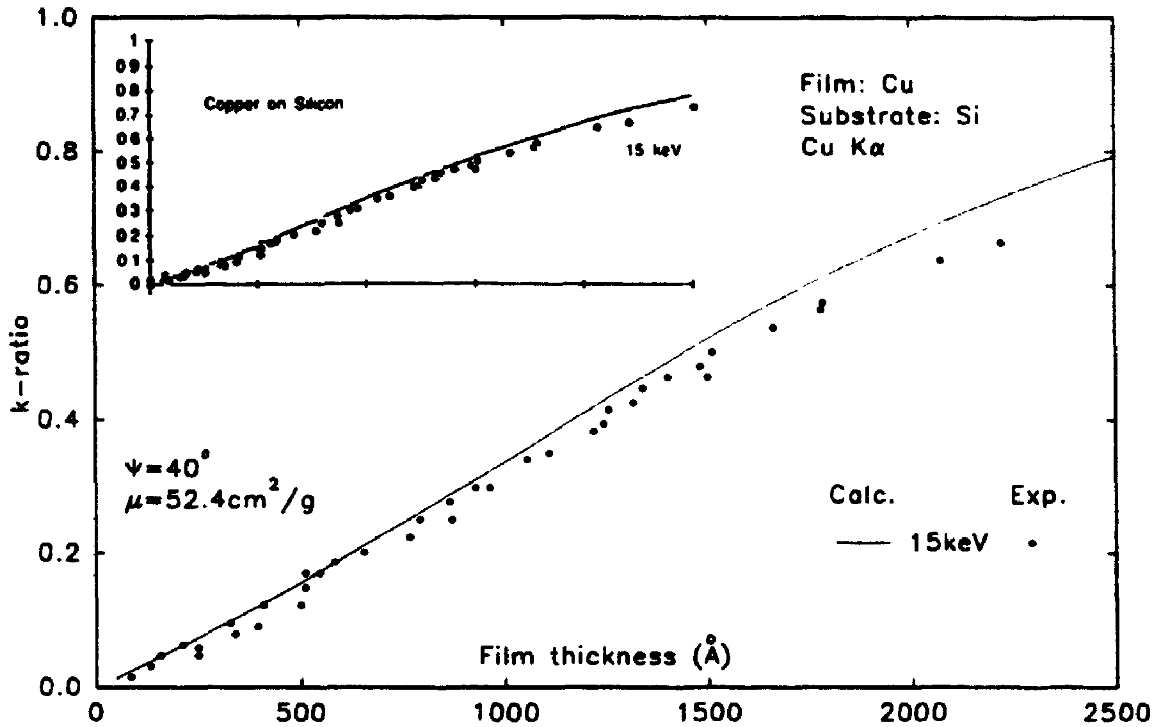

Figure 97a. Comparison of calculated k−ratios with those measured by Packwood et al. [181] for Cu films on Si substrate at 15 keV electron energy. The corner plot [181,Fig.5] is copyrighted and reprinted with the permission of San Francisco Press, Inc.

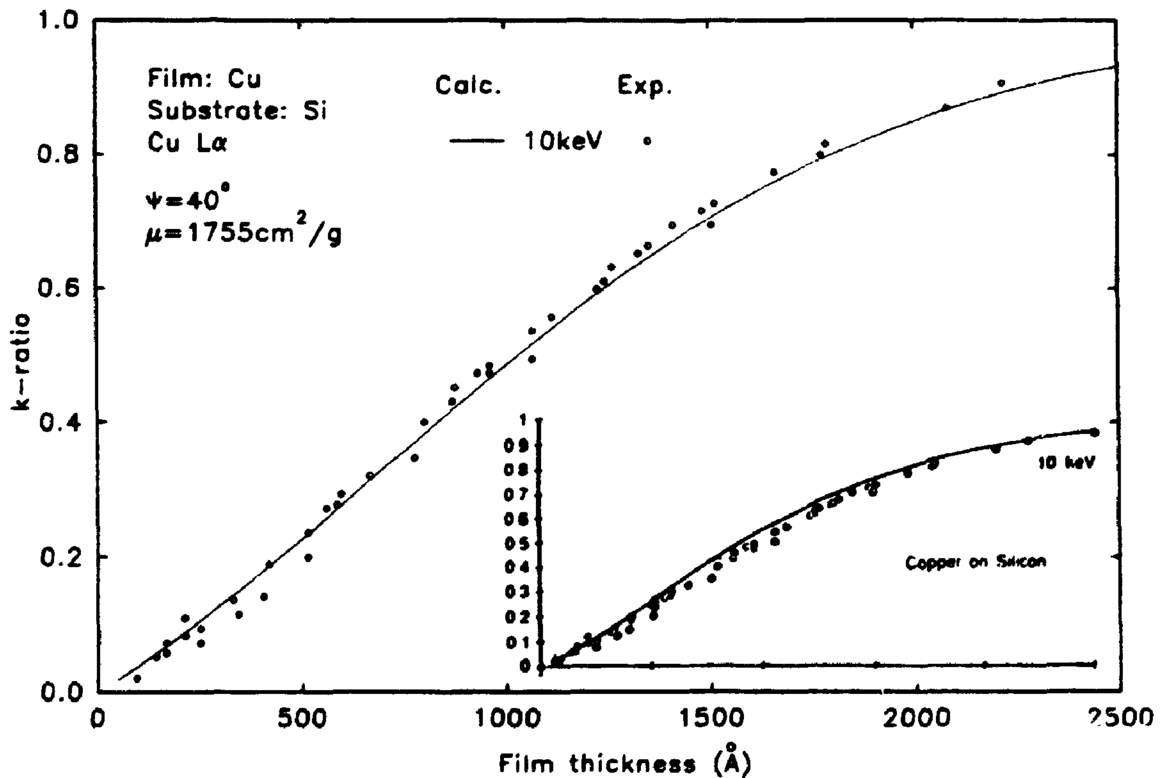

Figure 97b. Comparison of calculated k−ratios with those measured by Packwood et al. [181] for Cu films on Si substrate at 10 keV electron energy. The corner plot [181,Fig.6] is copyrighted and reprinted with the permission of San Francisco Press, Inc.

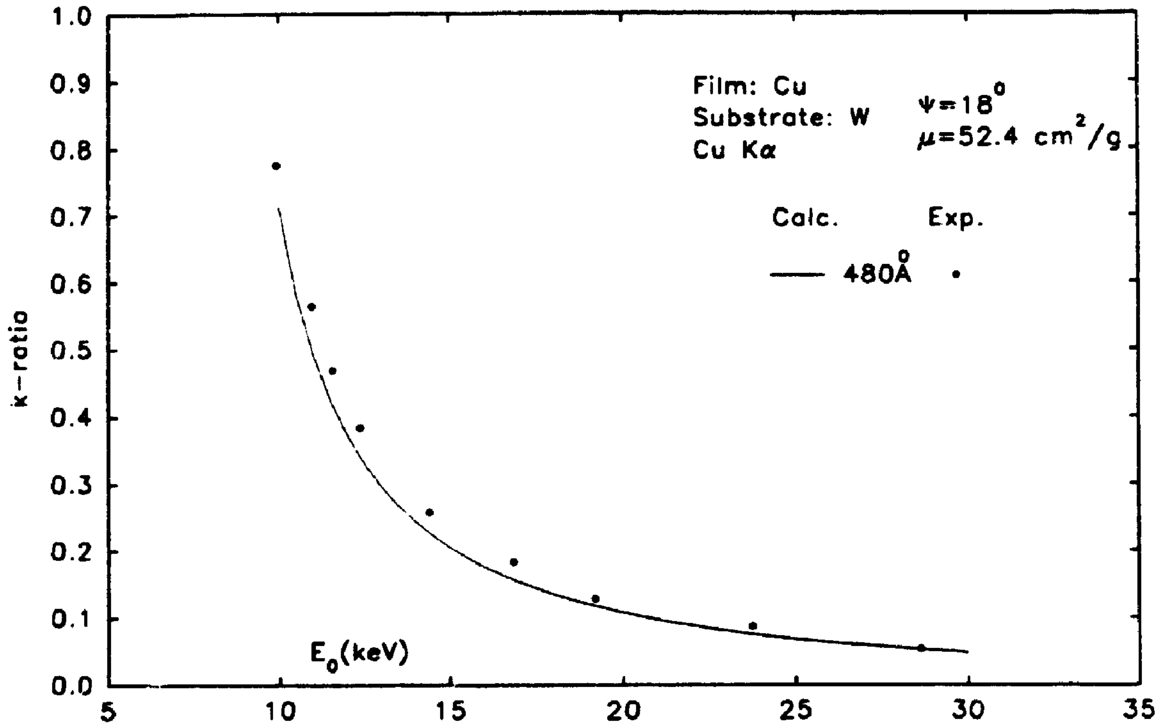

Figure 98a. Comparison of calculated k-ratios with those measured by Pouchou and Pichoir [75] for a Cu film on W substrate at different electron energies.

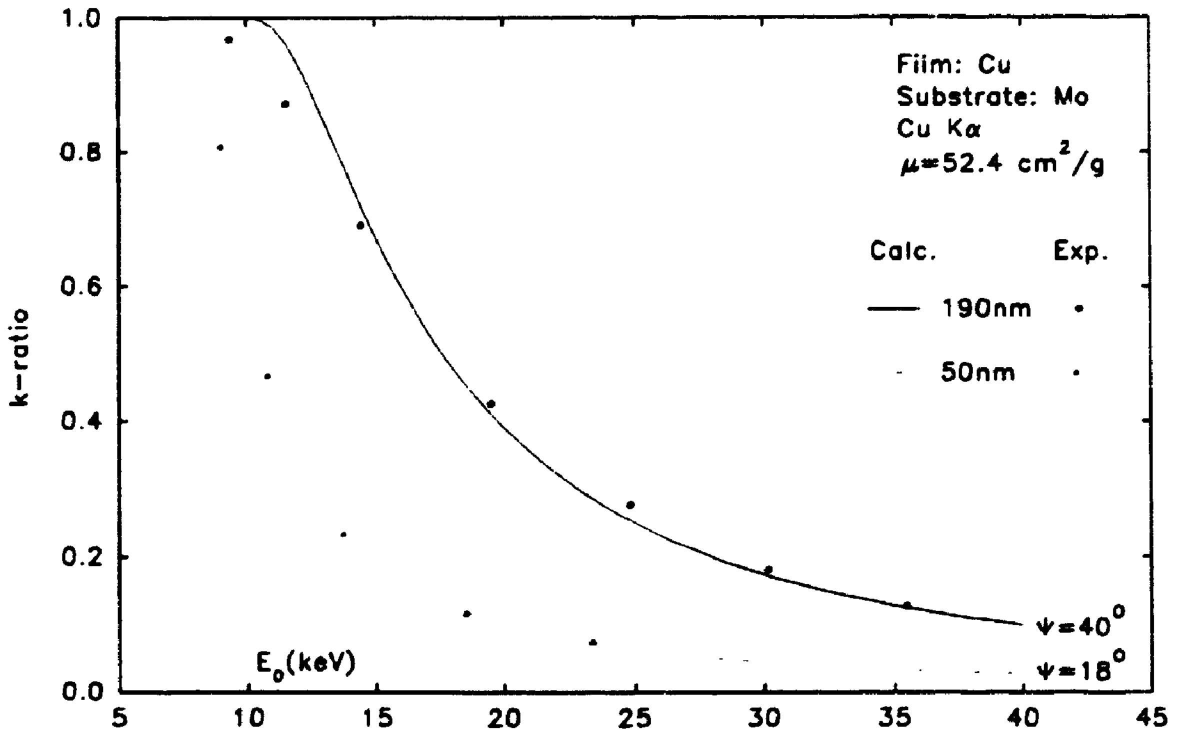

Figure 98b. Comparison of calculated k-ratios with those measured by Pouchou and Pichoir [75] for two Cu films on Mo substrate at different electron energies.

99a and b show data from Packwood et al. [181] for copper films on lead and tin. For these data, in support of the observations about the Pouchou and Pichoir data, the predicted k-ratios tend to be a bit high at 15 keV but are almost exact at 20 keV.

If a materials analyst is presented with a specimen of a film A on a substrate B of unknown thickness, the thickness can be readily determined by measuring the k-ratio and directly reading the corresponding thickness from the appropriate curves which are known as the 'working curves'. In practice, standard films of specified thickness are unlikely to be available so the analyst has to calculate the working curve using a technique su h as Monte Carlo simulation rather than determining the curve by actual measurements. Even so, this is too time consuming. The present model provides a highly efficient and accurate way to calculate film thickness based on a given measured k-ratio. Recall from Eqn. (76) that the only unknown is ρt which is the film thickness. In general, a successive approximation process was found to be very efficient in that the final film thickness converged in three or four iterations. Calculated film thicknesses using this method were compared with experimental measurements from Reuter [133] and Willich [155] and are summarized in Tables 9a and 9b respectively. As pointed out by Reuter, the true thicknesses of the films were determined by chemical analysis and thus these data provide an absolute test for the thickness measurements. The results from the graphical method proposed by Bishop and Poole [135] are also included as a comparison. In the case of Al film on B substrate at 4 keV which is a very low electron energy, the four aluminum f'lm thickness values tend to be slightly low compared with the chemical values, with

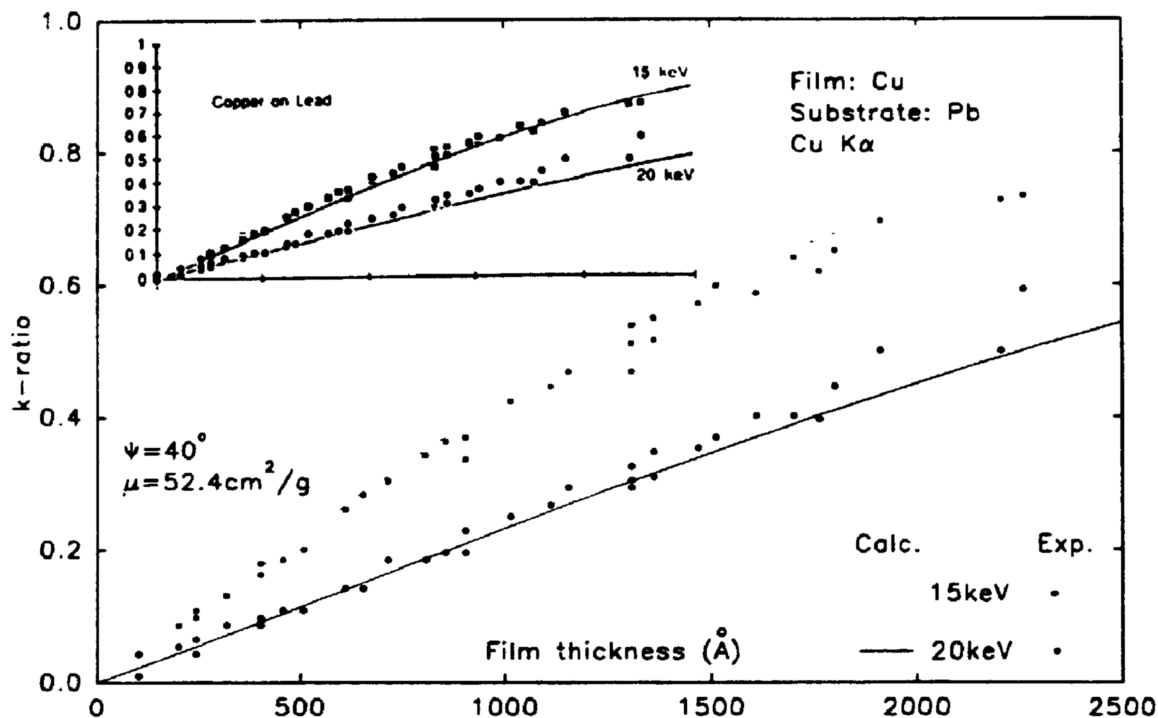

Figure 99a. Comparison of calculated k−ratios with those measured by Packwood et al. [181] for Cu films on Pb substrate at 15 and 20 keV electron energies. The corner plot [181,Fig.5] is copyrighted and reprinted with the permission of San Francisco Press, Inc.

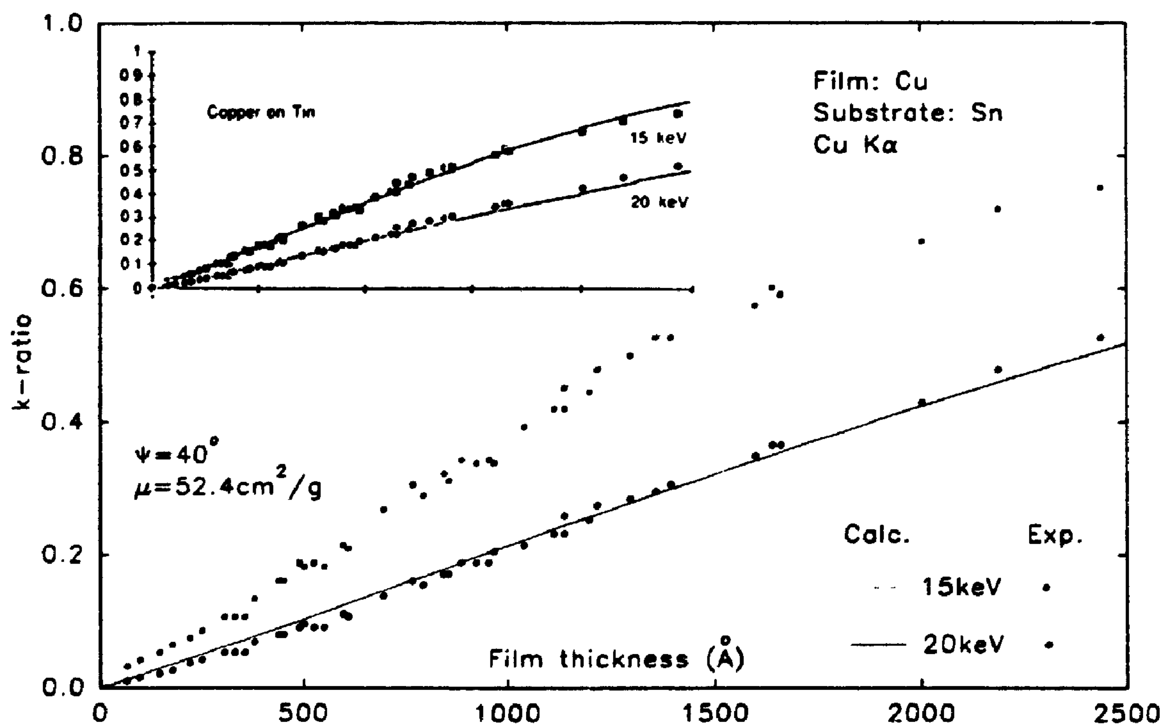

Figure 99b. Comparison of calculated k−ratios with those measured by Packwood et al. [181] for Cu films on Sn substrate at 15 and 20 keV electron energies. The corner plot [181,Fig.5] is copyrighted and reprinted with the permission of San Francisco Press, Inc.

Table 9a. Comparison of calculated film thicknesses from various methods using the measured k-ratio data from Reuter [133], take off angle(Ψ=52.5°).

Film	Substrate	E_o (keV)	E_c (keV)	μ (cm^2/g)	k-ratio	Thickness ($\mu g/cm^2$)			
						Chemical method	Reuter method	Graphical method	This work
Al(Z=13)	Boron(Z=5)	4	1.56	426	0.407	14.5	14.6	12.1	13.5
Al(Z=13)	Boron(Z=5)	4	1.56	426	0.182	7.3	7.0	5.8	6.5
Al(Z=13)	Boron(Z=5)	4	1.56	426	0.109	4.4	4.3	3.7	4.1
Al(Z=13)	Boron(Z=5)	4	1.56	426	0.084	3.4	3.3	2.9	3.2
Al(Z=13)	Iron(Z=26)	30	1.56	426	0.073	73	83	64	70
Al(Z=13)	Gold(Z=79)	30	1.56	426	0.093	73	85	69	68
Cu(Z=29)	Al_2O_3(Z=10)	30	8.98	54	0.063	83	72	79	85
Cu(Z=29)	Al_2O_3(Z=10)	10	0.933	1900	0.433	83	71	71	83
Ni(Z=28)	Al_2O_3(Z=10)	6	0.871	3500	0.612	48	45	39	49
Ni(Z=28)	Al_2O_3(Z=10)	12	0.871	3500	0.232	48	43	44	51
Ni(Z=28)	Al_2O_3(Z=10)	20	0.871	3500	0.131	48	40	37	46
Ni(Z=28)	Al_2O_3(Z=10)	15	8.329	59	0.094	26	23	23	29
Ni(Z=28)	Al_2O_3(Z=10)	18	8.329	59	0.053	25	23	22	25
Ni(Z=28)	Al_2O_3(Z=10)	22	8.329	59	0.035	26	24	21	26

Table 9b. Comparison of calculated film thicknesses with the measured k-ratio data from Willich [155], take off angle(Ψ=40°).

Film	Substrate	E_o (keV)	E_c (keV)	μ (cm^2/g)	k-ratio	Thickness ($\mu g/cm^2$)	
						Mechanical stylus	This work
Cu(Z=29)	Al(Z=13)	15	0.933	1755	0.138	52±2	49
Cu(Z=29)	Ti(Z=22)	15	0.933	1755	0.164	52±2	53
Cu(Z=29)	Ni(Z=28)	15	0.933	1755	0.179	52±2	55
Cu(Z=29)	Mo(Z=42)	15	0.933	1755	0.200	52±2	55
Cu(Z=29)	W(Z=74)	15	0.933	1755	0.221	52±2	55

better agreement for thinner films which is what one would expect for low electron energy. However, the values from the model do fall between the graphical method of Bishop and Poole and the Reuter method. The same comments can be made for the aluminum films on the higher atomic number substrates of iron and gold at the very much higher electron energy of 30 keV. For the copper and nickel films on the Al_2O_3 substrate, the agreement between this model and the chemical values is very good. The constancy of predicted film thickness with electron energy for the same film is not perfect but the variation is certainly acceptable. The predictions of this model overall are much better than either the Reuter or graphical models for this data set. Recently, Willich [155] made some k-ratio measurements for Cu on various substrates at 15 keV. A mechanical stylus was used to measure the film thicknesses which were presumably deposited simultaneously. The calculated film thicknesses agree well with the measured thicknesses and are reasonably consistent with substrate atomic number except for the fall off for low atomic number.

6.6 SOURCES OF ERROR

The model has been demonstrated to perform well for a wide variety of published data. The poorest agreement is for those systems measured with low overvoltage ratios. This is the same region in which bulk analysis using a $\phi(\rho z)$ approach is subject to question. Because of the formulation of the model in terms of a ratio to the bulk curve, as more accurate $\phi(\rho z)$ equations are developed, this model can be adapted to them and the result should lead to an improved agreement.

In the case of bulk as well as thin film analysis, a good knowledge of the x-ray mass absorption coefficients is required, in particular for low energy x-ray lines. Some of these mass absorption coefficients are the source of a high level of uncertainty. A comparison of the values from different authors reveals that there are still very large differences and, moreover, new values are always being published. The situation is made worse because many of the published data sets do not state the choice of mass absorption coefficient. In general, for medium to high energy x-ray lines, the table by Heinrich [182] gives reasonably complete mass absorption coefficients whereas the tables by Henke et al. [183] represent the most updated compilation for low energy x-ray lines. A good comparison of various mass absorption coefficient values, in particular for low energy x-ray lines, can be found in the paper by Sevov et al. [184]. Selected mass absorption values have been revised by Pouchou and Pichoir [185].

For some film-substrate combinations, characteristic fluorescence is important. This has not been considered in this thesis. Cox et al. [186] reported that the fluorescence effect could contribute a major source of error but only when the substrate radiation has an energy slightly greater than the critical excitation energy of the film element. A typical example is in the case of aluminum coatings on silicon which is an important system in the semiconductor industry and chromium coating on iron for corrosion resistance purposes. A correction of up to 16% is possible depending on the film thickness for the above mentioned system. The thin film fluorescence correction proposed by Cox et al. can be incorporated in the present model.

CHAPTER 7

CONCLUSIONS

A multiple scattering Monte Carlo model used to simulate bulk $\phi(\rho z)$ curves was extensively modified to include electron straggling and Mott multiple scattering angular distributions. As a consequence, plots of $\ln(\phi(\rho z))$ versus $(\rho z)^2$ are linear in agreement with the behaviour of experimentally measured $\phi(\rho z)$ curves. The substitution of Mott scattering for Rutherford scattering results in a net transfer of ionizations from the peak area to the tail of the distribution.

More than 300 thin film $\phi(\rho z)$ curves were calculated using the modified model. The ratio between the thin film and bulk $\phi(\rho z)$ values can be described by

$$Ratio = 1 \pm (m1(\rho z) + c1)^{8}$$

where the positive sign is for low atomic number films on high atomic number substrates and the negative sign is for the opposite. ρz is the depth from the specimen surface and the expression holds up to the interface. General values for m1 and c1 were derived which are applicable to all film/substrate combinations in the electron energy range for practical EPMA. Because of the formalism, the equations can be used with any bulk $\phi(\rho z)$ expression for quantitative thin film analysis. Thin film k-ratios calculated from this model agreed well with experimental data from the literature.

7.1 FUTURE WORK

Substrate $\phi(\rho z)$ curves from film/substrate samples can also be used for film thickness measurement by comparing substrate x-ray intensity with the corresponding standard. Some alterations are required in the present Monte Carlo program to accommodate these calculations. Since the generated x-rays now must pass through both the substrate and the film before reaching the detector, the measured substrate x-ray intensity has to be corrected both for the absorption in the substrate and the film. The limits of integration instead of from zero (surface of film) to ρt (film thickness) as in the case of film, need to be changed from ρt to infinity in the case of substrate. If modelled and parameterized properly, substrate $\phi(\rho z)$ curves can also give accurate film thickness measurements as an alternative to film $\phi(\rho z)$ curves. In fact, it was pointed out by Brown [118] that in strongly absorbing situations the substrate k ratio can be more sensitive than the film k ratio in particular for very thin film thickness measurement.

APPENDIX 1

FORTRAN PROGRAM TO CALCULATE BULK $\phi(\rho z)$ CURVES

(RUTHERFORD SCATTERING)

```
ccccccccccccccccccccccccccccccccccccccccccccccccccccccccccccccccccccccc
c
c This program calculates bulk φ(ρz) curves based on Rutherford multiple scattering
c  angles by Werner and Heydenreich from a set of input parameters which include:-
c     EO :  Incident electron energy
c     VK : Critical excitation potential
c     NZ :  Atomic number
c       A :  Atomic weight
c  NPAS:  Number of steps
c   NUM:  Number of trajectories
c
c The output will be stored in a file named 'DUM.DAT' which include an electron
c energy table (EN(200)), an electron distribution table (IXF(64,200)) and data to
c calculate bulk φ(ρz) curves (ROZ(64), PHI(64))
c
c The computation process can be summarized in the following way:-
c  1) Read in the initial input parameters
c  2) Calculate the mean ionization potential using the expression from Berger and
c       Seltzer
c  3) Calculate the x-ray range with lower limit of integration set to the critical
c      excitation potential
c  4) Use Runge Kutta method to determine and store electron energies at each step
c       in the electron energy table
c  5) Start the first electron trajectory using normal incidence angle
c  6) Introduce electron straggling so that the previously calculated step size for each
c      trajectory will be subject to change according to a gaussian distribution of values
c  7) Calculate the electron scattering angle using the expression from Werner and
c       Heydenrich after each interaction
c  8) Calculate the azimuthal angle
c  9) Check the new electron position, if the position is negative, then the electron is
c      considered backscattered and the corresponding counter is incremented.
c      Otherwise the position and energy of the electron inside the target are updated
c      and stored in the electron distribution table
c10) For the same trajectory, calculate the next new electron position by finding a new
c      scattering angle and azimuthal angle.  This process will continue until the
c      electron is backscattered from the target or the electron energy falls below the
c      critical excitation potential
c11) Start the next electron trajectory and continue until all trajectories are complete
c12) Calculate the bulk φ(ρz) curve using the data from the electron distribution table
c       since the number of electrons and the energy of each electron is known in each
c       and every layer in the target
c
ccccccccccccccccccccccccccccccccccccccccccccccccccccccccccccccccccccccc
```

```
      PROGRAM TSM56
      PARAMETER(ME=9)
      PARAMETER (MP=200)
      PARAMETER (MPP=401)
      PARAMETER (MMP=64)
C     PARAMETER (MAG=128)
      CHARACTER*1 QU
      DIMENSION NZ(ME),C(ME),A(ME),VK(ME)
      DIMENSION EN(MPP),IXF(MMP,MP),IXB(MMP,MP),IBAC(MP),IBB(MP)
     &,ROZ(MMP),PHI(MMP)
      DIMENSION ALP(MP),EFFZ(ME)
      COMMON NZ,A,VK,C,EO,RANGE,E14,EN,IXF,IXB,IBAC,IBB,ROZ,PHI,ISTART
      COMMON ALP,EFFZ
C     COMMON/LUI/LU5,LU6,LU7
C     DATA LU5,LU6,LU7/5,5,7/
C     DATA ISTART/490623069/
      OPEN(UNIT=7,FILE='DUM.DAT')
      OPEN(6,FILE='CON')
      OPEN(5,FILE='CON')
C Input
    1 WRITE(6,100)
  100 FORMAT(' Acceleration voltage (kV) ? ')
      READ(5,200,ERR=1) EO
  200 FORMAT(F12.0)
      WRITE(6,101)
  101 FORMAT(' Input constants of elements present in the target'/
     &' the simulation will be done for the first input element')
C Initialization for pure target
      JO=1
      JJA=1
      JJM=1
      C(1)=1.
C simulated element
    2 WRITE(6,102)
  102 FORMAT(' Atomic number ? ')
      READ(5,201,ERR=2) NZ(1)
  201 FORMAT(I6)
    3 WRITE(6,103)
  103 FORMAT(' Atom weight ? ')
      READ(5,200,ERR=3) A(1)
    4 WRITE(6,104)
  104 FORMAT(' Excitation voltage (kV) ? ')
      READ(5,200,ERR=4) VK(1)
    5 WRITE(6,105)
  105 FORMAT(' Is it a pure target ( Y or N ) Def[Y] ? ')
      READ(5,202,ERR=5) QU
  202 FORMAT(A1)
      IF((QU.NE.'N').AND.(QU.NE.'n')) GO TO 20
C Complex target
    7 WRITE(6,106)
  106 FORMAT(' Weight fraction of the calculated element ? ')
      READ(5,200,ERR=7) C(1)
    8 WRITE(6,107)
  107 FORMAT(' Number of companions  ? ')
      READ(5,201,ERR=8) JJD
      IF(JJD.LE.0) GO TO 8
      JJM=JJD+1
C Companions
      DO 9 J=1,JJD

      WRITE(6,108) J
```

```
  108 FORMAT('       Companion no.',I2)
   10 WRITE(6,102)
      READ(5,201,ERR=10) NZ(J+1)
   11 WRITE(6,103)
      READ(5,200,ERR=11) A(J+1)
   12 WRITE(6,104)
      READ(5,200,ERR=12) VK(J+1)
   13 WRITE(6,109)
  109 FORMAT(' Weight fraction ? ')
      READ(5,200,ERR=13) C(J+1)

    9 CONTINUE
C Parameters of the Simulation
C Xray range is employed -> nswr=2
   20 NSWR=2

C NUM is the number of simulated trajectories
C NPAS is the number of steps dividing the range
   21 WRITE(6,110) MMP-13
  110 FORMAT(' Number of steps  (< ',I3,' ? ')
      READ(5,201,ERR=21) NPAS
      IF((NPAS.LE.0).OR.(NPAS.GT.45)) GO TO 21
   22 WRITE(6,111)
  111 FORMAT(' Number of traectories ? ')
      READ(5,201,ERR=22) NUM
      ANUM=NUM
C Display input
      WRITE(6,112)
  112 FORMAT('       Target identification'/
     &' no.     Z        A        EK       C            ')
      WRITE(6,113)
  113 FORMAT(/)
      WRITE(6,203) (J,NZ(J),A(J),VK(J),C(J),J=1,JJM)
203   FORMAT(2X,I2,3X,I3,4X,F6.2,4X,F7.4,4X,F6.4)
      WRITE(6,204) EO,NPAS,NUM
  204 FORMAT('       Simulation parameters'/
     &' Acceleration voltage :',F6.3/
     &' Number of steps      :',I3/
     &' Number of trajectories :',I6)
C Proceed to mc calculation
      CALL RESU(JO,JJM,JJA,ANUM,NPAS,NSWR)
      CLOSE(UNIT=7)
      STOP
      END
C Control the simulation and output some balance
      SUBROUTINE RESU(JO,JM,JJA,ANUM,NPAS,NSWR)
      PARAMETER (ME=9)
      PARAMETER (MP=200)
      PARAMETER (MPP=401)
      PARAMETER (MMP=64)
C     PARAMETER (MAG=128)
      CHARACTER*2 SYMB(ME),ATSY(100)
      DIMENSION NZ(ME),A(ME),VK(ME),C(ME),EN(MPP),IXF(MMP,MP),
     &IXB(MMP,MP),IBAC(MP),IBB(MP),ROZ(MMP),PHI(MMP),ALOPHI(MMP)
      DIMENSION ALP(MP),EFFZ(ME)
      COMMON NZ,A,VK,C,EO,RANGE,E14,EN,IXF,IXB,IBAC,IBB,ROZ,PHI,ISTART
      COMMON ALP,EFFZ
C     COMMON/LUI/LU5,LU6,LU7
      DATA ATSY/'H','HE','LI','BE','B','C','N','O','N','NE','NA','MG'
     &,'AL','SI','P','S','CL','AR','K','CA','SC','TI','V','CR','MN'
     &,'FE','CO','NI','CU','ZN','GA','GE','AS','SE','BR','KR'
     &,'RB','SR','Y','ZR','NB','MO','TC','RU','RH','PD','AG','CD','IN'
     &,'SN','SB','TE','I','XE','CS','BA','LA','CE','PR','ND','PM','SM'
     &,'EU','GD','TB','DY','HO','ER','TM','YB','LU','HF','TA','W','RE'
```

```
     &,'OS','IR','PT','AU','HG','TI','PB','BI','PO','AT','RN','FR','RA'
     &,'AC','TH','PA','U','NP','PU','AM','CM','BK','CF','ES','FM'/
      WRITE(7,200) JM
  200 FORMAT(1X,I2,' <- Number of elements')
      WRITE(7,201)
  201 FORMAT(' Atom symbol(s) and weight fraction(s)')
      DO 1 J=JO,JM
      I=NZ(J)
      SYMB(J)=ATSY(I)
    1 CONTINUE
      WRITE(7,202) (SYMB(J),C(J),J=JO,JM)
  202 FORMAT(10(3X,A2,':',F6.4))
      WRITE(7,203) NPAS
  203 FORMAT(1X,I3,' <- Number of steps')
      NUM=ANUM
      WRITE(7,204) NUM
  204 FORMAT(1X,I6,' <- Number of trajectories')
      WRITE(7,205) EO
  205 FORMAT(1X,F5.2,' <- Acceleratlon voltage')
      WRITE(7,*) JJA
C     Trajectory sampling
      CALL E10(JO,JM,JJA,ANUM,NPAS,NSWR,RETRO1,RETRO2)
      RANG3=1000.*RANGE
      WRITE(7,206) RANG3
 206  FORMAT(1X,E15.8,' <- Range ( mg/cm2 )')
      WRITE(7,207)
 207  FORMAT(' Half step and full step energies')
      DO 2 I=1,MP,5
      J=I+MP+1
      WRITE(7,208) I,EN(I),EN(J)
 2    CONTINUE
  208 FORMAT(I3,3X,2(4X,F6.3))
      NPASS=2*MP+1
      TOT1=0.0
      DO 118 I=1,MP
C     WRITE(7,*) IBAC(I),IBB(I)
      TOT1=TOT1+IBAC(I)
 118  CONTINUE
      WRITE(7,*) TOT1
C Output electron distribution
      WRITE(7,209)
 209  FORMAT(' Electron distribution')
      CALL PRINT(NPAS)
C     WRITE(7,210) (IBB(I),I=1,MP)
C210  FORMAT(' BB',12(3X,I6))
      IF(NSWR.EQ.2) GO TO 23
      WRITE(7,211) RETRO1,RETRO2
 211  FORMAT(1X,F7.4,4X,F7.4,' <- Retrol , Retro2')
C Xray from Derian target
C     CALL XRAB(JJA,ALOPHI,NPAS,ANUM,NPASS,RXB,RXBO,RXBBO)
C     WRITE(7,212)
C212  FORMAT(' Derian target distribution')
C     DO 3 J=1,NPASS
C     WRITE(7,213) J,ROZ(J),ALOPHI(J)
C  3  CONTINUE
 213  FORMAT(1X,I3,3X,2(6X,E15.8))
C     WRITE(7,214) RXB,RXBO,RXBBO
C214  FORMAT(1X,3(E15.8,4X),'<- RXB,RXBO,RXBBO')
C     X-RAY FROM THE REGULAR TARGET
   23 CALL XRAF(JJA,ALOPHI,NPAS,ANUM,NPASS,RXF,RXFO)
      WRITE(7,215)
  215 FORMAT(' Phi(roz) distributlon')
      DO 4 J=1,NPASS
      WRITE(7,213) J,ROZ(J),ALOPHI(J)
```

```
    4   CONTINUE
C TOTAL AMOUNT
        WRITE(7,216) RXF,RXFO
  216 FORMAT(1X,2(E15.8,4X),' <- RXF,RXFO')
        RXFO=RXF+RXB+RXBBC
        RXBO=RXB+RXBBO
        WRITE(7,217) RXFO,RXBO
  217 FORMAT(1X,2(E15.8,4X),' <- RXF+RXB+RXBBO , RXB+RXBBO')
        RETURN
        END
C E10
C                        RoutineE10
C           Argument list
C input : JO       index of the first element of the target
C       : JJA      index of the calculated element
C       : JM       index of the last element of the target

C       : ANUM     number of trajectories (real)

C       : NPAS number of intervals dlviding the range
C       : NSWR lf 1 :-full range ; if 2 : xrays range
C output: RETRO1 backscattering coefficient
C       : RETRO2 fraction of electrons entering again the target
C              ( forw - back -> forw )
C         common
C scalar: E14 electron encrgy at the surface layer
C       : ISTART seed of the pseudo random number selector
C array : NZ        atomic numbers
C       : A        atom weights
C       : VK        excitation potentials
C       : C        weight fractions
C       : EO       incident electron energies
C       : EN       half step and full step electron mean energies
C       : IXF      table of transmited electrons
C       : IXB        " backscattered electrons
C       : IBAC     energy distribution of backscattered electrons
C       : IBB      the same as before (2th backscat. )
C       : ROZ      depth ( in mass thickness unit )
C       : PHI      phi-ro-z
C         parameters
C
C            ME       maximum number of elements in the target
C            MP       number of steps
C           MPP       dimension of the energy table
C           MAG       number of angles of equal scattering probability
C
C          function
C
C           EI          exponential integral
C           URAN        pseudo random number selector
C
        SUBROUTINE E10(JO,JM,JJA,ANUM,NPAS,NSWF,RETRO1,RETRO2)
        PARAMETER (ME=9)
        PARAMETER (MP=200)
        PARAMETER (MPP=401)
        PARAMETER (MMP=64)
C       PARAMETER (MAG=128)
        PARAMETER (NRD=3)
        DIMENSION NZ(ME),A(ME),VK(ME),C(ME),EN(MPP),AB(ME),
       &AC(ME),GA(4),RD(NRD),JJJ(99),ALP(MP),EFFZ(ME),LIM(99),N(99)
        DIMENSION IXF(MMP,MP),IXB(MMP,MP),IBAC(MP),IBB(MP),PHI(MMP),
       &P(MP),RES(MP),ROZ(MMP)
C       DIMENSION ABCD(50,MP)
        COMMON NZ,A,VK,C,EO,RANGE,E14,EN,IXF,IXB,IBAC,IBB ROZ,PHI,ALP
```

```
      COMMON EFFZ
C     COMMON/LUI/LU5,LU6,LU7
      DATA NMAX1,NAN,PI,P180/128,128,3.14159265,.174532925E-1/
C
C ECRAN is a constant used in the calculation of the screening parameter
      DATA ECRAN/1./
      DATA ISTART/490623069/
C
C Statement function calculating sine from cosine in argument
      SI(X)=SQRT(1.-X**2)
  100 FORMAT(' WARNING - Slow convergence for step no.',I3)
C      NUM : number of sampled trajectories
C       ED : the popular constant of the Bethe's formula (1.166)
C       BB : real converion of the atomic number of the emitting element
C       AA : mean ionizatlon potentiel of the emitting element
      NUM=ANUM
      ED=SQRT(EXP(1.)/2.)
      BB=NZ(JJA)
      AA=(9.76*BB+58.5/BB**.19)/1000.
C Determination of a minimum energy limit for calculatlng the
C  Bethe,s range
C   first find the greater mean ionization potential
C
      DO 15 JJ=JO,JM
      BB=NZ(JJ)
      AB(JJ)=A(JJ)/(7.85E4*(BB**1.00)*C(JJ))
      AC(JJ)=(9.76*BB+58.5/BB**.19)/1000.
      IF(AC(JJ).GT.AA) AA=AC(JJ)
      AC(JJ)=ED/AC(JJ)
   15 CONTINUE
      GO TO (16,17),NSWR
C Lower limit for full range calculation
 16   ZA=1.03**AA
      GO TO 18
C Lower limit for xrays range calculation
   17 ZA=VK(JJA)
C Range calculation
   18 SM=.0
      ED=.0
      DO 19 JJ=JO,JM
      ED=ED+ALOG(AC(JJ))/AB(JJ)
      SM=SM+1./AB(JJ)
   19 CONTINUE
      ED=ED/SM
      V=EXP(ED)
      RANGE=1./SM/V**2*(EI(2.*(ED+ALOG(EO)))-
     &EI(2.*(ED+ALOG(ZA))))
C Calculation of half step and full step electron mean energies
      H=MP
      H=RANGE/H/4.
      AA=H/2.
      BB=H/6.
      EA=EO
      NPAS2=2*MP
      DO 20 I=1,NPAS2
      DO 11 J=1,2
      EB=EA
      DO 25 IP=1,4
      GA(IP)=.0
      DO 26 JJ=JO,JM
      GA(IP)=GA(IP)+ALOG(AC(JJ)*EB)/AB(JJ)/EB
   26 CONTINUE
      GO TO (27,27,28,25),IP
   27 EB=EA-AA*GA(IP)
```

```
      GO TO 25
   28 EB=EA-H*GA(IP)
   25 CONTINUE
      EA=EA-BB*(GA(1)+2.*(GA(2)+GA(3))+GA(4))
      IF(I.NE.1) GO TO 11
      IF(J.EQ.1) E14=EA
   11 CONTINUE
      EN(I)=EA
   20 CONTINUE
      IF(EN(NPAS2).LT.VK(JJA)) EN(NPAS2)=VK(JJA)
C Energy sorting
C                   EN(I) I 1 -> NPAS : half step mean energy
C                   EN(NPAS+1) : incident electron energy
C                   EN(I) I NPAS+2 -> 2*NPAS+2 : full step mean energy
      DO 12 I=2,MP
      EN(NPAS2+1)=EN(I)
      DO 12 J=I,NPAS2
      EN(J)=EN(J+1)
   12 CONTINUE
      EN(NPAS2+1)=EN(MP+1)
      EN(MP+1)=EO
      WRITE(7,*) E14
C     TRAJECTORY SAMPLING
C    TABLE INITIALIZATION
      DO 58 I=1,MP
      IBAC(I)=0
      IBB(I)=0
      ALP(I)=0.0
      DO 58 J=1,MMP
      IXF(J,I)=0
      IXB(J,I)=0
  58  CONTINUE
      DO 149 K=1,99
      JJJ(K)=0
 149  CONTINUE
C H IS THE INCIDENT ANGLE
      H=.0
      WONE=0.0
      TOTZ=0.0
      DO 613 JJ=JO,JM
      EFFZ(JJ)=0.0
  613 CONTINUE
      DO 614 JJ=JO,JM
      BB=NZ(JJ)
      WONE=WONE+C(JJ)*(1.+.8/BB)*(BB**(4./3.))/A(JJ)
  614 CONTINUE
      WONE=WONE*RANGE*1.E+06/0.443
      DO 615 JJ=JO,JM
      BB=NZ(JJ)
      EFFZ(JJ)=C(JJ)*(1.+.8/BB)*(BB**(4./3.))/A(JJ)
      TOTZ=TOTZ+EFFZ(JJ)
  615 CONTINUE
      ZEFF=0.0
      DO 616 JJ=JO,JM
      BB=NZ(JJ)
      ZEFF=ZEFF+EFFZ(JJ)/TOTZ*BB**(2./3.9)
  616 CONTINUE
      ZEFF=ZEFF**(3.9/2.)
      LIM(1)=6
      LIM(2)=7
      LIM(3)=9
      LIM(4)=12
      LIM(5)=15
      LIM(6)=20
```

```
      LIM(7)=25
      LIM(8)=32
      LIM(9)=40
      LIM(10)=49
      LIM(11)=59
      LIM(12)=72
      LIM(13)=87
      LIM(14)=102
      LIM(15)=120
      LIM(16)=140
      LIM(17)=160
      LIM(18)=184
      LIM(19)=207
      LIM(20)=231
      LIM(21)=255
      LIM(22)=279
      LIM(23)=302
      LIM(24)=324
      LIM(25)=343
      LIM(26)=362
      LIM(27)=376
      LIM(28)=387
      LIM(29)=396
      LIM(30)=399
      DO 157 I=31,60
      LIM(I)=LIM(61-I)
 157  CONTINUE
      RRD=0.0
      RII=0.0
      DO 297 J=1,99
      N(J)=0
  297 CONTINUE
      DO 59 IT=1,NUM
C start one trajectory
C   NSW1 1 -> electron moving in the forward direction
C   NSW1 2 -> backscattered electron
C   NSW2 1 -> the counter of backscattered has already been incremented
C   NSW2 1 -> the counter of backscattered must been incremented
      NSW1=1
      NSW2=1
      Y=0.0
      AA=COS(H)
      IST=0
      JII=0
      STEP=0.0
  159 CALL URAN(ISTART,NRD,RD)
      RRD=(RD(1)-0.5)*6.0
      DO 762 II=1,60
      RII=II
      IF((RRD.LT.(RII/10.-3.)).AND.(RRD.GT.(RII/10.-3.1))) GO TO 763
      GO TO 762
  763 N(II)=N(II)+1
      IF(N(II).LE.LIM(II)) GO TO 999
      GO TO 159
  762 CONTINUE
  999 Y=0.5*(1.+0.56*(RD(1)-0.5))
      IST=(45.*(1.+0.56*(RD(1)-0.5)))+0.5
      J=Y+1.0
      I=1./FLOAT(IST)/4.*FLOAT(MP)+0.5
      IXF(J,I)=IXF(J,I)+1
      IF(IST.EQ.45) WRITE(5,*) IT,IST
      JJJ(1)=1./FLOAT(IST)/2.*FLOAT(MP)+0.5
      DO 35 K=2,IST
      KK=K-1
```

```
      STEP=IST
      JII=FLOAT(KK)*(1.-1./2./STEP)/(STEP-1.)*FLOAT(MP)+
     &1./FLOAT(IST)/2.*FLOAT(MP)+0.5
      JJJ(K)=JII
   35 CONTINUE
      STEPL=45./STEP
      DO 60 K=1,IST
      I=JJJ(K)
C "free path" sampling
      CALL URAN(ISTART,NRD,RD)
      BB=RD(1)
      Y=Y+AA*BB/STEPL
      IF(Y.GT.0.) GO TO 47
C move backward
      IF(NSW1.EQ.2) GO TO 62
      NSW1=2
      NSW2=2
      GO TO 62
C move forward
   47 IF(NSW1.EQ.2) GO TO 61
C deflection sampling
C  62 ALP(I)=(1.+.8/Z)**1.3*(RANGE*1.E+06/FLOAT(IST))**1.3
C    &*(Z**2.4)*4.34E-03/((.443*AAA)**1.3)/(EN(I)**2.3)
C  62 IF(K.GE.2) GO TO 911
   62 ALP(I)=4.34E-03*ZEFF**(2./3.)*(WONE**1.3)/45.0**1.3
     &/(EN(I+MP+1)**2.30)
C     GO TO 912
C 911 ALP(I)=(WONE*(1.-1./2./FLOAT(IST))/(FLOAT(IST)-1.))**(1.3)
C    &*4.34E-03*ZEFF**(2./3.)/(EN(I+MP+1)**2.30)
      C1=1.-(2.*ALP(I)*RD(2))/(1.+ALP(I)-RD(2))
      C2=SI(C1)
      C3=COS(2*PI*RD(3))
      AA=AA*C1+SI(AA)*C2*C3
      Y=Y+(1.-BB)*AA/STEPL
      IF(Y.LE.0.) GO TO(49,48),NSW1
      GO TO (63,61),NSW1
C update the table of electron position inside the target
   63 J=Y+1.0
      IXF(J,I)=IXF(J,I)+1
      GO TO 60
C backscattered electron
   49 NSW1=2
      NSW2=2
C update the table of electron position outide the target
C              ( simulation of the Derian experiment )
   48 J=Y-1.5
      J=-J
      IXB(J,I)=IXB(J,I)+1
      GO TO (60,67),NSW2
   67 IBAC(I)=IBAC(I)+1
      NSW2=1
   60 CONTINUE
      GO TO 59
C again in the target after being backscattered
   61 IF(NSW2.EQ.2) IBAC(I)=IBAC(I)+1
      IBB(I)=IBB(I)+1
   59 CONTINUE
C     CALCULATION OF BACKSCATTERING COEFFICIENTS
      IF(NSWk.EQ.2) GO TO 23
      RETRO1=.0
      RETRO2=.0
      DO 33 I=1,MP
      C1=IBAC(I)
      RETRO1=RETRO1+C1
```

```
      C1=IBB(I)
      RETRO2=RETRO2+C1
C     WRITE(7,*) IBAC(I),IBB(I)
   33 CONTINUE
      RETRO1=RETRO1/ANUM
      RETRO2=RETRO2/ANUM
      WRITE(7,*) RETRO1,RETRO2
   23 RETURN
      END
C PRINT
      SUBROUTINE PRINT(NPAS)
      PARAMETER (ME=9)
      PARAMETER (MP=200)
      PARAMETER (MPP=401)
      PARAMETER (MMP=64)
      DIMENSION NZ(ME),C(ME),A(ME),VK(ME),EN(MPP),IXF(MMP,MP),MOREB(99)
     &,IXB(MMP,MP),IBAC(MP),IBB(MP),ROZ(MMP),PHI(MMP),MORE(99,99)
      COMMON NZ,A,VK,C,EO,RANGE,E14,EN,IXF,IXB,IBAC,IBB,ROZ,PHI,ISTART
      COMMON/LUI/LU5,LU6,LU7
  103 FORMAT(1X,3X,10(3X,I3))
  101 FORMAT(1X,I3,10(1X,I5),1X,I5,1X,I5)
  111 FORMAT(' BS',10(1X,I5),1X,I5,1X,I5)
      DO 150 I=1,99
      MOREB(I)=0
      DO 149 J=1,99
      MORE(J,I)=0
  149 CONTINUE
  150 CONTINUE
      IS=10
      NTA=MP/IS
      IF(NTA.NE.0) GO TO 10
      IMIN=1
      GO TO 50
   10 DO 15 IT=1,NTA
      IADD=0
      IMIN=(IT-1)*IS
      IMAX=IS+IMIN
      IMIN=IMIN+1
      WRITE(7,103) (I,I=IMIN,IMAX)
C     DO 31 J=1,NPAS
C     K=NPAS+1-J
C     WRITE(7,101) K,(IXB(K,I),I=IMIN,IMAX)
C  31 CONTINUE
      DO 332 I=IMIN,IMAX
      IADD=IADD+IBAC(I)
  332 CONTINUE
      IF(IT.EQ.1) GO TO 168
      GO TO 169
  168 MOREB(IT)=IADD
      GO TO 170
  169 MOREB(IT)=MOREB(IT-1)+IADD
  170 WRITE(7,111) (IBAC(I),I=IMIN,IMAX),IADD,MOREB(IT)
      DO 334 J=1,MMP
      IADDD=0
      DO 333 I=IMIN,IMAX
      IADDD=IADDD+IXF(J,I)
 333  CONTINUE
      IF(IT.EQ.1)  GO TO 171
      GO TO 172
 171  MORE(J,IT)=IADDD
      GO TO 173
 172  MORE(J,IT)=MORE(J,(IT-1))+IADDD
 173  WRITE(7,101) J,(IXF(J,I),I=IMIN,IMAX),IADDD,MORE(J,IT)
      IF(IADDD.EQ.0)  GO TO 15
```

```
 334   CONTINUE
  15   CONTINUE
       IF(MP-IS*(MP/IS).EQ.0) GO TO 20
       IMIN=IMAX+1
  50   WRITE(7,103) (I,I=IMIN,MP)
C      DO 34 J=1,NPAS
C      K=NPAS+1-J
C      WRITE(7,101) K,(IXB(K,I),I=IMIN,NPAS)
C 34   CONTINUE
       WRITE(7,111) (IBAC(I),I=IMIN,MP)
       DO 32 J=1,MMP
       WRITE(7,101) J,(IXF(J,I),I=IMIN,MP)
  32   CONTINUE
  20   RETURN
       END
C EXPONENTIAL INTEGRAL
       FUNCTION EI(X)
       EI=ALOG(X)+X
       TN=X
       N=1
  300  AN=N
       IF(AN.GT.2.*X.AND.TN.LT.1.E-06) GO TO 400
       TN=TN*X*AN/(AN+1.)**2
       EI=EI+TN
       N=N+1
       GO TO 300
  400  RETURN
       END
C Select three random numbers - RAN is a system library function
C  ISTART : seed
C  NRD : number of sampled random numbers
C  RD      : random numbers in the range ( 0.,1. ), limits excluded
       SUBROUTINE URAN(ISTART,NRD,RD)
       DIMENSION RD(NRD)
       DO 1 I=1,NRD
    2  RD(I)=RAN(ISTART)
       IF((RD(I).GT.0.).AND.(RD(I).LT.1.)) GO TO 1
       GO TO 2
    1  CONTINUE
       RETURN
       END
       FUNCTION RAN(L)
       L=MOD(16807*L,2147483647)
       RAN=REAL(L)*4.6566128752459E-10
       RETURN
       END
C Calculation of Xray depth distribution in the target
C      Output:
C               ALOPHI log(phi(roz)
C               RXF total xray generation inside the target
C               RXFO total xray that would be generated inside
C                    the target in the absence of backscattering
C               NPASS index of the last layer giving a significant
C                    contribution
       SUBROUTINE XRAF(JJA,ALOPHI,NPAS,ANUM,NPASS,RXF,RXFO)
       PARAMETER (ME=9)
       PARAMETER (MP=200)
       PARAMETER (MPP=401)
       PARAMETER (MMP=64)
C      PARAMETER (MAG=128)
       DIMENSION NZ(ME),A(ME),VK(ME),C(ME),EN(MPP),IXF(MMP,MP),ALP(MP),
      &IXB(MMP,MP),IBAC(MP),IBB(MP),ROZ(MMP),PHI(MMP),ALOPHI(MMP)
       COMMON NZ,A,VK,C,EO,RANGE,E14,EN,IXF,IXB,IBAC,IBB,ROZ,PHI,ISTART
       COMMON ALP,EFFZ
```

```
      POWE=0.8
      COISO=1./EO**POWE/VK(JJA)**(2.-POWE)
     &*ALOG(EO/VK(JJA))
      NSW=1
      NPASS=MMP
C     PHI(1)=1./E14**POWE/VK(JJA)**(2.-POWE)
C    &*ALOG(E14/VK(JJA))
      PHI(1)=0.0
      RPAS=NPAS
      ROZ(1)=RANGE/RPAS/2.
      RXFO=.0
      DO 9 I=1,MP
      K=I
      IF(EN(K)/VK(JJA).LE.1.) GO TO 30
      AA=IXF(1,I)
      PHI(1)=PHI(1)+AA/ANUM/EN(K)**POWE/VK(JJA)**(2.-POWE)
     &*ALOG(EN(K)/VK(JJA))
    9 CONTINUE
      I=MMP
   30 NPAS1=I
      NPAS2=MP
      ALOPHI(1)=ALOG10(PHI(1)/COISO)
      RXF=PHI(1)/2.
      DO 10 J=2,NPAS1
      PHI(J)=.0
      J1=J-1
      RXFO=RXFO+1./EN(J1)/VK(JJA)*ALOG(EN(J1)/VK(JJA))
      GO TO (4,10),NSW
    4 ROZ(J)=J1
      ROZ(J)=ROZ(J)*RANGE/RPAS
      DO 11 I=J1,NPAS2
      K=I
      AA=IXF(J,I)
      PHI(J)=PHI(J)+AA/ANUM/EN(K)**POWE/VK(JJA)**(2.-POWE)
     &*ALOG(EN(K)/VK(JJA))
   11 CONTINUE
      IF(PHI(J).EQ.0.) GO TO 24
      ALOPHI(J)=ALOG10(PHI(J)/COISO)
      RXF=RXF+PHI(J)
      GO TO 10
   24 NPASS=J-1
      NSW=2
   10 CONTINUE
      IF(EN(NPAS1)/VK(JJA).GT.1.) RXFO=RXFO+1./EN(NPAS1)/VK(JJA)
     &*ALOG(EN(NPAS1)/VK(JJA))
      AA=RANGE/COISO/RPAS
      RXF=RXF*AA
      RXFO=RXFO*AA
      RETURN
      END
```

APPENDIX 2

FORTRAN PROGRAM TO CALCULATE BULK $\phi(\rho z)$ CURVES

(MOTT SCATTERING)

```
ccccccccccccccccccccccccccccccccccccccccccccccccccccccccccccccccccccccccc
c
c This program calculates bulk φ(ρz) curves based on Mott multiple scattering angles
c  from a set of input parameters which include:-
c     EO :  Incident electron energy
c     VK : Critical excitation potential
c     NZ :  Atomic number
c       A :  Atomic weight
c  NPAS:  Number of steps
c   NUM:  Number of trajectories
c The output will be stored in a file named 'DUM.DAT' which include an electron
c energy table (EN(200)), an electron distribution table (IXF(64,200)) and data to
c calculate bulk φ(ρz) curves (ROZ(64), PHI(64))
c The computation process can be summarized in the following way:-
c  1) Read in the initial input parameters
c  2) Calculate the mean ionization potential using the expression from Berger and
c       Seltzer
c  3) Calculate the x-ray range with lower limit of integration set to critical excitation
c       potential
c  4) Use Runge Kutta method to determine and store electron energies at each step
c       in the electron energy table
c  5) Start the first electron trajectory using normal incidence angle
c  6) Introduce electron straggling so that the previously calculated step size for each
c      trajectory will be subject to change according to a gaussian distribution of values
c  7) Depending on the atomic number of the target , read in the 8 appropriate
c      constants from previously stored tables (MOTT4.TXT and MOTT6.TXT) to
c      calculate the Mott single scattering angle from the expression by Drouin et al..
c      Also required is the Rutherford multiple scattering angle from Werner and
c      Heydenreich.  The Rutherford single scattering angle is also needed.  The Mott
c      multiple scattering angle can now be calculated according to Eqn. 73 in chapter
c      6 in this thesis
c  8) Calculate the azimuthal angle
c  9) Check the new electron position, if the position is negative, then the electron is
c      considered backscattered and the corresponding counter is incremented.
c      Otherwise the position and energy of the electron inside the target are updated
c      and stored in the electron distribution table
c10) For the same trajectory, calculate the next new electron position by finding a new
c      scattering angle and azimuthal angle.  This process will continue until the
c      electron is backscattered from the target or the electron energy falls below the
c      critical excitation potential
c11) Start the next electron trajectory and continue until all trajectories are complete
c12) Calculate the bulk φ(ρz) curve using the data from the electron distribution table
c       since the number of electrons and the energy of each electron is known in
c       each and every layer in the target
c
ccccccccccccccccccccccccccccccccccccccccccccccccccccccccccccccccccccccccc
```

```
      PROGRAM MOTT42
      PARAMETER(ME=9)
      PARAMETER (MP=200)
      PARAMETER (MPP=401)
      PARAMETER (MMP=64)
C     PARAMETER (MAG=128)
      CHARACTER*1 QU
      DIMENSION NZ(ME),C(ME),A(ME),VK(ME)
      DIMENSION EN(MPP),IXF(MMP,MP),IXB(MMP,MP),IBAC(MP),IBB(MP)
     &,ROZ(MMP),PHI(MMP)
      DIMENSION ALP(MP),EFFZ(ME),IX(99)
      DIMENSION YY1(99),YY2(99),YY3(99),YY4(99)
      DIMENSION YY5(99),YY6(99),YY7(99),YY8(99)
      COMMON NZ,A,VK,C,EO,RANGE,E14,EN,IXF,IXB,IBAC,IBB,ROZ,PHI,ISTART
      COMMON ALP,EFFZ
C     COMMON/LUI/LU5,LU6,LU7
C     DATA LU5,LU6,LU7/5,5,7/
C     DATA ISTART/490623069/
      OPEN(UNIT=7,FILE='DUM.DAT')
      OPEN(UNIT=8,FILE='MOTT4.TXT')
      OPEN(UNIT=9,FILE='MOTT6.TXT')
      OPEN(6,FILE='CON')
      OPEN(5,FILE='CON')
C Input
    1 WRITE(6,100)
  100 FORMAT(' Acceleration voltage (kV) ? ')
      READ(5,200,ERR=1) EO
  200 FORMAT(F12.0)
      WRITE(6,101)
  101 FORMAT(' Input constants of elements present in the target'/
     &' the simulation will be done for the first input element')
C Initialization for pure target
      JO=1
      JJA=1
      JJM=1
      C(1)=1.
C simulated element
    2 WRITE(6,102)
  102 FORMAT(' Atomic number ? ')
      READ(5,201,ERR=2) NZ(1)
  201 FORMAT(I6)
    3 WRITE(6,103)
  103 FORMAT(' Atom weight ? ')
      READ(5,200,ERR=3) A(1)
    4 WRITE(6,104)
  104 FORMAT(' Excitation voltage (kV) ? ')
      READ(5,200,ERR=4) VK(1)
    5 WRITE(6,105)
  105 FORMAT(' Is it a pure target ( Y or N ) Def[Y] ? ')
      READ(5,202,ERR=5) QU
  202 FORMAT(A1)
      IF((QU.NE.'N').AND.(QU.NE.'n')) GO TO 20
C Complex target
    7 WRITE(6,106)
  106 FORMAT(' Weight fraction of the calculated element ? ')
      READ(5,200,ERR=7) C(1)
    8 WRITE(6,107)
  107 FORMAT(' Number of companions  ? ')
      READ(5,201,ERR=8) JJD
      IF(JJD.LE.0) GO TO 8
      JJM=JJD+1
```

```
C Companions
      DO 9 J=1,JJD

      WRITE(6,108) J
  108 FORMAT('         Companion no.',I2)
   10 WRITE(6,102)
      READ(5,201,ERR=10) NZ(J+1)
   11 WRITE(6,103)
      READ(5,200,ERR=11) A(J+1)
   12 WRITE(6,104)
      READ(5,200,ERR=12) VK(J+1)
   13 WRITE(6,109)
  109 FORMAT(' Weight fraction ? ')
      READ(5,200,ERR=13) C(J+1)

    9 CONTINUE
C Parameters of the Simulation
C Xray range is employed -> nswr=2
   20 NSWR=2

C NUM is the number of simulated trajectories
C NPAS is the number of steps dividing the range
   21 WRITE(6,110) MMP-13
  110 FORMAT(' Number of steps  (< ',I3,' ? ')
      READ(5,201,ERR=21) NPAS
      IF((NPAS.LE.0).OR.(NPAS.GT.45)) GO TO 21
   22 WRITE(6,111)
  111 FORMAT(' Number of traectories ? ')
      READ(5,201,ERR=22) NUM
      ANUM=NUM
C Display input
      WRITE(6,112)
  112 FORMAT('        Target identification'/
     &' no.      Z         A        EK        C              ')
      WRITE(6,113)
  113 FORMAT(/)
      WRITE(6,203)  (J,NZ(J),A(J),VK(J),C(J),J=1,JJM)
203   FORMAT(2X,I2,3X,I3,4X,F6.2,4X,F7.4,4X,F6.4)
      WRITE(6,204) EO,NPAS,NUM
  204 FORMAT('        Simulation parameters'/
     &' Acceleration voltage :',F6.3/
     &' Number of steps       :',I3/
     &' Number of trajectories :',I6)
C Proceed to mc calculation
      DO 123 I=1,94
      READ(8,124) IX(I),YY1(I),YY2(I),YY3(I),YY4(I)
  124 FORMAT(3X,I2,4(4X,F10.7))
  123 CONTINUE
      CONC=YY1(NZ(1))
      COND=YY2(NZ(1))
      CONE=YY3(NZ(1))
      CONF=YY4(NZ(1))
      WRITE(7,125) CONC,COND,CONE,CONF
  125 FORMAT(3X,4(3X,F10.7))
      DO 126 I=1,94
      READ(9,127) IX(I),YY5(I),YY6(I),YY7(I),YY8(I)
  127 FORMAT(3X,I2,3X,F8.6,3(3X,F13.10))
  126 CONTINUE
      COC=YY5(NZ(1))
      COD=YY6(NZ(1))
      COE=YY7(NZ(1))
      COF=YY8(NZ(1))
      WRITE(7,128) COC,COD,COE,COF
  128 FORMAT(3X,F8.6,3(3X,F13.10))
```

```
      CALL RESU(JO,JJM,JJA,ANUM,NPAS,NSWR,CONC,COND
     &,CONE,CONF,COC,COD,COE,COF)
      CLOSE(UNIT=9)
      CLOSE(UNIT=8)
      CLOSE(UNIT=7)
      STOP
      END
C Control the simulation and output some balance
      SUBROUTINE RESU(JO,JM,JJA,ANUM,NPAS,NSWR,CONC,COND
     &,CONE,CONF,COC,COD,COE,COF)
      PARAMETER (ME=9)
      PARAMETER (MP=200)
      PARAMETER (MPP=401)
      PARAMETER (MMP=64)
C     PARAMETER (MAG=128)
      CHARACTER*2 SYMB(ME),ATSY(100)
      DIMENSION NZ(ME),A(ME),VK(ME),C(ME),EN(MPP),IXF(MMP,MP),
     &IXB(MMP,MP),IBAC(MP),IBB(MP),ROZ(MMP),PHI(MMP),ALOPHI(MMP)
      DIMENSION ALP(MP),EFFZ(ME)
      COMMON NZ,A,VK,C,EO,RANGE,E14,EN,IXF,IXB,IBAC,IBB,ROZ,PHI,ISTART
      COMMON ALP,EFFZ
C     COMMON/LUI/LU5,LU6,LU7
      DATA ATSY/'H','HE','LI','BE','B','C','N','O','N','NE','NA','MG'
     &,'AL','SI','P','S','CL','AR','K','CA','SC','TI','V','CR','MN'
     &,'FE','CO','NI','CU','ZN','GA','GE','AS','SE','BR','KR'
     &,'RB','SR','Y','ZR','NB','MO','TC','RU','RH','PD','AG','CD','IN'
     &,'SN','SB','TE','I','XE','CS','BA','LA','CE','PR','ND','PM','SM'
     &,'EU','GD','TB','DY','HO','ER','TM','YB','LU','HF','TA','W','RE'
     &,'OS','IR','PT','AU','HG','TI','PB','BI','PO','AT','RN','FR','RA'
     &,'AC','TH','PA','U','NP','PU','AM','CM','BK','CF','ES','FM'/
      WRITE(7,200) JM
  200 FORMAT(1X,I2,' <- Number of elements')
      WRITE(7,201)
  201 FORMAT(' Atom symbol(s) and weight fraction(s)')
      DO 1 J=JO,JM
      I=NZ(J)
      SYMB(J)=ATSY(I)
    1 CONTINUE
      WRITE(7,202) (SYMB(J),C(J),J=JO,JM)
  202 FORMAT(10(3X,A2,':',F6.4))
      WRITE(7,203) NPAS
  203 FORMAT(1X,I3,' <- Number of steps')
      NUM=ANUM
      WRITE(7,204) NUM
  204 FORMAT(1X,I6,' <- Number of trajectories')
      WRITE(7,205) EO
  205 FORMAT(1X,F5.2,' <- Acceleratlon voltage')
      WRITE(7,*) JJA
C     Trajectory sampling
      CALL E10(JO,JM,JJA,ANUM,NPAS,NSWR,RETRO1,RETRO2
     &,CONC,COND,CONE,CONF,COC,COD,COE,COF)
      RANG3=1000.*RANGE
      WRITE(7,206) RANG3
  206 FORMAT(1X,E15.8,' <- Range ( mg/cm2 )')
      WRITE(7,207)
  207 FORMAT(' Half step and full step energies')
      DO 2 I=1,MP,5
      J=I+MP+1
      WRITE(7,208) I,EN(I),EN(J)
    2 CONTINUE
  208 FORMAT(I3,3X,2(4X,F6.3))
      NPASS=2*MP+1
      TOT1=0.0
      DO 118 I=1,MP
```

```
C     WRITE(7,*) IBAC(I),IBB(I)
      TOT1=TOT1+IBAC(I)
 118  CONTINUE
      WRITE(7,*) TOT1
C Output electron distribution
      WRITE(7,209)
 209  FORMAT(' Electron distribution')
      CALL PRINT(NPAS)
C     WRITE(7,210) (IBB(I),I=1,MP)
C210  FORMAT(' BB',12(3X,I6))
      IF(NSWR.EQ.2) GO TO 23
      WRITE(7,211) RETRO1,RETRO2
 211  FORMAT(1X,F7.4,4X,F7.4,' <- Retrol , Retro2')
C Xray from Derian target
C     CALL XRAB(JJA,ALOPHI,NPAS,ANUM,NPASS,RXB,RXBO,RXBBO)
C     WRITE(7,212)
C212  FORMAT(' Derian target distribution')
C     DO 3 J=1,NPASS
C     WRITE(7,213) J,ROZ(J),ALOPHI(J)
C  3  CONTINUE
 213  FORMAT(1X,I3,3X,2(6X,E15.8))
C     WRITE(7,214) RXB,RXBO,RXBBO
C214  FORMAT(1X,3(E15.8,4X),'<- RXB,RXBO,RXBBO')
C     X-RAY FROM THE REGULAR TARGET
  23  CALL XRAF(JJA,ALOPHI,NPAS,ANUM,NPASS,RXF,RXFO)
      WRITE(7,215)
  215 FORMAT(' Phi(roz) distributlon')
      DO 4 J=1,NPASS
      WRITE(7,213) J,ROZ(J),ALOPHI(J)
   4  CONTINUE
C TOTAL AMOUNT
      WRITE(7,216) RXF,RXFO
  216 FORMAT(1X,2(E15.8,4X),' <- RXF,RXFO')
      RXFO=RXF+RXB+RXBBO
      RXBO=RXB+RXBBO
      WRITE(7,217) RXFO,RXBO
  217 FORMAT(1X,2(E15.8,4X),' <- RXF+RXB+RXBBO , RXB+RXBBO')
      RETURN
      END
C E10
C                    RoutineE10
C          Argument list
C input : JO      index of the first element of the target
C       : JJA     index of the calculated element
C       : JM      index of the last element of the target

C       : ANUM    number of trajectories (real)

C       : NPAS number of intervals dlviding the range
C       : NSWR lf 1 :-full range ; if 2 : xrays range
C output: RETRO1 backscattering coefficient
C       : RETRO2 fraction of electrons entering again the target
C               ( forw - back -> forw )
C        common
C scalar: E14 electron encrgy at the surface layer
C       : ISTART seed of the pseudo random number selector
C array : NZ       atomic numbers
C       : A       atom weights
C       : VK       excitation potentials
C       : C       weight fractions
C       : EO      incident electron energies
C       : EN      half step and full step electron mean energies
C       : IXF     table of transmited electrons
C       : IXB       " backscattered electrons
```

```
C       : IBAC    energy distribution of backscattered electrons
C       : IBB     the same as before (2th backscat. )
C       : ROZ     depth ( in mass thickness unit )
C       : PHI     phi-ro-z
C        parameters
C
C          ME      maximum number of elements in the target
C          MP      number of steps
C         MPP      dimension of the energy table
C         MAG      number of angles of equal scattering probability
C
C         function
C
C          EI       exponential integral
C          URAN     pseudo random number selector
C
      SUBROUTINE E10(JO,JM,JJA,ANUM,NPAS,NSWR,RETRO1,RETRO2
     &,CONC,COND,CONE,CONF,COC,COD,COE,COF)
      PARAMETER (ME=9)
      PARAMETER (MP=200)
      PARAMETER (MPP=401)
      PARAMETER (MMP=64)
C     PARAMETER (MAG=128)
      PARAMETER (NRD=3)
      DIMENSION NZ(ME),A(ME),VK(ME),C(ME),EN(MPP),AB(ME),
     &AC(ME),GA(4),RD(NRD),JJJ(99),ALP(MP),EFFZ(ME),LIM(99),N(99)
      DIMENSION IXF(MMP,MP),IXB(MMP,MP),IBAC(MP),IBB(MP),PHI(MMP),
     &P(MP),RES(MP),ROZ(MMP)
C     DIMENSION ABCD(50,MP)
      COMMON NZ,A,VK,C,EO,RANGE,E14,EN,IXF,IXB,IBAC,IBB ROZ,PHI,ALP
      COMMON EFFZ
C     COMMON/LUI/LU5,LU6,LU7
      DATA NMAX1,NAN,PI,P180/128,128,3.14159265,.174532925E-1/
C
C ECRAN is a constant used in the calculation of the screening parameter
      DATA ECRAN/1./
      DATA ISTART/490623069/
C
C Statement function calculating sine from cosine in argument
      SI(X)=SQRT(1.-X**2)
  100 FORMAT(' WARNING - Slow convergence for step no.',I3)
C      NUM : number of sampled trajectories
C       ED : the popular constant of the Bethe's formula (1.166)
C       BB : real converion of the atomic number of the emitting element
C       AA : mean ionizatlon potentiel of the emitting element
      NUM=ANUM
      ED=SQRT(EXP(1.)/2.)
      BB=NZ(JJA)
      AA=(9.76*BB+58.5/BB**.19)/1000.
C Determination of a minimum energy limit for calculatlng the
C  Bethe,s range
C   first find the greater mean ionization potential
C
      DO 15 JJ=JO,JM
      BB=NZ(JJ)
      AB(JJ)=A(JJ)/(7.85E4*(BB**1.00)*C(JJ))
      AC(JJ)=(9.76*BB+58.5/BB**.19)/1000.
      IF(AC(JJ).GT.AA) AA=AC(JJ)
      AC(JJ)=ED/AC(JJ)
   15 CONTINUE
      GO TO (16,17),NSWR
C Lower limit for full range calculation
 16   ZA=1.03**AA
      GO TO 18
```

```
C Lower limit for xrays range calculation
   17 ZA=VK(JJA)
C Range calculation
   18 SM=.0
      ED=.0
      DO 19 JJ=JO,JM
      ED=ED+ALOG(AC(JJ))/AB(JJ)
      SM=SM+1./AB(JJ)
   19 CONTINUE
      ED=ED/SM
      V=EXP(ED)
      RANGE=1./SM/V**2*(EI(2.*(ED+ALOG(EO)))-
     &EI(2.*(ED+ALOG(ZA))))
C Calculation of half step and full step electron mean energies
      H=MP
      H=RANGE/H/4.
      AA=H/2.
      BB=H/6.
      EA=EO
      NPAS2=2*MP
      DO 20 I=1,NPAS2
      DO 11 J=1,2
      EB=EA
      DO 25 IP=1,4
      GA(IP)=.0
      DO 26 JJ=JO,JM
      GA(IP)=GA(IP)+ALOG(AC(JJ)*EB)/AB(JJ)/EB
   26 CONTINUE
      GO TO (27,27,28,25),IP
   27 EB=EA-AA*GA(IP)
      GO TO 25
   28 EB=EA-H*GA(IP)
   25 CONTINUE
      EA=EA-BB*(GA(1)+2.*(GA(2)+GA(3))+GA(4))
      IF(I.NE.1) GO TO 11
      IF(J.EQ.1) E14=EA
   11 CONTINUE
      EN(I)=EA
   20 CONTINUE
      IF(EN(NPAS2).LT.VK(JJA)) EN(NPAS2)=VK(JJA)
C Energy sorting
C                   EN(I) I 1 -> NPAS : half step mean energy
C                   EN(NPAS+1) : incident electron energy
C                   EN(I) I NPAS+2 -> 2*NPAS+2 : full step mean energy
      DO 12 I=2,MP
      EN(NPAS2+1)=EN(I)
      DO 12 J=I,NPAS2
      EN(J)=EN(J+1)
   12 CONTINUE
      EN(NPAS2+1)=EN(MP+1)
      EN(MP+1)=EO
      WRITE(7,*) E14
C     TRAJECTORY SAMPLING
C    TABLE INITIALIZATION
      DO 58 I=1,MP
      IBAC(I)=0
      IBB(I)=0
      ALP(I)=0.0
      DO 58 J=1,MMP
      IXF(J,I)=0
      IXB(J,I)=0
  58  CONTINUE
      DO 149 K=1,99
      JJJ(K)=0
```

```
 149   CONTINUE
C H IS THE INCIDENT ANGLE
       H=.0
       WONE=0.0
       TOTZ=0.0
       DO 613 JJ=JO,JM
       EFFZ(JJ)=0.0
  613  CONTINUE
       DO 614 JJ=JO,JM
       BB=NZ(JJ)
       WONE=WONE+C(JJ)*(1.+.8/BB)*(BB**(4./3.))/A(JJ)
  614  CONTINUE
       WONE=WONE*RANGE*1.E+06/0.443
       DO 615 JJ=JO,JM
       BB=NZ(JJ)
       EFFZ(JJ)=C(JJ)*(1.+.8/BB)*(BB**(4./3.))/A(JJ)
       TOTZ=TOTZ+EFFZ(JJ)
  615  CONTINUE
       ZEFF=0.0
       DO 616 JJ=JO,JM
       BB=NZ(JJ)
       ZEFF=ZEFF+EFFZ(JJ)/TOTZ*BB**(2./3.9)
  616  CONTINUE
       ZEFF=ZEFF**(3.9/2.)
       LIM(1)=6
       LIM(2)=7
       LIM(3)=9
       LIM(4)=12
       LIM(5)=15
       LIM(6)=20
       LIM(7)=25
       LIM(8)=32
       LIM(9)=40
       LIM(10)=49
       LIM(11)=59
       LIM(12)=72
       LIM(13)=87
       LIM(14)=102
       LIM(15)=120
       LIM(16)=140
       LIM(17)=160
       LIM(18)=184
       LIM(19)=207
       LIM(20)=231
       LIM(21)=255
       LIM(22)=279
       LIM(23)=302
       LIM(24)=324
       LIM(25)=343
       LIM(26)=362
       LIM(27)=376
       LIM(28)=387
       LIM(29)=396
       LIM(30)=399
       DC 157 I=31,60
       LIM(I)=LIM(61-I)
 157   CONTINUE
       RRD=0.0
       RII=0.0
       DO 297 J=1,99
       N(J)=0
  297  CONTINUE
       DO 59 IT=1,NUM
C start one trajectory
```

```
C   NSW1 1 -> electron moving in the forward direction
C   NSW1 2 -> backscattered electron
C   NSW2 1 -> the counter of backscattered has already been incremented
C   NSW2 1 -> the counter of backscattered must bee incremented
      NSW1=1
      NSW2=1
      Y=0.0
      AA=COS(H)
      IST=0
      JII=0
      STEP=0.0
  159 CALL URAN(ISTART,NRD,RD)
      RRD=(RD(1)-0.5)*6.0
      DO 762 II=1,60
      RII=II
      IF((RRD.LT.(RII/10.-3.)).AND.(RRD.GT.(RII/10.-3.1))) GO TO 763
      GO TO 762
  763 N(II)=N(II)+1
      IF(N(II).LE.LIM(II)) GO TO 999
      GO TO 159
  762 CONTINUE
  999 Y=0.5*(1.+0.56*(RD(1)-0.5))
      IST=(45.*(1.+0.56*(RD(1)-0.5)))+0.5
      J=Y+1.0
      I=1./FLOAT(IST)/4.*FLOAT(MP)+0.5
      IXF(J,I)=IXF(J,I)+1
      IF(IST.EQ.45) WRITE(5,*) IT,IST
      JJJ(1)=1./FLOAT(IST)/2.*FLOAT(MP)+0.5
      DO 35 K=2,IST
      KK=K-1
      STEP=IST
      JII=FLOAT(KK)*(1.-1./2./STEP)/(STEP-1.)*FLOAT(MP)+
     &1./FLOAT(IST)/2.*FLOAT(MP)+0.5
      JJJ(K)=JII
  35  CONTINUE
      STEPL=45./STEP
      DO 60 K=1,IST
      I=JJJ(K)
C "free path" sampling
      CALL URAN(ISTART,NRD,RD)
      BB=RD(1)
      Y=Y+AA*BB/STEPL
      IF(Y.GT.0.) GO TO 47
C move backward
      IF(NSW1.EQ.2) GO TO 62
      NSW1=2
      NSW2=2
      GO TO 62
C move forward
   47 IF(NSW1.EQ.2) GO TO 61
C deflection sampling
C   62 ALP(I)=(1.+.8/Z)**1.3*(RANGE*1.E+06/FLOAT(IST))**1.3
C     &*(Z**2.4)*4.34E-03/((.443*AAA)**1.3)/(EN(I)**2.3)
C   62 IF(K.GE.2) GO TO 911
   62 ALP(I)=4.34E-03*ZEFF**(2./3.)*(WONE**1.3)/45.0**1.3
     &/(EN(I+MP+1)**2.30)
C     GO TO 912
C 911 ALP(I)=(WONE*(1.-1./2./FLOAT(IST))/(FLOAT(IST)-1.))**(1.3)
C    &*4.34E-03*ZEFF**(2./3.)/(EN(I+MP+1)**2.30)
      C1=1.-(2.*ALP(I)*RD(2))/(1.+ALP(I)-RD(2))
      C1=(ACOS(C1))*180.0/PI
      E1=30.0
      ALPH=10.0**(CONC+COND*ALOG10(E1)+CONE*ALOG10(E1)**2
     &+CONF/(EXP(ALOG10(E1))))
```

```
      BETA=COC+COD*SQRT(E1)*ALOG(E1)+COE*ALOG(E1)/E1
     &+COF/E1
      IF(BETA.GT.1.0)  BETA=1.0
      RMAX=(COS(180.0**BETA/180.0*PI)-1.0)*(1.0+ALPH)/
     &(COS(180.0**BETA/180.0*PI)-1.0-2.0*ALPH)
      RSTAR=RMAX*RD(2)
      AMCO=COS((ACOS(1.0-2.0*ALPH*RSTAR/(1.0+ALPH-RSTAR))
     &*180.0/PI)**(1.0/BETA)*PI/180.0)
      AMSCO=(ACOS(AMCO))*180.0/PI
      ALPH=4.34E-03*ZEFF**(2./3.)/E1
      ARSCO=1.0-2.0*ALPH*RD(2)/(1.+ALPH-RD(2))
      ARSCO=(ACOS(ARSCO))*180.0/PI
      C1=C1+(AMSCO-ARSCO)
      C1=COS(C1*PI/180.0)
      C2=SI(C1)
      C3=COS(2*PI*RD(3))
      AA=AA*C1+SI(AA)*C2*C3
      Y=Y+(1.-BB)*AA/STEPL
      IF(Y.LE.0.) GO TO(49,48),NSW1
      GO TO (63,61),NSW1
C update the table of electron position inside the target
   63 J=Y+1.0
      IXF(J,I)=IXF(J,I)+1
      GO TO 60
C backscattered electron
   49 NSW1=2
      NSW2=2
C update the table of electron position outide the target
C           ( simulation of the Derian experiment )
   48 J=Y-1.5
      J=-J
      IXB(J,I)=IXB(J,I)+1
      GO TO (60,67),NSW2
  67  IBAC(I)=IBAC(I)+1
      NSW2=1
  60  CONTINUE
      GO TO 59
C again in the target after being backscattered
   61 IF(NSW2.EQ.2) IBAC(I)=IBAC(I)+1
      IBB(I)=IBB(I)+1
   59 CONTINUE
C     CALCULATION OF BACKSCATTERING COEFFICIENTS
      IF(NSWR.EQ.2) GO TO 23
      RETRO1=.0
      RETRO2=.0
      DO 33 I=1,MP
      C1=IBAC(I)
      RETRO1=RETRO1+C1
      C1=IBB(I)
      RETRO2=RETRO2+C1
C     WRITE(7,*) IBAC(I),IBB(I)
   33 CONTINUE
      RETRO1=RETRO1/ANUM
      RETRO2=RETRO2/ANUM
      WRITE(7,*) RETRO1,RETRO2
   23 RETURN
      END
C PRINT
      SUBROUTINE PRINT(NPAS)
      PARAMETER (ME=9)
      PARAMETER (MP=200)
      PARAMETER (MPP=401)
      PARAMETER (MMP=64)
      DIMENSION NZ(ME),C(ME),A(ME),VK(ME),EN(MPP),IXF(MMP,MP),MOREB(99)
```

```
     &,IXB(MMP,MP),IBAC(MP),IBB(MP),ROZ(MMP),PHI(MMP),MORE(99,99)
      COMMON NZ,A,VK,C,EO,RANGE,E14,EN,IXF,IXB,IBAC,IBB,ROZ,PHI,ISTART
      COMMON/LUI/LU5,LU6,LU7
  1U3 FORMAT(1X,3X,10(3X,I3))
  101 FORMAT(1X,I3,10(1X,I5),1X,I5,1X,I5)
  111 FORMAT(' BS',10(1X,I5),1X,I5,1X,I5)
      DO 150 I=1,99
      MOREB(I)=0
      DO 149 J=1,99
      MORE(J,I)=0
  149 CONTINUE
  150 CONTINUE
      IS=10
      NTA=MP/IS
      IF(NTA.NE.0) GO TO 10
      IMIN=1
      GO TO 50
   10 DO 15 IT=1,NTA
      IADD=0
      IMIN=(IT-1)*IS
      IMAX=IS+IMIN
      IMIN=IMIN+1
      WRITE(7,103) (I,I=IMIN,IMAX)
C     DO 31 J=1,NPAS
C     K=NPAS+1-J
C     WRITE(7,101) K,(IXB(K,I),I=IMIN,IMAX)
C  31 CONTINUE
      DO 332 I=IMIN,IMAX
      IADD=IADD+IBAC(I)
  332 CONTINUE
      IF(IT.EQ.1) GO TO 168
      GO TO 169
  168 MOREB(IT)=IADD
      GO TO 170
  169 MOREB(IT)=MOREB(IT-1)+IADD
  170 WRITE(7,111) (IBAC(I),I=IMIN,IMAX),IADD,MOREB(IT)
      DO 334 J=1,MMP
      IADDD=0
      DO 333 I=IMIN,IMAX
      IADDD=IADDD+IXF(J,I)
 333  CONTINUE
      IF(IT.EQ.1)  GO TO 171
      GO TO 172
 171  MORE(J,IT)=IADDD
      GO TO 173
 172  MORE(J,IT)=MORE(J,(IT-1))+IADDD
 173  WRITE(7,101) J,(IXF(J,I),I=IMIN,IMAX),IADDD,MORE(J,IT)
      IF(IADDD.EQ.0)  GO TO 15
 334  CONTINUE
  15  CONTINUE
      IF(MP-IS*(MP/IS).EQ.0) GO TO 20
      IMIN=IMAX+1
  50  WRITE(7,103) (I,I=IMIN,MP)
C     DO 34 J=1,NPAS
C     K=NPAS+1-J
C     WRITE(7,101) K,(IXB(K,I),I=IMIN,NPAS)
C 34  CONTINUE
      WRITE(7,111) (IBAC(I),I=IMIN,MP)
      DO 32 J=1,MMP
      WRITE(7,101) J,(IXF(J,I),I=IMIN,MP)
  32  CONTINUE
  20  RETURN
      END
C EXPONENTIAL INTEGRAL
```

```
      FUNCTION EI(X)
      EI=ALOG(X)+X
      TN=X
      N=1
  300 AN=N
      IF(AN.GT.2.*X.AND.TN.LT.1.E-06) GO TO 400
      TN=TN*X*AN/(AN+1.)**2
      EI=EI+TN
      N=N+1
      GO TO 300
  400 RETURN
      END
C Select three random numbers - RAN is a system library function
C  ISTART : seed
C  NRD : number of sampled random numbers
C  RD       : random numbers in the range ( 0.,1. ), limits excluded
      SUBROUTINE URAN(ISTART,NRD,RD)
      DIMENSION RD(NRD)
      DO 1 I=1,NRD
    2 RD(I)=RAN(ISTART)
      IF((RD(I).GT.0.).AND.(RD(I).LT.1.)) GO TO 1
      GO TO 2
    1 CONTINUE
      RETURN
      END
      FUNCTION RAN(L)
      L=MOD(16807*L,2147483647)
      RAN=REAL(L)*4.6566128752459E-10
      RETURN
      END
C Calculation of Xray depth distribution in the target
C     Output:
C               ALOPHI log(phi(roz)
C               RXF total xray generation inside the target
C               RXFO total xray that would be generated inside
C                     the target in the absence of backscattering
C               NPASS index of the last layer giving a significant
C                     contribution
      SUBROUTINE XRAF(JJA,ALOPHI,NPAS,ANUM,NPASS,RXF,RXFO)
      PARAMETER (ME=9)
      PARAMETER (MP=200)
      PARAMETER (MPP=401)
      PARAMETER (MMP=64)
C     PARAMETER (MAG=128)
      DIMENSION NZ(ME),A(ME),VK(ME),C(ME),EN(MPP),IXF(MMP,MP),ALP(MP),
     &IXB(MMP,MP),IBAC(MP),IBB(MP),ROZ(MMP),PHI(MMP),ALOPHI(MMP)
      COMMON NZ,A,VK,C,EO,RANGE,E14,EN,IXF,IXB,IBAC,IBB,ROZ,PHI,ISTART
      COMMON ALP,EFFZ
      FOWE=0.8
      COISO=1./EO**POWE/VK(JJA)**(2.-POWE)
     &*ALOG(EO/VK(JJA))
      NSW=1
      NPASS=MMP
C     PHI(1)=1./E14**POWE/VK(JJA)**(2.-POWE)
C    &*ALOG(E14/VK(JJA))
      PHI(1)=0.0
      RPAS=NPAS
      ROZ(1)=RANGE/RPAS/2.
      RXFO=.0
      DO 9 I=1,MP
      K=I
      IF(EN(K)/VK(JJA).LE.1.) GO TO 30
      AA=IXF(1,I)
      PHI(1)=PHI(1)+AA/ANUM/EN(K)**POWE/VK(JJA)**(2.-POWE)
```

```
     &*ALOG(EN(K)/VK(JJA))
   9 CONTINUE
     I=MMP
  30 NPAS1=I
     NPAS2=MP
     ALOPHI(1)=ALOG10(PHI(1)/COISO)
     RXF=PHI(1)/2.
     DO 10 J=2,NPAS1
     PHI(J)=.0
     J1=J-1
     RXFO=RXFO+1./EN(J1)/VK(JJA)*ALOG(EN(J1)/VK(JJA))
     GO TO (4,10),NSW
   4 ROZ(J)=J1
     ROZ(J)=ROZ(J)*RANGE/RPAS
     DO 11 I=J1,NPAS2
     K=I
     AA=IXF(J,I)
     PHI(J)=PHI(J)+AA/ANUM/EN(K)**POWE/VK(JJA)**(2.-POWE)
     &*ALOG(EN(K)/VK(JJA))
  11 CONTINUE
     IF(PHI(J).EQ.0.) GO TO 24
     ALOPHI(J)=ALOG10(PHI(J)/COISO)
     RXF=RXF+PHI(J)
     GO TO 10
  24 NPASS=J-1
     NSW=2
  10 CONTINUE
     IF(EN(NPAS1)/VK(JJA).GT.1.) RXFO=RXFO+1./EN(NPAS1)/VK(JJA)
     &*ALOG(EN(NPAS1)/VK(JJA))
     AA=RANGE/COISO/RPAS
     RXF=RXF*AA
     RXFO=RXFO*AA
     RETURN
     END
```

APPENDIX 3

FORTRAN PROGRAM TO CALCULATE THIN FILM $\phi(\rho z)$ CURVES BY THE MONTE CARLO METHOD

```
cccccccccccccccccccccccccccccccccccccccccccccccccccccccccccccccccccccccccccc
c
c This program calculates film ϕ(ρz) curves based on Rutherford multiple scattering
c  angles by Werner and Heydenreich from a set of input parameters which include:-
c     EO :  Incident electron energy
c     VK : Critical excitation potential
c     NZ :  Film atomic number
c       A :  Film atomic weight
c THICK: Thickness of film in μg/cm2
c      ZS : Substrate atomic number
c      AS: Substrate atomic weight
c   NPAS:  Number of steps
c    NUM:  Number of trajectories
c
c The output will be stored in a file named 'DUM.DAT' which include an electron
c energy table (EN(200)) for the film, an electron distribution table (IXF(79,200)) for
c  the film and data to calculate the film ϕ(ρz) curve (ROZ(79), PHI(79))
c
c The computation process can be summarized in the following way:-
c  1) Read in the initial input parameters
c  2) Calculate the mean ionization potential using the expression from Berger and
c       Seltzer
c  3) Calculate the x-ray range with lower limit of integration set to critical excitation
c       potential
c  4) Use Runge Kutta method to determine and store electron energies at each step
c       in the electron energy table for the film medium as if it was a bulk target
c  5) Read in data from a previously stored substrate electron energy table
```

```
c  6) Start the first electron trajectory using normal incident angle
c  7) Introduce electron straggling so that the previously calculated step size for each
c      trajectory will be subject to change according to a gaussian distribution of values
c  8) Calculate the electron scattering angle using the expression from Werner and
c       Heydenreich after each interaction.  The first interaction is assumed to occur in
c       the film
c  9) Calculate the azimuthal angle
c 10) Check the new electron position, if the position is negative, then the electron is
c      considered backscattered and the corresponding counter is incremented.  If the
c      position is positive, then still need to check if it is smaller or larger than the film
c      thickness.  If smaller, data from the film need to be substituted into the Werner
c      and Heydenreich expression to calculate the scattering angle, also the position
c      and energy of the electron are updated and stored in the film electron
c      distribution table.  If larger, data from the substrate were used instead to
c      calculate the scattering angle.  The position and energy of the electron will be
c      updated but will not be stored in any table.
c 11) For the same trajectory, calculate the next new electron position by finding a
c      new scattering angle and azimuthal angle.  This process will continue until the
c      electron is backscattered from the target or the electron energy falls below the
c      critical excitation potential and that could occur either in the film or substrate
c 12) Start the next electron trajectory and continue until all trajectories are complete
c 13) Calculate the film φ(ρz) curve using the data from the film electron distribution
c       table since the number of electrons and the energy of each electron is known in
c       each and every layer in the film
c
cccccccccccccccccccccccccccccccccccccccccccccccccccccccccccccccccccccccccccccc
```

```
      PROGRAM THIN23
      PARAMETER(ME=9)
      PARAMETER (MP=200)
      PARAMETER (MPP=401)
      PARAMETER (MMP=79)
C     PARAMETER (MAG=128)
      CHARACTER*1 QU
      DIMENSION NZ(ME),C(ME),A(ME),VK(ME),ENS(MPP),IX(MP)
      DIMENSION EN(MPP),IXF(MMP,MP),IXB(2,2),IBAC(MP),IBB(MP)
     &,ROZ(MMP),PHI(MMP)
      DIMENSION ALP(MP),EFFZ(ME),ALPS(MP)
      COMMON ENS
      COMMON NZ,A,VK,C,EO,RANGE,E14,EN,IXF,IXB,IBAC,IBB,ROZ,PHI,ISTART
      COMMON ALP,EFFZ
C     COMMON/LUI/LU5,LU6,LU7
C     DATA LU5,LU6,LU7/5,5,7/
C     DATA ISTART/490623069/
      OPEN(UNIT=7,FILE='DUM.DAT')
      OPEN(UNIT=8,FILE='ENE24.TXT')
      OPEN(6,FILE='CON')
      OPEN(5,FILE='CON')
C Input
    1 WRITE(6,100)
  100 FORMAT(' Acceleration voltage (kV) ? ')
      READ(5,200,ERR=1) EO
  200 FORMAT(F12.0)
      WRITE(6,101)
  101 FORMAT(' Input constants of elements present in the target'/
     &' the simulation will be done for the first input element')
C Initialization for pure target
      JO=1
      JJA=1
      JJM=1
      C(1)=1.
C simulated element
    2 WRITE(6,102)
  102 FORMAT(' Atomic number ? ')
      READ(5,201,ERR=2) NZ(1)
  201 FORMAT(I6)
    3 WRITE(6,103)
  103 FORMAT(' Atom weight ? ')
      READ(5,200,ERR=3) A(1)
    4 WRITE(6,104)
  104 FORMAT(' Excitation voltage (kV) ? ')
      READ(5,200,ERR=4) VK(1)
    5 WRITE(6,105)
  105 FORMAT(' Is it a pure target ( Y or N ) Def[Y] ? ')
      READ(5,202,ERR=5) QU
  202 FORMAT(A1)
      IF((QU.NE.'N').AND.(QU.NE.'n')) GO TO 20
C Complex target
    7 WRITE(6,106)
  106 FORMAT(' Weight fraction of the calculated element ? ')
      READ(5,200,ERR=7) C(1)
    8 WRITE(6,107)
  107 FORMAT(' Number of companions  ? ')
      READ(5,201,ERR=8) JJD
      IF(JJD.LE.0) GO TO 8
      JJM=JJD+1
C Companions
```

```
      DO 9 J=1,JJD

      WRITE(6,108) J
  108 FORMAT('       Companion no.',I2)
   10 WRITE(6,102)
      READ(5,201,ERR=10) NZ(J+1)
   11 WRITE(6,103)
      READ(5,200,ERR=11) A(J+1)
   12 WRITE(6,104)
      READ(5,200,ERR=12) VK(J+1)
   13 WRITE(6,109)
  109 FORMAT(' Weight fraction ? ')
      READ(5,200,ERR=13) C(J+1)

    9 CONTINUE
C Parameters of the Simulation
C Xray range is employed -> nswr=2
   20 NSWR=2

C NUM is the number of simulated trajectories
C NPAS is the number of steps dividing the range
   21 WRITE(6,110) MMP+51
  110 FORMAT(' Number of steps  (< ',I3,' ? ')
      READ(5,201,ERR=21) NPAS
      IF((NPAS.LE.0).OR.(NPAS.GT.130)) GO TO 21
   22 WRITE(6,111)
  111 FORMAT(' Number of traectories ? ')
      READ(5,201,ERR=22) NUM
      ANUM=NUM
C Display input
      WRITE(6,112)
  112 FORMAT('      Target identification'/
     &' no.     Z        A       EK       C             ')
      WRITE(6,113)
  113 FORMAT(/)
      WRITE(6,203) (J,NZ(J),A(J),VK(J),C(J),J=1,JJM)
203   FORMAT(2X,I2,3X,I3,4X,F6.2,4X,F7.4,4X,F6.4)
      WRITE(6,204) EO,NPAS,NUM
  204 FORMAT('      Simulation parameters'/
     &' Acceleration voltage :',F6.3/
     &' Number of steps       :',I3/
     &' Number of trajectories :',I6)
C Proceed to mc calculation
      DO 123 I=1,200
      READ(8,124) IX(I),ENS(I),ENS(I+201)
  124 FORMAT(I3,3X,2(4X,F6.3))
  123 CONTINUE
      CALL RESU(JO,JJM,JJA,ANUM,NPAS,NSWR)
      CLOSE(UNIT=8)
      CLOSE(UNIT=7)
      STOP
      END
C Control the simulation and output some balance
      SUBROUTINE RESU(JO,JM,JJA,ANUM,NPAS,NSWR)
      PARAMETER (ME=9)
      PARAMETER (MP=200)
      PARAMETER (MPP=401)
      PARAMETER (MMP=79)
C     PARAMETER (MAG=128)
      CHARACTER*2 SYMB(ME),ATSY(100)
      DIMENSION NZ(ME),A(ME),VK(ME),C(ME),EN(MPP),IXF(MMP,MP),
     &IXB(2,2),IBAC(MP),IBB(MP),ROZ(MMP),PHI(MMP),ALOPHI(MMP)
      DIMENSION ALP(MP),EFFZ(ME),ALPS(MP),ENS(MPP)
      COMMON ENS
```

```
      COMMON NZ,A,VK,C,EO,RANGE,E14,EN,IXF,IXB,IBAC,IBB,ROZ,PHI,ISTART
      COMMON ALP,EFFZ
C     COMMON/LUI/LU5,LU6,LU7
      DATA ATSY/'H','HE','LI','BE','B','C','N','O','N','NE','NA','MG'
     &,'AL','SI','P','S','CL','AR','K','CA','SC','TI','V','CR','MN'
     &,'FE','CO','NI','CU','ZN','GA','GE','AS','SE','BR','KR'
     &,'RB','SR','Y','ZR','NB','MO','TC','RU','RH','PD','AG','CD','IN'
     &,'SN','SB','TE','I','XE','CS','BA','LA','CE','PR','ND','PM','SM'
     &,'EU','GD','TB','DY','HO','ER','TM','YB','LU','HF','TA','W','RE'
     &,'OS','IR','PT','AU','HG','TI','PB','BI','PO','AT','RN','FR','RA'
     &,'AC','TH','PA','U','NP','PU','AM','CM','BK','CF','ES','FM'/
      WRITE(7,200) JM
  200 FORMAT(1X,I2,' <- Number of elements')
      WRITE(7,201)
  201 FORMAT(' Atom symbol(s) and weight fraction(s)')
      DO 1 J=JO,JM
      I=NZ(J)
      SYMB(J)=ATSY(I)
    1 CONTINUE
      WRITE(7,202) (SYMB(J),C(J),J=JO,JM)
  202 FORMAT(10(3X,A2,':',F6.4))
      WRITE(7,203) NPAS
  203 FORMAT(1X,I3,' <- Number of steps')
      NUM=ANUM
      WRITE(7,204) NUM
  204 FORMAT(1X,I6,' <- Number of trajectories')
      WRITE(7,205) EO
  205 FORMAT(1X,F5.2,' <- Acceleratlon voltage')
      WRITE(7,*) JJA
C     Trajectory sampling
      CALL E10(JO,JM,JJA,ANUM,NPAS,NSWR,RETRO1,RETRO2)
      RANG3=1000.*RANGE
      WRITE(7,206) RANG3
 206  FORMAT(1X,E15.8,' <- Range ( mg/cm2 )')
      WRITE(7,207)
 207  FORMAT(' Half step and full step energies')
      DO 2 I=1,MP
      J=I+MP+1
      WRITE(7,208) I,EN(I),EN(J),ENS(I),ENS(J)
 2    CONTINUE
  208 FORMAT(I3,3X,4(4X,F6.3))
      NPASS=2*MP+1
      TOT1=0.0
      DO 118 I=1,MP
C     WRITE(7,*) IBAC(I),IBB(I)
      TOT1=TOT1+IBAC(I)
 118  CONTINUE
      WRITE(7,*) TOT1
C Output electron distribution
      WRITE(7,209)
 209  FORMAT(' Electron distribution')
      CALL PRINT(NPAS)
C     WRITE(7,210) (IBB(I),I=1,MP)
C210  FORMAT(' BB',12(3X,I6))
      IF(NSWR.EQ.2) GO TO 23
      WRITE(7,211) RETRO1,RETRO2
 211  FORMAT(1X,F7.4,4X,F7.4,' <- Retro1 , Retro2')
C Xray from Derian target
C     CALL XRAB(JJA,ALOPHI,NPAS,ANUM,NPASS,RXB,RXBO,RXBBO)
C     WRITE(7,212)
C212  FORMAT(' Derian target distribution')
C     DO 3 J=1,NPASS
C     WRITE(7,213) J,ROZ(J),ALOPHI(J)
C  3  CONTINUE
```

```
 213   FORMAT(1X,I3,3X,2(6X,E15.8))
C      WRITE(7,214) RXB,RXBO,RXBBO
C214   FORMAT(1X,3(E15.8,4X),'<- RXB,RXBO,RXBBO')
C      X-RAY FROM THE REGULAR TARGET
  23   CALL XRAF(JJA,ALOPHI,NPAS,ANUM,NPASS,RXF,RXFO)
       WRITE(7,215)
  215 FORMAT(' Phi(roz) distribution')
       THICK=50.000
       THICK=THICK*130./(RANGE*1.E+06)
       JCAL=THICK+1.0
       DO 4 J=1,JCAL
       WRITE(7,213) J,ROZ(J),ALOPHI(J)
   4   CONTINUE
C TOTAL AMOUNT
       WRITE(7,216) RXF,RXFO
  216 FORMAT(1X,2(E15.8,4X),' <- RXF,RXFO')
       RXFO=RXF+RXB+RXBBO
       RXBO=RXB+RXBBO
       WRITE(7,217) RXFO,RXBO
  217 FORMAT(1X,2(E15.8,4X),' <- RXF+RXB+RXBBO , RXB+RXBBO')
       RETURN
       END
C E10
C                        RoutineE10
C            Argument list
C input : JO        index of the first element of the target
C       : JJA       index of the calculated element
C       : JM        index of the last element of the target

C       : ANUM      number of trajectories (real)

C       : NPAS number of intervals dividing the range
C       : NSWR lf 1 :-full range ; if 2 : xrays range
C output: RETRO1 backscattering coefficient
C       : RETRO2 fraction of electrons entering again the target
C                ( forw - back -> forw )
C          common
C scalar: E14 electron encrgy at the surface layer
C       : ISTART seed of the pseudo random number selector
C array : NZ         atomic numbers
C       : A         atom weights
C       : VK         excitation potentials
C       : C         weight fractions
C       : EO        incident electron energies
C       : EN        half step and full step electron mean energies
C       : IXF       table of transmited electrons
C       : IXB         " backscattered electrons
C       : IBAC      energy distribution of backscattered electrons
C       : IBB       the same as before (2th backscat. )
C       : ROZ       depth ( in mass thickness unit )
C       : PHI       phi-ro-z
C          parameters
C
C             ME        maximum number of elements in the target
C             MP        number of steps
C            MPP        dimension of the energy table
C            MAG        number of angles of equal scattering probability
C
C           function
C
C            EI         exponential integral
C            URAN       pseudo random number selector
C
      SUBROUTINE E10(JO,JM,JJA,ANUM,NPAS,NSWR,RETRO1,RETRO2)
```

```
      PARAMETER (ME=9)
      PARAMETER (MP=200)
      PARAMETER (MPP=401)
      PARAMETER (MMP=79)
C     PARAMETER (MAG=128)
      PARAMETER (NRD=3)
      DIMENSION NZ(ME),A(ME),VK(ME),C(ME),EN(MPP),AB(ME),ENS(MPP),
     &AC(ME),GA(4),RD(NRD),JJJ(196),ALP(MP),EFFZ(ME),LIM(99),N(99)
      DIMENSION IXF(MMP,MP),IXB(2,2),IBAC(MP),IBB(MP),PHI(MMP),
     &P(MP),RES(MP),ROZ(MMP),ALPS(MP),JJS(196),IXFF(2,2)
C     DIMENSION ABCD(50,MP)
      COMMON ENS
      COMMON NZ,A,VK,C,EO,RANGE,E14,EN,IXF,IXB,IBAC,IBB ROZ,PHI,ALP
      COMMON EFFZ
C     COMMON/LUI/LU5,LU6,LU7
      DATA NMAX1,NAN,PI,P180/128,128,3.14159265,.174532925E-1/
C
C ECRAN is a constant used in the calculation of the screening parameter
      DATA ECRAN/1./
      DATA ISTART/490623069/
C
C Statement function calculating sine from cosine in argument
      SI(X)=SQRT(1.-X**2)
  100 FORMAT(' WARNING - Slow convergence for step no.',I3)
C       NUM : number of sampled trajectories
C        ED : the popular constant of the Bethe's formula (1.166)
C        BB : real converion of the atomic number of the emitting element
C        AA : mean ionizatlon potentiel of the emitting element
      NUM=ANUM
      ED=SQRT(EXP(1.)/2.)
      BB=NZ(JJA)
      AA=(9.76*BB+58.5/BB**.19)/1000.
C Determination of a minimum energy limit for calculatlng the
C  Bethe,s range
C   first find the greater mean ionization potential
C
      DO 15 JJ=JO,JM
      BB=NZ(JJ)
      AB(JJ)=A(JJ)/(7.85E4*(BB**1.00)*C(JJ))
      AC(JJ)=(9.76*BB+58.5/BB**.19)/1000.
      IF(AC(JJ).GT.AA) AA=AC(JJ)
      AC(JJ)=ED/AC(JJ)
   15 CONTINUE
      GO TO (16,17),NSWR
C Lower limit for full range calculation
 16   ZA=1.03**AA
      GO TO 18
C Lower limit for xrays range calculation
   17 ZA=VK(JJA)
C Range calculation
   18 SM=.0
      ED=.0
      DO 19 JJ=JO,JM
      ED=ED+ALOG(AC(JJ))/AB(
      SM=SM+1./AB(JJ)
   19 CONTINUE
      ED=ED/SM
      V=EXP(ED)
      RANGE=1./SM/V**2*(EI(2.*(ED+ALOG(EO)))-
     &EI(2.* ED+ALOG(ZA))))
C Calculation of half step and full step electron mean energies
      H=MP
      H=RANGE/H/4.
      AA=H/2.
```

```
      BB=H/6.
      EA=EO
      NPAS2=2*MP
      DO 20 I=1,NPAS2
      DO 11 J=1,2
      EB=EA
      DO 25 IP=1,4
      GA(IP)=.0
      DO 26 JJ=JO,JM
      GA(IP)=GA(IP)+ALOG(AC(JJ)*EB)/AB(JJ)/EB
   26 CONTINUE
      GO TO (27,27,28,25),IP
   27 EB=EA-AA*GA(IP)
      GO TO 25
   28 EB=EA-H*GA(IP)
   25 CONTINUE
      EA=EA-BB*(GA(1)+2.*(GA(2)+GA(3))+GA(4))
      IF(I.NE.1) GO TO 11
      IF(J.EQ.1) E14=EA
   11 CONTINUE
      EN(I)=EA
   20 CONTINUE
      IF(EN(NPAS2).LT.VK(JJA)) EN(NPAS2)=VK(JJA)
C Energy sorting
C                     EN(I) I 1 -> NPAS : half step mean energy
C                     EN(NPAS+1) : incident electron energy
C                     EN(I) I NPAS+2 -> 2*NPAS+2 : full step mean energy
      DO 12 I=2,MP
      EN(NPAS2+1)=EN(I)
      DO 12 J=I,NPAS2
      EN(J)=EN(J+1)
   12 CONTINUE
      EN(NPAS2+1)=EN(MP+1)
      EN(MP+1)=EO
      WRITE(7,*) E14
C     TRAJECTORY SAMPLING
C   TABLE INITIALIZATION
      DO 58 I=1,MP
      IBAC(I)=0
      IBB(I)=0
      ALP(I)=0.0
      ALPS(I)=0.0
      DO 58 J=1,MMP
      IXF(J,I)=0
  58  CONTINUE
      IXB(1,1)=0
      IXB(1,2)=0
      IXB(2,1)=0
      IXB(2,2)=0
      IXFF(1,1)=0
      IXFF(1,2)=0
      IXFF(2,1)=0
      IXFF(2,2)=0
      DO 149 K=1,196
      JJJ(K)=0
      JJS(K)=0
 149  CONTINUE
C H IS THE INCIDENT ANGLE
      THICK=50.000
      THICK=THICK*130./(RANGE*1.E+06)
      ZS=47.0
      AS=107.90
      H=.0
      WONE=0.0
```

```
      WONES=0.0
      TOTZ=0.0
      DO 613 JJ=JO,JM
      EFFZ(JJ)=0.0
  613 CONTINUE
      DO 614 JJ=JO,JM
      BB=NZ(JJ)
      WONE=WONE+C(JJ)*(1.+.8/BB)*(BB**(4./3.))/A(JJ)
  614 CONTINUE
      WONE=WONE*RANGE*1.E+06/0.443
      WONES=(1.+.8/ZS)*(ZS**(4./3.))/AS
      WONES=WONES*627.958/0.443
      DO 615 JJ=JO,JM
      BB=NZ(JJ,
      EFFZ(JJ)=C(JJ)*(1.+.8/BB)*(BB**(4./3.))/A(JJ)
      TOTZ=TOTZ+EFFZ(JJ)
  615 CONTINUE
      ZEFF=0.0
      DO 616 JJ=JO,JM
      BB=NZ(JJ)
      ZEFF=ZEFF+EFFZ(JJ)/TOTZ*BB**(2./3.9)
  616 CONTINUE
      ZEFF=ZEFF**(3.9/2.)
      LIM(1)=6
      LIM(2)=7
      LIM(3)=9
      LIM(4)=12
      LIM(5)=15
      LIM(6)=20
      LIM(7)=25
      LIM(8)=32
      LIM(9)=40
      LIM(10)=49
      LIM(11)=59
      LIM(12)=72
      LIM(13)=87
      LIM(14)=102
      LIM(15)=120
      LIM(16)=140
      LIM(17)=160
      LIM(18)=184
      LIM(19)=207
      LIM(20)=231
      LIM(21)=255
      LIM(22)=279
      LIM(23)=302
      LIM(24)=324
      LIM(25)=343
      LIM(26)=362
      LIM(27)=376
      LIM(28)=387
      LIM(29)=39[illegible]
      LIM(30)=399
      DO 157 I=31,60
      LIM(I)=LIM(61-I)
  157 CONTINUE
      RPD=0.0
      RII=0.0
      DO 297 J=1,99
      N(J)=0
  297 CONTINUE
      DO 59 IT=1,NUM
C start one trajectory
C   NSW1 1 -> electron moving in the forward direction
```

```
C   NSW1 2 -> backscattered electron
C   NSW2 1 -> the counter of backscattered has already been incremented
C   NSW2 1 -> the counter of backscattered must bee incremented
      NSW1=1
      NSW2=1
      Y=0.0
      AA=COS(H)
      IST=0
      JII=0
      STEP=0.0
  159 CALL URAN(ISTART,NRD,RD)
      RRD=(RD(1)-0.5)*6.0
      DO 762 II=1,60
      RII=II
      IF((RRD.LT.(RII/10.-3.)).AND.(RRD.GT.(RII/10.-3.1))) GO TO 763
      GO TO 762
  763 N(II)=N(II)+1
      IF(N(II).LE.LIM(II)) GO TO 999
      GO TO 159
  762 CONTINUE
  999 Y=0.5*(1.+0.60*(RD(1)-0.5))
      IST=(130.*(1.+0.60*(RD(1)-0.5)))+0.5
      J=Y+1.0
      I=1./FLOAT(IST)/1.384*FLOAT(MP)+0.5
      IXFF(J,I)=IXFF(J,I)+1
      IXF(J,I)=IXFF(J,I)
      IF(IST.EQ.130) WRITE(5,*) IT,IST
      JJJ(1)=1./FLOAT(IST)/0.692*FLOAT(MP)+0.5
      DO 35 K=2,IST
      KK=K-1
      STEP=IST
      JII=FLOAT(KK)*(1.-1./0.692/STEP)/(STEP-1.)*FLOAT(MP)+
     &1./FLOAT(IST)/0.692*FLOAT(MP)+0.5
      JJJ(K)=JII
   35 CONTINUE
      STEPL=130./STEP
      KK=0
      IC=0
      ICC=10
      DO 60 K=1,IST
      I=JJJ(K)
C "free path" sampling
      CALL URAN(ISTART,NRD,RD)
      BB=RD(1)
      Y=Y+AA*BB/STEPL
      IF(Y.GT.0.) GO TO 47
C move backward
      IF(NSW1.EQ.2) GO TO 62
      NSW1=2
      NSW2=2
      GO TO 62
C move forward
   47 IF(NSW1.EQ.2) GO TO 61
C deflection sampling
C  62 ALP(I)=(1.+.8/Z)**1.3*(RANGE*1.E+06/FLOAT(IST))**1.3
C    &*(Z**2.4)*4.34E-03/((.443*AAA)**1.3)/(EN(I)**2.3)
C  62 IF(K.GE.2) GO TO 911
   62 IF((IC.EQ.0).AND.(Y.LE.THICK)) GO TO 803
      IF((IC.EQ.0).AND.(Y.GE.THICK)) GO TO 802
      IF((IC.EQ.1).AND.(Y.GE.THICK)  GO TO 800
      IF((IC.EQ.1).AND.(Y.LE.THICK)) GO TO 801
  803 IC=0
      ICC=10
      KK=KK+1
```

```
      ALP(I)=4.34E-03*ZEFF**(2./3.)*(WONE**1.3)/130.0**1.3
     ',`(EN(JJJ(KK)+MP+1)**2.30)
      GO TO 393
  802 IC=1
      ICC=20
      DO 805 ISUB=1,199
      IF((EN(JJJ(KK+1)+MP+1).LE.ENS(MP+1+ISUB)).AND.
     &(EN(JJJ(KK+1)+MP+1).GE.ENS(MP+2+ISUB))) GO TO 806
  805 CONTINUE
  806 IF(ABS(EN(JJJ(KK+1)+MP+1)-ENS(MP+1+ISUB)).LE.
     &ABS(EN(JJJ(KK+1)+MP+1)-ENS(MP+2+ISUB))) GO TO 807
      GO TO 833
  807 ALPS(I)=4.34E-03*ZS**(2./3.)*(WONES**1.3)/130.0**1.3
     &/(ENS(ISUB+MP+1)**2.30)
      ALP(I)=ALPS(I)
      DO 811 KK=1,(IST-K)
      JJS(KK)=FLOAT(MPP-(MP+1+ISUB))/FLOAT(IST-K)*FLOAT(KK)
     &+FLOAT(MI+1+ISUB)+0.5-FLOAT(MP+1)
  811 CONTINUE
      KK=0
      GO TO 393
  833 ALPS(I)=4.34E-03*ZS**(2./3.)*(WONES**1.3)/130.0**1.3
     &/(ENS(ISUB+MP+2)**2.30)
      ALP(I)=ALPS(I)
      DO 810 KK=1,(IST-K)
      JJS(KK)=FLOAT(MPP-(MP+2+ISUB))/FLOAT(IST-K)*FLOAT(KK)
     &+FLOAT(MP+2+ISUB)+0.5-FLOAT(MP+1)
  810 CONTINUE
      KK=0
      GO TO 393
  800 IC=1
      ICC=40
      KK=KK+1
      ALPS(I)=4.34E-03*ZS**(2./3.)*(WONES**1.3)/130.0**1.3
     &/(ENS(JJS(KK)+MP+1)**2.30)
      ALP(I)=ALPS(I)
      GO TO 393
  801 IC=0
      ICC=30
      DO 812 IFM=1,199
      IF((ENS(JJS(KK+1)+MP+1).LE.EN(MP+1+IFM)).AND.
     &(ENS(JJS(KK+1)+MP+1).GE.EN(MP+2+IFM))) GO TO 813
  812 CONTINUE
  813 IF(ABS(ENS(JJS(KK+1)+MP+1)-EN(MP+1+IFM)).LE.
     &ABS(ENS(JJS(KK+1)+MP+1)-EN(MP+2+IFM))) GO TO 814
      GO TO 834
  814 ALP(I)=4.34E-03*ZEFF**(2./3.)*(WONE**1.3)/130.0**1.3
     &/(EN(IFM+MP+1)**2.30)
      DO 816 KK=1,(IST-K)
      JJJ(KK)=FLOAT(MPP-(MP+1+IFM))/FLOAT(IST-K)*FLOAT(KK)
     &+FLOAT(MP+1+IFM)+0.5-FLOAT(MP+1)
  816 CONTINUE
      KK=0
      GO TO 393
  834 ALP(I)=4.34E-03*ZEFF**(2./3.)*(WONE**1.3)/130.0**1.3
     &/(EN(IFM+MP+2)**2.30)
      DO 815 KK=1,(IST-K)
      JJJ(KK)=FLOAT(MPP-(MP+2+IFM))/FLOAT(IST-K)*FLOAT(KK)
     &+FLOAT(MP+2+IFM)+0.5-FLOAT(MP+1)
  815 CONTINUE
      KK=0
      GO TO 393
C     GO TO 912
C 911 ALP(I)=(WONE*(1.-1./2./FLOAT(IST))/(FLOAT(IST)-1.))**(1.3)
```

```
C     &*4.34E-03*ZEFF**(2./3.)/(EN(I+MP+1)**2.30)
  393 C1=1.-(2.*ALP(I)*RD(2))/(1.+ALP(I)-RD(2))
      C2=SI(C1)
      C3=COS(2*PI*RD(3))
      AA=AA*C1+SI(AA)*C2*C3
      Y=Y+(1.-BB)*AA/STEPL
      IF(Y.LE.0.) GO TO(49,48),NSW1
      GO TO (63,61),NSW1
C update the table of electron position inside the target
   63 J=Y+1.0
C     IXF(J,I)=IXF(J,I)+1
      IF(J.GE.80) GO TO 60
      IF(ICC.EQ.10) IXF(J,JJJ(KK))=IXF(J,JJJ(KK))+1
      IF(ICC.EQ.20) IXF(J,(ISUB+1))=IXF(J,(ISUB+1))+1
      IF(ICC.EQ.30) IXF(J,(IFM+1))=IXF(J,(IFM+1))+1
      IF(ICC.EQ.40) IXF(J,JJS(KK))=IXF(J,JJS(KK))+1
      GO TO 60
C backscattered electron
   49 NSW1=2
      NSW2=2
C update the table of electron position outide the target
C          ( simulation of the Derian experiment )
   48 J=Y-1.5
      J=-J
C     IXB(J,I)=IXB(J,I)+1
      GO TO (60,67),NSW2
  67  IBAC(I)=IBAC(I)+1
      NSW2=1
  60  CONTINUE
      GO TO 59
C again in the target after being backscattered
   61 IF(NSW2.EQ.2) IBAC(I)=IBAC(I)+1
      IBB(I)=IBB(I)+1
   59 CONTINUE
C     CALCULATION OF BACKSCATTERING COEFFICIENTS
      IF(NSWR.EQ.2) GO TO 23
      RETRO1=.0
      RETRO2=.0
      DO 33 I=1,MP
      C1=IBAC(I)
      RETRO1=RETRO1+C1
      C1=IBB(I)
      RETRO2=RETRO2+C1
C     WRITE(7,*) IBAC(I),IBB(I)
   33 CONTINUE
      RETRO1=RETRO1/ANUM
      RETRO2=RETRO2/ANUM
      WRITE(7,*) RETRO1,RETRO2
   23 RETURN
      END
C PRINT
      SUBROUTINE PRINT(NPAS)
      PARAMETER (ME=9)
      PARAMETER (MP=200)
      PARAMETER (MPP=401)
      PARAMETER (MMP=79)
      DIMENSION NZ(ME),C(ME),A(ME),VK(ME),EN(MPP),IXF(MMP,MP),MOREB(99)
     &,IXB(2,2),IBAC(MP),IBB(MP),ROZ(MMP),PHI(MMP),MORE(MMP,99)
      DIMENSION ENS(MPP)
      COMMON ENS
      COMMON NZ,A,VK,C,EO,RANGE,E14,FN,IXF,IXB,IBAC,IBB,ROZ,PHI,ISTART
      COMMON/LUI/LU5,LU6,LU7
  103 FORMAT(1X,3X,10(3X,I3))
  101 FORMAT(1X,I3,10(1X,I5),1X,I5,1X,I5)
```

```
  111 FORMAT(' BS',10(1X,I5),1X,I5,1X,I5)
      DO 150 I=1,99
      MOREB(I)=0
      DO 149 J=1,MMP
      MORE(J,I)=0
  149 CONTINUE
  150 CONTINUE
      IS=10
      NTA=MP/IS
      IF(NTA.NE.0) GO TO 10
      IMIN=1
      GO TO 50
   10 DO 15 IT=1,NTA
      IADD=0
      IMIN=(IT-1)*IS
      IMAX=IS+IMIN
      IMIN=IMIN+1
      WRITE(7,103) (I,I=IMIN,IMAX)
C     DO 31 J=1,NPAS
C     K=NPAS+1-J
C     WRITE(7,101) K,(IXB(K,I),I=IMIN,IMAX)
C  31 CONTINUE
      DO 332 I=IMIN,IMAX
      IADD=IADD+IBAC(I)
  332 CONTINUE
      IF(IT.EQ.1) GO TO 168
      GO TO 169
  168 MOREB(IT)=IADD
      GO TO 170
  169 MOREB(IT)=MOREB(IT-1)+IADD
  170 WRITE(7,111) (IBAC(I),I=IMIN,IMAX),IADD,MOREB(IT)
      DO 334 J=1,MMP
      IADDD=0
      DO 333 I=IMIN,IMAX
      IADDD=IADDD+IXF(J,I)
 333  CONTINUE
      IF(IT.EQ.1)  GO TO 171
      GO TO 172
 171  MORE(J,IT)=IADDD
      GO TO 173
 172  MORE(J,IT)=MORE(J,(IT-1))+IADDD
 173  WRITE(7,101) J,(IXF(J,I),I=IMIN,IMAX),IADDD,MORE(J,IT)
      IF(IADDD.EQ.0)  GO TO 15
 334  CONTINUE
  15  CONTINUE
      IF(MP-IS*(MP/IS).EQ.0) GO TO 20
      IMIN=IMAX+1
  50  WRITE(7,103) (I,I=IMIN,MP)
C     DO 34 J=1,NPAS
C     K=NPAS+1-J
C     WRITE(7,101) K,(IXB(K,I),I=IMIN,NPAS)
C 34  CONTINUE
      WRITE(7,111) (IBAC(I),I=IMIN,MP)
      DO 32 J=1,MMP
      WRITE(7,101) J,(IXF(J,I),I=IMIN,MP)
  32  CONTINUE
  20  RETURN
      END
C EXPONENTIAL INTEGRAL
      FUNCTION EI(X)
      EI=ALOG(X)+X
      TN=X
      N=1
  300 AN=N
```

```
      IF(AN.GT.2.*X.AND.TN.LT.1.E-06) GO TO 400
      TN=TN*X*AN/(AN+1.)**2
      EI=EI+TN
      N=N+1
      GO TO 300
  400 RETURN
      END
C Select three random numbers - RAN is a system library function
C  ISTART : seed
C  NRD : number of sampled random numbers
C  RD       : random numbers in the range ( 0.,1. ), limits excluded
      SUBROUTINE URAN(ISTART,NRD,RD)
      DIMENSION RD(NRD)
      DO 1 I=1,NRD
    2 RD(I)=RAN(ISTART)
      IF((RD(I).GT.0.).AND.(RD(I).LT.1.)) GO TO 1
      GO TO 2
    1 CONTINUE
      RETURN
      END
      FUNCTION RAN(L)
      L=MOD(16807*L,2147483647)
      RAN=REAL(L)*4.6566128752459E-10
      RETURN
      END
C Calculation of Xray depth distribution in the target
C     Output:
C              ALOPHI log(phi(roz)
C              RXF total xray generation inside the target
C              RXFO total xray that would be generated inside
C                     the target in the absence of backscattering
C              NPASS index of the last layer giving a significant
C                     contribution
      SUBROUTINE XRAF(JJA,ALOPHI,NPAS,ANUM,NPASS,RXF,RXFO)
      PARAMETER (ME=9)
      PARAMETER (MP=200)
      PARAMETER (MPP=401)
      PARAMETER (MMP=79)
C     PARAMETER (MAG=128)
      DIMENSION NZ(ME),A(ME),VK(ME),C(ME),EN(MPP),IXF(MMP,MP),ALP(MP),
     &IXB(2,2),IBAC(MP),IBB(MP),ROZ(MMP),PHI(MMP),ALOPHI(MMP)
      DIMENSION ENS(MPP)
      COMMON ENS
      COMMON NZ,A,VK,C,EO,RANGE,E14,EN,IXF,IXB,IBAC,IBB,ROZ,PHI,ISTART
      COMMON ALP,EFFZ
      POWE=0.8
      COISO=1./EO**POWE/VK(JJA)**(2.-POWE)
     &*ALOG(EO/VK(JJA))
      NSW=1
      NPASS=MMP
C     PHI(1)=1./E14**POWE/VK(JJA)**(2.-POWE)
C    &*ALOG(E14/VK(JJA))
      PHI(1)=0.0
      RPAS=NPAS
      ROZ(1)=RANGE/RPAS/2.
      RXFO=.0
      DO 9 I=1,MP
      K=I
      IF(EN(K)/VK(JJA).LE.1.) GO TO 30
      AA=IXF(1,I)
      PHI(1)=PHI(1)+AA/ANUM/EN(K)**POWE/VK(JJA)**(2.-POWE)
     &*ALOG(EN(K)/VK(JJA))
    9 CONTINUE
      I=MMP
```

```
30 NPAS1=I
   NPAS2=MP
   ALOPHI(1)=ALOG10(PHI(1)/COISO)
   RXF=PHI(1)/2.
   DO 10 J=2,NPAS1
   PHI(J)=.0
   J1=J-1
   RXFO=RXFO+1./EN(J1)/VK(JJA)*ALOG(EN(J1)/VK(JJA))
   GO TO (4,10),NSW
 4 ROZ(J)=J1
   ROZ(J)=ROZ(J)*RANGE/RPAS
   DO 11 I=J1,NPAS2
   K=I
   AA=IXF(J,I)
   PHI(J)=PHI(J)+AA/ANUM/EN(K)**POWE/VK(JJA)**(2.-POWE)
  &*ALOG(EN(K)/VK(JJA))
11 CONTINUE
   IF(PHI(J).EQ.0.) GO TO 24
   ALOPHI(J)=ALOG10(PHI(J)/COISO)
   RXF=RXF+PHI(J)
   GO TO 10
24 NPASS=J-1
   NSW=2
10 CONTINUE
   IF(EN(NPAS1)/VK(JJA).GT.1.) RXFO=RXFO+1./EN(NPAS1)/VK(JJA)
  &*ALOG(EN(NPAS1)/VK(JJA))
   AA=RANGE/COISO/RPAS
   RXF=RXF*AA
   RXFO=RXFO*AA
   RETURN
   END
```

APPENDIX 4

SUMMARY OF THE SET OF EQUATIONS TO CALCULATE THIN FILM $\phi(\rho z)$ CURVES

THIN FILM $\Phi(\rho z)$ EQUATION

$$\Phi(\rho z)_{Film} = \Phi(\rho z)_{Bulk} * RATIO$$

For Low Z film on High Z substrate :

$$RATIO = 1 + (m1*\rho z + c1)^{6} \qquad 0 < \rho z < \rho t$$

$$c1 = c3 - (\rho t/(\mu g/cm^{2}))^{2.00} * e^{c2}$$

$$c2 = -3.5050*\ln((E_{o} - (E_{c}/3))/keV) - 2.7132$$

$$c3 = 1.094*(|\Delta\eta|*(1-\eta_{Film}))^{0.133642}$$

$$m1 = \{[1/(e^{c4}*(\rho t_{norm})^{0.02275})] - c1\}/\rho t$$

$$c4 = 0.3853*(1+|\Delta\eta|*(1-\eta_{Film}))^{-4.2374}$$

For High Z film on Low Z substrate :

$$RATIO = 1 - (m1*\rho z + c1)^{6} \qquad 0 < \rho z < \rho t$$

$$c1 = c3 - (\rho t/(\mu g/cm^{2}))^{2.00} * e^{c2}$$

$$c2 = -3.2946*\ln((E_{o} - (E_{c}/2))/keV) - 3.3330$$

$$c3 = 0.9396*(|\Delta\eta|*(1+\eta_{Substrate}))^{0.110121}$$

$$m1 = \{[1/(e^{(c4-0.04719)} * e^{0.02049*|\ln(10\rho t_{norm})|})] - c1\}/\rho t$$

$$c4 = 0.4471*(1+|\Delta\eta|*(1+\eta_{Substrate}))^{-3.2531}$$

APPENDIX 5

FORTRAN PROGRAM TO CALCULATE THIN FILM $\phi(\rho z)$ CURVES BY EQUATIONS

```
cccccccccccccccccccccccccccccccccccccccccccccccccccccccccccccccccccccccccccc
c
c This program calculates and stores a generated bulk φ(ρz) curve and bulk φ(ρz)
c curve corrected for absorption data in a file named 'TRR205.DAT'. This program
c also calculates and stores a film φ(ρz) curve both uncorrected and corrected for
c absorption data in 'TRR305.DAT'. These files can be imported into any plotting
c software for a graphical display. Relevant information and constants calculated from
c the computation process are selectively stored in 'TRR105.DAT'. The entire bulk
c φ(ρz) data and the bulk φ(ρz) data only up to the film thickness are stored in
c 'NNN105.DAT'. This program also calculates one k-ratio value and that depends on
c the set of user input values which include:
c        EO = Incident electron energy
c        EC = Critical excitation potential of the x-ray line of interest
c        XZ = Film atomic number
c         A = Film atomic weight
c    THICK = Film thickness in μg/cm²
c       SXZ= Substrate atomic number
c     NUM2= Number of equal intervals to carry out the  integration for a chosen φ(ρz)
c              curve
c     RMAC= Mass absorption coefficient
c       ANG= X-ray take off angle in degrees
c
c The 'DIMENSION' arrays that are used in this program include:-
c B1, B2  refer to the (ρz, φ(ρz)) values for the entire bulk φ(ρz) curve for the film
c              material
c F1, B9  refer to the (ρz, φ(ρz)) values for the bulk φ(ρz) curve only up to the input
c              film thickness
c     CO  refers to the constants related to c1, c2, c3, m1 and c4 for low Z film on
c              high Z substrate and vice versa (equations were shown in Appendix 4)
c     R2   refers to the ratio required to convert the corresponding bulk φ(ρz) curve to
c              film φ(ρz) curve at a particular film thickness.
c     CF   refers to the calculated film φ(ρz) values
c    AB2   refers to the bulk φ(ρz) values after correction for absorption
c    ACF   refers to the film φ(ρz) values after correction for absorption
c
```

c

c Based on the input values, the program calculates the following:-

c CSC: cosecant of the x-ray take off angle

c U: overvoltage ratio

c BSF: bulk backscatter coefficient from Love, Cox and Scott for the film material

c SBSF: bulk backscatter coefficient from Love, Cox and Scott for the substrate
c material

c PHIO: bulk $\phi(o)$ value from Love, Cox and Scott for the film material

c ALP: parameters in calculating bulk $\phi(\rho z)$ curve for the film material using
c BET: Brown and Packwood expression for α, β and γ_0
c GAM:

c STEPB: the width of each interval for the entire bulk $\phi(\rho z)$ curve depending on
c NUM2

c STEPF: the width of each interval for bulk $\phi(\rho z)$ curve only up to the particular
c film thickness of interest

c B1, B2: data points for the entire bulk $\phi(\rho z)$ curve governed by STEPB
c (see DO 280 LOOP)

c F1, B9: data points for the bulk $\phi(\rho z)$ curve only up to the particular film thickness
c of interest governed by STEPF (see DO 180 LOOP)

c CO: depending on whether the situation is low Z film on high Z substrate or
c high Z film on low Z substrate, then apply the appropriate equations from
c Appendix 4 to calculate c1, c2, c3, m1 and c4 for the value of 'Ratio'

c R2: the ratio required to convert the corresponding bulk $\phi(\rho z)$ curve to film
c $\phi(\rho z)$ curve at a particular film thickness

c CF: film $\phi(\rho z)$ values

c AB2: bulk $\phi(\rho z)$ values after correction for absorption (see DO 250 LOOP)

c ACF: film $\phi(\rho z)$ values after correction for absorption (see DO 250 LOOP)

c AREAB: integration of bulk $\phi(\rho z)$ curve after correction for absorption (see DO
c 110 LOOP)

cAREACF: integration of film $\phi(\rho z)$ curve after correction for absorption (see DO
c 110 LOOP)

c RATCK: film k-ratio for the particular set of input parameters

c

cccccccccccccccccccccccccccccccccccccccccccccccccccccccccccccccccccccccc

```
      PROGRAM ERR8
      REAL IU
      DIMENSION B1(300),B2(300),AB2(300),F1(300)
      DIMENSION ACF(300),B9(300)
      DIMENSION CO(10),R2(300),CF(300)
      OPEN(2,FILE='CON')
      OPEN(UNIT=5,FILE='NNN105.DAT')
      OPEN(UNIT=6,FILE='TRR305.DAT')
      OPEN(UNIT=7,FILE='TRR205.DAT')
      OPEN(UNIT=8,FILE='TRR105.DAT')
      WRITE(2,*)'INPUT EO,EC,BULK ATM# ,ATM WT,FILM THICK,SUBAT...'
      READ(2,*) EO,EC,XZ,A,THICK,SXZ
      WRITE(2,*)'INPUT NUM2,RMAC,ANG'
      READ(2,*) NUM2,RMAC,ANG
      IEIGHT=8
      RMAC=RMAC*1.0E-06
      CSC=1.0/SIN(ANG*3.141592654/180.0)
      BSF=0.0
      BSF30=0.0
      ETA=-52.3791+XZ*(150.48371+XZ*(-1.67373+0.00716*XZ))
      ETA=ETA/10000.
      GETA=(-1112.8+30.289*XZ-0.15498*XZ*XZ)/10000.0
      BSF=ETA*(1.0+GETA*LOG(EO/20.0))
      BSF30=ETA*(1.0+GETA*LOG(30.0/20.0))
      SBSF=0.0
      SBSF30=0.0
      ETA=-52.3791+SXZ*(150.48371+SXZ*(-1.67373+0.00716*SXZ))
      ETA=ETA/10000.
      GETA=(-1112.8+30.289*SXZ-0.15498*SXZ*SXZ)/10000.0
      SBSF=ETA*(1.0+GETA*LOG(EO/20.0))
      SBSF30=ETA*(1.0+GETA*LOG(30.0/20.0))
      U=EO/EC
      GU=-0.59299+21.55329/U-30.55248/U/U+9.59218/U/U/U
      IU=3.43378-10.7872/U+10.97628/U/U-3.62286/U/U/U
      PHIO=1.0+(BSF/(1.0+BSF))*(IU+GU*LOG(1.0+BSF))
      GAM=5.0*3.141592654*U/(U-1.0)/LOG(U)*(LOG(U)-5.0+5.0
     &*U**(-0.2))
      BSJ=XZ*(9.76+58.82*XZ**(-1.19))*1.0E-03
      ALP=0.395*XZ**0.95/A/(EO**1.25)*(LOG(1.166*EO/BSJ)/
     &(EO-EC))**0.5
      BET=0.4*ALP*XZ**0.6
      WRITE(8,*) BSF,BSF30,SBSF,SBSF30
      WRITE(8,*) BSF,PHIO,BSJ
      WRITE(8,*) ALP,BET,GAM
      B1(1)=0.0
      F1(1)=0.0
      B2(1)=PHIO
      B9(1)=PHIO
      I=0
50    I=I+1
      B1(I+1)=B1(I)+EO-4.0
      B2(I+1)=GAM*(1.0-((GAM-PHIO)/GAM)*EXP(-BET*B1(I+1)))
     &*EXP(-(ALP**2.0)*(B1(I+1))**2.0)
      DUM=5.0E-03*(1.0+(EC/EO)**1.0)*(1.0-(XZ/100.0)**2.0)
      IF((B2(I+1)).LE.(DUM)) GO TO 160
      GO TO 50
160   STEPB=B1(I)/(NUM2-1)
      XRANGE=B1(I)
      STEPF=THICK/(NUM2-1)
      WRITE(8,*) XRANGE,THICK
      NUM3=NUM2-1
      DO 280 J=1,NUM3
```

```
      B1(J+1)=STEPB*J
      B2(J+1)=GAM*(1.0-((GAM-PHIO)/GAM)*EXP(-BET*B1(J+1)))
     &*EXP(-(ALP**2.0)*(B1(J+1))**2.0)
 280  CONTINUE
      DO 180 J=1,NUM3
      F1(J+1)=STEPF*J
      B9(J+1)=GAM*(1.0-((GAM-PHIO)/GAM)*EXP(-BET*F1(J+1)))
     &*EXP(-(ALP**2.0)*(F1(J+1))**2.0)
 180  CONTINUE
      DO 90 K=1,NUM2
      WRITE(5,*) B1(K),B2(K),F1(K),B9(K)
 90   CONTINUE
       RANGE=XRANGE
       ETAF=BSF30
       ETAS=SBSF30
       DETA=ABS(ETAF-ETAS)
       FETAS=ETAF-ETAS
       ZF=XZ
       ZS=SXZ
       BIT=(1.0+((EC/EO)**1.0)*(1.0+FETAS/DETA)**1.0E-09)
     & *0.0835*FETAS/DETA
       IF(ZF.GT.ZS) GO TO 20
       CO(1)=-3.505041801*LOG(EO-EC*(0.4165+BIT))-2.713164382
       CO(2)=(DETA*(1.0-ETAF))**0.133640497*EXP(0.089751805)
       CO(3)=(DETA*(1.0-ETAF)+1.0)**(-4.237370618)
     & *EXP(-0.953803219)
       BEGIN=THICK**2.0*EXP(CO(1))-CO(2)
       PRODUCT=BEGIN*((THICK/RANGE)**0.022746964)*EXP(CO(3))
       GO TO 80
 20    CO(1)=-3.29457620*LOG(EO-EC*(0.4165+BIT))-3.332989881
       CO(2)=(DETA*(1.0+ETAS))**0.110122169*EXP(-0.062321491)
       CO(3)=(DETA*(1.0+ETAS)+1.0)**(-3.253062862)
     & *EXP(-0.804942195)
       CO(4)=CO(3)-0.09081404
       BEGIN=THICK**2.0*EXP(CO(1))-CO(2)
       IF((THICK/RANGE).LE.(0.1)) GO TO 60
       PRODUCT=BEGIN*(THICK/RANGE)**0.020493884*EXP(CO(3))
       GO TO 80
 60    PRODUCT=BEGIN*(THICK/RANGE)**(-0.020493884)*EXP(CO(4))
 80    RINT=PRODUCT*THICK/(1.0+PRODUCT)
       SLOPE=RINT/BEGIN
       IF(SLOPE.GT.(0.0)) GO TO 187
       PRODUCT=1.0E-06-1.0
       RINT=PRODUCT*THICK/(1.0+PRODUCT)
       SLOPE=RINT/BEGIN
 187   WRITE(8,*) EO,EC,ZF,ZS
       WRITE(8,*) DETA,RANGE,THICK,NUM2
       WRITE(8,*) CO(1),CO(2),CO(3),CO(4)
       WRITE(8,*) BEGIN,PRODUCT,RINT,SLOPE
       IF(ZF.GT.ZS) GO TO 12
       DO 10 J=1,NUM2
       R2(J)=1.0+((F1(J)-RINT)/SLOPE)**IEIGHT
       IF((F1(J)-RINT).LT.(0.0)) R2(J)=1.0
       CF(J)=B9(J)*R2(J)
 10    CONTINUE
       GO TO 13
 12    DO 14 J=1,NUM2
       R2(J)=1.0-((F1(J)-RINT)/SLOPE)**IEIGHT
       IF((F1(J)-RINT).LT.(0.0)) R2(J)=1.0
       CF(J)=B9(J)*R2(J)
 14    CONTINUE
 13    AREAB=0.0
       AREACF=0.0
       DO 250 L=1,NUM2
```

4 of/de 4

PM-1 3½"x4" PHOTOGRAPHIC MICROCOPY TARGET
NBS 1010a ANSI/ISO #2 EQUIVALENT

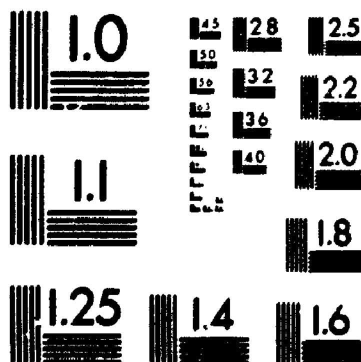

```
      AB2(L)=B2(L)*EXP(-RMAC*B1(L)*CSC)
      ACF(L)=CF(L)*EXP(-RMAC*F1(L)*CSC)
      WRITE(7,*) L,B1(L),B2(L),AB2(L)
      WRITE(6,*) L,F1(L),CF(L),ACF(L)
250   CONTINUE
      DO 110 K=2,NUM2
      AREAB=AREAB+(AB2(K)+AB2(K-1))*(B1(K)-B1(K-1))*0.5
      AREACF=AREACF+(ACF(K)+ACF(K-1))*(F1(K)-F1(K-1))*0.5
      WRITE(8,*) K-1,K ˜REACF,AREAB
110   CONTINUE
      RATCK=AREACF/AREAB
      WRITE(8,*) RMAC,CSC
      WRITE(8,*) AREACF,AREAB,RATCK
      WRITE(2,*) RATCK
      CLOSE(UNIT=8)
      CLOSE(UNIT=7)
      CLOSE(UNIT=6)
      CLOSE(UNIT=5)
      STOP
      END
```

APPENDIX 6

FORTRAN PROGRAM TO CALCULATE FILM K-RATIOS AS A FUNCTION OF ELECTRON ENERGY

```
cccccccccccccccccccccccccccccccccccccccccccccccccccccccccccccccccccccccc
c
c This program calculates the film k-ratios as a function of incident electron energy
c and stores the data into a file named 'DUM.DAT' which can be imported into any
c plotting software for a graphical display. The program requires some user input
c values which include:
c     EOL = Lowest electron energy chosen for the calculation
c     EOH = Highest electron energy chosen for the calculation
c       EC = Critical excitation potential of the x-ray line of interest
c       XZ = Film atomic number
c         A = Film atomic weight
c  THICK = Film thickness in μg/cm2
c     SXZ= Substrate atomic number
c   NUM2= Number of equal intervals to carry out the integration for a chosen φ(ρz)
c            curve
c   RMAC= Mass absorption coefficient
c     ANG= X-ray take off angle in degrees
c
c The 'DIMENSION' arrays that are used in this program include:-
c B1, B2  refer to the (ρz, φ(ρz)) values for the entire bulk φ(ρz) curve for the film
c           material
c F1, B9  refer to the (ρz, φ(ρz)) values for the bulk φ(ρz) curve only up to the input
c           film thickness
c    CO  refers to the constants related to c1, c2, c3, m1 and c4 for low Z film on
c           high Z substrate and vice versa (equations were shown in Appendix 4)
c    R2  refers to the ratio required to convert the corresponding bulk φ(ρz) curve to
c           film φ(ρz) curve at a particular film thickness.
c    CF  refers to the calculated film φ(ρz) values
c   AB2  refers to the bulk φ(ρz) values after correction for absorption
c   ACF  refers to the film φ(ρz) values after correction for absorption
c
```

```
c
c Based on the input values, the program calculates the following:-
c     CSC:  cosecant of the x-ray take off angle
c       U:  overvoltage ratio
c     BSF:  bulk backscatter coefficient from Love, Cox and Scott for the film material
c    SBSF:  bulk backscatter coefficient from Love, Cox and Scott for the substrate
c           material
c    PHIO:  bulk φ(o) value from Love, Cox and Scott for the film material
c     ALP:  parameters in calculating bulk φ(ρz) curve for the film material using
c     BET:  Brown and Packwooc expression for α, β and γ0
c     GAM:
c   STEPB:  the width of each interval for the entire bulk φ(ρz) curve depending on
c           NUM2
c   STEPF:  the width of each interval for bulk φ(ρz) curve only up to the particular
c           film thickness of interest
c  B1, B2:  data points for the entire bulk φ(ρz) curve governed by STEPB
c           (see DO 280 LOOP)
c  F1, B9:  data points for the bulk φ(ρz) curve only up to the particular film thickness
c           of interest governed by STEPF (see DO 180 LOOP)
c      CO:  depending on whether the situation is low Z film on high Z substrate or
c           high Z film on low Z substrate, then apply the appropriate equations from
c           Appendix 4 to calculate c1, c2, c3, m1 and c4 for the value of 'Ratio'
c      R2:  the ratio required to convert the corresponding bulk φ(ρz) curve to film
c           φ(ρz) curve at a particular film thickness
c      CF:  film φ(ρz) values
c     AB2:  bulk φ(ρz) values after correction for absorption (see DO 250 LOOP)
c     ACF:  film φ(ρz) values after correction for absorption  (see DO 250 LOOP)
c  AREAB:  integration of bulk φ(ρz) curve after correction for absorption (see DO
c           110 LOOP)
cAREACF:  integration of film φ(ρz) curve after correction for absorption (see DO
c           110 LOOP)
c  RATCK:  film k-ratio versus incident electron energy at an interval of 1 keV (see
c           DO 991 LOOP)
c
cccccccccccccccccccccccccccccccccccccccccccccccccccccccccccccccccccccccccccccccc
```

```
      PROGRAM ERR11
      REAL IU
      DIMENSION B1(300),B2(300),AB2(300),F1(300)
      DIMENSION ACF(300),B9(300)
      DIMENSION CO(10),R2(300),CF(300)
      OPEN(2,FILE='CON')
      OPEN(UNIT=3,FILE='DUM.DAT')
C     OPEN(UNIT=5,FILE='NNN103.DAT')
C     OPEN(UNIT=6,FILE='TRR303.DAT')
C     OPEN(UNIT=7,FILE='TRR203.DAT')
C     OPEN(UNIT=8,FILE='TRR103.DAT')
      WRITE(2,*)'INPUT EOL,EOH,EC,BULK ATM# ,ATM WT,FILM THICK,SUBATM#'
      READ(2,*) EOL,EOH,EC,XZ,A,THICK,SXZ
      WRITE(2,*)'INPUT NUM2,RMAC,ANG'
      READ(2,*) NUM2,RMAC,ANG
      IEOL=EOL*2.0
      IEOH=EOH*2.0
      IEIGHT=8
      RMAC=RMAC*1.0E-06
      CSC=1.0/SIN(ANG*3.141592654/180.0)
      BSF=0.0
      BSF30=0.0
      DO 991 IEO=IEOL,IEOH
      EO=FLOAT(IEO)/2.0
      ETA=-52.3791+XZ*(150.48371+XZ*(-1.67373+0.00716*XZ))
      ETA=ETA/10000.
      GETA=(-1112.8+30.289*XZ-0.15498*XZ*XZ)/10000.0
      BSF=ETA*(1.0+GETA*LOG(EO/20.0))
      BSF30=ETA*(1.0+GETA*LOG(30.0/20.0))
      SBSF=0.0
      SBSF30=0.0
      ETA=-52.3791+SXZ*(150.48371+SXZ*(-1.67373+0.00716*SXZ))
      ETA=ETA/10000.
      GETA=(-1112.8+30.289*SXZ-0.15498*SXZ*SXZ)/10000.0
      SBSF=ETA*(1.0+GETA*LOG(EO/20.0))
      SBSF30=ETA*(1.0+GETA*LOG(30.0/20.0))
      U=EO/EC
      GU=-0.59299+21.55329/U-30.55248/U/U+9.59218/U/U/U
      IU=3.43378-10.7872/U+10.97628/U/U-3.62286/U/U/U
      PHIO=1.0+(BSF/(1.0+BSF))*(IU+GU*LOG(1.0+BSF))
      GAM=5.0*3.141592654*U/(U-1.0)/LOG(U)*(LOG(U)-5.0+5.0
     &*U**(-0.2))
      BSJ=XZ*(9.76+58.82*XZ**(-1.19))*1.0E-03
      ALP=0.395*XZ**0.95/A/(EO**1.25)*(LOG(1.166*EO/BSJ)/
     &(EO-EC))**0.5
      BET=0.4*ALP*XZ**0.6
C     WRITE(8,*) BSF,BSF30,SBSF,SBSF30
C     WRITE(8,*) BSF,PHIO,BSJ
C     WRITE(8,*) ALP,BET,GAM
      B1(1)=0.0
      F1(1)=0.0
      B2(1)=PHIO
      B9(1)=PHIO
      I=0
   50 I=I+1
      B1(I+1)=B1(I)+EO-4.0
      B2(I+1)=GAM*(1.0-((GAM-PHIO)/GAM)*EXP(-BET*B1(I+1)))
     &*EXP(-(ALP**2.0)*(B1(I+1))**2.0)
      DUM=5.0E-03*(1.0+(EC/EO)**1.0)*(1.0-(XZ/100.0)**2.0)
      IF((B2(I+1)).LE.(DUM)) GO TO 160
      GO TO 50
  160 STEPB=B1(I)/(NUM2-1)
```

```
      XRANGE=B1(I)
      STEPF=THICK/(NUM2-1)
C     WRITE(8,*) XRANGE,THICK
      NUM3=NUM2-1
      DO 280 J=1,NUM3
      B1(J+1)=STEPB*J
      B2(J+1)=GAM*(1.0-((GAM-PHIO)/GAM)*EXP(-BET*B1(J+1)))
     &*EXP(-(ALP**2.0)*(B1(J+1))**2.0)
  280 CONTINUE
      DO 180 J=1,NUM3
      F1(J+1)=STEPF*J
      B9(J+1)=GAM*(1.0-((GAM-PHIO)/GAM)*EXP(-BET*F1(J+1)))
     &*EXP(-(ALP**2.0)*(F1(J+1))**2.0)
 180  CONTINUE
      DO 90 K=1,NUM2
C     WRITE(5,*) B1(K),B2(K),F1(K),B9(K)
  90  CONTINUE
       RANGE=XRANGE
       ETAF=BSF30
       ETAS=SBSF30
       DETA=ABS(ETAF-ETAS)
       FETAS=ETAF-ETAS
       ZF=XZ
       ZS=SXZ
       BIT=(1.0+((EC/EO)**1.0)*(1.0+FETAS/DETA)**1.0E-09)
     & *0.0835*FETAS/DETA
       IF(ZF.GT.ZS) GO TO 20
       CO(1)=-3.505041801*LOG(EO-EC*(0.4165+BIT))-2.713164382
       CO(2)=(DETA*(1.0-ETAF))**0.133640497*EXP(0.089751805)
       CO(3)=(DETA*(1.0-ETAF)+1.0)**(-4.237370618)
     & *EXP(-0.953803219)
       BEGIN=THICK**2.0*EXP(CO(1))-CO(2)
       PRODUCT=BEGIN*((THICK/RANGE)**0.022746964)*EXP(CO(3))
       GO TO 80
   20  CO(1)=-3.29457620*LOG(EO-EC*(0.4165+BIT))-3.332989881
       CO(2)=(DETA*(1.0+ETAS))**0.110122169*EXP(-0.062321491)
       CO(3)=(DETA*(1.0+ETAS)+1.0)**(-3.253062862)
     & *EXP(-0.804942195)
       CO(4)=CO(3)-0.09081404
       BEGIN=THICK**2.0*EXP(CO(1))-CO(2)
       IF((THICK/RANGE).LE.(0.1)) GO TO 60
       PRODUCT=BEGIN*(THICK/RANGE)**0.020493884*EXP(CO(3))
       GO TO 80
   60  PRODUCT=BEGIN*(THICK/RANGE)**(-0.020493884)*EXP(CO(4))
   80  RINT=PRODUCT*THICK/(1.0+PRODUCT)
       SLOPE=RINT/BEGIN
       IF(SLOPE.GT.(0.0)) GO TO 187
       PRODUCT=1.0E-06-1.0
       RINT=PRODUCT*THICK/(1.0+PRODUCT)
       SLOPE=RINT/BEGIN
C      WRITE(8,*) EO,EC,ZF,ZS
C      WRITE(8,*) DETA,RANGE,THICK,NUM2
C      WRITE(8,*) CO(1),CO(2),CO(3),CO(4)
C      WRITE(8,*) BEGIN,PRODUCT,RINT,SLOPE
  187  IF(ZF.GT.ZS) GO TO 12
       DO 10 J=1,NUM2
       R2(J)=1.0+((F1(J)-RINT)/SLOPE)**IEIGHT
       IF((F1(J)-RINT).LT.(0.0)) R2(J)=1.0
       CF(J)=B9(J)*R2(J)
   10  CONTINUE
       GO TO 13
   12  DO 14 J=1,NUM2
       R2(J)=1.0-((F1(J)-RINT)/SLOPE)**IEIGHT
       IF((F1(J)-RINT).LT.(0.0)) R2(J)=1.0
```

```
      CF(J)=B9(J)*R2(J)
   14 CONTINUE
   13 AREAB=0.0
      AREACF=0.0
      DO 250 L=1,NUM2
      AB2(L)=B2(L)*EXP(-RMAC*B1(L)*CSC)
      ACF(L)=CF(L)*EXP(-RMAC*F1(L)*CSC)
C     WRITE(7,*) L,B1(L),B2(L),AB2(L)
C     WRITE(6,*) L,F1(L),CF(L),ACF(L)
  250 CONTINUE
      DO 110 K=2,NUM2
      AREAB=AREAB+(AB2(K)+AB2(K-1))*(B1(K)-B1(K-1))*0.5
      AREACF=AREACF+(ACF(K)+ACF(K-1))*(F1(K)-F1(K-1))*0.5
C     WRITE(8,*) K-1,K,AREACF,AREAB
  110 CONTINUE
      RATCK=AREACF/AREAB
C     WRITE(8,*) RMAC,CSC
C     WRITE(8,*) AREACF,AREAB,RATCK
C     WRITE(2,*) RATCK
      WRITE(3,*) EO,RATCK,RINT,SLOPE
  991 CONTINUE
C     CLOSE(UNIT=8)
C     CLOSE(UNIT=7)
C     CLOSE(UNIT=6)
C     CLOSE(UNIT=5)
      STOP
      END
```

APPENDIX 7

FORTRAN PROGRAM TO CALCULATE FILM K-RATIOS AS A FUNCTION OF FILM THICKNESS

```
cccccccccccccccccccccccccccccccccccccccccccccccccccccccccccccccccccccccc
c
c  This program calculates the film k-ratios as a function of film thicknesses and stores
c  the data into a file named 'DUM.DAT' which can be imported into any plotting
c  software for a graphical display.  The program requires some user input values
c  which include:
c        EO =  Incident electron energy
c        EC = Critical excitation potential of the x-ray line of interest
c        XZ = Film atomic number
c          A = Film atomic weight
c THICKL = Thinnest film thickness in μg/cm²  for the calculation
c THICKH = Thickest film thickness in μg/cm²  for the calculation
c       SXZ= Substrate atomic number
c    NUM2= Number of equal intervals to carry out the  integration for a chosen φ(ρz)
c              curve
c    RMAC= Mass absorption coefficient
c      ANG= X-ray take off angle in degrees
c
c The 'DIMENSION' arrays that are used in this program include:-
c B1, B2  refer to the (ρz, φ(ρz)) values for the entire bulk φ(ρz) curve for the film
c            material
c F1, B9  refer to the (ρz, φ(ρz)) values for the bulk φ(ρz) curve only up to the input
c            film thickness
c     CO  refers to the constants related to c1, c2, c3, m1 and c4 for low Z film on
c            high Z substrate and vice versa (equations were shown in Appendix 4)
c     R2   refers to the ratio required to convert the corresponding bulk φ(ρz) curve to
c            film φ(ρz) curve at a particular film thickness.
c     CF   refers to the calculated film φ(ρz) values
c   AB2   refers to the bulk φ(ρz) values after correction for absorption
c   ACF   refers to the film φ(ρz) values after correction for absorption
c
```

```
c
c Based on the input values, the program calculates the following:-
c      CSC:  cosecant of the x-ray take off angle
c        U:  overvoltage ratio
c      BSF:  bulk backscatter coefficient from Love, Cox and Scott for the film material
c     SBSF:  bulk backscatter coefficient from Love, Cox and Scott for the substrate
c            material
c     PHIO:  bulk φ(o) value from Love, Cox and Scott for the film material
c      ALP:  parameters in calculating bulk φ(ρz) curve for the film material using
c      BET:  Brown and Packwood expression for α, β and γ0
c      GAM:
c    STEPB:  the width of each interval for the entire bulk φ(ρz) curve depending on
c            NUM2
c    STEPF:  the width of each interval for bulk φ(ρz) curve only up to the particular
c            film thickness of interest
c   B1, B2:  data points for the entire bulk φ(ρz) curve governed by STEPB
c            (see DO 280 LOOP)
c   F1, B9:  data points for the bulk φ(ρz) curve only up to the particular film thickness
c            of interest by governed by STEPF (see DO 180 LOOP)
c       CO:  depending on whether the situation is low Z film on high Z substrate or
c            high Z film on low Z substrate, then apply the appropriate equations from
c            Appendix 4 to calculate c1, c2, c3, m1 and c4 for the value of 'Ratio'
c       R2:  the ratio required to convert the corresponding bulk φ(ρz) curve to film
c            φ(ρz) curve at a particular film thickness
c       CF:  film φ(ρz) values
c      AB2:  bulk φ(ρz) values after correction for absorption (see DO 250 LOOP)
c      ACF:  film φ(ρz) values after correction for absorption  (see DO 250 LOOP)
c   AREAB:  integration of bulk φ(ρz) curve after correction for absorption (see DO
c            110 LOOP)
cAREACF:  integration of film φ(ρz) curve after correction for absorption (see DO
c            110 LOOP)
c   RATCK:  film k-ratio versus film thickness with 25 data points (see DO 991 LOOP)
c
cccccccccccccccccccccccccccccccccccccccccccccccccccccccccccccccccccccccccccc
```

```
      PROGRAM ERR12
      REAL IU
      DIMENSION B1(300),B2(300),AB2(300),F1(300)
      DIMENSION ACF(300),B9(300)
      DIMENSION CO(10),R2(300),CF(300)
      OPEN(2,FILE='CON')
      OPEN(UNIT=3,FILE='DUM.DAT')
C     OPEN(UNIT=5,FILE='NNN103.DAT')
C     OPEN(UNIT=6,FILE='TRR303.DAT')
C     OPEN(UNIT=7,FILE='TRR203.DAT')
C     OPEN(UNIT=8,FILE='TRR103.DAT')
      WRITE(2,*)'INPUT EO,EC,BULK ATM# ,ATM WT,THICKL,THICKH,SUBATM#'
      READ(2,*) EO,EC,XZ,A,THICKL,THICKH,SXZ
      WRITE(2,*)'INPUT NUM2,RMAC,ANG'
      READ(2,*) NUM2,RMAC,ANG
      ITHICL=THICKL*1.0
      ITHICH=THICKH*1.0
      IEIGHT=8
      RMAC=RMAC*1.0E-06
      CSC=1.0/SIN(ANG*3.141592654/180.0)
      BSF=0.0
      BSF30=0.0
      DO 991 ITHICK=ITHICL,ITHICH,25
      THICK=FLOAT(ITHICK)/1.0
      THICK=THICK*0.1050
      ETA=-52.3791+XZ*(150.48371+XZ*(-1.67373+0.00716*XZ))
      ETA=ETA/10000.
      GETA=(-1112.8+30.289*XZ-0.15498*XZ*XZ)/10000.0
      BSF=ETA*(1.0+GETA*LOG(EO/20.0))
      BSF30=ETA*(1.0+GETA*LOG(30.0/20.0))
      SBSF=0.0
      SBSF30=0.0
      ETA=-52.3791+SXZ*(150.48371+SXZ*(-1.67373+0.00716*SXZ))
      ETA=ETA/10000.
      GETA=(-1112.8+30.289*SXZ-0.15498*SXZ*SXZ)/10000.0
      SBSF=ETA*(1.0+GETA*LOG(EO/20.0))
      SBSF30=ETA*(1.0+GETA*LOG(30.0/20.0))
      U=EO/EC
      GU=-0.59299+21.55329/U-30.55248/U/U+9.59218/U/U/U
      IU=3.43378-10.7872/U+10.97628/U/U-3.62286/U/U/U
      PHIO=1.0+(BSF/(1.0+BSF))*(IU+GU*LOG(1.0+BSF))
      GAM=5.0*3.141592654*U/(U-1.0)/LOG(U)*(LOG(U)-5.0+5.0
     &*U**(-0.2))
      BSJ=XZ*(9.76+58.82*XZ**(-1.19))*1.0E-03
      ALP=0.395*XZ**0.95/A/(EO**1.25)*(LOG(1.166*EO/BSJ)/
     &(EO-EC))**0.5
      BET=0.4*ALP*XZ**0.6
C     WRITE(8,*) BSF,BSF30,SBSF,SBSF30
C     WRITE(8,*) BSF,PHIO,BSJ
C     WRITE(8,*) ALP,BET,GAM
      B1(1)=0.0
      F1(1)=0.0
      B2(1)=PHIO
      B9(1)=PHIO
      I=0
   50 I=I+1
      B1(I+1)=B1(I)+EO-4.0
      B2(I+1)=GAM*(1.0-((GAM-PHIO)/GAM)*EXP(-BET*B1(I+1)))
     &*EXP(-(ALP**2.0)*(B1(I+1))**2.0)
C     DUM=5.0E-03*(1.0+(EC/EO)**1.0)*(1.0-(XZ/100.0)**2.0)
C     IF((B2(I+1)).LE.(DUM)) GO TO 160
      IF((B2(I+1)).LE.(1.0E-05)) GO TO 160
```

```
      GO TO 50
  160 STEPB=B1(I)/(NUM2-1)
      XRANGE=B1(I)
      STEPF=THICK/(NUM2-1)
C     WRITE(8,*) XRANGE,THICK
      NUM3=NUM2-1
      DO 280 J=1,NUM3
      B1(J+1)=STEPB*J
      B2(J+1)=GAM*(1.0-((GAM-PHIO)/GAM)*EXP(-BET*B1(J+1)))
     &*EXP(-(ALP**2.0)*(B1(J+1))**2.0)
  280 CONTINUE
      DO 180 J=1,NUM3
      F1(J+1)=STEPF*J
      B9(J+1)=GAM*(1.0-((GAM-PHIO)/GAM)*EXP(-BET*F1(J+1)))
     &*EXP(-(ALP**2.0)*(F1(J+1))**2.0)
 180  CONTINUE
      DO 90 K=1,NUM2
C     WRITE(5,*) B1(K),B2(K),F1(K),B9(K)
  90  CONTINUE
       RANGE=XRANGE
       ETAF=BSF30
       ETAS=SBSF30
       DETA=ABS(ETAF-ETAS)
       FETAS=ETAF-ETAS
       ZF=XZ
       ZS=SXZ
       BIT=(1.0+((EC/EO)**1.0)*(1.0+FETAS/DETA)**1.0E-09)
     & *0.0835*FETAS/DETA
       IF(ZF.GT.ZS) GO TO 20
       CO(1)=-3.505041801*LOG(EO-EC*(0.4165+BIT))-2.713164382
       CO(2)=(DETA*(1.0-ETAF))**0.133640497*EXP(0.089751805)
       CO(3)=(DETA*(1.0-ETAF)+1.0)**(-4.237370618)
     & *EXP(-0.953803219)
       BEGIN=THICK**2.0*EXP(CO(1))-CO(2)
       PRODUCT=BEGIN*((THICK/RANGE)**0.022746964)*EXP(CO(3))
       GO TO 80
   20  CO(1)=-3.29457620*LOG(EO-EC*(0.4165+BIT))-3.332989881
       CO(2)=(DETA*(1.0+ETAS))**0.110122169*EXP(-0.062321491)
       CO(3)=(DETA*(1.0+ETAS)+1.0)**(-3.253062862)
     & *EXP(-0.804942195)
       CO(4)=CO(3)-0.09081404
       BEGIN=THICK**2.0*EXP(CO(1))-CO(2)
       IF((THICK/RANGE).LE.(0.1)) GO TO 60
       PRODUCT=BEGIN*(THICK/RANGE)**0.020493884*EXP(CO(3))
       GO TO 80
   60  PRODUCT=BEGIN*(THICK/RANGE)**(-0.020493884)*EXP(CO(4))
   80  RINT=PRODUCT*THICK/(1.0+PRODUCT)
       SLOPE=RINT/BEGIN
       IF(SLOPE.GT.(0.0)) GO TO 187
       PRODUCT=1.0E-06-1.0
       RINT=PRODUCT*THICK/(1.0+PRODUCT)
       SLOPE=RINT/BEGIN
C      WRITE(8,*) EO,EC,ZF,ZS
C      WRITE(8,*) DETA,RANGE,THICK,NUM2
C      WRITE(8,*) CO(1),CO(2),CO(3),CO(4)
C      WRITE(8,*) BEGIN,PRODUCT,RINT,SLOPE
  187  IF(ZF.GT.ZS) GO TO 12
       DO 10 J=1,NUM2
       R2(J)=1.0+((F1(J)-RINT)/SLOPE)**IEIGHT
       IF((F1(J)-RINT).LT.(0.0)) R2(J)=1.0
       CF(J)=B9(J)*R2(J)
   10  CONTINUE
       GO TO 13
   12  DO 14 J=1,NUM2
```

```
      R2(J)=1.0-((F1(J)-RINT)/SLOPE)**IEIGHT
      IF((F1(J)-RINT).LT.(0.0)) R2(J)=1.0
      CF(J)=B9(J)*R2(J)
   14 CONTINUE
   13 AREAB=0.0
      AREACF=0.0
      DO 250 L=1,NUM2
      AB2(L)=B2(L)*EXP(-RMAC*B1(L)*CSC)
      ACF(L)=CF(L)*EXP(-RMAC*F1(L)*CSC)
C     WRITE(7,*) L,B1(L),B2(L),AB2(L)
C     WRITE(6,*) L,F1(L),CF(L),ACF(L)
  250 CONTINUE
      DO 110 K=2,NUM2
      AREAB=AREAB+(AB2(K)+AB2(K-1))*(B1(K)-B1(K-1))*0.5
      AREACF=AREACF+(ACF(K)+ACF(K-1))*(F1(K)-F1(K-1))*0.5
C     WRITE(8,*) K-1,K,AREACF,AREAB
  110 CONTINUE
      RATCK=AREACF/AREAB
C     WRITE(8,*) RMAC,CSC
C     WRITE(8,*) AREACF,AREAB,RATCK
C     WRITE(2,*) RATCK
      WRITE(3,*) THICK/0.1050,RATCK
C     WRITE(3,*) THICK,RATCK
  991 CONTINUE
C     CLOSE(UNIT=8)
C     CLOSE(UNIT=7)
C     CLOSE(UNIT=6)
C     CLOSE(UNIT=5)
      STOP
      END
```

APPENDIX 8

FORTRAN PROGRAM TO CALCULATE UNKNOWN FILM THICKNESS FROM THE K-RATIO

```
ccccccccccccccccccccccccccccccccccccccccccccccccccccccccccccccccccccccccccc
c
c This program calculates an unknown film thickness from a given measured k-ratio.
c The computation generates a first estimate of the film thickness and then starts an
c iterative process to calculate the final true film thickness. The criterion of when the
c iterative process can be terminated is based on comparing how close the calculated
c k-ratio is to the measured k-ratio. The program requires some user input values
c which include:
c       EO = Incident electron energy
c       EC = Critical excitation potential of the x-ray line of interest
c       XZ = Film atomic number
c        A = Film atomic weight
c     RATK = Measured k-ratio
c      SXZ= Substrate atomic number
c     NUM2= Number of equal intervals to carry out the integration for a chosen ϕ(ρz)
c           curve
c     RMAC= Mass absorption coefficient
c      ANG= X-ray take off angle in degrees
c
c The 'DIMENSION' arrays that are used in this program include:-
c B1, B2  refer to the (ρz, ϕ(ρz)) values for the entire bulk ϕ(ρz) curve for the film
c         material
c F1, B9  refer to the (ρz, ϕ(ρz)) values for the bulk ϕ(ρz) curve only up to the
c         estimated film thickness
c     CO  refers to the constants related to c1, c2, c3, m1 and c4 for low Z film on
c         high Z substrate and vice versa (equations were shown in Appendix 4)
c     R2  refers to the ratio required to convert the corresponding bulk ϕ(ρz) curve to
c         film ϕ(ρz) curve at an estimated film thickness.
c     CF  refers to the calculated film ϕ(ρz) values based on an estimated film
c         thickness
c    AB2  refers to the bulk ϕ(ρz) values after correction for absorption
c    ACF  refers to the film ϕ(ρz) values after correction for absorption based on an
c         estimated film thickness
c
```

```
c
c Based on the input values, the program calculates the following:-
c     CSC:  cosecant of the x-ray take off angle
c       U:  overvoltage ratio
c     BSF:  bulk backscatter coefficient from Love, Cox and Scott for the film material
c    SBSF:  bulk backscatter coefficient from Love, Cox and Scott for the substrate
c           material
c    PHIO:  bulk φ(o) value from Love, Cox and Scott for the film material
c     ALP:  parameters in calculating bulk φ(ρz) curve for the film material using
c     BET:  Brown and Packwood expression for α, β and γ0
c     GAM:
c   STEPB:  the width of each interval for the entire bulk φ(ρz) curve depending on
c           NUM2
c   STEPF:  the width of each interval for bulk φ(ρz) curve only up to the estimated
c           film thickness
c  B1, B2:  data points for the entire bulk φ(ρz) curve governed by STEPB
c           (see DO 280 LOOP)
c  F1, B9:  data points for the bulk φ(ρz) curve only up to the estimated film thickness
c           of interest governed by STEPF (see DO 180 LOOP)
c      CO:  depending on whether the situation is low Z film on high Z substrate or
c           high Z film on low Z substrate, then apply the appropriate equations from
c           Appendix 4 to calculate c1, c2, c3, m1 and c4 for the value of 'Ratio'
c      R2:  the ratio required to convert the corresponding bulk φ(ρz) curve to film
c           φ(ρz) curve at an estimated film thickness
c      CF:  film φ(ρz) values based on estimated film thickness
c     AB2:  bulk φ(ρz) values after correction for absorption (see DO 250 LOOP)
c     ACF:  film φ(ρz) values after correction for absorption  (see DO 250 LOOP)
c  AREAB:  integration of bulk φ(ρz) curve after correction for absorption (see DO
c           110 LOOP)
cAREACF:  integration of film φ(ρz) curve after correction for absorption (see DO
c           110 LOOP)
c  RATCK:  Calculated film k-ratio.  Subsequant estimates on the film thickness was
c           done through the DO 340 LOOP
c
cccccccccccccccccccccccccccccccccccccccccccccccccccccccccccccccccccccccccccc
```

```
      PROGRAM ERR10
      REAL IU
      DIMENSION B1(300),B2(300),AB2(300),F1(300)
      DIMENSION ACF(300),B9(300)
      DIMENSION CO(10),R2(300),CF(300)
      OPEN(2,FILE='CON')
C     OPEN(UNIT=5,FILE='NNN103.DAT')
C     OPEN(UNIT=6,FILE='TRR303.DAT')
C     OPEN(UNIT=7,FILE='TRR203.DAT')
C     OPEN(UNIT=8,FILE='TRR103.DAT')
      WRITE(2,*)'INPUT EO,EC,BULK ATM# ,ATM WT,K RATIO,SUBATM#'
      READ(2,*) EO,EC,XZ,A,RATK,SXZ
      WRITE(2,*)'INPUT NUM2,RMAC,ANG'
      READ(2,*) NUM2,RMAC,ANG
      IEIGHT=8
      RMAC=RMAC*1.0E-06
      CSC=1.0/SIN(ANG*3.141592654/180.0)
      BSF=0.0
      BSF30=0.0
      ETA=-52.3791+XZ*(150.48371+XZ*(-1.67373+0.00716*XZ))
      ETA=ETA/10000.
      GETA=(-1112.8+30.289*XZ-0.15498*XZ*XZ)/10000.0
      BSF=ETA*(1.0+GETA*LOG(EO/20.0))
      BSF30=ETA*(1.0+GETA*LOG(30.0/20.0))
      SBSF=0.0
      SBSF30=0.0
      ETA=-52.3791+SXZ*(150.48371+SXZ*(-1.67373+0.00716*SXZ))
      ETA=ETA/10000.
      GETA=(-1112.8+30.289*SXZ-0.15498*SXZ*SXZ)/10000.0
      SBSF=ETA*(1.0+GETA*LOG(EO/20.0))
      SBSF30=ETA*(1.0+GETA*LOG(30.0/20.0))
      U=EO/EC
      GU=-0.59299+21.55329/U-30.55248/U/U+9.59218/U/U/U
      IU=3.43378-10.7872/U+10.97628/U/U-3.62286/U/U/U
      PHIO=1.0+(BSF/(1.0+BSF))*(IU+GU*LOG(1.0+BSF))
      GAM=5.0*3.141592654*U/(U-1.0)/LOG(U)*(LOG(U)-5.0+5.0
     &*U**(-0.2))
      BSJ=XZ*(9.76+58.82*XZ**(-1.19))*1.0E-03
      ALP=0.395*XZ**0.95/A/(EO**1.25)*(LOG(1.166*EO/BSJ)/
     &(EO-EC))**0.5
      BET=0.4*ALP*XZ**0.6
C     WRITE(8,*) BSF,BSF30,SBSF,SBSF30
C     WRITE(8,*) BSF,PHIO,BSJ
C     WRITE(8,*) ALP,BET,GAM
      B1(1)=0.0
      F1(1)=0.0
      B2(1)=PHIO
      B9(1)=PHIO
      I=0
   50 I=I+1
      B1(I+1)=B1(I)+EO
      B2(I+1)=GAM*(1.0-((GAM-PHIO)/GAM)*EXP(-BET*B1(I+1)))
     &*EXP(-(ALP**2.0)*(B1(I+1))**2.0)
      DUM=5.0E-03*(1.0+(EC/EO)**1.0)*(1.0-(XZ/100.0)**2.0)
      IF((B2(I+1)).LE.(DUM)) GO TO 160
      GO TO 50
  160 STEPB=B1(I)/(NUM2-1)
      XRANGE=B1(I)
C     STEPF=THICK/(NUM2-1)
C     WRITE(8,*) XRANGE,THICK
      NUM3=NUM2-1
      DO 280 J=1,NUM3
```

```
      B1(J+1)=STEPB*J
      B2(J+1)=GAM*(1.0-((GAM-PHIO)/GAM)*EXP(-BET*B1(J+1)))
     &*EXP(-(ALP**2.0)*(B1(J+1))**2.0)
  280 CONTINUE
      THICK=XRANGE*RATK
      LL=0
  340 LL=LL+1
      STEPF=THICK/NUM3
      DO 180 J=1,NUM3
      F1(J+1)=STEPF*J
      B9(J+1)=GAM*(1.0-((GAM-PHIO)/GAM)*EXP(-BET*F1(J+1)))
     &*EXP(-(ALP**2.0)*(F1(J+1))**2.0)
 180  CONTINUE
C     DO 90 K=1,NUM2
C     WRITE(5,*) B1(K),B2(K),F1(K),B9(K)
C 90  CONTINUE
       RANGE=XRANGE
       ETAF=BSF30
       ETAS=SBSF30
       DETA=ABS(ETAF-ETAS)
       FETAS=ETAF-ETAS
       ZF=XZ
       ZS=SXZ
       BIT=(1.0+((EC/EO)**1.0)*(1.0+FETAS/DETA)**1.0E-09)
     & *0.0835*FETAS/DETA
       IF(ZF.GT.ZS) GO TO 20
       CO(1)=-3.505041801*LOG(EO-EC*(0.4165+BIT))-2.713164382
       CO(2)=(DETA*(1.0-ETAF))**0.133640497*EXP(0.089751805)
       CO(3)=(DETA*(1.0-ETAF)+1.0)**(-4.237370618)
     & *EXP(-0.953803219)
       BEGIN=THICK**2.0*EXP(CO(1))-CO(2)
       PRODUCT=BEGIN*((THICK/RANGE)**0.022746964)*EXP(CO(3))
       GO TO 80
   20  CO(1)=-3.29457620*LOG(EO-EC*(0.4165+BIT))-3.332989881
       CO(2)=(DETA*(1.0+ETAS))**0.110122169*EXP(-0.062321491)
       CO(3)=(DETA*(1.0+ETAS)+1.0)**(-3.253062862)
     & *EXP(-0.804942195)
       CO(4)=CO(3)-0.09081404
       BEGIN=THICK**2.0*EXP(CO(1))-CO(2)
       IF((THICK/RANGE).LE.(0.1)) GO TO 60
       PRODUCT=BEGIN*(THICK/RANGE)**0.020493884*EXP(CO(3))
       GO TO 80
   60  PRODUCT=BEGIN*(THICK/RANGE)**(-0.020493884)*EXP(CO(4))
   80  RINT=PRODUCT*THICK/(1.0+PRODUCT)
       SLOPE=RINT/BEGIN
C      WRITE(8,*) EO,EC,ZF,ZS
C      WRITE(8,*) DETA,RANGE,THICK,NUM2
C      WRITE(8,*) CO(1),CO(2),CO(3),CO(4)
C      WRITE(8,*) BEGIN,PRODUCT,RINT,SLOPE
       IF(ZF.GT.ZS) GO TO 12
       DO 10 J=1,NUM2
       R2(J)=1.0+((F1(J)-RINT)/SLOPE)**IEIGHT
       IF((F1(J)-RINT).LT.(0.0)) R2(J)=1.0
       CF(J)=B9(J)*R2(J)
   10  CONTINUE
       GO TO 13
   12  DO 14 J=1,NUM2
       R2(J)=1.0-((F1(J)-RINT)/SLOPE)**IEIGHT
       IF((F1(J)-RINT).LT.(0.0)) R2(J)=1.0
       CF(J)=B9(J)*R2(J)
   14  CONTINUE
   13  AREAB=0.0
       AREACF=0.0
       DO 250 L=1,NUM2
```

```
      AB2(L)=B2(L)*EXP(-RMAC*B1(L)*CSC)
      ACF(L)=CF(L)*EXP(-RMAC*F1(L)*CSC)
C     WRITE(7,*) L,B1(L),B2(L),AB2(L)
C     WRITE(6,*) L,F1(L),CF(L),ACF(L)
 250  CONTINUE
      DO 110 K=2,NUM2
      AREAB=AREAB+(AB2(K)+AB2(K-1))*(B1(K)-B1(K-1))*0.5
      AREACF=AREACF+(ACF(K)+ACF(K-1))*(F1(K)-F1(K-1))*0.5
C     WRITE(8,*) K-1,K,AREACF,AREAB
 110  CONTINUE
      RATCK=AREACF/AREAB
C     WRITE(8,*) RMAC,CSC
C     WRITE(8,*) AREACF,AREAB,RATCK
      WRITE(2,*) LL,THICK,RATCK
      IF((ABS(RATCK-RATK)).LE.(0.0001)) GO TO 190
      THICK=THICK*RATK/RATCK
      GO TO 340
C     CLOSE(UNIT=8)
C     CLOSE(UNIT=7)
C     CLOSE(UNIT=6)
C     CLOSE(UNIT=5)
 190  STOP
      END
```

REFERENCES

[1] Packwood, R.H. and Brown, J.D. (1981) X-ray Spectr. 10, p. 138-146.

[2] Karduck, P., Ammann, N. and Rehbach, W.P. (1990) Microbeam Analysis (San Francisco Press), p. 21-31.

[3] Ding, Z.J. and Wu, Z. (1994) J. Phys. D: 27(2), p. 387-392.

[4] Henoc, J. and Maurice, F. (1991) in Electron Probe Quantitation (Plenum, New York) edited by Heinrich, K.F.J. and Newbury, D.E., P. 105-143.

[5] Heinrich, K.F.J. (1981) Electron Probe Microanalysis (Van Nostrand, New York).

[6] Scott, V.D. and Love, G. (1983) Quantitative Electron Probe Microanalysis (Ellis Horwood Limited, Chichester).

[7] Heinrich, K.F.J. and D.E. Newbury, eds. (1991) Electron Probe Quantitation (Plenum, New York).

[8] Reed, S.J.B. (1993) Electron Microprobe Analysis (Cambridge University Press).

[9] Scott, V.D., Love, G. and Reed, S.J.B. (1995) in Quantitative Electron-Probe Microanalysis, 2nd edition, Ellis Horwood Series in Physics and Its Applications.

[10] Wittry, D.B. and Sun, S. (1990) J. Appl. Phys. 67, p. 1633.

[11] Wittry, D.B. and Sun, S. (1990) J. Appl. Phys. 68, p. 387.

[12] Wittry, D.B. and Sun, S. (1991) J. Appl. Phys. 69, p. 3886.

[13] Bastin, G.F. and Heijligers, H.J.M. (1986) X-ray Spectr. 15, p. 135.

[14] Castaing and Deschamps (1955) J. Physique et le Radium 16, p. 304-317.

[15] Brown, J.D. and Parobek, L. in 6th ICXOM (Osaka, 1971) edited by G. Shinoda, K. Kohra and T. Ichinokawa, University of Tokyo Press, Tokyo, p. 163 (1972).

[16] Karduck, P. and Rehbach, W. in ref. [7], p. 203.

[17] Castaing, R. and Henoc, J. (1966) in 4th ICXOM (Orsay, 1965) edited by R. Castaing, P. Deschamps and J. Philibert, Hermann, Paris, p. 120.

[18] Shimizu, R., Murata, K. and Shinoda, G. in ref. [17], p. 127.

[19] Sewell, D.A., Love, G. and Scott, V.D. (1985) J. Phys. D18, p. 1233.

[20] Brown, J.D. Adv. Electron. Electron Phys. Suppl. 6, 45 (1969).

[21] Brown, J.D. and Parobek, L. Adv. X-ray Anal. 16, p. 198 (1973).

[22] Brown, J.D. and Parobek, L. X-ray Spectrom. 5, p. 36 (1976).

[23] Parobek, L. and Brown, J.D. X-ray Spectrom. 7, p. 26 (1978).

[24] Karduck, P. and Rehbach, W. in Microbeam Analysis 1988, edited by D.E. Newbury, p. 277. San Francisco Press, San Francisco (1988).

[25] Rehbach, W. and Karduck, P. in 11th ICXOM (London, Ontario, 1986) edited by J.D. Brown and R.H. Packwood, p. 244, London, Ont. (1987).

[26] Rehbach, W. and Karduck, P. in ref. [24], p. 285.

[27] Heinrich, K.F.J. in ref. [5], p. 265.

[28] Brown, J.D. in Electron beam interactions with solids, p. 139 (1982) SEM, Inc., AMF O'Hare (Chicago), IL 60666, U.S.A.

[29] Scott, V.D. and Love, G. in ref. [6], p. 175.

[30] Karduck, P. and Rehbach, W. in ref. [7], p. 194.

[31] Scott, V.D., Love, G. and Reed, S.J.B. (1995) in ref. [9], p. 128.

[32] Sewell, D.A., Love, G. and Scott, V.D. (1987) J. Phys. D: Appl. Phys. 20, p. 1567-1573.

[33] Packwood, R., Parker, C. and Moore, V.E. in ref. [24], p. 258.

[34] Pouchou, J.L., Pichoir, F. and Boivin, D. (1990) in ICXOM 12th (Cracow), p. 52-59, 1989.

[35] Castaing, R. (1951), Ph.D. thesis, University of Paris, Paris.

[36] Philibert, J. (1963) in 3rd ICXOM, Ed. H.H. Pattee, V.E. Cosslett, A. Engstrom, Academic Press, New York (1963), p. 379-393.

[37] Heinrich, K.F.J. in ref. [5], p. 271.

[38] Scott, V.D., Love, G. and Reed, S.J.B. (1995) in ref. [9], p. 123.

[39] Duncumb, P. and Shields, P.K. (1966) in the Electron Microprobe edited by T.D. Mckinley, K.F.J. Heinrich and D.B. Wittry, Wiley, New York, p. 284.

[40] Duncumb, P., Shields, P.K. and Casas, C-da (1969) in X-ray optics and microanalysis (Eds. G. Mollenstedt, K.H. Gaukler) Springer Verlag Berlin, p. 146.

[41] Love, G., Cox, M.G.C. and Scott, V.D., J. Phys. D8, p. 1686 (1975).

[42] Scott, V.D. and Love, G. in ref. [7], p. 19-30.

[43] Thomas, P.M. (1963), Brit. J. Appl. Phys., 14, p. 397.

[44] Bishop, H.E. (1968), J. Phys. D: Appl. Phys. 1, p. 673.

[45] Duncumb, P. and Reed, S.J.B. (1968) NBS Spec. Publ. 298 (Washington: U.S. Dept. Commerce), p. 133-154.

[46] Springer, G. (1966), Mikrochim. Acta, 3, p. 587.

[47] Love, G., Cox, M.G.C. and Scott, V.D. (1977) J. Phys. D: Appl. Phys., 10, p.7.

[48] Philibert, J. and Tixier, R. (1968) in ref. [45], p. 13-34.

[49] Love, G., Cox, M.G.C. and Scott, V.D. (1978) J. Phys. D: Appl. Phys. 11, p. 7-22.

[50] Pouchou, J.L. and Pichoir, F. in ref. [7], p. 31.

[51] Castaing, R. (1960) Advances in Electronics and Electron Physics, vol. 113, ed. L.L. Marton, p. 317-386.

[52] Reed, S.J.B. (1965) Brit. J. Appl. Phys. 16, p. 913-926.

[53] Reed, S.J.B. (1990) in ref. [2], p. 109-114.

[54] Armstrong, J.T. and Buseck, P.R. XRS 14: p. 172 (1985).

[55] Springer, G. (1967) Neues Jahrb Mineral Abhandl 106, p. 241-256.

[56] Henoc, J. (1968) in ref. [45], p. 197-214.

[57] Springer, G. and Rosner, B. (1969) X-ray optics and microanalysis (Eds. G. Mollenstedt, K.H. Gaukler) Springer Verlag Berlin, p. 170-174.

[58] Lenard, P. (1895) Ann. Phys. Lpz. 56, p. 255.

[58a] Criss, J. and Birks, L.S. (1966) in ref. [39], p. 217-236.

[59] Bishop, H.E. (1974) J. Phys. D: Appl. Phys. 7, p. 2009-2020.

[60] Wittry, D.B. (1958) J. Appl. Phys. 29, p. 1543.

[61] Kyser, D. (1972) in ref. [15], p. 147-156.

[62] Tanuma, S. and Nagashima, K. (1983) Mikrochim Acta I, p. 299-313.

[63] Tanuma, S. and Nagashima, K. (1984) Mikrochim. Acta III, p. 265-274.

[64] Buchner, A.R. and Pitsch, W. (1971) Zeit für Metallkunde 62, p. 392-400.

[65] Buchner, A.R. and Pitsch, W. (1972) Z. metallkde, 63, p. 398.

[66] Buchner, A.R. and Stienen, J.P.M. (1975) Microchim. Acta Supp. 6, p. 227.

[67] Buchner, A.R. (1987) in ref. [25], p. 262-264.

[68] Brown, J.D. and Robinson, W.H. (1979) Microbeam Analysis, p. 238.

[69] Brown, J.D. and Packwood, R.H. (1982) X-ray Spectr. 11, p. 187.

[70] Bastin, G., Van Loo, J. and Heijligers, H. (1984) X-ray Spectr. 13, p. 91-97.

[71] Bastin, G., Heijligers, H. and Van Loo, J. (1986) Scanning 8, p. 45-67.

[72] Tirira, J. and Riveros, J. (1987) X-ray Spectr. 16, p. 27.

[73] Tirira, J., Giogrio, M. del and Riveros, J. (1987) X-ray Spectr. 16, p. 243.

[74] Giorgio, M. del, Trincavelli, J. and Riveros, J. (1990) X-ray Spectr. 19, p. 261.

[75] Pouchou, J.L. and Pichoir, F. in X-ray optics and microanalysis edited by Sevely, J., Maurice, F., Jouffrey, B. and Tixier, R. Editions de Physique, Paris (1984) p. 47-50.

[76] Pouchou, J.L. and Pichoir, F. La Recherche Aerospatiale Partie I, p. 167-191 (1984).

[77] Pouchou, J.L. and Pichoir, F. in ref. [25], p. 249.

[78] Pouchou, J.L. and Pichoir, F.M.A. in ref. [24], p. 315-318.

[79] Love, G., Sewell, D.A. and Scott, V.D. in ref. [75], p. 21-25.

[80] Sewell, D.A., Love, G. and Scott, V.D. in ref. [19], p. 1244-1268.

[81] Gaber, M. (1992) X-ray Spectr. 21, p. 215-221.

[82] Merlet, C. (1992) 13th ICXOM, Manchester 1991, p. 123-127.

[83] August, H.J. and Wernisch, J. (1991) X-ray Spectr. 21, p. 131-140.

[84] August, H.J. and Wernisch, J. (1991) in ref. [83], p. 141-148.

[85] Scott, V.D. and Love, G. (1990) Scanning 12, p. 193-202.

[86] Riveros, J. and Castellano, G. (1993) X-ray Spectr. 22, p.3-10

[87] Scott, V.D., Love, G. and Reed, S.J.B. (1995) in ref. [9], p. 170.

[88] Green, M. (1963) Proc. Phys. Soc. 82, p. 204.

[89] Bishop, H.E. (1966) Ph.D. thesis, University of Cambridge.

[90] NBS Spec. Publ. 460 (Washington: U.S. Dept. Commerce) edited by K.F.J. Heinrich, D.E. Newbury and H. Yakowitz (1976).

[91] Joy, D.C. (1995) Monte Carlo Modeling for Electron Microscopy and Microanalysis (Oxford University Press, New York).

[92] Bethe, H.A. Ann. Phys. (Leipzig) 5, p. 325 (1930)

[93] Berger, M.J. and Seltzer, S.M. (1964), Nat. Res. Council Publ. 1133 (Washington: Nat. Acad. Sciences), p. 205.

[94] Reimer, L. (1985) Scanning Electron Microscopy vol. 45 (Springer-Verlag, Berlin) p. 57.

[95] Scott, V.D., Love, G. and Reed, S.J.B. (1995) in ref. [9], p. 216.

[96] Goudsmit, S. and Saunderson, J.L. (1940) Phys. Rev. 57, p. 24.

[97] Powell, C.J. (1990) in Microbeam Analysis 1990, p. 13.

[98] Rez, P. (1984) X-ray Spectr. 13, p. 55-59.

[99] Tung, C.J., Ashley, J.C. and Ritchie, R.H. (1979), 26, p. 4874-4878.

[100] Landau, L. (1944) J. Phys. USSR, 8, p. 201-205.

[101] Merlet, C. (1992) x-ray Spectr. 21, p. 229-238.

[102] Werner, U. and Heydenreich, J. (1984) Ultramicroscopy, 15, p. 17-28.

[103] Mott, N.F. (1929) Proc. R. Soc. A124, p. 425-442.

[104] Kotera, M., Murata, J. and Nagami, J. (1981) J. Appl. Phys. 52, p. 997-1003.

[105] Kotera, M., Murata, J. and Nagami, J. (1981) J. Appl. Phys. 52, p. 7403-7408.

[106] Reimer, L. and Lodding, R. (1984) Scanning 6, p. 128-151.

[107] Reimer, L. and Stelter, D. (1986) Scanning 8, p. 265-277.

[108] Czyzewski, Z., Maccallum, Do., Romig, A. and Joy, D.C. (1990) J. Appl. Phys. 68, p. 3066-3072.

[109] Drouin, D., Gauvin, R. and Joy, D.C. (1994) Scanning 16, p. 67-77.

[110] Murata, K., Kotera, M. and Kawata, H. (1989) 12th ICXOM, Cracow, p. 163-168.

[111] Murata, K., Kotera, M. and Nagami, K. (1983) J. Appl. Phys. 54, p. 1110-1114.

[112] Ding, Z.J. and Wu, Z. (1993) Phys. D: Appl. Phys. 26, p. 507-516.

[113] Murata, K., Kotera, M. and Nagami, K. (1983) J. Appl. Phys. 54, p. 1110-1114.

[114] Nassiopoulou, A.G. and Valamontes, E. (1988) EUREM 88, York, England in Inst. Phys. Conf. Ser. No. 93, Vol. 2, Ch. 4, p. 157-158.

[115] Butz, R. and Wagner, H. (1970) Phys. Stat. Sol. (a) 3, p. 325-331.

[116] Butz, R. and Wagner, H. (1973) Surf. Sci. 34, p. 693-704.

[117] Wendt, M., Krajewski, T. and Bimberg, R. (1976) Phys. Stat. Sol. (a) 36, p. 253-261.

[118] Brown, J.D. (1983) Spectrochim. Acta 38B, p. 1411.

[119] Brown, J.D. (1988) Microbeam Analysis 1988, p. 271-272.

[120] Murata, K. and Sugiyama, K. (1989) J. Appl. Phys. 66, p. 4456-4461.

[121] Hasegawa, S., Daimon, H. and Ino, S. (1987) Surf. Sci. 186, p. 138.

[122] Pouchou, J.L. and Pichoir, F. (1990) Scanning 12, p. 212-224.

[123] Scott, V.D., Love, G. and Reed, S.J.B. (1995) in ref. [9], p. 105.

[124] Bastin, G.F. and Heijligers, H.J.M. (1988) Microbeam Analysis, p. 325-328.

[125] Sweeny, W.E., Seebold, E.E. and Birks, L.S. (1960) J. Appl. Phys. 31, p. 1061-1064.

[126] Cockett, G.H. and Davis, C.D. (1963) Br. J. Appl. Phys. 14, p. 813-816.

[127] Marshall, D.J. and Hall, T.A. (1966) in ref. [17], p. 374-381.

[128] Marshall, D.J. and Hall, T.A. (1968) J. Phys. D, 1, p. 1651-1656.

[129] Philibert, J. and Penot, D. (1966) in ref. [17], p. 365-373.

[130] Philibert, J. and Tixier, R. (1968) J. Phys. D., 2, p. 685-694.

[131] Colby, J.W. (1968) Adv. X-ray Anal., 11, p. 287-305.

[132] Djuric, B. and Cerovic, D. (1969) 5th ICXOM, Springer, Berlin, p. 99-103.

[133] Reuter, W. (1972) 6th ICXOM, Tokyo, p. 121-130.

[134] Reuter, W., Kuptsis, J.D., Lurio, A. and Kyser, D.F. (1975) J. Phys. D: Appl. Phys., Vol. 11, p. 2633-2642.

[135] Bishop, H.E. and Poole, D.M. (1973) J. Phys. D: Appl. Phys., 6, p. 1142-1158.

[136] Bishop, H.E. and Poole, D.M. (1992) 13th ICXOM, Manchester, p. 135-137.

[137] Bolon, R.B. and Lifshin, E. (1973) Proc. VIth Annual SEM Symposium, ed. by O. Johari and I. Corvin, p. 385, Illinois Research Institute.

[138] Hutchins, G.A. in Characterization of Solid Surfaces (1974), ed. by Kane, P.F. and Larrabee, G.B. Plenum Press, New York, p. 469.

[139] Kyser, D.F. and Murata, K. (1974) IBM J. Res. Dev. 18, p. 352-363.

[140] Yakowitz, H., Newbury, D.E. (1976) SEM I, IITRI, Chicago, p. 151-162.

[141] Duzevic, D. and Bonefacic, A. (1978) X-ray Spectrom., 7, p. 152-155.

[142] Cvikevich, S. and Pihl, C. (1979) Microbeam Analysis, p. 39-42.

[143] Hunger, H.J. and Kuchler, L. (1979) Phys. Stat. Sol. (a), 56, K45-K48.

[144] Murata, K., Cvikevich, S. and Kuptsis, J.D. (1984) J. de Physique, Colloque, 45, C-2, p. 13-16.

[145] Sewell, D.A., Hall, I.D., Love, G., Partridge, J.P. and Scott, V.D. (1984) J. de Physique Colloq. 45, C-2, p. 33-36.

[146] Packwood, R.H. and Milliken, K.S. (1985) CANMET-Report PMRL 85-25(TR).

[147] Packwood, R.H. (1986) Microbeam Analysis, p. 268-270.

[148] Packwood, R., Remond, G. and Brown, J.D. (1987) 11th ICXOM, London, Canada, p. 274.

[149] Packwood, R.H., Remond, G. and Holloway, P.H. (1988) Surf. Interf. Anal., 11, p. 127.

[150] Willich, P., Obertop, D. and Tolle, H.J. (1985) X-ray Spectrom. 14, p. 84-88.

[151] Willich, P. (1986) 11th ICXOM, London, Canada, p. 238-243.

[152] Willich, P. and Obertop, D. (1988), Surface Interface Analysis, 13, p. 20-24.

[153] Willich, P. and Obertop, D. (1989) J. de Physique, Colloque C-5, p. 285-294.

[154] Willich, P. and Schiffmann, K. (1990) Proc. 12th Int. Cong. for Electron Microscopy, p. 226-227.

[155] Willich, P. (1992) Mikrochim. Acta (Suppl.) 12, p. 1-17.

[156] Churms, C.L. and Kritzinger, S. (1986) Proc. 11th Int. Cong. on Electron Microscopy, Kyoto, p. 607-608.

[157] Brown, J.D. (1986) Applied Surface Science, Vol. 26, p. 294-305.

[158] August, H.J. (1987) Scanning 9, p. 145-155.

[159] August, H.J. (1991) Scanning 13, p. 393-403.

[160] August, H.J. (1992) Mikrochim. Acta (Suppl.), 12, p. 131-137.

[161] Hunger, H.J. (1988) Scanning 10, p. 65-72.

[162] Waldo, R.A. (1988) Microbeam Analysis, p. 310-314.

[163] Gillies, A.D., Fitzgerald, A.G. and Watton, H.L.L. (1989) EMAG-MICRO89, London in Inst. Phys. Conf. Ser. No. 98, Chap. 7, p. 319-322.

[164] Cazaux, J., Jbara, O. and Thomas, X. (1990) Surf. Interf. Anal., Vol. 15, p. 567-581.

[165] Fitzgerald, A.G., Gillies, A.D. and Watton, H.L.L. (1990) Surf. Interf. Anal., Vol. 16, p. 163-167.

[166] Fitzgerald, A.G. (1993) Journal of Microscopy, Vol. 170, Pt. 2, p. 97-110.

[167] Fitzgerald, A.G., Gillies, A.D. and Ploessi, A. (1993) EMAG93, Liverpool in Inst. Phys. Conf. Ser. No. 138, Section 2, p. 103-106.

[168] Bastin, G.F., Heijligers, H.J.M. and Dijkstra, J.M. (1990) Microbeam Analysis, p. 159.

[169] Bastin, G.F., Heijligers, H.J.M. and Dijkstra, J.M. (1990) in Proc. XII Int. Cong. for Electron Microscopy, San Francisco Press, San Francisco, p. 216-217.

[170] Bastin, G.F., Dijkstra, J.M., Heijligers, H.J.M. and Klepper, D. (1992) Mikrochim. Acta (Suppl.) 12, p. 93-97.

[171] Karduck, P. and Ammann, N. (1990) Proceedings of the 12th Int. Cong. for Electron Microscopy, p. 14-15.

[172] Ammann, N. and Karduck, P. (1990) Proceedings of the 12th Int. Cong. for Electron Microscopy, p. 214-215.

[173] Ammann, N. and Karduck, P. (1990) Microbeam Analysis, p. 150.

[174] Wernisch, J. (1992) Int. Summer School on Diagnostics and Applications of Thin Films, Czechoslovakia, 1991 (Bristol: Institute of Physics), p. 21-45.

[175] Laurie, K.G., Love, G. and Scott, V.D. (1992) ICXOM 13th, Manchester, p. 153-156.

[176] Scott, V.D. and Love, G. (1992) X-ray Spectrom., 21, p. 27-35.

[177] Mackenzie, A.P. (1993) Rep. Prog. Phys. 56, p. 557-604.

[178] Scott, V.D., Love, G. and Reed, S.J.B. (1995) in ref. [9], p. 234.

[179] Heinrich, K.F.J. (1981), see ref. [5], p. 244.

[180] Heinrich, K.F.J. (1981), see ref. [5], p. 245.

[181] Packwood, R.H., Moore, V. and Thomas, S. (1989) Microbeam Analysis, p. 211-215.

[182] Heinrich, K.F.J. (1986) 11th ICXOM, p. 67-119.

[183] Henke, B.L., Gullikson, E.M. and Davis, J.C. (1993), Atom Data Nuclear Data Tables, 54, p. 181.

[184] Sevov, S., Degischer, H.P., August, H.J. and Wernisch, J. (1989) Scanning 11, p. 123-134.

[185] Pouchou, J.L. and Pichoir, F. in ref. [7], p. 63.

[186] Cox, M.G.C., Love, G. and Scott, V.D. (1979) J. Phys. D. 12, p. 1441-1451.